SED

Student Experiment Description

Document ID: RX1314_MUSCAT_v5-0_9Aug13.pdf

Mission: REXUS 13/14

Team Name: MUSCAT

Experiment Title: **MU**ltiple **S**pheres for **C**haracterization of **A**tmospheric **T**emperatures

Team: Ólafía Lára Lárusdóttir
Darri Kristmundsson
Andreas Myleus
Emilio Lozano
Marco Tito Bordogna
Miguel Galrinho
Leo Fidjeland
Anders Haponen
Anton Hou
Benjamin Oakes
Marcus Lindh
Markus Fjällid
Marcus Lejon

Team Contact Address: Space and Plasma Physics
School of Electrical Engineering
Royal Institute of Technology (KTH)
SE-100 44 Stockholm
Sweden

Email: muscatexperiment@gmail.com

Website: www.muscatexperiment.se

Version:	Issue Date:	Document Type:	Valid from:
5.0	August 11, 2013	**Spec**	August 11, 2013

Issued by:
Ó.L. Lárusdóttir, D. Kristmundsson, A. Myleus, E. Lozano, M.T. Bordogna, M. Galrinho, L. Fidjeland, A. Haponen, A. Hou, B.D. Oakes, M. Lindh, M. Fjällid, M. Lejon

Approved by:
Nickolay Ivchenko and Gunnar Tibert.

Change Record

Version	Date	Changed chapters	Remarks
0.0	2012-01-4	New Version	Blank Book 2012
1.0	2012-02-16	All	Preliminary Design Review
2.0	2012-06-11	All	Critical Design Review
2.1	2012-06-15	All	Feedback before CDR
2.2	2012-06-18	File name and dates	Feedback before CDR
2.3	2012-07-19	Ch. 1, 2, 3, 4, 5 and 6 as well as appendix	Feedback after CDR
2.4	2012-08-03	Ch. 4 and 6 as well as appendix	
3.0	2012-09-23	Ch. 1, 2, 3, 4, 5, 6 as well as appendix	
4.0	2013-02-07	Ch. 3.1.1, 3.2.1, 4.3.1, 4.5.2.6, 6 as well as appendix	Feedback after EAR
4.1	2013-04-20	Ch. 6.1.1, 6.1.4, 6.2.12, 6.3 and 6.4	
5.0	2013-08-09	Ch. 3, 5, 6, 7	

Contents

Abstract

The scientific objective of MUSCAT is to develop a proof of concept of a technique to conduct high-resolution multiple point measurements of mesospheric and stratospheric temperatures and vertical wind profiles using active spherical probes. Furthermore the technological objective is to demonstrate multiple small deployable sub-payloads that are reliable, robust and easy to manufacture. As the experiment is designed as a standalone standard module only requiring power supply and ejection initiation from the rocket, it will provide means of adding middle atmospheric temperature- and wind profile measurements to any mesospheric rocket mission. Post flight analysis will be conducted to derive the temperature from GPS measurements and fundamental principles of fluid mechanics.

Preface

MUSCAT, MUltiple Spheres for Characterization of Atmospheric Temperatures is a sounding rocket experiment developed at the Division of Space and Plasma Physics at the School of Electrical Engineering and the Division of Solid Mechanics at the School of Engineering Sciences at The Royal Institute of Technology (KTH), together with the Department of Meteorology at Stockholm University (MISU).

MUSCAT will be launched from the Swedish Space Corporation's Esrange Space Centre in March 2013 as part of the REXUS/BEXUS. The REXUS/BEXUS programme is realised under a bilateral agency agreement between the German Aerospace Center (DLR) and the Swedish National Space Board (SNSB). The Swedish share of the payload has been made available to students from other European countries through a collaboration with the European Space Agency (ESA). EuroLaunch, a cooperation between the Esrange Space Center of the Swedish Space Corporation (SSC) and the Mobile Rocket Base (MORABA) of DLR, is responsible for the launch campaign management and operations of the launch vehicles.

Abbreviations

ADC	Analog to Digital Converter
CDR	Critical Design Review
COG	Centre Of Gravity
DSSS	Direct-sequence spread spectrum
ESA	European Space Agency
ESRANGE	European Sounding Rocket Launching Range
ESTEC	European Space Research and Technology Centre, ESA (Noordwijk, The Netherlands)
FFU	Free Falling Unit
FPGA	Field Programmable Gate Array
GPS	Global Positioning System
I/O	Input/Output
IF	Intermediate Frequency
IPR	Integration Progress Review
KTH	Kungliga Tekniska Högskolan
LO	Liftoff
MUSCAT	MUltiple Spheres for the Characterization of Atmospheric Temperatures
PCB	Printed Circuit Board
PDR	Preliminary Design Review
RAIN	Rocket deployed Atmospheric probes conducting Independent measurements in Northern Sweden
RF	Radio Frequency
RMU	Rocket Mounted Unit
RXSM	REXUS Service Module
SED	Student Experiment Documentation
SMHI	Swedish Meteorological and Hydrological Institute
SODS	Start of Data Storage
SOE	Start Of Experiment
SPP	Space and Plasma Physics
SQUID	Spinning QUad Ionospheric Deployer
SSC	Swedish Space Corporation
STX	Satellite Transmitter
SU	Stockholm Universitet
TBC	To Be Confirmed
TBD	To Be Determined
VHDL	Very High speed integrated Description Language
WBS	Work Breakdown Structure

Chapter 1

Introduction

1.1 Scientific Background

During the past two decades there has been considerable interest expressed in middle-atmosphere temperature measurements due to the influence of temperature on the motions and dynamics of the region, its interrelationship with chemical species and the electrical structure and in general the morphology of events occurring there. For any of those studies, atmospheric temperature is one of the main variables needed.

There are a few ways to obtain middle-atmospheric temperatures through passive methods, each with its advantages and disadvantages. The height resolution of satellites and LIDAR measurements is insufficient for regional atmospheric studies. LIDARs are often limited by both clouds and daylight as well as requiring long integration times, up to many hours, to be able to find temperatures; satellites only measure at very sparse vertical locations and they also need complicated retrieval techniques to derive the temperature. Other methods such as airplane and balloon measurements are limited by the altitude that they can reach (approximately up to 30 km). Therefore there is a strong need for precise *in-situ* measurements to verify retrieved temperatures from existing remote sensing techniques such as the ones mentioned above where the temperatures are derived from inversion techniques.

1.2 Experiment Objectives

Primary Objectives:

- Proof of concept of a multi-point deployable sub-payload for the derivation of temperature and density profiles in middle atmosphere;
- Acquisition of data with high accuracy and resolution;

Secondary Objectives:

- Derivation, using multi-point measurements, of the horizontal structure of temperature and density profiles;
- Using multi-point measurements to capture horizontal wind data at different altitudes;

- Demonstrate sub-payloads that are reliable, robust and easy to manufacture.

1.3 Experiment Overview

The experiment involves ejecting four spherical probes, or Free Falling Units (FFU), from a REXUS rocket module. The module, called a Rocket Mounted Unit (RMU), carries the FFUs to an altitude of approximately 60 km where they are ejected from the rocket at a spin of 4 Hz. The FFUs will then continue to a maximum altitude of roughly 90 km. Upon ejection, the FFUs start a data gathering phase, recording raw GPS data as they travel through the atmosphere.

At an altitude of 5 km the data gathering phase is complete and the FFUs deploy parachutes in order to slow them down and switch from raw GPS data gathering to recording and transmitting commercial GPS coordinates to the ground crew, which locates and retrieves them upon landing. The GPS data is then analysed to obtain information about the velocity and acceleration of the FFUs during the free fall. These data are used, along with the drag coefficent of the FFUs, to derive the atmospheric density and temperature profiles.

1.4 Team

1.4.1 Contact Point

Address	MUSCAT Team,Ólafía Lára Lárusdóttir Space and Plasma Physics School of Electrical Engineering Royal Institute of Technology (KTH) Teknikringen 31, Stockholm SE-10044 Sweden
Email	muscatexperiment@gmail.com
Website	www.muscatexperiment.se

1.4.2 Team members

Team Leader	**Ólafía Lára Lárusdóttir** (Iceland) MSc Electrical Engineering, Electrophyiscis KTH, Sweden (2nd year of 2) BSc Electrical Engineering, University of Iceland Project management, electrical design, verification, GPS data analysis and antenna design
Mechanical Team Leader	**Darri Kristmundsson** (Iceland) MSc Aerospace Engineering, KTH, Sweden (2nd year of 2) BSc Mechanical Engineering, University of Iceland Project management, documentation, mechanical design
Mechanical Team	**Andreas Myleus** (Sweden) MSc Aerospace Engineering, KTH, Sweden (2nd year of 2) BSc Mechatronics, KTH, Sweden

Outreach, software and landing system
Emilio Lozano (Spain)
MSc Aerospace Engineering, KTH, Sweden (2nd year of 2)
BSc Aircraft Engineering, Polytechnic University of Madrid, Sweden
Mechanical design, structural analysis, and manufacturing

Marco Tito Bordogna (Italy)
MSc Aerospace Engineering, KTH, Sweden (2nd year of 2)
BSc Aerospace Engineering, Politecnico di Milano, Italy
Mechanical design of FFU, manufacturing and scientific questions

Marcus Lejon (Sweden)
MSc Aerospace Engineering, KTH, Sweden (2nd year of 2)
BSc Aeronautical Engineering, Mälardalen University, Sweden
Descent analysis, drag estimation, thermal analysis
Member up until December 1st, 2012

Miguel Galrinho (Portugal)
Visiting student at KTH
MSc Aerospace Engineering, TU Delft
Manufacturing and test design
Member up until December 1st, 2012

Electrical Team

Benjamin Donald Oakes (Sweden, Australia)
MSc Electrical Engineering (Electrophysics), KTH, Sweden (2nd year of 2)
BSc Electrical Engineering, Örebro University, Sweden
Antenna design
Member up until June 1st, 2012

Anton Hou (Sweden)
Civ.Ing(BSc + MSc) Electrical Engineering, KTH, Sweden (4th year of 5)
Power supply system
Member up until June 1st, 2012

Anders Haponen (Sweden)
Civ.Ing(BSc + MSc) Electrical Engineering, KTH, Sweden (4th year of 5)
Power supply system
Member up until June 1st, 2012

Leo Fidjeland (Sweden)
Civ.Ing(BSc + MSc) Engineering Physics, KTH, Sweden (3rd year of 5)
GPS experiment, localisation, hardware programming and scientific questions
Member up until September 1st, 2012

Marcus Lindh (Sweden)
Civ.Ing(BSc + MSc) Electrical Engineering, KTH, Sweden (4th year of 5)
Design, manufacturing, programming and testing of Data acquisition system and RMU electrical system

Markus Fjällid (Sweden)

Civ.Ing(BSc + MSc) Electrical Engineering, KTH, Sweden (4th year of 5)
Design, manufacturing, programming and testing of Data acquisition system and RMU electrical system

Chapter 2

Experiment Requirements

2.1 Functional Requirements

The FFUs shall:

F1.1 record GPS signals in local memory after ejection from rocket until parachute deployment;

F1.2 switch to internal power upon ejection from the RMU;

F1.3 deploy a parachute upon receiving a signal from an internal pressure sensor;

F1.4 transmit their positions during the recovery phase;

F1.5 record data on acceleration, angular rate, temperature and pressure to a local memory.

F1.6 provide the capability to switch on or off all electrical components inside the FFU except for the logic circuits.

F1.7 provide the capability to be charged by using an umbilical connector.

The FFUs should:

F1.8 fall without tumbling.

The RMU shall:

F2.1 hold the FFUs inside the rocket prior to ejection;

F2.2 eject four FFUs;

F2.3 charge the FFUs batteries while the FFUs are inside the rocket;

F2.4 provide an umbilical connection to the FFUs;

F2.5 provide a connection to the RXSM.

F2.6 be capable to turn on or off all electrical components inside the FFU except for the logic circuits.

The RMU should:

F2.7 record video footage of the ejection of the FFUs.

2.2 Performance Requirements

The RMU should:

P1.1 eject the FFUs at an initial speed of 5-10 m/s before the despinning of the rocket.

P1.2 charge the FFU batteries with 4.2 V and 1 A current while inside the rocket.

P1.3 record video footage that is at least 720 pixels and 30 frames per second of the ejection of the FFUs.

The FFUs shall:

P2.1 deploy their parachutes at 5$\pm$1 km altitude.

P2.2 transmit their positions for a 24 hour recovery period.

P2.3 record GPS raw data at a sampling rate of $>$ 4 Msamples/s between ejection and parachute deployment.

P2.4 record internal sensor data at a sampling rate of $>$ 100 samples/s from before the liftoff to after landing.

The FFUs should:

P2.5 have landing velocities no greater than 10 m/s.

The Thermal Cutter shall:

P3.1 cut the constraining fishing line within 4 seconds of activation.

2.3 Design Requirements

The RMU shall:

D1.1 have FFU ejection openings dimensioned so that the structural integrity of the rocket is not compromised;

D1.2 have eject able hatches that are appropriately sized to avoid jamming;

D1.3 provide specified charging line to FFU batteries until ejection.

D1.4 provide short-circuit protection for each FFU.

The RMU constraining steel cable shall:

D2.1 have an adequate margin of safety against tensile failure.

The FFUs shall:

D3.1 each house a parachute, parachute deployment system and electronics system;

D3.2 each have a spherical shape with diameter 124 mm and a smooth surface;

D3.3 each have batteries with sufficient power and capacity for the environmental conditions during flight and after landing;

D3.4 transmit radio beacon and satellite modem data at frequencies that comply with legal requirements;

D3.5 not interfere with the REXUS RF transmission;

D3.6 have a sufficient memory for storing data collected during flight;

D3.7 provide stable 1.5 V, 2.8 V, 3 V, 3.3 V and 5 V voltage(s) to their various electrical components

D3.8 withstand shocks

The FFUs should:

P4.1 fall with the antenna facing towards zenith.

Mechanical components shall:

D5.1 conform to tolerances as specified by design requirements and analysis.

The full system shall:

D6.1 withstand a sinusoidal vibration level of 0.124 m/s between 10 Hz and 50 Hz and a level of 4.0 g between 50 Hz and 2000 Hz with a sweep rate of 4 octaves per minute.

D6.2 withstand random vibration levels of $12.7g_{rms}$ along both the longitudinal and lateral axes over a frequency range from 20 Hz to 2000 Hz.

D6.3 operate at temperatures in the range between -30 °C and 60 °C (electronic components)

D6.4 operate at temperatures in the range between -30 °C and 150 °C (outer surfaces)

D6.5 not interfere with the electronics of the rocket or any of the other experiments;

D6.6 have electrical components that can withstand all stages of the mission;

2.4 Operational Requirements

The RMU shall:

O1.1 be loaded using a safe and efficient procedure;

O1.2 have an FFU ejection system that is initiated by Esrange by a flight event timeline command.

The FFUs shall:

O2.1 disable power to their transmission sub-systems and their parachute deployment system until FFU ejection;

O2.2 work independently of any control from the ground or RMU after lift off;

O2.3 land within the Esrange recovery zone.

The RMU ejection system shall:

O3.1 be secured by safety straps during handling.

Chapter 3

Project Planning

3.1 Work Breakdown Structure

Figure 3.1 presents the Work Breakdown Structure of the MUSCAT project. This provides a general overview of the task division amongst the different areas of the project.

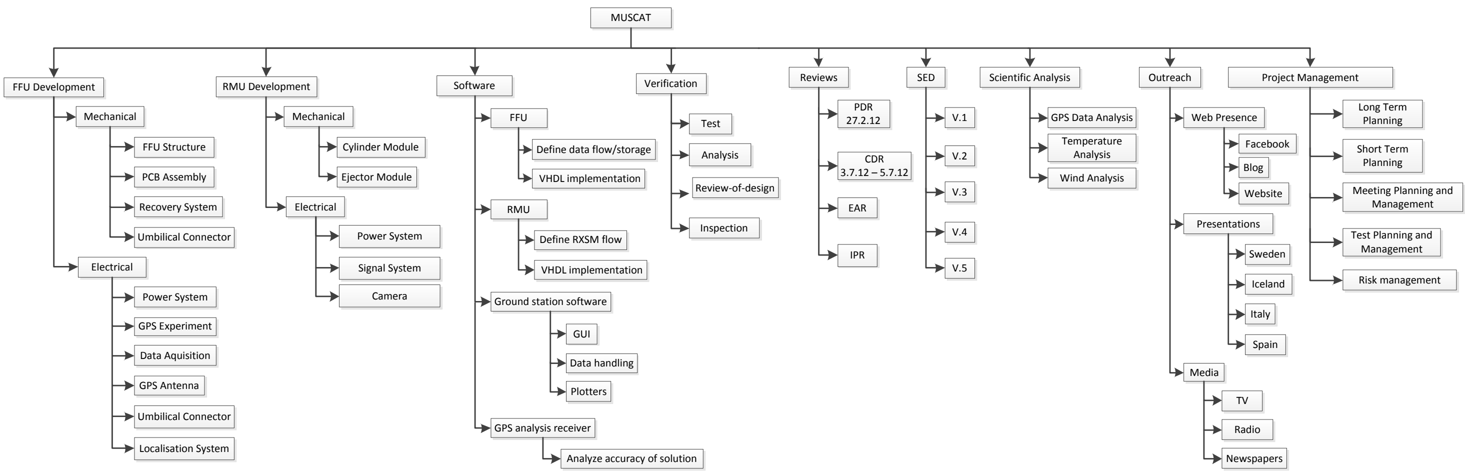

Figure 3.1: Work Breakdown Structure

3.1.1 Planning Summary

A plan has been made with Microsoft Project 2010 and has served as a guideline for the team. The plan has been updated every week with comments from team members, which are relayed at smaller team meetings. Each team member has the responsibility to detail what they need to do in order to finish each project before the assigned deadlines. The project managers will then provide the team with feedback on how best to proceed in order to meet all deadlines. Following is the outline of how the plan has been and how it is for the future.

In the first prototyping stage between mid February and mid April 2012, the entire MUSCAT team participated in the preparation of two fully functional FFUs and a detailed design of the RMU. Two drop tests were conducted in April and May. This period corresponds to the spring semester of the Swedish academic year so that the group's bachelor thesis students use the prototype design, testing, construction and drop tests for their final thesis reports. Two drop test were made and the drop test reports can be found in appendices B.4 and B.5.

Preparation for the Critical Design started in early May and ended in the beginning of June 2012. After this review comments from CDR were taken care of, which included the re-design of the ejection system, and the main focus was put on producing and verifying components for the experiment. During the summer months from mid June to the end of August the team size diminished due to the electrical team finishing their bachelor theses. Five extra FFUs were assembled from August to end of January.

Preparation for the IPR started in mid-September. The IPR allowed us to report on the progress made with our development and our assembly process. Most of the parts for the RMU were delivered by mid-October, with the rest being delivered/manufactured in November, December, January and February. The five new FFUs were verified formally and informally from early October until late January. During November the assembly of the RMU was not completed as planned due to delayed shipment of the rocket cylinder, and work on the project was more or less halted in the second half of December due to Christmas vacation. In January, the RMU was assembled and tested in a live fire ejection test, following which EAR was conducted.

Verification of the full experiment with the full REXUS system was conducted by ESA and SSC in the period of February to end of April 2013. MUSCAT team members participated in most of these tests. The launch of the MUSCAT experiment was successful the 9th of May.

The MUSCAT experiment participated in ESA PAC Symposium in June 2013 and data analysis is ongoing.

3.2 Resources

The following section presents the team members' availabilities over the coming project phase along with the project's budget details.

3.2.1 Manpower

Table 3.1 outlines team members' availabilities in the August 2013 to September 2013 period. Our team now consists of eight masters students, thereof three inactive students which are working on their thesis far away but are available for work on SED, programming and consulting.

Team Member	**Responsibility**	**Availability**
Ólafía Lára Lárusdóttir	Project management, GPS data analysis, outreach,	10%
Darri Kristmundsson	Project management, outreach and documentation	10%
Andreas Myleus	Outreach, consulting and software programming	5%
Emilio Lozano	Consulting and outreach	5%

Marco Tito Bordogna	Documentation, outreach, data analysis and scientific questions	10%
Marcus Lindh	Documentation	5%
Markus Fjällid	Documentation	5%

Table 3.1: Manpower over the August - September 2013 period.

3.2.2 Budget

Table 3.2 outlines the estimated costs of the MUSCAT experiment. Not taken into account in this table are the costs the experiment module and the pyro cutters.

Item	**Estimated Cost [€]**
Travel	3,500
Electrical Components	2,500
PCBs	3,000
Mechanics	3,500
Machining	7,000
Verification	2,000
Outreach	500
TOTAL	22,000

Table 3.2: Budget

3.2.3 External support

3.2.3.1 Supervisors

Dr. Nickolay Ivchenko, Associate Professor, Space and Plasma Physics, KTH
Dr. Gunnar Tibert, Associate Professor, Mechanics, KTH
Dr. Anders Ellgardt, Researcher, Electrical Engineering, KTH
Dr. Jörg Gumbel, Associate Professor, Meteorology, SU
Kristoffer Hultgren, PhD student, Meteorology, SU
Peggy Achtert, PhD student, Meteorology, SU
Nicola Schlatter, PhD student, Space and Plasma Physics, KTH

3.2.3.2 Sponsors

Swedish National Space Board (SNSB)
EuroLaunch a cooperation between the Esrange Space Center of the Swedish Space Corporation (SSC) and the Mobile Rocket Base (Moraba)
German Aerospace Center (DLR)
European Space Agency (ESA)
The Royal Institute of Technology (KTH)
Stockholm University
Mimmin

Evonik Industries
LIROS Ropes
Lesjöfors
Lindhtech.

3.3 Outreach

MUSCAT team members have been very active in the outreach program with regularly updating the team blog, sharing videos and photos and giving presentations. The following section summarises each of these items.

3.3.1 Website

URL: `http://www.muscatexperiment.se`

Figure 3.2: The MUSCAT Experiment Website.

The current website provides a congestive overview of the project along with links to other project resources, such as the blog. General information about the project, the scientific objective of the experiment and the team members are presented. Information about the REXUS/BEXUS programme, sponsors and the universities is included also. A contact form is also incorporated into the website, allowing interested people to find out more about the project by contacting the team directly.

3.3.2 Blog

URL: `http://muscatexperiment.wordpress.com`

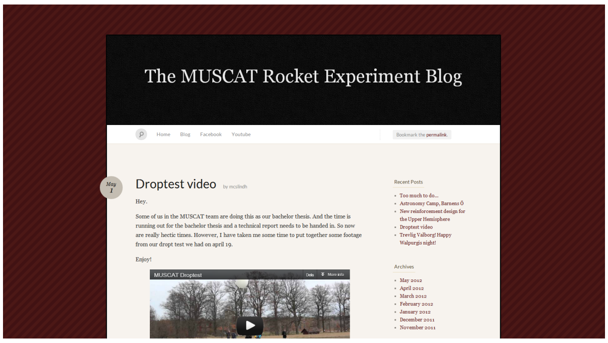

Figure 3.3: The MUSCAT Experiment Blog on 1st May.

We chose to separate the blog from the website with a Wordpress for the user-friendliness. It will be easier for every team member to edit and upload content to it with their own account. The blog is intended to be more extroverted and dynamic and here we will post regular updates on how the project moves on in a general way, but also more specifically on how electronics, mechanics and outreach progresses.

Our goal is to update the blog as often as we can. We have had a schedule during the spring where each of the 12 team members is responsible for the blog one day each over a 2 week period. During the summer some members will leave and almost no blogging will be done regularly, due to the project taking a holiday. A new schedule will be done in the autumn when the new team is gathered again.

3.3.3 Facebook

URL: `http://www.facebook.com/muscatexperiment`

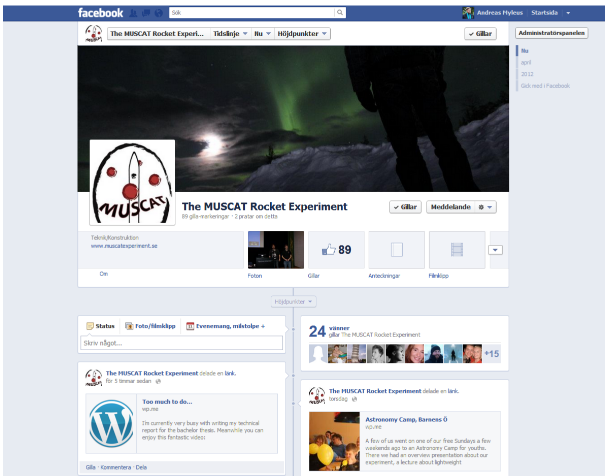

Figure 3.4: The MUSCAT Experiment Facebook Page on 1st May.

Like many other organisations, businesses or persons in the modern world we decided to generate followers and advertise ourselves through Facebook. Our page is called The MUSCAT Rocket Experiment. Here we have basic information about the experiment, but the page is mainly used to spread the blog updates to everyone who "Likes" the page. The posts can then be discussed and shared on Facebook. Whenever a post is added on the Wordpress page, it is shared to the Facebook page.

3.3.4 YouTube

URL: `http://www.youtube.com/muscatexperiment`

A Youtube channel, muscatexperiment, is used to store relevant videos of our progress, which are posted on the blog. There is a link to the channel from the website and the blog.

3.3.5 Interactions so far

- November 2012 we visited one presentation that the RAIN-team arranged at "Vetenskapens hus" (Science house) for high school students. Here one got a good feeling of how a presentation could be arranged and we also meet the person responsible for the current cooperation with the RAIN-team. The intention is to extend the cooperation with "Vetenskapens hus" to the MUSCAT team.
- The two Icelandic members of the team had 2 school presentations in Iceland about the experiment during Christmas 2011.

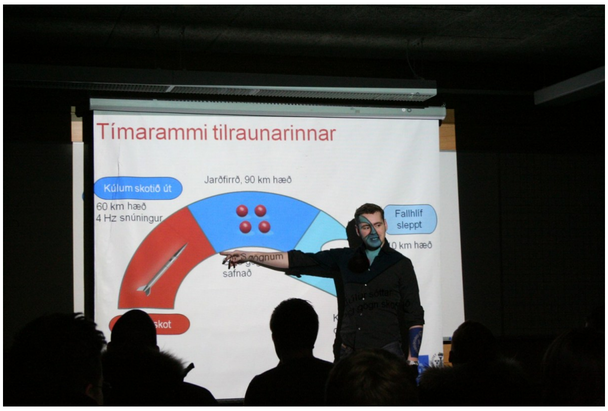

Figure 3.5: Outreach in Iceland.

- March 2012 we had a presentation about the experiment in general for the 100 most promising high-school students in Sweden at Tekniska Museet. It was during an exhibition called "Utställningen" where the 100 best high-school projects are shown. We got to present during the first day of the week long event as "What can you do later at the University?".

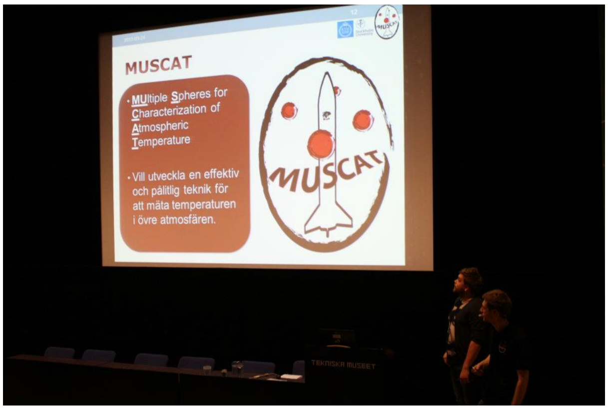

Figure 3.6: Outreach at Tekniska Museet in Stockholm.

- April 2012 we participated in a 2 day Master Fair for Aerospace Engineering. We got to talk to Bachelor students who are choosing their Master in the autumn about REXUS and MUSCAT. They got to visit all of the workshops we use and see all the prototypes we have built.
- April 2012 four of us went to an Astronomy Camp outside Stockholm and had a 2 hour presentation about the experiment in general, lightweight structures, rocket propulsion and GPS. We also demonstrated the recovery system that we will use on our FFUs.

Figure 3.7: Outreach at Astronomy Camp.

- The five Bachelor students have handed in their thesis' and held presentations of their work in the end of May 2012:
  - Construction and Analysis of a GPS and Localization System for Sounding Rocket Experiment
    Date: 15 May & 25 May
  - Data Acquisition System in the MUSCAT Experiment
    Date: 25 May
  - Power System in the MUSCAT Experiment
    Date: 25 May
- We have done three guest blog posts in a Swedish Space Blog (Rymdkanalen.se).

- September 2012 we promoted our experiment and previous KTH REXUS experiments to other Aerospace and Electrical Engineering students during guest lectures. This was also an opportunity to recruit students for a possible new REXUS team.
- September 2012 we got an article published in an engineering student magazine at Instituto Superior Tecnico in Lisbon.
- October 2012 we went to Mälardalens Högskola in Västerås to present REXUS and MUSCAT for Aeronautical Engineering students. We also had presentations about the new REXUS applications to KTH students.
- October 2012 we also had presentations at KTH about the previous REXUS teams from KTH, and informed about the new application period.
- October 2012 we visited ICES Embedded Industry Market Day at KTH.
- January 2013 we had an article published about MUSCAT in Leonardo Times at TU Delft.
- During the launch campaign in May 2013 we had 2 articles published, one in the biggest newspaper in Iceland and one in a local newspaper in Sweden.

3.4 Risk Register

Table 3.3 indicates the codes that are used in the Risk Register presented in Table 3.4

Primary ID	Description	Secondary ID	Description
TC	Technical implementation	.R	Inside rocket
MS	Mission (operational performance)	.F	FFU fall
SF	Safety	.L	Experiment recovery
VE	Vehicle	.A	Multiple phases
PE	Personnel	.P	Pre-launch preparations

Table 3.3: Risk register legend

Risk ID	Risk	Probability	Severity	PxS	Actions	Reference/ Remarks
TC.A10	Critical deformation of FFU shape due to thermal effects significantly changes drag coefficient	A	3	very low	Perform thermal analysis	
TC.A20	Internal electromagnetic interferences	A	4	very low	Shield high frequency components	
TC.A30	Error in the FPGA code	A	4	very low	Test the code extensively	
TC.A2	Antenna transmissions are blocked after ejection	A	4	very low	Do extensive testing	Risk deleted

TC.A3	Electromagnetic interferences	B	3	low	make sure lines are decoupled and impedance matched properly to prevent oscillations	Risk deleted
TC.F1	Separation of FFU upper hemisphere due to random vibrations	B	2	very low	Vibration tests	Risk deleted
TC.F2	Sensors might be improperly calibrated	B	3	low	Ask manufacturer for calibration and test with calibrated equipment	Risk deleted
MS.R10	Rocket cylinder loses structural integrity	A	5	low	FE analysis on the structure	Appendix B.2
MS.R21	Failure of ejection system: Pyro cutter activates prematurely	A	5	low	Let SSC handle the pyrocutter	
MS.R22	Failure of ejection system: Pyro cutter does not activate	A	3	very low	Let SSC handle the pyrocutter	
MS.R30	Failure of ejection system: Structural failure of spring	A	3	very low	Test ejection system in rotation with and without spring	
MS.R4	Battery Malfunction	A	2	very low	Test the battery and whether it is charging	
MS.R40	Failure of ejection system: Excessive thermal expansion of structure causes moving parts to jam	A	4	low	Perform thermal analysis	
MS.R50	Failure of ejector structure during rocket powered flight	A	3	very low	Ejector beam analysis	Appendix B.9
MS.F10	Failure of deployment system: Thermal cutters do not cut	B	3	low	Perform thermal tests to ensure cutting at low temperatures	

MS.F20	Failure of deployment system: Parachute does not open properly	A	3	very low	Verify parachute packing procedure and deployment in a drop test	Appendix F.1
MS.F30	Hot gas enters RMU during re-entry and affects other experiments	A	3	very low	Have two aluminium plates placed on the upper and lower part of the rocket module	
MS.F40	Thermal failure of FFU during re-entry leading to loss of FFU due to outer skin melting	A	3	low	Re-entry thermal analysis	
MS.A10	Failure of deployment system: Pressure sensor initiates parachute deployment at the wrong altitude	B	3	low	Perform vacuum and drop tests	
MS.A21	Battery malfunction due to vacuum exposure	A	3	very low	Test the battery in vacuum chamber	
MS.A22	Battery failure due to exposure to cold	A	2	very low	Perform thermal test on battery	Appendix B.1
MS.A30	Loose screws/bolts cause damage	A	3	very low	Use locktight glue and nylon nuts	
MS.A40	FFUs are not correctly assembled	A	3	very low	Follow assembly procedure	Appendix F.1
MS.A50	FFUs are incorrectly placed in the RMU	A	3	very low	Follow assembly procedure, place markings on FFUs	
MS.L10	FFU hits hard surface upon landing and is damaged, causing loss of data	C	2	low	Verify design during drop tests	Appendix B.4

MS.L20	RMU fills up with snow which damages other experiments	B	3	low	Have two aluminium plates placed on the upper and lower part of the rocket module	
MS.L30	FFU PCB comes in contact with snow and shorts	A	3	very low	Cover PCB with epoxy resin	
MS.L40	Localization system loses reception after landing	D	1	low	Store the last coordinate sent from the FFU	
MS.L50	One or more FFUs are not recovered due to difficult terrain	B	2	very low	Secondary recovery plan	
SF.P10	RMU ejects FFUs while on ground	A	5	low	Secure with failsafe straps	
SF.P2	Handling of ejector module springs cause injury	A	5	low	Handle springs with a safe and efficient procedure	Removed
SF.L10	FFU hits somebody or his property	A	4	very low	Reduce FFU drift by deploying the parachute at a suitable altitude based on drift calculations	
SF.L11	FFU hits somebody or his property during the sky diving test	A	4	very low	Plan the drop very well so that the FFU lands in an empty space	
SF.R10	Antenna transmits while inside rocket before launch	A	5	low	Test rocket pin mode	
VE.R10	Failure of restraining cable due to thermal loads	A	5	low	Thermal analysis of cable	
PE.P10	One or more team members are unexpectedly unavailable for more than one week	E	1	low	Schedule buffer time	

PE.P20	One or more team members unexpectedly leave the project	B	2	very low	Schedule buffer time	
PE.P30	Unequal workload on team members	B	2	low	Redistribute workload	
PE.P40	Team is unavailable for big project events	B	2	very low		
PE.P50	One or more person gets injured in the sky diving test	A	5	low	Follow sky diving safety procedure and let a professional drop the FFUs	

Table 3.4: Risk register

3.5 Heritage

MUSCAT inherits a large amount of knowledge from previous KTH teams, especially the RAIN team. Heritage items which we intend to make use of:

- Solutions for the localization system
- Parachute design
- Spring-based ejection system
- Thermocutter and winch design for the parachute release mechanism
- Project management tools: Basecamp, Dropbox, Microsoft Project
- Outreach program structure (high school visits)
- Documentation
- GPS experiment solutions
- Power system and battery solutions
- VHDL code modules for FFU and RMU firmware.
- PC software for GPS post-processing.

Chapter 4

Experiment Description

4.1 Experiment Setup

The MUSCAT experiment contains two main subsystems. The first one is the rocket mounted unit (RMU) and the second one is the four free falling units (FFUs). The RMU includes the inner structure and the rocket cylinder. The RMU is where the FFUs are housed.The FFUs are atmospheric probes that contain the electronic devices used to perform the experiment. The main purpose of the RMU is to keep the FFUs in place until the ejection altitude is reached and eject them at this altitude. In the RMU the FFUs are housed in individual cages that are attached to the inner structure of the rocket cylinder. While the FFUs are in the rocket, each FFU is connected with a five pin connector to the RMU. These five pins are used to ground the FFUs, transmit information from and to the FFUs, charge them and activating the sleep mode. The FFUs are not active when they are inside the RMU. The FFUs are activated when the FFUs are ejected from the RMU. The RMU is connected to the RXSM. The RXSM allows us to control the camera, monitor the FFUs and charge the FFUs.

4.2 Experiment Interfaces

4.2.1 Mechanical

The MUSCAT RMU, shown in figure 4.1, consists of a cylinder module and an ejector module. The RMU is attached to the rocket modules above and below by means of screwed joints, which are unmodified as provided with the rocket cylinder. The rocket cylinder is custom-made with four openings for deployment of the four FFUs. In order to match the strength of the original module, the modified rocket cylinder has been reinforced by increasing the wall thickness. In the RMU no bulkheads are used.

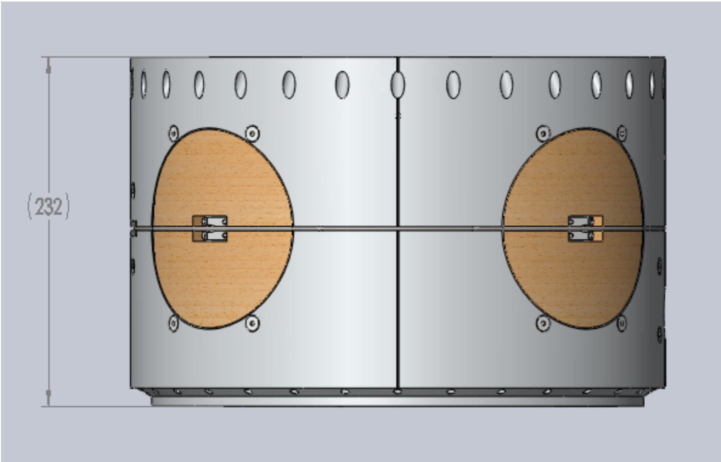

Figure 4.1: The MUSCAT RMU, housed in a 220mm REXUS module.

4.2.1.1 Hot Gas Protection

To prevent thermal damage to the payload and service systems due to hot gases entering the module during re-entry and provide protection from snow entering the module upon landing, the MUSCAT RMU is isolated from the rest of the rocket by cover plates made of aluminium. Cables running through the module will be housed inside an aluminium shielded tunnel located below the D-Sub bracket.

4.2.1.2 Ejector Module Interface

The ejector module contains a spring-based ejection system which is activated by cutting a steel wire with a pair of pyrocutters. The pyrocutters are operated by Eurolaunch.

4.2.1.3 D-Sub Brackets

A D-sub bracket is placed directly below the top collar of the rocket module at 180°. The positioning of the bracket is shown in figure 4.2. The D-sub bracket is used to hold D-sub connectors that lead to the experiments located above MUSCAT.

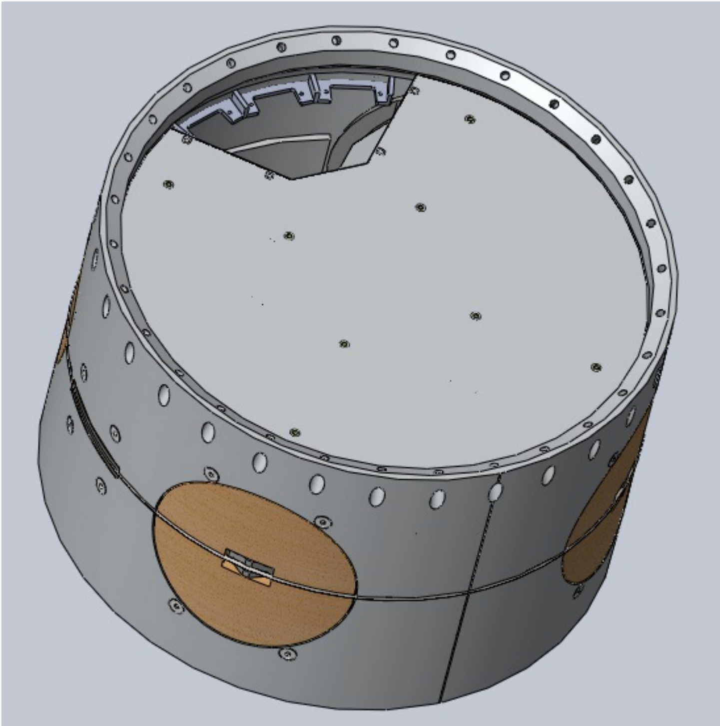

Figure 4.2: D-sub bracket, located at 180°.

4.2.2 Electrical

The RXSM connector interface to the RMU is compliant with the specifications in [1]. The RXSM connector is used for communicating with the FFUs and RMU as well as charging the battery prior to launch. The data pins on the RXSM connector are used to send commands to the experiment and to read out data so the experiment status can be monitored during flight. The interface between the RMU and the FFUs consists of a pin header connection to each FFU.

4.2.2.1 RXSM Connector

The RXSM cable (from the rocket to the RMU) shall have a female connector (section 7.6 of the REXUS user manual [1]). The RMU shall have a male connector (section 7.6.1 of the REXUS user manual [1]). The RXSM-connector is connected to the RMU to power the RMU. The connector is also used for transmitting data to the RXSM, which in turn forwards the data to ground via telemetry. For data transfer a 38.4 kbit/second downlink and 38.4 kbit/second uplink are used. The camera will be switched on by a command to RMU and will be activated before rocket launch. The charge pin can be used to charge the FFUs' internal batteries. The RXSM connector complies with [1], using the pins listed in Table 4.1.

Pin	Pin name	Notes
1	+28 V	Experiment Power
2	Spare	Not connected.
3	SODS	Not connected.
4	SOE	Not connected.

5	LO	Not connected.
6	EXP out+	Non inverted experiment data to RXSM.
7	EXP out-	Inverted experiment data to RXSM.
8	28 V Ground	Power ground.
9	28 V	Experiment Power
10	28V Charging	Not used (option)
11	Spare	From rocket
12	UTE	Not connected
13	EXP in+	Non inverted control data to the experiment
14	EXP in-	Inverted control data to the experiment
15	28V Ground	Power ground

Table 4.1: The RXSM connector pin configuration.

4.2.2.2 Communication

The FFU and RMU send down sensor values, housekeeping data and status to the ground station. The FFU is connected to the RMU through a umbilical pin connection. The RMU then communicates with the ground station through the RXSM. For testing, commands can be sent to the FFUs and RMU to turn on or off different systems, except for the transmission system and the thermal cutter in the FFU which are disabled while the FFU is in the rocket. Before the launch, mission mode is initiated by sending a command to the RMU which tells the FFU to enter the mode.

4.2.2.3 Umbilical Connector

The RMU is connected to the FFU via an umbilical connector. The FFU have a female socket and the RMU has a male connector for each FFU. The umbilical connector can be used for communication with the FFUs, charging of the FFU batteries and activating the FFU sleep mode. During flight, the umbilical connector is connected to the RMU until FFU ejection. The umbilical connector pin configuration is listed in Table 4.2.

Pin #	Pin Name	Function
1	GND	Ground
2	BATT	Battery charge input
3	RX	Communication from the RMU
4	TX	Communication to the RMU
5	Rocket	Prevents RF systems and parachute deployment from activating, also used for activating FFU sleep mode.

Table 4.2: The umbilical connector pin configuration.

4.2.2.4 Power transfer to the FFU

The umbilical connector is used to charge the FFUs' internal batteries which, in turn, power the FFUs. The power input lines to the FFUs are reverse polarity protected by series diodes. This means that there is no risk of the FFU batteries powering external equipment in reverse.

4.2.3 Radio Frequencies

While inside the rocket all radio transmitters inside the FFUs are disabled. Each FFU contains two transmitters and two receivers but only two antennas, the main antenna and beacon antenna. After the ejection of the FFUs the main antenna receives GPS L1 signals (at 1575.42 MHz, see table 4.3) with a MAXIM Universal GPS Receiver [2] until parachute deployment at 5 km. After parachute deployment the preamplified signal is redirected to a GPS module ET-318 [3]. The GPS engine board acquires position of the FFU and sends this information to the FPGA. The FPGA manages the data from the GPS engine board and sends it to a satellite modem STX2 [4] and a VHF Narrow band FM transmitter. The STX2 modem centre frequency 1615 MHz. The STX2 modem uses DSSS modulation and each STX2 modem has a unique ID that is hardware based and is not modifiable. This unit ID is sent with the STX message as can be seen in the data sheet [4] which allows us to distinguish between the different FFUs. The resolution of the STX2 is 2.5 MHz. The power level of the STX2 is 18 dBm$\pm$2 dB. The STX2 is a commercial product available globally from the Globalstar service. The FFUs will all have TX1 transmitters from Radiometrix with different centre frequencies, 173.250 MHz, 173.275 MHz, 173.300 MHz and 173.325 MHz. All TX1 have a modulation bandwidth at -3 dB of 7 kHz and the power level of 10 dBm, see table 4.3. The frequencies for the TX1 transmitters will be applied for by Esrange. All frequencies used comply with the frequencies forbidden in [1].

Frequency (MHz)	RX/TX	Unit	Bandwidth	Power(max)
1575.42	RX	MAX2769		
1575.42	RX	ET-318		
1615	TX	STX2	2.5 MHz	20 dBm
173.250	TX	TX1	7 kHz	11.5 dBm
173.275	TX	TX1	7 kHz	11.5 dBm
173.300	TX	TX1	7 kHz	11.5 dBm
173.325	TX	TX1	7 kHz	11.5 dBm

Table 4.3: The Radio Frequencies.

4.3 Experiment Components

4.3.1 Mechanical

Tables 4.4, 4.5 and 4.6 summarize the dimensions of the mechanical components. Note that mass figures come from direct measurements of FFU prototypes and mass analysis of RMU through CAD software. A detailed list and drawings of the mechanical components can be found in appendix C.1 to C.42.

Component	Mass [kg]
FFU (x4)	$\sim$ 0.4 (each)
RMU	10.5
Experiment total mass	12.1

Table 4.4: Mass properties

Component	
FFU diameter (mm)	124
FFU volume (mm^3)	998306
FFUs expected COG position	Within 10 mm of the centre on the rotational axis

Table 4.5: FFU dimensions

Component	
RMU diameter (mm)	356
RMU height (mm)	232
RMU footprint area (m^2)	0.681
RMU expected COG position	Within 20 mm of the centre on the rotational axis

Table 4.6: RMU dimensions

4.3.2 Electrical

The electrical components' datasheets can be found in references.

4.4 Scientific Design

The purpose of the MUSCAT experiment is a proof of concept of a method to derive temperature and density profile in the middle-atmosphere. The temperature and density profiles of the atmosphere are derived from data stored in the FFUs during flight. While each probe is falling the forces acting on it, and the direction of the total velocity vector are illustrated for a 2D case in Figure 4.3.

The forces are acting the FFU is the gravity force (mg) and the drag force denoted in Figure 4.3 as F_D. Using the equation of motion (Newtons second law), it is possible to write a system of equations for the forces acting in the vertical and horizontal directions respectively.

$$\begin{cases} ma_V = mg - \frac{1}{2}\rho_\infty AC_D|V_\infty|V_\infty \cos\theta \\ ma_H = \frac{1}{2}\rho_\infty AC_D|V_\infty|V_\infty \sin\theta \end{cases} \tag{4.1}$$

Where m is the mass of the sphere, g is the acceleration due to gravity, ρ is the density of the atmosphere, V is the velocity, A is a reference area (maximum cross section area for a sphere) and CD is the drag coefficient. The subscript ∞ denotes free-stream conditions. From the equation of motion in the vertical direction, an equation for the density can be obtained, as shown in Eq. (4.2).

$$\rho_\infty = -\frac{2m(a_V + |g|)}{AC_D|V_\infty|V_\infty \cos\theta} \tag{4.2}$$

In order to calculate ρ, the MUSCAT experiment needs to record: position, velocity and acceleration of each FFU. The FFUs will carry an antenna which will receive GPS raw signal, and internal sensors. By using Eq. (4.2), the hydrostatic equation shown in Eq. (4.3) and the equation of state for perfect gasses shown in Eq. (4.4) it is possible to derive a temperature profile at various altitudes [5] [6].

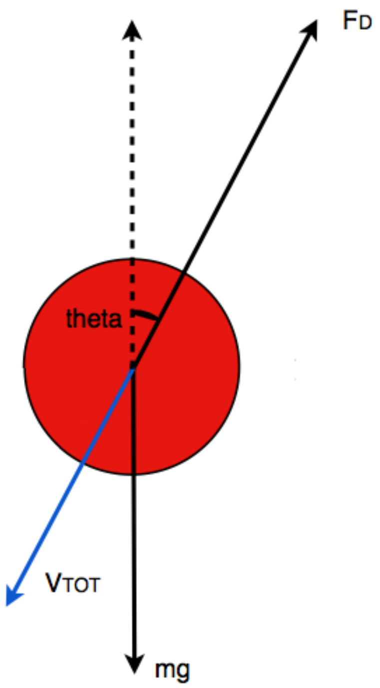

Figure 4.3: External forces and direction of the velocity vector for a FFU

$$dp = -\rho_\infty g dz \tag{4.3}$$

$$p = \rho_\infty R T_\infty \tag{4.4}$$

Where dp is a small change in pressure, dz is a small change in altitude, R is the specific gas constant and T_∞ is the temperature in the free-stream in Kelvin.

Equation (4.3) and (4.4) are combined and integrated with respect to the altitude between two limits. The result is shown in Eq. (4.5).

$$T_\infty(h) = T_\infty(0)\frac{\rho_\infty(0)}{\rho_\infty(h)} + \frac{1}{\rho_\infty(h)R}\int_{z(h)}^{z(0)} \rho_\infty g \,\mathrm{d}z \tag{4.5}$$

Where $T_\infty(0)$ and $\rho_\infty(0)$ is the temperature and density at the beginning of the fall, respectively. A detailed derivation of Eq. (4.5) can be found in Appendix B.8.

The coefficient of drag, C_D, is important for the above calculations. The FFUs have a spherical shape in order to retain a constant cross sectional area (A) independent of orientation. This enable the team to model the drag coefficient of the probe with good accuracy for a wide range or Mach and Reynolds number. The approach to obtain the value of C_D for the Reynolds numbers and Mach numbers which the sphere will experience during the fall, can also be found in Appendix B.8.

4.5 Mechanical Design

The MUSCAT experiment is composed of the RMU and four FFUs. The FFUs are housed inside an ejector module inside the RMU during the rocket launch and subsequent rocket powered flight.

4.5.1 Free Falling Unit (FFU)

The Free Falling Unit is shown in figure 4.4. The FFU consists of a spherical structure, a recovery system and a PCB assembly. The FFU is 124 mm of diameter and the mass is approximately 0.4 kg.

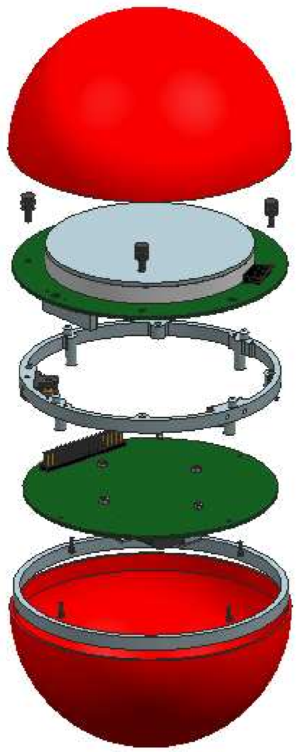

Figure 4.4: FFU Exploded view

4.5.1.1 PCB Assembly

The PCBs play an important structural role in the FFU since all electronic components are mounted on them and so they have to withstand the loads of all those components in all phases of the mission (launch, ejection, free fall and landing). The FFUs have two PCBs: *the top PCB* and the *bottom PCB*.

The antenna is placed on the upper surface of the top PCB and the battery is mounted on the underside of the bottom PCB using a cage. The electrical connection between the PCBs is provided by a vertical multi pin connector, see section 4.6.1. The top PCB is screwed onto the *internal metal ring* using custom made *eyebolts* as shown in figure 4.5.

Top PCB has a diameter of 121 mm and a thickness of approximately 1.6 mm. The *internal metal ring* has an external diameter of 115 mm and a variable thickness (3-5 mm). The metal rings are made out of aluminum.

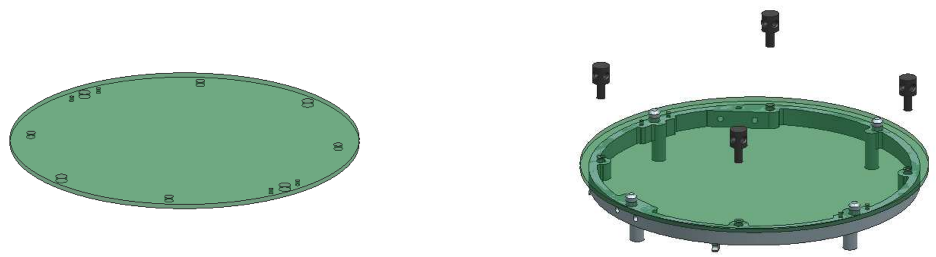

(a) *Top PCB* (b) *Top PCB with eyebolt*

Figure 4.5: FFU: Top PCB

The bottom PCB, with a diameter of 112 mm, is placed beneath the top PCB and fixed to extensions from the *internal metal ring* (figure 4.6).

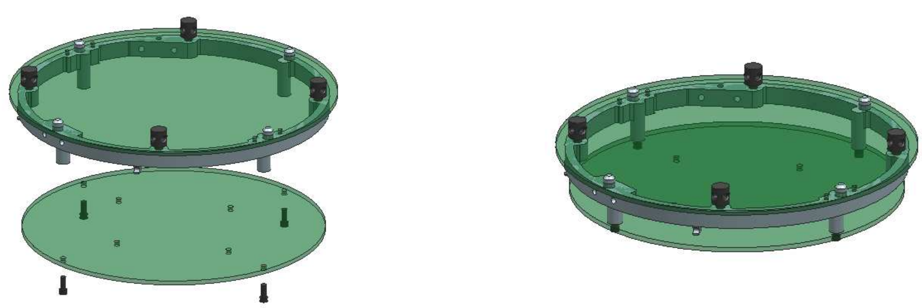

(a) (b)

Figure 4.6: FFU: Bottom PCB

4.5.1.2 Spherical Shells

An *upper hemisphere*, made of Glass Fiber Reinforced Polymer (GFRP) with a outer diameter of 124 mm and 1 mm thickness, is attached to the PCB. Inside the upper hemisphere a rib ring (figure 4.7) is attached. Movement and/or rotation of the upper hemisphere with respect to the PCB is prevented by matching the holes in the rib ring with truncated cone shaped elements of the *internal metal ring*. A fishing line is then used to create a removable vertical constraint, as discussed in the section 4.5.1.3. The assembly of the PCB and the upper hemisphere is shown in figure 4.8.

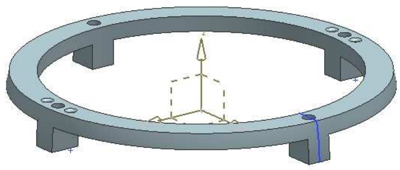

(a) *Rib Ring*

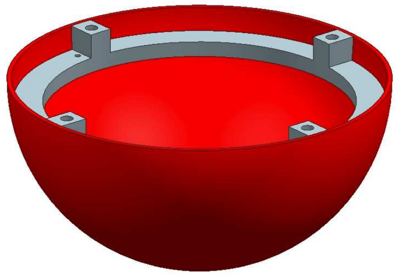

(b) *Rib Ring inside Upper Hemisphere*

Figure 4.7: FFU: Rib Ring with Upper Hemisphere

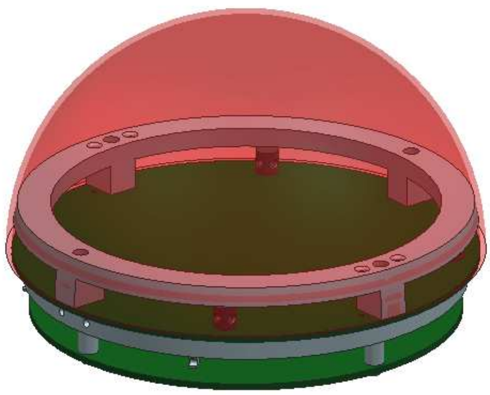

Figure 4.8: FFU: PCBs with Upper Hemisphere

A *lower hemisphere* is attached, using epoxy resin, to an *external metal ring* made of aluminum with external diameter of 121 mm and 3 mm thickness (figure 4.9).

(a)

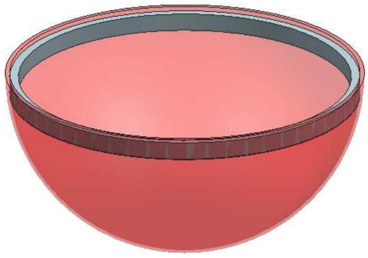

(b)

Figure 4.9: FFU: Lower Hemisphere with External Metal ring

The contact surface between the *external metal ring* and the *internal metal ring* is threaded. This allows the assembly of the upper hemisphere/PCB section and the lower hemisphere, respectively, as shown in figure 4.10.

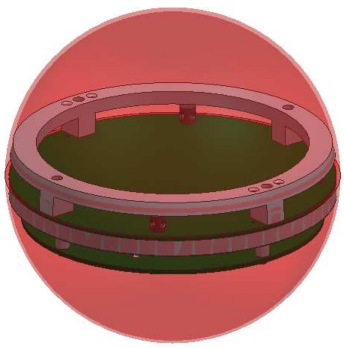

Figure 4.10: The complete FFU structural assembly

A report was made about the Spherical Shell as a project for a course MUSCAT team members took. The report can be found in the appendix G.1.

4.5.1.3 Recovery System

During flight, the parachute is housed beneath the upper hemisphere of the FFU. For the assembly of the upper hemisphere with the PCB the fishing line (i.e Spectra Fiber Rope) has to pass through the holes marked 1-10 as shown in figure 4.11. The line is tightened using a custom made winch (figure 4.12).

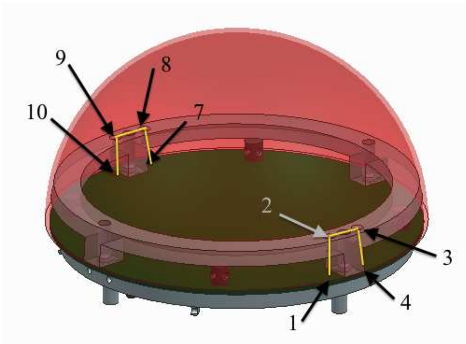

(a)

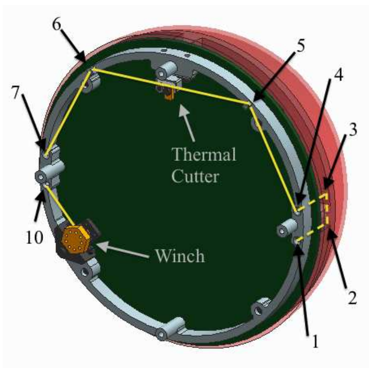

(b)

Figure 4.11: FFU: Position of holes

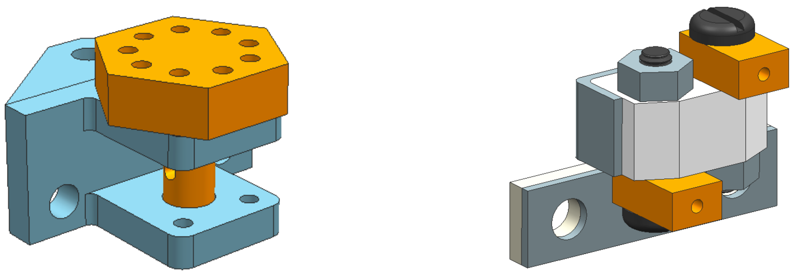

(a) (b)

Figure 4.12: FFU: Winch and Thermal Cutter

During the assembly of the upper hemisphere with the PCB the fishing line will also pass through a custom made thermal cutter (figure 4.12) placed under the top PCB, as shown in figure 4.13.

The winch and the thermal cutter are based on a solution from RAIN [7]. The thermal cutter is made of a kanthal wire held by two copper spacers. The copper spacers are fixed to the plastic insulator that is held in position by the cutter base. The winch is made of a winch base and the winch rotor, both are made of aluminium.

Once the FFU reaches the parachute deployment altitude the thermal cutter is activated. When the vertical constraint on the upper hemisphere is removed the parachute is deployed. Both winch and thermal cutter are custom made and are designed to be clamped to the internal metal ring.

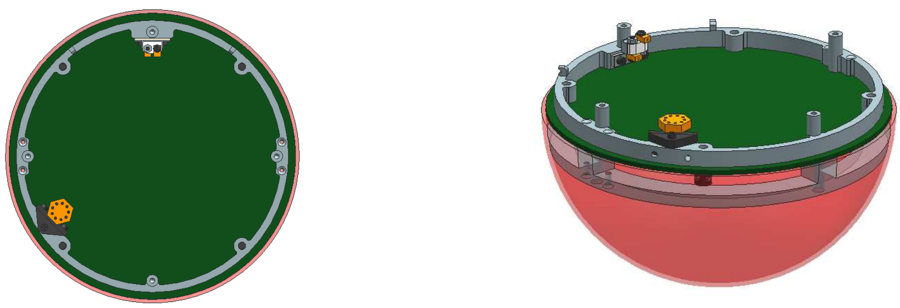

(a) (b)

Figure 4.13: FFU: Position of Thermal Cutter

A single Top Flight ThinMill 30" X-shape is used for each FFU. A cross parachute has been selected based on its resistance to drift. This parachute has also been chosen based on its thin fabric to minimize weight. It is rated from the supplier to be sufficient for payload weights of 450-600 g, this will give a terminal velocity of 5 m/s.

The parachute is made of rip-stop nylon fabric with a density of only 28 g/m^2. The parachute ropes are made out of braided nylon, and eight of these from the parachute are secured with a sewn knot to a 1.5 m long Dyneema rope. The rope is provided by Liros Ropes and can withstand loads up to 3500 N. The four cords that are used to connect the middle cord to the FFU are also made from Dyneema and are tied and sewn together with the middle cord. In the other end they are tied and sewn to the eyebolts of the FFU. The cord setup between the parachute and FFU is shown in (Appendix F).

An analysis of the required strength of the middle cord is done based on [8]. The required strength of the cord was calculated to be 960 N, with a safety factor of 2. We also require the cord to be at most 2 mm in diameter, to be able to fit it through the eyebolts on the FFU. Since Dyneema rope can withstand the load it has been chosen as the material for the parachute lines. A parachute cord twisting report can be found in appendix B.7.

4.5.2 Rocket Mounted Unit (RMU)

The RMU, shown in figure 4.14 consists of a rocket cylinder, the ejector module and hatches, a pyrocutter module and rocket mounted electronics. The rocket cylinder is a modified REXUS rocket cylinder, in which four 134 mm diameter holes are evenly spaced around the perimeter. The ejector module is connected to the modified cylinder via four collars. The ejector module serves the purpose of guiding FFU cages out of the rocket by a extension spring based ejection mechanism. To keep the springs extended during flight a steel cable is strapped into a groove around the RMU, constraining the movement of the hatches and therefore the movement of the whole ejection system. This steel cable is cut by two pyrocutters at the ejection time to release the FFUs.

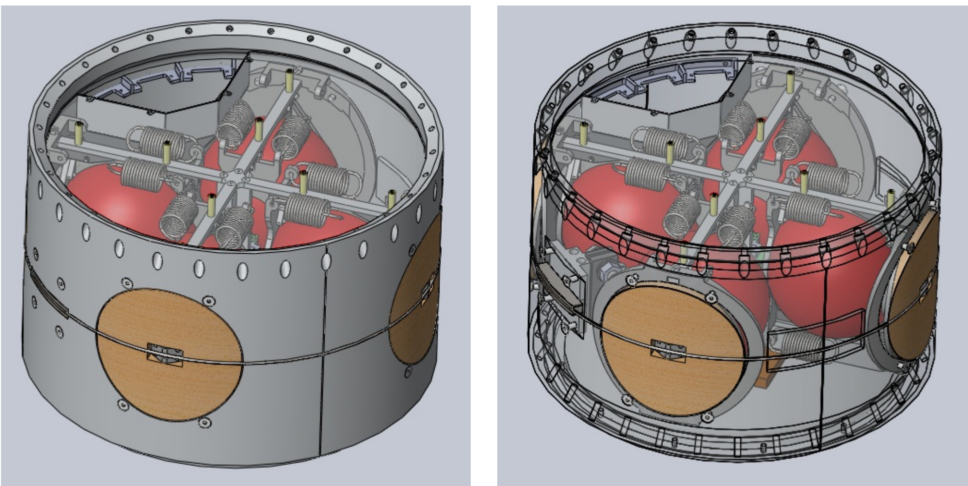

(a) *Solid view* (b) *See-through view*

Figure 4.14: RMU views

The rocket cylinder openings will be referred to as 45°, 135°, 225° and 315° as shown in figure 4.15.

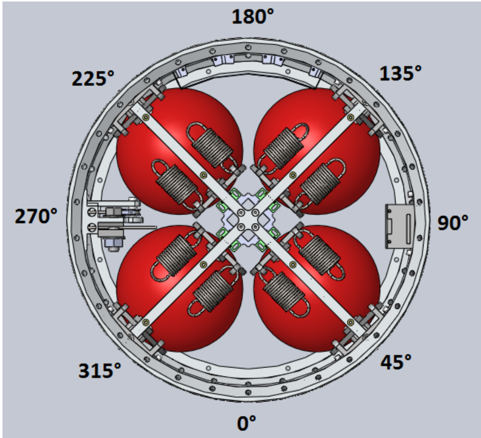

Figure 4.15: Rocket cylinder openings at 45°, 135°, 225° and 315°.

To protect other experiments from hot gases and snow, when our hatches have been ejected, two aluminium plates are placed on the upper and the lower part of the rocket module (figure 4.16).
Both plates have a thickness of 0.5 mm. The lower plate is clamped to the holes that are supposed to be used for the bulkhead. An opening in the lower plate allows the cables to enter in the rocket module. The upper plate is clamped to the ejector module and is placed above the collars and at the same height as the D-SUB bracket. A tunnel made out of aluminium will protect the cables running through the module. This tunnel is fixed at both ends to the aluminium plates as shown in figure 4.17.

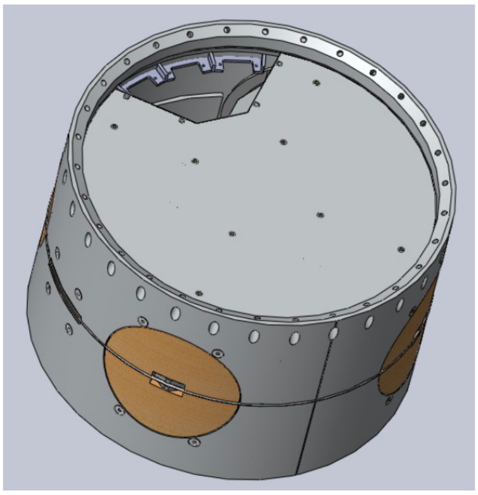

(a) *Upper plate at the top of the RMU*

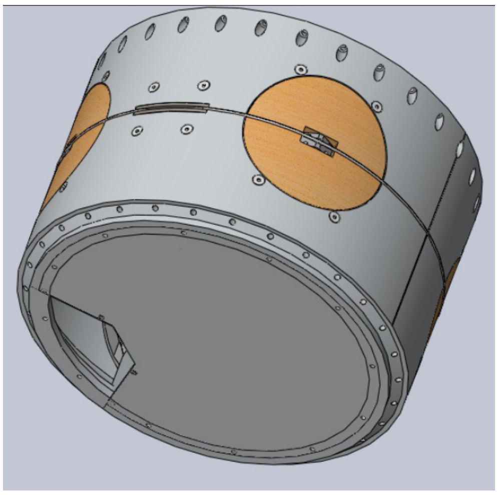

(b) *Lower plate at the bottom of the RMU*

Figure 4.16: Gas protection plate positions in the RMU

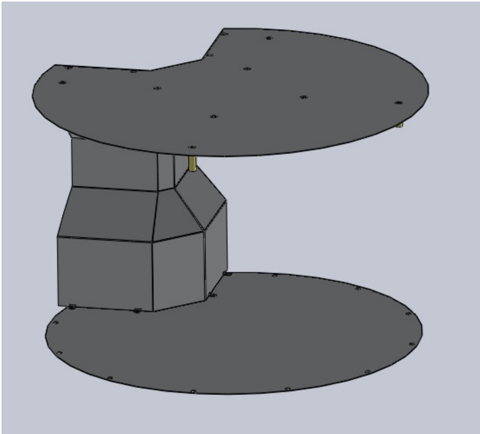

Figure 4.17: Gas protection tunnel and plates

4.5.2.1 Modified Rocket Cylinder

The rocket cylinder is a modified 220 mm REXUS rocket module. Multiple modifications need to be performed on the standard module in order to accommodate the required four openings, the cable groove and to install the required additional components. A thorough structural analysis of the strength and stiffness of the rocket module with four 134-mm-diameter perpendicular holes on the cylindrical surface shows that increasing the wall thickness from 4 to 8 mm will ensure the stiffness and strength of the module without reinforcement around the holes. The analysis is included in appendix B.2. Due to the groove running around the module, additional material is added at 0, 90, 180 and 270 to strengthen the module, as shown in figure 4.19.

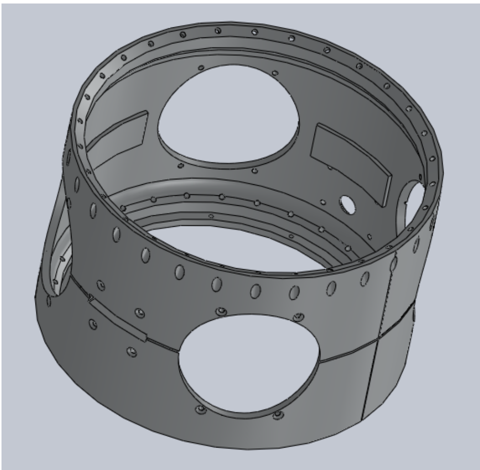

Figure 4.18: Modified rocket cylinder.

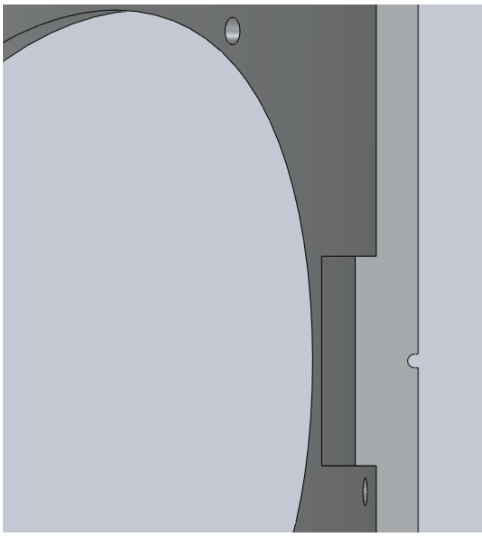

Figure 4.19: Cable groove and reinforcements at 0°, 90°, 180° and 270°.

4.5.2.2 Ejector Module

The ejector module consists of a rail system, connecting collars and four FFU cages. Each FFU cage is connected to a collar by four extension springs. The rail system consists of two aluminium crosses. Each cross has four rails, constraining the FFU cages and guiding them during ejection. During the rocket powered flight these rails serve as structural support for the FFU cages. An analysis of the rail strength is included in appendix B.9. The FFU cages are split in two halves for FFU deployment and general access, as shown in figure 4.20. The FFU cages are manufactured from the same material as the crosses. The extension springs required for the ejector module are located at the point where the crosses are docked to the four collars. The springs are attached to the FFU cages and pull the FFU cages out of the rocket during ejection. The movement of the ejector module is constrained by a 2.5mm diameter steel cable strapped around the cylinder module, securing the hatches. The cable is made of austenitic SS316 alloy and consists of 7 wound threads. An analysis of the cable can be found in appendix B.11. The selection of the extension springs is detailed in appendix B.10.

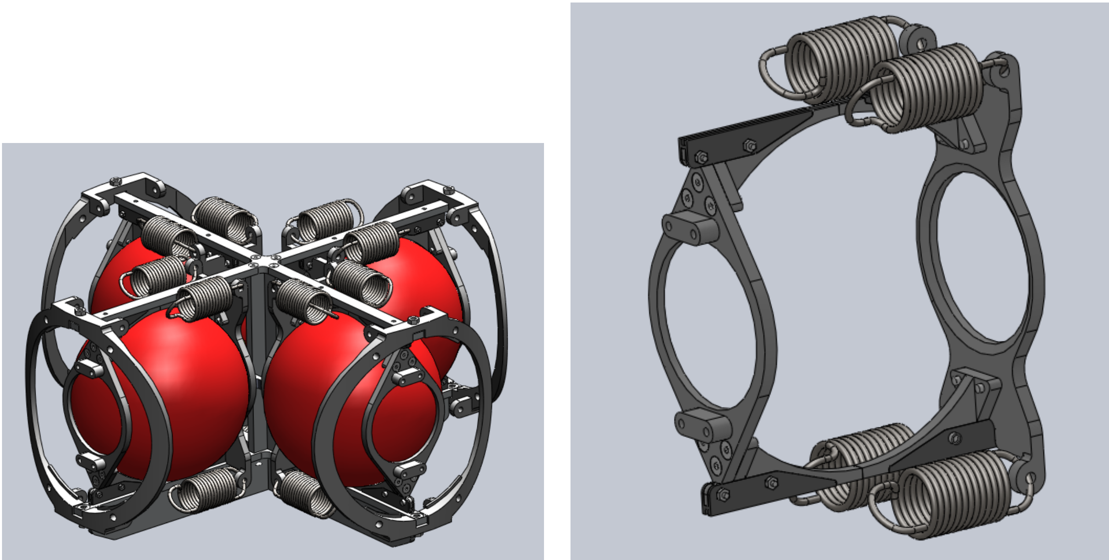

(a) *The ejector module* (b) *FFU cage*

Figure 4.20: Ejector module and FFU cage

4.5.2.3 FFU Cage

The housing of each FFU is a cage made out of aluminium alloy. The FFU cage is a structure which secures the FFU without transmitting any derived load from the ejector system to the FFU. The connecting piece between the FFU cage and the cross, refered to as slider, is made of teflon to minimize friction during ejection. The FFU cage contains two sub-assemblies, the inner half which pushes the FFU out of the rocket during ejection, and the outer half which connects to the hatch and constrains radial motion of the cage until ejection. A simulation of this is shown in video [9]. Each cage half consists of a ring connected to two ribs. A teflon slider is mounted on each rib. The outer ring is connected to the hatch and the inner ring is connected to the extension springs used for ejection. To ensure personal safety while loading the cages, a "remove before flight" safety camp is put between the inner ring and the collar piece, preventing accidental ejection.

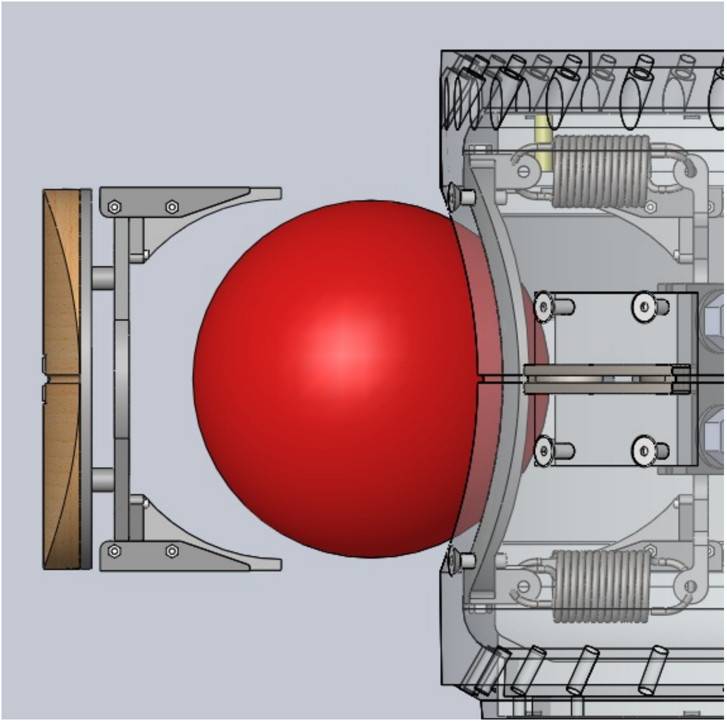

Figure 4.21: A view of the FFU ejection.

4.5.2.4 Hatches

The hatches are thin flat sections with a diameter of 132 mm. These sections are layered with cork which is flushed against the rocket skin. The cork is glued to the hatch using high-temperature Epoxy. On the outer side of each hatch there is a fork to guide the constraining steel cable as shown in figure 4.22. The cable tenses against the fork and is untouched by the cork. The hatch is connected on the inner side to the FFU cage. When the constraining cable is tightened, each hatch is pressed into the rocket cylinder and rests against an extrusions on the collar as shown in figure 4.22.

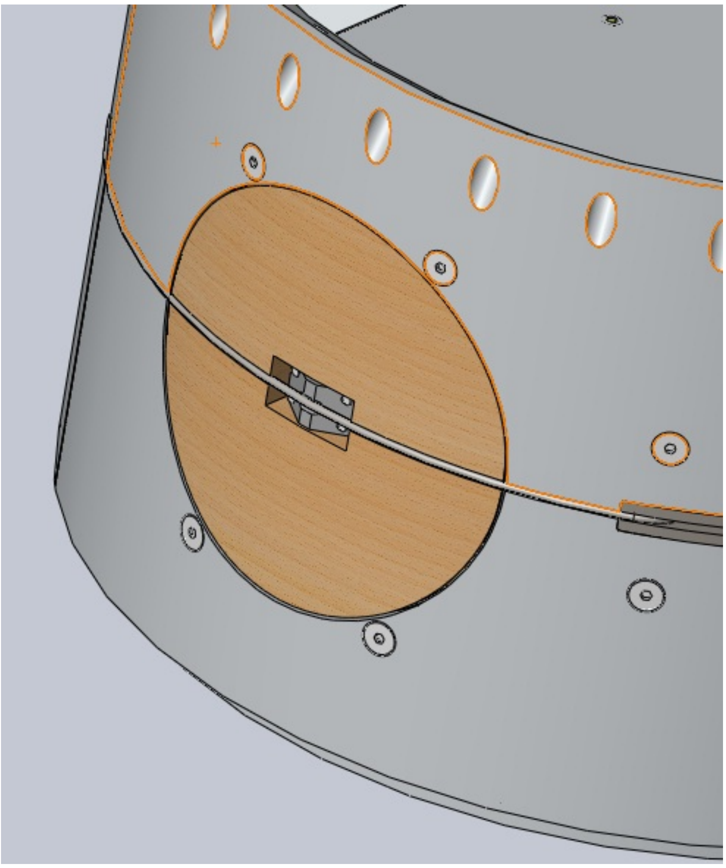

Figure 4.22: A hatch being constrained by the steel cable.

4.5.2.5 Pyrocutter Module

The pyrocutter assembly consists of two pyrocutters which are placed inside a pyrocutter bracket. The pyrocutter bracket is mounted on the inside of the rocket skin at 270° as shown in figure 4.23.

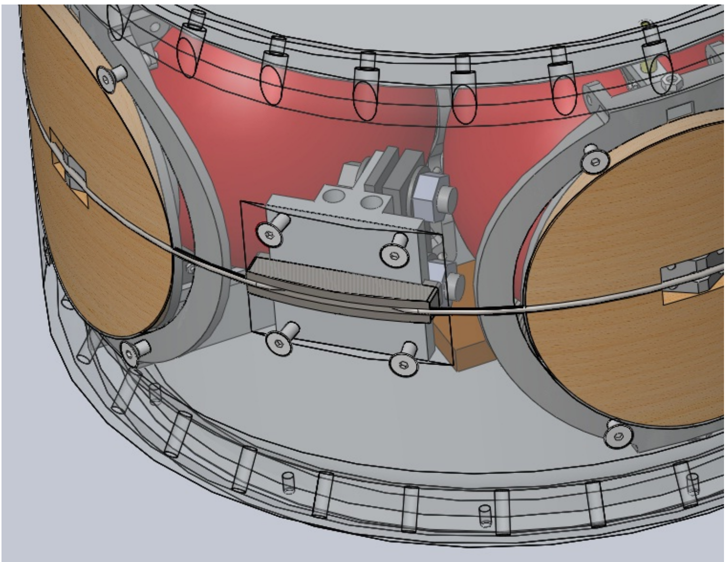

Figure 4.23: Pyrocutter assembly mounted on the rocket skin

The steel cable has a thimble on one end which is bolted at position 1 in figure 4.24. The cable passes through the first pyrocutter at position 2 and enters a cable guide made of steel at position 3. The cable guide ensures a safe turning radius for the cable while guiding it through the rocket skin and into the cable groove. The cable runs around the module, securing each hatch, and re-enters the cable guide at position 4. It then passes through the second pyrocutter at position 5 before being secured between two ruffled steel plates at position 6.

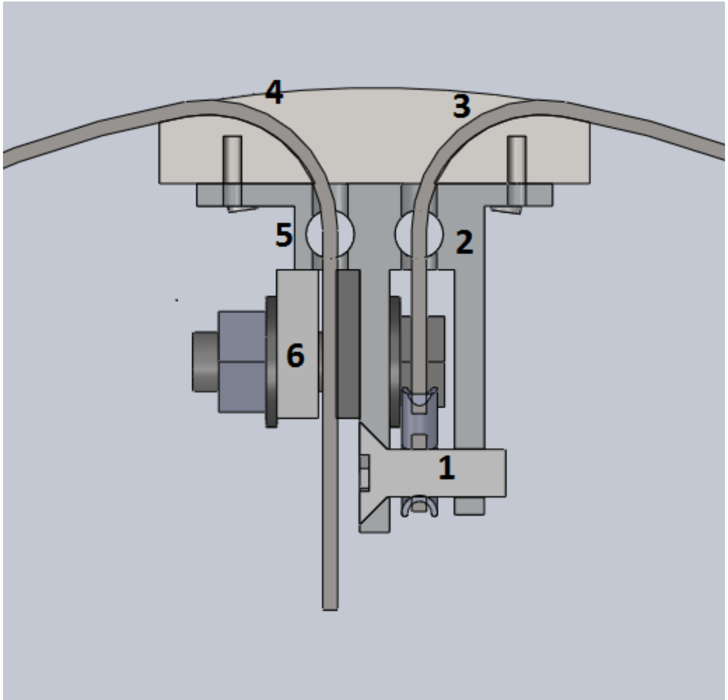

Figure 4.24: Functional diagram of pyrocutter assembly.

The two steel plates are bolted to the pyrocutter bracket by two M10 bolts, which also provide clamping for the cable as shown in figure 4.25. After clamping the cable, a sleeve of aluminium/copper will be crimped around the loose end of the cable to prevent slipping.

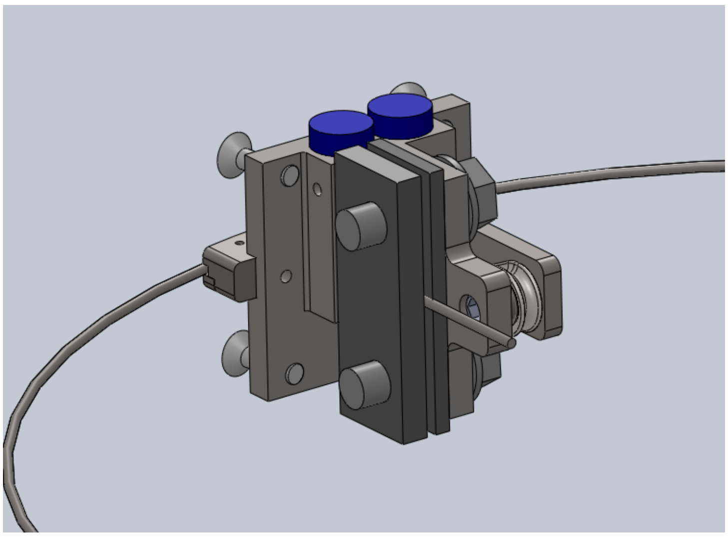

Figure 4.25: Ruffled steel plates clamping the steel cable.

4.5.2.6 Camera

A camera and its protective housing is placed at 90°. The camera housing is mounted onto the cylinder interior via four M5 bolts as shown in figure 4.26.The camera box assembly is form by a hollow rectangular structure and a lid that will be screwed to it. The hollow rectangular structure is attached to the RMU module with four screws from each corner. The lid is attached to the hollow rectangular structure with four screws. The camera will be inserted in the empty volume created between the lid and the skin of the RMU, see figure 4.26.

(a) *Camera front view*

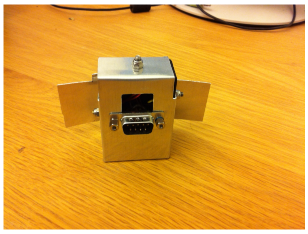

(b) *Camera back view*

Figure 4.26: GoPro Hero 3 camera and camera mount.

4.5.2.7 Umbilical

A five pin umbilical connection is provided between each FFU and the RMU.

The pin type and model used for the male connector is SAMTEC - TSW-106-13-G-S-RA - HEADER. The female connector is TE CONNECTIVITY / AMP - 5535676-5. The male connector is attached to a platform mounted in the middle between the upper and the lower cross of the ejection system and located behind the FFU cage. The female connector is soldered on the top side of the top PCB of the FFU, so it is located along the FFU equator.

The male umbilical is mounted on a platform in the middle of the RMU. The mounting of the male umbilical connector with the platform allows adjustments in the radial direction (with respect to the rocket cylinder). This is achieved by means of "loose" holes for the mounting screws connecting the umbilical PCB to the platform: the pins are adjusted by sliding the umbilical PCB, and then the screws are tightened. The umbilical connection is shown in figure 4.27.

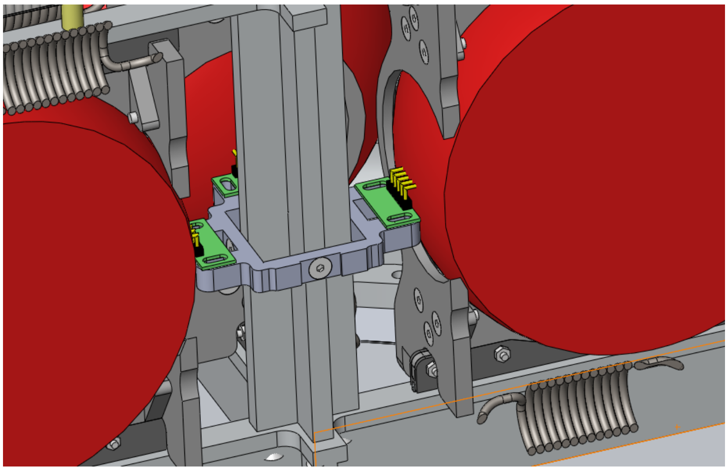

Figure 4.27: Umbilical connection between FFU and RMU.

Since the male umbilical connectors are fixed, the sliding movement of the FFU cage will unplug the male from the female part of the umbilical connector, when the FFUs are ejected.

4.5.2.8 RMU PCB

Most of the RMU electronics will be placed on a PCB in the center of the RMU beneath the ejector module as shown in figure 4.28. Electronics not mounted directly on the PCB are connected by wires running from the PCB to the umbilical connection, the RXSM and the camera.

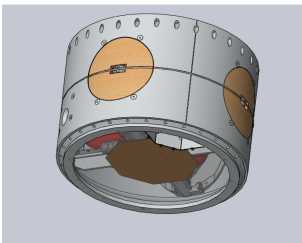

(a) *Placement of the RMU electronics bottom view*

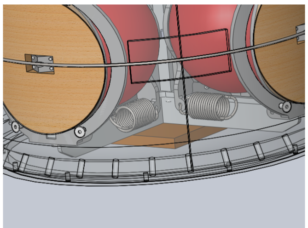

(b) *Placement of the RMU electronics close up*

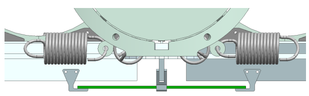

(c) *Placement of the RMU electronics side view*

Figure 4.28: Placement of the RMU electronics

4.6 Electronics Design

Schematics of our electronics design are provided in appendices D.1 to D.5.

4.6.1 FFU

The electrical systems of the FFUs consists of four parts: the GPS-experiment, the localisation system, a data acqusition system and a power system. This is implemented in two different PCBs: top and bottom.

The top PCB consists of the GPS-experiment and localization system, including the antennas. The bottom PCB consists of the data acquisition and power systems. The primary objective of the electrical system is to receive and store raw GPS data. The localization system provides a position and transmits it for retrieval of the probes. A block diagram of the entire electrical system of the FFUs is shown in 4.29. Each FFU has an inbuilt fuse connected in series with the battery. This is an important detail when testing and developing the FFUs. The fuse will be short circuit in the flight version of the FFUs..

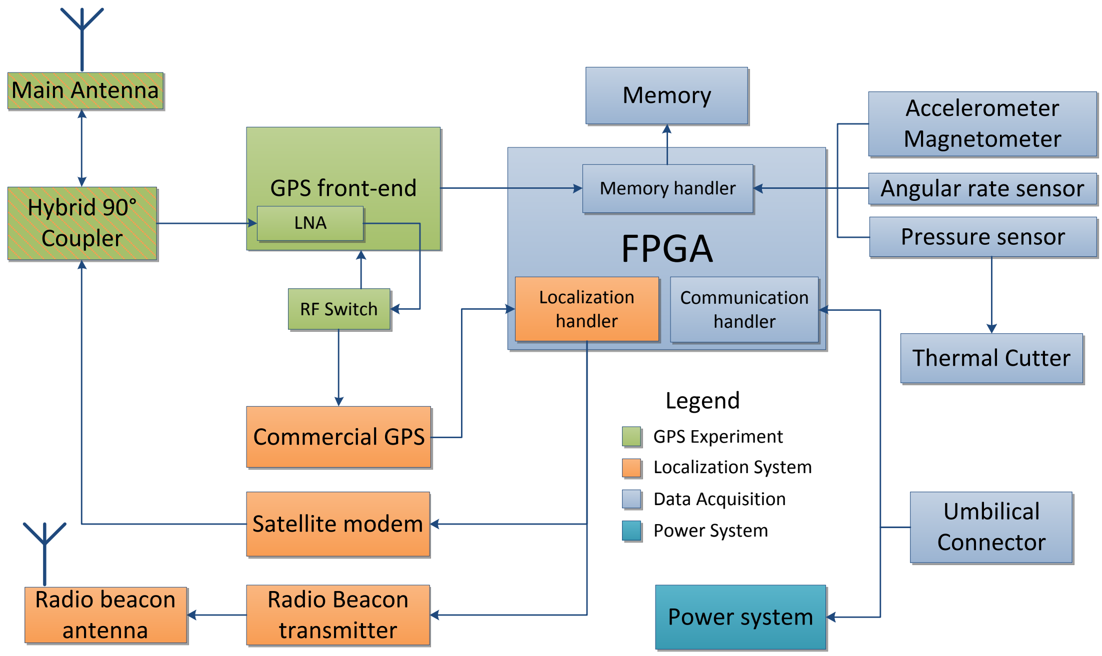

Figure 4.29: Block diagram of FFU electrical system

4.6.1.1 GPS Experiment

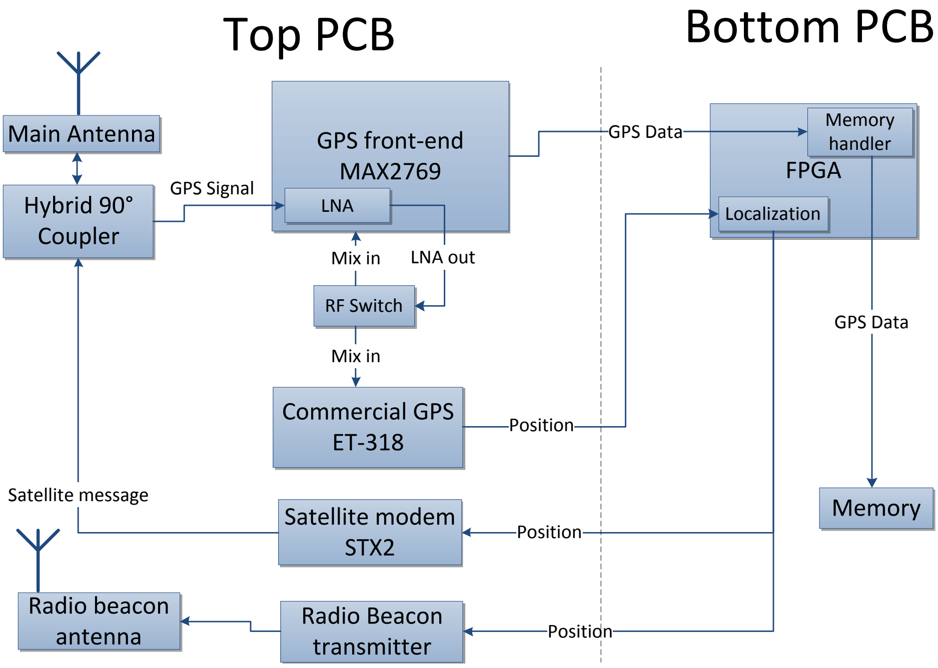

Figure 4.30: Concept diagram of the GPS experiment and Localization system.

To be able to save the raw GPS signal it needs to be filtered, mixed and digitized. This is done in the GPS front-end receiver MAX2769 from Maxim [2]. The GPS signal is first amplified in a LNA (Low Noise Amplifier). This is a typical amplifier for very weak signals and reduces the loss of GPS signal strength in the coming processing. The signal then comes out of the front-end again and is routed through an RF switch of type PE4230 from Peregrine [10]. This switch makes it possible to choose whether to route the signal back into the front-end or to the commercial GPS and is controlled from the FPGA. After the signal is sent back into the front-end, it is mixed down to a desirable IF frequency. This is then sampled and digitized, and sent into the FPGA to be written to the memory.

The MAX2769 GPS front-end is controlled through a 3-wire serial interface: the CS (chip select), SCLK (serial clock) and SDATA (serial data) signals. The settings are contained inside the front-end through 10 serial shift registers, each consisting of a 28 bit word with the MSB (Most Significant Bit) sent first [2]. A 4-bit register address is also transmitted. The transmission protocol is shown in Fig. 4.31.

When the CS signal is put low, the registers are ready to receive new settings. On the rising edge SCLK, a new bit is shifted into the register. When all 32 bits are transmitted, the CS signal is put high again. Out of the 10 available settings 8 are used, the last two are reserved for test mode [2]. The registers are sent with 4 ms distance and only every register is transmitted once per FPGA reset. The settings used are shown in Table 4.7.

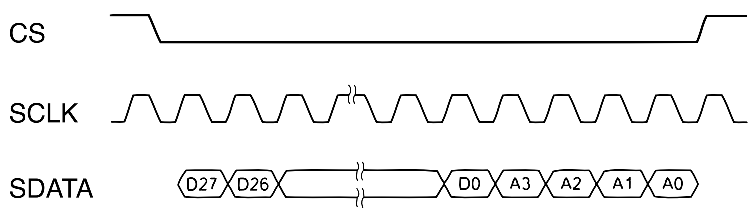

Figure 4.31: Transmission protocol through the 3-wire serial interface of the front-end.

Table 4.7: Register settings in the front-end. Address is in binary and value in hex. With the exception of the LNA1 port selection, these settings are ported from RAIN [7].

Adress	Value	Description
0000	A295563	Activates LNA1, a 5th order LP filter with a double-sided bandwidth of 4.2MHz
0001	0550288	Selects only the I-channel with 2-bit resolution where MSB is polarity and LSB magnitude
0010	D6FE1DC	Disables DSP-interface
0011	9CC0000	f_{samp} is set to $f_{TCXO}/2$. IF frequency is set to be calculated with fractional PLL.
0100	0180010	$N_{DIV} = 96$ and $R_{DIV} = 1$.
0101	0FE0070	$F_{DIV} = 99584$
0110	8000000	Default, only used with DSP-interface.
0111	10061B2	Default, only used with DSP-interface.

4.6.1.2 Localisation System

After parachute deployment, the RF-signal is rerouted from the front-end to a commercial GPS chip through the RF- switch. This commercial GPS is of type ET-318 from GlobalSat [3]. This out of the box GPS chip can after fast setup acquire a position of the FFU and send this to the FPGA. The position is then sent through a satellite modem of type STX2 from Axonn [4]. The STX2 can send short messages of up to 9 bytes to the Globalstar service. These messages can then be viewed online by logging in with an account to which the unique ID of each chip has been registered. A radio beacon transmitter of type TX1 from Radiometrix also transmits the acquired position modulated into it's HF signal at approx 170MHz [11]. The TX1 transmitter chip is used with it's own antenna. This makes it possible to take a bearing on the FFU when using a directed receiver antenna at the same frequency. While the FFU is in recovery phase, the position of the commercial GPS is modulated into the beacon signal for redundancy purposes. When in the low power phase, only the carrier wave is transmitted.

4.6.1.3 Sensors and Data Acquisition

A FPGA is the central control unit in the FFU. It controls all subsystems and will be recording the data during flight into a non-volatile memory. An ADC with inbuilt multiplexer will be used to cycle through different analog signals to monitor. This includes currents and voltages in the FFU for housekeeping and testing purpose. The sensors that we will use are a 3-axis digital accelerometer with magnetometer, a 3-axis digital angular rate sensor and an analog pressure sensor. The conceptual diagram of the system is shown in figure 4.32.

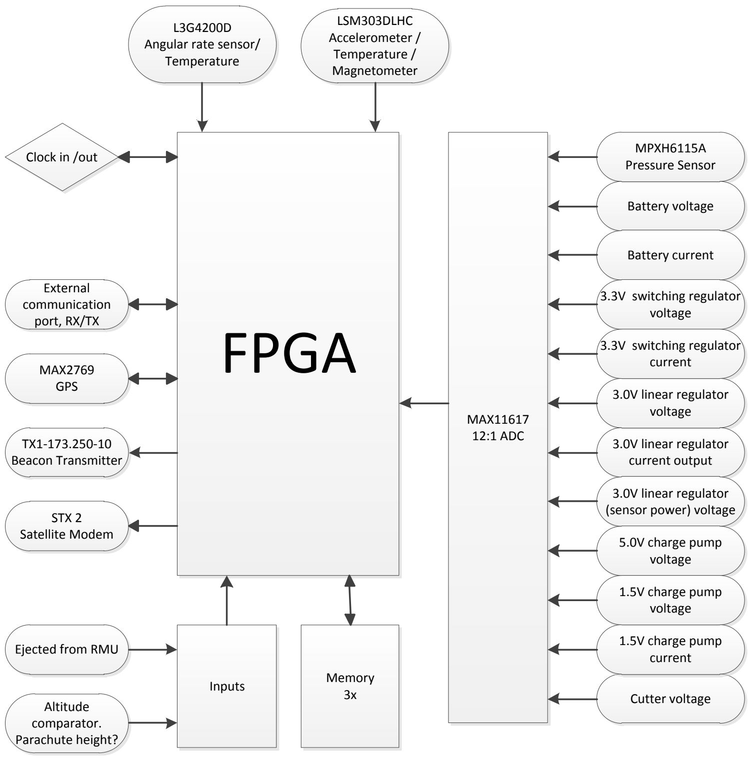

Figure 4.32: Conceptual diagram of the data acquisition system

4.6.1.3.1 ADC

The MAX11617[12] is an analog to digital converter with inbuilt 12:1 MUX. It has 12 bit resolution and is digitally controlled over I^2C. This particular ADC has a very low power consumption which is a good feature in our project. The ADC can be configured to cycle through all the inputs and sample the voltages to digital values. The ADC features an internal voltage reference when calculating the digital representation of the measured signal. The voltage reference is 2.048 V.

Some signals measured have a too high voltage. They are thus connected to the ADC through a resistor voltage divider. The gain factor corresponding to each channel is described in table 4.8.

Table 4.8: ADC channel input gain adjustments

Channel	Measure	Gain factor
0	THE_PRESSURE	2/5
1	V_BAT_MON	1/2
2	V_I_BAT_MON	1
3	V_1.5V_MON	1
4	I_1.5V_MON	1
5	V_5V_MON	5/14
6	V_CUTTER_MON	1/2
7	V_3.3V_MON	1/2
8	I_3.3_MON	1
9	V_3V_SENS_MON	1/2
10	V_3V_MEM_MON	1/2
11	I_3V_MEM_MON	1

The transfer function for the ADC is 1 $LSB = (VREF/2^N)$ [V], where N is the number of bits = 12.

1 LSB = 2048/4096 mV=0.5 mV.

4.6.1.3.2 Pressure Sensor

The pressure sensor is manufactured by Freescale Semiconductor and the specific model is MPXH6115A6U[13]. This is an analog pressure sensor with the measuring range of 15 to 115 kPa. The sensor is connected to the first input on our ADC through a voltage divider.

The transfer function of the pressure sensor is $V_{out} = V_S \cdot (0.009 \cdot P - 0.095) \pm E$, where P = the pressure, V_S = supply voltage = 5.0 V, V_{out} = output voltage from pressure sensor, E = error term specified in datasheet [13].

4.6.1.3.3 Current Sensors

For current monitoring of the electronics, dedicated current monitoring ICs have been used from MAXIM. The reason for using these chips instead of making our own current sensing circuit with operational amplifiers is that this is more accurate. They require smaller space on the PCB, fewer additional components and their price was quite low which makes it a convenient solution.

MAX9929F[14] is a bidirectional current monitor used for measuring the battery current. It has a voltage output that is linear to the current measured.

There are two versions of this current monitor IC available, MAX9928[14] and MAX9929. The first one (MAX9928) has a current output. The second one (MAX9929) has a voltage output. The schematic as in figure 4.33 has been designed to work with both versions of the current sensing IC. When MAX9929 with voltage output is used, R14DC shall not be soldered to the PCB.

When MAX9929 is used it works as a voltage amplifier with the gain $A_v = 50\ V/V$. The voltage is measured across a $\frac{4}{300}\Omega$ (three 0.04 Ω resistors in parallel) shunt resistor.

From this the current can be calculated according to equation 4.6. With the chosen shunt resistor and the given gain the current can be read out as the voltage measured on I_BAT_MON times 3/2. The gain accuracy is specified to 1.0%.

$$I_{bat} = \frac{(I\_BAT\_MON)/50}{4/300} = \frac{3}{2} I\_BAT\_MON \tag{4.6}$$

As the current monitor is bidirectional it can measure current in both directions. The voltage output is though always positive so a current direction output is available on the IC. The direction output is in our design connected to a LED (D1DC) that will light up when current is going into the battery. This indicates that the battery is charging. The current direction output is also connected to the FPGA.

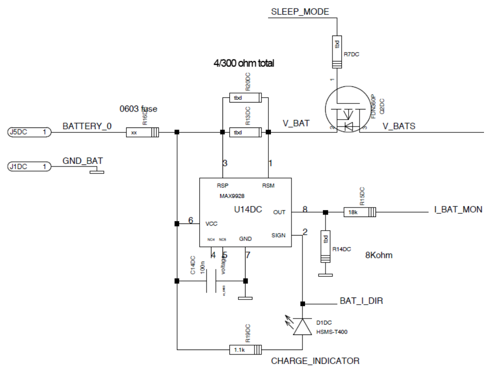

Figure 4.33: Battery current monitor with charge indicator

When measuring unidirectional currents, MAX4372F[15] current monitors have been used. We have a total of three of these on our bottom PCB. These currents monitors do also have a voltage output like MAX9929 with the gain $A_v = 50\ V/V$. The accuracy is stated to be 0.18 %.

They do all measure the voltage across a shunt resistor but in this case they have other values.

The current for the satellite modem is calculated from the voltage drop measured across R18DC=0.04 Ω:

$$I_{STX2} = \frac{(I\_3.3V\_MON)/50}{0.04} \tag{4.7}$$

The current for the FPGA core is calculated from the voltage drop measured across R21DC=0.68 Ω:

$$I_{FPGAcore} = \frac{(I\_1.5V\_MON)/50}{0.68} \tag{4.8}$$

The current for the memories is calculated from the voltage drop measured across R24DC=0.68 Ω:

$$I_{memory} = \frac{(I\_3V\_MEM\_MON)/50}{0.68} \tag{4.9}$$

4.6.1.3.4 Angular Rate Sensor (Gyroscope)

The gyro, L3G4200D[16], uses the I^{2}C communication protocol. It has 16 bits resolution and high shock survivability and is ultra-stable over temperature and time. That was some of the key features that made us choose this particular sensor. It has a selectable measure range of ±250/±500/±2000 dps and a selectable bandwidth of 100/200/400/800 Hz. The sampling rate can be set to 100/200/400/800 Hz. The gyro is configured by changing values in the sensors register. To enable the sensor and all axis the CTRL_REG1 is set to 00100000. The scale is set to ±2000dps by changing CTRL_REG4 to 00100011. The remaining settings is default. Output data rate is 100 Hz and bandwidth is 12.5 Hz. More details can be can be found in the datasheet[16].

4.6.1.3.5 Accelerometer

The 3D accelerometer, LSM303DLHC[17], has a resolution of 12 bits per axis and can acceleration from -16 g to +16 g. It has also an inbuilt 3D magnetometer to detect the orientation and an inbuilt temperature sensor. The temperature sensor is not needed in the experiment but can be used for temperature compensation of the sensor according to the datasheet [17]. The bandwidth can be adjusted between 1-5376 Hz. The sampling rate for the accelerometer can be set to 1/10/25/50/100/200/400 Hz. The sampling rate for the magnetometer can be set to 0.75/1.5/3.0/7.5/15/30/75/220 Hz.

To configure the sensor register values are changed. The register CTRL_REG1 is changed to 01100111. This makes the sensor use 200 Hz output data rate and enables all three axis. The remaining accelerometer settings are default. This means range is ±2 g and bandwidth 22.2 Hz. The magnetometer is set to continuous conversion mode by editing the register MR_REG_M to 00000000. The rest of the setting is default and can be viewed in the datasheet[17] among other details.

4.6.1.4 Thermal Cutter

To deploy the parachute, the fishing line holding the upper hemisphere will be cut off by a thermal cutter. The output of the pressure sensor is compared to a reference voltage (defined in hardware by a resistor divider) by a comparator. The logic output of the comparator (high when the pressure is below the threshold) is provided to the FPGA. An output is activated by the FPGA logic a pre-defined time after the pressure increases above the threshold. The output controls a MOSFET switch powering the thermal cutter from the battery. The fishing line is cut by heating a metal wire which is touching the fishing line. The metal wire is connected in series with current limiting 1.3 Ohm resistance. The wire and resistors are connected to the battery through the MOSFET, and will draw 2.0-2.5 A. The time before the line is cut is approximately 3-4 s according to Appendix B.3.

4.6.1.5 Main antenna

The main antenna was designed to receive GPS signals at 1575.42 MHz with right hand circular polarization and transmit signals at 1615 MHz with left hand circular polarization. The center frequency of the antenna was chosen to be 1.597 GHz, with a fractional -10 dB return loss bandwidth of 3%. The antenna was designed to match to 50 Ω. After careful consideration (appendix G.2) the antenna built and used in the FFUs is a circular patch antenna with two feeds connected to a 90 degree hybrid coupler. The antenna was designed using analytical methods from Antenna Theory Analysis and Design by Constantine A. Balanis [18] and optimized using Computer Simulation Technology [19].

Patch antennas are generally quite narrowband. In order to increase the bandwidth of the antenna a substrate, ROHACELL 31, with a dielectric constant of $\epsilon_r \approx 1$ at 2 GHz was used. The substrate was available at KTH and it had a height of 9 mm. Furthermore two feeds were used, placed symmetrically around the center since that arrangement decreases losses [20]. In figure 4.34 one can see how the model looked like in CST. The circular patch we ended with had a radius of 47 mm. A 0.035 mm FR-4 layer was used as a support structure for the patch, beneath that the 9 mm ROHACELL 31 was placed and finally a ground plane was placed under the substrate that is the same size as the top PCB in the FFU. The feeds of the antenna were placed 22 mm from the center. The antenna was simulated with all disturbing objects around and also with the sphere on top.

In figure 4.34 one can see the final model used to simulate the antenna without the sphere. With the sphere on top the center frequency became lower, which made the signal better for receiving GPS signals. In figures 4.34 and 4.35 the simulation results without sphere can be seen.

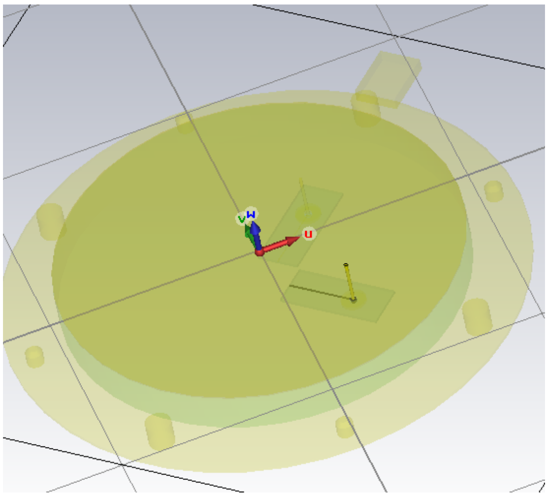

(a) *The final CST model of the circular patch antenna*

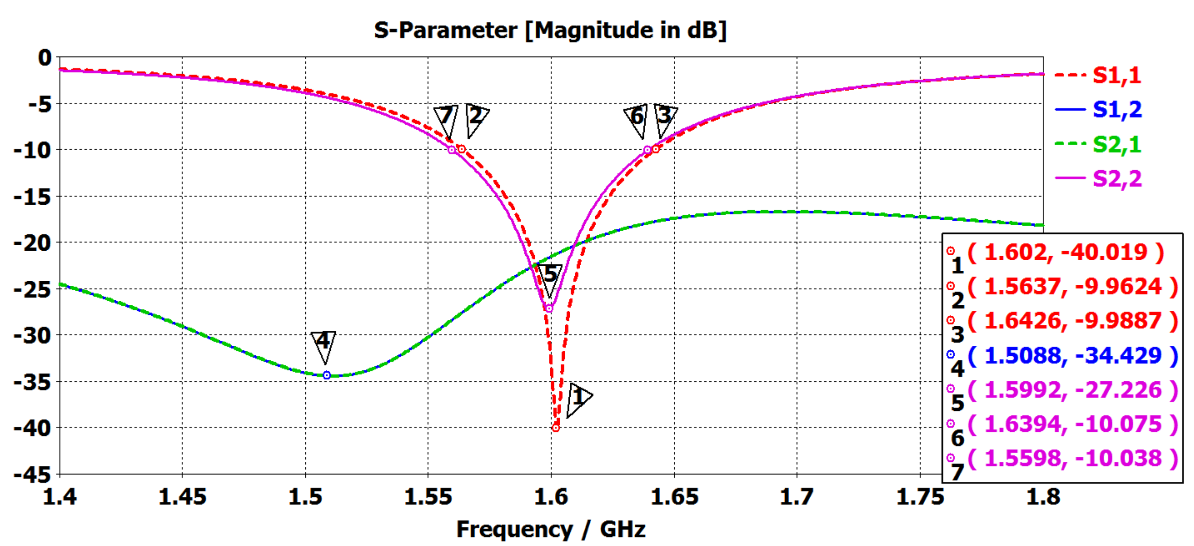

(b) *The s parameters of the simulated antenna*

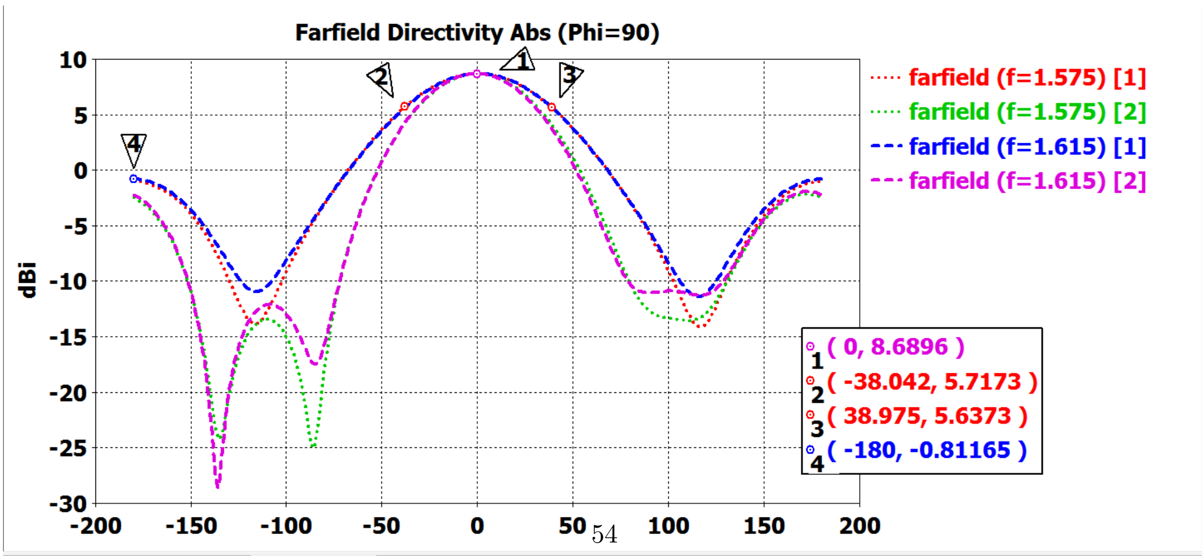

(c) *The directivity of the simulated antenna*

Figure 4.34: Simulations in CST

As can be seen from figures 4.34 and 4.35 the results for 1.575 GHz and 1.615 GHz are quite good. The antenna has according to the simulations a fractional -10 dB return loss bandwidth of ca. 5%. The halfpower beamwidht is around 80 ° and the axial ratio is less than 3 dB for the halfpower beamwidth of the simulted antenna.

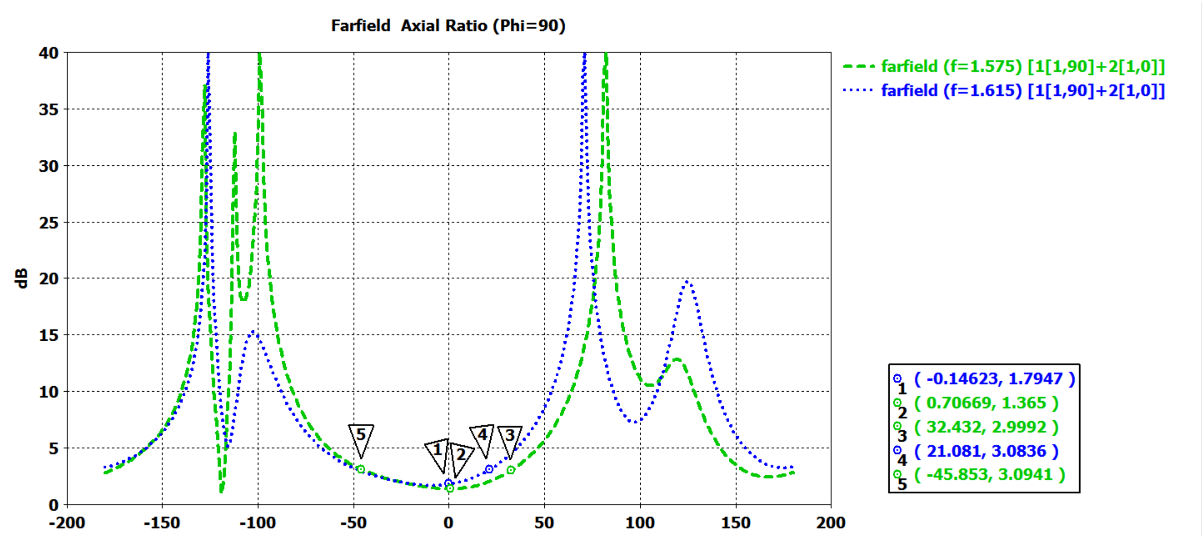

(a) *The Axial ratio of the simulated antenna for left hand circular polarization for both frequencies. The 3 dB points are marked*

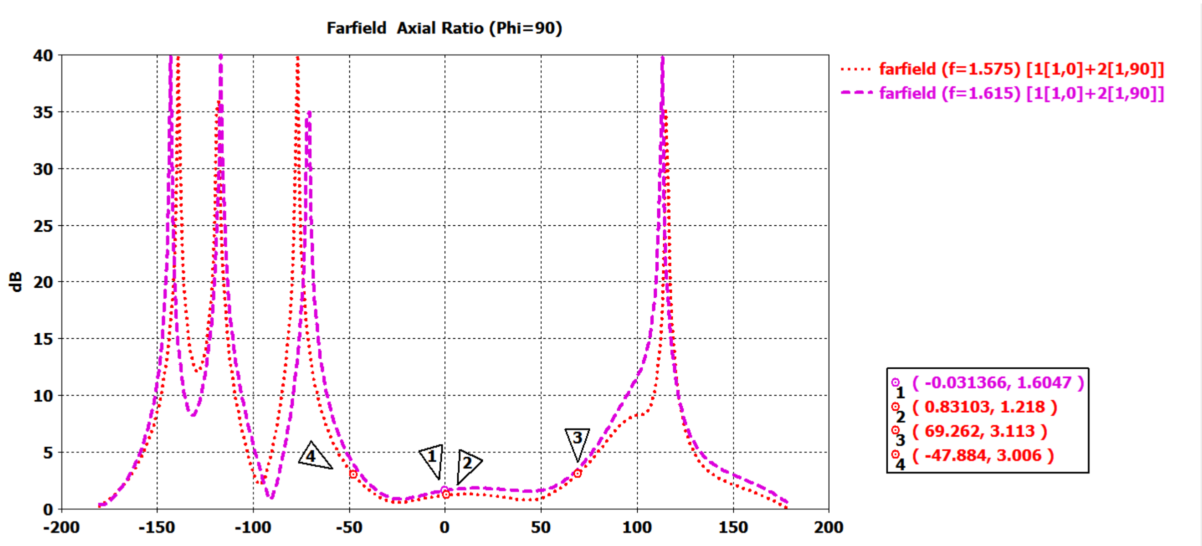

(b) *The Axial ratio of the simulated antenna for right hand circular polarization, for both frequencies. The 3 dB points are marked*

Figure 4.35: Simulations in CST continued

The hybrid coupler was designed using AWR environment and then it was simulated using CST. The dimensions of the hybrid coupler can be seen in figure 4.36a. The thickness of the hybrid coupler is 0.035 mm and it is sandwiched in between FR-4 layers in the PCB, which in turn are sandwiched between two ground planes in the top PCB. From the figures one can see the lengths and widths of the coupler, where the dimensions are the same on both figure a and b.

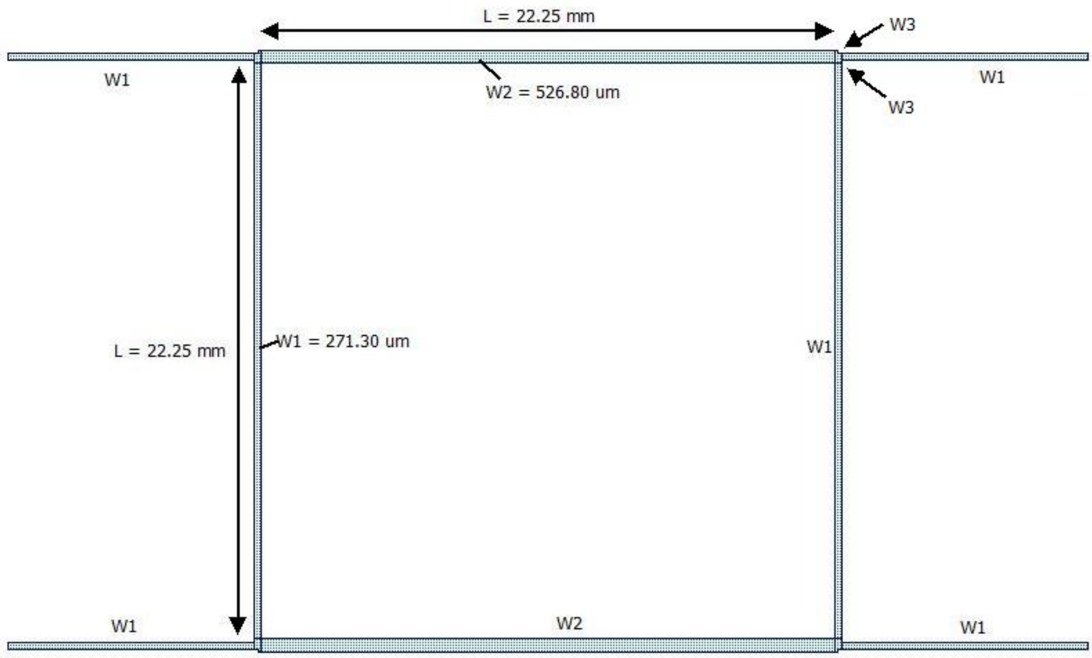

Figure 4.36: The hybrid coupler, where $W3 = \frac{W1-W2}{2}$

A test antenna was built using fake cones and eyebolts made of aluminum rods cut to the same height as the real eye bolts and cones will have. This was done because the cones and eyebolts had not arrived in March when the tests and measurements of the antenna were made. The test antenna consisted of the patch, the substrate, ground plane and the hybrid coupler.

First the S_{21} parameter of the antenna was measured in order to gain information about the bandwidth of the antenna. This was done with a Vector Network Analyzer using SMA connectors connected to both input ports of the hybrid coupler. The measurement results can be seen in figure 4.37 b. The axial ratio was measured using a robot and a horn antenna. The main antenna was the receiving antenna. One input port of the antenna was connected to the vector network analyzer which was connected to a computer while the other port was terminated with 50 Ω impedance. The horn antenna was designed for higher frequencies and it was almost at it's cut off at the frequencies we were looking at, so it transmitted a very weak signal. The measurement results for 1.6 GHz can be seen in figure 4.37.

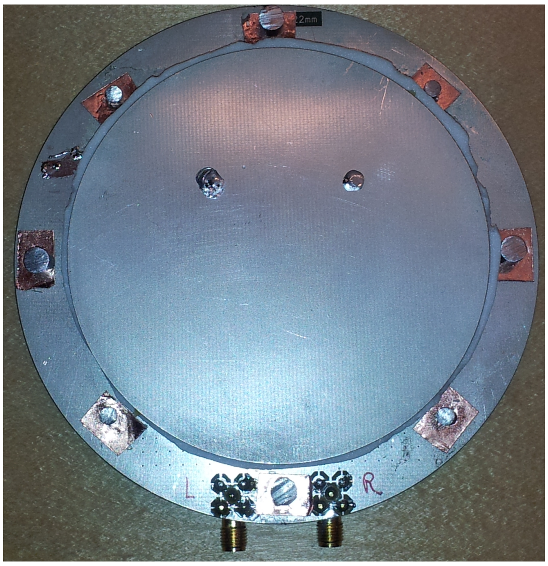

(a) *A built antenna for tests*

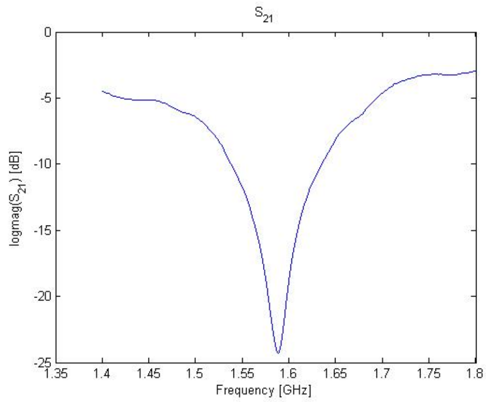

(b) S_{12}*-parameter measurement of the hybrid coupler and the antenna*

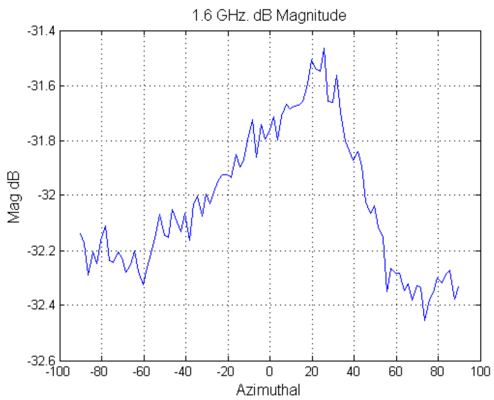

(c) *Axial ratio of the test antenna when connected to the port for RHCP*

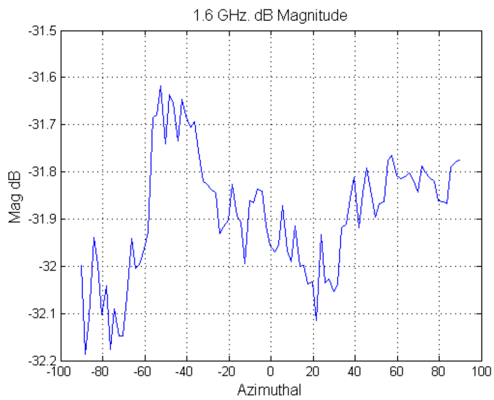

(d) *Axial ratio of the test antenna when connected to the port for LHCP*

Figure 4.37: Measurements of the antenna

As can be seen from figures 4.37b-d the fractional -10 dB return bandwidth is 6.3 %. Furthermore the half-power beamwidth is 70° which is OK for our purpose, but it could be better. The polarization as can be seen from figure 4.37 is very circular, the axial ratio is 1 dB for RHCP and 0.6 dB for LCHP.
Finally the antenna was tested in the drop test. The STX could send out messages that was received by Global Star satellites and the commercial GPS was able to get a position fix.

4.6.2 RMU

The RMU electronics is based on the RAIN RMU but is expanded to be able to communicate with four FFUs, comparing to RAIN that only used two. Figure 4.38 shows a conceptual diagram of the electronic system.

Inside the RMU the RS-422 signals levels are converted to standard LVTTL which are then connected to a

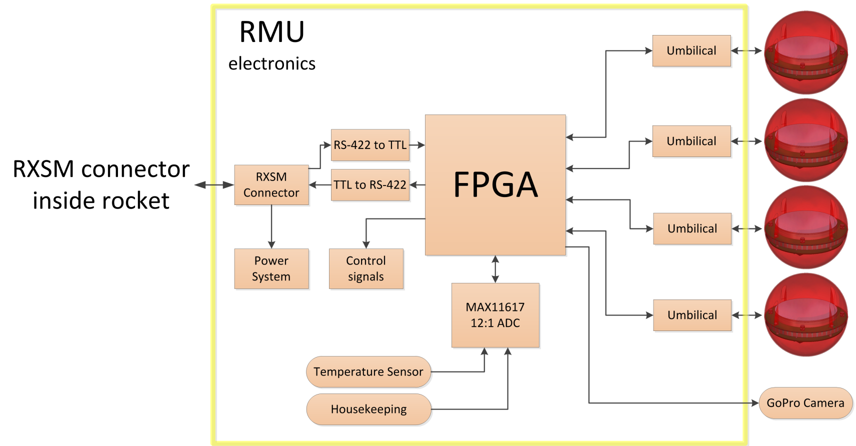

Figure 4.38: Conceptual diagram of the RMU electronics design

FPGA. The FPGA inside the RMU will work as a data switch. The schematics of the RMU electronics are in progress and preliminary schematics can be found in appendices D.6 to D.8.

4.6.2.1 FPGA

The RMU contains an FPGA in order to communicate with the FFUs. The status of the FFUs is sent to the RXSM which will then transmit to the ground via telemetry. The aim of this is for us to be able to supervise FFU functionality up until their ejection from the rocket. The RMU FPGA controls the RMU data acquisition system and the camera. The RMU IS also able to send commands to the FFUs, such as putting them in mission mode.

4.6.2.2 Data Acquisition system

The RMU have an inbuilt housekeeping system keeping track of voltages and inside temperature in the RMU. The same type of ADC will be used as in the FFUs to convert analog signals to digital values. The circuit will not contain any memories for saving data but can instead be read out in real-time using the RXSM connection.

4.6.2.3 Camera

The RMU also contains a camera that is used to observe the ejection of the FFUs. The purpose of this is to verify that the FFUs have been ejected properly and for calculation of ejection speed. This camera uses the same power supply as RMU electronics and is down converted with a linear regulator to 4.1 V.

The RMU camera is placed on the inner skin of the rocket looking out through a hole. The RMU FPGA is used to switch the camera on. The camera is an HD Hero camera manufactured by GoPro, which is intended for use in rugged conditions. The camera will be modified so that it can be securely fastened to the rocket module with a case developed by SQUID. During launch the part of the camera looking out through the rocket wall is exposed to high temperatures that could possibly destroy the camera. To ensure survival during launch a small window protecting the camera lens from the outside environment will be placed in between the rocket cylinder and the camera lens.

The camera recording is initiated shortly before launch of the rocket and is switched off after the rocket has landed. All recorded footage is saved on a 32GB SD card that will be salvaged for post-flight analysis after the RMU returns.

4.6.2.4 Turning the MUSCAT Experiment Off

Powering down the RMU puts FFUs to sleep mode. They can be put to sleep mode by a command to RMU even while the RMU is powered.

4.6.2.5 Ejection System

The ejection is controlled by Eurolaunch. The pyrocutter is activated by the current supplied from the RXSM. It will cut the steel constraint cable, which will in turn release the springs from their elongated state, ejecting the FFUs out of the rocket. The FFUs will be ejected from the rocket before the de-spinning of the rocket.

4.7 Power System

There are two power systems, one of the FFU and another of the RMU

4.7.1 FFU

When the FFUs are mounted in the rocket the batteries are recharged by the RMU through the umbilical connections. After the FFUs have been ejected they depend on the internal batteries for providing power to the electrical components. The power system in each FFU primarily consists of a rechargeable lithium-ion battery and voltage regulators. The required voltages for full functionality of the FFUs are 1.5 V, 2.8 V, 3.0 V, 3.3 V and 5 V. To minimize distortion in collected data, LDO regulators are used for the ADC, GPS frontend, memories, antenna switch and digital sensors (accelerometer, gyro/magnetic sensor). The ADC, memories and digital sensors run on 3.0 V while the GPS frontend and antenna switch run on 2.8 V. The pressure sensor and some operational amplifiers are powered by a charge pump regulator since they require 5.0 V supply and low current. Switching regulators provide power for the commercial GPS as well as the satellite modem. A charge pump regulator is used to supply 1.5 V to the FPGA core. Figure 4.39 illustrates which components are active during each phase of the experiment.

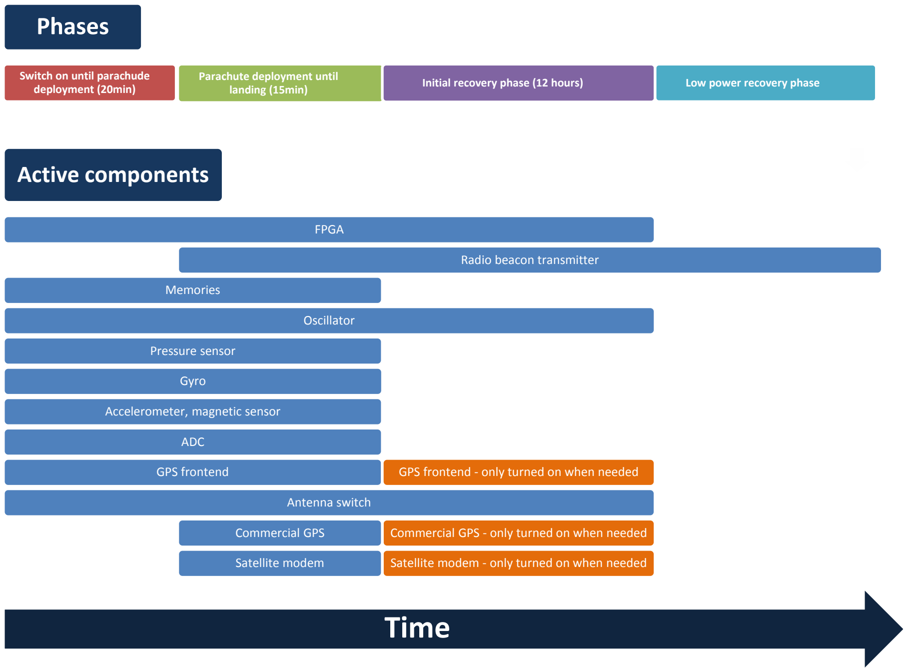

Figure 4.39: Flowchart of active system

4.7.1.1 Blocking of Transmitters and Cutter While Inside the Rocket

As a precautionary measure all transmitters and the cutter are shut off while the FFUs are mounted in the RMU, this is called rocket mode. This is implemented with a pin in the umbilical connection, called ROCKET. When the ROCKET pin is connected it prevents the FPGA from powering the satellite modem, radio beacon and the cutter.

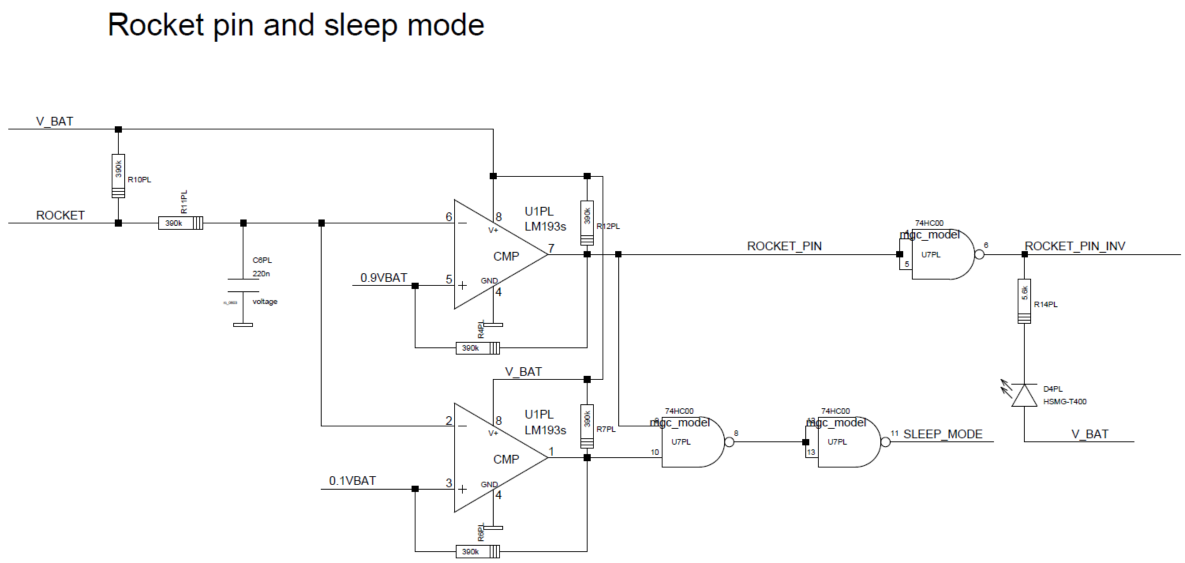

Figure 4.40: Circuit diagram of rocket pin and sleep mode

4.7.1.2 Sleep Mode and Rocket Mode

The FFUs are in the rocket mode when the umbilical connection is engaged. To deactivate the whole experiment (all the FFUs), sleep mode can be initiated. When sleep mode is initiated, power is switched off to all electrical components inside the FFU except for the logic circuits. This means that the FFUs will be almost fully deactivated.

Sleep mode and rocket mode are enabled through the umbilical link which has a dedicated pin (ROCKET) for these modes. It is implemented with comparators and logic ICs to enable or disable the modes based on the voltage on ROCKET pin. The circuit diagram of rocket pin and sleep mode is illustrated in Figure 4.40.

If the ROCKET voltage is pulled down to ground by the RMU, sleep mode and rocket mode will be enabled. If the ROCKET voltage is set to half the battery voltage by the RMU, only rocket mode will be enabled. If the ROCKET voltage is set to battery voltage both rocket mode and sleep mode will be disabled. If the ROCKET voltage is left floating an internal pull-up will force the ROCKET voltage to battery voltage. This also prevents the sleep mode or rocket mode from accidentally being enabled after ejection. Since the ROCKET mode must be enabled while the FFU is in the RMU the RMU was designed so that it cannot set the ROCKET voltage to battery voltage. The RMU was also designed so that the FFUs will enter sleep mode if the FPGA in the RMU is powered down. This implementation guarantees that the FFU transmitters and cutters are disabled by the rocket mode when the FFU is in the RMU. It also makes it possible to shut off all components in the FFU except the logic, either by command or by powering down the RMU. Table 4.9 shows the voltage level configuration of the ROCKET pin for the different modes.

ROCKET voltage	Rocket mode	Sleep mode
Battery voltage	Disabled (off)	Disabled (off)
Half the battery voltage	On	Off
Ground	On	On

Table 4.9: ROCKET voltage level configuration

4.7.1.3 Power Budget

The purpose of the power budget is to estimate the capacity needed for battery. Figure 4.39 illustrates which components are active during each phase of the experiment.

Tables 4.10, 4.11 and 4.12 estimate the energy consumption during three of the four phases of the experiment: switch-on until parachute deployment, parachute deployment until landing and initial recovery phase. The last phase is a low power recovery phase, which shall last until the battery dies and is therefore not included in the power budget.

Component	**1.5 V**	**2.8 V**	**3.0 V**	**5.0 V**	**Duty factor**
FGPA	10 mA		25 mA		100%
Memories			45 mA		100%
Pressure sensor				6.0 mA	100%
Gyro			6.1 mA		100%
Accelerometer, magnetic sensor			0.11 mA		100%
A/D converter			0.9 mA		100%
GPS frontend		15 mA			100%
Antenna switch		0.029mA			100%
Total mean current	10 mA	15 mA	77 mA	6.0 mA	
Energy consumed (20 minutes)	5.0 mWh	14 mWh	77 mWh	10 mWh	

Table 4.10: Energy consumption from switch-on until parachute deployment

Component	**1.5 V**	**2.8 V**	**3.0 V**	**3.3 V**	**5.0 V**	**Duty factor**
FGPA	10 mA		25 mA			100%
Memories			45 mA			100%
Pressure sensor					6.0 mA	100%
Gyro			6.1 mA			100%
Accelerometer, magnetic sensor			0.11 mA			100%
A/D converter			0.9 mA			100%
GPS frontend		15 mA				100%
Antenna switch		0.029 mA				100%
Commercial GPS				40 mA		100%
Satellite modem				500 mA		1%
Radio beacon transmitter			9.5 mA			100%
Total mean current	10 mA	15 mA	86 mA	45.00 mA	6.0 mA	
Energy consumed (15 minutes)	3.8 mWh	10 mWh	64 mWh	37 mWh	7.5 mWh	

Table 4.11: Energy consumption from parachute deployment until landing

Component	1.5 V	2.8 V	3.0 V	3.3 V	Duty factor
FGPA	10 mA		25 mA		100%
GPS frontend		15 mA			100%
Antenna switch		0.029 mA			100%
Commercial GPS				40 mA	10%
Satellite modem				500 mA	1%
Radio beacon transmitter			9.5 mA		100%
Total mean current	10 mA	15 mA	35 mA	9 mA	
Energy consumed (12 hours)	180 mWh	505 mWh	1242 mWh	356 mWh	

Table 4.12: Energy consumption during initial recovery phase

4.7.1.4 Battery Selection

After discharge tests at low temperatures (Appendix E) the lithium-ion battery Saft MP 144350 [21] was chosen due to its high capacity at low temperatures. The capacity for the battery is approximated from the test data to 6.2 Wh at -30°C. According to the power budget approximately 2.5 Wh are consumed by the FFU after ejection until low power recovery phase, this means that as long as the total efficiency for the voltage regulation is above 50% the battery should have enough capacity to last for 24 hours at the temperature -30°C.

4.7.2 RMU

The power supply from the RXSM is going to be used by both the RMU and the FFUs during the experiment. The "+28 V" will be used to power the RMU's circuitry and camera. The "28 V Charging Power" from the RXSM will be used to recharge the battery of each FFU while they are still contained in the RMU. Separate 4.2 V regulators will be used to charge the batteries, so that if one regulator would fail the other FFUs would not be affected. The power lines between the RMU and each FFU will be fused to prevent damaging the batteries, rocket or FFU.

4.8 Firmware Design

The firmware is written in VHDL using a development environment called "Libero Project Manager" provided by Actel. The code is programmed into the FPGAs and thereby controls all the functionalities in the FFUs and RMU. The main parts of the code are the memory handling and data acquisition from the GPS and the sensors. Furthermore, the different phases described earlier are detected and activated using the firmware. The firmware in the FFUs consists of many code modules connected together. Figure 4.41 shows a simplified concept of how the data acqusition system works in the FPGA. All sensors and data sources are connected to a packet MUX that switches the MUX output to the correct input. The output from the MUX is sent to a memory buffer which buffers the data. When the buffer is full it writes the data to the memory module which is connected to the physical memory. When the memory is full, a switch will change so that data is written to another memory. The design have 3 memories in total. Schematics of the firmware design can be found in appendix F.1.

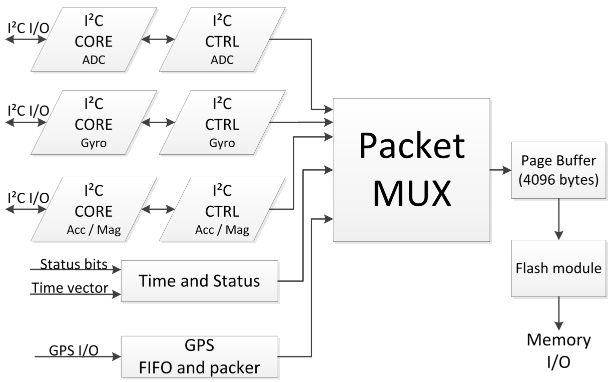

Figure 4.41: Conceptual diagram of the firmware of the data acquisition system

4.8.1 Timing

The system is synchronized by an FPGA global clock vector displayed in Table 4.13. The highest frequency, 32.768 MHz in m_time(0), is generated from the external oscillator. For every next step in the vector the frequency is divided by two down to 250 Hz at m_time(17). A 8 bit counter with roll over at 250 is then clocked from m_time(17) which creates the rest of the time vector. Because the 8 bit counter has a roll over at 250, the most significant bit will change at 1 Hz rate which is the 25th element in the m_time vector. All the processes are run and timed from this clock vector allowing the system to do different tasks but still be synchronized.

Table 4.13: Time vector

System clock vector		Description
M_TIME[0] =	32.768 MHz	Oscillator frequency
M_TIME[1] =	16.384 MHz	Memory
M_TIME[2] =	8.192 MHz	
M_TIME[3] =	4.096 MHz	Read clock from buffer to memory IC
M_TIME[4] =	2.048 MHz	
M_TIME[5] =	1.024 MHz	
M_TIME[6] =	512 kHz	
M_TIME[7] =	256 kHz	I²C Core and Controller
M_TIME[8] =	128 kHz	
M_TIME[9] =	64 kHz	
M_TIME[10] =	32 kHz	
M_TIME[11] =	16 kHz	
M_TIME[12] =	8 kHz	
⋮	⋮	
M_TIME[25] =	1 Hz	

4.8.2 Communication

The FFU has two connections for communication and battery charging. One is the umbilical connector on the top board. The umbilical connection is used when the FFU is mounted in the RMU. The other connector is a pin header located on the bottom side of the bottom PCB. It is used for reprogramming the FPGA with new firmware, charging the battery and data connection. The pinout is given in table 4.14.

Table 4.14: Bottom connector

Pin #	Pin name	Description
1	JTAG_TCK	Programming pin
2	GND	Ground
3	JTAG_TDO_M	Programming pin
4		not used
5	JTAG_TMS	Programming pin
6	VJTAG	Programming pin
7	V+3.3_OSC	Programming pin
8	TRST	Programming pin
9	JTAG_TDI_M	Programming pin
10	GND	Ground
11	V_BAT	For battery charging
12	GND	Ground
13	UART_RX	Serial communication from computer/RMU
14	UART_TX	Serial communication to computer/RMU
15	UART_USB_BUFFER	RTS signal from Serial port
16	GND	Ground

Data readout is done using the pin header on the bottom PCB. This can also be done with the umbilical connector but at a much lower data rate. The standard speed for communication in the FFU is set to 38400 Band with one stop bit and no flow control. The umbilical connector does not have a flow control pin that is required for high speed readouts. However, by pressing the command 'T' the FFU is switched to turbo mode and the bottom header can be used for high speed read outs. Data rates up to 2MBits can then be achieved. Communication with the FFU is done using a USB to serial adapter based on the FT232 chip[22] and a terminal software with logging capabilities.

4.8.3 Commands in test mode / mission mode

Commands can be sent to the FFU from a computer using a serial port to switch between two operational modes. The default mode when power on a FFU is test mode. In test mode commands can be sent to the FPGA to switch on and off voltage regulators, change states and read/erase memory. The defined commands are given in table 4.15. Some commands are very critical. To access these, two buttons needs to be pressed in correct order. The memory erasing for example is only executed after the command sent is 'J' followed by 'Q'. This is a safety feature to avoid accidental memory erasing.

From test mode one can enter the second mode called mission mode. Mission mode is what will be used during the actual rocket launch. In mission mode all commands are disabled and the FPGA waits for the FFU to be ejected from the rocket. When it is ejected the data acquisition starts.

To deactivate mission mode the FFU needs to be reset. Reset can be done either by short circuiting the reset pins on the bottom PCB or by setting the FFU in deep sleep mode for a second.

4.8.4 Mission mode phase initiation

The different phases of the mission mode are described in figure 4.39. The first phase starts when the FFUs are ejected from the RMU and is trigged by the ROCKET_PIN in the umbilical connection. The second phase is initiated when the pressure sensor senses a pressure corresponding to an altitude of approximately 5 km. The third phase is initiated by a timer 15 min after the second phase is initiated. The fourth phase depends on the battery voltage. When is drops below a threshold value the phase is initiated.

Table 4.15: Commands for FFU

Command	**Description**	**Note**
JN	Enable memory saving	Toggle command
JQ	Erase memory	
Ji	Start mission mode	
a	Read out from memory	Toggle command
F	Read out the current memory address	
R	Rewind memory	
T	Toggle Turbo mode	Toggle command. After toggled, FFU is set to turbo mode. This enables high speed readout.
S	Enable STX2	Toggle command
s	Sensors and memory power	Toggle command
L	3.3 V switched power regulator enable /disable	Toggle command
C	Cutter engage	Toggle command
G	GPS frontend power	Toggle command
P	Pressure sensor and comparator power	Toggle command
g	GPS commercial awake	
B	Beacon power	Toggle command

4.8.5 Memory Packets

The data that is collected from all the sensors on-board is written to the memory in packets. Each packet contains 8 bytes. There are eight different kind of packets as described in TABLE 4.16. To be able to separate the different packets from each other identification bits have been implemented. The first two bits in the packet describe what it contains and the rest of the bits are packet type specific. The bits that are not in use in the packet are set as binary zeros or grouped to lengths of 4 bits and set to intuitive hex values. The accelerometer packets for example always begin with 2ACC, and ADC packets begin with either 01AD, 02AD or 03AD. This makes it very easy to determine packet types when observing the raw data saved into the memories.

Table 4.16: Memory Packets

Gyroscope	Packet type	ID	temp	OUT_X_L	OUT_X_H	OUT_Y_L	OUT_Y_H	OUT_Z_L	OUT_Z_H
	b00	b00 xC	8 bits	8 bits	8 bits	8 bits	8 bits	8 bits	8 bits

ADC ch 0-3	Packet type	ID	AIN0	AIN1	AIN2	AIN3
	b00	b00 x1AD	PRESSURE	V_BAT_MON	V_I_BAT_MON	V_1.5V_MON
ADC ch 4-7	Packet type	ID	AIN4	AIN5	AIN6	AIN7
	b00	b00 x2AD	I_1.5V_MON	V_5V_MON	V_CUTTER_MON	V_3.3V_MON
ADC ch 8-11	Packet type	ID	AIN8	AIN9	AIN10	AIN11
	b00	b00 x3AD	I_3.3_MON	V_3V_SENS_MON	V_3V_MEM_MON	I_3V_MEM_MON

Accelerometer	Packet type	ID	OUT_X_L	OUT_X_H	OUT_Y_L	OUT_Y_H	OUT_Z_L	OUT_Z_H
	b00	b10 xACC	8 bits	8 bits	8 bits	8 bits	8 bits	8 bits
Magnetometer	Packet type	ID	OUT_X_L	OUT_X_H	OUT_Y_L	OUT_Y_H	OUT_Z_L	OUT_Z_H
	b00	b11 xACC	8 bits	8 bits	8 bits	8 bits	8 bits	8 bits

Time / Status	Packet type	Seconds since reset	Time within seconds	Binary zeros	Status bits
	b01	18 bits	8 bits	24 bits	12 bits
GPS	Packet type	Raw GPS data			
	b11	62 bits			

4.8.5.1 Gyroscope Packet

Contains data of the rotation for X, Y and Z axis. Each axis has 16 bit resolution and thus requires two bytes each. The packet also contains 8 bit temperature data from the sensor. The temperature can be used for temperature compensating of the sensor. It is only calibrated for delta T measurements.

4.8.5.2 ADC Packet

There are three different ADC packets. Each packet contains 4 ADC channels.

4.8.5.3 Accelerometer Packet

Contains data of the acceleration in X, Y and Z axis. Each axis has 12 bit resolution.

4.8.5.4 Magnetometer Packet

Contains data of the magnetic field in X, Y and Z axis. Each axis has 12 bit resolution.

4.8.5.5 Time/Status Packet

The time and status packet contains information about how long time has passed since last system reset, status of output ports and other interesting signals. The list of status bits is displayed in table 4.17. More status bits will most likely be implemented as the project continues.

Table 4.17: Status bits

Bit	Name	Description
1	Mission_mode_int	Mission mode activated
2	GPS_EXP_OFF	GPS experiment off
3	-	not implemented
4	GPS_Awake	Commercial GPS awake
5	STX_PWR_ON	Satellite modem on
6	Sensors_OFF	Sensors off
7	Beacon_PWR_ON	Beacon transmitter on
8	Pressure_en	Pressure sensor enabled
9	CUTTER_ENGAGE	Cutter activated
10	Charge_Pin	Battery is charging
11	Rocket_Pin	Connected to rocket
12	ALT_COMP	Pressure sensor comparator

4.8.5.6 GPS Packet

Contains 62bits of raw GPS data.

4.8.6 FPGA Overview

The FPGA used in this project is the A3P250 from Actel[23]. This particular model is in the ProASIC3 family and is low cost and low power which suits this project very well. It comes in a VQ100 package and is based on non-volatile flash technology. This makes it possible to reprogram in system. The FPGA has 68 I/O pins which are placed around the four sides of the VQ100 package. Each side of the FPGA can run on different voltages and our design uses 3.3 V and 3.0 V levels. These levels are both in the range of the standard LVTTL. The FPGA core runs on 1.5 V from a dedicated voltage regulator.

4.8.7 Status LEDs

To get a fast overview of the systems status during testing some LEDs have been implemented. Different blink patterns indicate status according to table 4.18. These messages are easily changed and very useful for debugging. The messages will be changed as the project continues.

4.9 Thermal Design

The temperature of the FFUs after ejection from the RMU is under investigation and will be presented in the report in Appendix B.8. Due to aerodynamic forces during the descent, the FFUs will reach a higher temperature than the temperature of the atmosphere. The temperature range for which components inside the FFUs are expected to be functional can be seen in table 4.19. The thermal cutter will be insulated from the FFU structure and will not heat up inside the rocket or heat up components during the recovery phase. The components will not produce any significant heat.

Table 4.18: Status LEDs

LED		Description
D1M, Blue	Single flash	FPGA up and running, memory power on
	Double flash	GPS Awake
	Triple flash	Mission mode activated
	Steady on	Inside rocket or zero G has been detected
D2M, Green	Single flash	STX Power is on
	Double flash	STX Send Enable
	Triple flash	Memory is enabled (saving)
	Steady on	Memory buffer is full or Cutter is cutting
D1DC, Green	On	Battery is charging
D4PL, Red	On	Rocket pin is connected
D2S, Orange	On	Pressure sensor comparator. Low altitude detected (high pressure), activates cutter

Component	min/max operating temperature [°C]	peak temperature [°C]
Electronics	-30/85	
Sattelite transmitter	-30/60	
Batteries	-30/80	up to 120

Table 4.19: Thermal table

4.10 Ground Support Equipment

The main objective is that the FFU will store all the data during the descent. When the probes have landed, all the systems will be turned off besides the commercial GPS transmitting a signal through the radio beacon and the satellite modem. Before the launch a computer is needed to be able to test the electric equipment, i.e reading the memory and analysing its data. A computer software called Muscateer will be used to test and verify the stability of the electrical systems before launch. Furthermore the muscateer software will also need to extract the data to a hard drive after recovery of the probes. We will bring a independent ground-based GPS receiver, to record the signals for comparison.

4.10.1 MuscatEer Software

The previous KTH REXUS team RAIN developed a software called RainMan in order to communicate with their FFUs and RMU while in the rocket. It also serves testing purposes and memory read-out capabilities. It is GUI based and written in C++ with the wxWidgets package. MUSCAT is very similar to RAIN in the meaning of having FFUs and a RMU. It was a natural process to take over RainMan and transform it into something useful for us. Thanks to the modular thinking when programming the RainMan, it was soon developed into the MuscatEer.

MuscatEer is used for direct connection to a FFU for debugging and testing purposes and for communicating with the RMU. MuscatEer is used to communicate with the experiment before launch to activate the mission mode in all FFUs and start the camera recording. During flight the RMU sends realtime values monitoring voltages, currents and temperature to the ground using RXSM connector. These values are displayed in MuscatEer and highlighted green if they are within certain predefined bounds.

4.10.2 Multicast Receiver and Tracking

The beacon receiver at Esrange consists of a cluster of single channel receivers. The receivers are connected to USB to serial adapters to a computer which runs a broadcaster software. All messages received on the beacon receivers are sent to the PC and broadcasted using multicast on a UDP network on a certain IP and port. In our case this was 224.100.100.113 : 6600. The receiver is located on the radar hill. An application used for processing these messages has been developed in C#. The application takes the incoming messages, filters them, rewrites them on a proper format and uploads them to a ftp-server. The messages are then displayed on a map on a web page.

The multicast receiver application filtered the messages according to receiver preambles and checked message length and validity. If a valid GPS message was received it was saved in a list waiting for upload at a certain rate, in our case 35 s, the messages saved in the list was processed and converted to log files. The logfiles have the same formatting as the STX2 messages uploaded to the FTP server. The logfiles were then automatically uploaded via FTP to the webserver in a similar way as the STX2 messages and became visible in the web tracker page. The developed application that process UDP messages and uploads them to the ftp server is shown in figure 4.42.

PHP / javascript code for a realtime tracker using Google maps was inherited from RAIN and was modified to suit MUSCAT. MUSCAT uses 4 FFUs instead of RAINs two and the beacon interpretation was redone. The tracker plots positions from both the satellite modem and the beacons by using log files saved on the webserver. By using a feature provided by Comtechmobile, the manufacturer of the sattelite modem, a message route can be set up to upload new messages to the ftp-server. The map GUI updates automatically every tenth second.

4.10.3 Pre-Flight

4.10.3.1 Communication Boards

The purpose of the communication board is to retrieve the data after the experiment as well as testing the FFU while it's not fully assembled. During testing the communication board will transfer information from the FFU's sensors and memory to a computer. The board is a USB to serial adapter based on the FT232 chip[22]. Data rates up to 2MBits can be achieved. The communication board is borrowed from the RAIN team.

4.10.3.2 Battery Charger

The FFU batteries is charged either by the inbuilt charger in the RMU or by a current regulated power supply. The power supply is set set to 4.2 V and limited to 1 A.

images/udp.png

Figure 4.42: The UDP to FTP application uploading beacon messages to the ftp/webserver

4.10.3.3 Computers

At least three computers are needed for pre- flight preparations. Each computer are equipped with the software required to communicate with the FFUs and RMU over the Comm/Charge board, to program the FFUs and RMU and to process test and flight data collected from the FFUs. One of these computers will also monitor the the FFUs when they are in the rocket on the launch-pad and when they still in the rocket during flight.

4.10.3.4 RMU Loading System

The FFU ejection is driven by 16 extension springs which each require approximately 123N for loading. The springs will be loaded using a loading frame and a custom-made winch mounted on the RMU, as shown in figure 4.43. During the loading, a "remove before flight" safety clamp and an internal safety block, shown in figure 4.44 is placed on the Ejector Module to constrain the springs while the steel cable is tightened around the RMU. When the steel cable has been tensioned, the safety clamp labeled "remove before flight" is removed.

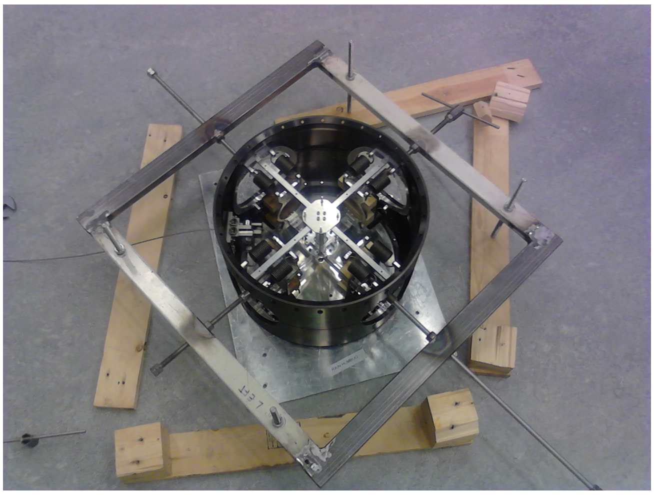

(a) *Loading of RMU*

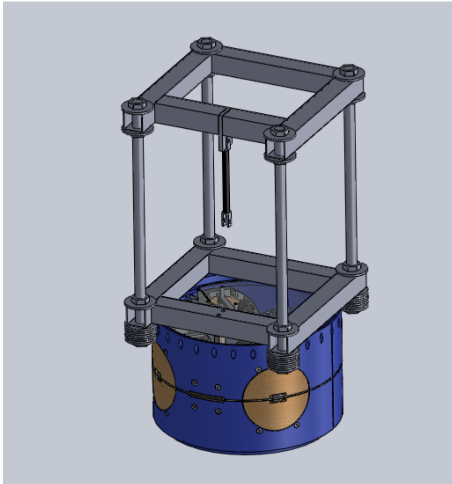

(b) *Loading winch assembly*

Figure 4.43: Loading of RMU with custom-made winch

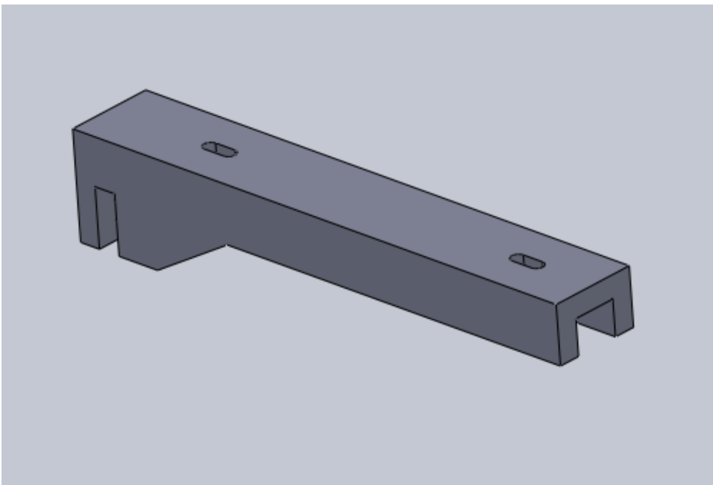

(a) *Remove before flight safety clamp*

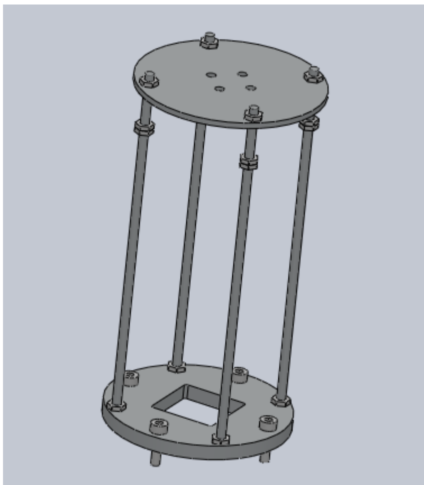

(b) *Safety block mounted on the central RMU assembly.*

Figure 4.44: Securing of RMU with RBF Safety Clamp and Safety Block

4.10.3.5 Spare Parts and Toolbox

A toolbox with all the necessary tools for the FFUs and the RMU will be available. Spare parts for the FFUs and the RMU will be brought to the launch campaign in case of an unplanned system fault.

4.10.3.6 Backup FFU

Backup FFUs will be prepared so that one of the flight FFUs can be replaced in the event of a major system failure. These FFUs will be the test FFUs that are in the best condition of the four.

4.10.3.7 Backup RMU board

A backup RMU board is available in the case that the flight board experiences a fatal system failure. This backup board is the RMU test board.

4.10.4 Flight

4.10.4.1 Real Time Data Readout Software

The MuscatEar software is used before launch to activate the MUSCAT Experiments mission mode inside all FFUs. It is then used trough the whole experiment timeline for monitoring the experiment.

4.10.4.2 Ground Based GPS Experiment FFUs

Two test FFUs will be used to run the GPS experiment on the ground during flight so that control data is collected for post-flight analysis.

4.10.5 Post-Flight

4.10.5.1 COMTECH Portal

The STX 2 satellite modem transmits commercial GPS coordinates to satellite which will then be available on COMTECH web portal. The transmitted messages can be viewed and downloaded from this portal. To access the portal go to the URL https://assetview.comtechmobile.com/portal/index.php

4.10.5.2 VHF Localization system receiver

MUSCAT will use receivers that Esrange will build at the frequencies of 173.250 MHz, 173.275 MHz, 173.300 MHz and 173,325 MHz.

4.10.5.3 Contingency RMU Loading Strap

The helicopter recovery crew will be provided with a set of straps to secure the RMU in case that ejection has not occured by the time the payload is recovered. These straps are included to ensure the safety of the recovery crew.

4.10.5.4 Unpacker Software

The Unpacker software was initially developed by RAIN, but it has been heavily modified in order to meet our specifications and protocols. The raw GPS and sensor data is packed in a different way in our memories. The software is written in C and is command-line type, and you start it by writing the path to a file you want to unpack. What the software does is that it uses a file with raw data from the memories of the FFUs as input. It then outputs one file with sensor packet data for the plotter to use and multiple files of raw GPS data for the GPS Software Receiver. This software is used because it would take too long for the GPS Software Receiver, that is written in MATLAB, to separate the raw GPS data packets from the sensor data packets.

The packets are all 64 bits long, or 16 x 4 bits hexadecimal letters long. An example packet in hexadecimal form:

`3AC3021C025FFFBE`

Or in binary form:

`0011101011000011000000100001110000000001001011111111111110111110`

The two first bits is the packet type. By looking at the two first bits of each row in the raw data, the software then sorts out which data goes in which file. The example above is a sensor data packet because of the first two *00* and would be appended directly to the sensor file. If the data packet begins with *11* it is a raw GPS packet. For the raw GPS data files that are produced it is a bit special, you have to remove the two first packet type bits and each following couple of 0s and 1s are then translated to either 0, 2, 4 or 6 in the following way:

```
00 = 4
01 = 2
10 = 6
11 = 0
```

What is then saved in the GPS data files are just combinations of 0, 2, 4 and 6, and this is what the GPS Software Receiver interprets.

4.10.5.5 Plotter Software

This MATLAB software has developed in order to be able to plot sensor data from the Unpacker. As input it gets a file with raw sensor packets and it then produces plots of different voltages, currents, states, angular rates, accelerations and magnetic orientation as a function of internal time.

Chapter 5

Experiment Verification and Testing

Verification will be accomplished by one or more of the following verification methods:

- **Test (T)**
  Requirements have to be verified by measuring system/product performance and functioning under various simulated conditions. This method is referred to as "Test".
- **Analysis (A)**
  Verification is achieved by performing theoretical or empirical evaluation by accepted techniques. This method is referred to as "Analysis".
- **Review-of-design (R)**
  Verification is achieved by validation of records or by evidence of validated design documents or when approved design reports, technical descriptions, engineering drawings unambiguously show the requirement is met. This method shall be referred as "Review-of-design".
- **Inspection (I)**
  Verification is achieved by visual determination of physical characteristics (such as construction features, hardware conformance to document drawing or workmanship requirements).This method shall be referred to as "Inspection".
- **Similarity (S)**
  Verification is performed by stating that a part of the experiment is similar to a part that has already been flown successfully. This method shall be referred to as "Similarity".

5.1 Verification Matrix

Functional		
ID	**Requirement text**	**Verification**
The FFUs shall:		
F1.1	Record GPS signals in local memory after ejection from rocket until parachute deployment.	A,R,S,T
F1.2	Switch to internal power upon ejection from the RMU.	R,S,T
F1.3	Deploy parachute upon receiving a signal from an internal pressure sensor.	R,S,T
F1.4	Transmit their positions during the recovery phase.	A,R,S,T
F1.5	Record data on acceleration, angular rate, temperature and pressure to a local memory.	R,S,T
F1.6	Provide the capability to switch on or off all electrical components inside the FFU except for the logic circuits.	R,T
F1.7	Provide the capability to be charged using an umbilical connector	S,R,I,T
The FFUs should:		
F1.7	Fall without tumbling.	T
The RMU shall:		
F2.1	Hold the FFUs inside the rocket prior to ejection.	A,R,I,T
F2.2	Eject four FFUs.	S,A,R,T
F2.3	Charge the FFUs batteries while the FFUs are inside the rocket.	S,R,I,T
F2.4	Provide an umbilical connection to the FFUs.	R,I,T
F2.5	Provide a connection to the RXSM.	S,R,I,T
F2.6	Be capable to turn on or off all electrical components inside the FFU except for the logic circuits.	R,I,T
The RMU should:		
F2.7	Record video footage of the ejection of the FFUs.	S,R,T
Performance		
ID	**Requirement text**	**Verification**
The RMU should:		
P1.1	Eject the FFUs at an initial speed of 5-10 m/s before the despinning of the rocket.	A,T
P1.2	Charge the FFU batteries with 4.2 V and 1 A current while inside the rocket.	T
P1.3	Record video footage that is at least 720 pixels and 30 frames per second of the ejections of the FFUs	I
The FFUs shall:		
P2.1	Deploy their parachutes at 5$\pm$1 km altitude.	A,I,S,T
P2.2	Transmit their positions for a 24 hour recovery period.	S,R,T
P2.3	Record GPS raw data at a sampling rate of $>$4 Msamples/s between ejection and parachute deployment.	S,R,T
P2.4	Record internal sensor data at a sampling rate of $>$100 samples/s from before the liftoff to after landing.	S,R,T
The FFUs should:		
P2.5	Have landing velocities no greater than 10 m/s.	A,I,T
The Thermal Cutter shall:		
P3.1	Cut the constraining fishing line within 4 seconds of activation.	T

Design		
ID	**Requirement text**	**Verification**
The RMU shall:		
D1.1	Have FFU ejection openings dimensioned so that the structural integrity of the rocket is not compromised.	A,R,T
D1.2	Have eject able hatches that are appropriately sized to avoid jamming.	R,I,T
D1.3	Provide specified charging line to FFU batteries until ejection.	R,I
D1.4	Provide short-circuit protection for each FFU.	R
The RMU constraining steel cable shall:		
D2.1	have an adequate margin of safety against tensile failure.	A,I
The FFUs shall:		
D3.1	Each house a parachute, parachute deployment system, and electronics system.	R,I
D3.2	Each have a spherical shape with diameter 124 mm and a smooth surface.	R,I
D3.3	Each have batteries with sufficient power and capacity for the environmental conditions during flight and after landing.	S,T
D3.4	Transmit radio beacon and satellite modem data at frequencies that comply with legal requirements.	A,T
D3.5	Not interfere with the REXUS RF transmission .	R,T
D3.6	Have a sufficient memory for storing data collected during flight.	S,T
D3.7	Provide stable 1.5 V, 2.8 V, 3 V, 3.3 V and 5 V voltage(s) to their various electrical components	R,S,T
D3.8	Withstand shocks.	T
The FFUs should:		
D4.1	Fall with the antenna facing towards zenith.	A,T
Mechanical components shall:		
D5.1	Conform to tolerances as specified by design requirements and analysis.	R
The full system shall:		
D6.1	Withstand a sinusoidal vibration level of 0.124 m/s between 10 Hz and 50 Hz and a level of 4.0 g between 50 Hz and 2000 Hz with a sweep rate of 4 octaves per minute.	A,T
D6.2	Withstand random vibration levels of $6.0g_{rms}$ along both the longitudinal and lateral axes over a frequency range from 20 Hz to 2000 Hz.	A,T
D6.3	Operate at temperatures in the range between -30 °C and 60 °C (electronic components)	S,I,T
D6.4	Operate at temperatures in the range between -30 °C and 150 °C (outer surfaces).	A,T
D6.5	Not interfere with the electronics of the rocket or any of the other experiments.	R,I,T
D6.6	Have electrical components that can withstand all stages of the mission.	S,I,T
Operational		
ID	**Requirement text**	**Verification**
The RMU shall:		
O1.1	Be loaded using a safe and efficient procedure.	S

O1.2	Have an FFU ejection system that is initiated by Esrange by a flight event timeline command.	R,T
The FFUs shall:		
O2.1	Disable power to their transmission sub-systems and their parachute deployment system until FFU ejection.	R,T
O2.2	Work independently of any control from the ground or RMU after lift off.	R,T
O2.3	Land within the Esrange recovery zone.	A,S
The RMU ejection system shall:		
O3.1	Be secured by safety straps during handling.	S,T

Table 5.1: Verification Matrix for the MUSCAT Experiment

5.2 Verification Plan

ID	Title	Type	Date	Facility	Requirement	Status
A.1	GPS Antenna Analysis	A	30/02/2012	KTH	F1.1, F1.4, D3.4	Completed
A.2	RMU Structural Finite Element Analysis	A	10/05/2012	KTH	D.1.1, D.6.1, D.6.2	Completed
A.3	RMU Rail Analysis	A	14/05/2012	KTH	F2.2, D6.1, D6.2	Completed
A.4	Spring Force Analysis	A	20/05/2012	KTH	F2.2, P1.1	Completed
A.5	RMU Constraint Cable Analysis	A	20/08/2012	KTH	F2.1, D2.1	Completed
A.6	Ejection analysis of the FFUs	A	14/09/2012	KTH	F2.2	Completed
A.7	Thermal analysis of FFU drop	A	02/10/2012	KTH	D6.4,D6.6	Completed
I.1	Data Sheet Inspection	I	13/09/2012	KTH	F1.3, F1.4, F1.5, P2.4, D2.1, D6.3, D6.4, D6.6	Completed
I.2	FFU Assembly Inspection	I	14/01/2013	KTH	D3.1, D3.2	Done
I.3	FFU status inspection (LED inspection)	I	16/01/2013	KTH	F1.7	Done
I.4	RMU Assembly Inspection	I	08/02/2013	KTH	F2.1, F2.2, F2.4, D1.2, D1.3	Done
I.5	RMU status inspection (LED inspection)	I	22/01/2013	KTH	F2.3, F2.6	Done

I.6	RMU connected to REXUS system inspection	I	22/01/2013	KTH	F2.5	Done
R.1	FFU Schematic Review	R	21/02/2012	KTH	F1.1, F1.7, F1.2, F1.3, F1.4, F1.5, F1.6, P2.3, P2.4, D3.1, D3.5, D3.7, D6.5, O2.1	Completed
R.2	FFU Drawing Review	R	21/02/2012	KTH	D3.1, D3.2, D5.1	Completed
R.3	FFU Layout Review	R	10/03/2012	KTH	F1.1, F1.2, F1.3, F1.4, F1.5, F1.6, F1.7, P2.3, P2.4, D3.1, D3.5, D3.7, D6.5, O2.1	Completed
R.4	RMU Drawing Review	R	18/05/2012	KTH	F2.1, F2.2, F2.4, D1.1, D.1.2, D5.1	Completed
R.5	RMU Schematic Review	R	12/09/2012	KTH	F.2.3, F.2.4, F.2.5, F.2.6, F.2.7, D1.3, D1.4, D6.5, O1.2	Completed
R.7	RMU Layout Review	R	28/09/2012	KTH	F.2.3, F.2.4, F.2.5, F.2.6, F.2.7, D1.3, D1.4, D6.5, O1.2	Completed
S.1	Electronic Components RAIN used (Memory, FPGA, Camera, Battery, GPS Front end, STX modem, Pressure sensor, Thermal cutter, Regulators and VHF transmitter)	S	Not Applicable	KTH	F1.1, F1.3, F1.4, F1.5, F2.3, P2.2, P2.3, P2.4, D3.3, D3.6, D3.7, D6.3, D6.6	Done
S.2	RAIN RMU loading procedure	S	Not Applicable	KTH	O1.1, O3.1	Done
S.3	RAIN FFUs land within Esrange recovery zone and lonterm thermal test	S	Not Applicable	KTH	P2.2, O2.3	Done

S.4	RAINs charging and communication system	S	Not Applicable	KTH	F1.7, F2.3, F2.5, F2.6	Done
S.5	RAIN RMU ejection system	S	Not Applicable	KTH	F2.2	Done
S.6	SQUID, RAIN camera system	S	Not Applicable	KTH	F2.7	Done
T.1	GPS Antenna Testing	T	10/03/2012	KTH	F1.1, F1.4, D3.4, D3.5	Completed
T.2	Thermal Cutter Test	T	10/04/2012	KTH	F1.3, P3.1	Completed
T.3	Drop Test 1	T	19/04/2012	Arboga Airfield	F1.1, F1.4, F1.5, P2.4, P2.5, P3.1	Completed
T.4	Drop Test 2	T	21/05/2012	Arboga Airfield	F1.1, F1.4, F1.5, P2.4, P2.5, P3.1	Completed
T.5	High altitude drop test	T	23/08/2012	Leo's skydiving club	F1.1, F1.3, F1.4, F1.5, F1.8, P2.1, P2.3, P2.4, P2.5, P3.1, D3.7, D3.8, D4.1	Completed
T.6	Informal Electrical FFU Systems Tests	T	14/01/2013	KTH	F1.1-F1.7, F2.3, P1.2, P2.1, P2.3, P2.4, P3.1, D1.4, D3.3, D3.5, D3.6, D3.7, D6.6, O2.1, O2.2	Done
T.7	RMU Communication Test	T	18/01/2013	KTH	F2.5, D6.5	Done
T.8	RMU Static Ejection Test	T	19/01/2013	KTH	F2.1, F2.2, P1.1, D1.1, D1.2, O3.1	Done
T.9	RMU Spinning Ejection Test	T	19/01/2013	KTH	F1.8, F2.1, F2.2, P1.1, D1.1, D1.2, D3.8, O3.1	Done
T.10	RMU/RXSM/FFU Electrical Functionality Tests	T	22/01/2013	KTH	F1.2, F1.6, F1.7, F2.3-F2.7, D3.8, O2.1	Done
T.13	GPS experiment test	T	March 2013	KTH	F1.1, P2.3	Done
T.11	Vibration Test	T	20/02/2013	DLR Bremen	F2.1, D1.2, D6.1, D6.2	Done

T.12	Bench Test	T	March 2013	DLR Bremen	F2.1, F2.3, F2.5, F2.6, F2.7, P2.4, D6.5, O1.2, O2.1, O2.2	Done
T.13	Recovery phase test	T	April 2013	KTH	F1.4, D3.4, D3.5	Done
T.14	Thermal and vacuum tests	T	May	KTH	F1.5, P2.2, P3.1, D3.3, D3.7, D6.3, D6.4, D6.6	Done

Table 5.2: Test Plan Matrix for the MUSCAT Experiment

Chapter 6

Launch Campaign Preparation

6.1 Flight Requirement Plan

This section summarises the dimensions and mass of the experiment, the safety risks to be avoided when handling the experiment, the electrical interfaces between the experiment and the RXSM, and the requirements for operating the experiment during launch campaign.

6.1.1 Experiment Dimensions

Tables 6.1, 6.2 and 6.3 summarise the dimensions of the mechanical components.

Component	Mass [kg]
FFU (x4)	$\sim$ 0.4 (each)
RMU	10.5
Experiment total mass	$\sim$ 12.1

Table 6.1: Experiment mass.

Component	Dimension
FFU diameter	124 mm
FFU volume	998306 mm^3
FFUs expected COG	$\pm$ 10 mm from the rotational axis

Table 6.2: FFU dimensions.

Component	Dimension
RMU diameter	356 mm
RMU height	232 mm
RMU footprint area	0.681 m^2
RMU expected COG	$\pm$ 20 mm from the rotational axis

Table 6.3: RMU dimensions.

A parts lists and drawings of all FFU and RMU components is given in Appendix C.

6.1.2 Safety Risks

The experiment's safety risks involve the handling of the experiment when its ejection springs are loaded and managing the pyro cutter used to initiate FFU ejection from the rocket. Below is a summary of the safety risks at each stage of the launch campaign along with an explanation of the redundant system used to counter this risk.

6.1.2.1 Battery Shipping

A number of Li-Ion batteries will be shipped to the launch site. The type of batteries used are Saft MP 144350 and they have a typical capacity of 2.6 AH at 0.5 A 20°C, 2.5 V cut-off. If the batteries are transported by a member of the MUSCAT-team, they will be transported according to IATA regulations and brought in the hand luggage on a possible flight. The batteries are approximately 7-8 Wh which is well below the allowed 160 Wh specified in the IATA regulations.

6.1.2.2 RMU Loading

A 555 N force is required to load the ejection system of the RMU. A custom-built RMU loading frame will be used to extend the springs inside the RMU. The spring extension procedure is discussed in Appendix F.2

After the spring extension procedure has been completed the springs are temporarily constrained in their extended state by remove before flight safety measures. Two systems of safety measures are used. The first system consists in four *safety clamps* placed on top of the upper cross, between the collar and the pusher plates of each cage. The second one is a circular *safety block* that connects the bottom parts of the pushing plates of the four each cage.

With the remove before flight safety measures in place, the FFUs are then loaded into the system along with the RMU hatches. A 2.5 mm diameter steel cable is then placed in the groove around the outside of the cylinder and tensioned with a custom-built cable tensioning mechanism to hold the springs extended. Once the cable has been tensioned and constrained inside the RMU, the steel cable is cut before the constraint point so as to get rid of excess cable. The loading frame is then disassembled and a remove before flight straps are fastened around the RMU as an additional redundancy for preventing spring release.

6.1.2.3 Flight Simulation Testing

During the final flight simulation test a full run through of the MUSCAT experiment flight timeline will be conducted, not including the ejection of the FFUs. The pyro cutter circuit will not be connected. An LED and resistor circuit will be used in its place. When the pyro cutter is signaled the LED will light up, indicating pyro cutter initiation. The real pyro cutter circuit will be connected after the flight simulation tests when it is deemed safe to do so by Eurolaunch. Both the remove before flight clamps and straps will be used as safe guards against an ejection failure at this stage of launch preparations.

6.1.2.4 Payload Stack Assembly

The safety measures are removed when the RMU is ready to be mounted to the payload stack. Before removing the safety measures a remove before flight *safety strap* is fastened around the RMU as safety measure during assembly. The strap remains fastened around the RMU until personnel are no longer working with the payload stack. Eurolaunch will be required to remove the safety strap before flight.

6.1.2.5 Pyrocutter

Two Cypres pyrocutters are used to initiate the ejection of the FFUs. The pyrocutters for flight version and any hot tests will be provided by Eurolaunch. Pyrocutters are not electrically connected to the MUSCAT experiment, and are activated by Eurolaunch. Responsibility for transporting, handling, installing, and operating the flight and hot tests pyrocutters is taken by Eurolaunch, who also are responsible for ensuring the safety procedures around the pyrocutters.

6.1.2.6 Recovery

In the unlikely event that the RMU ejection system is fully or partially loaded, the recovery crew will be notified prior to the helicopter flight (together with the coordinates of the FFUs). A heavy duty strap is provided to the recovery crew to secure the hatches in position by tightening it around the circumference of the module over the wire groove. This system keeps the springs constrained and prevents surprise ejections during payload handling and transportation. A procedure for mounting these straps to the rocket module will also be provided.

6.1.3 Electrical Interfaces

The electrical interfaces with the REXUS rocket are summarised in Table 6.4.

REXUS Electrical Interfaces		
Service module interface required? Yes		
	Number of service module interfaces:	1
	TV channel required?	No
Up/Downlink (RS-422) required? Yes		
	Data rate - downlink	38.4 kbit/s
	Data rate - uplink	38.4 kbit/s
Power system: Service module power required? Yes		
	Peak power consumption	10 W
	Average power consumption	3 W
	Total energy consumption after lift-off (until T+600s)	0.5 Wh
	Power ON	1200 s before lift-off
	Power OFF	600 s after lift-off
	Battery recharging through service module:	Yes
Experiment signals: Signals from service module required? No		
	LO	No
	SOE	No
	SODS	No

Table 6.4: Electrical Interfaces

6.1.3.1 Communication

The MUSCAT experiment uses the up/downlink. The uplink is used to turn on the FFUs and start the GoPro camera prior launch. The uplink is also used for setting the FFUs in mission mode. The downlink is used to send down housekeeping data from the FFUs and the RMU.

6.1.3.2 Experiment Deactivation

The FFUs can be deactivated by the RMU by activating sleep mode. The FFUs will also enter sleep mode if the RMU is powered down. When the FFUs are switched off only the logic circuits for the sleep mode are powered.

6.1.3.3 FFU Charging

The MUSCAT experiment uses the charge line for charging the FFUs' batteries. The RMU does not need to be powered (+28V line) for the charger to work but can be. The FFUs are charged both when they are turned on and off. The FFUs will be recharged when the charge line is provided.

6.1.4 Launch Site Requirements

- A work area for preparation of the MUSCAT experiment. The working area should be indoors and at room temperature. It should have electricity sockets and internet connection at least for four computers. One big table or two small tables and at least four chair are needed. Running water should be close by.
- The MUSCAT experiment requires its payload to be kept at a temperature above 10° C on the launch pad prior to launch.
- MUSCAT experiment requires use of the Esrange VHF receiver system for receiving the position of the FFUs during the parachute descent
- All pyrocutters, for flight and any hot tests required by Eurolaunch, are to be provided and handled by Eurolaunch.
- RXSM shall control the initiation of the pyro cutter during the flight.
- The REXUS rocket shall be spinning during the ejection of the FFUs.
- Helicopter assisted tracking and recovery to recover the FFUs post-flight.
- The helicopter recovery crew shall be provided by the MUSCAT team with RMU ejection system safety straps to constrain the RMU ejection system in case of an unsuccessful FFU ejection. The RMU handling and safety procedure will be provided by the MUSCAT team.
- If possible, MUSCAT experiment would also like to use of Esrange's Lidar the night prior to launch.

6.2 Preparation and Test Activities at Esrange

The activities that the MUSCAT team will perform during the launch campaign are described in the following sections.

6.2.1 Team Organization

Six MUSCAT team members will be present at the launch campaign to conduct the necessary preparation, launch and post launch activities.

Role	Name	Responsibilities
Team Leader	Ólafía Lára Lárusdóttir	Management of launch campaign activities and primary MUSCAT interface with Eurolaunch
Ground Control	Markus Fjallid	Monitors RMU status during launch. Handles RMU electronics and software.
FFU Officer	Marcus Lindh	Monitors FFU status. Handles FFU software.
Assembly & Maintenance Officers	Darri Kristmundsson, Marco Tito Bordogna	RMU/FFU assembly and maintainance
Recovery Officer	Andreas Myleus	Relays GPS position from Globastar satellite to Esrange ground control during experiment recovery
Lidar Operator	Peggy Achtert	Operates Lidar

6.2.2 Workspace Preparation

The MUSCAT team will set up MUSCAT's allocated workspace upon arriving at Esrange. All equipment and tools will be unpacked and organized. Furthermore the FFUs and RMU will be inspected for any damage that may have occurred during transportation to Esrange. At this stage a network switch will be set up and to provide an internet connection to the MUSCAT team.

6.2.3 FFU Assembly

Two test FFUs, four flight FFUs and one space flight FFU will each have had their base assemblies completed before arrival at Esrange. While at Esrange the recovery systems for each flight FFU will need to be assembled. The two test FFUs will be assembled so that they can be used in the ground-based GPS experiment during the flight simulation tests and the actual flight.

The four flight FFUs will be integrated into the full experiment assembly before flight simulation testing. These FFUs will also have their recovery systems prepared at Esrange before their FFU functionality tests.

The spare flight FFU will have been prepared using the same procedures used for the flight FFUs. In the event that any of the flight FFUs are not working nominally, there will be the option of replacing the not working flight FFU with the spare flight FFU. The assembly procedures for the flight FFUs are provided in appendix F.1.

6.2.4 FFU Functionality Checks

After the FFUs have undergone inspection and recovery system assembly they will undergo basic functionality testing where each on board system will be activated and monitored for nominal operation. Voltage and current levels, the data acquisition system, the recovery system, the GPS experiment and the localisation system will be checked. After an FFU has undergone the basic functionality test its batteries shall be fully charged.

6.2.5 RMU Loading

The assembly of the RMU without the FFUs and without the extension of the ejection springs will occur before arrival at Esrange. At Esrange, the RMU will be loaded before the flight simulation tests.

The RMU loading procedure involves the extension and constraint of the RMU ejection springs, insertion of the FFUs and RMU hatches, and the tensioning of the steel cable used to constrain the ejection springs. The RMU loading mechanism and tensioning mechanism are shown in figure 4.43. The pyro cutter used to initiate the ejection of the FFUs shall be provided by Eurolaunch and will be included in the assembly after the flight simulation tests. During the flight simulation tests an LED and resistor circuit will be used instead of the cutter circuit. The procedure is outlined in Appendix F.2.

6.2.6 Full System Functionality Checks

After the FFUs have been loaded into the RMU the communication between the RMU and the FFUs will be tested in addition to a full check of the FFU sensor readings. The RMU camera and temperature sensor will also undergo a functionality test.

6.2.7 Flight Simulation Testing

The fully assembled MUSCAT experiment with flight FFUs shall be provided for the flight simulation tests. During all countdowns the MUSCAT ground control team will rehearse their flight monitoring procedures. The FFUs shall not be ejected from the RMU during any of the flight simulation tests. In addition, the team will rehearse running the ground based GPS experiments during at least one of the flight simulation tests at Radar Hill with test FFUs.

6.2.8 Payload Assembly

Before MUSCAT is put into the payload stack, the remove before flight safety clamps shall be removed and the safety block shall be put in the raised position. They will not be accessible after payload assembly. During and after payload assembly the ejection constraint straps secured around the rocket module will act as the redundant ejection spring constraint system.

6.2.9 Ground Based Experiment Measurements

In order to get undisturbed GPS data to correlate with the data acquired by the experiment during flight, two GPS measurement stations will be set up outside Esrange. These stations consist of FFUs. Two measurements will be made. The first one will be a test, where the FFU Officers will go to Radar Hill and perform the GPS measurement with two FFUs. The collected GPS data will be read out overnight and analysed.

Before launch and the final flight simulation test the FFU officers will need to position themselves at Radar Hill. The ground-based GPS experiment will be activated 65 seconds prior to the rocket flight. The data will be collected the entire time the FFUs are falling.

6.2.10 Lidar Measurements

If possible, MUSCAT would like to perform lidar measurements the night before the launch to obtain a temperature profile for comparison with experiment data. The LIDAR is often operated by MISU (Department of Meteorology at Stockholm University) when there are campaigns at Esrange. A PhD student from MISU, involved in MUSCAT, will be there as usual and operate it. This will not interfere with the REXUS launch campaign.

6.2.11 Ground Control Experiment Monitoring

The MUSCAT ground control will be responsible for monitoring the FFUs during the flight simulation tests as well as the flight. A primary ground control terminal with two controllers will be responsible for monitoring the health of the experiment, giving status updates about the experiment when required to do so and activating or deactivating the experiment at defined points in the timeline.

A backup ground control terminal with two standby controllers running the same ground support program will be ready in the case that the primary ground control station fails. Half of the flight simulation tests will be monitored by the primary ground control crew and the other half will be monitored by the backup crew. This is to ensure that both teams are fully prepared to perform the necessary ground control tasks.

6.2.12 Preparation and test activity timeline

Procedures which must be carried out	**Time**	**Who**
Workspace preparation	Day 1	Full Team
Prepare LIDAR Experiment	TBD	Lidar Operator
Inspect FFUs	Day 2	FFU Officer, Assembly & Maintenance Officers
FFU Assembly	Day 3	Assembly & Maintenance Officers
FFU Functionality Checks	Day 3	FFU Officer, Team Leader, Recovery Officer
RMU Loading	Day 4	Assembly & Maintenance Officers, Ground Control
Full System Functionality Test	Day 4	FFU Officer, Recovery Officer, Ground Control, Team Leader
Flight Simulation Testing	Day 4	Full Team

Payload Assembly	Day 5	Assembly & Maintenance Officers
Ground Based GPS Experiment Measurements	TBD	FFU Officer, Recovery Officer
Ground Control Experiment Monitoring	TBD	Ground Control

Table 6.6: Preparation and test activities

6.3 Timeline for Countdown and Flight

Table 6.7 contains the flight timeline of the MUSCAT experiment.

MUSCAT Timeline				
Action	**Time [h:mm:ss]**	**Duration**	**Expected altitude**	**Responsible**
Take pictures and video for outreach Ground control check	t-2:20:00 t-2:20:00	4:00:00	Ground Ground	Andreas Myleus Markus Fjällid, Marcus Lindh
GPS experiment ground station set up Radar Hill	t-2:00:00	50 min	Ground	Andreas Myleus, Marco Tito Bordogna
Payload test: MUSCAT activation and status check	t-1:15:00	14 min	Ground	Markus Fjällid, Marcus Lindh
Erase all memories	t-00:10:00		Ground	Markus Fjällid, Marcus Lindh
MUSCAT RMU is powered and monitored	t-00:15:00	5 mins	Ground	Markus Fjällid, Marcus Lindh
RXSM connection confirmed			Ground	Marcus Lindh, Markus Fjällid
All loggers started			Ground	Markus Fjällid
Data rotor switched off			Ground	Marcus Lindh, Markus Fjällid
FFU 1 check memory empty			Ground	Marcus Lindh, Markus Fjällid
FFU 2 check memory empty			Ground	Marcus Lindh, Markus Fjällid
FFU 3 check memory empty			Ground	Marcus Lindh, Markus Fjällid
FFU 4 check memory empty			Ground	Marcus Lindh, Markus Fjällid
Confirm empty memories			Ground	Marcus Lindh, Markus Fjällid
FFU 1 memory rewinded			Ground	Marcus Lindh, Markus Fjällid

FFU 2 memory rewinded			Ground	Marcus Lindh, Markus Fjällid
FFU 3 memory rewinded			Ground	Marcus Lindh, Markus Fjällid
FFU 4 memory rewinded			Ground	Marcus Lindh, Markus Fjällid
MUSCAT FFUs are turned on and put into mission mode	t-00:10:00		Ground	Marcus Lindh, Markus Fjällid
Safe mode on			Ground	Marcus Lindh, Markus Fjällid
Data rotor switched on			Ground	Marcus Lindh, Markus Fjällid
The mission mode is activated. Confirm to Mark Ólafía Lára Lárusdóttir			Gound	t-00:05:00
RMU camera starts to record	t-00:05:00		Ground	Marcus Lindh, Markus Fjällid
Service module switched to internal power	t-00:02:00		Ground	
FFU 1 mission mode status green	t-00:01:50		Ground	Marcus Lindh, Markus Fjällid
FFU 2 mission mode status green	t-00:01:50		Ground	Marcus Lindh, Markus Fjällid
FFU 3 mission mode status green	t-00:01:50		Ground	Marcus Lindh, Markus Fjällid
FFU 4 mission mode status green	t-00:01:50		Ground	Marcus Lindh, Markus Fjällid
LIFT OFF	t		Ground	
Motor burnout	t+00:00:26			
Pyro-cutter initiation	t+00:01:05			
FFUs ejection	t+00:01:05			
Rocket de-spin	t+00:01:10			
FFUs and RMU reach apogee	t+0:02:20		80 km altitude above ground	
MUSCAT FFUs go into recovery mode	t+00:06:00		5 km altitude above ground	
RMU camera stops recording	t+00:08:00			
RMU power down	t+00:10:00			
Loggers stopped	t+00:10:30			
Satellite message from FFU 1				Andreas Myleus
Satellite message from FFU 2				Andreas Myleus

Satellite message from FFU 3				Andreas Myleus
Satellite message from FFU 4				Andreas Myleus
FFU touchdown	t+0:20:00		Ground	

Table 6.7: Flight Timeline

6.4 Post Flight Activities

The post flight activities include FFUs and RMU recovery, read out of data from all FFUs and the RMU camera and detailed documentation of the flight and post flight events.

6.4.1 Localisation

After landing, the FFUs will transmit their GPS position to the Globalstar satellite network along with a radio beacon signal that has its GPS position modulated into it. The transmitted radio beacon signals will have center frequency of 173.250 MHz, 173.275 MHz, 173.300 MHz and 173.325 MHz. The modulation bandwidth of the transmitters at -3 dB is 7 kHz and the power level is from 4-11 dBm. The center frequency of the Globalstar signals will be 1615 MHz, the resolution is 2.5 MHz and the power level i 18 dBm$\pm$2 dB. MUSCAT shall use the antenna system provided by Esrange.

The MUSCAT ground control team will receive the FFU GPS positions from the Globalstar satellite network via the Comtech Mobile Datacom assetview portal.

6.4.2 Recovery

The helicopter recovery crew responsible for collecting the FFUs shall be given one set (per FFU) of the GPS coordinates for recovery, and an indication of whether any ejection anomalies have been detected during the flight. In the latter case a safety strap should be put around the circumference of the MUSCAT module as a safety measure. The helicopter crew shall also use VHF beacon signals for near-range localisation of the FFUs. Upon finding an FFU the recovery team shall take photos of it and it's landing site so as to document how the FFU landed.

The FFUs that were used to run the GPS ground experiments will be brought back from Radar Hill by two team members.

In the unfortunate case that none of the FFUs will be found during recovery a small part of the team will try to retrieve the FFUs the day after launch. This will be done via snowmobiles with a few people from Kiruna that are experienced snow mobile drivers provided that the weather will be OK and Esrange accepts it. If this will not be allowed a plan C will be made.

6.4.3 RMU Inspection and Data Read Out

The RMU will be photographed in order to document the state it returns in. The Camera SD card is then retrieved and contents saved and analysed for FFU ejection data.

6.4.4 FFU Data Read Out

The FFU data are read out from all FFUs. The readout is done twice for each FFU, and a backup copy of both files is made immediately after the readout. Unpacking to retrieve the sensor and housekeeping data is performed, and plotting of the overview of the complete flight. The sensor and GPS data are saved for the evaluation, which will continue upon return to KTH.

6.4.5 Pack Up

The day after launch the workspace will be cleaned up, the FFUs, the RMU and all experiment ground support equipment packed in order to be ready for transport back to Stockholm. The data will then be further analysed in Stockholm.

6.4.6 Post Flight Activities Timeline

Procedures which must be carried out	**Time**	**Who**
Recover GPS ground experiments	Directly after launch	Darri Kristmundsson, Marco Tito Bordogna
Read data out from ground FFUs	Directly after ground FFUs recovery	Ólafía Lára Lárusdóttir
Read data out from flight FFUs	Directly after flight FFUs recovery	Marcus Lindh, Markus Fjällid
Read RMU camera data out	Directly after RMU recovery	Markus Fjällid
Analyse GPS experiment data	Directly after recovery	Ólafía Lára Lárusdóttir
Prepare presentation on MUSCAT experiment performance	Directly after recovery	Ólafía Lára Lárusdóttir, Darri Kristmundsson, Andreas Myleus
Document recovery photo and video	Directly after recovery	Andreas Myleus
Document post-flight activity	Directly after each activity	Full Team
Workspace clean up and experiment pack up	Day after launch	Full Team
Depart for Stockholm	A few days after launch	Full Team

Table 6.8: Post flight activities

Chapter 7

Data analysis plan and experiment reports

7.1 Data analysis

7.1.1 GPS Data Analysis

7.1.1.1 Software Receiver

The raw GPS data is analyzed in a software receiver constructed by Erik Lindén of RAIN [7]. The software receiver is written in MATLAB, and operates in two parts: Tracking satellites and obtaining a navigational solution.

7.1.1.1.1 Tracking

Since the GPS signal is a CDMA protocol, the method of listening to a message from a specific satellite is by correlating the received signal with replication of the C/A code of that satellite. The software receiver goes through every GPS satellite, constructs its PRN code and correlates this with a specified second of the collected data. Since the Doppler shift in the GPS signal affects the frequency of the bits sent in its message, the software receiver searches a specified frequency range. A lock is evaluated using a "tent" curve fit through a sliding frame of correlation attempts, indicating the start time of a positive code correlation (CST). When an initial signal has been locked, it is tracked with a PLL loop to get a higher precision than the curve fitting method. The signal is then tracked for a specified time and the tracking results are saved to be used in the navigational solution. In addition, Ionospheric data from IGS is also used to compensate for the effects of electron content in the atmosphere. Accelerometer and magnetometer data can also be used to determine the orientation of the FFU.

7.1.1.1.2 Solution

The standard real-time approach to calculating a position in the GPS system is by using the navigational message transmitted from each satellite, or broadcast ephemeris. The software receiver however uses ephemeris data from the International GNSS Service (IGS). This data, after some processing, gives a significantly higher precision of the GPS satellite position. A navigational solution requires a successful track of at least 4 satellites. The time message in the ephemeris (with corrected time from the IGS products) gives, by counting the number of CSTs from the time message start, the exact time of a satellite at any given CST. Knowing the exact time, the pseudorange (distance from satellite to GPS receiver) for each satellite can be calculated, using this time the position information in the processed IGS products mentioned above. With more than 4 pseudoranges, the position is overdetermined and is therefore calculated in a least square sense. The velocity is measured independent of the pseudorange calculation using the output of the PLL loop tracing the carrier frequency. Calculating the Doppler shift of this signal, the velocity of the antenna projected on the line of sight vector to each satellite is determined. Since at least 4 satellites are locked, the complete velocity vector of the FFU can be determined. Using these methods, the position and velocity measurements are not coupled. This means that the higher accuracy in the velocity is not used when calculating the position. For example, the position can be very noisy, and jump several meters per sample, even though the velocity vector is almost constant. To give a better connection between these two variables, a global optimization problem is set up coupling the velocity and position. This is minimized in a least squared sense to give position and velocity of the FFU over the entire interval.

7.1.2 Scientific Analysis

The data from the GPS experiment and the internal sensors will be combined to get the acceleration in each point in time. From the acceleration the horizontal wind and density will be derived. Using the density and hydrostatic equilibrium the temperature will be found by methods described in section 4.4

7.2 Final Experiment Report

7.2.1 Campaign

7.2.1.1 Preparation activities during launch campaign

During the preparation phase the team followed the guidelines stated in Chapter 6. During the arrival date the team prepared the working zone unpacking all the equipment and checking any visible damage on the experiment. Electrical check up were performed on both FFU's and RMU's electronic to ensure they functionality.

Several test involving the major system of the experiment have been tested. Those tests verified the functionality of: RMU-FFU communication, FFU mission mode activation, parachute deployment system, data acquisition system, recovery system via radio beacon and recovery system via satellite modem. During those test some issues were discovery in the data acquisition system for two FFUs. One FFU has been replaced with the spare FFU. The second FFU was fixed using spare components.

After performing all the mentioned test and fixing the issues, the FFU were assembled in flight configuration and loaded on the RMU ready for payload assembly. From this point any change has been made to the experiment. For the rest of the preparation activities the team participated to all the payload test.

7.2.1.2 Flight performance

The RMU was kept at temperatures above 20°C during flight countdown to maintain operational temperatures of the FFU thermal cutters. MORABA carried this out by gas burners at the rocket silo, and the RMU temperature was monitored from the REXUS team ground station. The batteries inside the FFUs where fully charged prior the launch.

The ejection system performed nominally ejecting the four FFUs at t+67 seconds. All parachutes were deployed and all FFUs switched from GPS experiment to commercial GPS for localization. Messages with the coordinates of the FFUs were received via radio beacon and satellite modem. The recovery of the FFUs went smooth and all FFUs have been recovered.

The data readout from the four FFUs gave us all necessary data for analysis.

- Doc, 2350 Mbyte data.
- Dopey, 2595 Mbyte data.
- Frankenstein, 1532 Mbyte data.
- Sleepy, 2582 Mbyte data.

The biggest part of the collected data is raw GPS data but about 0.02% of the total size of the data are internal sensor and housekeeping data.

The power consumption of the MUSCAT RMU was on a fairly constant level until FFU ejection when it dropped a little. Until ejection the measured current from the RXSM was 0.16 A, giving 4.5 W of power. After the ejection the current dropped to 0.08 A, 2.24 W. These numbers were well within the specified limits.

7.2.1.3 Recovery

All four FFUs were recovered in pristine condition with no visual damages sustained during re-entry or landing. All four top hemispheres were lost after ejection, as was to be expected.
The crash of the REXUS 13 rocket did not damage the MUSCAT RMU. Inspection of the RMU gas protection showed two small gaps along the heat shielding tape at the plate intersections, but the origin of these could either be due to the launch vibrations or the rocket crash. Both pyrocutters performed optimally and the cut steel wire was cleanly ejected along with all four hatches. No hatches were recovered as was to be expected.

7.2.1.4 Post flight activities

Once the RMU was disassembled from the rocket stack it was taken to the MUSCAT packing area. The GoPro camera SD card was removed and backed up to a portable computer. The RMU was inspected for damage by removing the upper gas protection plate, which required removing the thermal protection tape.
The flight FFUs were brought to the team workspace. The hardware was visually inspected without any sight of damage. The bottom hemispheres were removed. A small amount of water was removed using paper towels. The flight data were read out onto a portable computer. The data were then read out a second time. The battery cable in each FFU was cut. The FFUs were placed in ESD protective bags for shipping back to Stockholm. From a mechanical standpoint, all FFUs and the RMU are in condition to be reused after the rocket flight.

7.3 Results

In this section the results obtained until the delivery of this 5th version of the SED are presented and commented. For what concerns the GPS data analysis the work is still ongoing, therefore only preliminary results are shown.

7.3.1 Technical results and scientific data evaluation

During the free fall the FFU collected both raw GPS data and inertial sensor data, three FFU out of four collect data for the whole duration of the mission while one recorded data only for 250 seconds. This is not affecting the scientific objective of the experiment since three FFUs are enough to obtain the horizontal structure of temperature and density profile and moreover in 250 seconds are enough to over most of the altitude rage the MUSCAT Experiment is interested in.

Both data the records started at FFU ejection and raw GPS data recording stopped at parachute deployment when the GPS experiment was shut off and the commercial GPS was used for localization. For what concerns the inertia sensors the data were recorder until recovery when the FFU was put in sleep mode.

7.3.1.1 Inertial sensor data

Inertial sensor data on board of the FFUs were accelerometers and gyroscopes. Figure 7.1 shows the values recorder by the accelerometer in z direction and x, y and z component of the angular rate. Upon ejection it the FFUs are affected by air drag, as it is shown in figure 7.1, where for the first 15 seconds the acceleration is negative.

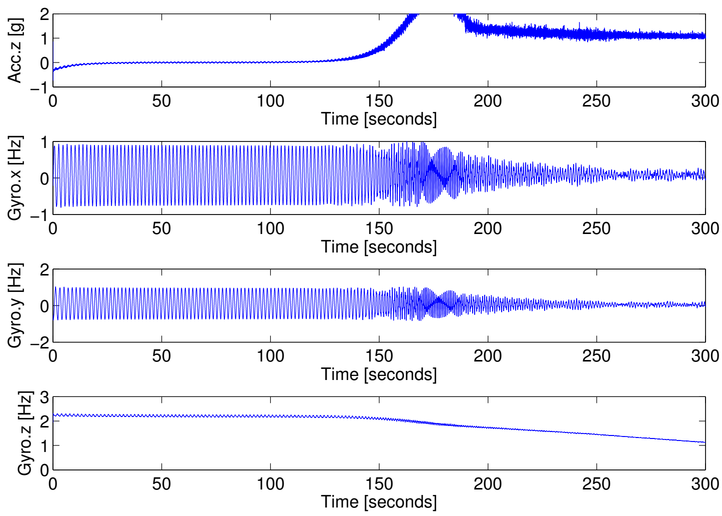

Figure 7.1: Acceleration in z direction and x, y and z component of the angular rate.

Figure 7.1 shows also that the FFUs had the antenna facing up during the reentry since the acceleration is positive. At ejection the rocket was spinning at 3.2 Hz, however the spin rate of the FFUs around the z-axis is lower and varies between 2.3 and 1.8 Hz, depending on FFU. For conservation of angular momentum the

FFUs should have continued to spin with the same angular speed, the reasons for this de-spin are still not clear. During the reentry phase the spin rate decreased, this is due to the fact that the increasing air density leads to higher air drag acting on the FFUs. On the x and y axis it is possible to see a clear precession motion of the FFU.

Inertial sensors identified also a systematic problem of the ejection system. Figure 7.2 shows the value of the gyros of all FFU in the y-axis. The y-axis is in the plane perpendicular to the spinning axis of the rocket and it is perpendicular to the FFU ejection. The figure show a systematic negative value at ejection for all the FFUs, this means that the ejection system introduced a non desired small torque during the ejection. However this did not disturb the dynamic of the free fall.

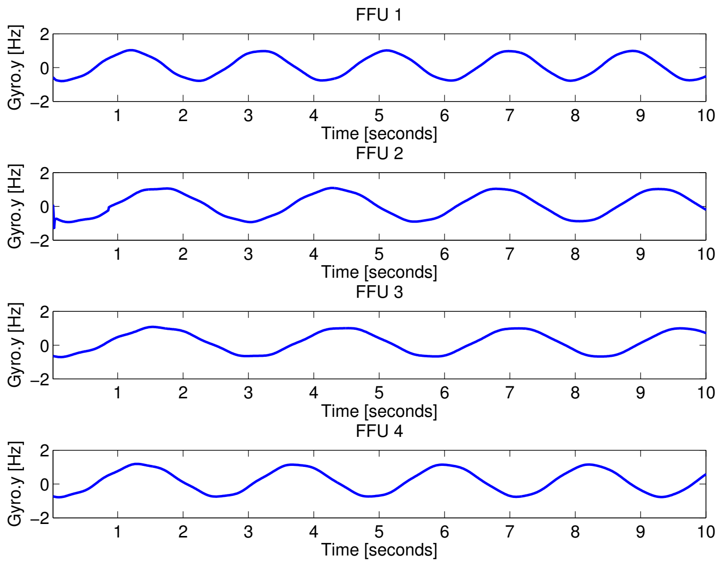

Figure 7.2: Tip off of the FFUs at ejection.

7.3.1.2 GPS data

The analysis of the raw GPS data is still on going (8th August, 2013). The free fall position and velocity have been calculated only for one FFU. The results are shown in figures 7.3 and 7.4. The FFU reached the apogee of 81 km 69 seconds after ejection and reached a maximum speed of 700 m/s.

7.3.2 Outlook

7.3.2.1 Further data evaluation

Quite a few things are left to be done. To summarise the main things are

1. to process the data from the raw GPS data for at least two more FFUs
2. to process the data further for three or four FFUs to get the horizontal wind and density and finally the temperature

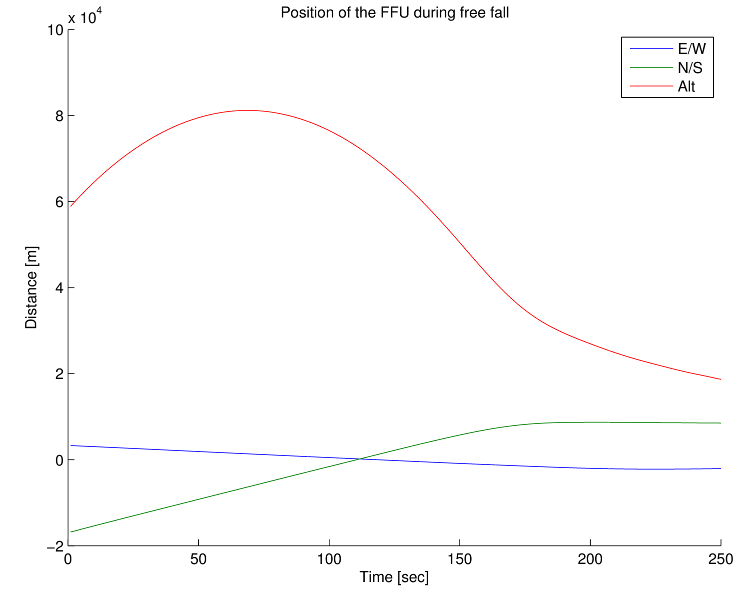

Figure 7.3: Position of the FFU in free fall.

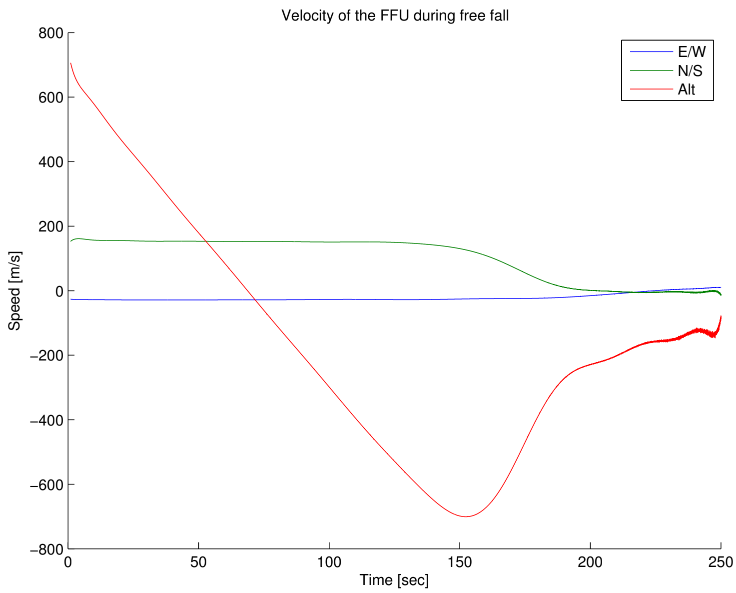

Figure 7.4: Velocity of the FFU in the free fall.

3. to compare the temperature data to reference data obtained with a LIDAR the 7th of May

We experienced msec of dropouts in our GPS data for three out of four FFUs, this causes problems in our software receiver so the software receiver needs to be updated in order to get a solution. Acquiring a complete solution for one satellite, if there are no dropouts, takes about two days due to a lot of data and limited computing power. We are missing personal with enough knowledge of software receiver to fix our software receiver, but we have people in training and they should be able to fix the software receiver in a few months.

The processing of horizontal wind, density and temperature profiles should not be as time consuming as the GPS analysis since the team has one student with the knowledge to derive this data, waiting for the processed GPS data. Comparing the LIDAR and the derived temperature data will not take much time and there are several persons that can readily do this.

7.3.2.2 Improvement of experiment and recommendations

Our experiment could have been improved in the following ways

1. The data saving can be improved so msec data dropouts will not occur
2. The data read out software could be improved so that touching the readout computer during readouts does not affect the readout
3. The unpacker can be improved so that if there are any anomalies in the data, the user gets a warning
4. The software receiver can be improved to handle msec dropouts

7.3.2.3 Planned presentations and publications

Future presentations and publications of the MUSCAT experiment are not completely planned but the following is to be planned

1. Present the results in high schools in Iceland,
2. The MUSCAT team supervisors plan to publish the results of our experiment in peer reviewed journal.
3. Present the results and or the team to students at KTH, to promote them to join a REXUS experiment.

7.4 Lessons learned

During a big project like REXUS/BEXUS the team members learn a lot of things. In this section the most important lessons learned are listed.

7.4.1 Project management

As a project manager one needs to plan many things and see the big picture. During the selection workshop we had presentations about project management. These presentations were very helpful but came quite late and would have been more useful earlier on in the start of the project. For future project managers, this is a step by step guide how to make an efficient plan.

1. Gather data.
   (a) Read through all guidelines given to you, SED guidelines, REXUS manual and possibly introduction to project management (if the project manager hasn't taken a course in project management)
   (b) Talk to all team members informally about how much time they have during the next few weeks, regularly

   (c) Think about what your requirements are and how you will fulfill them and how you will verify that you fulfill them.

2. Make a work breakdown structure in verbal form
3. From the work breakdown structure, create Gantt charts, with deadlines that have a few weeks lead time and what team member is responsible for which task.
4. Communicate the plan with others
5. Update the plan
   (a) Check if availability has changed
   (b) Check if tasks have changed
   (c) Check if you need more time for some tasks
6. Repeat the last two steps until the project is done.

Teams are all about communication. It is important to have formal meetings but it is also important to talk together frequently informally. It is very important to spend time on preparing meetings a week in advance. It is also important that team members know and feel they are responsible for their tasks.
Requirements are important but if one doesn't have a way of verifying the requirement it is useless. When making the requirements, plan the verification, step by step so one realises if there is something that can't be verified.

7.4.2 Outreach

We have learned that when posting blog posts on the internet, people are more interested in seeing pictures and videos than reading text. The most viewed posts we have contain a lot of pictures and videos.

7.4.3 Flight campaign

It is important to read the REXUS user manual to prepare for the flight campaign. Think about what the team needs to check before launching it's experiment. Write down everything that is critical for the experiment to work, even small things, like attaching cables. Do not trust that someone else will do something for you and check that it has been done before integration. Be sure to check off all the things on the list and have a person dedicated to the check list to ensure everything is done as planned. Do not have things that are not critical to the experiment working. Prepare the check list before the bench test so it can be tried in advance.

References

[1] Euro Launch, *REXUS User Manual*, 7.3 ed., 2011. http://www.rexusbexus.net/images/stories/rexus/rx_ref_usermanual_v7-3_31aug11.pdf retrieved 2012-02-13.

[2] MAXIM, *MAX2769 Universal GPS Receiver*, 2 ed., 2006. MAX2769 Datasheet.

[3] USGlobalSat, *User guide ET-318*, 1.3.1 ed. http://www.usglobalsat.com/store/download/52/et318_ug.pdf accessed 2011-05-03.

[4] Axonn, *Gen 2 Satellite Transmitter Product Data Sheet*, 1.4 ed., 2005.

[5] F. Schmidlin, "The inflatable sphere: A techique for the accurate measurement of middle atmosphere temperatures," *Journal of Geophysical Research*, December 1991.

[6] F. L. B. et. al., "Upper-Air Density and Temperature by the Falling-Sphere Method," *Journal of Applied Physics*, vol. 27, no. 7, 1956.

[7] W. Reid *et al.*, *RAIN Student Experiment Documentation*. Royal Institute of Technology (KTH), 3 ed., September 2011.

[8] G. Casselbrant *et al.*, *SQUID Student Experiment Documentation*. Royal Institute of Technology (KTH), 5 ed., April 2011.

[9] MUSCAT Rocket Experiment, *Video Simulation of FFU Ejection*, 12 2011. http://www.youtube.com/watch?v=AjUDkoLGGks&context=C3ecbc68ADOEgsToPDskK_r9Pb-BjnH8Ka9stcPxXK.

[10] Peregrine Semiconductor, *Datasheet PE4230*, 2005. http://www.peregrine-semi.com/pdf/datasheets/pe4230ds.pdf accessed 2011-05-26.

[11] Radiometrix, *Datasheet TX1/RX1*, 2 ed., 2005. http://www.radiometrix.com/files/additional/tx1rx1.pdf accessed 2011-05-04.

[12] Maxim Integrated Products Inc., *MAX11617*. http://datasheets.maxim-ic.com/en/ds/MAX11612-MAX11617.pdf accessed 2012-02-13.

[13] Freescale Semiconductor Inc., *MPXH6115A*. http://www.freescale.com/files/sensors/doc/data_sheet/MPXA6115A.pdf accessed 2012-02-13.

[14] Maxim Integrated Products Inc., *MAXIM MAX9928/MAX9929*. http://datasheets.maxim-ic.com/en/ds/MAX9928F-MAX9929F.pdf accessed 2012-05-26.

[15] Maxim Integrated Products Inc., *MAXIM MAX4372T/F/H*. http://datasheets.maxim-ic.com/en/ds/MAX4372-MAX4372T.pdf accessed 2012-05-26.

[16] STMicroelectronics, *L3G4200D*. http://www.st.com/internet/com/TECHNICAL_RESOURCES/TECHNICAL_LITERATURE/DATASHEET/CD00265057.pdf accessed 2012-02-13.

[17] STMicroelectronics, *LSM303DLHC*. http://www.st.com/internet/com/TECHNICAL_RESOURCES/TECHNICAL_LITERATURE/DATASHEET/DM00027543.pdf accessed 2012-02-13.

[18] C. A. Balanis, *Antenna Theory Analysis and Design*. John Wiley & Sons, 3 ed., 2005.

[19] *CST Computer Simulaiton Technology AG*, 2012. http://www.test.org/doe/ accessed 2012-02-13.

[20] P. Hall, "Probe compensation in thick microstrip patches," *Electronics letters*, vol. 23, May 1987.

[21] Saft, *Saft MP 144250*. http://www.saftbatteries.com/doc/Documents/liion/Cube572/MP144350_1009.ff6efb8d-6aab-45ef-ae7a-7fe4af5b011d.pdf accessed 2012-02-13.

[22] Future technology Devices International Ltd., *FT232R USB UART IC*. http://www.ftdichip.com/Support/Documents/DataSheets/ICs/DS_FT232R.pdf accessed 2012-05-26.

[23] Actel, *ProASIC3 FPGA Fabric User's Guide*, 2010. http://www.actel.com/documents/PA3_UG.pdf accessed 2011-05-07.

Appendix A

Experiment reviews

REXUS / BEXUS

Experiment Preliminary Design Review

Flight: REXUS 13

Payload Manager: Mark Fittock

Experiment: MUSCAT

Location: Esrange, Kiruna, Sweden **Date:** Thu 01 Mar, 2012

1. Review Board members

Mark Uitendaal	SSC Esrange (Chair)
Olle Persson	SSC Esrange
Hans Henriksson	SSC Esrange
Per Baldemar	SSC Esrange
Mikael Inga	SSC Solna
Mark Fittock	DLR Bremen
Martin Siegl	DLR Bremen
Markus Pinzer	DLR MORABA
Nils Hoeger	DLR MORABA
Alexander Schmidt	DLR MORABA
Andreas Grillenberger	DLR RT
Koen de Beule	ESA Technical Directorate
Natacha Callens	ESA Education Office
Paul Stevens	ESA Education Office (Minutes)

2. Experiment Team members

Ólafía Lára Lárusdottir
Andreas Myleus
Emilio Lozano
Marco Tito Bordogna
Leo Fidjeland
Marcus Lindh

3. General Comments

- SED
  - The document was generally very good. It was clear, concise and very well presented and formatted.
  - It was noted that Chapter 6 was deleted from the SED. This section is very important from a launch and operations point of view, so please ensure that it is included prior to submission of SED v2-0.
  - Chapter 7 was well done, which was very much appreciated by the panel. Chapter 4.3 was also a nice addition.
  - For future versions of the SED, please include the Change Record, as this helps us track any changes or updates made to your documentation. Please also ensure that any additional material or information referenced within the main body of the SED, is included in the Appendices at the end of the document.

- Presentation
    - The presentation was generally well delivered. It was clear, concise, informative and well structured. However it was noted that the WBS section, at the end of the presentation, could have been more concise.
    - For future reference, it is recommended that you try to engage more with your audience; maintain regular eye contact and try not to read directly from the slides.

<u>4. Panel Comments and Recommendations</u>

- Requirements and constraints (SED chapter 2)
    - The requirements and constraints section were generally well thought out. The Functional and Operational requirements were particularly well done.
    - However, it was noted that there were mistakes in the Performance requirements, e.g. for P1.2 your experiment is required to withstand $6.0g_{rms}$. EuroLaunch recommends you use $12.7g_{rms}$ as the qualification level. You also seem to have confused some Performance requirements with Design requirements.

- Mechanics (SED chapter 4.2.1 & 4.4)
    - **It is strongly recommended that you elaborate on the RMU design, prior to submission of SED v2-0. Please provide information on where the electronics will be located and how they will be protected. Please also provide details on thermal protection methods.**
    - Kapton tubing is recommended for thermal insulation, and protection against snow on impact. However, it is recommended that you assess this methods' effectiveness based on the RAIN flight before committing to it.
    - The mass of the RMU is very high at present, due to the module hatch stiffeners. Although this is a good approach, the design should be optimised further if possible, to reduce mass.
    - **The FEA conducted on the module, is very much appreciated. However, please consider the cable groove circumnavigating the module, as this could be a source of structural weakness. It is recommended that you run further FEA, with the cable groove incorporated into your model.**
    - The use of Teflon coating for the RMU guiderails is a good idea.
    - If the temperature sensors are only to be used for internal monitoring of the FFU's, then their function should be separated in the requirements to reflect this.
    - It is recommended that you manufacture spare flight models of the FFU's, so that you always have four pre-loaded flight versions that aren't being used for testing. Ideally 8-10 should be manufactured.

- Electronics and data management (SED chapter 4.2.2, 4.2.3, 4.5 & 4.7)
    - **Please elaborate on electrical interface definitions as soon as possible, and include detailed electrical schematics, in the next version of the SED.**
    - **It was noted that there was no mention of the RMU electronics design in the SED. Please do not neglect this element of the design. It is recommended that you make good use of any heritage from the RAIN experiment.**
    - Please ensure that the FFU's have sufficient battery capacity, to handle all functions and events.
    - Please also be careful with your battery selection, as Lithium batteries can be difficult to transport. It is recommended that you research battery shipping regulations, and take these into account before making your selection.
    - **The FFU wire antenna is a potential single point failure. If they fail, you lose contact. Please be careful with this element of the design, and ensure that they are robust enough to handle the dynamics of ejection and free-fall. Verify your design rigorously.**
    - It is recommended that you use SND fuses where possible, as they are easier to implement.
    - Please ensure that the pyro cutter is well protected, both mechanically and electrically, and cannot be damaged or prematurely activated during integration or flight.
    - It is recommended that you make use of the LO, SOE and SODS signals. It is desirable to be able to power up/down the FFUs on demand, and this function is easiest to implement using these digital inputs.

- Please be aware that magnetometers can be adversely affected by the high iron content in the ground, at Kiruna.

- Thermal (SED chapter 4.2.4 & 4.6)
    - **The thermal analysis section of the SED will need to be elaborated prior to submission of SED v2-0, including preliminary calculations and conclusions.**
    - It is recommended that you provide a table outlining the thermal ranges of individual components.
    - It is recommended that you provide some form of heating for your FFU batteries. Battery performance can degrade at extreme low temperatures, so please look into this.
    - It is also recommended that you thermally isolate any sensitive components within your design, to prevent unwanted heat transfer.
    - Details on your thermal protection system, i.e. the Kapton tube, should be included in your thermal analysis.
    - Please consider the effects of the extreme thermal/vacuum environment on your thermal cutter system.

- Software (SED chapter 4.8)
    - It is recommended that you make good use of RAINs software design, but please don't neglect this element of the design, and be sure to include any modifications or updates to the code in the SED.
    - It is strongly recommended that you recruit a dedicated software engineer into the team, to handle any problems or modifications to the software.

- Verification and testing (SED chapter 5)
    - The verification matrix is generally good, but please pay close attention to your verification methods. Inspection is used too often as a means of verification, which is incorrect. Please follow the guidelines outlined in the verification presentation.
    - The test plan is very good, especially the use of cross-referencing. The panel commends you for this.
    - Please try to optimise the FFU loading procedure. A lot of time is wasted during test campaigns when the FFU's are loaded/unloaded, particularly at spin/balance. This is primarily due to the amount of time needed to set up the loading mechanism.

- Safety and risk analysis (SED chapter 3.4)
    - This section was generally well done, with most of the major technical risks correctly identified.
    - It is recommended that you incorporate project planning risks into your risk register; including loss of personnel through illness, injury or withdrawal. Manufacturing and integration risks should also be included, such as damage to critical components, late delivery of materials etc. Please give as much thought as possible to all risks
    - Please ensure that the FFU loading procedure is as safe as possible. Include safety straps, locking mechanisms and eye protection for personnel into the test package.

- Launch and operations (SED chapter 6)
    - Please define your post-flight recovery procedure and requirements prior to submission of SED v2-0. You will be advised on Esrange's recovery policy in due course.
    - **It is strongly recommended that you confer with StrathSat-R, regarding your localisation frequencies. In the event that you are located in the same payload, you do not want to have signal clashes.**
    - **Please be aware that you need permits for certain electromagnetic frequencies in Sweden, so please ensure that you identify your required frequencies as early as possible and apply for permission.**

- Organisation, project planning & outreach (SED chapters 3.1, 3.2 & 3.3)
    - Please clarify and improve your Gantt chart dependencies. At present they are a little confusing.
    - **With such a large group, team management will be challenging. It is recommended that you**

weigh up your required man-hours against the availability of your team. Please do not underestimate the amount of work involved.
  - In the event that the FFU localisation system fails, and they are not recovered at the same time as the payload; you should factor the cost of manually recovering them into your project budget.
  - Please include all organiser logos on your website, and be sure to include all sponsorship information in your SED.
  - The outreach conducted to date has been excellent. The panel was very impressed by your efforts and encourage you to keep it up.

- Others
  - Your experiment module should be available by August 2012. Once your design is fixed, we will ask you to provide CAD models and engineering drawings. The module will then be manufactured and dispatched to you.
  - In the meantime, you should consider building an RMU mock-up to test your ejection mechanism.

5. Internal Panel Discussion

- Summary of main actions for the experiment team
  - **The RMU design requires more focus. In particular the RMU electronics and systems need to be defined in greater detail. This will be scrutinised at the CDR.**
  - Make sure you have adequate software competence in your team. It is important that you understand the system in-depth, so that you can develop and de-bug your software if necessary.
  - The following addendums to the SED will be required to clarify your experiment design:
    - Will you require any digital signals from RXSM, i.e. LO, SOE and SODS? If so, for what purpose?
    - Please provide detailed electrical schematics as soon as possible.
    - Please provide a software development plan. Will you have to update the RAIN software code for your experiment? If so, how and who will do it? Please provide flow diagrams, if possible.
    - Please provide some initial clarification on the RMU mechanical design. Where will your PCB be mounted? Define your thermal protection system (kapton tube?) etc.
    - Please define which internal FFU sensors will be used, and for what purpose.
  - Review and address all discrepancy items and inconsistencies listed within this report, prior to submission of SED v2-0.

- PDR Result: pass / conditional pass / not passed
  - **Pass** – subject to submission of the above SED addendums.

- Next SED version due
  - SED v2-0

REXUS
Experiment Critical Design Review

Flight:	**REXUS 13**
Payload Manager:	Mark Fittock
Experiment:	MUSCAT
Location:	DLR, Oberpfaffenhofen, Germany **Date:** 05/07/2012

1. Review Board members

Mark Fittock	DLR Bremen
Juergen Knof	DLR MORABA
Tobias Ruhe	DLR MORABA
Nils Hoger	DLR MORABA
Marcus Hoerschgen	DLR MORABA
Frank Hassenflug	DLR MORABA
Natacha Callens	ESA Education Office
Alex Kinaird	ESA Education Office (minutes)
Koen DeBeule	ESA Technical Directorate – Chair
Mikael Inga	SSC Solna
Jianning Li	SSC Solna

2. Experiment Team members

Emilo Lozana (KTH)

Marco Tito Bordogna (KTH)

Darri Kristmundsson (KTH)

Markus Fjallid (KTH)

3. General Comments

- Presentation
  - The presentation was generally very good.
  - For future reference try and engage the audience more, make eye contact and try not to read directly from the slides.

- SED
  - The progression of your SED from PDR was, in general, quite disappointing, you might want to consider a side by side comparison of the two versions to see this for yourself.
  - In general with such a large document you should try and include conclusions at the end of sections and/or chapters.
  - Try and be more concise.
  - You should be careful and consistent with units (see density on page 33).
  - On page 165 you refer to a terrorist cutter, be careful with spelling and grammar, try and have someone outside you team read through a document before submission.
  - Be careful with your versioning!
  - Try and stick to the format of the SED guidelines, don't move or delete chapters.
  - **Provide a phone number for your team in the SED**

4. Panel Comments and Recommendations

- Requirements and constraints (SED chapter 2)
  - It seems there is still a little confusion between performance and design.
  - You don't seem to have included many critical performance requirements e.g.: Include how and how fast etc. you will measure the temperature.

- Mechanics (SED chapter 4.2.1 & 4.4)
  - Your FEA was reviewed by an expert at ESA who provided the following comments:
    - In your FEA the type of element and meshing is good, but consider changes to increase accuracy and efficiency, if you want more advice please ask the organisers for it.
    - Try and focus on best achievable solution in the document rather than a number of options.
    - No need for elastic strength analysis.
    - Perhaps consider a full dynamic load analysis.
    - You seem to have used best approach, assuming manufacturing is not an issue and boundary conditions are correct.
  - You should ensure you give an overview of all the system (RMU and FFU, module and bulkhead), include sketches and dimensions (top, side view etc.).
  - Bear in mind that in general the FFU is not considered critical for the rocket.
  - **The major point of concern for the panel with respect to your mechanical design is the hatch system. The panels' concern is for the possible aerodynamic effects of your current system and possibility of premature release of the hatches. As such you should implement the following design changes:**
    - **Hatches should be flush with the surface.**
    - **Implement a solution where the wire feeds through the inside of the module, or in a groove, in general find a better solution for the fixation.**
    - **Find a solution which protects the hook.**
    - **The hook and/or cable fixation is to be inside the rocket.**
    - **Include dimensions and specifications of wire.**
    - **You should outline all of the above clearly in your document.**
    - **If you need more advice on this you should contact the organisers ASAP.**
  - With regards to your Kapton protection you should think carefully about this design, you should either:
    - Implement a sufficient system around your tunnel which protects other modules
      or
    - Implement a system with a top and bottom cover which protects other modules (such as a plastic or aluminium plate) but with consideration for the cable routing.
  - You should provide some kind of mechanical protection for your electronics board. This is important for the first section of the flight where you need it to operate. A simple protection would be sufficient here.
  - The panel commend your idea of using comparison for analysis in the FEA, but suggest you should include more analysis than just buckling (if you have completed more analysis you need to make this clear in the document).
  - Due to the length of your document it is suggested that you only include the final solution of analyses with a mention of the tradeoff and a focus on the final analysis.
  - Please include the boundary conditions and constraints in your analysis.
  - Only include the two required load cases in the report.
  - For the bending moment analysis consider continuing performing the analysis by comparison (with an unmodified module).
  - Be sure, in all cases, to include your safety factors (assumed and calculated).
  - Do not neglect temperature effects in your design and/or analysis.
  - You should clearly label the point of peak stresses in your diagrams/results.
  - Your FEA should also include the blocking mechanism of the hatches.

- You should clearly show how the lower cross is attached to the structure and this attachment should be subject to an FEA.
- **In general there is not enough information about the mechanical interface, please expand on this (see the SED guidelines)** .
- D-SUB bracket is upside down in the CAD model, please correct this.
- Please include assembly drawings where/when available.
- As with all the sections please include a concise conclusion to the mechanical section(s).

- Electronics and data management (SED chapter 4.2.2, 4.2.3, 4.5 & 4.7)
  - It is not clear if you use signals (LO, SOE etc.), make this clear in your document. If you have signal reception as heritage only then make this clear (preferably modify the design!).
  - It seems you have a lot of charging circuits but a lack of back current protection – this is simple to correct, please implement a design change here.
  - One of your capacitors is incorrectly labelled as 100nF instead of 100μF – correct this.
  - Be clear about the role of fuses, for example there role in launch and/or testing only, include this in the document.
  - It is suggested the use of stacked MOSFETs is not standard, this can normally be avoided using logic and reducing the power stack – this is a suggestion for future work.
  - Remove references that are "unsure what this is".
  - **You should provide the required frequency information ASAP.**
  - You should check the transmission slots etc. for the globalstar system, ask for help from the organisers if you need coordination with other teams/Eurolaunch.
  - Make it clear in the document whether and when you transmit raw GPS data and global GPS data. Include the expected timings/events for these transmissions.
  - Include the type and design umbilical connector to your FFUs in the report. Also include how the separation occurs.

- Thermal (SED chapter 4.2.4 & 4.6)
  - Page 63 is missing the parameter regarding the skin of the FFU.
  - See above (mechanical) for the Kapton tape comments/thermal protection comments.

- Software (SED chapter 4.8)
  - There is not much description about what happens in the FPGA, you should describe more in the document, specifically about what triggers what; (e.g. pressure sensor for the parachute) and how this is handled.
  - Be aware that an error in the FPGA code can be fatal, this should at least be included in the risk register.
  - Much of the software seems like it's copied and pasted from previous designs, make clear that you don't do this by documenting it properly.
  - In general it was felt much more useful detail could be provided on the software design

- Verification and testing (SED chapter 5)
  - In the verification matrix you are using inspection far too much: e.g. design requirement 4.1 – you should verify through test not inspection.
  - In general re-think your verification method (especially inspection).
  - The panel commend you cross coupling between the verification matrix and the requirements.
  - The panel recognise that all major required tests are included.
  - The battery must be tested in vacuum and inspected after the full FFI test.
  - You shall perform a shaker test to qualification level for your hatch system.

- Safety and risk analysis (SED chapter 3.4)
  - MS.R1: this risk should be lower now, the risk register should be 'live' i.e. updated when you mitigate a risk.
  - Please ensure you update the risk register before each version.
  - If a risk is removed (by the removal of hardware for example) then don't remove the risk from the table but include a remark such as 'risk deleted'.
  - The sky diver test should be included in the risk matrix.

- In general the sky diver seems risky, you should address this test carefully, ensure this is performed after your vacuum test.

- Launch and operations (SED chapter 6)
  - Include the full procedure for securing the module upon recovery and during operations/transport.
  - Please include in your procedures a method to inform the recovery team about whether the telemetry indicates a successful ejection.
  - Please clarify how the LIDAR should be operation (if at all) and any restrictions (if any) it would have on the launch.
  - Be sure to look at the requirements for battery shipping (also include this in safety if necessary).
  - You should never refer to other chapters in chapter 6 – this section should be standalone.
  - You should include the pyro safety information in this section and the safety section.
  - Your preparation activities should be well documented, they will be much easier and less hectic if you plan (although it's still envisaged they will be intensive due to your design).
  - **In general your chapter 6 needs considerable improvement before it reaches CDR standard.**

- Organisation, project planning & outreach (SED chapters 3.1, 3.2 & 3.3)
  - You should clarify how many team members you have and you should include this in the planner.
  - The Gantt chart in the appendix only shows dates, not tasks, please correct this.
  - Please include the sponsors in the document.
  - Consider adding more experiment design and evolution and pictures on the website.
  - Post more on Facebook.
  - Be aware of the dangers of a late IPR with respect to your development timeline.

<u>5. Internal Panel Discussion</u>

- Summary of main actions for the experiment team:
  - **Update your hatch deployment system.**
  - **Complete your chapter 6 with the comments here and the SED guidelines.**
  - **Provide the required frequency information to the correct parties.**

- CDR Result: not passed.

- Next SED version due

  - You should provide an updated **SED v2-3** outlining your new mechanical design ASAP. The deadline set for this is the **19th of July at 4pm** but it is strongly suggested you provide this earlier.
  - Following acceptance of your new mechanical design you should provide a further **version 2-4** to close the other points covered in this report, at a minimum you should address the highlighted (**bold)** points. The deadline for this is **5th of August.**
  - **Version 3-0** (subject to passing the CDR) will be due around 1 week before your IPR, provisionally due on the **24th of September.**

REVIEW

Flight: RX-13

Experiment: MUSCAT

Review location: KTH, Stockholm, Sweden

Date: 08Oct2012

Review Panel

Mikael Inga – SSC

Experiment Team members

Ólafía Lára Lárusdóttir

MUSCAT Team

Nickolay Ivchenko (Associate Professor)

PICTURES

FFU parts and parachute

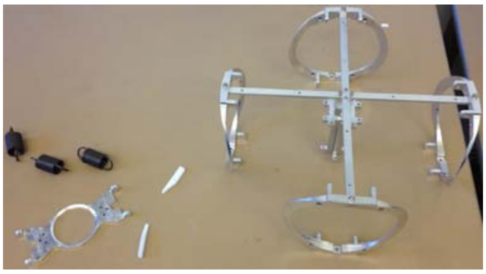

RMU Mechanical parts

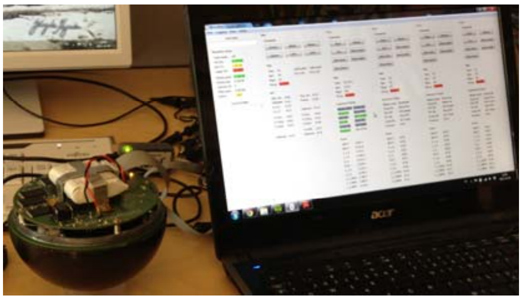

Test FFU and GSE SW

GENERAL COMMENTS

- Time to put everything together and start testing on complete flight systems.

PANEL COMMENTS AND RECOMMENDATIONS

Science

- Will meet objectives.

Requirements and constraints (SED chapter 2)

- Updated, but just rearranged.

Mechanics (SED chapter 4.2.1 & 4.4)

- RMU mechanical design frozen, parts for delivery at end of October.
- FFU mechanical design froze, FM completed in late October.
- All parts in house, end October for assembly.

Electronics and data management (SED chapter 4.2.2, 4.2.3, 4.5 & 4.7)

- FFU FM PCBs delivered but not populated.
- FFU Transmitters in house, all long-lead items in house.
- RMU design frozen, PCBs will be ordered.

Thermal (SED chapter 4.2.4 & 4.6)

- No comments.

Software (SED chapter 4.8)

- FFU 95% done.
- No GPS position via beacons, shortage of memory buffer (due to long NMEA msg.).
- RMU 20% done (reuse of RAIN SW).
- GSE SW 80% done.

Verification and testing (SED chapter 5)

- Revise test plan to make is realizable (Prioritize tests, combine tests etc.).
- Shaker test to be done on complete mechanical system. (Vibration levels?)

Safety and risk analysis (SED chapter 3.4)

- No comments.

Launch and operations (SED chapter 6)

- Charge line?

Organisation, project planning & outreach (SED chapters 3.1, 3.2 & 3.3)

- Most of the team will be gone in December.
- Keep web alive.
- Revise test plan to make is realizable.

SED

- No comments.

End-to-end Test

- Only Test of FFU (TM) to GSE SW (No RMU).

Others

- No comments.

FINAL REMARKS

Summary of major actions for the experiment team

- Finalize flight FFUs and RMU and start testing.

IPR Result: pass / conditional pass / fail

- Pass.

Next SED version due

- EAR

Summary of actions for EuroLaunch

- Check ETAG Tracking, handheld, position format.
- Esrange ETAG multi-channel RX progress?
- Shaker test to be done? Levels? Where? When?
- TRW Pyro cutters?
- Charge line? Details?
- RXSM Connector? (in module).
- Team requests EAR in 1st week of December.

REVIEW

Flight: RX-13

Experiment: MUSCAT

Review location: KTH, Stockholm, Sweden

Date: 22Jan2013

Review Panel

Mikael Inga – SSC

Experiment Team members

Ólafía Lára Lárusdóttir

Markus Fjällid

Marcus Lindh

Marco Tito Bordogna

PICTURES

MUSCAT Module

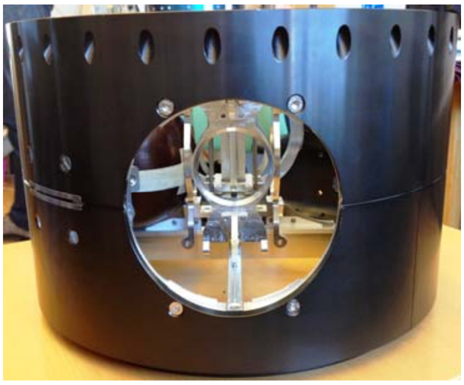

MUSCAT Module

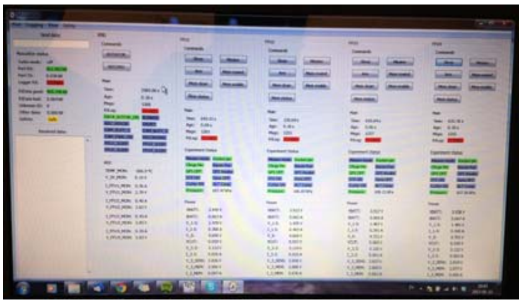

EGSE Software GUI

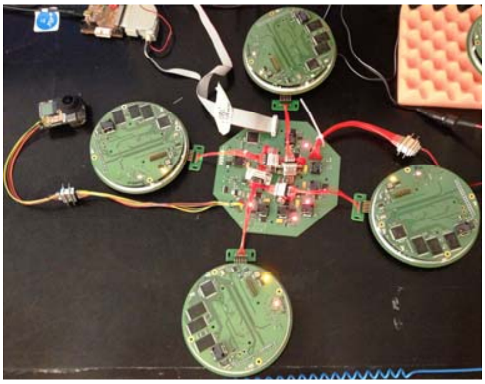

RMU and FFUs electronics, end-to-end test

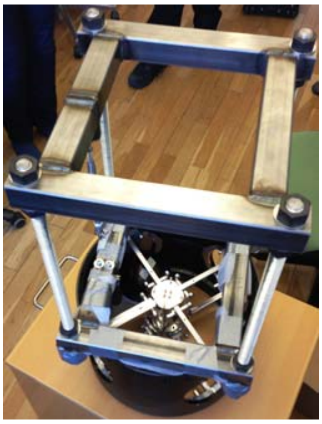

Wire Tension Tool

Hatch Tool

GENERAL COMMENTS

- Experiment almost finalized, all parts are available and the final assembly of ejection system, RMU and FFUs remains.

PANEL COMMENTS AND RECOMMENDATIONS

Science

- Ok.

Requirements and constraints (SED chapter 2)

- No changes.

Mechanics (SED chapter 4.2.1 & 4.4)

- Final assembly of ejections system and locking of nuts/bolts remains.
- Integration of Electronics (RMU and FFUs) remains.
- Implement some cover/protection of PCBS to avoid dirt/short-circuits.
- FFUs (4 Flight + 2 spares), final assembly/integration remains.
- RMU (1 Flight+ 1 spare), final assembly/integration remains.
- Wire tension system: unsure of tension, measure it somehow.
- Module covers (hot gas protection) still to be manufactured.
- Placement of D-sub connector still to be finalized.
- Camera mechanics still to be manufactured.

Electronics and data management (SED chapter 4.2.2, 4.2.3, 4.5 & 4.7)

- Electronics finalized.
- FFUs electronics finalized.

- Spare RMU still to be soldered.
- Bring 2 USB-Serial converters and cable to tests and campaign.
- Routing of the TRW cutters cables still to be finalized.

Thermal (SED chapter 4.2.4 & 4.6)

- No comments.

Software (SED chapter 4.8)

- On-board Software finalized.
- EGSE Software almost done.
- EGSE Software, Loss of communication handling to be looked at.
- EGSE Software, Engineering to scientific values conversion to be calibrated.

Verification and testing (SED chapter 5)

- Shaker test to be done at Integration week (fully assembled experiment with springs)
- Thermal test of thermal cutters still to be done.

Safety and risk analysis (SED chapter 3.4)

- Wire tension? Coarse measurement necessary.

Launch and operations (SED chapter 6)

- Handling of FFU GPS positions, still to be finalized with help of SSC.

Organisation, project planning & outreach (SED chapters 3.1, 3.2 & 3.3)

- Outreach person left for master thesis, outreach still to be kept alive.
- Some outreach already planned.
- Ship experiment latest 7th of February to Bremen (Integration week).

SED

- No comments.

End-to-end Test

- Successfully done with REXUS Service Simulator (RXSM).

Others

- Check with RAIN about the shipment of the experiment.

FINAL REMARKS

Summary of major actions for the experiment team

- Final assembly of the flight hardware.
- Finalize EGSE Software (calibrations, Loss of communication handling).
- Finalize handling of FFU GPS positions during/after flight.

EAR Result: pass / conditional pass / fail

- Pass

Next SED version due

- SED (Ver. 4) Delivery?

Summary of actions for EuroLaunch

- D-sub brackets with correct (different) radius.
- ETAG/beacon operations and interface to pos-net.
- SSC will provide a transport box (also battery box).
- More TRW Cutters for test/flight

Appendix B

Test Reports

This appendix includes reports on each of the test conducted.

Battery capacity test at different temperatures

Anders Haponen, Anton Hou

February 8, 2012

Abstract

Discharge tests at low temperatures revealed that the Moli ICP103450CA [reference to datasheet] battery did not function properly at a temperature of -30° C, this was more or less expected since the capacity for that temperature was not specified in the datasheet. The stored energy for the Saft MP 144350 [reference to datasheet] was approximated from the test data to 6.2 Wh at -30° C, compared to the claimed 7-8 Wh.

Nomenclature

$V(t)$	= Battery voltage under load as a function of time
R	= Load resistance
P_{mean}	= Mean power during discharge
t_{total}	= Total discharge time
E	= Total discharged energy

1 Background

The battery test was performed to compare the two alternatives for the batteries in the FFUs. The batteries were tested by discharging them over a constant resistive load at different temperatures. The batteries were placed in a temperature chamber and were connected to a resistor on the outside, where the voltages were meassured. The voltage over each battery was logged using a measurement plotting system from HP (7090A [reference]). To avoid damaging the batteries the load was disconnected from each battery before the battery reached its specified cut off voltage.

To ensure that the batteries were equally charged for each test they were recharged until the recharge current reached 2% of the recommended maximum recharge current according to recommendations in the datasheet.

2 Method for estimating battery capacity

One method to compute the energy is to first calculate the mean power and then multiplying by the total time:

$$E = P_{mean}t_{total}, \tag{1}$$

where the mean power can be written as:

$$P_{mean} = \frac{(V(t)^2)_{mean}}{R} \tag{2}$$

This substitution is useful since the resistance is constant. Since our data were not digitized we had to approximate the mean square voltage.

3 Results

At -30° C the Moli battery reached its cut off voltage just from the temperature drop. The battery was also tested at -25° C, at this temperature the stored energy was approximated to 2-3 Wh. To confirm that the specific battery used for testing was not defect it was also tested at room temperature. At room temperature the stored energy was approximated to 6.5 Wh, compared to the claimed 7.4 Wh. The Saft battery was tested at -30° C and its stored energy was approximated to 6.2 Wh, compared to the claimed 7-8 Wh.

4 Conclusion

Based on the results in this report and the and the fact that a temperature of -25° C is not uncommon during a night in Kiruna and the capacity of the Moli battery at this temperature was not high enough, the recommended action would be to use the Saft battery.

A Discharge curves

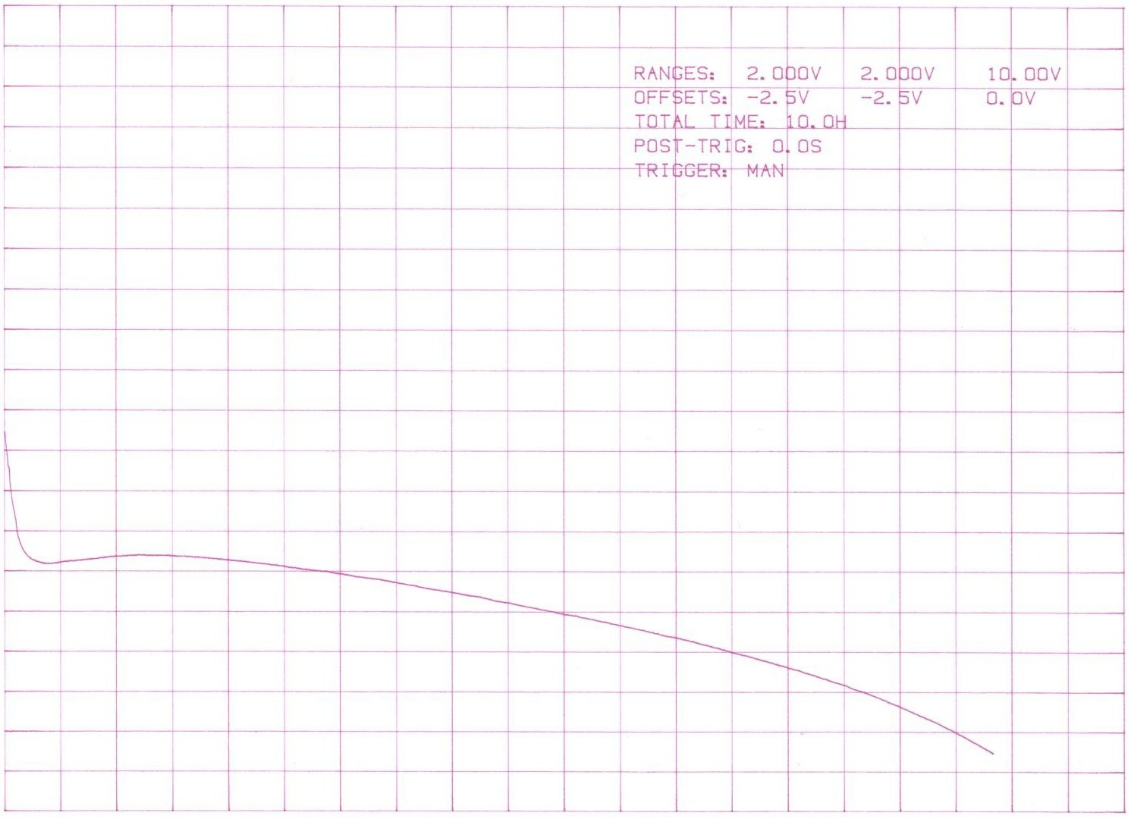

Figure 1: Discharge curve for the Saft battery at -30° C

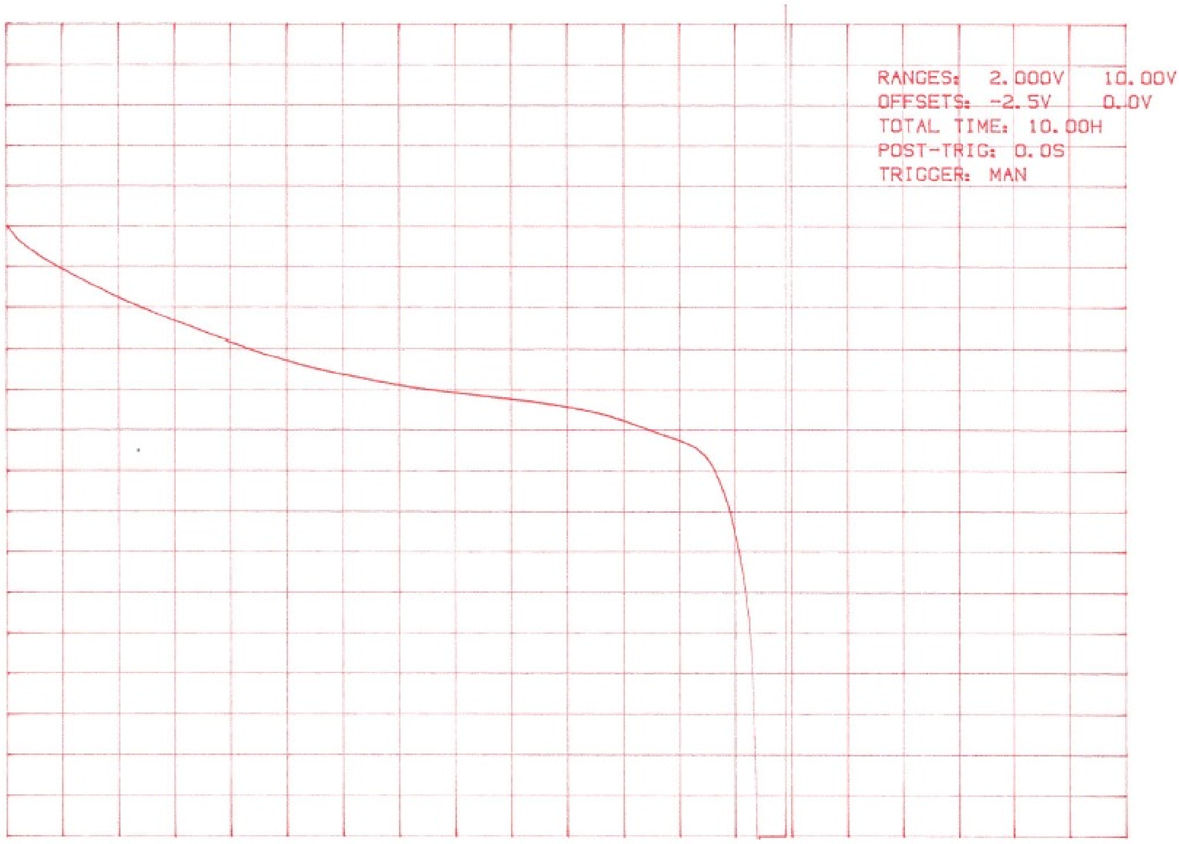

Figure 2: Discharge curve for the Moli battery at room temperature

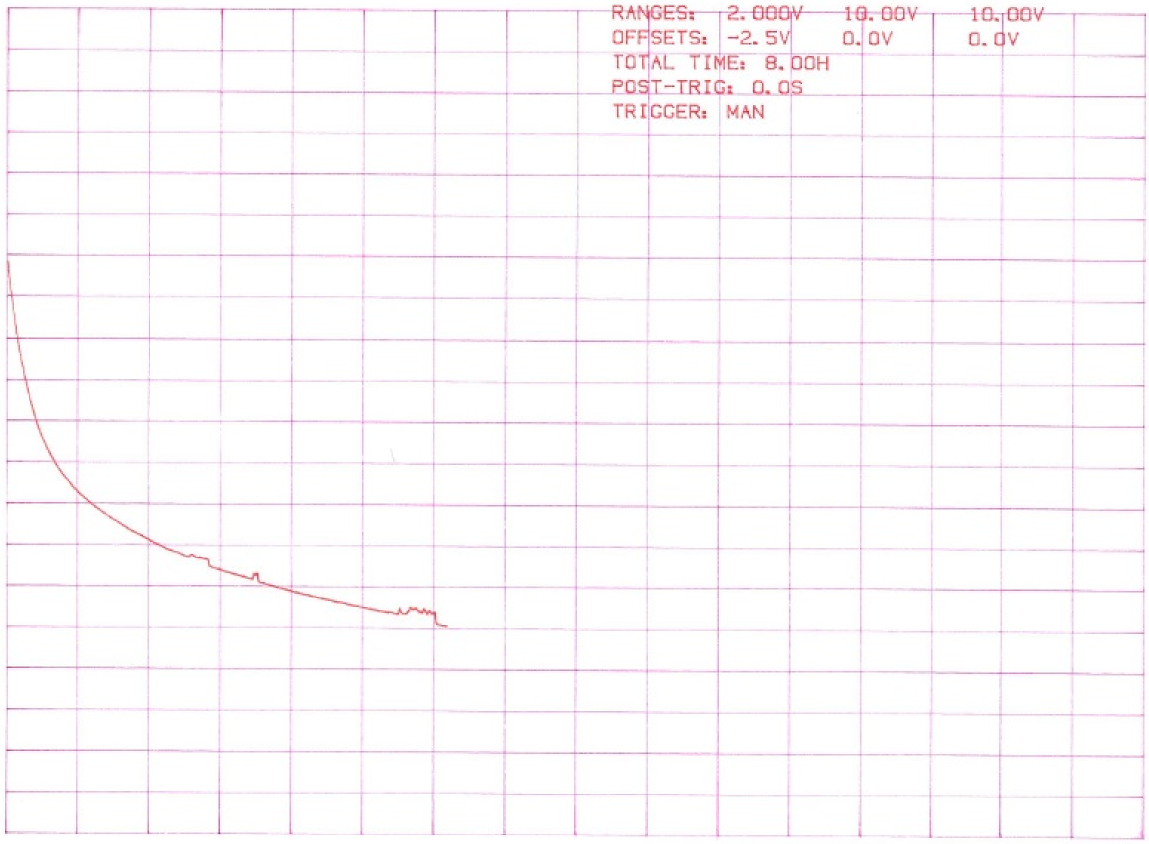

Figure 3: Discharge curve for the Moli battery at -25° C

Structural analysis of the modified and unmodified REXUS rocket modules.

Emilio J. Lozano

July 19, 2012

List of symbols and abbreviations

MUSCAT - Multiple Spheres for Characterization of Atmospheric Temperature.
RMU - Rocket mounted unit.
FFU - Free falling unit.
ω - Slenderness parameter from EUROCODE 9.
α - Angle of the circular sector swept by the openings in the weakest section in the modified module.
D -Outer diameter of the module.
R - Outer radius of the module.
H - Length of the shell structure.
t - Thickness of the thin-walled section of the module.
d- Diameter of the openings.
FEM – Finite element method.
I_x - Moment of inertia of the section with respect to the x axis.
I_y - Moment of inertia of the section with respect to the y axis.
C_x - Influence coefficient of the boundary conditions according to EUROCODE 9
A - Area of the section.
E - Young modulus.
ν - Poisson ratio.
$\sigma_{cr,x,EUROCODE9}$ - Normal critical stress according to the EUROCODE 9 formulation.
$\sigma_{cr,x,Timoshenko}$ - Normal critical stress according to the Timoshenko formulation.
$\sigma_{cr,x,ABAQUS}$ - Normal critical stress according to the ABAQUS FEM analysis.
$\sigma_{cr,x,ABAQUS,X\ reinforcement}$- Normal critical stress in the case X of reinforcement
CAD - Computer aided design
BSR - Back support reinforcement
D' - Diameter of the module with the groove ad the weakest section
D''- Diameter of the back support reinforcement of the of the module
t' - Thickness of the module at the weakest section when the groove is implemented
t'' - Thickness of the back support reinforcement
β - Angle of the circular sector swept by the openings of the back support reinforcements.
ECSS - European Cooperation for Space Standardization
χ - Reduction factor for axial load
ω_0 - Heat affected zone factor compression
ω_x - Heat affected zone factor bending
N_{Ed} - Axial compressive force
N_{Rd} - Axial capacity of the cross-section
M_{Ed} - Bending moment according to first order theory

Abstract

This report presents the structural analysis of the modified rocket module to determine the changes required to achieve the same strength and stiffness as the unmodified rocket module.

The equal-strength-and-equal-stiffness design approach was chosen because of the lack of information about the loads the module is subjected to during launch, both in terms of load type and the magnitudes. A literature review on sounding rocket launch loads revealed that the very little information is available. Thus, it was determined that designing the modified module so that:

1. the factor of safety against elastic buckling,
2. the cross-section area (axial strength), and
3. the moment of inertia (bending strength)

are equal to those of the unmodified module would be the most safe and accuracy approach in the absence of launch load information. Both the unmodified module, which we know is flight proven, and the modified module were therefore subjected to the same type of analysis.

The following analyses and conclusions were performed and drawn, respectively:

- **Sections 2.2.2-2.2.4, 3.4 and 3.5**: The elastic buckling under axial load of the unmodified module was analysed. The finite element results are only 5% higher than the analytical solutions and the mesh is refined until the solution converges. The elastic buckling analysis shows that the finite element model is valid and that the module will yield before buckling. This tells us that we can use a section analysis to compare the capacities of the modules.

- **Sections 4.1.3**: The elastic buckling load of the modified module with four openings, increased wall thickness, circumferential groove for the cable and the strengthening of the skin due to the groove is analysed and found to have a slightly higher elastic buckling strength than the unmodified module. This means that both modules will have the same factor of safety against buckling, so simple section analysis can be used to compare their load bearing capacities.

- **Section 3.1:** The simple Ramberg-Osgood elastic-plastic material model for the aluminium alloy, proposed in Eurocode 9, is introduced for the elastic-plastic analysis of the modules subjected to axial, bending and combined axial and bending loads. An elastic-plastic material model is required to investigate the effects of stress concentrations due the various openings in the modified module.

- **Section 3.2:** The upper and lower edges of the modules are simply supported, i.e. the translational degrees of freedom are constrained to prevent ovalisation of the upper and lower rings. These boundary conditions have been found to be accurate as the assembly of modules means that there in fact are two rings preventing ovalisation. Analyses of a stack of three modules have shown that the simply supported boundary conditions represent the behaviour of the module in the module stack. In addition, both the unmodified and the

modified modules are analysed with the same boundary conditions, so the comparison is accurate.

- **Section 3.4:** A uniform mesh size was shown to be good for the convergence of the elastic buckling load, but a non-uniform mesh was implemented to more accurately capture the stress concentrations around the openings.

- **Section 4.1:** The increase of the wall thickness for the modified module is determined to get at least the same elastic buckling load, cross-section area and moment of inertia as the unmodified module. Preliminary analysis of various strengthening measures showed that the increasing the wall thickness was the most mass optimum strategy.

- **Section 4.1.2**: The stress concentrations in the modified module for axial load were analysed and found to be acceptable. Parts of the module will be in the plastic region, but the module could still tolerate the load level corresponding to a factor of safety of 2.

- **Section 4.1.4:** The capacity of the modules for combined axial load (from launch acceleration), shear and bending loads (from gravity and vibrations) are analysed. Stress concentrations are found to be worst in the groove close to the openings, but in a limited region. The stress concentration factors for extrapolated sounding rocket load levels, found in literature, are not critical despite being above the yield strength of the material as the regions of high stresses are very small. An interaction formula for the combined axial load and bending load is derived from Eurocode 9, which describes that capacity of the module for any combination of axial and bending loads.

- **Section 6:** A thermal analysis to study the displacement of the module under heating is performed. The analysis of the module with the collar and the cross shows that the stresses induced by the thermal loads are not critical, partly because the screw connection of the crosses has some play which can adjust for the thermal displacements.

- **Section 7:** The pretension of the cable to keep the hatches closed during launch results in radial forces on the collar, which are screwed to the module. The effect of the cable pretension is a stress concentration in the cable groove close to the openings, but the stress levels are below the yield strength and the region is small, so this load case is not critical.

To summarise, the updated and extended analysis of the modified module confirms that the proposed design seems to be safe for launch as the modules have equal cross-section areas and moments of inertia and the stress concentration regions in the modified module are small for realistic load levels.

Analysis results		
Unmodified module		**Percentage with respect to initial properties(%)**
Wall thickness (mm)	4	100
Mass (kg)	4.58	100
Critical buckling stress (MPa)	1005	100
Cross-section area (mm^2)	4423	100
Moment of inertia ($x10^7$ mm^4)	6.85	100
Stress concentration at the openings (MPa)	Not relevant	Not relevant
Parts in the assembly	1	----
Modified module (134mm openings) groove + groove reinforcement		**----**
Mean wall thickness (mm)	8	200
Maximum wall thickness (mm)	12	300
Minimum wall thickness (mm)	8	200
Mass (kg)	5.39	118
Critical buckling stress (MPa)	1017	101
Cross-section area (mm^2)	4795	108
Moment of inertia ($x10^7$ mm^4)	7.05	102
Stress concentration factors at the openings	Compression=7 Bending=5 Combined=4	Not relevant
Safety factor under realistic stress level	1.97	---
Reference safety factor	1.1 [12]	---
Parts in the assembly	1	----

1. Introduction

The need of this study arises from the structural modification with four openings of the standard rocket module demanded by the MUSCAT experiment. These four openings are needed in order to be able to release FFUs. The aims of this study of the rocket module are:

- Quantify the loss of stiffness and strength in the rocket module when the four openings are implemented

-Suggest a way to reinforce the modified rocket module such the modified rocket module has the same stiffness and strength of the original unmodified rocket module.

The initial approach of assessing the stiffness and strength loss is by assessing the stiffness of the buckling critical stress through a linear elastic buckling analysis for axial compression. The behaviour against specific launch loads has not been considered as a reliable approach because the absence of information about the loads during the mission. That approach would also be more time consuming because it requires a more elaborated dynamic analysis. Furthermore, the approach of trying to match the same stiffness and strength of the unmodified rocket module is more reliable because the unmodified rocket module has been tested under reliable conditions. This means that if the modified module that has the same stiffness and strength as the unmodified rocket module, it should be able to stand the same loads. This has been done by using the interaction formula stated in EUROCODE 9[2] for combined loading conditions in cylindrical shells as it can be seen in page 46. Although the approach of not evaluating the load will not be as refined as the evaluation of the loads it is known according to [7] the margin of safety can absorb the discrepancies.

2. Load bearing capacity assessment

2.1. Openings placement

The openings in the rocket module are located in the middle position of the thin-walled section of the rocket module. The thin-walled section of the rocket module is the 150 mm long section where the thickness of the wall is 4 mm. The denomination thin-walled comes from the value of the ratio between the thickness of the rocket module and its radius which is 0.02 for this case. The value of this ratio according to Vensel [8] allows the treatment of the sections as a thin shell (thin-walled section) because according to Vense [8*]"If the ratio mentioned above is negligible in comparison with the unity the shell structure can be considered as a thin shell ".* The section denoted as the thin-walled section can be seen in the Figure 1.

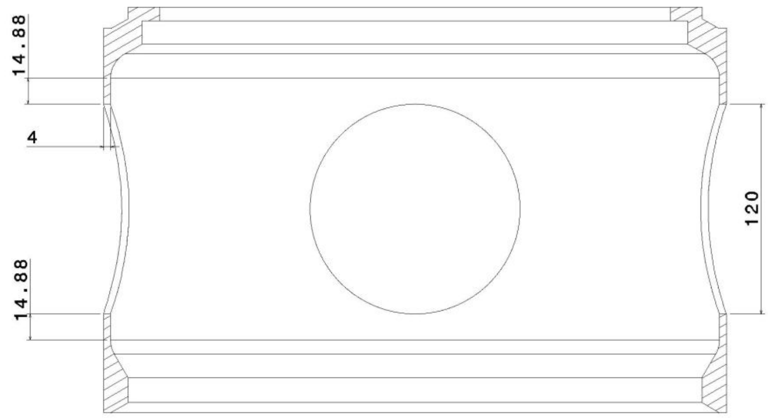

Figure1: Section of the rocket module.

The location of the opening in the middle of the thin-walled section of Figure 1 is motivated by the nature of the loads that the rocket module will be subjected to during the mission among other practical considerations like a smooth transition from the section where the screws are attached to the thin-walled section. The loads will be applied from the top and the bottom part because the rocket module will be installed over the rocket engine with other rocket modules over it so the modified rocket module will be subjected to the thrust of the rocket engine and the inertia forces of the upper rocket modules. Therefore according to [1], which suggests that the opening should be as far as possible from the extreme where the load is implemented in order to increase the stiffness and strength. The most appropriate location of the openings in the modified RMU should be in the middle of the thin-walled section because it is there where the distance is the same from the areas where the loads are applied. The openings are separated by 90 degrees in angle to have the maximum possible separation. The maximum angular separation is desirable because the greater the distance between opening the lower influence it will exist between them.

2.2. Classical load bearing capacity assessment

The initial assessment of the stiffness and strength is through elastic buckling analysis of a cylindrical shell under axial compression. This analysis is performed assuming that the section is a hollow cylinder of 4 mm thickness with an effective length of 150 mm. The assumption of considering the 150 mm section is on the safe side since the top and bottom rings increase the stiffness and strength of the rocket module. The main aim of this stage is by means of the EUROCODE 9[2] and the Timoshenko [3] classical buckling formulations establish the reference value of the critical buckling stress of the cylindrical shell for the validation of the subsequent FEM calculations. Therefore if the rocket module without openings has the same load capacity as the modified rocket module with opening, the associated stiffness of both configurations should be the same.

2.2.1. Classical section analysis

The assessment of the stiffness and strength cannot be conceived without the calculation of the geometric characteristics of the involved sections. Therefore an analysis of the weakest section is performed and compared with the characteristics of the unmodified section in order to obtain a first estimate of the size of the stiffeners around the openings.

Unmodified RMU section

Figure 2 shows the characteristic section of the unmodified module

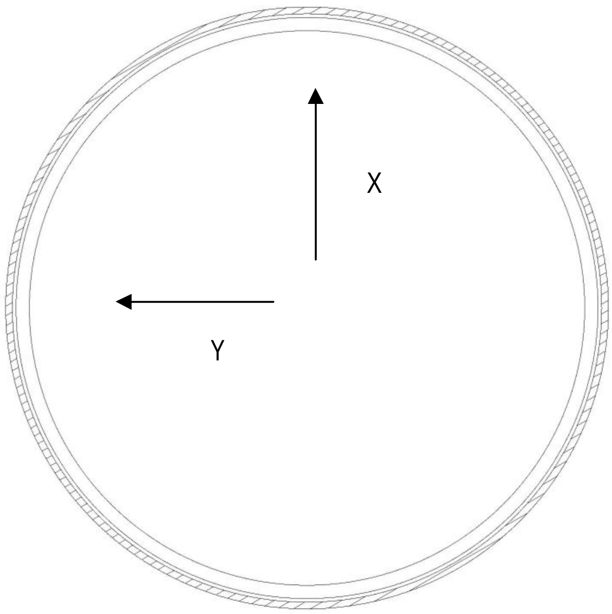

Figure 2, Unmodified section geometry

The properties of the section relevant for the stiffness and strength are the moment of inertia (*I*), area (*A*) and Young's modulus (*E*). Young's modulus is a property of the material: therefore it is the same for the sections of the modified and unmodified rocket module. Then the affected properties of the section are the moment of inertia and the area. In the case of the unmodified section, the moment of inertia and the area are obtained from Equations (1) and (2) for the thin-walled section of the rocket module

$$A_{unmodified\ RMU} = \frac{\pi}{4}[D^2 - (D-2t)^2] \quad (1)$$

$$I_{unmodified\ RMU} = \frac{\pi}{64}[D^4 - (D-2t)^4] \quad (2)$$

where D is the diameter of the section and t is the thickness of the thin-walled section.

For this case $A_{unmodified\ RMU}$ =4423mm^2 and $I_{unmodified\ RMU}$ =6.852x10^7 mm^4.

Modified rocket module section

Figure 3 shows the characteristic section of the modified module at the point where the openings reach their bigger diameter. At this point any reinforcement can be seen figure 3 because the purpose in this step is to analyze the loss of section properties. The respective reinforcements and modification will be treated in coming sections

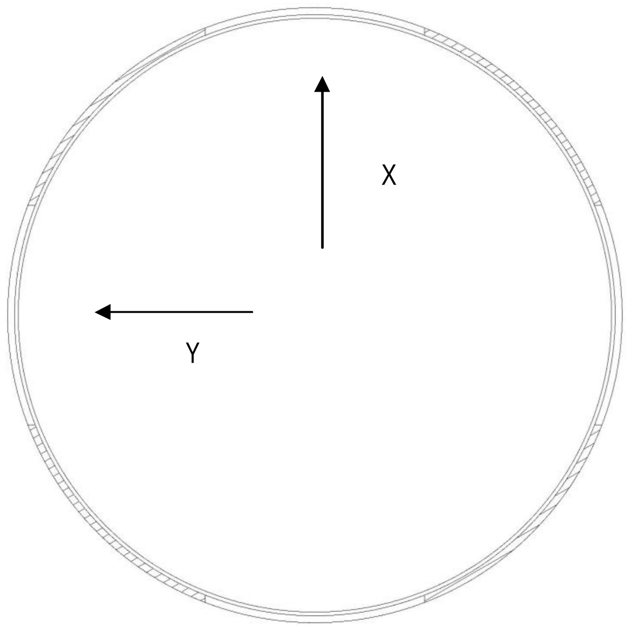

Figure 3: Modified section geometry.

Beside the previously mentioned parameter the diameter of the openings is a new factor that will influence the characteristic parameters of the section .For the modified section the area and the moment of inertia as functions of the diameter (*d*) of the openings can be expressed by means of Equations (4) ,(5) ,(6) and (7). Moreover, Equation (3) expresses the relationship between α and the dimensions of the rocket module. A view to Figure 4 is recommended in order to understand the upcoming variable α.

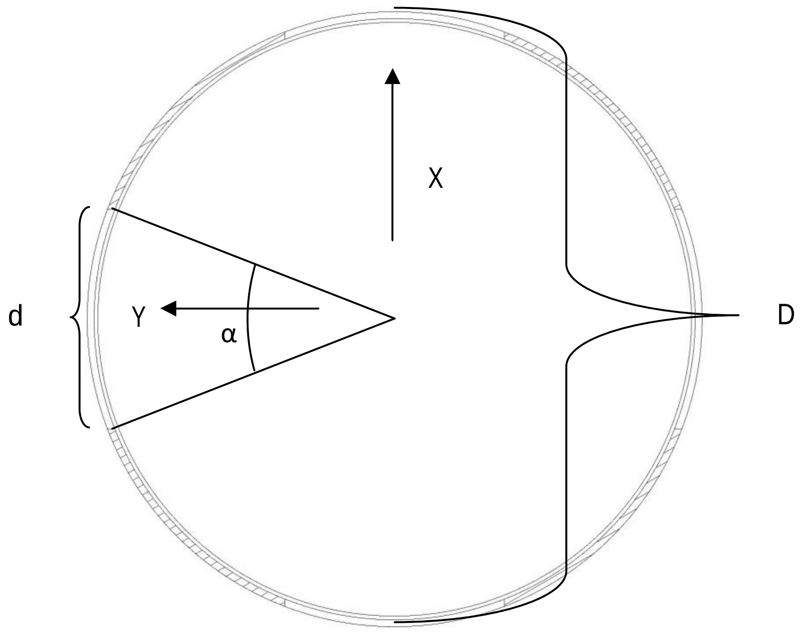

Figure 4: Modified section geometry with the definition of α.

$$*\,\alpha = \arcsin\left(\frac{d}{D}\right) \tag{3}$$

$$A_{modified\ RMU} = \frac{\pi}{4}\left[D^2 - (D-2t)^2\right] - 4\alpha\left[\frac{D^2}{4} - \left(\frac{D}{2} - t\right)^2\right] \tag{4}$$

$$I_{x,circle\ segment} = \frac{[R^4 - (R-t)^4]}{4}(\alpha + \sin(\alpha)\sin(\alpha)) \tag{5}$$

$$I_{y,circle\ segment} = \frac{[R^4 - (R-t)^4]}{4}(\alpha - \sin(\alpha)\sin(\alpha)) \tag{6}$$

$$I_{modified\ RMU} = I_{unmodified\ RMU} - 2I_{x,circle\ segment} - 2I_{y,circle\ segment} \tag{7}$$

In the case of the modified rocket module there are three measurements of the opening that were analyzed. The maximum opening diameter was set to 134 mm. The second measurement is a minimum diameter for the opening set by the minimum space required by the electrical team to fit all the equipment needed. The minimum opening diameter was set to 120 mm. The third measurement studied was a solution in between of the other ones, and this measurement is a diameter of 124 mm (The same diameter than the FFU) for the openings, with this size of the openings the electrical team get extra place for equipment. Nevertheless the analysis will be performed in a worse case scenario which means openings of 134 mm in the modified rocket module. With the openings of 134 mm the area, the moment of inertia of the modified section is shown in Table 1. Furthermore a percentage ratio comparing the modified section with the unmodified section has been included.

Openings diameter	$A_{Modified\ section}(mm^2)$	$I_{Modified\ section}\ (x10^7 mm^4)$	% of unmodified rocket module area	% of unmodified rocket module area
134mm	2211	3.48	49.9	50.7

Table 1: Geometric characteristics of the modified section

Table 1 shows that the impact of the increment of the diameter of the openings is not negligible at all.

2.2.2. EUROCODE 9[2] routine for critical stress assessment

The EUROCODE 9[2] for aluminium design of shell structures is the code used in Europe for the design of aluminium shell structures for civil engineering structures. The idea of using this source as a verification method comes from the well proven functioning of the expressions and assumptions that are presented in this code. According to EUROCODE 9[2] depending on the slenderness parameter ω of the shell structure, there are a set of parameters that influence the out coming results. The influence parameters are chosen according to dimensionless parameter ω. The parameter ω is defined as $\omega = H/\sqrt{Rt}$, ω can be defined as a dimensionless parameter that expresses the slenderness of the shell . Furthermore, ω is used in EUROCODE 9[2] to classify the cylindrical shell into short, medium or long shells. According to the EUROCODE 9[2] and due to its complexity and further influences in the critical buckling stress assessment a mathematical routine was developed. Giving the input of the geometry of the shell, the routine gave as a result the value ω=5.62. Moreover, according to the result ω=5.62 the rocket module is classified as a medium length shell. With the parameter ω and the material properties of the aluminium 7020-T6 provided in the EUROCODE9[4], the critical stress in the axial direction for the approximated module can be derived with Equation (8)

$$\sigma_{cr,x,EUROCODE9} = 0.605 E C_x \frac{t}{R} \tag{8}$$

where C_x is a coefficient that introduces the influence of the boundary conditions. For a medium length shell there is no influence of the boundary conditions on the critical buckling stress. Therefore, the value of C_x in this case is 1. From [8], the critical axial stress is $\sigma_{cr,x}$ = 965 MPa.

2.2.3. Timoshenko critical stress assessment

The classical evaluation of the axial critical stress is done according to Timoshenko [3].

$$\sigma_{cr,x,Timoshenko} = \frac{Et}{R\sqrt{3(1-\nu^2)}} \tag{9}$$

Inserting the data corresponding to the RMU in (9),t he estimation of critical stress is $\sigma_{cr,x,Timoshenko}$=975 MPa , for $\nu = 0.33$

2.2.4. Summary for the classical assessment of the load bearing capacity section

The aim of the previous sections was to calculate the critical buckling stress of the simplified rocket module geometry in order to obtain a value of critical buckling stress to validate the reliability of the coming FEM calculations. These calculations were done with two different approaches with the purpose of having more data to compare. The results of the sections 2.2.2 and 2.2.1 should be interpreted as values where the stiffness is involved, because it should be kept in mind that the aim of this study is the assessment of the associated stiffness by means of the critical buckling stress that the module can withstand. Furthermore, the result from Timoshenko [3] is 1% larger than the value from EUROCODE 9[2] , which was expected since the EUROCODE 9[2] should lead to results that are more on the safe side. Another fact from EUROCODE 9[2] that must be mentioned is that the screw holes with all their dimensions smaller than $\sqrt{Rt/4}$ can be neglected for the analysis. This fact has not so much importance in the classical assessment because all the calculations are done taking into account only the thin-walled section. Nevertheless this should be taken into account in the FEM calculations where a whole model is implemented in the software according to the recommendations and assumptions that EUROCODE 9[2] allows.

Finally, it should be remarked that the values presented in table 2, are not the values that should be achieved with the inclusion of the reinforcement in the modified RMU during the coming FEM calculations. The aim of these values is to provide a solid validation to set a starting point for the coming FEM analysis.

$\sigma_{cr,x,Timoshenko}$	975 MPa
$\sigma_{cr,x,EUROCODE\ 9}$	965 MPa

Table 2: Critical stresses obtained by means of classical analysis.

3. FEM analysis considerations

3.1. Material model

The material model used to model the aluminium alloy used, in this case 7020-T6, is the Ramberg-Osgood stress-strain model [10]. This model is specially suited for the description of aluminium alloy because it was developed with this purpose. The Ramberg-Osgood stress-strain model is specially suited for modelling of the yielding behaviour of aluminium alloys until the ultimate strength and the transition between linear behaviour and the behaviour after the yielding strength. The Ramberg-Osgood stress-strain model is Equation (10)

$$\varepsilon = \frac{\sigma}{\mathrm{E}} + K\left(\frac{\sigma}{\mathrm{E}}\right)^{\mathrm{n}} \tag{10}$$

Where *K* and *n* are constants that depend on the material under study. The exponent *n* can be computed using the Steinhardt[11] approach as the yield strength of the material expressed in MPa divided by 10.*E* is the Young's modulus of the material. In order to implement this model in the FEM software there are a set of parameters that should be calculated, because the Ramberg-Osgood stress-strain model is implemented according equation 11.

$$\varepsilon = \frac{\sigma}{\mathrm{E}} + \alpha\frac{\sigma_0}{\mathrm{E}}\left(\frac{\sigma}{\sigma_0}\right)^{\mathrm{n}} \tag{11}$$

The parameters present in (11) are the same than in (10) but in the case of (11) σ_0 is the yield strength of the material and α is a parameter that depends on the material. The parameter used in the FEM software to implement this model can be seen in table 3.

Parameter	Value
E	70 GPa
n	28
σ_0	280 MPa
α	0.5

Table 3: Parameter for the deformation plasticity application of ABAQUS[5].

3.2. Boundary conditions

The boundary conditions do not have influence for the critical buckling stress for this case according to EUROCODE9[2].Nevertheless the boundary conditions have a influence in this comparison of critical buckling because for a fair comparison the boundary conditions must be the same for each FEM model. Therefore a load case and a set of boundary conditions have been defined. The area where the pressure is located is the marked area that can be appreciated in Figure 5.

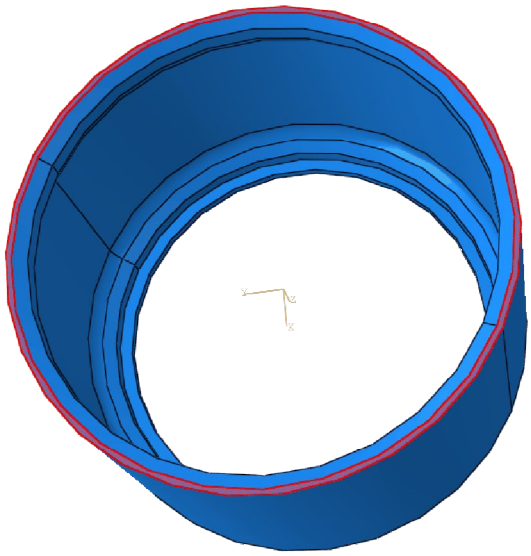

Figure 5: Loading area.

The area marked in figure 6, is the area where the translational degrees of freedom that ABAQUS requires to constrain the part to simply supported conditions have been constrained.

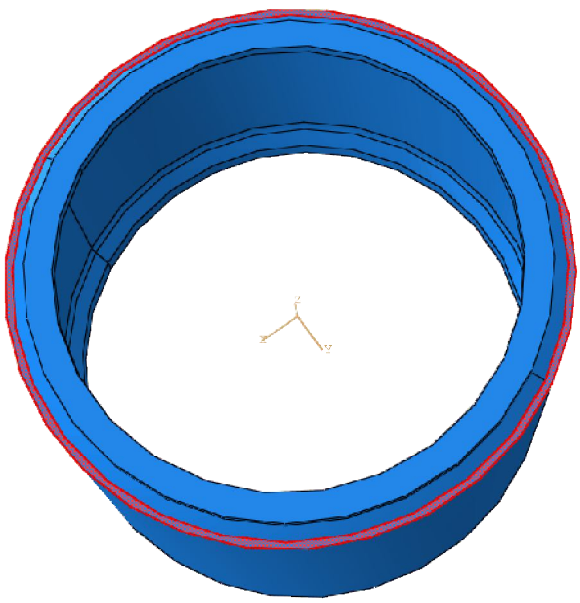

Figure 6: Boundary implementation area.

In Figure 7, view of the model with both constrains can be seen. In (7), pointed with BC1, the constrains of the upper support of the module can be seen. This boundary condition constrains the displacement in plane. This means that the displacement of the area pointed with BC1 can only been in the vertical direction. This decision has been done because the assembly of the rocket do not allow oval deformations during the deformation. The rotations are not constrained because this are it is not clamped in the assembly of the rocket. In (7). Pointed with BC2, the boundary conditions of the lower support of the module can be seen. The logic beneath this boundary condition is the same as in the case of BC1 but constraining the vertical degree of freedom in order to not allow free solid displacements.

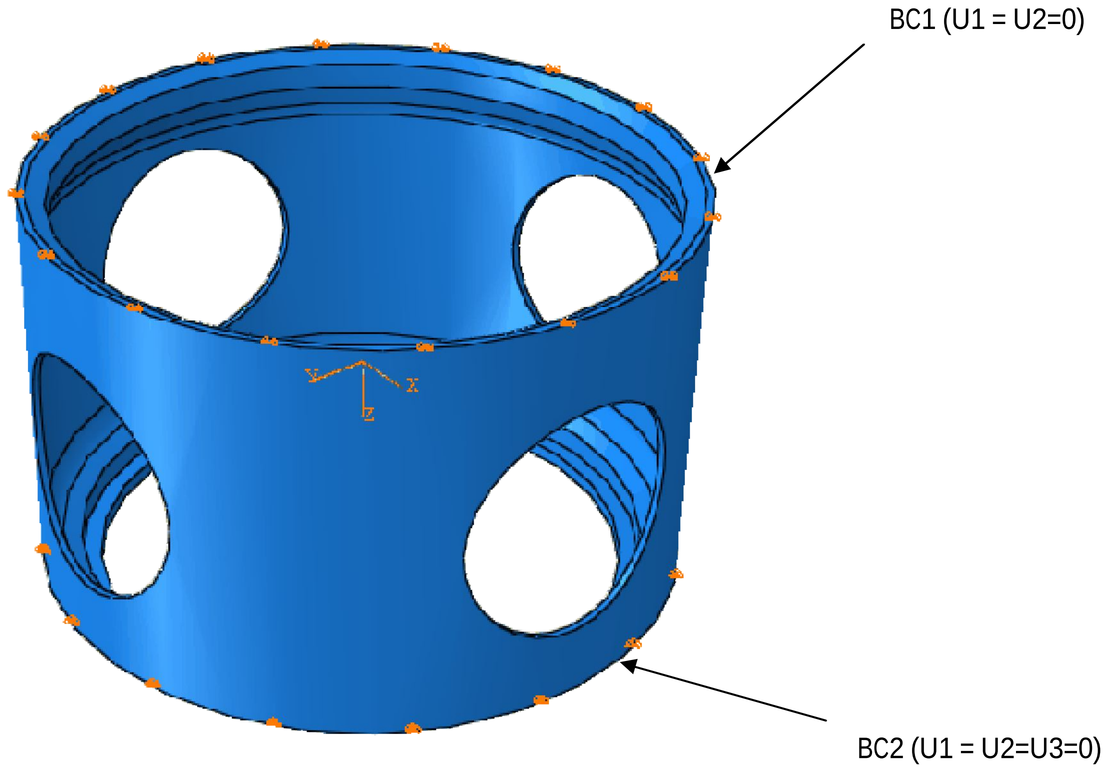

Figure 7: Isometric view of the boundary conditions

3.3. Element type

The element type selected to perform the FEM analysis was the C3D10I. This is an element with a 10-node general purpose tetrahedron with improved surface stress formulation [5]. This element is a tetrahedral shaped element which is the most powerful tool that ABAQUS has to mesh complicates geometries as the ones that are being implemented in this study. The use of this element in automatic meshing and in semi-automatic meshing as is the case in this study, leads to an unstructured mesh. This means that the distribution of elements is not perfectly symmetric and the stress are not perfectly symmetric even if the load case and geometry are perfectly symmetric. This will be clearly visible in the illustrations of the analyses.

3.4. Mesh size assessment

The size of the mesh is the characteristic length of the elements used to mesh the corresponding geometry. Depending of the characteristic length of the mesh the meshing process will converge to a better solution or not. For this case the characteristic length of 20, 15, 10, 7.5, 5, 4.5 and 4 have analyzed in order to get an impression of the convergence of the solution. The results can be seen in figure 8 to 14. It should be mentioned that the FEM analysis to compare strengths of the different configurations of the rocket module (Buckling analysis) have been performed with the characteristic length of 5 because of its better performance in terms of time and computational power . For the assessment of the stress concentrations assessment a partitioned mesh has been implemented. The development of the partitioned mesh is discussed later in this section.

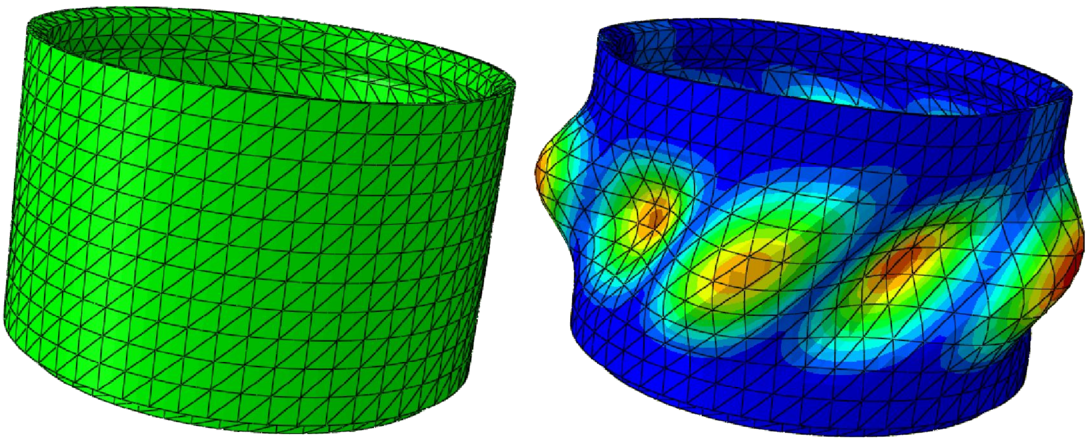

Figure 8: FEM models with characteristic element length of 20.Critical buckling stress =1184 MPa.

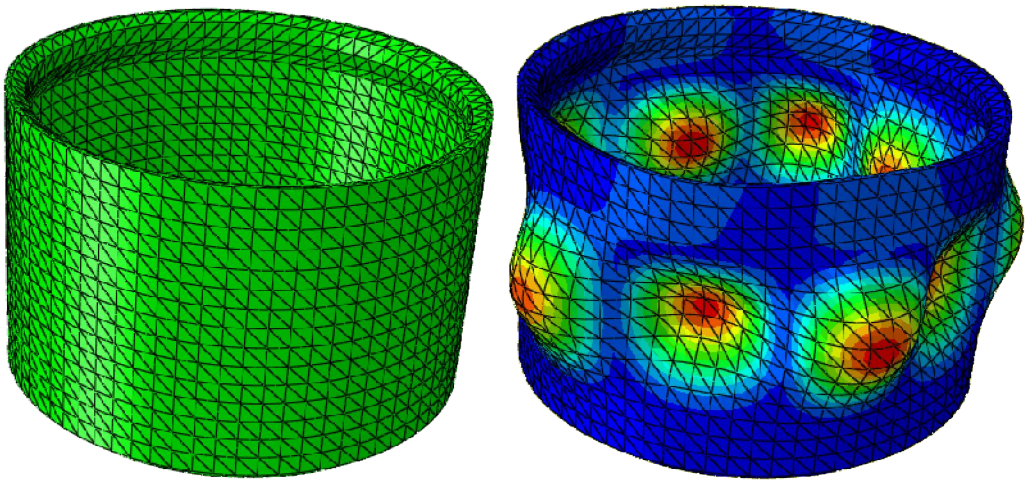

Figure 9: FEM models with characteristic element length of 15.Critical buckling stress=1169 MPa.

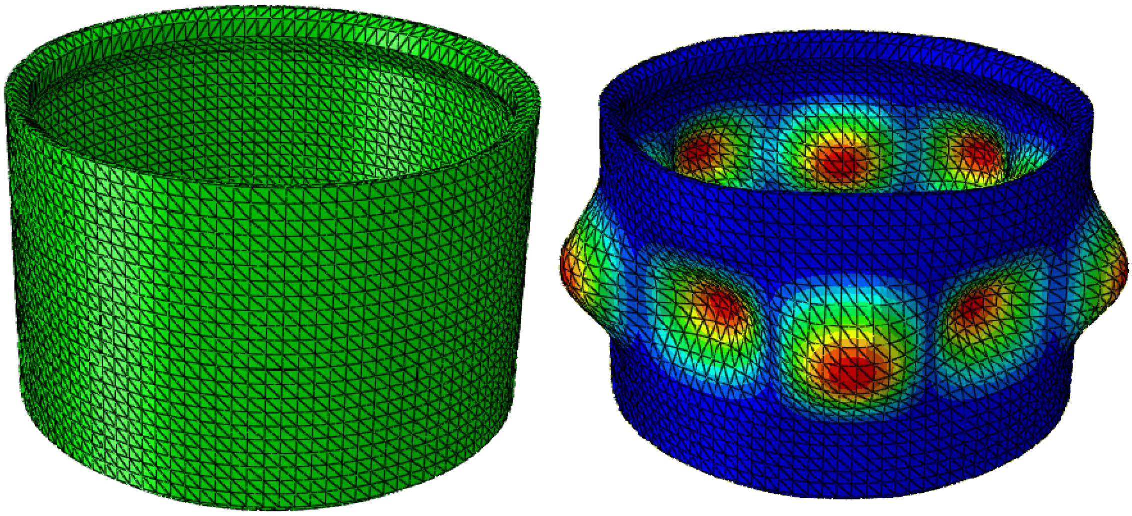

Figure 10: FEM models with characteristic element length of 10.Critical buckling stress=1041 MPa.

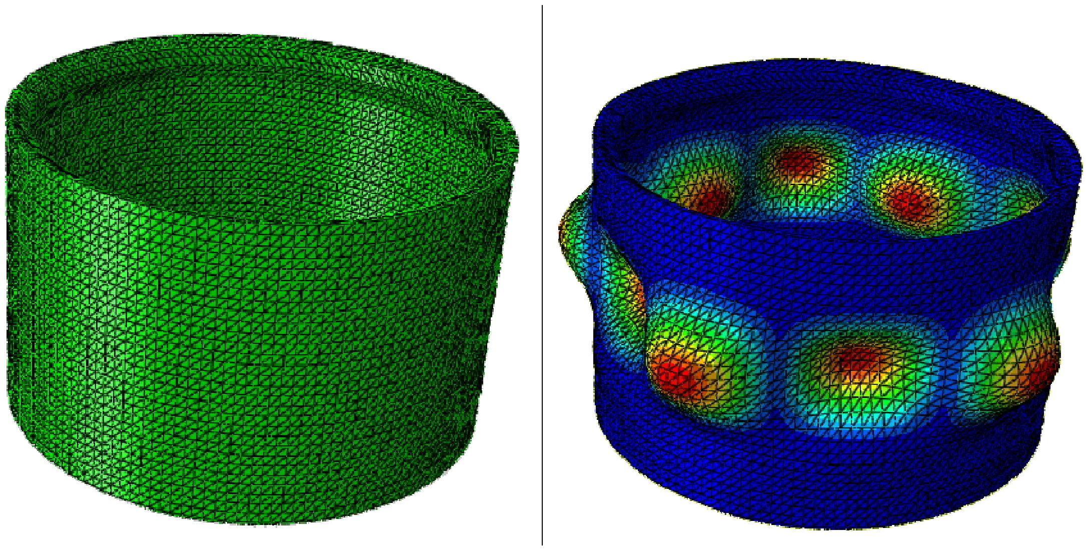

Figure 11: FEM models with characteristic element length of 7.5. Critical buckling stress=1023 MPa.

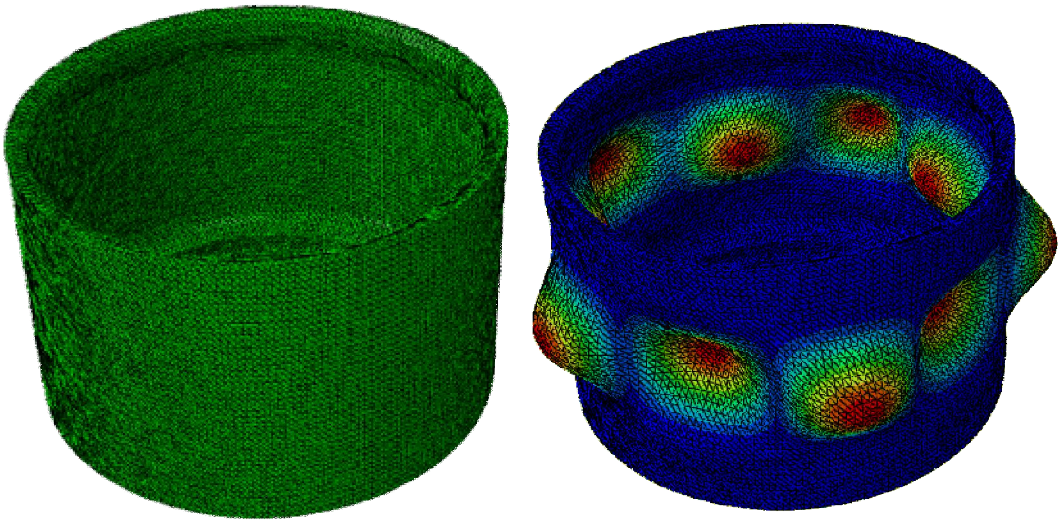

Figure 12: FEM models with characteristic element length of 5. Critical buckling stress=1017 MPa.

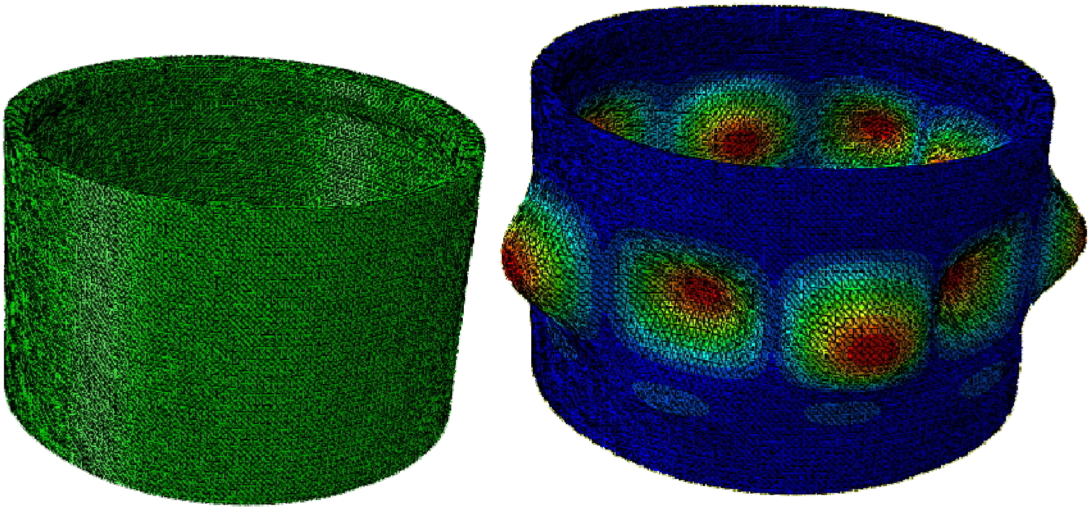

Figure 13: FEM models with characteristic element length of 4.5. Critical buckling stress=1017 MPa.

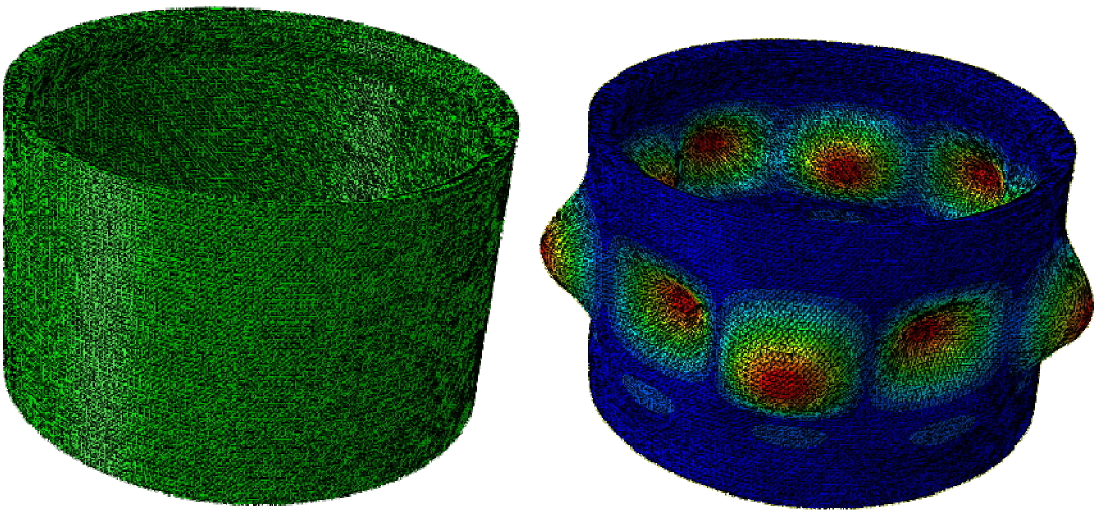

Figure 14: FEM models with characteristic element length of 4. Critical buckling stress=1017 MPa.

As it can be appreciated the values of the critical buckling stress converge to a solution when the mesh is refined. Furthermore when the mesh is refined a tendency to a smother displacement field can be seen in the first buckling mode. The values for the critical buckling load associated with the first buckling mode have been calculated for different reference element sizes. The values can be seen in Table 4

Reference element size	Critical buckling load (MPa)
20	1169
19	1331
18	1136
17	1097
16	1210
15	1041
14	1132
13	1039
12	1068
11	1033
10	1023
9	1026
8	1025
7.5	1017
7	1023
6	1020
5	1017
4.5	1017
4	1017

Table 4: Critical buckling load for different reference element sizes

As it can be appreciated the values of the critical buckling stress converge to a solution when the mesh is refined. This tendency can be clearly seen in Figure 15, where the data from Table 4 have been plotted and fitted with a polynomial curve.

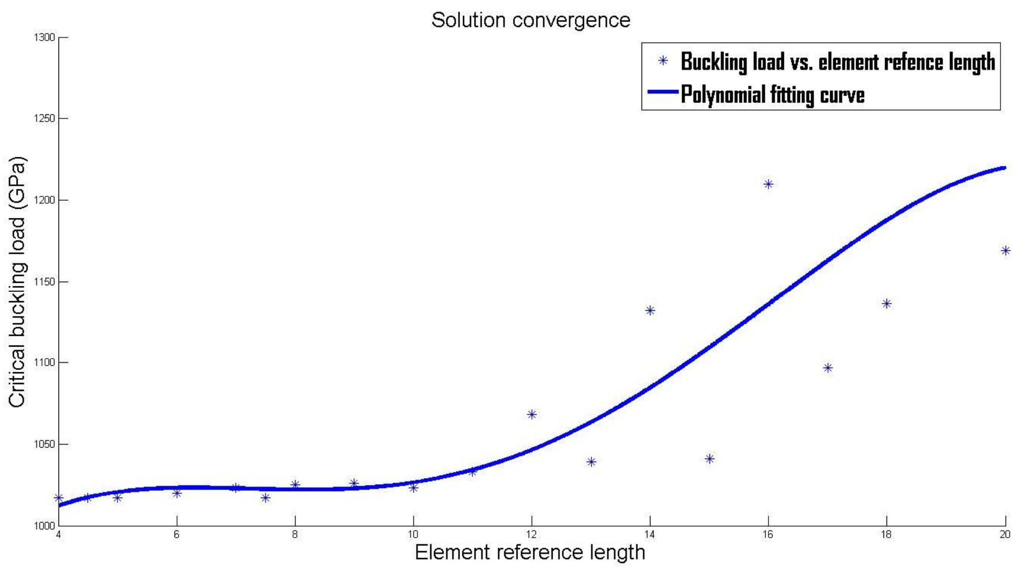

Figure 15: Solution convergence plot.

Furthermore when the mesh is refined a tendency to a smoother displacement field can be seen in the representation of the first buckling mode. The implications of the convergence seen in Figure 15, are that the following ones.

-Convergence of the solution of the FEM is not fully reached at element characteristic length of 4. Therefore partitions where the element length can be decreased should be placed at the points where the accuracy of peak stresses is important.

-In the case of the comparison of strength by means of buckling analysis no partitions are required because the different configuration are meshed in the same way with the same element characteristic length. Thus the expected error is the same in both.

As mentioned above, in the cases when the refinement of the stresses is critical partitions with refined meshes are required. In the case of the MUSCAT experiment these partitions will be locates in the places where stress concentrations are expected. These locations are in the circumferential groove and around the openings. The partition suggested can be seen in Figure 16.

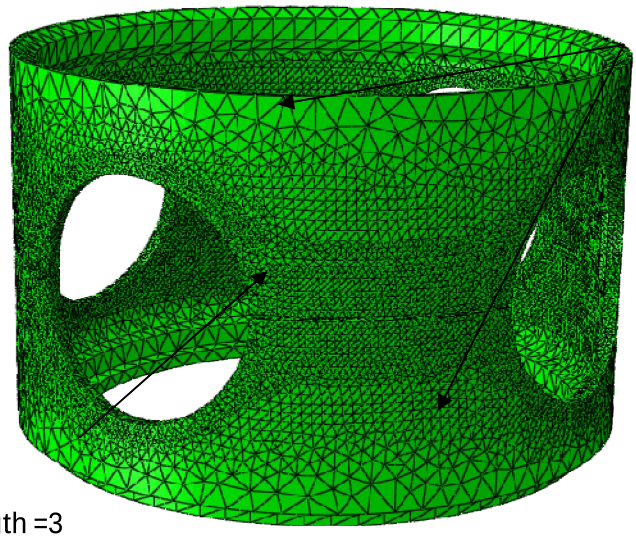

Figure 16: Meshed partition illustration.

The partitions cover 25 mm above and below the circumferential groove and 10 mm around the openings. In the analysis where no groove was present but stress concentration has to be considered in the analysis a partition with circular projections of 25 mm with centre at the weakest section are implemented. This partition can be seen in Figure 17. The elements in these partitions have a characteristic length of 3 while outside the partitions the characteristic length has been maintained in 5 to obtain a good result in low stress areas. In this case the element characteristic length could be maintained small outside the partitions because the areas with refined meshes are smaller than the area with refined mesh when the groove is present.

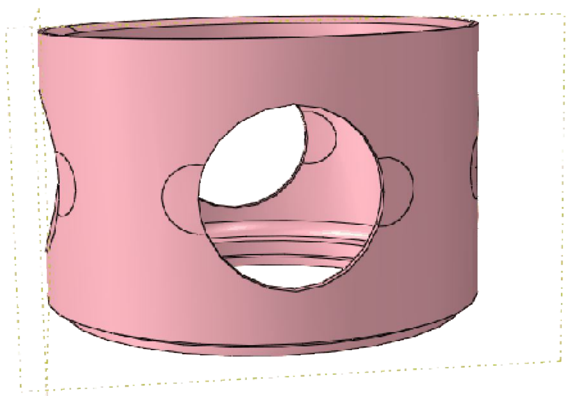

Figure 17: Openings sides partitions.

The variation of size that can be seen is due to the transition from the characteristic element length of 10 to 3 because the continuity that the mesh has to guarantee. A more clear geometry of the partitions created when the groove is present can be seen in Figure 18 as well as the different seeding of the different edges.

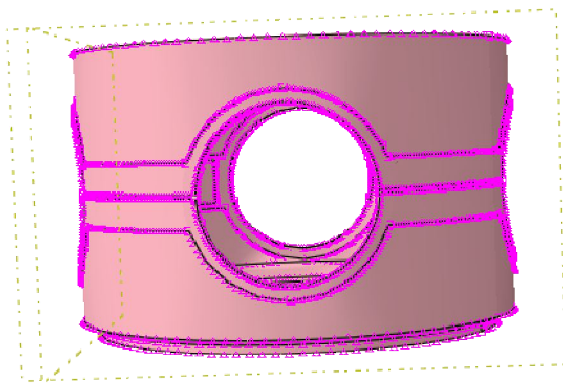

Figure 18: Geometry and seeding of the partition when the groove is present

In this partition the average size of the element is 5 in the part but with the definition of element with characteristic length of 3 gives more accuracy in the areas where the stress concentration is expected. This partition represents an optimization with the respect the fully automatic mesh because of the higher accuracy of the solution that can be achieved employing the same computational power as in a uniform fully automatic mesh.

3.5. FEM load bearing capacity assessment

The FEM stiffness and strength assessment has been performed using the well known FEM software ABAQUS. The first step in the FEM calculations was to verify the values obtained with the EUROCODE 9 [2] expressions and the expression suggested by Timoshenko [3]. Therefore a model of the unmodified rocket module was submitted for analysis. The Figure 19 is the unmodified rocket module without the holes of the screws.

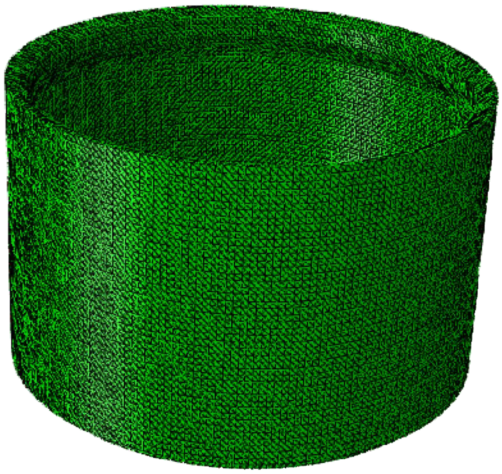

Figure 19: FEM model of the unmodified module meshed.

The critical stress obtained from the FEM software for this configuration is $\sigma_{cr,x,ABAQUS}$ = 1017 MPa. This result is reasonably close to the analytical solutions, indicating that the FEM software is providing realistic results. The result presented above corresponds with the first mode of the RMU. A representation of this first mode provided by ABAQUS can be seen in Figure 20.

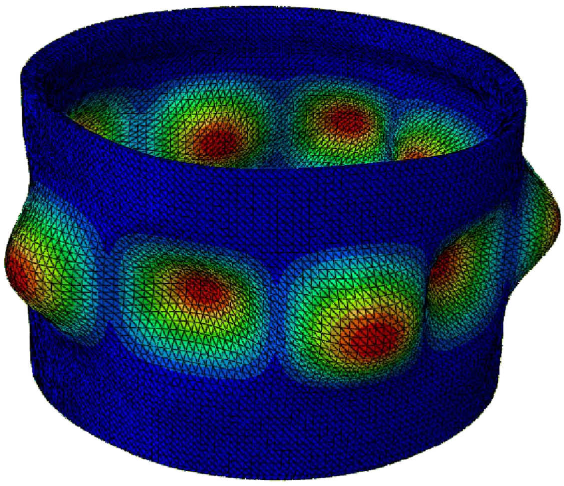

Figure 20: First buckling mode of the unmodified rocket module.

With these similar results that have been obtained by EUROCODE 9, Timoshenko and the FEM software ABAQUS, it can be said that the ABAQUS model has been verified.

3.6. FEM assessment of load bearing capacity

The idea of this entire study is to compare critical buckling stresses as measure of the associated strength of each configuration. To evaluate the loss of load bearing capacity of the modified rocket module an analysis of the critical stress in the modified rocket module should be performed. This analysis is needed because depending on how low is the stiffness and strength, the modified will require certain reinforcement. To perform the analysis a modified rocket module like the module showed in Figure 21 was implemented in the FEM software.

.

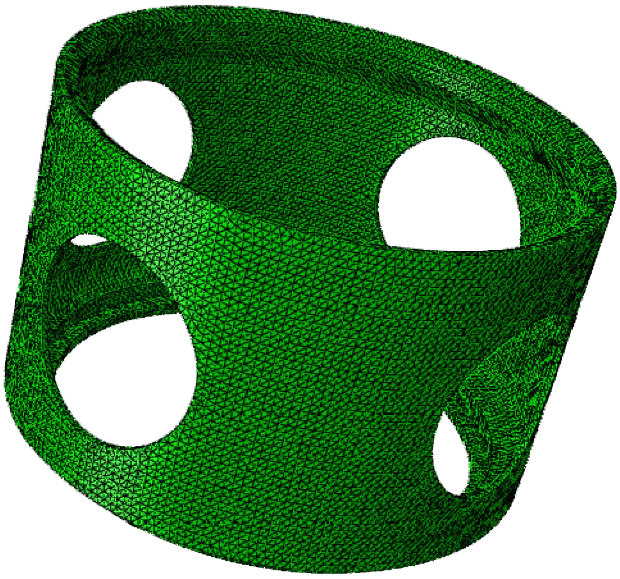

Figure 21: Modified rocket module meshed.

After the analysis performed by the FEM software the value obtained for the critical buckling stress was the following one $\sigma_{cr,x,ABAQUS,MODIFIED}$ = 207 MPa.

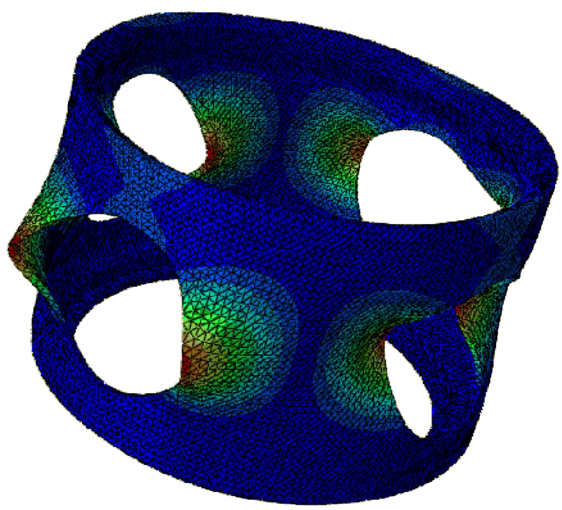

Figure 22: First buckling mode of modified rocket module.

This value, corresponding with the first mode that can be seen in Figure 22, means a loss of stiffness and strength of 79.7% compared with the unmodified module. This loss of capacity of stiffness and strength could affect the integrity of the rocket. Therefore, the rocket cylinder should be reinforced in order to increase the bearing load capacity until the level of the load bearing capacity of the unmodified rocket cylinder.

4. Reinforcement approach analysis

4.1. Thickening of thin walled section

The approach that has been considered suitable to stiffen the module until an appropriate level of strength is thickening the wall of the thin walled section. This approach is based in the idea that the bending stiffness and the critical buckling load depends on the product of the Young's modulus and the moment of inertia, according to Timoshenko[3]. Therefore maximizing this product the bending stiffness and the buckling critical load will increase. There are two means to increase the mentioned product but only one can be influenced by a design parameter. The member of the product that can be maximized is the moment of inertia that depends on the thickness. The Young's modulus cannot be modified because the module is manufactured with a specific material that cannot be modified.

The modification of the moment of inertia with this approach is done by thickening the thin walled section of the module where the openings are placed. This method shows an initial advantage due to the fact that thickening is more efficient in term of inertia added than the concentrated area concept of the reinforcements. This can be proved as follows:

Supposed the moment of inertia of a ring like the one that can be seen in Figure 24, the moment of inertia of such geometry is defined by Equations (12.a) and (12.b)

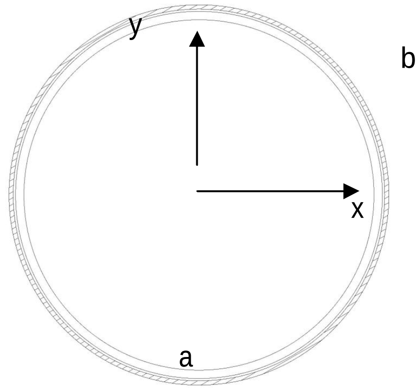

Figure 24: Ring for efficient area location demonstration.

$$I_{ring,x} = \frac{\pi}{4}\left(r_{exterior}^4 - r_{interior}^4\right) \tag{12.a}$$

$$I_{ring,y} = \frac{\pi}{4}\left(r_{exterior}^4 - r_{interior}^4\right) \tag{12.b}$$

If the thickness is increased by means of decreasing the inner radius multiplying this one by a factor δ smaller than one greater than zero (The outer radius cannot be modified because it is a parameter set by the manufacturing of the module).Then the moment of inertia in with respect to the *x* and *y* axes become Equation (13.a) and equation (13.b)

$$I_{ring,x\delta} = \frac{\pi}{4}\left(r_{exterior}^4 - r_{interior}^4\delta^4\right) \tag{13.a}$$

$$I_{ring,y\delta} = \frac{\pi}{4}\left(r_{exterior}^4 - r_{interior}^4\delta^4\right) \tag{13.b}$$

And the total inertia added by decreasing the radius until $r_{interior}\delta$ is equal to Equation (14)

$$\Delta Inertia_{total} = \left(I_{ring,x\delta} + I_{ring,y\delta}\right) - \left(I_{ring,x} + I_{ring,y}\right) = \frac{\pi r_{int}^4(1-\delta^4)}{2} \tag{14}$$

While the inertia added by concentrating in position a (Figure 24) the same area that the increase of thickness generates can be computed as Equations (15.a)and (15.b)

$$I_{concentrated,x} = \pi r_{int}^2(1-\delta^2)(r_{interior} - r_{interior}\sqrt{\pi(1-\delta^2)})^2) \tag{15.a}$$

$$I_{concentrate,y} = 0 \tag{15.b}$$

Equating (14) and the addition of (15.a) and (15.b) a ratio between the inertia added by incrementing the thickness and the inertia added by inserting the equivalent area in a certain point. This ratio can be seen in Equation 16

$$\frac{(1+\delta^2)}{2(1+\pi(1-\delta^2)-2\sqrt{\pi(1-\delta^2)})} = 1 \tag{16}$$

The positive roots (negative roots will imply negative inertia, fact without physical meaning) of (16) will be the $\delta's$ that are in the transition points from being more efficient to add a concentrated mass or to increase the thickness. The roots of equation (16) are

$$\delta_1 = \frac{\sqrt{4\pi^2 - 12\pi + 1}}{2\pi} \approx 0.228$$

$$\delta_2 = 1$$

These results means that for the case of the concentrated area located in position a of Figure 24 (This location where a concentrated mass can create maximum inertia with respect to on axis) than only if the inner radius is decreased by 73% then a concentrated mass in position a will add more inertia for the same area. The root $\delta_2 = 1$ means that if no thickness is added, hence no inertia is created. Then the concentrated area to create the same inertia is the same, nothing. A plot of the shape of (16) for the range where δ was defined above (0 , 1) can be seen in Figure 25

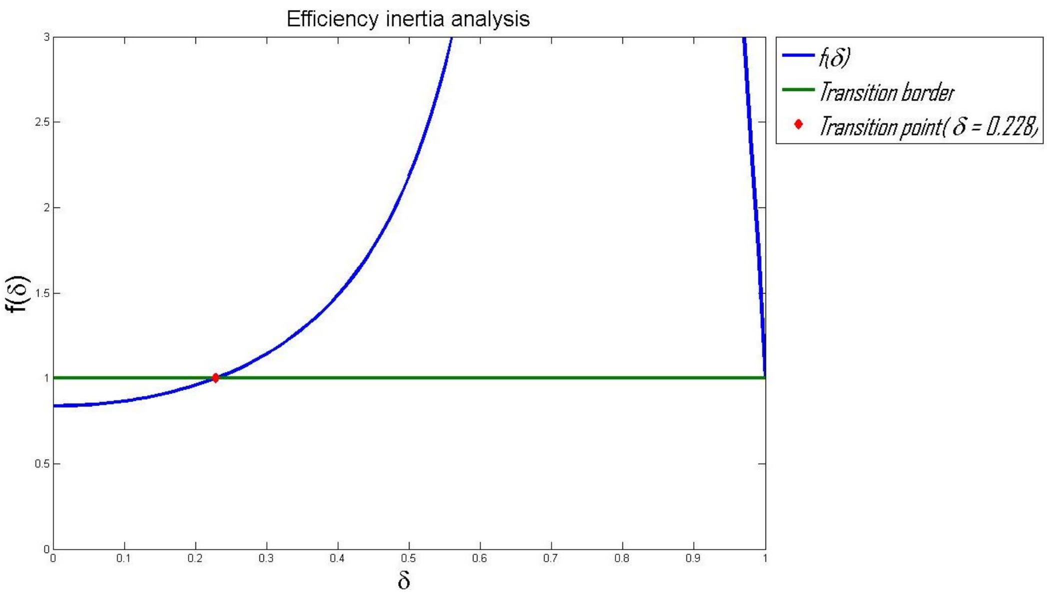

Figure 25: Inertia analysis.

For the case of a concentrated area in position (b) of Figure 24 the influence of in the total inertia will be the same because the inertia created with respect to each axis will be half but the same in each axis. Therefore the same analysis is valid for a concentrated mass in position b and can be generalized for any position around the ring.

After this first evaluation the thickening of the wall appears as a more efficient way to add inertia to a section. Therefore is a suitable method to increase the bending stiffness and the critical buckling load associated with the section.

4.1.1. Classical evaluation of stiffening by thickening the thin walled section approach

In addition to the coming FEM analysis a classical analysis to validate the results should be performed. The analysis that will be performed to evaluate the influence in the critical buckling load of the thickening of the thin walled section is a classical buckling analysis. The main assumption to perform this analysis is to assume that after the modification of the module with the four opening there are four plates left that will carry the loads. This geometry can be seen in Figure 26.

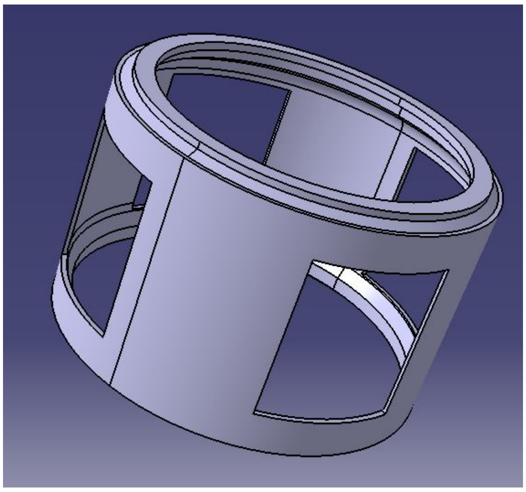

Figure 26: Idealized module.

Under the mentioned assumption mentioned above and assuming that the plates are not curved to be conservative assuming a configuration weaker than what in reality is. The support conditions in these calculations are clamped in both edges of the plate in order to simulate the real support conditions. The critical buckling load of each plate can be predicted according to Timoshenko[3] by means of Equation (17) and the critical stress by means of Equation (18)

$$P_{cr} = \frac{\pi^2 \mathrm{E} I}{L^2} \tag{17}$$

$$\sigma_{cr} = \frac{P_{cr}}{bh} = \frac{\pi^2 \mathrm{E} I}{bhL^2} \tag{18}$$

Where *b* is the width of the plate, *h* is the thickness, *L* is the effective length, *E* the Young's modulus and *I* the area moment of inertia of the weakest section of the plate. Equation (18) can be simplify by developing Equation (19), where the width of the plate has no influence on the buckling load

$$\sigma_{cr} = \frac{\pi^2 \mathrm{E} h^2}{3L^2} \tag{19}$$

Considering Equation (21) and different wall thicknesses an evaluation of the critical buckling stress have been performed with the different combinations. The results are presented in Table 5

Thickness(mm)	h=4	h=5	h=6	h=7	h=8	h=9	h=10
σ_{cr}(MPa)	163	255	368	501	655	829	1023

Table 5: Critical buckling stresses 4 plates model

From the result shown in Table 5 it can be concluded that for thicknesses above 8 mm to be conservative the module is stiff enough in buckling. The module can be consider stiff enough under buckling conditions because the aluminium 7020-T6 used in this case has a yield strength of 280 MPa according to Eurocode 9 [9].

These conservative values for the critical buckling load can be compared with the values obtained with the FEM software ABAQUS [5] .For the case of thickness 8 mm the calculations showed to be a reasonable value for the new thickness of the wall. The critical buckling load estimated by ABAQUS[5] is 1080 MPa. This value is above the yield strength of the material and fulfil the requirement of matching the same strength according with the calculation performed according EUROCODE 9[2] for the unmodified module, the calculation by the classical analysis with Timoshenko[3]'s and the result provided by ABAQUS[5] for the unmodified module. Furthermore, this result confirms the conservative assumptions that were made previous the analysis by means of assuming four plates carrying the load. The first buckling mode can be seen in Figure 27, the smoothness and uniformity of the harmonic shape of the mode is a sign of the validity of the analysis.

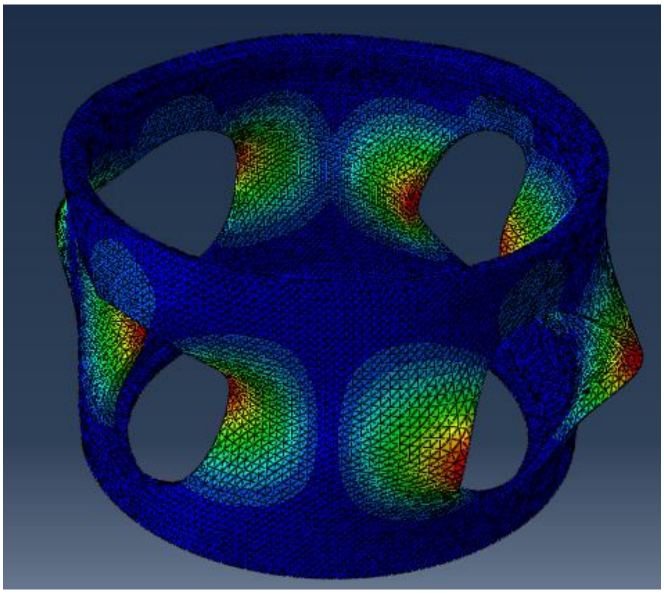

Figure 27: First buckling mode of 8 mm modified module 130 mm openings.

The case of 8mm thickness appear to be quite conservative, therefore a more critical configuration of the modified module was studied to set a lower limit closer to the strength of the unmodified module critical buckling load. The more critical configuration analysed with the FEM software was a 8 mm thickness module with 134 mm openings. The critical buckling stress obtained from the FEM software was 1029 MPa. This value is more than three times the yield strength of the material used and it is above the critical buckling stress of the unmodified module which is 1005 MPa. The first buckling mode can be seen in Figure 28, the smoothness and uniformity of the harmonic shape of the mode is a sign of the validity of the analysis because if the same in the analysis in the unmodified module and both have the same characteristic element length.

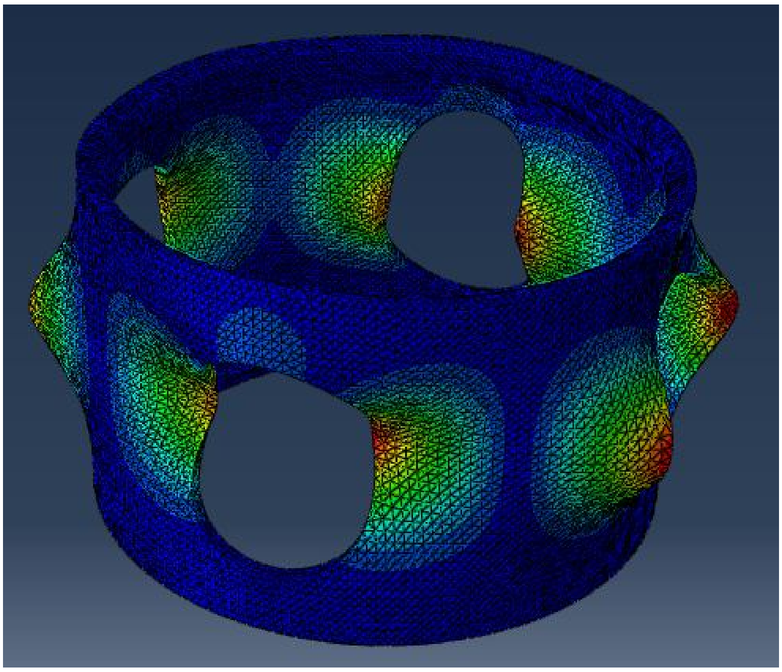

Figure 28: First buckling mode of 8mm modified module 134mm openings

After the confirmation that for a value of thickness of 8 mm the strength of the module is at the same level at the strength of the unmodified one and it is over the yield strength of the material by a factor of three, which is a good safety factor. The next and final step in this classical analysis is the calculations of the weakest section to confirm that the properties in the weakest section of the modified module match the properties of the unmodified module. This is important because under linear elasticity Navier's equation shows that if two sections have the same moment of inertia and area they can bear the same load assuming that all the characteristics of the material remain unmodified. The area of the unmodified module section can be computed as it shown in Equation (20) and the moment of inertia can be computed as it can be seen in Equation (21)

$$A_{unmodified\ RMU} = \frac{\pi}{4}[D^2 - (D-2t)^2] \quad (20)$$

$$I_{unmodified\ RMU} = \frac{\pi}{64}[D^4 - (D-2t)^4] \quad (21)$$

Introducing the appropriate parameters in (20) and (21) the following values are obtained

$A_{unmodified\ RMU}$ =4423mm^2 $I_{unmodified\ RMU}$ =6.852x10^7 mm^4.

The moment of inertia and the area of the modified section with the thickness of 8 mm can be computed in a similar way to the one followed in Equation (20) and Equation (21). The equations to compute the area and moment of inertia of the modified section are Equation (22) and Equation (23)

$$A_{modified\ RMU} = \frac{\pi}{4}[D^2 - (D-2t)^2] - 4\alpha(R^2 - (R-t)^2) \quad (22)$$

$$I_{modified\ RMU} = \frac{\pi}{64}[D^4 - (D-2t)^4] - \left[2\frac{(R^4-(R-t)^4)}{4}(\alpha + \sin(\alpha)\cos(\alpha))\right] - \left[2\frac{(R^4-(R-t)^4)}{4}(\alpha - \sin(\alpha)\cos(\alpha))\right] \quad (23)$$

α is the angle covered by the opening and can be computed as follows

$$\alpha = \arcsin\left(\frac{d_{openingd}}{D_{module}}\right) \tag{24}$$

Introducing the appropriate parameters in (22) and (23) the following values are obtained for openings of 130mm in diameter.

$A_{modified\ RMU130}$ =4583mm^2 $I_{modified\ RMU130}$ =6.942 x10^{7}mm^4.

Openings up to 134mm can be acceptable, for this case the area is still bigger than for the unmodified module but the moment of inertia is slightly smaller as it can be seen in the following results

$A_{modified\ RMU134}$ =4448mm^2 $I_{modified\ RMU134}$ =6.738 x10^{7}mm^4.

After these results it can be concluded that openings of 130 mm with a thicker wall of 8 mm thickness is a configuration stronger than the unmodified module with a wall thickness of 4mm. Furthermore, opening up to 134 mm in diameter could be used because the remaining area is still bigger than the area of the unmodified module and the moment of inertia is only 1.6% smaller than in the moment of inertia of the unmodified module. This small variation can be absorbed by the factor of safety present in the buckling analysis.

4.1.2. FEM analysis of stiffening by thickening the thin walled section

In the FEM analysis performed to evaluate this approach has been decided to induce a strain of 0.4% of the height of the module in compression to simulate a maximum admissible deformation. This means that compression of 0.88 mm has been prescribed n the vertical direction. The boundary conditions used in the analysis are the ones stated in section 3.2. The value of 0.4% has been set according to the limit set by the material of 0.2% deformation as strain yield limit multiplied by two to include a safe margin in the analysis. This analysis has been performed in the modified module of 8mm wall thickness and 134 mm openings without the presence of the groove. The result of the FEM analysis of the 8mm wall thickness and 134 mm openings can be seen in Figure 29.

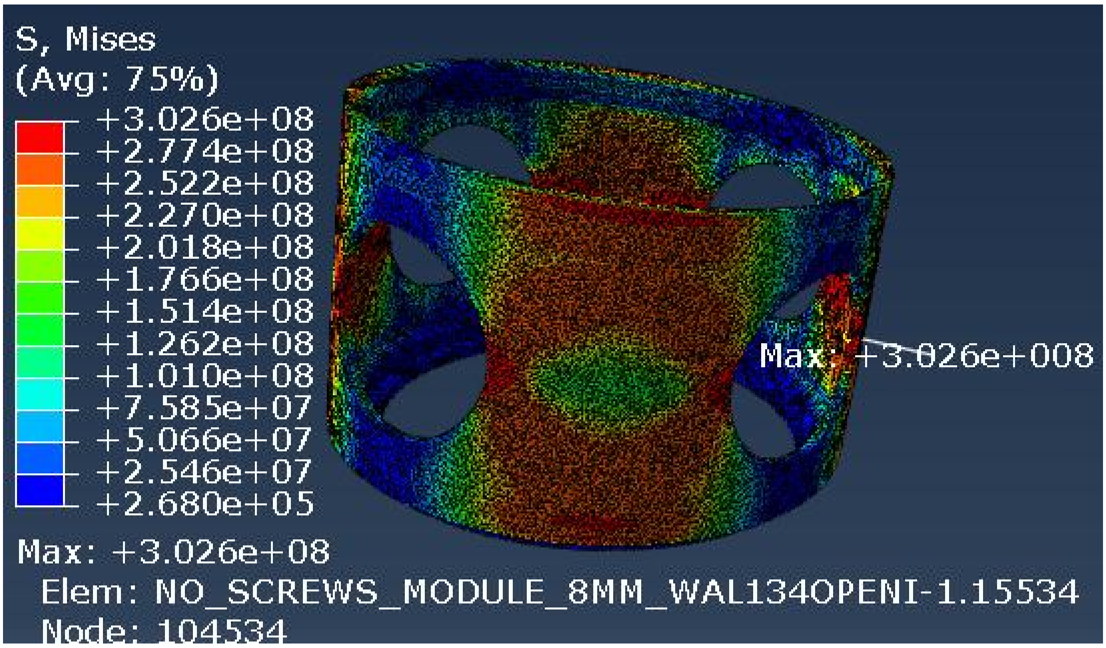

Figure 29: Compression 2% of 8mm modified module 134mm openings.

From this analysis there are two conclusions than can be drawn. The first conclusion is that for a limit strain deformation of 2% the stresses that appear are 300 MPa which is in the order of magnitude of the yield strength of the material used. The second conclusion is that there are concentrations of stress in the weakest section of the module that are the highest stresses. Hence an evaluation of the stress concentration factor should be performed afterwards.

4.1.3. Groove implementation analysis

In the design of the MUSCAT experiment rocket cylinder a groove has to be implemented to protect the cable from the direct incidence of hot supersonic flow. The groove is to be implemented in the weakest section of the rocket cylinder. The mission of the aforementioned groove is to house the cable present in the ejection system. The dimensions of the cable are 2.5 mm in diameter; therefore the dimensions that are estimated for the groove are the dimensions that can be seen in Figure 30.

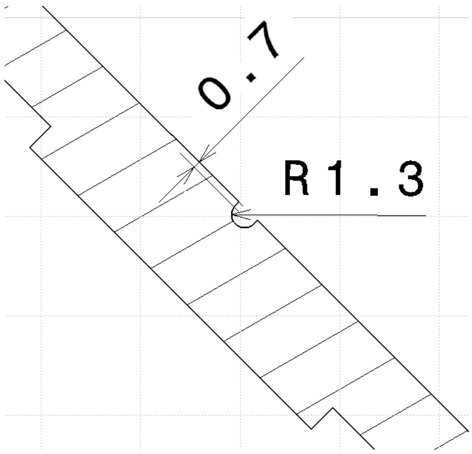

Figure 30: Draft of groove section.

The design of the groove is composed by a semicircle of radius 1.3 plus a prolongation up to the surface of the rocket cylinder of 0.7mm. The covering distance that the groove can provide to the cable is thus 2 mm. As it can be noted from the above mentioned dimension of the cable is 2.5 mm. There is 0.5 mm of the cable that will not be housed inside the groove. This protruding portion should not suffer of heating due to its proximity to the skin of the rocket cylinder.

The introduction of the groove meant a decrease of area and moment of inertia at the weakest section of the rocket cylinder. Therefore, a reinforcement to counteract the negative effect of the groove has to be implemented. The solution achieved is to leave extra-material in the back of the groove while the rocket module is milled out during its manufacturing process. An illustration of this reinforcement can be seen in Figure 31.

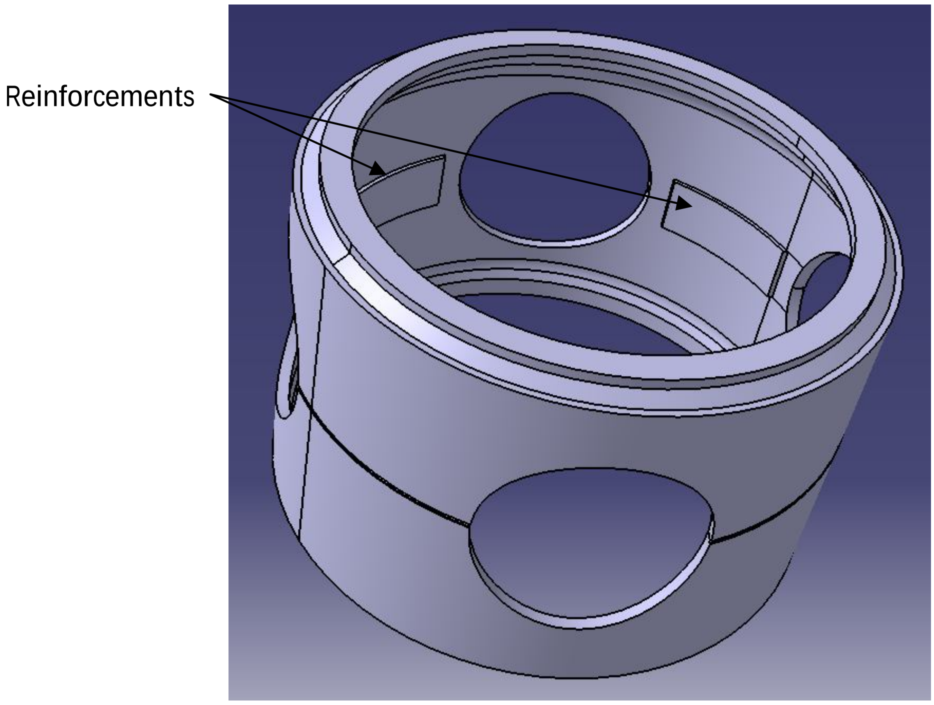

Figure 31: Back support reinforcements for the groove.

It can be noticed in Figure 31, the reinforcements do not cover the entire circumferential length of the inner side of the rocket cylinder, this due to the location of the collars of the ejection system that will cover the distance between the reinforcements and the openings. It should be mention that the stiffening effect of the collar have not been included in this strength and section analysis in order to be conservative because the collars will provide extra stiffness and strength when they are included in the assembly. A draft of the studied geometry can be seen in Figure 32.a and Figure 32.b. In the design of the RMU extensions until the collars, this means that the final reinforcements are bigger and hence they will provide more stiffness. This final pointed assumption makes the calculations more conservative from the stiffness and strength point of view

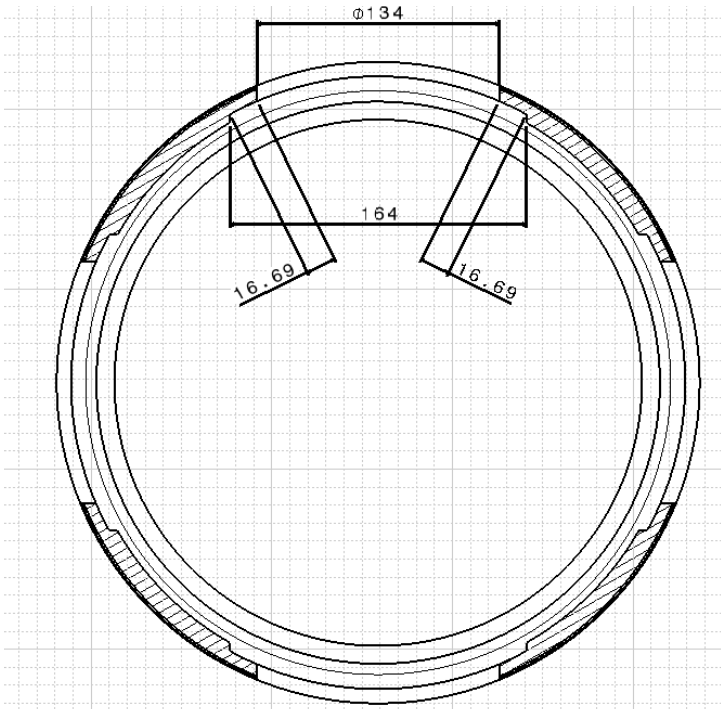

Figure 32.a: Upper view.

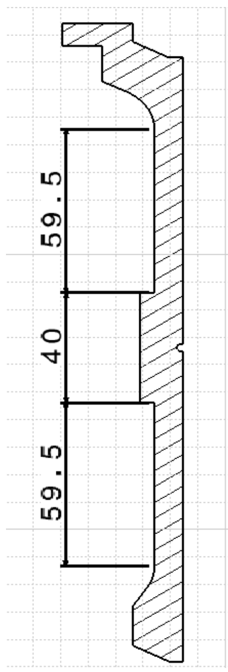

Figure 32.b: Section view

The radial dimension required by the reinforcements are determined by Equation 25, Equation 26, Equation 27 and Equation 28 and the aim of having the same moment of inertia and area as the unmodified module.

$$A_{modified\ RMU+BSR} = \frac{\pi}{4}\left[D'^2 - (D' - 2t')^2\right] - 4\alpha\left(R'^2 - (R' - t')^2\right) \tag{25}$$

$$I_{mod\ \mathrm{G}-RMU} = \frac{\pi}{64}\left[D'^4 - (D' - 2t')^4\right] - \left[2\frac{(R'^4 - (R' - t')^4)}{4}(\alpha + \sin(\alpha)\cos(\alpha))\right] - \left[2\frac{(R'^4 - (R' - t')^4)}{4}(\alpha - \sin(\alpha)\cos(\alpha))\right] \tag{26}$$

$$I_{BSR} = \frac{\pi}{64}\left[D''^4 - (D'' - 2t'')^4\right] - \left[2\frac{(R''^4 - (R'' - t'')^4)}{4}(\beta + \sin(\beta)\cos(\beta))\right] - \left[2\frac{(R''^4 - (R'' - t'')^4)}{4}(\beta - \sin(\beta)\cos(\beta))\right] \tag{27}$$

$$I_{\mathrm{mod\ G}-RMU+BSR} = I_{mod\ \mathrm{G}-RMU} + I_{BSR} \tag{28}$$

The values obtained for a thickness of the back support reinforcement of 4mm are the following ones:

$$A_{modified\ RMU+BSR} = 4795\ \mathrm{mm}^2$$

$$I_{\mathrm{mod\ G}-RMU+BSR} = 7.05\times10^7\mathrm{mm}^4$$

These values represent 108 % of the unmodified module in the case of the area and 102 % on the case of the moment of inertia. It should be noted that this values are at the weakest section of the modified module. Therefore the rest of sections that can be found in the modified module have even larger section area and area moment of inertia that the unmodified module.

The vertical dimensioning of the back support introduced to reinforce the grooved area is controlled by the load bearing capacity evaluated by means of the buckling strength of each configuration. The parameter to be studied is the shown in Figure 33 and denoted as A

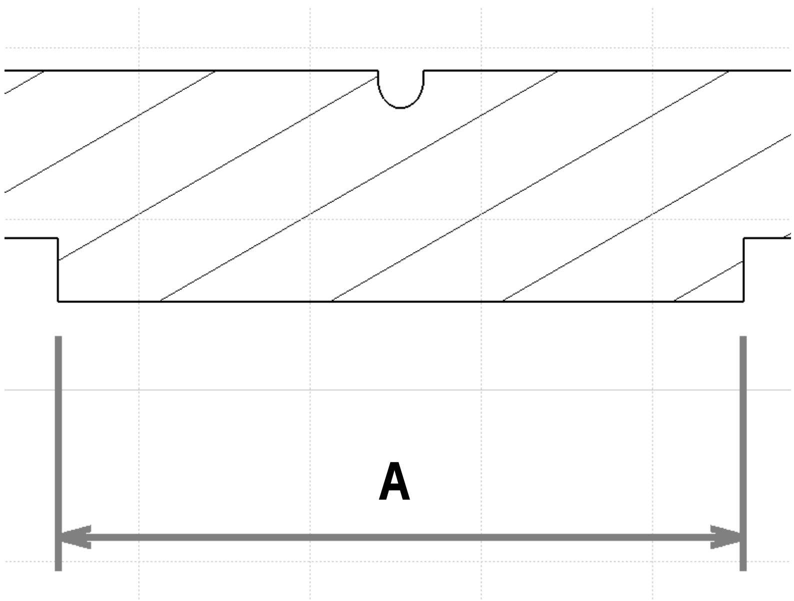

Figure 33: Vertical length of the back support reinforcement.

Different configurations in terms of the vertical length of the reinforcement have been studied and the different results can be seen in Table 6

Reinforcement vertical length (mm)	Strength (MPa)	% Of unmodified module strength
20	1043	103
30	1080	107
40	1096	109
50	1176	117

Table 6: Results of the different vertical length of the BSR.

After the results obtained above the dimensions of the reinforcements are 4x40 mm as it can be seen in Figure 34

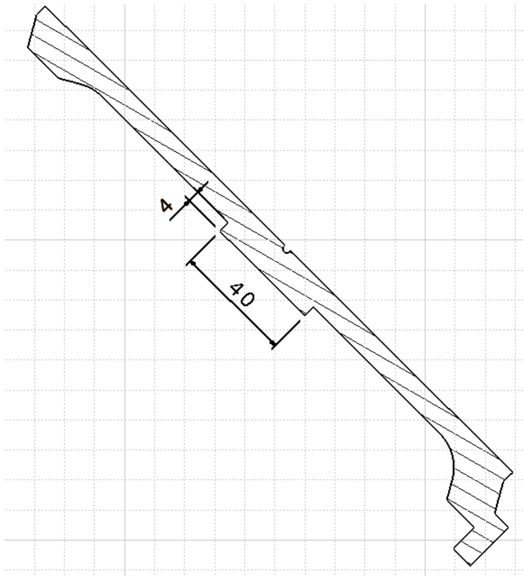

Figure 34: Reinforcement final dimensions

4.1.4. Stress concentration analysis under compression and bending loads

The stress concentration analysis is based in comparing the data collected from similar modules that have used in the same way as the MUSCAT module and have had successful launches. In the analysis of [7] a rocket manufactured in aluminium 6061-T6 (Yield strength of 240 MPa [9]) showed that the maximum stresses appeared in the screw holes with a maximum value of 52 MPa and the maximum stress in the skin of the module was 6 MPa . The concentration of stresses in the screws is not considered in this analysis because that part had not suffered modifications in the MUSCAT module and the validity of analysis of the module remain valid. In this analysis only the stresses in the skin will be taken into account because it is the area of the module where the modifications are to be implemented. Equation (27) shows the ratio between the stresses in the skin in the module of reference [7] and the yield strength of the material used in that module.

$$\frac{\sigma_{0.2}}{\sigma_{Max\ skin}} = \frac{240}{6} \approx 40 \tag{27}$$

With this ratio between the yield strength of the material in module in (7) and the stress in the skin during the launch, a value for the admissible skins stress for the MUSCAT module can be extrapolated. The reference module was submitted to 13 g of acceleration during launch, in the case of the MUSCAT module this value will be assumed double, 26 g. This is done because the maximum acceleration during launch can reach 21 g therefore a margin of safety is incorporated in these calculations. Assuming double the acceleration, double of stresses can be assumed as a right correlation. In this case the skin stress is set to 20 MPa instead of 12 MPa in order to include more safety margin in the calculations. Hence extrapolating the factor obtained in Equation (27) to the MUSCAT module a estimation of the skin stress can be done as showed in Equation (28)

$$\frac{\sigma_{0.2}}{\sigma_{Max\ skin}} = \frac{280}{20} \approx 14 \tag{28}$$

Where 20 MPa is the skin stress in the thin walled section expected in the MUSCAT module. The next step in the analysis is to obtain the load that can induce 20 MPa in the skin of the module. This load can be estimated by equilibrium of forces. Because if the internal stress has to be 20MPa in the skin the external load has to be the 20 MPa multiplied by the area where the 20 MPa are applied (The cross section of the thin walled section of the module) this can be done as showed in Equation 29

$$\sigma A = P_{equivalent} = 20\ MPa \times A_{RMU\,t=8mm_{no}openings} = 175\text{kN} \tag{29}$$

Distributing this equivalent load in the contact surface of the module in the FEM software a corroboration analysis can be done. This analysis was performed and the results can be seen in Figure 35

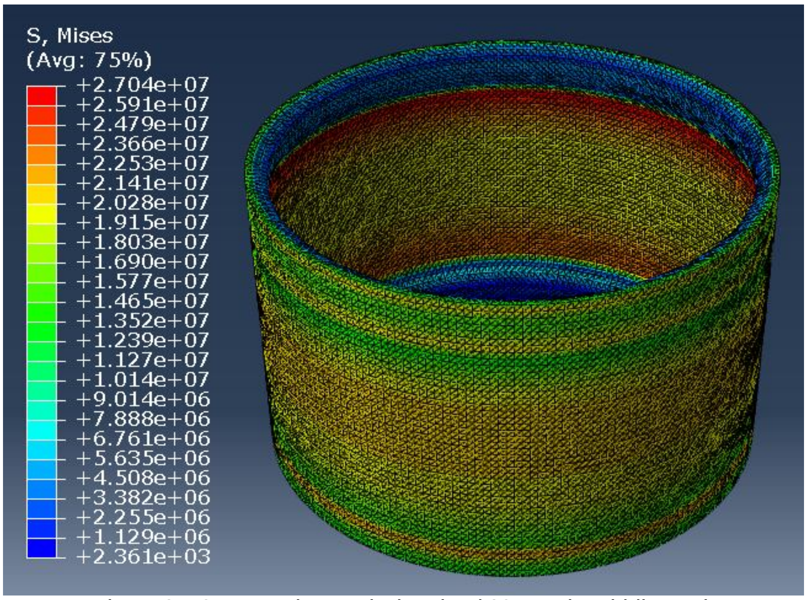

Figure 35: Compression equivalent load 20 MPa in middle section

The middle section, where the opening will be placed, is submitted to 20 MPa as it was expected. In the transition section appears a concentration of stresses but as mention before that section will not be significantly affected by the modification implemented in the MUSCAT module, hence the original analysis of the manufacturer remain valid. Also it should be mentioned that the extrapolation is taken from a peak value in a reduced area in the module of reference [7] while in this cases a more critical loading condition is induced because the entire section is loaded with thee extrapolated load of reference [7]

The same analysis was performed for the more critical configuration of 8 mm thickness and 134 mm openings and the results can be seen in Figure 36

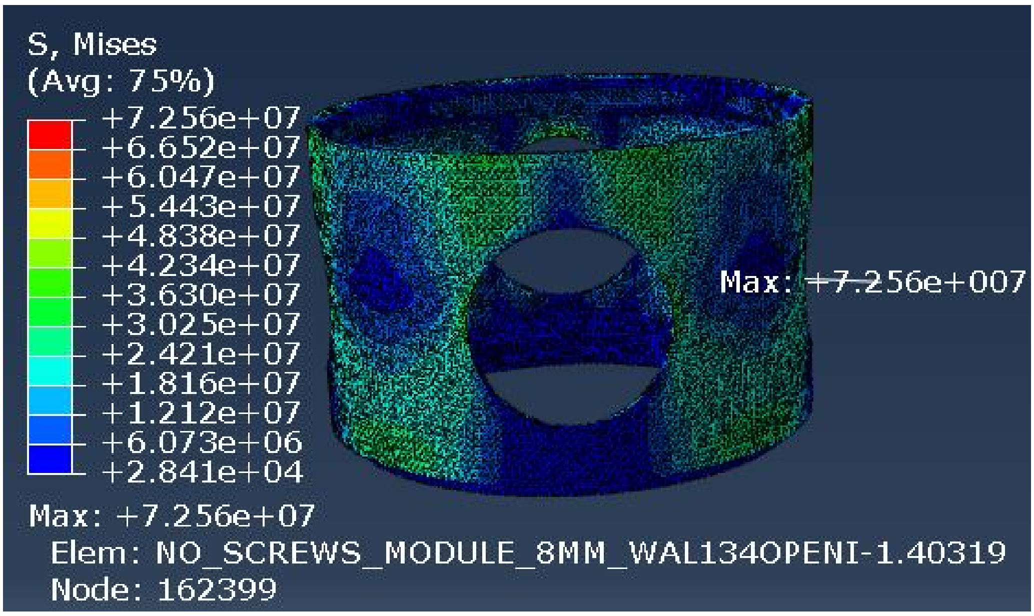

Figure 36: Stress concentration for 134 mm openings

As it was expected the bigger the openings the bigger the concentration of stresses. In the case of the 134 mm opening the maximum stress present under a realistic level of stress is three times lower than the yield strength of the material used in the MUSCAT module. Therefore, the configuration with 134 mm openings can be used without compromising the structural integrity of the module because the maximum stresses are 73 MPa under realistic loading conditions. However, in the MUSCAT mechanical lay-out of the RMU there is a circumferential groove that would lead to stress concentrations. This stresses concentration has also been evaluated under the same load cases used above and the results can be seen in Figure 37

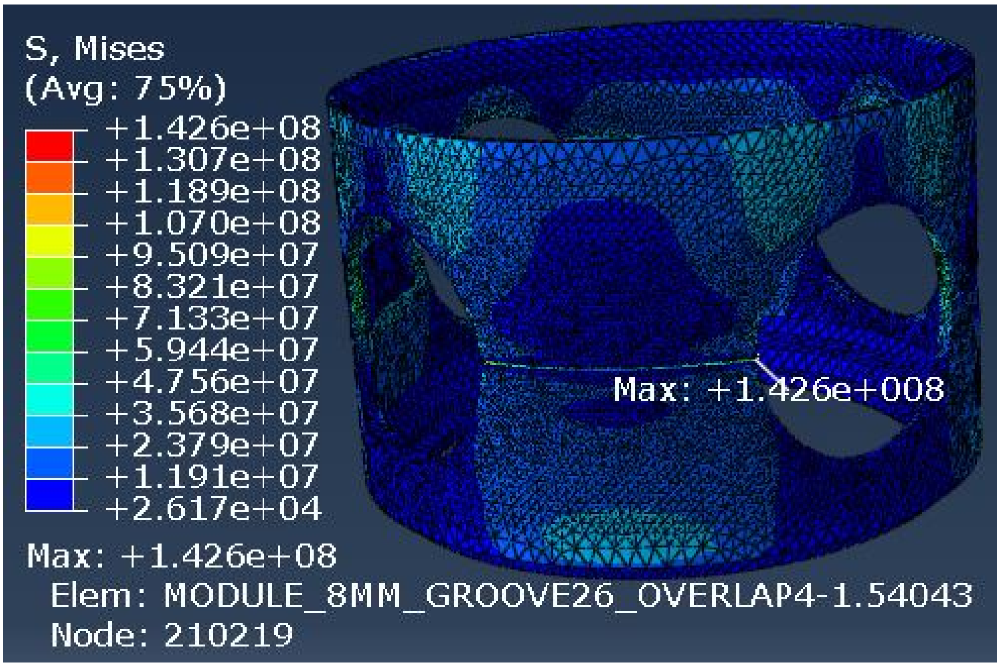

Figure 37: Stress concentration analysis including the groove

The stresses that resulted from the stress concentration analysis of the groove were 142 MPa. This means that there is a margin of safety of almost 2 (1.97) taking the yield strength of aluminium 7020 T6 as reference. This safety factor can be considered enough, because according to ECSS in reference [12], the safety factor for aerospace structure when the yield strength is taken as reference, should be 1.1 as minimum. In Figure 38, a more detailed view of an analysis with refined mesh can be seen. According to the legend of the contour plot in Figure 38, the peak of the stress concentration remains around 140 MPa. The area affected by the stress concentration is really small and affect even few elements. However, by comparing this stress with the stress in the skin of the unmodified module for the same stress a stress concentration factor can be stated as follows

$$\frac{\sigma_{MUSCAT\ 20MPa}}{\sigma_{Unmodified\ 20MPa}} = \frac{140}{20} \approx 7$$

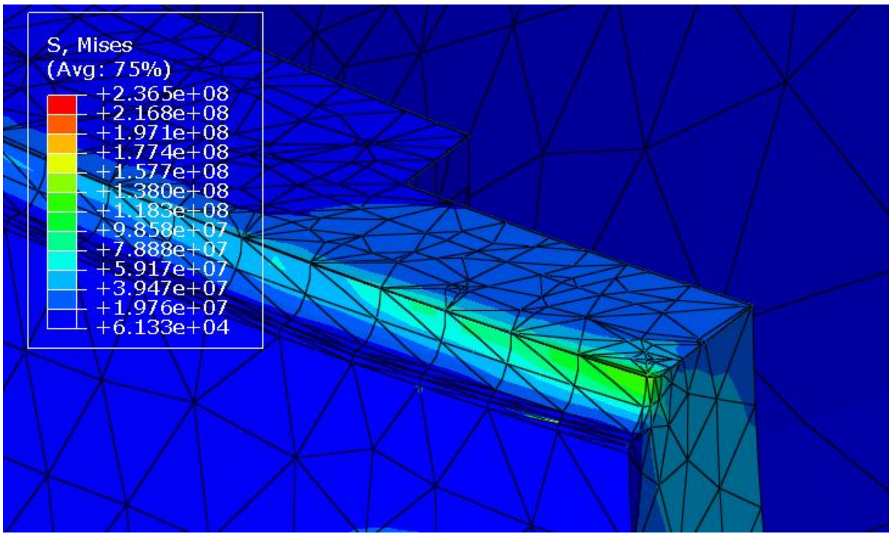

Figure 38: Stress concentration detailed view.

In order to give an idea of the affected element in the stress concentration a path following the surface of the groove has been created as it can be seen in Figure 39

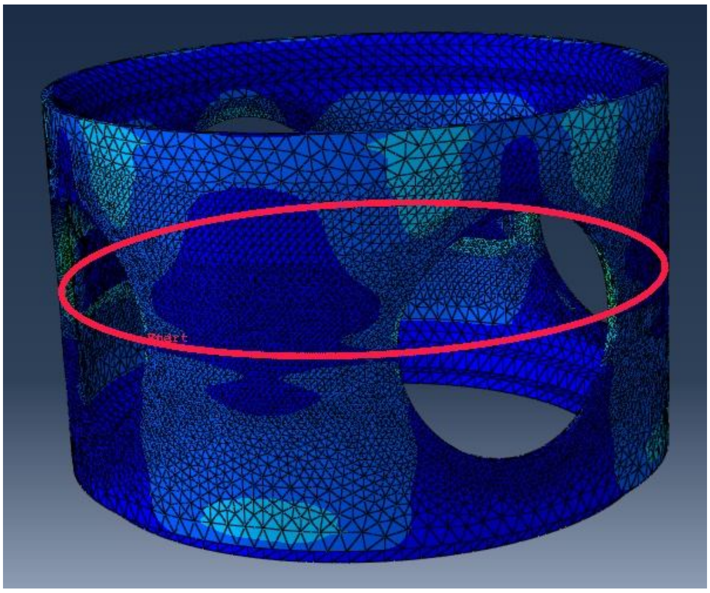

Figure 39: Illustration of the path following the surface of the groove.

The stresses along the path following the surface of the groove have been plotted versus the normalized length along the path. The mentioned plot can be seen in Figure 40

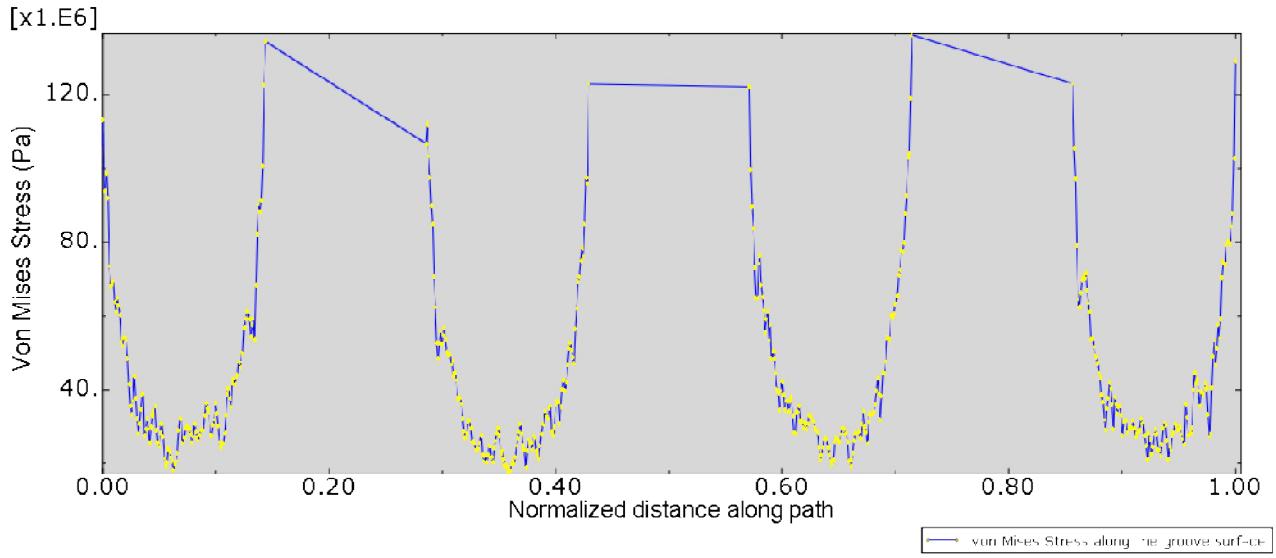

Figure 40: Plot of the stresses along the path versus normalized distance.

In figure 40, it can be seen that the number of elements affected by the stress concentration is really small. Because the path is composed by 1000 equally spaced along the surface of the groove and there never more than 10 points (The points are located in the nodes of the elements) over the zone of high stress concentration. To summarise the results pointed out so far, it can be said that the stress concentration under buckling load are inside reasonable limits because the lowest safety facto derived is 1.97 which is inside the limit of 1.1 marker by the standards [12] .

In the case of bending loads the approach is to assembly the module in the configuration that will be used in the launch and apply pure bending load in two different configurations. The configuration of the payload where the MUSCAT module will be launch is 220mm module (MUSCAT)+220mm module+120mm module+nose cone adaptor. The configuration for the FEM software will be set o three 220 mm modules because it has similar length and it is more efficient in terms of computing time will be more efficient because this study is interested in the MUSCAT module not in the parts that carry the loads until it. The mesh of the modules that are not the MUSCAT module will be coarser for identical reasons. The configuration is important because depending on the location of module the total bending moment is different. Therefore, an approximation of the above mentioned configuration will be used in the analysis. The boundary conditions for this case will be pinned in the lower part of the MUSCAT module simulating the attachment o the rocket engine. This configuration can be seen in Figure 41

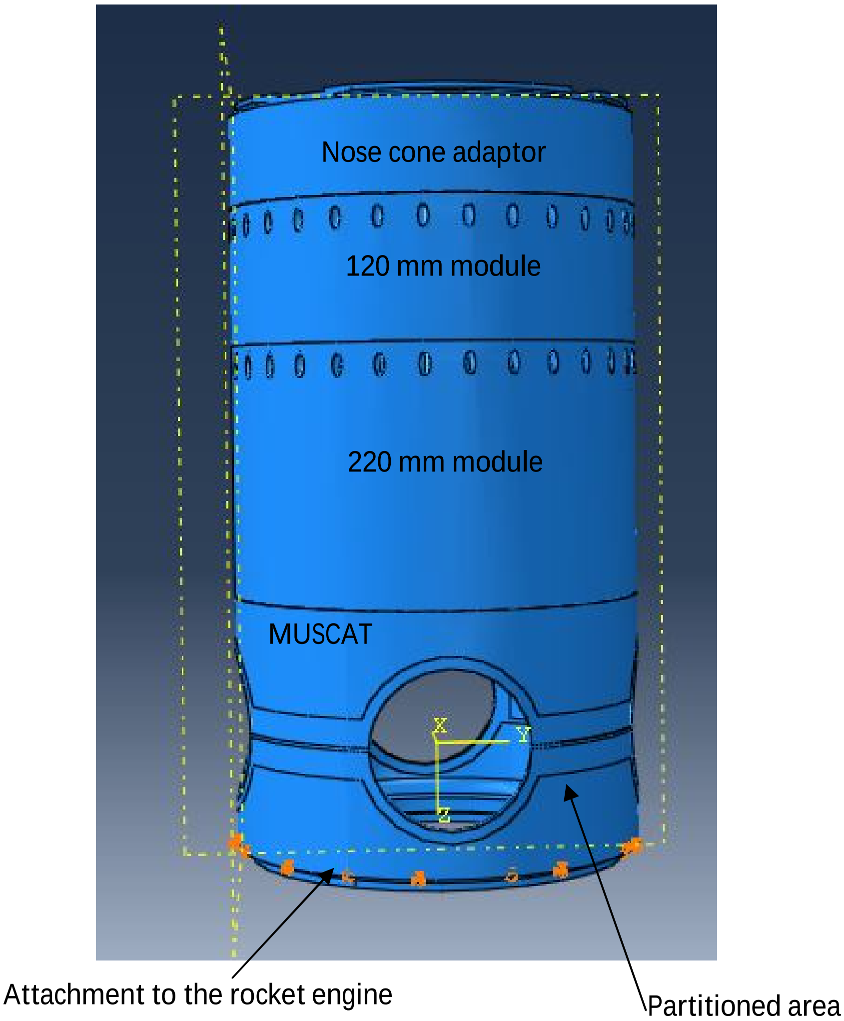

Figure 41: Position definition of FEM model.

The two load cases will be one with the force pointing above the opening as it can be seen in Figure 42.a and a second case where the bending load point 45 degress from the first case, in the direction where no opening is implemented. The last mentioned configuration can be seen in Figure 42.b. Both load cases are implemented in the FEM software as surface shear in the upper part of the upper module. This kind of force has been chosen because then the location of the resultant force is known and the bending moment acting in the MUSCAT module can be easily derived. In the FEM analysis the holes for the attaching screws between modules have been excluded. This is because of the meshing problems that they could cause and because they are located in an area that it is not affected by the modifications of the Muscat experiment. Therefore the analysis of the manufacturer remains valid in this area.

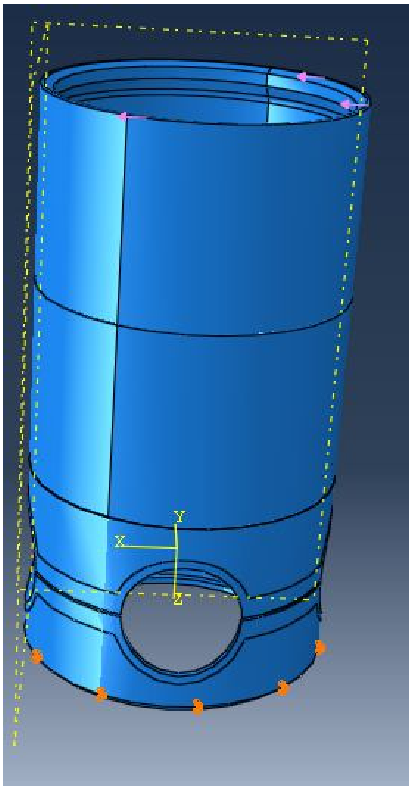

Figure 42.a: Load case 1

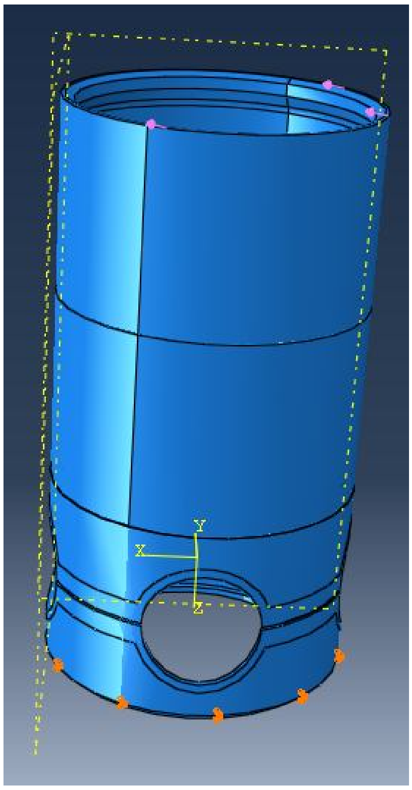

Figure 42.b: Load case 2

The aims of this analysis are two; the first one is to derive a stress concentration factor for the case of bending and the second one id to derive the bending load that can induce yielding in the MUSCAT module. This bending load will be used in the report to derive the load combination that the MUSCAT module can stand.

The results from the load case one mentioned above can be seen in Figure 43.a while the result of the analysis under the load case two can be seen in Figure 43.b. AS it was expected the load case two is more critical than the load case one. With the bending load set to 10MN, yielding is present in the stress concentration areas although it is not extended.

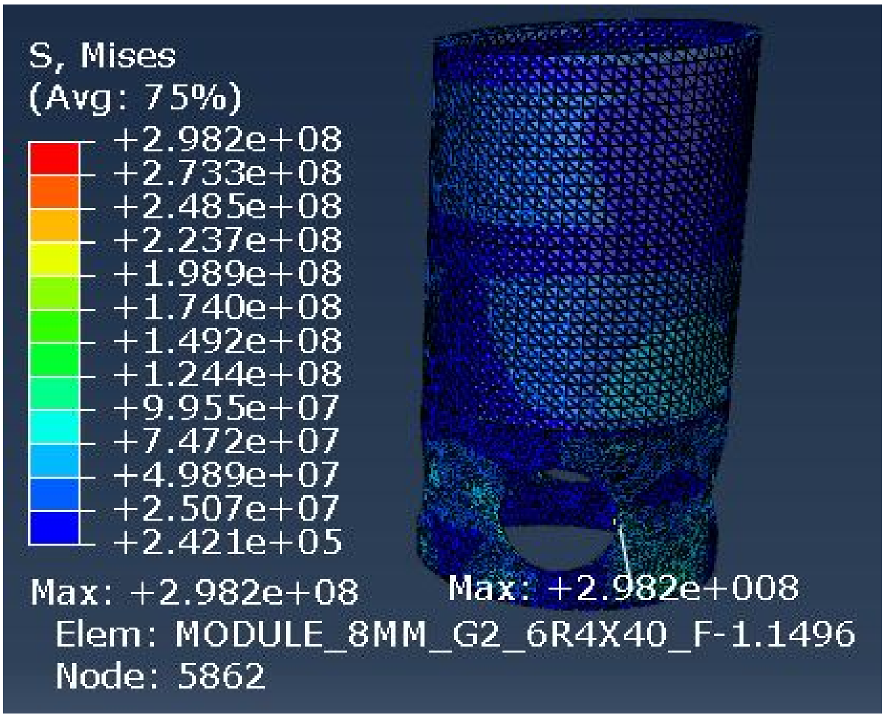

Figure 43.a: Results load case 1

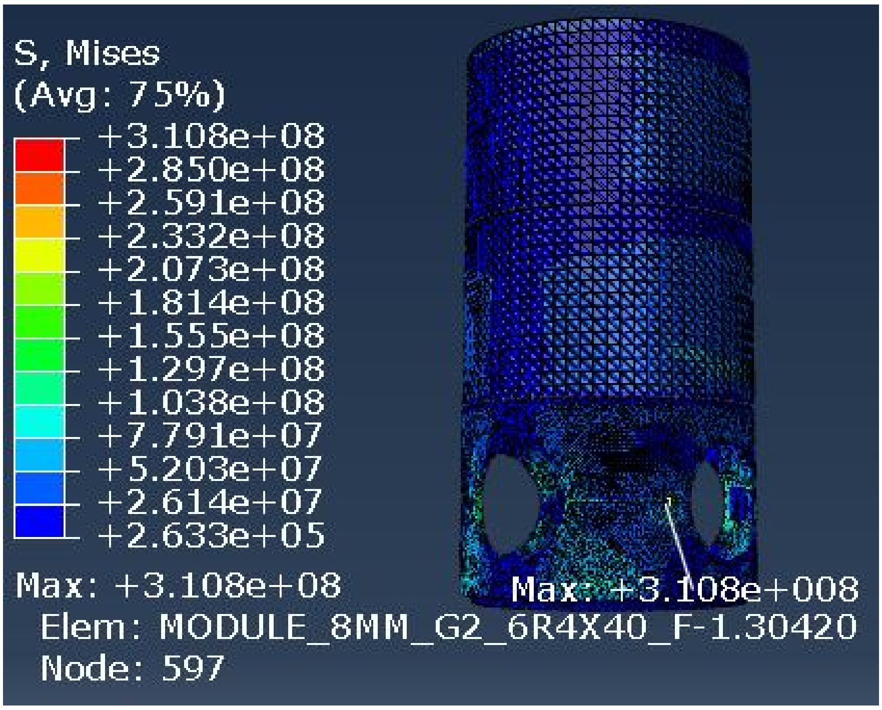

Figure 43.b: Results load case 2

In order to establish a concentration of stress factor in relation to the unmodified module the same load mentioned above (10MN as a shear load in the top of ht upper module) was set in a similar model with three unmodified modules. The FEM model used can be seen in Figure 44. It is done under the same assumptions as the previous assembly of three modules.

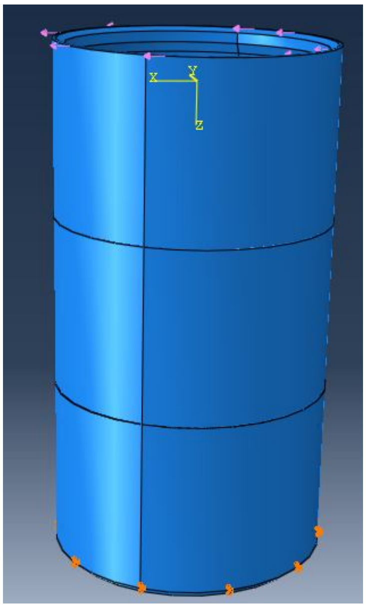

Figure 44: FEM model

The results from this analysis can be seen in Figure 45. As it was expected the level of stresses is more uniform and the absolute value smaller. According the contour plot of Figure 46, the maximum stress in the skin of the unmodified module located in the same position of the MUSCAT module is between 62MPa and 69 MPa. In order to be conservative the maximum stress in the skin of the unmodified module can be assumed 62 MPa. Thus, the stress concentration factor by comparing the stress in the skin of the unmodified with the stress in the skin of the MUSCAT module under the same load conditions (bending load) is

$$\frac{\sigma_{MUSCAT\ bending}}{\sigma_{Unmodified\ bending}} = \frac{301}{62} \approx 5$$

Figure 45: Results of unmodified modules in pure bending.

Another interesting case for this section of stress concentrations is to analyze the case where bending and compression are combined. Therefore an analysis with the 10 MN and the 20MPa loads in the same model has been performed for a configuration including the MUSCAT module and another configuration with unmodified modules only. The loads have been applied in the upper modules in the same way as it has been done in the previous analyses. The result of the analysis concerning the configuration with the MUSCAT module can be seen in Figure 46.

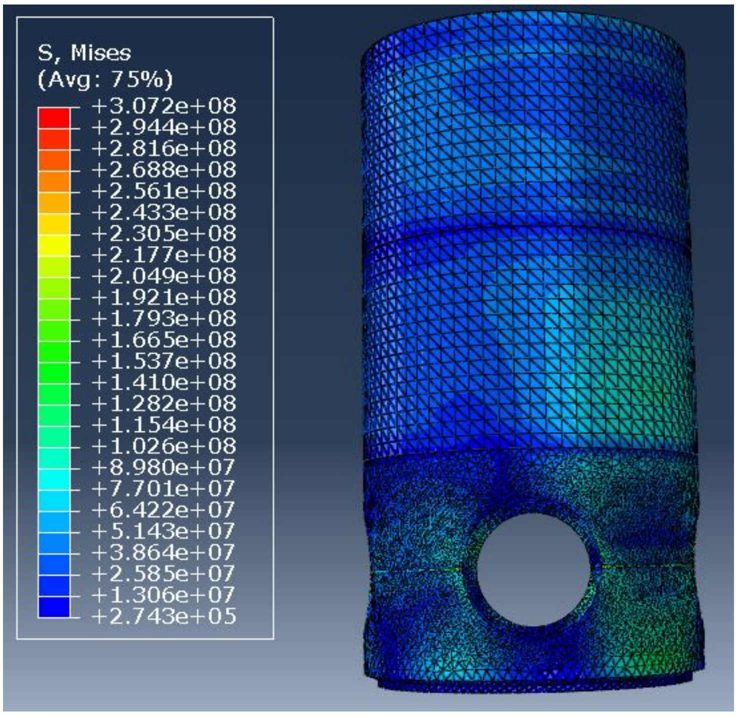

Figure 46: Results bending compression combination.

Due to difficulty to spot the stress concentration area a neared view can be seen in Figure 47. In this contour plot the stress peak can be up to 280MPa

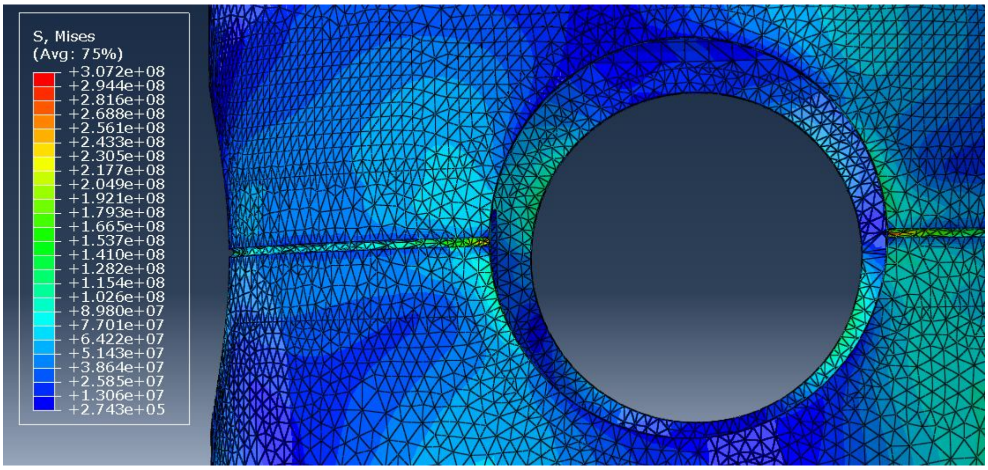

Figure 47: Detailed view of results bending compression combination.

The same analysis has been performed for the configuration with only unmodified modules and the results can be seen in Figure 48

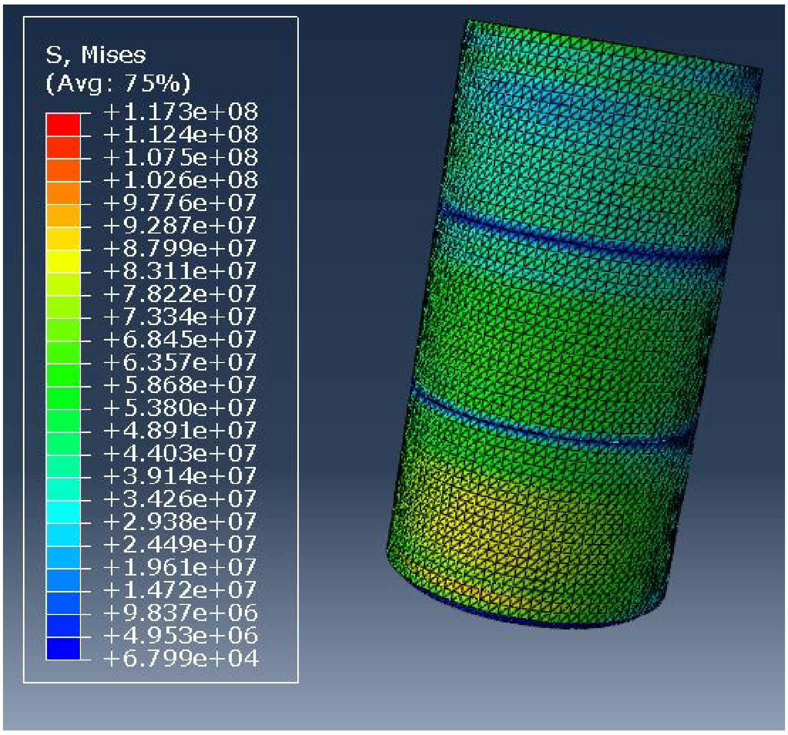

Figure 48: Results bending compression combination.

In this contour plot the maximum stress present in the unmodified module located in the position of the MUSCAT module are between 83 MPa and 87 MPa. In order to be conservative the smaller value will be taken. Assuming 83 MPa as the maximum skin stress, a stress concentration factor can be established as follows.

$$\frac{\sigma_{MUSCAT\ bending+compression}}{\sigma_{Unmodified\ bending+compression}} = \frac{280}{83} \approx 4$$

This means that for the case of combined loads the stress concentrations factor with respect the unmodified module is the lowest among the case of bending (KF=5) and compression (KF=7)

The combination of load studied in this case has been chosen because there were results from individual applications and conclusion could be drawn. However, a more general deduction of the set of combinations that this module can stand can be derived and compared according to [2]. According to [2], the resistance of a pipe cross-section for combined axial compression and bi-axial bending is given by Equation (30)

$$\left(\frac{N_{Ed}}{\chi_{\min}\omega_x N_{Rd}}\right) + \frac{1}{\omega_0}\left[\left(\frac{M_{y,Ed}}{M_{y,Rd}}\right)^{1.7} + \left(\frac{M_{z,Ed}}{M_{z,Rd}}\right)^{1.7}\right]^{0.6} \leq 1.00 \qquad (30)$$

where N_{Ed} is the axial compressive force, N_{Rd} is the axial capacity of the cross-section, M_{Ed} is the bending moment according to first order theory, ω_0 and ω_x are the heat affected zone factors (equal to 1 if there are no welds) and χ is the reduction factor for buckling. As we have an axial symmetric cross-section, we can set one of the bending moments to zero. With no reduction due to heat affected zones, i.e. no welding, the formula simplifies to Equation (31)

$$\left(\frac{N_{Ed}}{\chi_{\min} N_{Rd}}\right)+\left(\frac{M_{Ed}}{M_{Rd}}\right)\leq 1.00 \tag{31}$$

The reduction factor χ can be obtained from [2] considering the slenderness parameter of the module and considering that the alloy used is heat treated. With these considerations it can be obtained from [2] that $\chi = 0.9$. Then 31 become Equation (32)

$$\left(\frac{N_{Ed}}{0.9 N_{Rd}}\right)+\left(\frac{M_{Ed}}{M_{Rd}}\right)\leq 1.00 \tag{32}$$

If the axial load capacity N_{Rd} and the bending moment capacity M_{Rd} are equal for both the unmodified and the modified modules, the interaction formula can safely be used to calculate the capacity against combined axial compression and bending. N_{Rd} is the area of the section multiplied the yield strength of the material and M_{Rd} is the yield strength of the material multiplied the moment of inertia. Therefore, in the case of the MUSCAT module where the area and moment of inertia of the weakest section are larger than the area and moment of inertia of section of the unmodified module, it can be guaranteed that the modified module can stand the same loads combinations than the unmodified module.

There two more places where stress concentration should be checked. One of these places is the camera opening than has not been included in the analysis so far because is not in the weakest section and in terms of structural strength does not represent a threat. The other place is the opening in the module where a steel guide will introduce the cable of the ejection system in the internal pyro-cutter. This has not been considered in the section analysis and in the strength analysis because this part is a solid steel part with only two small holes for the cable that is inserted in the module. However, a compression test has been performed to see if the stress level in these places is higher than in the stress concentration area pointed in previous analyses. The same optimization procedure in the meshing has been followed to increase the accuracy of the solution in the required areas, the part has been partitioned a manually meshed to include smaller elements in the surroundings of the critical places. The results can be seen in Figure 49 and Figure 50.

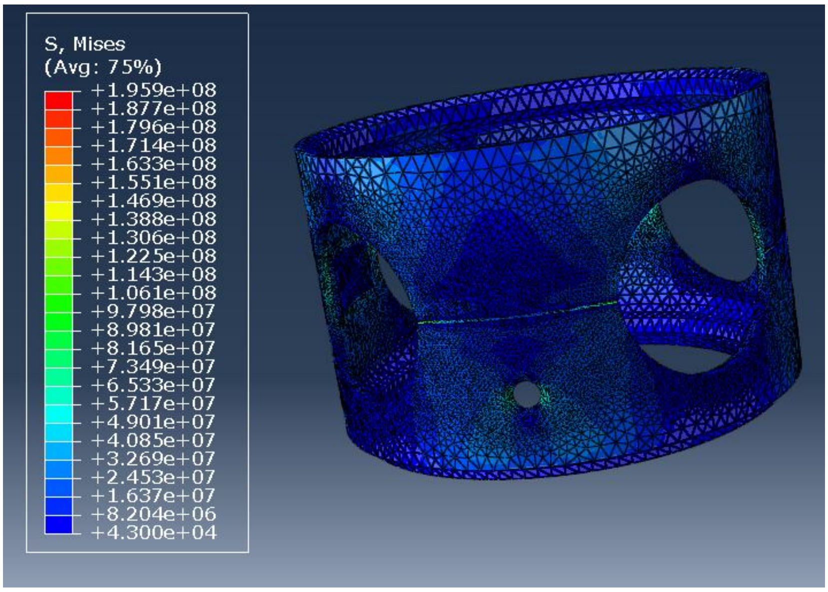

Figure 49: Camera opening stress concentration

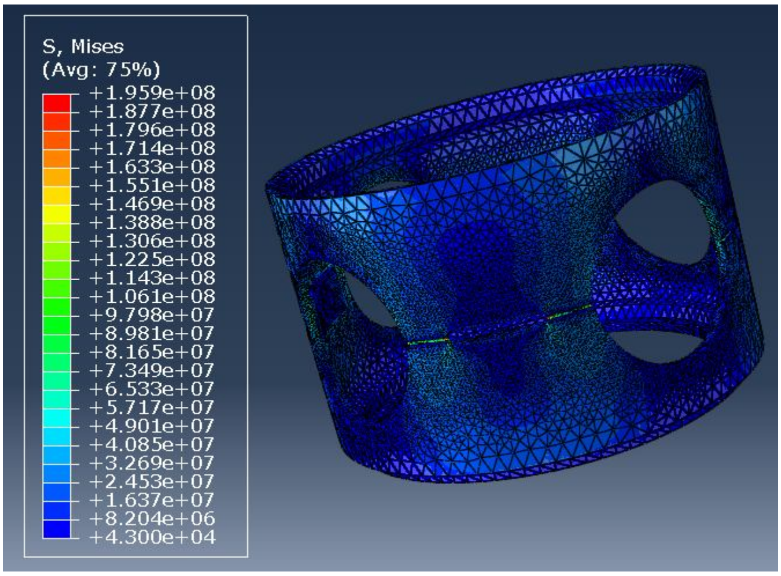

Figure 50: Pyro-cutter access hole stress concentration

As it can be seen in Figure 49 and Figure 50, there are stress concentrations. However according to the contour plot the level of these concentration of stresses is not higher that the stress concentrations detected in the sides of the openings if previous analyses.

5. Mass evaluation of the module

An evaluation of the mass of the modified module plus the reinforcement should be performed. This analysis have been done using the measuring function of CATIA V5 [6] with the density of 2700kg/m^3 provided for aluminium alloy 7020-T6 by EUROCODE 9[4]. The mass has been evaluated for the modified reinforced module with opening of 134 mm. The mass for the modified module with 8 mm wall thickness, the groove for the cable, reinforcements for the groove and openings of 134 mm is 5.39 kg. The mass of the unmodified 220mm module is 4.58 kg. This means an increment in mass with respect the unmodified module of 0.81 kg for the modified module with 134 mm openings. All these estimations have done using a parametric model implemented in CATIA V5 [6] that can be seen in Figure 51

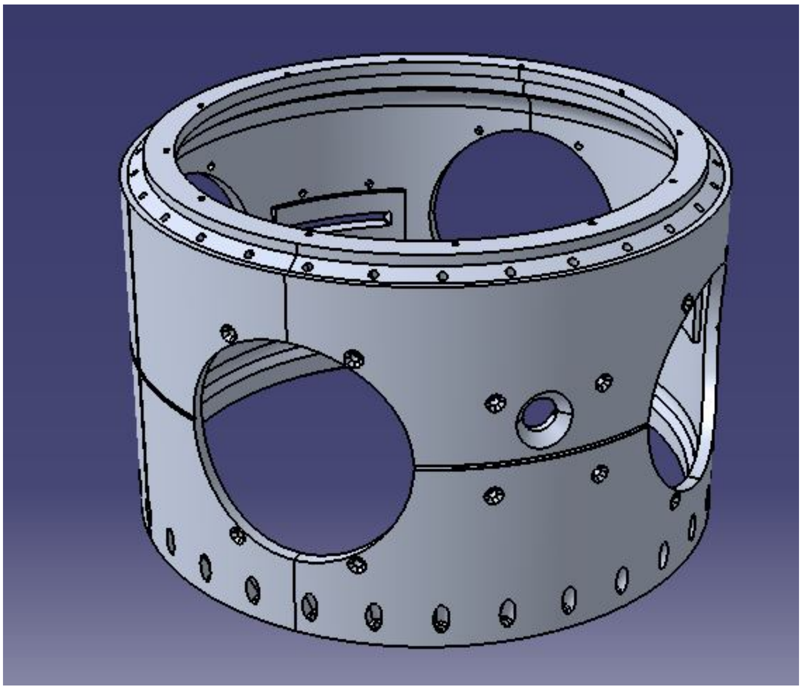

Figure 51: model used in the measurement of the mass.

6. Thermal analysis of the module

The thermal analysis of the modified module consist in heating up the module until the 120 degrees Celsius mentioned in the REXUS manual and check that the displacements induced by the change in temperature can be tolerated by the mechanical components of inside the module. The results of this analysis can be seen in Figure 52, in this contour plot the points where the collar will be attached are in light green which means that the maximum displacement can be 1.9 mm. This displacement can be absorbed by the crosses and associated thermal expansions.

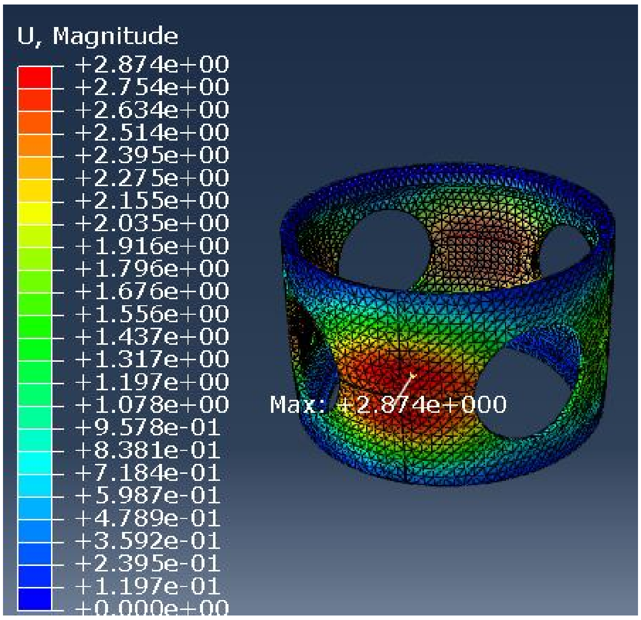

Figure 52: Displacement field induced by temperature increment.

Furthermore, it should be noted that this is steady state solution and this is worse case scenario because the characteristic time of the heat transfer process will not allow to reach a steady state at the maximum temperature mentioned in the REXUS manual.

The same analysis has been carried out for the unmodified module in order to establish a comparison and the result can be seen in Figure 53. The displacement in the unmodified module is slightly smaller. This is due to the no inclusion of the steel guide in the thermal analysis of the modified module because considering the steel guide for the cables of the ejection system; both modules have the same strength and stiffness.

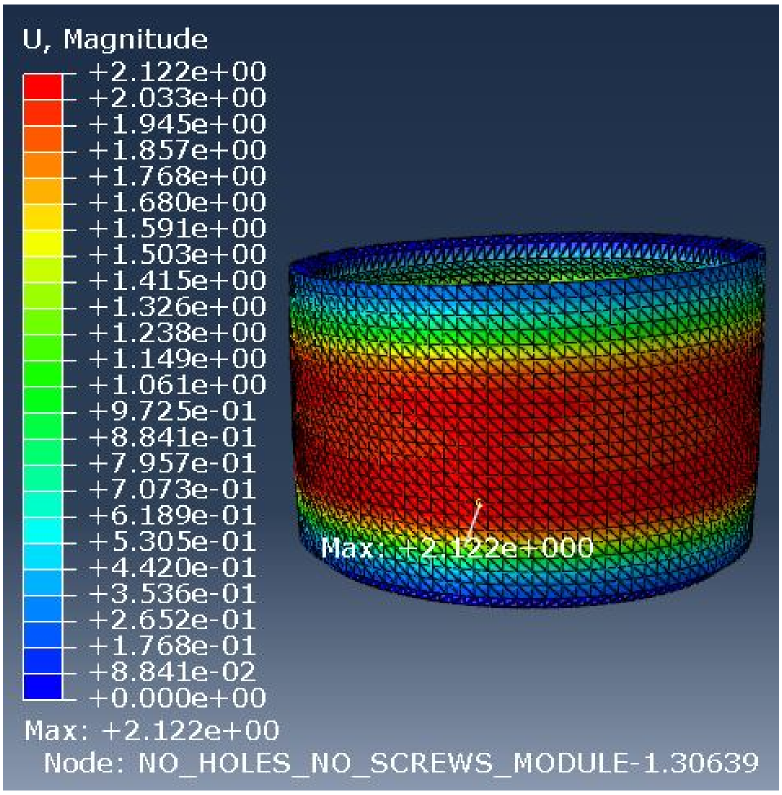

Figure 53: Displacement field induced by temperature increment.

A thermal analysis of the modified module containing the collars and the lower cross was considered important in order to check the stress and displacements that the thermal loads can induce in the structure. The results of this analysis can be seen in Figure 54 where the stress caused by the thermal load can be seen an in Figure 55 where the displacement due to the thermal loads can be seen

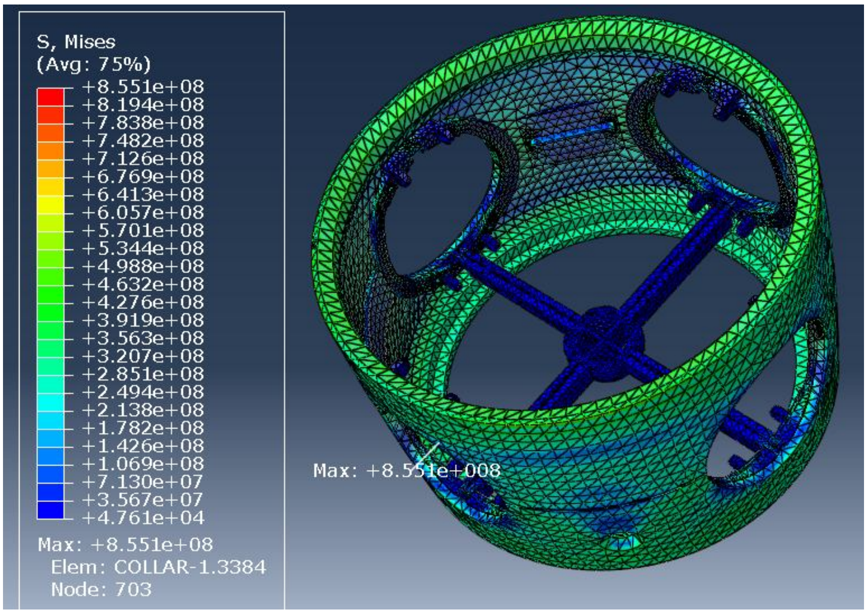

Figure 54: Stresses field induced by temperature increment.

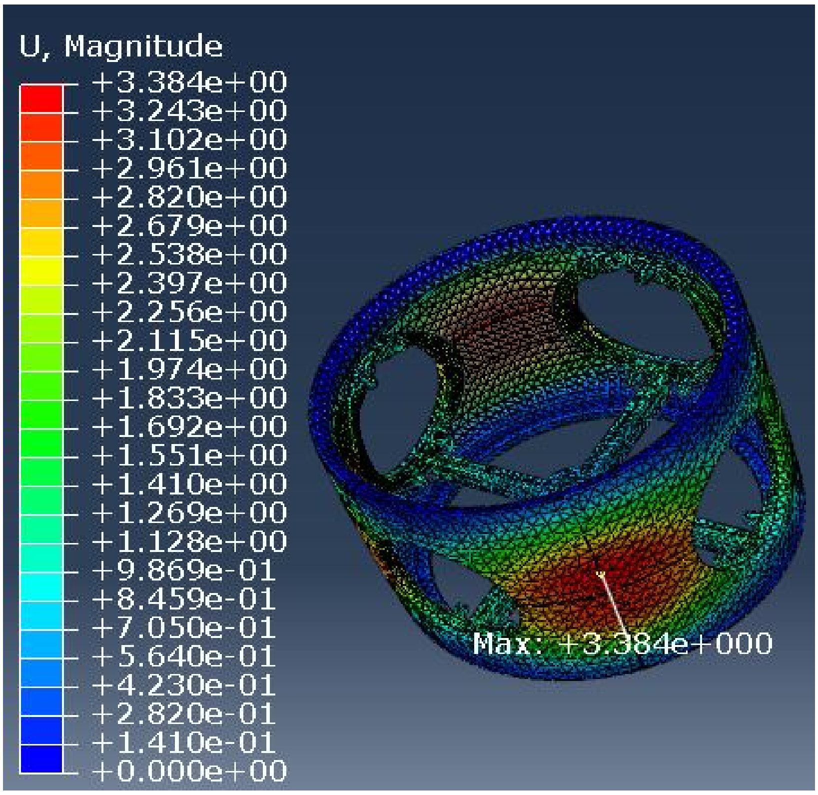

Figure 55: Displacement field induced by temperature increment.

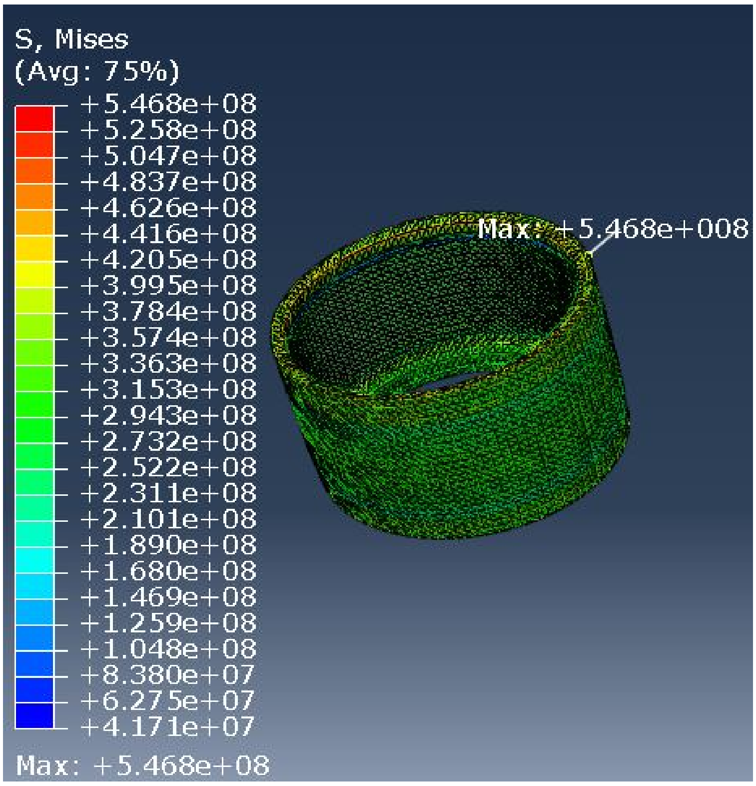

Figure 56: Stresses field induced by temperature increment

In this analysis the boundary condition of simply supported of both ends of the rocket were used to simulate the assembly constrains of the rocket when the module is mounted. The conclusion that can be obtained from this thermal analysis is that the inner structure can get stresses due to the thermal loads. The displacement experimented by the unmodified module and the MUSCAT module are really close therefore the MUSCAT module can handle the thermal loads of the mission. The stresses induced by the thermal load in both modules are almost the same, thus the stress concentration due to thermal loads is negligible(Figure 54 and Figure 56). Finally, it should emphasized that this a extreme case where the steady state of the solution is reached, during the flight this will not happen because the characteristic time of the heat transfer problem is long in comparison with the duration of the high temperature load. Furthermore, the 120 degrees are expected only in the skin not in the entire module.

7. Module assembly considerations

7.1. Hatches pressure over the collar

According to design requirements the hatches cannot protrude at any time during the flight from the rocket module. Therefore an analysis to derive the tension in the cable required to avoid this was conducted. The tension in the cable for the hatches to push over the stoppers placed in the collars with 0.98 kN. A FEM analysis has been conducted to analyse this and according to the contour plot that can be seen in Figure 57, the stress in the collars as well as in the module and in the inner structure are far below the yield strength of the material.

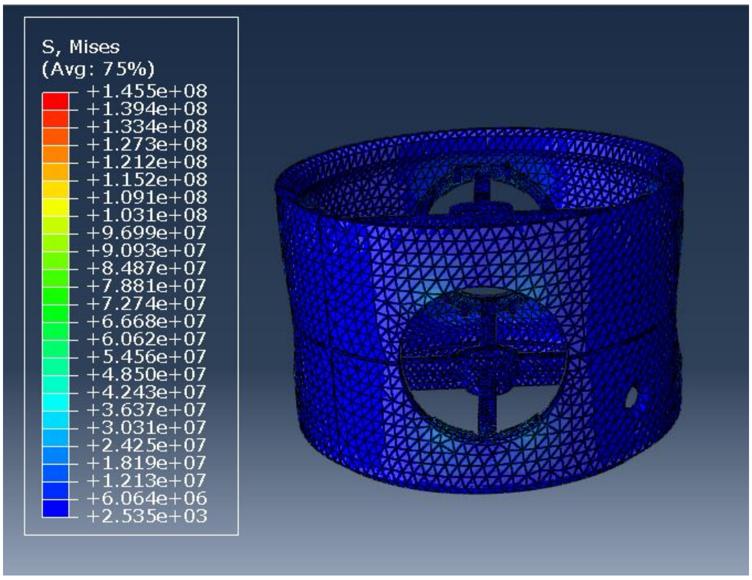

Figure 57: Pressure of the hatches analysis result

7.2. Cable influence

The cable is pretension in order to avoid the hatches to move and therefore the rocket module is also compressed perpendicular to the hoop direction. The pressure derived from the cable tension can be obtained as it is shown in Equation (33) using an analogy with a differential portion of a pressure vessel equations and the cable.

$$P_{cable} = \frac{\sigma_{cable}\, t_{cable}}{r_{cable}} = \frac{600 \times 2.5}{176} = 8.5MPa \tag{33}$$

A FEM analysis has been performed with this load and the compression load used in section 6 (20 MPa) in order t o see if the cable pretension has a visible influence in the stress concentration factor. The results from this analysis can be seen in Figure 58.

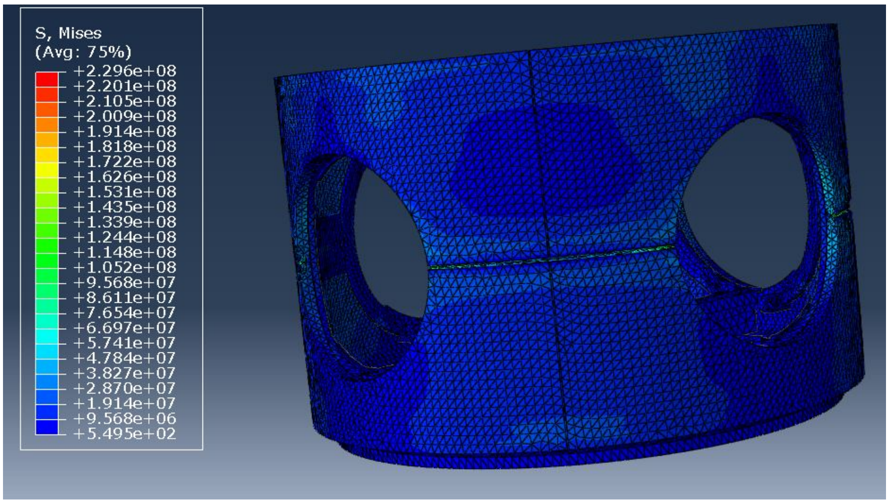

Figure 58: Stress concentration considering cable effect.

It is difficult to see the peaks of stresses, therefore a path following the groove has been created and plotted as can be seen in Figure 59. From this pace it can easily appreciated that the stress peak remain in the same values as in the analysis where the effect of the cable was not considered.

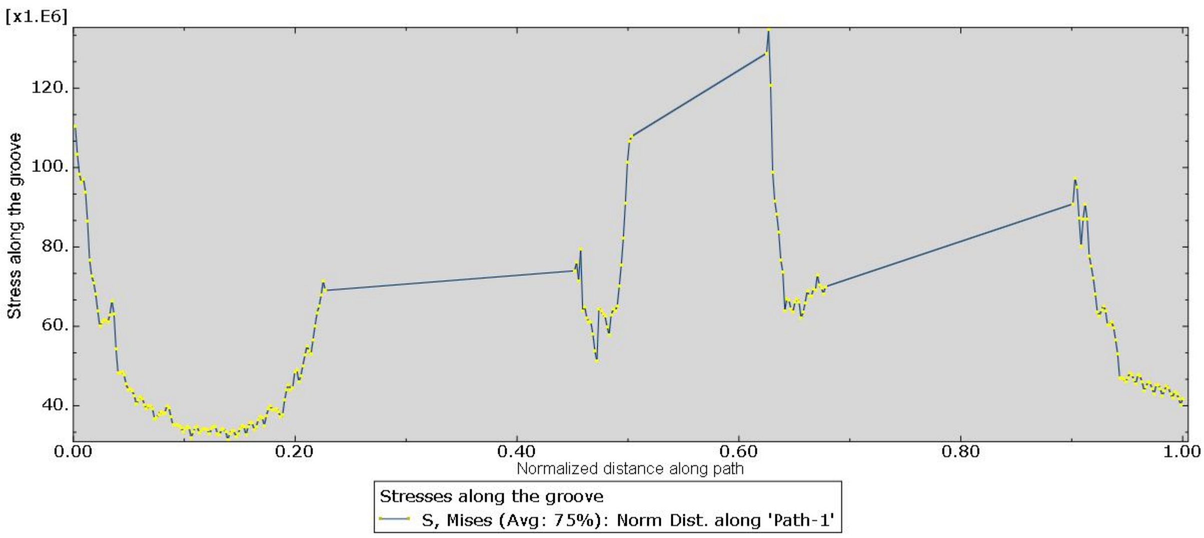

Figure 50: Path along the groove considering cable effect.

7.3. Cross-collar attachment strength evaluation

The connection between the crosses and the collars is done by a screw, that in this case will be simulated with a “TIE” constrain between two partitions. The load for this connection are mainly shear caused by the acceleration of the crosses during flight and the acceleration of the FFUs and cages over the lower cross. This analysis has been performed and it can be seen in Figure 60.

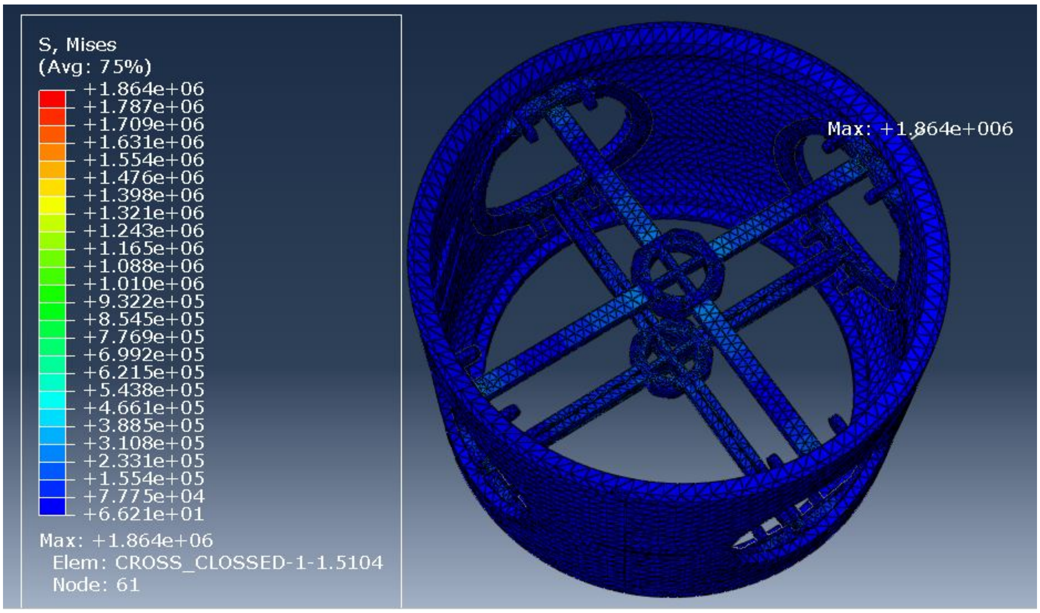

Figure 60: Stresses in the cross-collar connection

It can be seen in the contour plot that the level of stress is far below the strength of the material, therefore there is no problem in terms of strength in the connection between the collars and the cross.

8. CONCLUSION

This report presents the structural analysis of the modified rocket module to determine the changes required to achieve the same strength and stiffness as the unmodified rocket module.

The conclusions were and drawn, respectively:

- **Sections 2.2.2-2.2.4, 3.4 and 3.5**: The elastic buckling under axial load of the unmodified module was analysed. The finite element results are only 5% higher than the analytical solutions and the mesh is refined until the solution converges. The elastic buckling analysis shows that the finite element model is valid and that the module will yield before buckling. This tells us that we can use a section analysis to compare the capacities of the modules.

- **Sections 4.1.3**: The elastic buckling load of the modified module with four openings, increased wall thickness, circumferential groove for the cable and the strengthening of the skin due to the groove is analysed and found to have a slightly higher elastic buckling strength than the unmodified module. This means that both modules will have the same factor of safety against buckling, so simple section analysis can be used to compare their load bearing capacities.

- **Section 3.1:** The simple Ramberg-Osgood elastic-plastic material model for the aluminium alloy, proposed in Eurocode 9, is introduced for the elastic-plastic analysis of the modules subjected to axial, bending and combined axial and bending loads. An elastic-plastic material model is required to investigate the effects of stress concentrations due the various openings in the modified module.

- **Section 3.2:** The upper and lower edges of the modules are simply supported, i.e. the translational degrees of freedom are constrained to prevent ovalisation of the upper and lower rings. These boundary conditions have been found to be accurate as the assembly of modules means that there in fact are two rings preventing ovalisation. Analyses of a stack of three modules have shown that the simply supported boundary conditions represent the behaviour of the module in the module stack. In addition, both the unmodified and the modified modules are analysed with the same boundary conditions, so the comparison is accurate.
- **Section 3.4:** A uniform mesh size was shown to be good for the convergence of the elastic buckling load, but a non-uniform mesh was implemented to more accurately capture the stress concentrations around the openings.

- **Section 4.1:** The increase of the wall thickness for the modified module is determined to get at least the same elastic buckling load, cross-section area and moment of inertia as the unmodified module. Preliminary analysis of various strengthening measures showed that the increasing the wall thickness was the most mass optimum strategy.

- **Section 4.1.2**: The stress concentrations in the modified module for axial load were analysed and found to be acceptable. Parts of the module will be in the plastic region, but the module could still tolerate the load level corresponding to a factor of safety of 2.

- **Section 4.1.4:** The capacity of the modules for combined axial load (from launch acceleration), shear and bending loads (from gravity and vibrations) are analysed. Stress concentrations are found to be worst in the groove close to the openings, but in a limited region. The stress concentration factors for extrapolated sounding rocket load levels, found in literature, are not critical despite being above the yield strength of the material as the regions of high stresses are very small. An interaction formula for the combined axial load and bending load is derived from Eurocode 9, which describes that capacity of the module for any combination of axial and bending loads.

- **Section 6:** A thermal analysis to study the displacement of the module under heating is performed. The analysis of the module with the collar and the cross shows that the stresses induced by the thermal loads are not critical, partly because the screw connection of the crosses has some play which can adjust for the thermal displacements.

- **Section 7:** The pretension of the cable to keep the hatches closed during launch results in radial forces on the collar, which are screwed to the module. The effect of the cable pretension is a stress concentration in the cable groove close to the openings, but the stress levels are below the yield strength and the region is small, so this load case is not critical.

To summarise, the updated and extended analysis of the modified module confirms that the proposed design seems to be safe for launch as the modules have equal cross-section areas and moments of inertia and the stress concentration regions in the modified module are small for realistic load levels.

References

1- **Numerical and experimental investigations of the response of aluminium cylinders with a cut-out subject to axial compression**
Haipeng Han, Jinquan Cheng, Farid Taheri, Neil Pegg
Thin-Walled Structures 44 (2006) 254–270

2- **Eurocode 9 (Design of aluminium structures)**
Part 1-5: Shell structures
BS EN 1999-1-5:2007

3- **Theory of elastic stability**
Stephen Timoshenko (1934)
ISBN 99-0942591-2

4- **Eurocode 9: Design of aluminium structures**
Part 1-1:General rules and rules for building
DD ENV 1999-1-1:2000

5- **ABAQUS user interface information**
Dassault Systemes Simulia Corp.
Rising Sun Mills
166 Valley Street
Providence, RI 02909-2499, USA

6- **Catia V5 R16**
Dassault Systemes
3DS
Rue Latécoère, 78140
Vélizy-Villacoublay, France

7- **Structural Dynamic Analysis of a Sounding Rocket during the Liftoff**
Hui-wen Hu, Yao-cheng Wang and WEI-Jun Lu
Composite Materials and Lightweight Laboratory, Department of Vehicle engineering,
National Pingtung University of Sciences and Technology.
I, Shuefu Road, Neipu, Pingtung, Taiwan, R.O.C.
Journal of Aeronautics, Astronautics and Aviation, Series A, Vol.41, No.2,PP.111-120(2009)

8- **Thin Plates and Shells Theory: Analysis, and Applications**
Eduard Ventsel and Theodor Krauthammer
CRC Press 2001
ISBN: 978-0-8247-0575-6

9- **Eurocode 9: Design of aluminium structures**
Part 1-2: General rules
General rules and rules for buildings
1999-1-1:2000

10- **Description of stress strain curves by three parameters**
Walter Ramber & Willian Osgood 1943
Document ID: 19930081614
Report number: NACA-TN-902
National Advisory Committee of Aeronautics (NACA)

11- **Remarks on the application of ENV1993-1-6 buckling curves to aluminium shells**
NSCC 2004(Nordic Steel Construction Conference)
Copenhagen, Denmark 7 – 9 June 2004
Mazzolani (Department of Structural Analysis and Design, University of Naples Federico II,)
Mandara (Department of Civil Engineering, Second University of Naples, Aversa (CE))
Di Lauro (Department of Civil Engineering, Second University of Naples, Aversa (CE))

12- **European Cooperation for Space Standardization (ECSS),**
Space engineering: structural factors of safety for spaceflight hardware.
ECSS-E-ST-32-10C, 6 March 2009

Thermal cutter sea-level test

Andreas Myleus

May 16, 2012

1 Introduction

The thermal cutter is the device that cuts the string that holds the top hemisphere in place. When the string is cut, the top hemisphere is released, which exposes the parachute to make sure it deploys. It was crucial for the balloon drop tests to make sure how long it took for the string to be cut from when the thermal cutter was initiated. Timing the time it took to cut the string was performed in a lab at SPP, KTH. The mean time of the cut was around 3-4 seconds, which was enough to make sure the parachute had time to deploy before the FFU hit the ground. During drop test 1, the cutter performed as intended and the data collected from drop test 1 confirmed this cut time.

2 Method for timing

The tests performed indoors was made the 17th of April. The first drop test was done the 19th of April.

- Case 1: The thermal cutter was attached to the inner metal ring and a power supply was adjusted to give 3.9V (the voltage of the battery). A string was held by hand over the kanthal wire that burns the string, and the thermal cutter was connected to the power supply. The current was noted and the time it took for the string to burn.
- Case 2: The same was done but with limiting the current in the power supply to simulate the resistor array that is on the bottom PCB.
- Case 3: Test the thermal cutter with the battery.
- Case 4: Test the cutter in the drop test.

3 Results

- Case 1: Current of around 3 A. Mean time of 1 second,
- Case 2: Current 2.2 A. Mean time of 3-4 seconds.
- Case 3: Mean time of 3-4 seconds.

- Case 4: Time of 3.5 seconds. Can be seen in Figure 1.

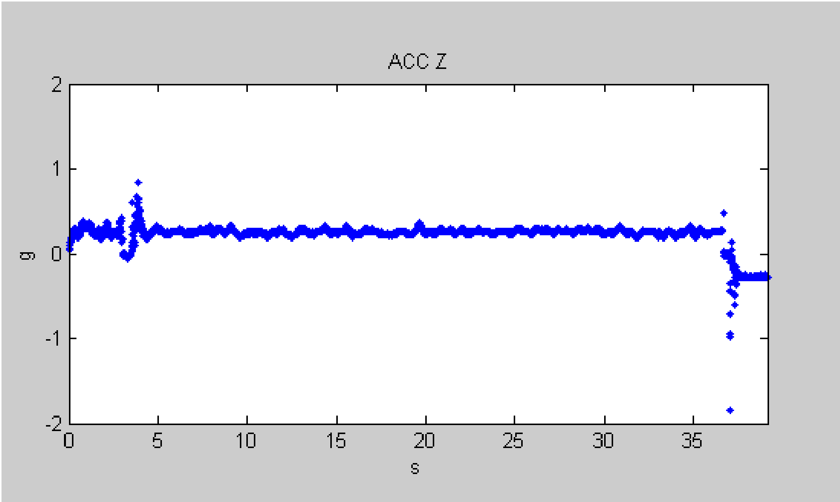

Figure 1: Acceleration of FFU in z-axis during Drop 1 in Drop Test 1.

The data is collected at the same time as the cutter is initiated. The acceleration in the z-axis of the FFU has a peak after 3.5 sec, which is the parachute deploying.

4 Conclusion

The thermal cutter achieves the performance needed for the first drop test at sea-level in Arboga during the spring. Cutting tests while simulating the conditions in the atmosphere that we will operate during the live free fall has to be done. Also cutting tests at very low temperatures, simulating the conditions at sea-level at Esrange, will be done.

MUSCAT Rocket Experiment

Drop Test Report

Darri Kristmundsson

May 16, 2012

Abstract

A drop test was performed at Aarboga airfield on April 19th 2012 to test the overall system performance of the MUSCAT FFU system. An FFU is attached to a balloon and hoisted up to a specified drop altitude, upon which a drop mechanism is activated. Upon entering free fall the FFU initiates a mission mode which includes collecting internal sensor data and activating a recovery system, which includes deploying a parachute. The goals of the test were not properly met due to equipment failures.

1 Goals and Objectives

- To verify the parachute deployment and packing procedure.
- To transmit and receive commercial GPS data in field conditions.
- To gather raw GPS data in field conditions which can be post-processed to find positions, acceleration and velocities of FFUs during free fall.
- To verify functionality of internal sensors and to post process sensor data to find drop altitude and velocities.

2 Background Information

2.1 Weather Balloon

A weather balloon was used to elevate the payload to drop altitude. The payload consisted of a test FFU, the drop mechanism and a length of tether anchoring the balloon to the ground.

2.2 Tether Winch Mechanism

A spool of 80 lb Berkley Fishing Fireline was attched to a winch, which was used to release and reel in the balloon.

2.3 Drop Mechanism

A remotely controlled drop mechanism is used for initiating the drops when the payload has reached the drop altitude. This drop mechanism consists of a cellphone which, when called, delivers a current through a Kanthal wire which is wrapped around the line connecting the FFU to the balloon. The Kanthal wire is heated by the current and cuts the FFU line about 7 seconds after the call has been placed.

2.4 Drop Test Mission Mode

When mission mode is initiated by sending a command to the FFU, it stops listening to new commands and waits for the accelerometers to detect the zero G of the free fall. When it is triggered, the FPGA sends a current through the thermal cutter, which cuts the fishing line constraining the upper hemisphere, thus initiating the parachute deployment. In addition, the FPGA also records accelerometer, magnetometer, pressure and angular rate data and writes these to the memory. The parachute deploys in approximately 4 seconds, slowing the FFU to a terminal velocity of 5-10 m/s vertically. Data gathering ends after 40 s and the memories can be read after FPGA reset.

2.5 FFU Recovery System

The FFU recovery system is thoroughly described in the MUSCAT Student Experiment Documentation. It consists of a parachute, a releasable upper hemisphere and a thermal cutter. The purpose of the recovery system is to bring the FFU to a safe terminal velocity of 8-10 m/s. For the drop test, a Top Flight 30" ThinMill X-shape parachute was used. It was connected to the FFU by four 20cm chords gathered at the end of a 1,5m line.

2.6 Dummy Test

To verify the functionality of the drop mechanism and to assess the balloon drift due to wind a dummy drop is performed with a dead payload. The dummy is a box with the same mass as an FFU, which weighs 396g.

2.7 Balloon Camera

To capture close-up footage of the parachute deployment, a GoPRO Hero digital camera is attached to the balloon and angled towards the payload.

2.8 Ground Camera

To document the drop, a ground based camera is kept on the balloon during ascent and FFU during drop.

3 Method

Following is a summary of procedures used during the drop test.

3.1 Balloon inflation

For the balloon inflation the following equipment is required:

- Cotton gloves for all personell
- Balloon
- Helium tank
- Pressure regulator
- Pressure regulator o-ring
- Wrench
- Balloon hose
- (Duct tape)
- Wire ties

The weather balloon is very sensitive to fat acids and must not come into direct contact with skin. Cotton gloves must be worn at all times while handling the balloon. The balloon can only be touched with bare hands at the base where it is visually thicker and more robust. Indoors inflation is recommended for avoiding wind complications. For pressure regulator positions, refer to figure 1. The inflation procedure is as follows:

- Spread a clean cover on the ground, large enough to uncpack the balloon on (c.a. 10 m^2)
- Gently unpack the balloon from its box and lay on the groundcover.
- Connect the pressure regulator (1) to the Helium tank. Make sure that o-ring is in place (see figure 2). Also make sure that both pressure regulator valves (2,4) are closed. Secure connection with wrench.
- Test the tank/regulator connection by slowly opening the tank valve (2). Listen carefully for leaks in the tank/regulator connection.
- Connect the balloon hose to pressure regulator (6) and balloon. Secure both ends with wire ties. Make sure only to place wire ties on the reinforced part of the balloon.
- Position 2-3 persons around the balloon to keep it properly spread during inflation.
- Regulate output pressure at c.a. 2-3 (4).
- Inflate balloon.
- Connect a mass equal to the payload to the balloon reinforcement. When the balloon can freely lift the mass and float around it is sufficiently inflated.
- Close tank valve (2). Secure balloon outlet with wire ties above the end of the hose.
- Secure balloon to a fixture on the ground and remove the hose.

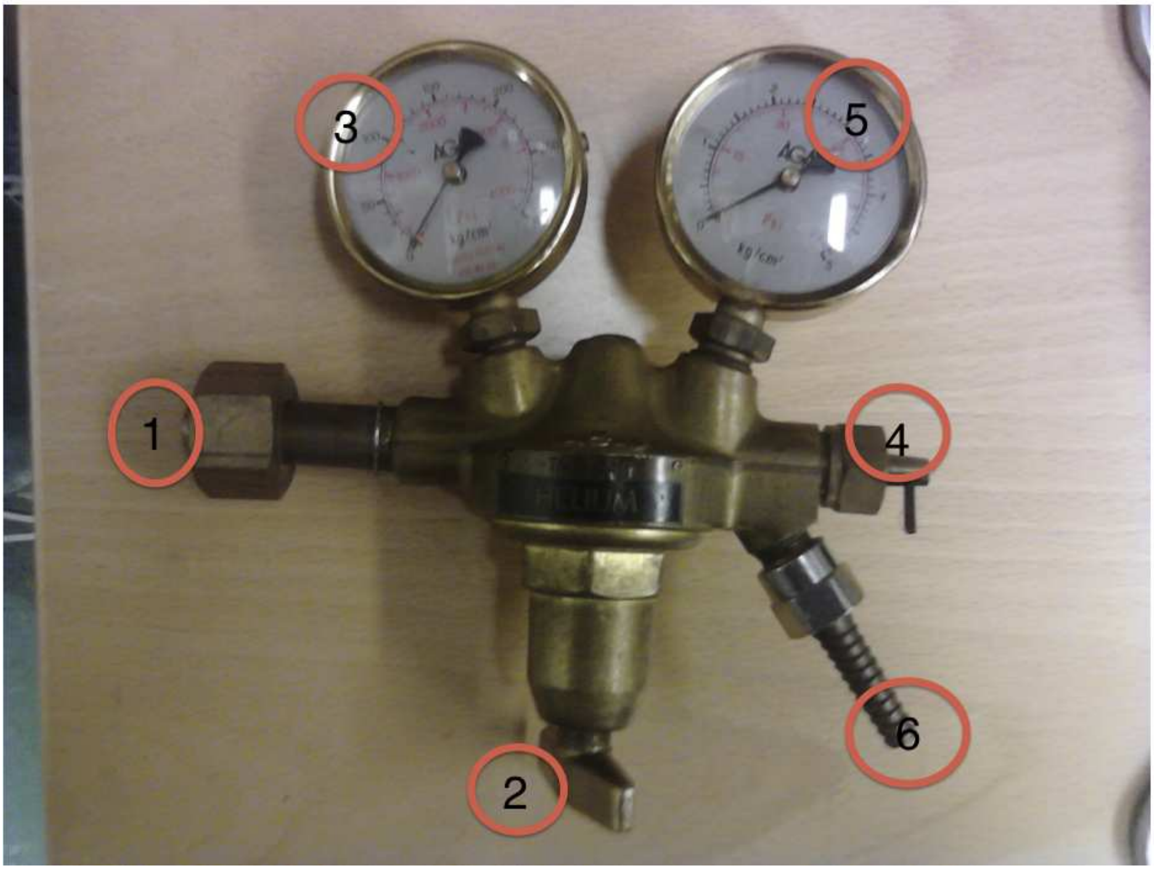

Figure 1. 1. Tank connector 2. Tank valve 3. Tank pressure meter 4. Output valve 5. Output pressure meter 6. Regulator output.

3.2 FFU Parachute Packing

A parachute packing procedure is available in the MUSCAT SED.

3.3 FFU Activation

- Connect the FFU to the Charge/Comm board using the bottom 16pin connector. Make sure the arrow on the connector is pointing to the arrow on the board.
- Connect the RAIN charge/Comm board to a computer using a USB cable.
- If the FFU battery needs to be charged, connect external power to the RAIN charge/Comm board to charge the .
- If the FFU needs to be programmed, connect the splitcable connected between the RAIN charge/Comm board to the FlashPro programmer.

Figure 2. Pressure regulator o-ring

- Use the program Teraterm to issue commands. Configure the program to use serial and the baud rate 38400. Write the commands in the text window.
- Make sure the data is on memory can be erased.
- Rewind the memory by pressing 'R'.
- Erase the memory by pressing 'JQ'.
- Press 'F' repetitively until '00000000' is returned, meaning the erase is done.
- Check that the memory is empty by pressing 'a' two times and see if you only get 'F's.
- Rewind the memory again by pressing 'R'.
- Check the memory address, press 'F' and see if it is '00000000'.
- Start mission mode by pressing 'Ji'.
- Verify that the blue LED is triple blinking, meaning mission mode.
- Remove the connector to the FFU.

3.4 Drop Test Procedure

After the payload has been secured to the balloon, the launch officers gradually give it line and report its approximate altitude to the test leader. Tracking officers positioned around the parameter report on balloon drift to estimate the wind conditions. When the balloon has reached its goal altitude, the test leader initiates the drop by placing a call to the drop mechanism. The recovery system officers proceed to retrieve the payload when it lands.

3.5 Post-drop Procedure

The FFU is inspected for structural failure and LED statues are recorded off the PCBs. In particular, the thermal cutter is inspected for damage. The FFU is connected to a computer and the data are read out and plotted according to the following procedure

- Connect the FFU to the Charge/Comm board using the bottom 16pin connector. Make sure the arrow on the connector is pointing to the arrow on the board.
- Connect the RAIN charge/Comm board to a computer using a USB cable.
- Reset the FFU by connecting the two reset test-points on the circuit board.
- Use the program Teraterm to issue commands. Configure the program to use serial and the baud rate 38400. Write the commands in the text window.
- Press 'T' to enable turbo readout.
- Switch to 2000000 Baud readout speed in Tera term and make sure flow block is activated.
- Enable logging in Teraterm
- Press 'a' to start readout.
- Check the log window that the counter is is increasing.
- Press 'a' again when only 'F's are displayed in the window.
- Pause and close logging in Teraterm.
- Make sure the data is plotted and verified before the memory is erased.

4 Observations

Of the four documented FFU drops, only 1 and 3 yielded useful data. The data from these two drops are documented in this chapter. As the drop activation was unexpected in both cases, no drop time was logged on the ground, but it can be estimated from gyro readings from the drops.

4.1 FFU Drop 1

The accelerometer, pressure sensor and gyro recordings from drop 1 are shown in figures 3, 4 and 5.

Ground observations of approximate drop altitude and terminal velocity are presented in table 4.1

4.2 FFU Drop 3

The accelerometer, pressure sensor and gyro recordings from drop 3 are shown in figures 6, 7 and 8. In this drop, the parachute deployment takes place 11 seconds after the data gathering commenses. Since data is only gathered for 40 seconds, the ground impact was not recorded during this drop, and the total drop time remains unknown.

Ground observations of approximate drop altitude and terminal velocity are presented in table 4.2

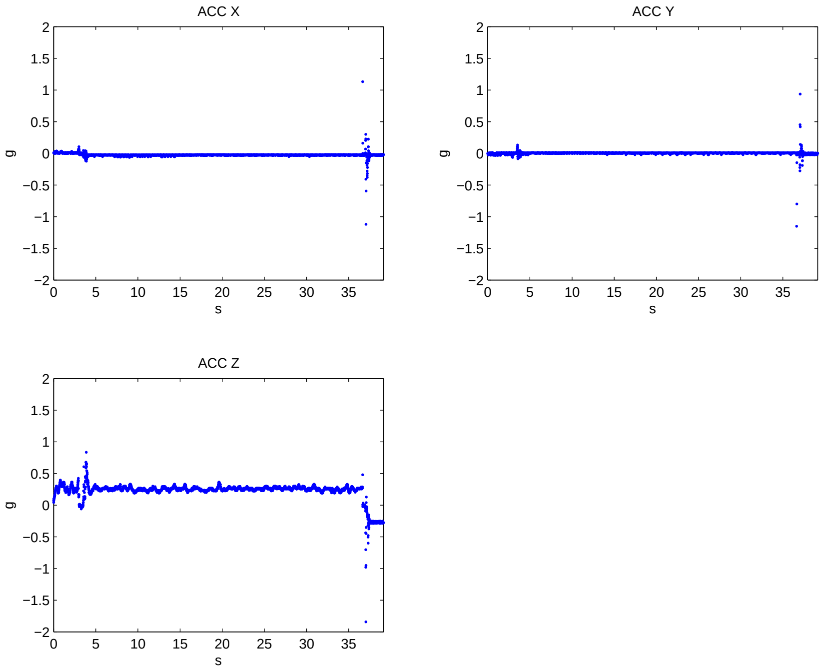

Figure 3. Accelerometer readings from drop 1

Table 1. Data collected during drop 1

	Value
Drop altitude (tether count) $[m]$	150
Drop altitude (pressure reading) $[m]$	138
Drop duration $[s]$	36.7
Free fall time $[s]$	3.66

Table 2. Data collected during drop 3

	Value
Drop altitude (tether count) $[m]$	150
Drop altitude (pressure reading) $[m]$	138
Drop duration $[s]$	$\geq$29
Free fall time $[s]$	11

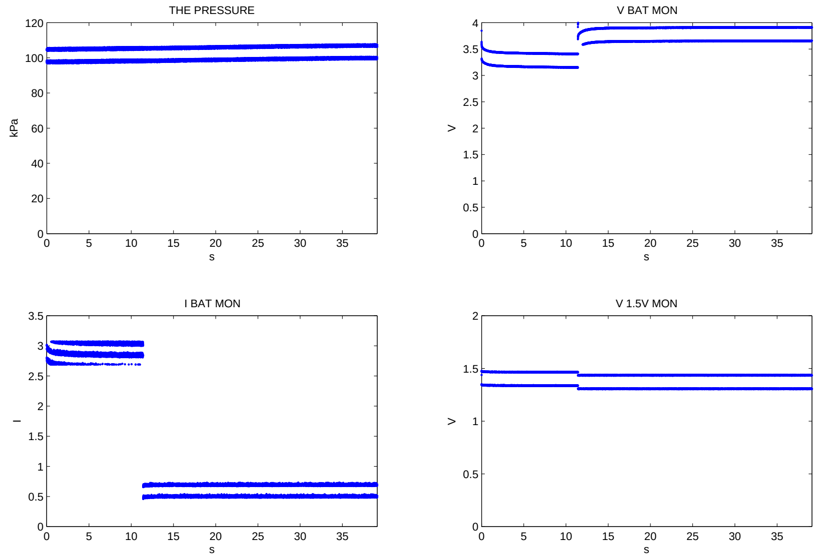

Figure 4. Pressure sensor readings from drop 1

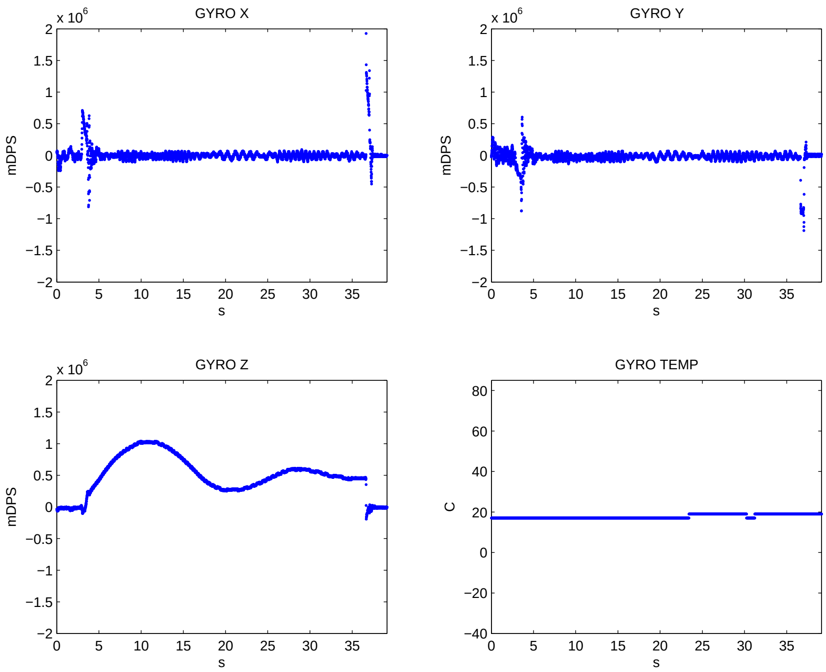

Figure 5. Gyro readings from drop 1

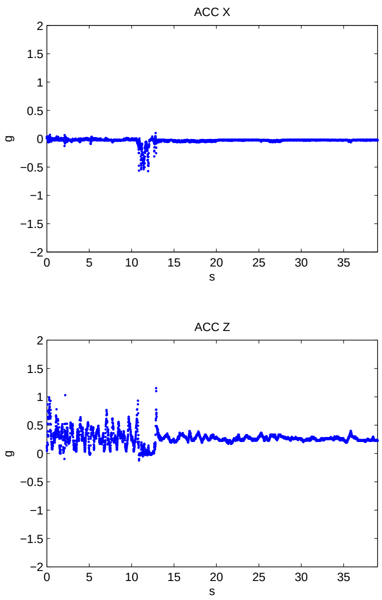

Figure 6. Accelerometer readings from drop 3

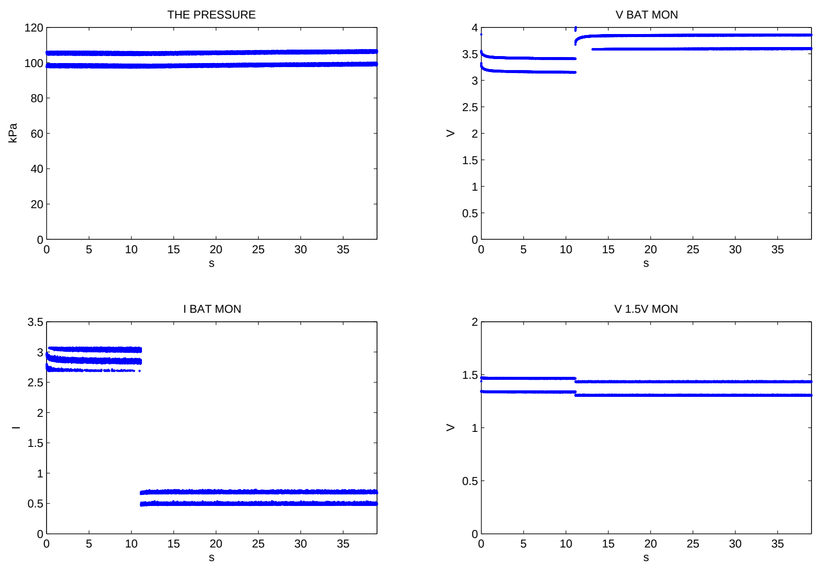

Figure 7. Pressure sensor readings from drop 3

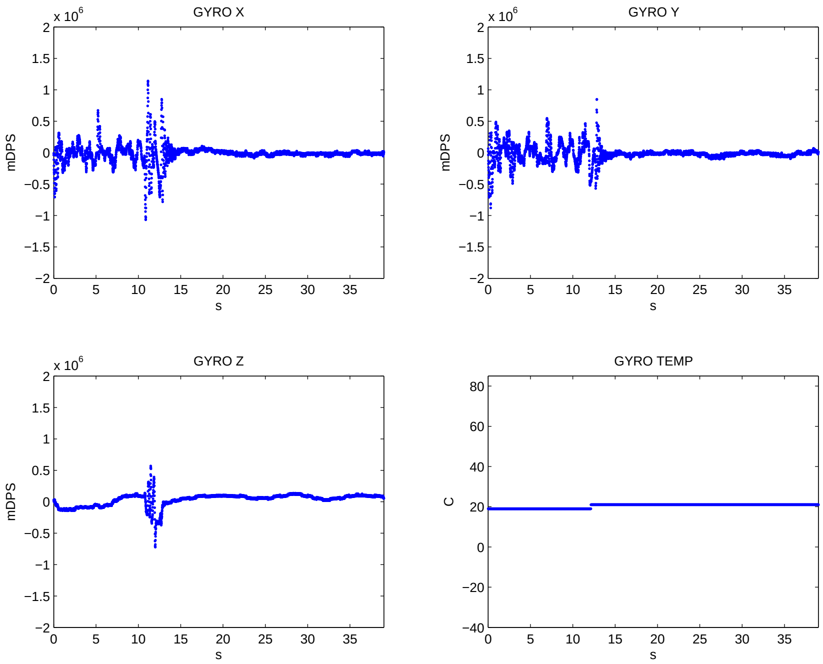

Figure 8. Gyro readings from drop 3

5 Results and Discussion

5.1 Estimation of Terminal Velocity

From the acceleration figures, it is clear that the parachute deployment causes a big shock on the FFU. We therefore assume that terminal velocity is reached almost instantly when the parachutes are deployed. From video observations, the free fall before full parachute deployment is estimated around 20 meters. It is then possible to estimate the terminal velocity by dividing the drop altitude minus the free fall by the parachute fall time. In case of drop 1, the terminal velocity is about 3.2 m/s. As the drop time is unknown for drop 3, no terminal velocity has been estimated for that drop

5.2 Parachute Tangling

Upon landing, it was observed that the parachute strings were twisted along the FFU zenith axis. This raises concerns as to weather this can cause the parachute to tangle and close when falling from a higher altitude. Observer on-site claims that the parachute strings were untangled until landing, and only tangled on ground. This issue will be tested further.

5.3 FFU Structural Problems

The FFU structure consists of two hemispheres. The lower hemispheres is attached to the PCBs and essentially carries all the measurement hardware. The upper hemisphere is ejected when the parachute is deployed. It is a thin hemispherical shell with four ribs glued to the inside, as shown in figure 9.

Figure 9. Upper hemisphere.

These ribs are used for constraining the upper hemisphere to the lower hemisphere before parachute ejection. For this interface to function, the ribs have to be precisely lined up with protrusions located on the internal metal ring of the lower hemisphere. Due to production difficulties, the upper hemisphere was not keeping its spherical shape and was developing an egg shape. This negatively affected the gluing of the ribs, which were coming loose due to stresses in the gluing surface of hte hemisphere. This led us to attempt two temporary solutions for the drop test. Firstly, a thin cylindrical plastic section was glued to the inside of the hemisphere as shown in figure 10.

Figure 10. Thin cylindrical section reinforcement.

When this reinforcement turned out to be insufficient for keeping a spherical shape of the hemisphere, an outer reinforcement was taped to the hemisphere, as shown in figure 11.

Figure 11. Outer reinforcement.

This solution provided a temporary fix for the egging issue.

5.4 Dummy Test

In preparation for the dummy test, the drop mechanism was tested on the ground. The mechanism had been inherited from RAIN and was tested the day before the drop test by people which were

not on-site during the drop test. During the drop mechanism test the batteries blew due to a faulty circuit. This also caused a malfunction in a mosfet. The circuit had to be rebuilt before initiating the dummy test. This took some time, as nobody on-site had knowledge of the drop mechanism circuit.
After fixing the mechanism, the dummy was sent up with the balloon and succesfully dropped. This gave an idea of the balloon drift and verified that the drop equipment was safe for a live payload.

5.5 FFU Tests

By the time the first FFU test was attempted, the wind had increased. This caused strong balloon drift. The FFU mission mode was designed to be triggered by a accelerometer sensing a free fall. The strong wind movement of the balloon and payload triggered the free fall sensor, which turned out to be too sensitive. This caused a recovery system deployment before a drop command was given from the ground team, which essentially released the bottom hemisphere from the top hemisphere and allowed the payload to deploy a parachute and fall to the ground.
Strong winds continued to cause problems during the following two drops. During the second FFU ascent, the strong wind caused shearing of the line connecting the FFU to the balloon, dropping the FFU at 3 meters altitude and initiating parachute deployment. Upon impact with the ground, one of the upper hemisphere ribs became unglued and the FFU had to be brought inside for repair, reset and repacking. During third drop, the free fall sensing was still too sensitive, deploying the FFU at 150 meters, again without a ground command.
During the fourth drop, a fast balloon deployment allowed a successful ascent. A drop command was given from the ground team, releasing activating the drop mechanism and releasing the FFU at 150 meters altitude. This time the parachute deployment and data gathering phase did not initiate, causing the FFU to plummit to the ground without deploying a parachute. upon impact the lower hemisphere buckled, and the cover of a satellite modem came loose and shorted the FFU bottom PCB. The cause of this error has been traced back to an error in the FPGA programming, which resulted in the FFU sensors not re-setting.

6 Conclusion

Of the four goals stated for the drop test, two failed and two were partially succesful.

- The parachute deployed when the hemispheres separated, but this deployment was not achieved during a FFU free fall, rather it happened when the upper hemisphere was still attached to the balloon and is therefore not representive of actual flight conditions. The parachute did however manage to deploy and achieve a reasonable terminal velocity, judging by the state of the FFUs when recovered. The exact terminal velocity was not determined and it is unknown if it was within the stated limits.
- Localization system was not functioning during the drop test and was not tested.
- Front end was not functioning during the drop test and was not tested.
- Internal sensors gathered data and were used to initialize mission mode, but were affected by a reset error, causing an FFU crash and catastrophic failure. Data recorded is not sufficiently accurate to determine correct drop altitude or terminal velocity.

The results of the drop test can be blamed on two things. Firstly, weather conditions were not ideal for the test, with strong wind causing problems with balloon operations and deployment and greatly delaying the team's efforts. Secondly, preparations were insufficient. Operational procedures were not properly documented and the team relied on hands-on knowledge of the individual team members to prepare the FFUs. This for example caused problems when the drop mechanism failed. Documentation of FFU subsystem testing in the days leading up to the drop test was also insufficient, leaving room for unexpected errors during FFU operations. Before a second drop test is to be attempted, testing and operational procedures need to be extensively documented and clarified to avoid unnecessary surprises during the drop test.

MUSCAT Rocket Experiment

Drop Test 2 Report

Andreas Myleus

November 25, 2012

Abstract

A second drop test was performed at Arboga airfield on May 21th 2012 to verify and test the overall system performance of the MUSCAT FFU system, due to the failed attempts in the last drop test. An FFU was attached to a balloon and hoisted up to a specified drop altitude, upon which a drop mechanism was activated. Upon entering free fall the FFU initiated a mission mode which included collecting internal sensor data and activating a recovery system, which includes deploying a parachute. The goals of the test were partially met, with emphasis on success.

1 Goals and Objectives

- To verify the parachute deployment and packing procedure.
- To transmit and receive commercial GPS data in field conditions.
- To gather raw GPS data in field conditions which can be post-processed to find positions, acceleration and velocities of FFUs during free fall.
- To verify functionality of internal sensors and to post process sensor data to find drop altitude and velocities.

2 Background Information

2.1 Weather Balloon

A weather balloon was used to elevate the payload to drop altitude. The payload consisted of a test FFU, the drop mechanism, see Appendix A, and a length of tether anchoring the balloon to the ground.

2.2 Tether Winch Mechanism

A spool of 80 lb Berkley Fishing Fireline was attched to a winch, which was used to release and reel in the balloon.

2.3 Drop Mechanism

A remotely controlled drop mechanism, see Appendix A, is used for initiating the drops when the payload has reached the drop altitude. This drop mechanism has been greatly improved from the previous one to make it more robust. It consists of a cellphone which, when called, delivers a current through a kanthal wire which is wrapped around the line connecting the FFU to the balloon. The kanthal wire is heated by the current and cuts the FFU line about 7 seconds after the call has been placed.

2.4 Drop Test Mission Mode

When mission mode is initiated by sending a command to the FFU, it stops listening to new commands and waits for the accelerometers to detect the zero G of the free fall. When it is triggered, the FPGA controls a current through the thermal cutter, which cuts the fishing line constraining the upper hemisphere, thus initiating the parachute deployment. In addition, the FPGA also records accelerometer, magnetometer, pressure and angular rate data and writes these to the memory. Data gathering ends after 80 s and the memories can be read after FPGA reset.

2.5 FFU Recovery System

The FFU recovery system is thoroughly described in the MUSCAT Student Experiment Documentation. It consists of a parachute, a releasable upper hemisphere and a thermal cutter. The purpose of the recovery system is to bring the FFU to a safe terminal velocity of below 10 m/s. For the drop test, a Top Flight 30" ThinMill X-shape parachute was used. It was connected to the FFU by four 20 cm chords gathered at the end of a 1,5 m line.

2.6 Dummy Test

To verify the functionality of the drop mechanism and to assess the balloon drift due to wind a dummy drop is performed with a dead payload. The dummy is a box with the same mass as an FFU, which weighs 396 g.

2.7 Balloon Camera

To capture close-up footage of the parachute deployment, a GoPRO Hero digital camera is attached to the balloon and angled towards the payload.

2.8 Ground Camera

To document the drop, a ground based camera is kept on the balloon during ascent and FFU during drop.

3 Method

Following is a summary of procedures used during the drop test.

3.1 Balloon inflation

For the balloon inflation the following equipment is required:

- Cotton gloves for all personnel
- Balloon
- Helium tank
- Pressure regulator
- Pressure regulator o-ring
- Wrench
- Balloon hose
- (Duct tape)
- Wire ties

The weather balloon is very sensitive to fat acids and must not come into direct contact with skin. Cotton gloves must be worn at all times while handling the balloon. The balloon can only be touched with bare hands at the base where it is visually thicker and more robust. Indoors inflation is recommended for avoiding wind complications. For pressure regulator positions, refer to figure 1. The inflation procedure is as follows:

- Spread a clean cover on the ground, large enough to uncpack the balloon on (c.a. 10 m^2)
- Gently unpack the balloon from its box and lay on the groundcover.
- Connect the pressure regulator (1) to the Helium tank. Make sure that o-ring is in place (see figure 2). Also make sure that both pressure regulator valves (2,4) are closed. Secure connection with wrench.
- Test the tank/regulator connection by slowly opening the tank valve (2). Listen carefully for leaks in the tank/regulator connection.
- Connect the balloon hose to pressure regulator (6) and balloon. Secure both ends with wire ties. Make sure only to place wire ties on the reinforced part of the balloon.
- Position 2-3 persons around the balloon to keep it properly spread during inflation.
- Regulate output pressure at c.a. 2-3 (4).
- Inflate balloon.

- Connect a mass equal to the payload to the balloon reinforcement. When the balloon can freely lift the mass and float around it is sufficiently inflated.
- Close tank valve (2). Secure balloon outlet with wire ties above the end of the hose.
- Secure balloon to a fixture on the ground and remove the hose.

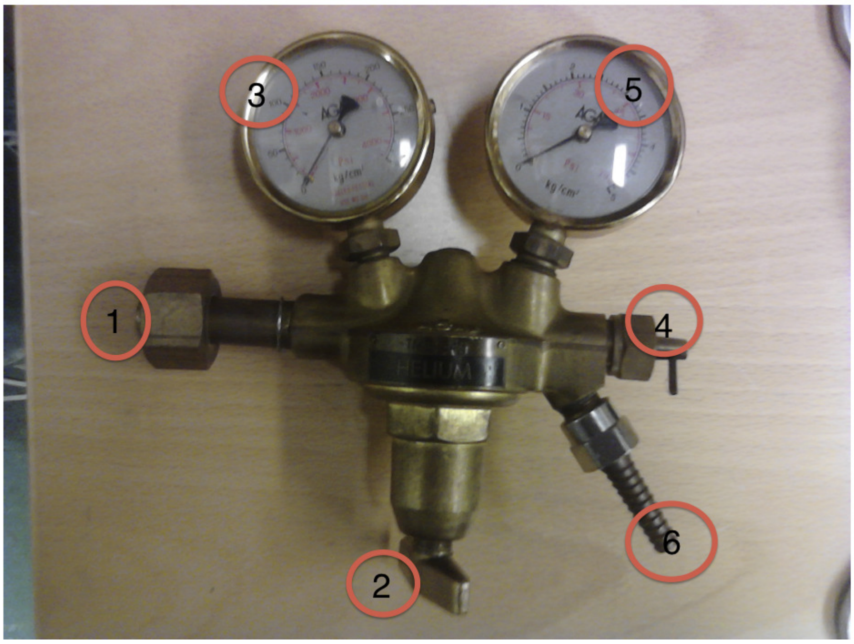

Figure 1. 1. Tank connector 2. Tank valve 3. Tank pressure meter 4. Output valve 5. Output pressure meter 6. Regulator output.

Figure 2. Pressure regulator o-ring.

3.2 FFU Parachute Packing

A parachute packing procedure is available in the MUSCAT SED.

3.3 FFU Activation

- Connect the FFU to the Charge/Comm board using the bottom 16pin connector. Make sure the arrow on the connector is pointing to the arrow on the board.
- Connect the RAIN charge/Comm board to a computer using a USB cable.
- If the FFU battery needs to be charged, connect external power to the RAIN charge/Comm board to charge the .
- If the FFU needs to be programmed, connect the splitcable connected between the RAIN charge/Comm board to the FlashPro programmer.
- Use the program Teraterm to issue commands. Configure the program to use serial and the baud rate 38400. Write the commands in the text window.
- Make sure the data is on memory can be erased.
- Rewind the memory by pressing 'R'.
- Erase the memory by pressing 'JQ'.
- Press 'F' repetitively until '00000000' is returned, meaning the erase is done.
- Check that the memory is empty by pressing 'a' two times and see if you only get 'F's.
- Rewind the memory again by pressing 'R'.
- Check the memory address, press 'F' and see if it is '00000000'.
- Start mission mode by pressing 'Ji'.
- Verify that the blue LED is triple blinking, meaning mission mode.
- Remove the connector to the FFU.

3.4 Drop Test Procedure

After the payload has been secured to the balloon, the launch officers gradually give it line and report its approximate altitude to the test leader. Tracking officers positioned around the parameter report on balloon drift to estimate the wind conditions. When the balloon has reached its goal altitude, the test leader initiates the drop by placing a call to the drop mechanism. The recovery system officers proceed to retrieve the payload when it lands.

3.5 Post-drop Procedure

The FFU is inspected for structural failure and LED statues are recorded off the PCBs. In particular, the thermal cutter is inspected for damage. The FFU is connected to a computer and the data are read out and plotted according to the following procedure

- Connect the FFU to the Charge/Comm board using the bottom 16pin connector. Make sure the arrow on the connector is pointing to the arrow on the board.
- Connect the RAIN charge/Comm board to a computer using a USB cable.
- Reset the FFU by connecting the two reset test-points on the circuit board.
- Use the program Teraterm to issue commands. Configure the program to use serial and the baud rate 38400. Write the commands in the text window.
- Press 'T' to enable turbo readout.
- Switch to 2000000 Baud readout speed in Tera term and make sure flow block is activated.
- Enable logging in Teraterm.
- Press 'a' to start readout.
- Check the log window that the counter is is increasing.
- Press 'a' again when only 'F's are displayed in the window.
- Pause and close logging in Teraterm.
- Make sure the data is plotted and verified before the memory is erased.

4 Results and Observations

Of the four documented FFU drops, data was only collected from the 3 last drops. In the first drop the zero-g detection failed. The second drop the zero-g and the FFU thermal cutter initiated, but the short fall did not separate the two hemispheres. Improvised pen springs were added to help separate the hemispheres, resulting in 2 successful parachute deployments. The data from these three drops are documented in this chapter.

4.1 FFU Drop 1

Zero-g detection failed, no data was stored. Thermal cutter did not initiate and parachute did not deploy. The glued external metal ring jumped out of position and the battery cage bent due to the impact on the ground.

Ground observations are presented in table 4.1.

Table 1. Data collected during Drop 1.

	Value
Drop altitude (tether count) [m]	200
Drop altitude (pressure reading) [m]	-
Drop duration [s]	5
Free fall time [s]	5

4.2 FFU Drop 2

Zero-g detection worked. Thermal cutter initiated, but the hemispheres did not separate and the parachute did not deploy. The satellite modem was torn off from its soldering points and the battery cage bent due to the impact on the ground. Only 5 s of data was gathered because the FFU reset itself after the impact.

Ground observations are presented in table 4.2. Accelerometer, pressure and gyroscope plots can be seen in Figure 3, Figure 4 and Figure 5.

Table 2. Data collected during drop 2.

	Value
Drop altitude (tether count) [m]	200
Drop altitude (pressure reading) [m]	174
Drop duration [s]	5
Free fall time [s]	5

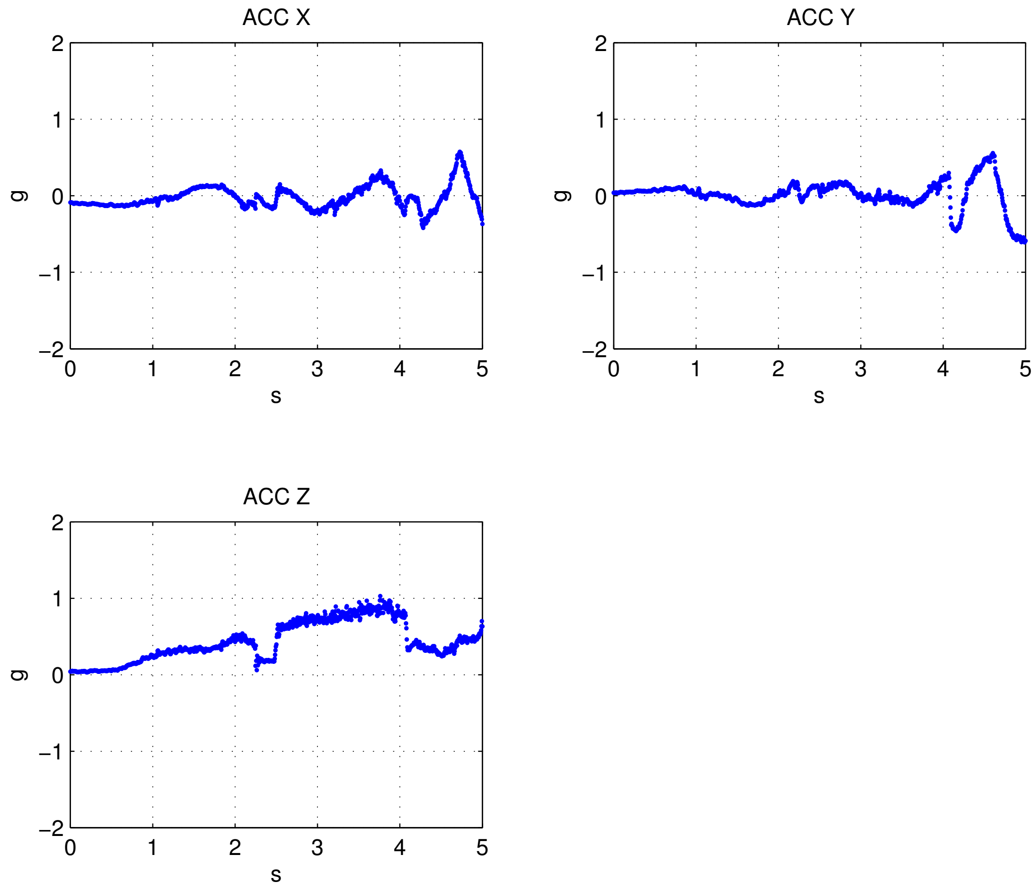

Figure 3. Accelerometer readings from Drop 2.

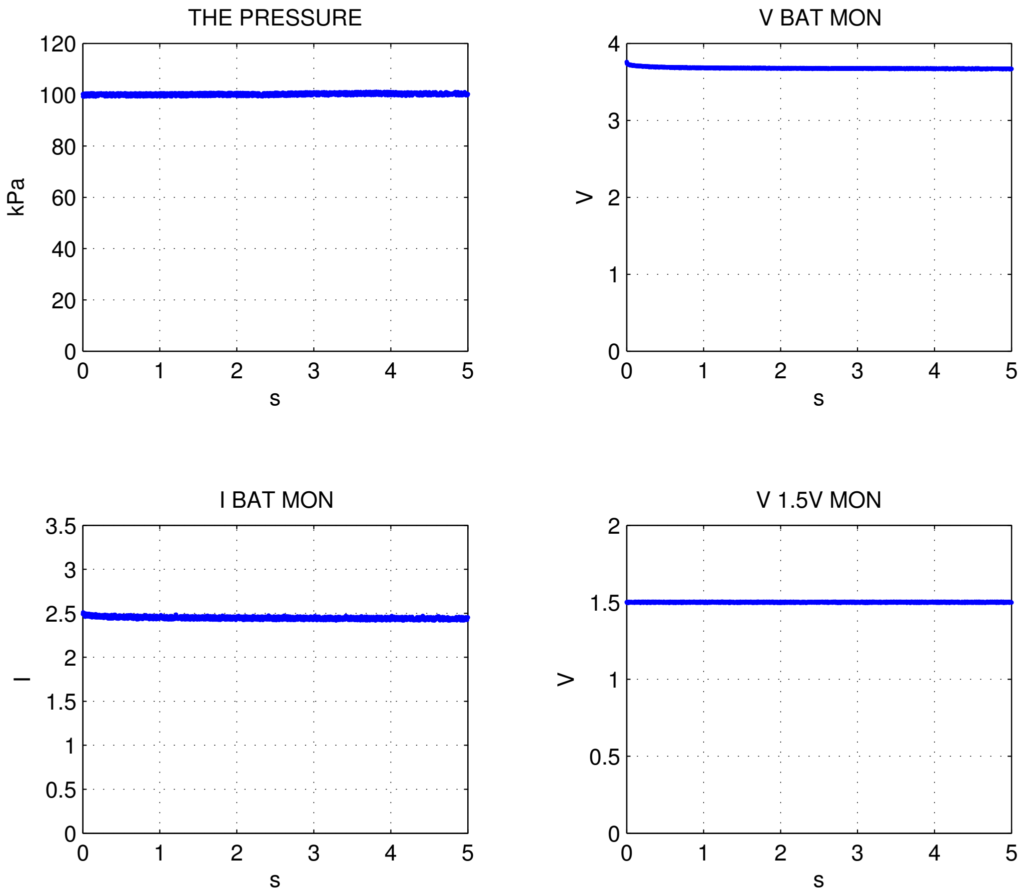

Figure 4. Pressure sensor readings from Drop 2.

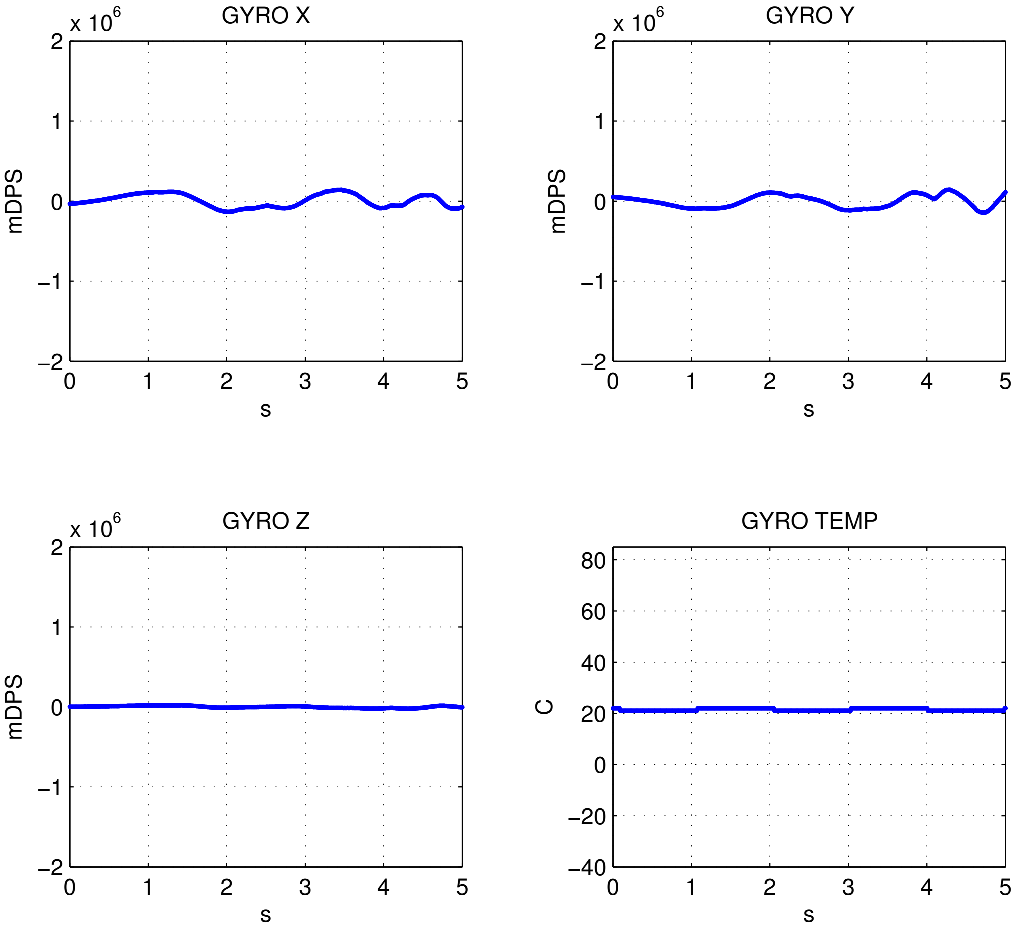

Figure 5. Gyro readings from Drop 2.

4.3 FFU Drop 3

Zero-g detection worked. Thermal cutter initiated, hemispheres separated with the help of improvised pen springs and the parachute deployed. The pressure sensor was damaged from the ground impacts of Drop 1 and 2 and gave no data.

Ground observations are presented in table 4.3. Accelerometer, pressure and gyroscope plots can be seen in Figure 6, Figure 7 and Figure 8.

Table 3. Data collected during drop 3.

	Value
Drop altitude (tether count) [m]	250
Drop altitude (pressure reading) [m]	-
Drop duration [s]	20
Free fall time [s]	3

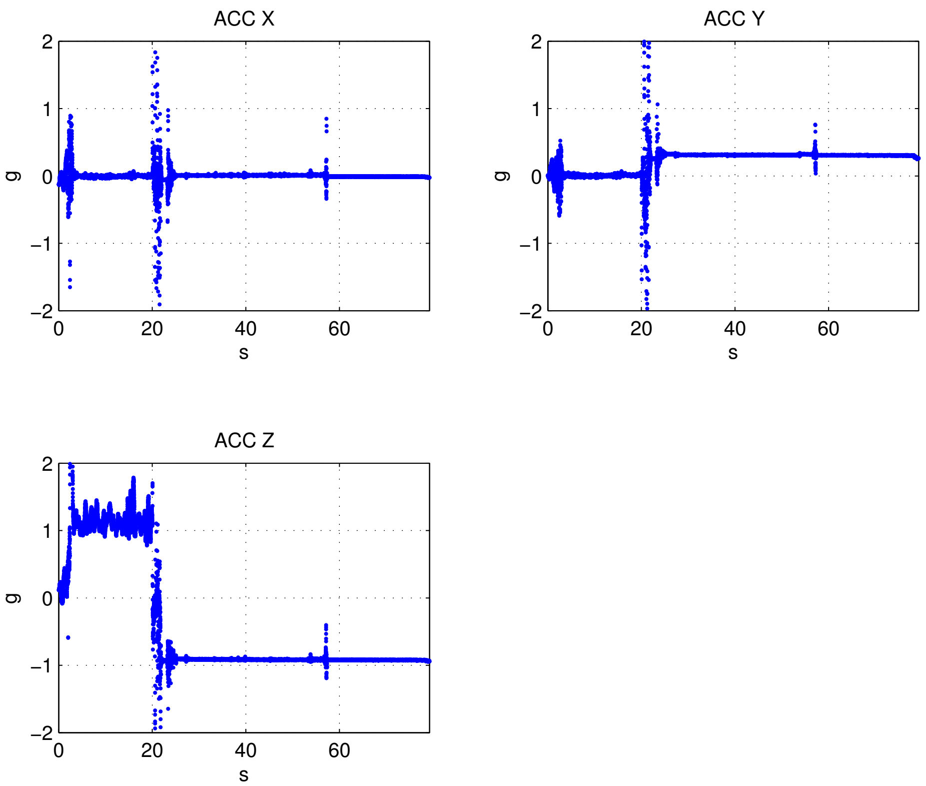

Figure 6. Accelerometer readings from Drop 3.

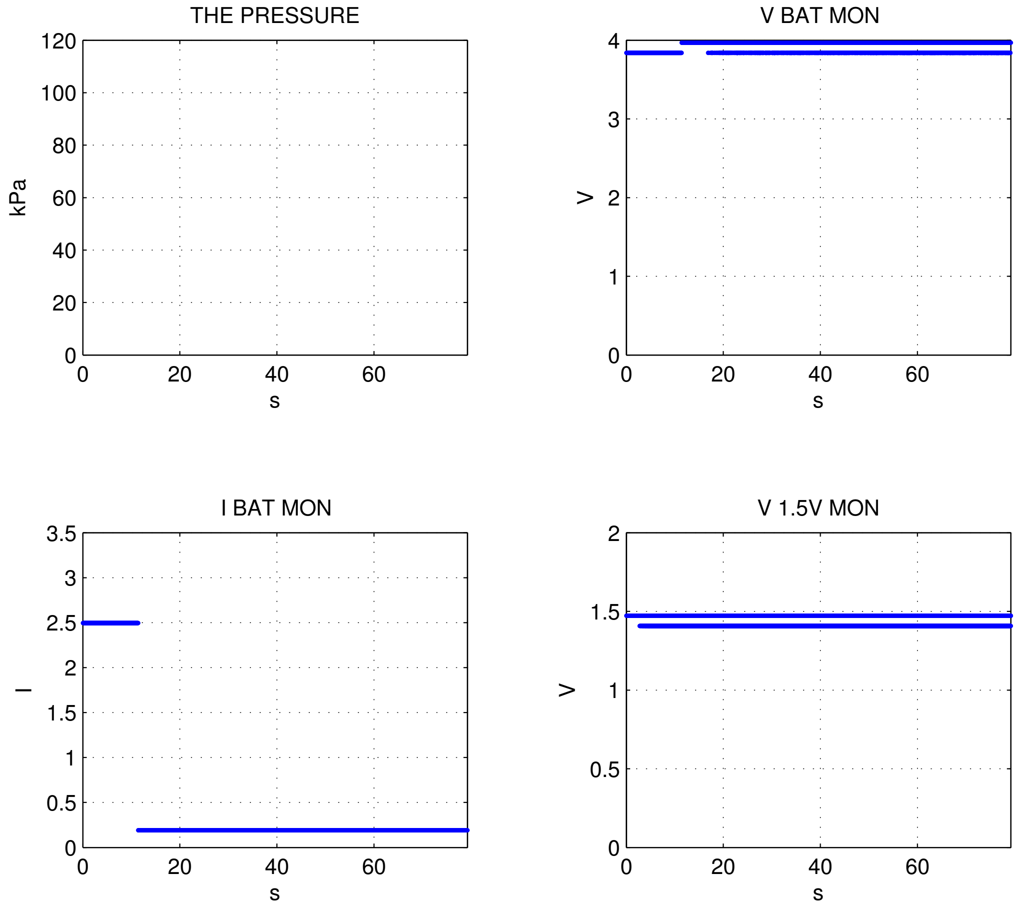

Figure 7. Pressure sensor readings from Drop 3.

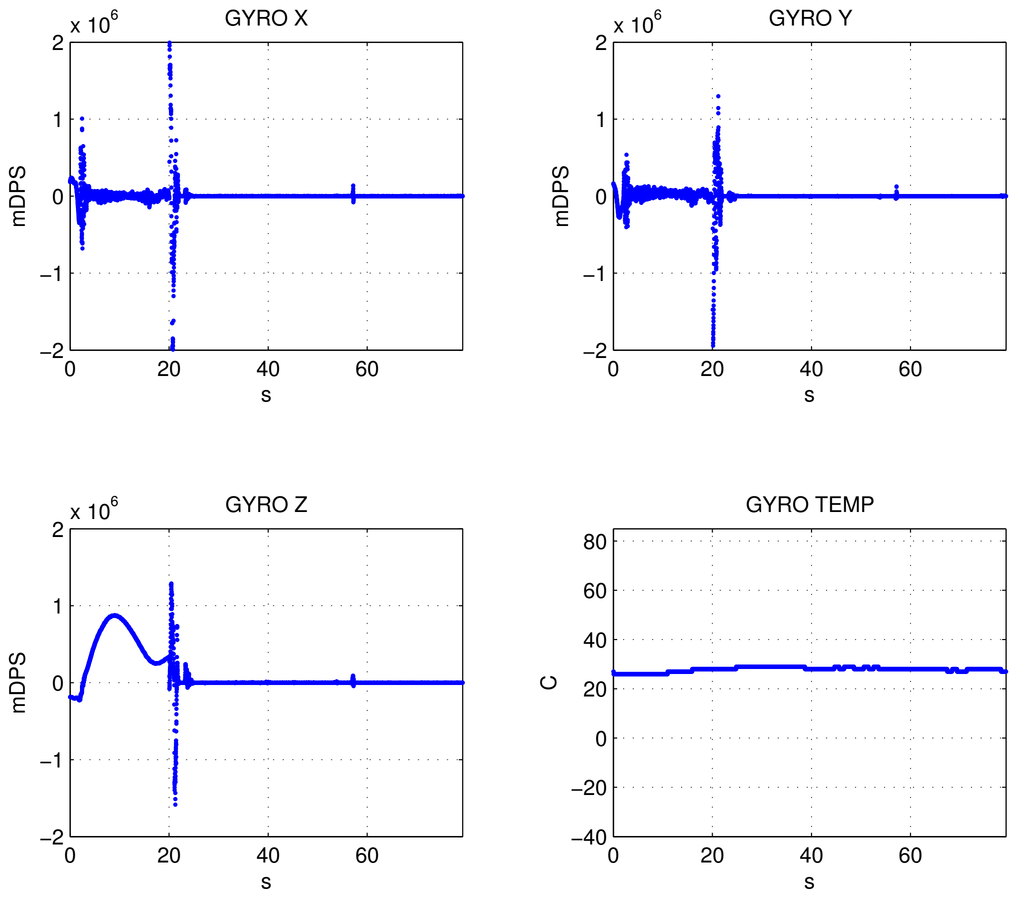

Figure 8. Gyro readings from Drop 3.

4.4 FFU Drop 4

Zero-g detection worked. Thermal cutter initiated, hemispheres separated with the help of improvised pen springs and the parachute deployed. The pressure sensor was damaged from the ground impacts from Drop 1 and 2 and gave no data.

Ground observations are presented in table 4.4. Accelerometer, pressure and gyroscope plots can be seen in Figure 9, Figure 10 and Figure 11.

Table 4. Data collected during drop 4.

	Value
Drop altitude (tether count) [m]	300
Drop altitude (pressure reading) [m]	-
Drop duration [s]	26
Free fall time [s]	3

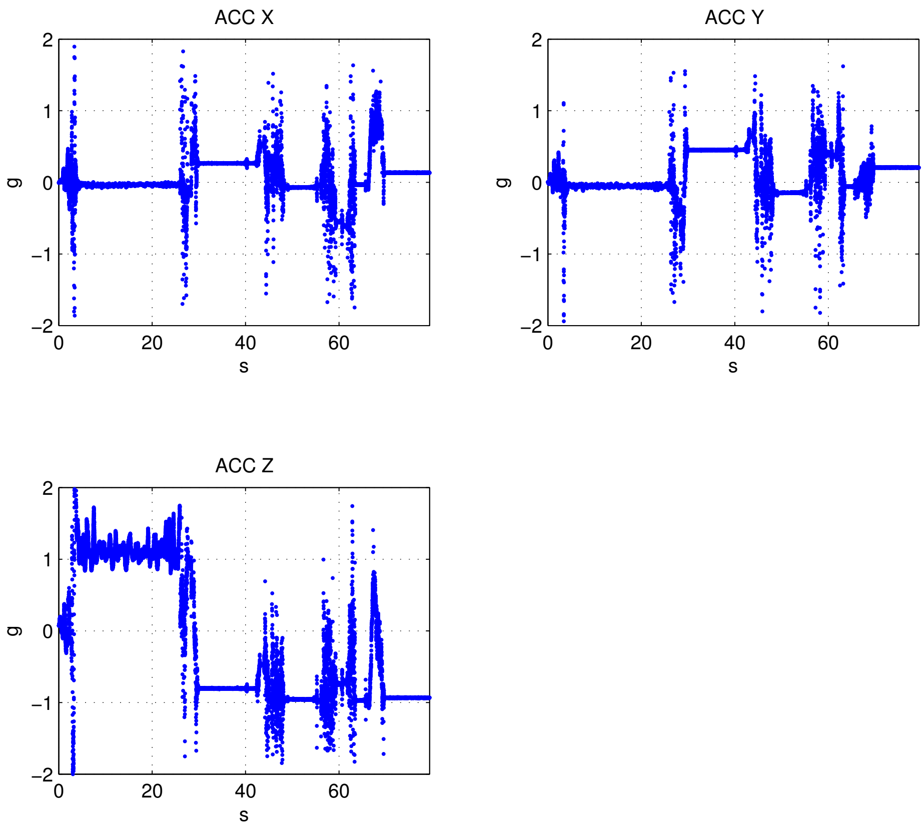

Figure 9. Accelerometer readings from Drop 4.

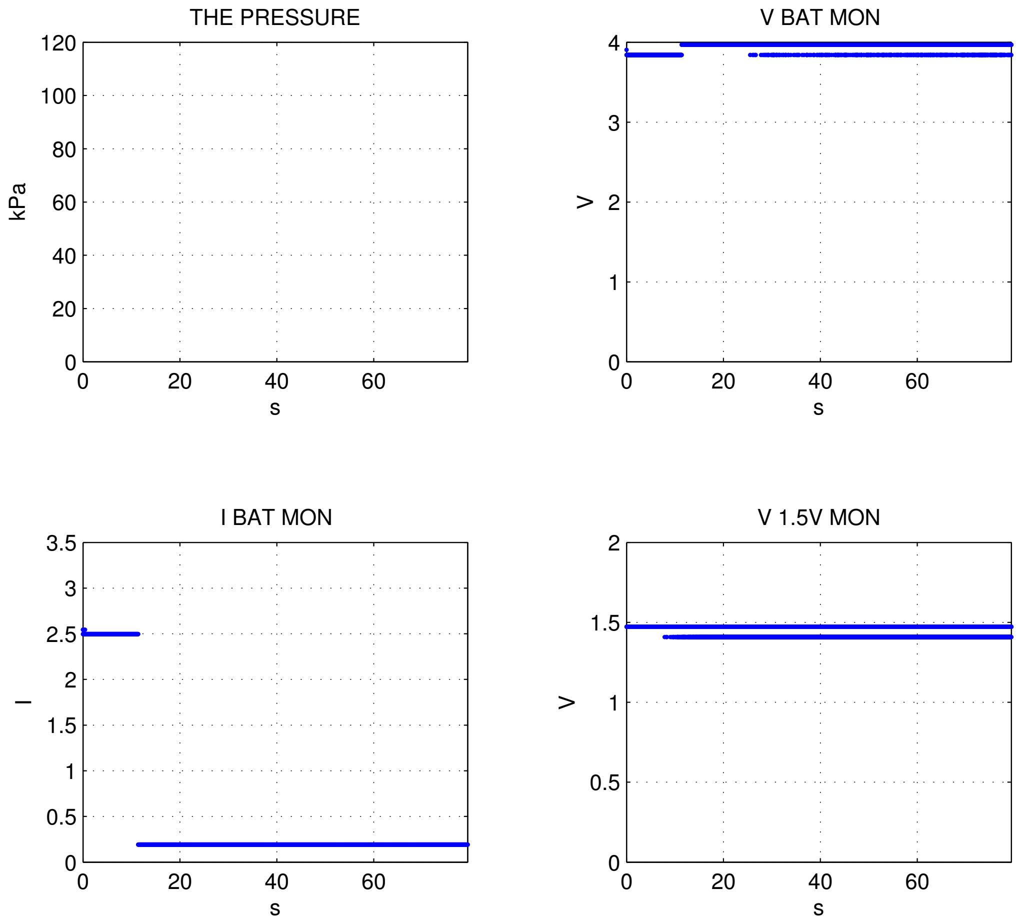

Figure 10. Pressure sensor readings from Drop 4.

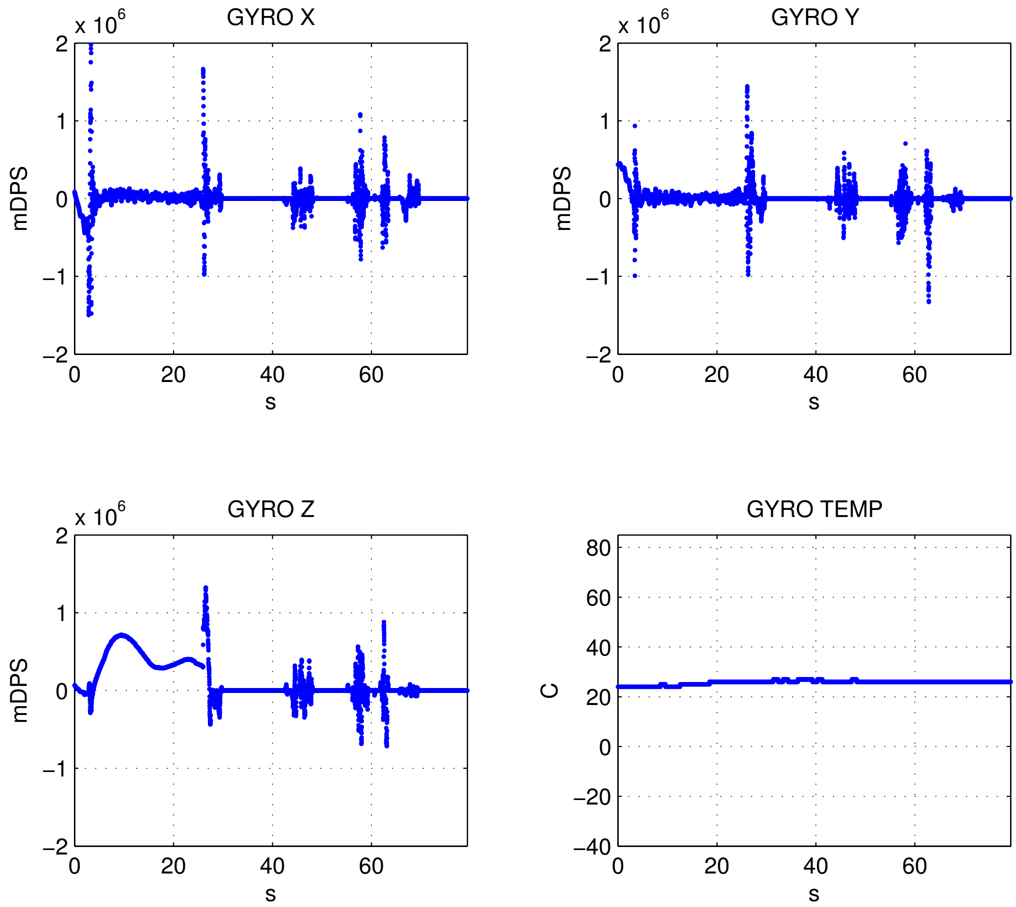

Figure 11. Gyro readings from Drop 4.

5 Discussion

5.1 Estimation of Terminal Velocity

From video observations and sensor data, the free fall takes 3 s, or around 45 m, and from previous observations it is estimated that it falls for 20 m before full parachute deployment. It is then possible to estimate the terminal velocity by dividing the drop altitude minus the free fall distance and the parachute deployment distance, with the fall time of the parachute.

In case of drop 3, the terminal velocity is about 10 m/s, and same for drop 4. These estimations are much higher than for drop 1 in drop test 1 (3.2 m/s). The difference between the drops are that in drop 1, drop test 1, the parachute is deployed instantaneously due to zero-g initiating too early. This means that the parachute reaches terminal velocity much sooner and one can assume linear decent speed after 20 m. But in the cases of drop test 2, the FFU falls for 3 s, and gaining speed so that it falls at approximately 30 m/s upon parachute deployment. This means that it takes more than 20 m for the FFU to reach terminal velocity, because it has to brake from 30 m/s instead of 0 m/s. Even with these estimations, the terminal velocity is within the requirements.

With the timings recorded in the drops we tried to simulate the terminal velocity of the parachutes in MATLAB to get a more accurate result than before. This gave the result of 6-7 m/s which can be more reasonable.

5.2 Parachute Tangling

Upon landing, it was observed in drop test 1 that the parachute strings were twisted along the FFU zenith axis. This raised concerns as to weather this can cause the parachute to tangle and close when falling from a higher altitude. Observer on-site claims that the parachute strings were untangled until landing, and only tangled on ground.

This issue was addressed more in this drop test and observers were located just next to the landing of the FFU to get a better picture if the tangling was because of the spinning during the fall or if it was only happening on the ground.

We observed that the parachute was tangled just before it hit the ground, but in these tests the free fall time was also much lower, which could mean that the relative rotation between the FFU and the parachute had not stabilized yet. The gyro plots in Figure 8 and Figure 11 show that the z-axis rotation is stabilizing, but has not yet reached a constant rotation. A longer fall would have been necessary. This will be investigated more in the High Altitude Drop Test. Different solutions with swivels and/or longer/shorter middle cords will be tested.

5.3 FFU Structural Problems

In drop 2 the hemispheres failed to separate and improvised pen springs were added so that the hemispheres would be able to separate directly when the fishing line is cut, instead of relying on the drag around the sphere to separate them. This will be implemented in a more robust way in the final design of the FFUs.

5.4 Dummy Test

In preparation for the real drop tests, the drop mechanism was tested on the ground with a dummy weight. The mechanism had been inherited from RAIN and greatly improved for robustness. The drop mechanism worked as intended on all drops.

5.5 FFU Tests

The weather conditions were better than last time on this drop test day. The zero-g in Drop 1 was too insensitive and did not trigger and resulting in a ground impact. This was tuned for Drop 2 and zero-g worked as intended, but the hemispheres did not separate and resulted in a ground impact. In Drop 3 and 4, the whole parachute deployment system, sensor data gathering (excluding pressure sensor) and localization system (except for beacon transmitter) worked as intended.

6 Conclusion

Of the four goals stated for the drop test, three were successful and one was partially successful.

- The parachute deployment worked partially during Drop 2 and as intended during Drop 3 and 4.
- Localization system was functioning during the drop tests, except for the beacon transmitter which is not yet been implemented.
- GPS Front-end was not functioning during the drop test and was not tested.
- Internal sensors gathered data and were used to initialize mission mode, but in Drop 1 the zero-g triggering was too insensitive. In Drop 2, 3 and 4 the sensor gathering worked as intended, except for the pressure sensor that broke after the ground impact in Drop 2. Data recorded is not sufficiently accurate to determine precise drop altitude or terminal velocity.

Even though some things did not go as intended, the overall results of the drop test can be regarded as a success. We were better prepared and weather conditions were better. Operational procedures were documented better this time. All systems had been made more robust and helped us to achieve what we wanted much more smoother without delays due to on-site repairs.

A Appendix

Droptest mechanism

The mechanism needs two batteries, one 3.7V Li-Ion (same as in the FFUs) and one 9v battery. The 3.7V battery is providing the phone and cutter with power and the 9V battery powers the logic.

3.7V Battery is connected to the right terminal. Cutter is connected to the left terminal.

How to use it:

1. Open the box
2. Connect 9 V battery
3. Connect 3.7 V battery and change the battery switch to on position
4. Start the phone by pressing the on/off button on the top. Tape the box cover together
5. Thread the fishing line through the teflon tube **over** the nichrome heating wire and secure it in the suspension ring by a proper knot.
6. ARM the cutter by switching the ARM switch. The ARM LED starts flashing red/blue
7. Call the phone to activate the cutter. (phone: 072-7712588). Arm LED goes off and the yellow cutter LED lits up and the cutter is cutting for a couple of seconds.
8. To reuse, repeat from step 5

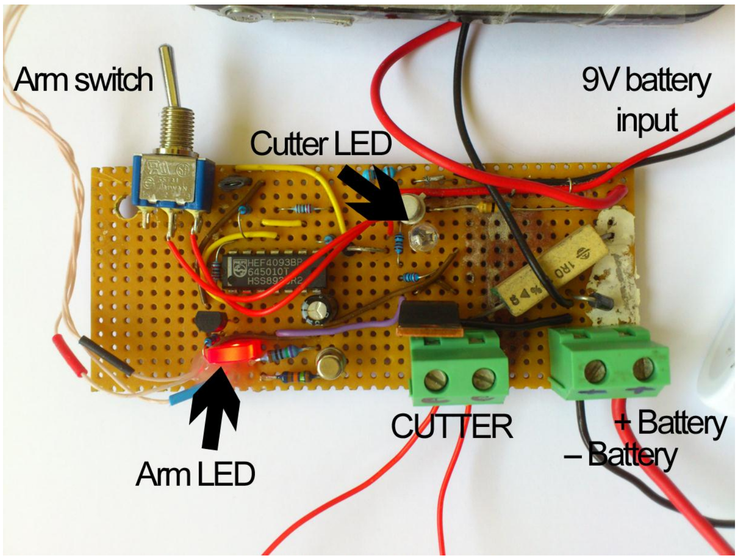

Droptest mechanism

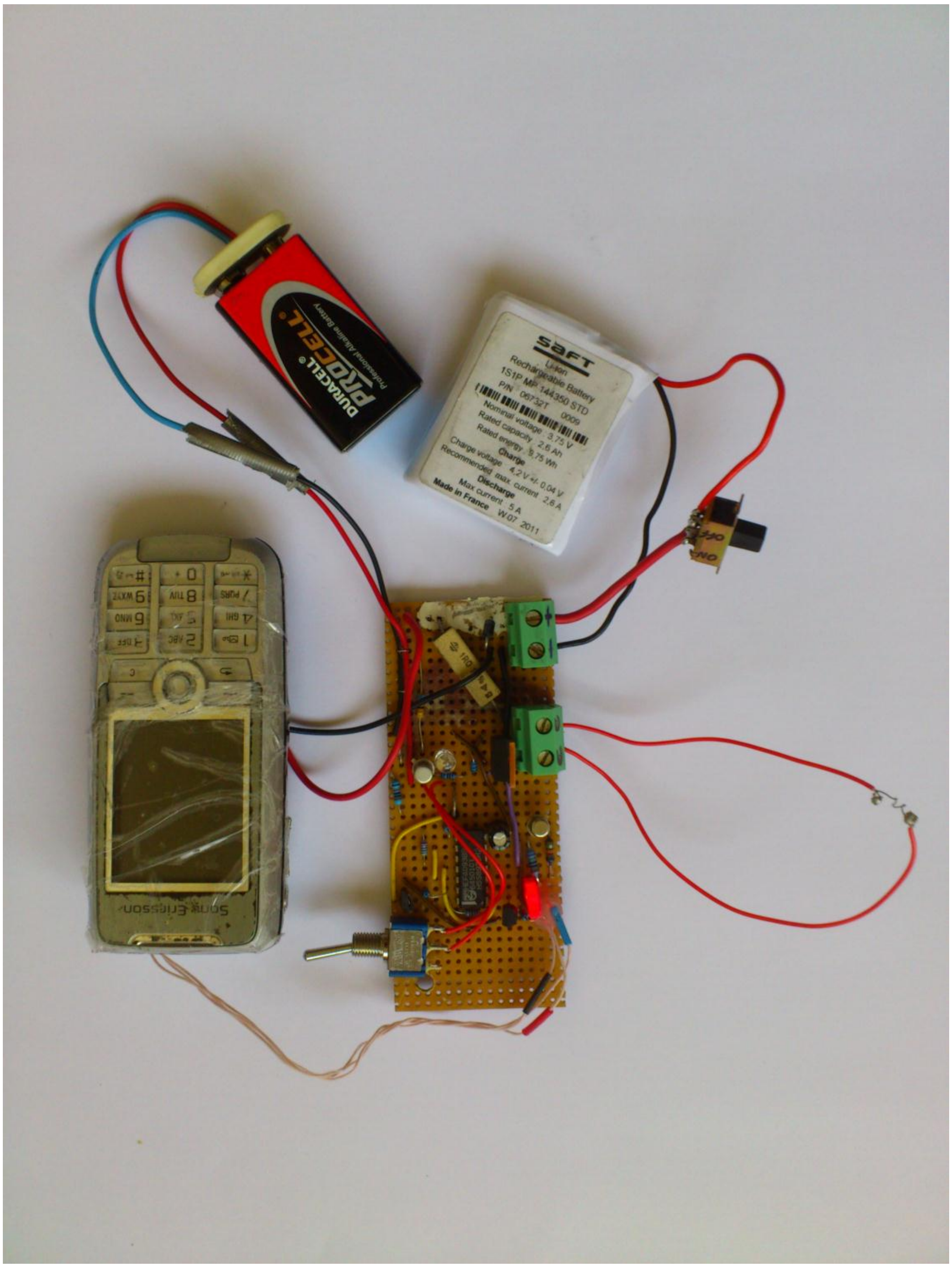

Latest update: 2012-09-17

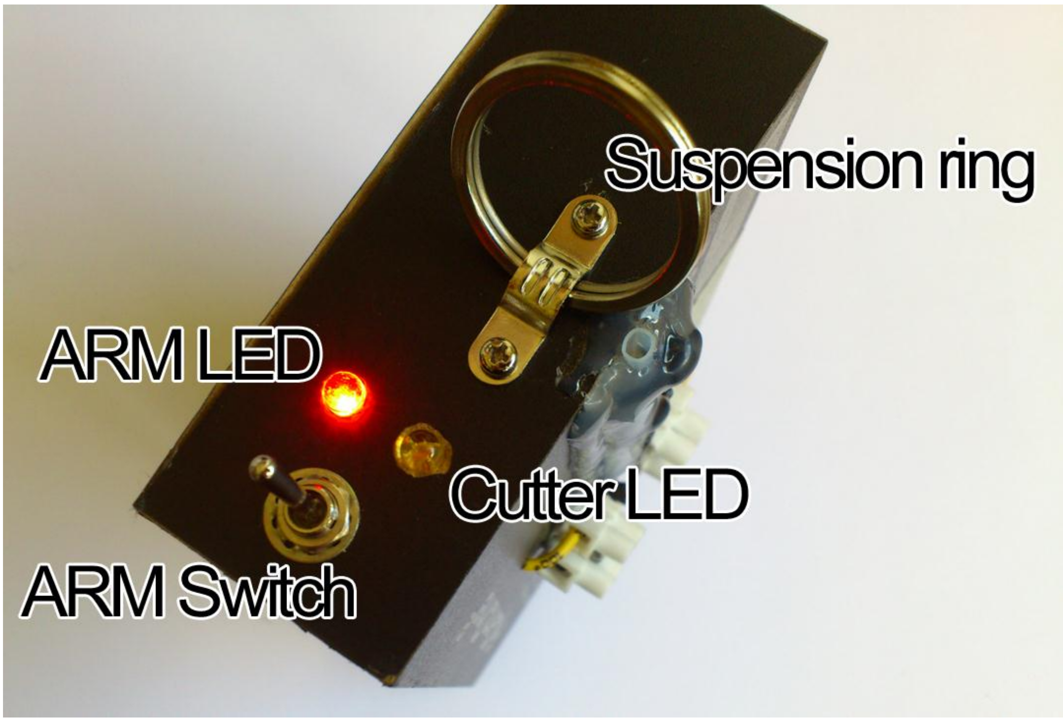
Suspension ring
ARM LED
Cutter LED
ARM Switch


FlyCamOne²
Technische Daten / Technical Data
Thread direction
Cutter
FC2000 FlyCamOne2
ACME the game company - Germany

Droptest mechanism

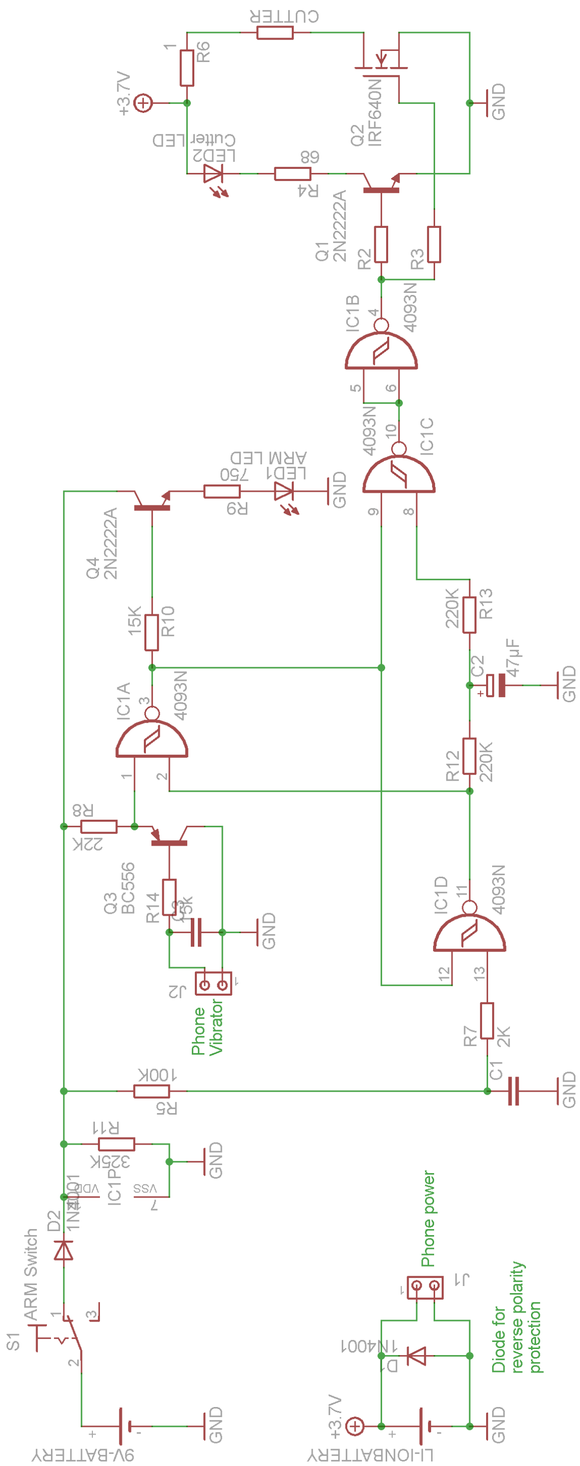

Latest update: 2012-09-17

MUSCAT Rocket Experiment

Drop Test 3 Report

Miguel Galrinho

September 14, 2012

Abstract

A third drop test was performed at Stockholms Fallskärmsklubb on August 29th 2012 to verify and test the overall performance of the MUSCAT FFU system. The main objective was to increase the confidence in the overall functionality of the system after the successful attempts of Drop Test 2, and to gather more data during the fall and at higher altitudes than in the previous drop tests. An FFU was taken by a skydiver and during the jump he would drop it at a specified altitude. Upon entering free fall the FFU would initiate a mission mode which included collecting internal sensor data and activating a recovery system, including the deployment of a parachute. The goals of the test were only partly met, with relevant failures.

1 Goals and Objectives

- To verify the parachute deployment and packing procedure.
- To transmit and receive commercial GPS data in field conditions.
- To gather raw GPS data in field conditions which can be post-processed to find positions, acceleration and velocities of FFUs during free fall.
- To verify functionality of internal sensors and to post process sensor data to find drop altitude and velocities.

2 Background Information

2.1 Drop Mechanism

A professional skydiver takes the FFU with him in an airplane from which he will jump. His task is to remove the safety trigger and drop the FFU during the jump. If possible, he should be able to follow it for a while and film the deployment of the parachute.

2.2 Drop Test Mission Mode

When mission mode is initiated by sending a command to the FFU, it stops listening to new commands and waits for the pressure sensor to detect a certain pressure around $92kPa$. When it is triggered, the FPGA controls a current through the thermal cutter, which cuts the fishing line constraining the upper hemisphere, thus initiating the parachute deployment. In addition, the FPGA also records accelerometer, magnetometer, pressure and angular rate data and writes these to the memory.

2.3 FFU Recovery System

The FFU recovery system is thoroughly described in the MUSCAT Student Experiment Documentation. It consists of a parachute, a releasable upper hemisphere and a thermal cutter. The purpose of the recovery system is to bring the FFU to a safe terminal velocity of below 10 m/s. For the drop test, a Top Flight 30" ThinMill X-shape parachute was used. It was connected to the FFU by four 20 cm chords gathered at the end of a 1,5 m line.

2.4 Drop Tests Plan

In total, five different tests were planned:

Dummy drop
Get the FFUs in the airplane until 1000m without dropping them. Descend inside the plane while holding the FFUs to verify mission mode, that is, if the cutter is triggered and at which hight, and if data is recorded.

First drop
Live drop at 1000m.

Second drop
Live drop at 2000m.

Third drop
Live drop at 3000m.

Fourth drop
Live drop at 4000m.

3 Method

Following is a summary of procedures used during the drop test.

3.1 FFU Parachute Packing

A parachute packing procedure is available in the MUSCAT SED.

3.2 FFU Activation

- Connect the FFU to the Charge/Comm board using the bottom 16pin connector. Make sure the arrow on the connector is pointing to the arrow on the board.
- Connect the RAIN charge/Comm board to a computer using a USB cable.

- If the FFU battery needs to be charged, connect external power to the RAIN charge/Comm board to charge it.
- If the FFU needs to be programmed, connect the splitcable connected between the RAIN charge/Comm board to the FlashPro programmer.
- Use the program Teraterm to issue commands. Configure the program to use serial and the baud rate 38400. Write the commands in the text window.
- Make sure the data is on memory can be erased.
- Rewind the memory by pressing 'R'.
- Erase the memory by pressing 'JQ'.
- Press 'F' repetitively until '00000000' is returned, meaning the erase is done.
- Check that the memory is empty by pressing 'a' two times and see if you only get 'F's.
- Rewind the memory again by pressing 'R'.
- Check the memory address, press 'F' and see if it is '00000000'.
- Start mission mode by pressing 'Ji'.
- Verify that the blue LED is triple blinking, meaning mission mode.
- Remove the connector to the FFU.

3.3 Drop Test Procedure

The team members would previously set with the skydiver where he was going to drop the FFU, taking special account to the wind speed and direction. The team members would position themselves around the area where the FFU was supposed to be dropped and fall. The skydiver that would drop the FFU should be located as soon as possible, so that it would be easier to spot the FFU once the parachute deployed. The FFU should not become out of sight so that the landing spot could be easily seen. Trying to detect the upper hemisphere should only be done if it would not compromise the detection of the landing spot of the FFU.

3.4 Post-drop Procedure

The FFU is inspected for structural failure and LED statues are recorded off the PCBs. In particular, the thermal cutter is inspected for damage. The FFU is connected to a computer and the data are read out and plotted according to the following procedure:

- Connect the FFU to the Charge/Comm board using the bottom 16pin connector. Make sure the arrow on the connector is pointing to the arrow on the board.
- Connect the RAIN charge/Comm board to a computer using a USB cable.
- Reset the FFU by connecting the two reset test-points on the circuit board.

- Use the program Teraterm to issue commands. Configure the program to use serial and the baud rate 38400. Write the commands in the text window.
- Press 'T' to enable turbo readout.
- Switch to 2000000 Baud readout speed in Tera term and make sure flow block is activated.
- Enable logging in Teraterm
- Press 'a' to start readout.
- Check the log window that the counter is is increasing.
- Press 'a' again when only 'F's are displayed in the window.
- Pause and close logging in Teraterm.
- Make sure the data is plotted and verified before the memory is erased.

4 Results and Observations

Despite the initial plan to have a dummy drop and four more drops after that, only two drops were made after the dummy. The main reasons for the changes in the plan were the unsuccessfulness of Drop 1 and the inappropriate weather conditions. Relevant data was recorded for Drop 2, but with some issues encountered on the clock package.

4.1 FFU Dummy Drop

For the dummy drop, two FFUs (*Oj* and *Glad*) were taken in the airplane until $4000m$. During the descent, mission mode was successfully verified: both of them deployed at the same altitude around $900m$, as measured by an altimeter that was taken in the plane. Moreover, during the post-drop procedure it was verified that sensor data was successfully recorded, but not GPS data. This was to be expected, since the FFUs were during the whole test inside the plane, where GPS signal reception is weak.

4.2 FFU Drop 1

Although the first drop was initially planned to be done at $1000m$, the fact that the dummy drop showed that the deployment takes place at $900m$ (and therefore too close to $1000m$) was determinant for the decision to increase the altitude of the first drop, that would take place at $1800m$.

Taking into account the wind, it was decided that one of the FFUs (*Oj*) should be dropped slightly off the landing field, such that the wind would make it drift to the inside.

In the first drop, the skydiver decided not to try to film the deployment of the parachute, since he wanted to use this drop to get used to the behaviour of the FFU upon dropping it.

During the jump, the skydiver was easily spotted, but the FFU could not be seen either by the team members or by the skydiver, who lost sight of it shortly after dropping it. The parachute deployment could not be seen by anyone on the field or by any of the skydivers that were jumping. Also, no GPS messages were received, and the FFU could not be recovered.

Either one of the following happened during the drop:

1. The parachute did not deploy and the FFU crashed.
2. The parachute deployed but could not be spotted and did not send any messages, and the wind drifted it away from the landing field.

The first option seems to be the most likely for the following reasons:

- No one could see the parachute deployment;
- No messages were sent;
- During the search, on foot and using a motorized paraglider, the FFU should have been easily spotted if it had an orange parachute opened around it.

Independently of the uncertainty about the parachute deployment, it is almost certain that the FFU fell on the crops' field next to the landing field. The possibility of recovering it is still positive since the crops will soon be harvested.

4.3 FFU Drop 2

After the failure of the first drop, the following decisions were taken:

- The altitude of the drop should be lowered to $1100m$ to avoid losing sight of the FFU.
- The FFU should be dropped just above the field, in case the parachute doesn't deploy and the wind doesn't drift the FFU to the landing field.

In this drop, another FFU (*Glad*) was successfully spotted upon parachute deployment, and it was recovered with the antenna down and almost no parachute tangling. Only the upper hemisphere was lost. Sensor data was recorded and is presented next, but only one GPS message was received.

The following should be commented about these plots:

- The package obtained from the clock is completely wrong, and therefore there is no way of knowing how correct the time axes is. Therefore, the time scale was chosen according to what the team members approximately remember about the duration of the experiment.
- According to this estimate, the part of the fall with the parachute deployed lasted for around 90 seconds (from 70 to 160).

Concerning the GPS message received, it was only one probably because of the time that it takes to synchronize and the fact that the FFU was turned upside-down when it was on the ground, and the signal must have been weak. The position that it transmitted was very accurate.

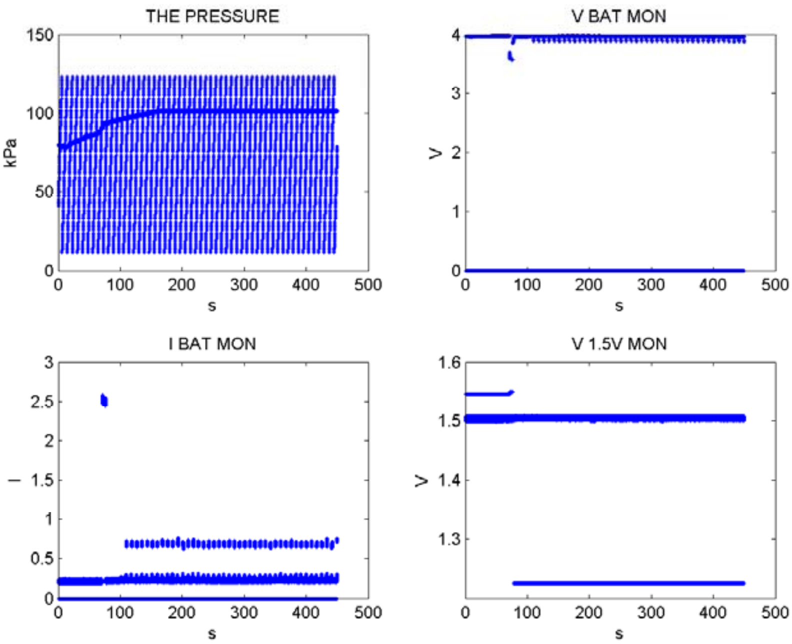
THE PRESSURE
kPa
s
V BAT MON
V
s
I BAT MON
I
s
V 1.5V MON
V
s

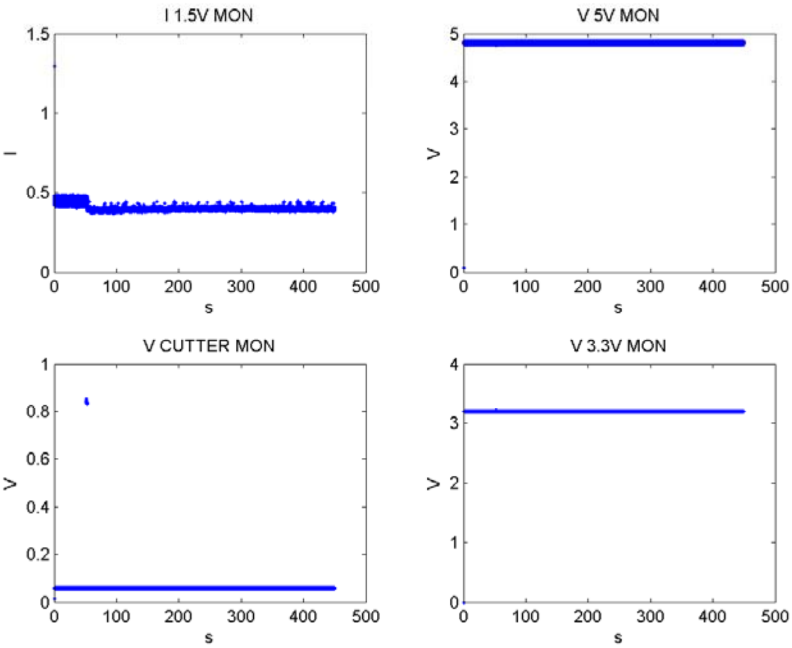
I 1.5V MON
I
s
V 5V MON
V
s
V CUTTER MON
V
s
V 3.3V MON
V
s

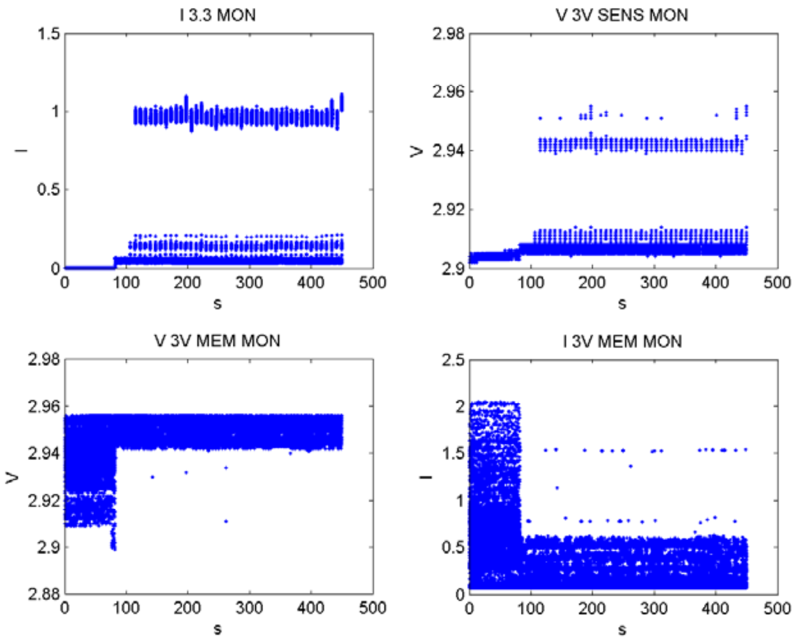
I 3.3 MON
V 3V SENS MON
V 3V MEM MON
I 3V MEM MON
I
V
s

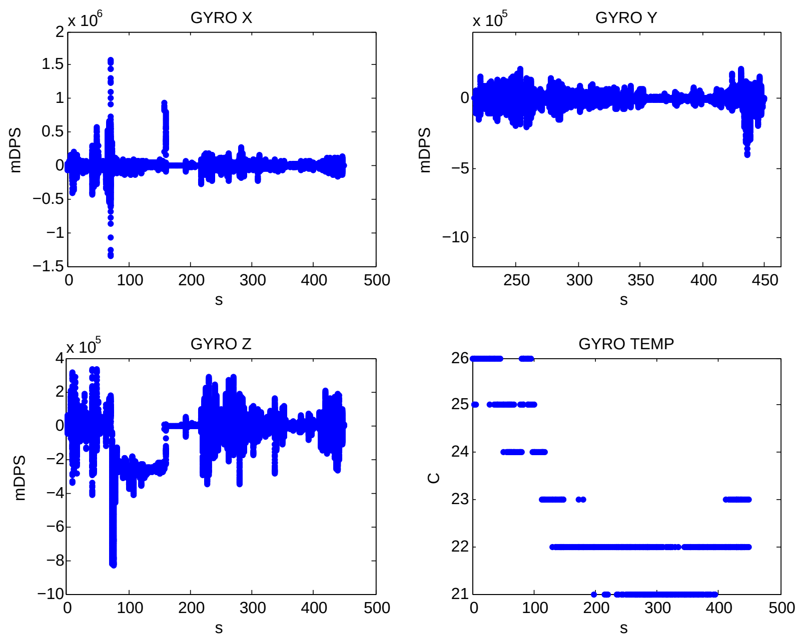
GYRO X
GYRO Y
GYRO Z
GYRO TEMP
x 10^6
x 10^5
mDPS
C
s

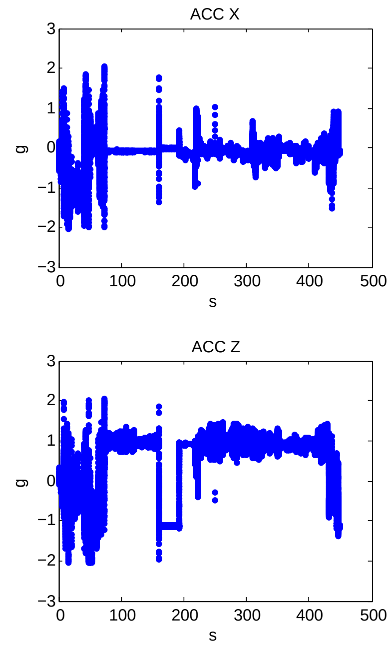
ACC X
ACC Y
ACC Z
g
s

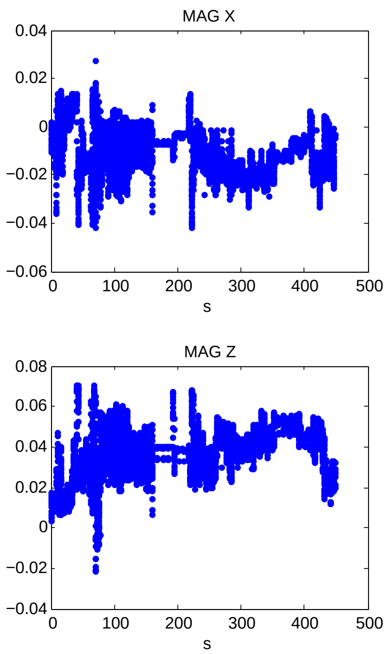
MAG X
MAG Y
MAG Z
s

5 Discussion

5.1 Parachute Tangling

The parachute tangling that had been reported in the previous Drop Test was not detected now. This supports the suspicions that had been made then, according to which the tangling would be due to the fact that the relative rotation between the FFU and the parachute hadn't stabilized yet. In fact, this time with a higher altitude drop, a significant tangling was not observed.

5.2 FFU Structural Problems

The problems during the first drop test are still not clear. On one hand, the non-deployment of the parachute seems strange after the successful dummy test, but on the other hand it is unlikely that the parachute deployed but no one could see it. Perhaps it might be possible to draw some conclusions later in case the FFU is found.

5.3 FFU Tests

The dummy test gave indications that the deployment system was working well for both FFUs. However, it is very likely that in the first drop the parachute did not deploy, although it is not possible to be completely sure without recovering the FFU. The second drop was successful, but the altitude at which the FFU was dropped was changed from the initial plan because of the failure of the first drop. Also, the recorded data has some problems in the clock package.

More drops were planed, but because of weather conditions they were not done.

6 Conclusion

The high altitude test failed in some matters and was successful in others.

- Failures:
  - The first FFU was lost, and most likely the parachute did not deploy.
  - The clock package recorded during the second drop has problems.
  - It was not possible to film the parachute deployment.
  - The tests were not done according to what was initially planned due to the failure of the first drop and to inadequate weather conditions.
- Success:
  - Both in the dummy test and in the second drop, the parachute deployed.
  - There was a GPS message received during the second drop, and it transmitted an accurate position.
  - It was possible to record sensor data that makes sense, despite the problems with the clock.

MUSCAT Rocket Experiment

Parachute cord twisting Test Report

Andreas Myleus

November 25, 2012

Abstract

After Drop Test 1 there was a concern regarding the parachute cords twisting and the parachute closing as the parachute spun during the descent. A simple test to get a feel for how the system behaved during spin was set up. Two different types of middle cords were used, a torsionally stiffer and a torsionally softer one. After looking at high-speed video footage, the conclusion was that the FFU followed the motion of the spinning parachute better with the stiffer one (the one that was used for the drop test), and no parachute cord twisting was observed. Further investigation will be made during Drop Test 2 and during the high altitude drop test.

1 Goals and Objectives

- To get a feel for how the spinning of the parachute affected the rest of the system, containing the parachute cords, the middle cord and the FFU.
- To test two different middle cords, one torsionally stiff, and one torsionally soft.

2 Background Information

This question was raised after observing that the parachute lines connecting to the middle cord had twisted after the first drop of Drop Test 1. There was no clear picture whether the twisting was caused by the parachute spinning and the middle cord connection to the FFU or if it was cause while the FFU was on the ground.

In Figure 1 one can see the observation made during Drop 1, Drop Test 1. In Figure 2 one can see the parachute set-up.

Figure 1. Parachute cord twist observation.

Figure 2. Parachute set-up.

3 Method

The test was performed in Sing-Sing at KTH, which contains a big open space in the middle of the building that enabled us to hang the FFU around 16 m down from one of the floors. Each floor could access the area in the middle. The FFU was hung in a fishing line to achieve the least amount of torsional torque as possible.

At the top someone held the fishing line, on a floor above the FFU someone filmed with a high-speed camera and on the bottom floor there was someone that spun the parachute. The parachute was filled with paper that weighed the same as the FFU to expand the parachute and to keep the same dynamics of the system as if it was falling. A marker was placed on the FFU to keep track of the relative motion of the FFU and the parachute. The test set-up can be seen in Figure 3.

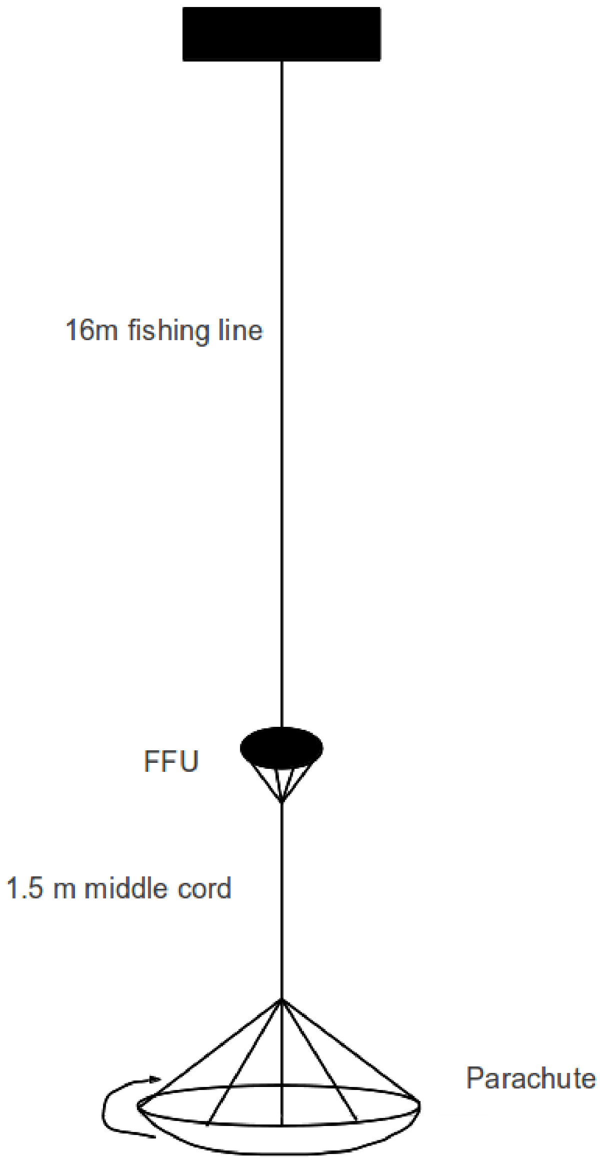

Figure 3. Test set-up.

4 Results and Observations

4.1 Soft middle cord

From the video footage one could see that the FFU did not follow the parachute very well. This caused the middle cord to twist instead of the parachute cords.

4.2 Stiff middle cord

From the video footage one could see that the FFU followed the parachute quite good and no twisting of any cords was observed.

5 Discussion

A preferable system would be to have a stable system in the sense of the relative motion between the FFU and the parachute. In other words the parachute would start to spin after deployment and the FFUs angular rate would oscillate around the middle cord, but after some time the FFU would spin with the same angular rate.

Different ideas on how to solve this problem have been discussed, using a swivel was one option, but to meet parachute opening shock a metal swivel would be needed and that would interfere with the GPS antenna. Therefore it was decided to test whether a stiff or a soft middle cord, where the stiffer one was the most desirable. More observations will be made during Drop Test 2. A high altitude drop test will most likely be performed and that would be a perfect time to try out different set-ups, with different middle cords lengths and stiffness over a longer fall. This would give hints on how to achieve a stable system that does not close, and swings into constant relative motion between the FFU and parachute within reasonable time.

Aerodynamic and Thermodynamic Analysis of a Falling Sphere

Marcus Lejon
KTH Royal Institute of Technology
SE-100 44 Stockholm

November 17th, 2012

The use of a falling sphere to determine the temperature, wind and density profiles of the atmosphere has been investigated in the present report. Four spheres are released from an altitude of 90 km. A polynomial fit of tabulated drag coefficient data is proposed to obtain the drag coefficient as a function of Mach and Reynolds numbers. The skin temperature of the spheres is determined from a simulation of the heat transfer from surrounding air to a thin-walled sphere made of glass-fiber reinforced epoxy. It is concluded that the spheres are expected survive the descent.

1 Introduction

Four spheres will be launched to an altitude of 90 km in a sounding rocket as a part of the MUSCAT (MUltiple Spheres for Characterization of Atmospheric Temperature) experiment. The rocket is planned to launch from the ESRANGE Space Center, Sweden, during the Spring of 2013. The spheres will be used to obtain the temperature, wind and density profiles of the atmosphere.

In the present report, an analysis is made of the aerodynamic considerations to determine the temperature, wind and density profiles of the atmosphere. Simulations are made to determine the range of Mach and Reynolds numbers as well as the duration of the descent.

Due to the low density of the atmosphere at high altitude, the spheres will accelerate to high velocities during the descent. When air is brought to rest relative to the sphere at the stagnation point, the temperature of the air is increased. An investigation is made in the present report to determine if the spheres will survive the descent with regards to temperature.

2 Aerodynamics

The aerodynamic drag can be calculated as

$$D = \frac{1}{2}\rho_\infty V_\infty^2 A C_D \tag{1}$$

where ρ is the density of the atmosphere, V is the velocity, A is a reference area (maximum cross section area for a sphere) and C_D is the drag coefficient. The subscript ∞ denotes free-stream conditions. That is, at a point sufficiently far upstream to be unaffected by the presence of the sphere.

The external forces acting on a falling sphere are shown in Fig. 1.

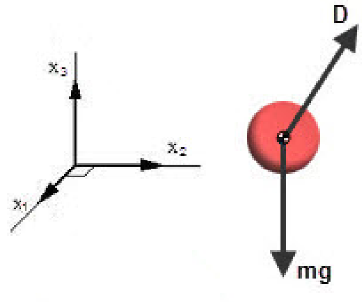

Figure 1: Coordinate axis and forces acting on the sphere.

The position of the sphere is given in a Cartesian coordinate system as a coordinate (x_1,x_2,x_3). The velocity in the three directions can be written in vector form as $\dot{\mathbf{x}}_1$, $\dot{\mathbf{x}}_2$ and $\dot{\mathbf{x}}_3$. The velocity V_∞, neglecting wind speeds, can be calculated as

$$V_\infty = \sqrt{\dot{x}_1^2 + \dot{x}_2^2 + \dot{x}_3^2} \tag{2}$$

The equation of motion in the vertical direction for the free falling sphere is

$$g - \frac{\rho_\infty A C_D |V_\infty|}{2m}\dot{x}_3 = \ddot{x}_3 \tag{3}$$

where g is the acceleration due to gravity. Since the initial altitude of the falling sphere is approximately 90 km, it is appropriate to consider an acceleration due to gravity which is dependent on the altitude [1]

$$g = \frac{GM'}{(R + x_3)^2} \tag{4}$$

where G is the universal gravitational constant and R is the radius of the Earth. M' is the sum of the mass of the Earth and the sphere. The mass of the sphere can here be neglected.

The drag coefficient is dependent on the Mach and Reynolds numbers [2]. The Mach number M is defined as

$$M_\infty = \frac{V_\infty}{a_\infty} = \frac{V_\infty}{\sqrt{\gamma R T_\infty}} \tag{5}$$

where a is the speed of sound, γ is the ratio of specific heats, R is the specific gas constant ($R = 287.04\ J/kgK$ for dry air) and T is the temperature in Kelvin.

The Reynolds number gives a measure of the ratio beween the inertial and viscous forces of the flow:

$$Re_\infty = \frac{\rho_\infty V_\infty L}{\mu_\infty} \tag{6}$$

where L is a reference length and μ is the dynamic viscosity of the flow medium. In the present report, the diameter of the sphere is used as the reference length. The dynamic viscosity is dependent on the temperature. The variation of μ for air is given by Sutherland's law [3]

$$\frac{\mu_\infty}{\mu_{\mathrm{ref}}} = \left(\frac{T_\infty}{T_{\mathrm{ref}}}\right)^{3/2} \frac{T_{\mathrm{ref}} + 110}{T_\infty + 110} \tag{7}$$

where μ_{ref} is a reference dynamic viscosity at a reference temperature T_{ref}. Values used here are $\mu_{\mathrm{ref}} = 1.7894 \cdot 10^{-5}$ and $T_{\mathrm{ref}} = 288.16$ K, [3].

2.1 Numerical Simulation

An estimation of the Mach number range during the descent has been obtained from a numerical simulation of a sphere released from rest at 90 km altitude. The properties of the atmosphere has been obtained using values published by the *U.S. Committee on Extension to the Standard Atmosphere.* The sphere diameter was set to 0.124 m and the mass of the sphere was set to 0.46 kg. The simulation was run with a Mach dependent drag coefficient [4]. The Mach number variation during the simulated fall is shown in Fig. 2.

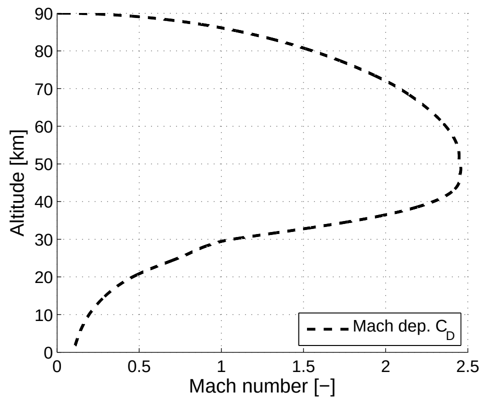

Figure 2: Altitude versus Mach number.

The Reynolds number for the same simulation is shown in Fig. 3.

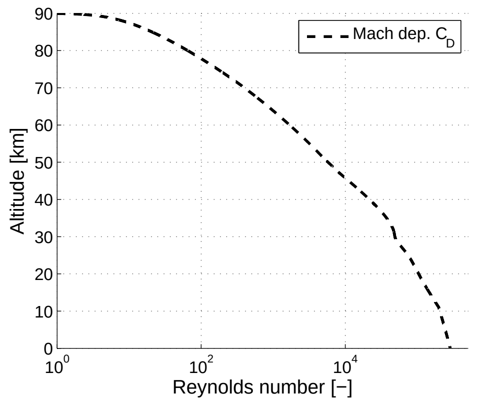

Figure 3: Reynolds number versus altitude.

The expected range for the Mach number is $0 \leq M_\infty \leq 2.5$ and the expected range of the Reynolds number is $0 \leq Re_\infty \leq 300\,000$.

2.2 The Drag Coefficient

To obtain the density and temperature profile of the atmosphere by the use of falling spheres, it is essential that the drag coefficient C_D of the spheres can be determined throughout the descent. Unless the drag coefficient can be established for a given flow field condition, a change of the acceleration of a sphere due to a change in the drag coefficient or a change of the atmospheric density cannot be distinguished from one another.

Mach and Reynolds numbers are two parameters which greatly affect the drag coefficient of a sphere. If a sphere has zero initial velocity and is released from 90 km altitude, it will experience a wide range of Mach and Reynolds numbers before impact on the Earth surface.

References [5], [6], [7] and [8] present tabulated data of the drag coefficient for a sphere for different Mach and Reynolds numbers. The uncertainty of the values found in reference [5], [6] are [7] are given as ±2%, while the values found in [8] have varying uncertainty. When gathering data for the present investigation, only values with an error equal or less than 2% has been used. Some values were further excluded due to the poor readability of the technical reports. The reports used to obtain the drag coefficient have used spheres with high surface quality. The roughness of the surface can change the drag coefficient considerable if the laminar boundary layer transitions to turbulent. High quality of the surface fineness of the spheres used in this experiment is therefore important to obtain good accuracy of the atmospheric density.

Reference [9] compares equations which can be used to determine the drag coefficient for creeping flow for a wide range of Reynolds numbers. The equation concluded in the report to give the best fit is

$$C_D = \frac{24}{Re_\infty}(1 + 0.150 Re_\infty^{0.681}) + \frac{0.407}{1 + \frac{8710}{Re_\infty}} \tag{8}$$

Eq. (8) has a root-mean square deviation of 1.77% when compared to experimental data according to reference [9]. Logarithmically distributed values of the drag coefficient calculated with Eq. (8) for Reynolds numbers in the range $10^{-3} - 2 \cdot 10^5$ have been used for this investigation. Values at higher Reynolds number would have been desirable, however, the equation is only valid for Reynolds numbers below $2 \cdot 10^5$.

An interpolation of all the scattered data was done with the TriScatteredInterp feature in the computational software MATLAB. Using the TriScatteredInterp feature, the value of C_D is obtained at a specified point by linear interpolation using a Delaunay triangulation of the tabulated data. The interpolation was done with the Mach number and the natural logaritm of the Reynolds number.

Using the drag coefficient obtained from TriScatteredInterp, a contour plot with contours of constant C_D can be generated. The result is shown in Fig. 4.

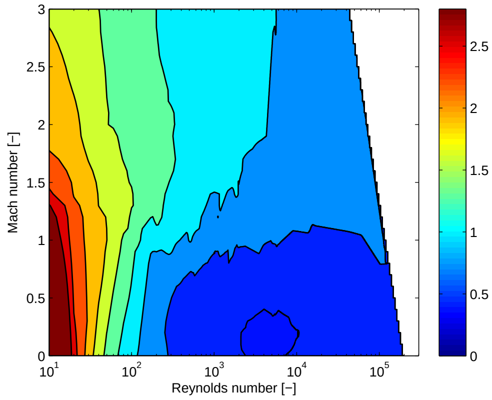

Figure 4: Drag coefficient contour plot.

Simulations show that values outside of the interpolated region (white region in Fig. 4) will be needed for the final part of the descent. At approximately 10 km altitude, the Reynolds number goes above $2 \cdot 10^5$. The drag coefficient change very little at high Reynolds numbers and the closest value at the same Mach number will be used. At 5 kilometers altitude the FFUs deploy a parachute and the drag coefficient for the sphere is not relevant for the remainder of the descent. The error induced by the interpolated method is neglectible. The uncertainty of the drag coefficient obtained with TriScatteredInterp is the same as for the measured data: 2%.

3 Density and Temperature Profile Calculation

The goal of the experiment with free-falling spheres is to obtain the wind, density and temperature profiles. Reference [2] gives a detailed description on the approach to obtain the density profile by the use of a falling sphere. A similar approach has been considered in the present report and is described in the following section. The key difference is that the wind speeds in the horizontal plane has been taken into account in the present report.

3.1 Theory

Equation (2) can be written to include the wind components

$$V'_\infty = \sqrt{(\dot{x}_1 - w_1)^2 + (\dot{x}_2 - w_2)^2 + (\dot{x}_3 - w_3)^2} \tag{9}$$

where w_1, w_2 and w_3 are the wind components in the x_1, x_2 and x_3 directions respectively. w_3 is set to zero in the calculations. The vertical winds will show as perturbations in the calculations.

Solving Eq. (3) for the density and considering horizontal winds gives the result

$$\rho_\infty = -\frac{(\ddot{x}_3 + |g|)2m}{AC_D V'_\infty \dot{x}_3} \tag{10}$$

The equations of motion in the x_1 and x_2 direction respectively can be written as

$$\ddot{x}_1 = -\frac{\rho_\infty AC_D(\dot{x}_1 - w_1)V'_\infty}{2m} \tag{11}$$

$$\ddot{x}_2 = -\frac{\rho_\infty AC_D(\dot{x}_2 - w_2)V'_\infty}{2m} \tag{12}$$

To obtain the temperature profile it is necessary to consider the ideal gas law:

$$p_\infty = \rho_\infty RT_\infty \tag{13}$$

and the hydrostatic equation:

$$\mathrm{d}p = -\rho_\infty g \, \mathrm{d}x_3 \tag{14}$$

where $\mathrm{d}p$ is a small change in pressure and $\mathrm{d}x_3$ is a small change in altitude.

Integration of Eq. (14)

$$p_\infty(h) = -\int_{x_3(0)}^{x_3(h)} \rho_\infty g \, \mathrm{d}x_3 + p_\infty(0) \tag{15}$$

where the integration limits are two altitudes, $x_3(0)$ and $x_3(h)$. The equation can be rewritten as

$$p_\infty(h) = \int_{x_3(h)}^{x_3(0)} \rho_\infty g \, \mathrm{d}x_3 + p_\infty(0) \tag{16}$$

The ideal gas law can be formulated for an altitude $x_3(0)$ and an altitude $x_3(h)$.

$$p_\infty(0) = \rho_\infty(0)T_\infty(0)R \tag{17}$$

$$p_\infty(h) = \rho_\infty(h)T_\infty(h)R \tag{18}$$

Solving for $T_\infty(h)$ and using Eq. (16)

$$T_\infty(h) = \frac{p_\infty(h)}{\rho_\infty(h)R} = \\ = \frac{p_\infty(0)}{\rho_\infty(h)R} + \frac{1}{\rho_\infty(h)R}\int_{x_3(h)}^{x_3(0)} \rho_\infty g \, \mathrm{d}x_3 \tag{19}$$

Replacing $p_\infty(0)$ by using Eq. (18)

$$T_\infty(h) = T_\infty(0)\frac{\rho_\infty(0)}{\rho_\infty(h)} + \frac{1}{\rho_\infty(h)R}\int_{x_3(h)}^{x_3(0)} \rho_\infty g \, \mathrm{d}x_3 \tag{20}$$

which is the equation used to calculate the temperature. $T(0)$ will be obtained from the *U.S. Committee on Extension to the Standard Atmosphere.* $T(0)$ is the temperature at the altitue where the calculation is initiated (around 90 km). The error induced by not knowing the actually value of $T(0)$ will be reduced as calculation proceeds and the density $\rho(h)$ is increased. The term with $T(0)$ in Eq. (20) will be around 10% of the total value approximately 14 km below the initial altitude [2].

3.2 Procedure

For the first iteration, the steps (i)–(vi) are done in the list below. For subsequent iterations, the first step is skipped and the temperature from the previous time step is used.

i. Guess initial value of T_∞ (from *U.S. Committee on Extension to the Standard Atmosphere*)
ii. μ_∞ is determined from the value of T_∞
iii. Mach and Reynolds number are calculated
iv. C_D is obtained from the polynomial
v. ρ_∞, w_1, w_2 are calculated from Eq. (10)–(12) (3 equations, 3 unknowns)
vi. Calculate $T_\infty(h)$ from Eq. (20).

3.3 Simulations

The drag coefficient obtained with the polynomial fit is used to simulate the fall of the sphere. The simulation is compared to the one made with a Mach dependent drag coefficient in Section 2.1. The Mach number and Reynolds number dependence on altitude during the fall are shown in Figs. 5 and 6.

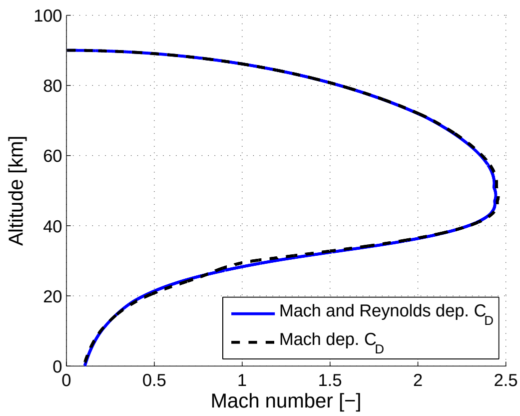

Figure 5: Altitude versus Mach number.

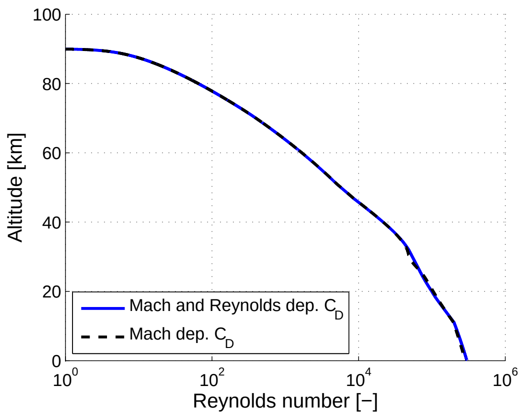

Figure 6: Altitude versus Reynolds number.

The difference in Mach and Reynolds numbers during the descent for the two simulations is shown to be small. The maximum deviation of the Mach number considering a Mach dependent drag coefficient compared to a the Mach and Reynolds number dependent drag coefficient, is 4%. The duration of the fall for the two simulations are also compared. Considering a Mach and Reynolds number dependent drag coefficient, the fall takes 503 seconds. Compared to a Mach dependent drag coefficient where the duration of the fall is 522 seconds.

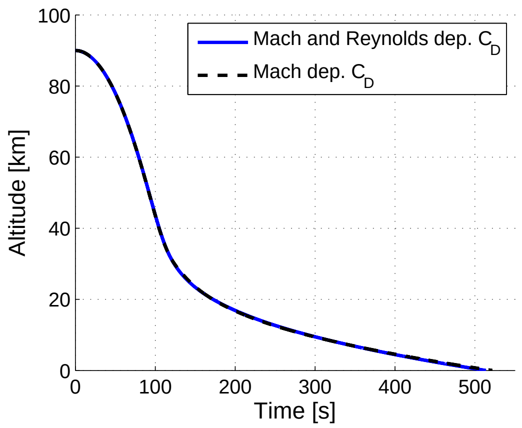

Figure 7: Altitude versus time.

A simulation has been done to determine the accuracy needed from the accelerometers to determine the density during the descent. The simulation is done with a Mach and Reynolds dependent drag coefficient.

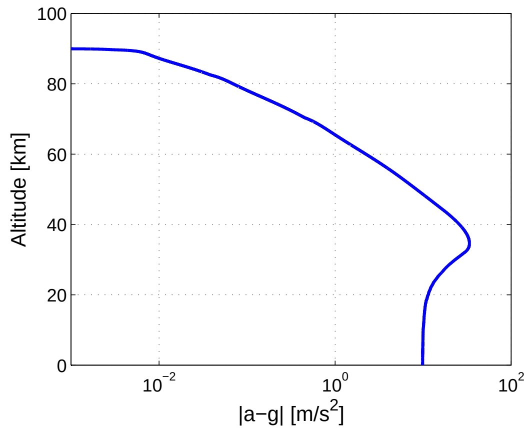

Figure 8: Acceleration in vertical direction due to aerodynamic forces throughout the descent.

4 Skin Temperature Evaluation

There is a small region of air which is slowed down to zero velocity relative to the sphere. This occur where the surface of the sphere is perpendicular to the onset flow. On a sphere this is considered a point, known as a stagnation point.

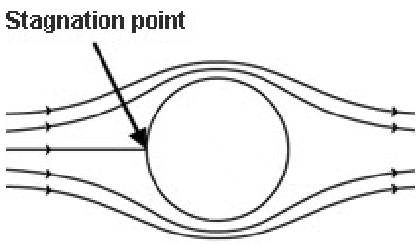

Figure 9: Stagnation point.

The temperature of the air is increased as it is brought to rest relative to the sphere. Due to the high maximum velocity of the spheres in this experiment, this temperature is evaluated to determine the temperature of the surface of the spheres.

4.1 Theory

4.1.1 Stagnation Temperature

The stagnation temperature can be obtained from the energy equation for steady one-dimensional flow

$$c_p T_\infty + \frac{V_\infty}{2} = c_p T_0 \tag{21}$$

where c_p is the specific heat of the air at constant pressure, T_∞ is the temperature of the free-stream, V_∞ is the velocity of the free-stream and T_0 is the total temperature if a fluid element is brought to rest adiabatically. The total temperature is found in the stagnation point.

4.1.2 Heat Transfer

A hollow sphere is considered with a radius of 62 mm and a shell thickness of 1 mm. The pressure inside the sphere is considered to be atmospheric pressure at sea level. The temperature of the air surrounding the sphere on all sides is considered to be the stagnation temperature. This is conservative and is expected to give an overestimation of the temperature of the sphere.

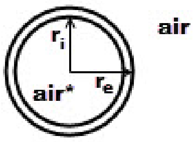

Figure 10: Sphere denotation.

Two boundary conditions are fulfilled as the sphere is heated

$$T(r_i) = T_{\text{air}*} \tag{22}$$

$$-\kappa \left.\frac{\partial T_s}{\partial r}\right|_{r_e} = h(T(r_e) - T_0) \tag{23}$$

where κ is the thermal conductivity of the shell material and h is the convective heat transfer coefficient. The temperature of the air outside of the sphere is denoted T_0 as in the stagnation temperature. The subscript s denotes the shell.

Eq. (22) states that the temperature of the surface of the sphere facing inwards has the same temperature as the air inside the sphere. Equation (23) states that the heat flow in the outer part of the shell is equal to the heat transfer by convection to the surface from the external air.

The convective heat transfer coefficient h is calculated with the equation shown in Eq. (24) from reference [10]. Isentropic flow is assumed and modified Newtonian theory is used to obtain the value 3.44. The predicted value was compared by the authors of reference [10] with experimental values obtained at different Reynolds numbers at Mach 3 and for varying surface roughness. The results showed a good agreement. In the simulation made in the present report, this relation is used for the whole external surface of the sphere.

$$3.44 = \frac{h}{\rho_\infty V_\infty c_p}\sqrt{\frac{\rho_\infty V_\infty D}{\mu_\infty}} \tag{24}$$

Solving for h and writing it using the Reynolds number

$$h = \frac{3.44\mu_\infty c_p \sqrt{Re_\infty}}{D} \tag{25}$$

The equation used to obtain the temperature of the air inside the sphere in time is

$$\rho_{\text{air}*} V_{\text{air}*} c_{\text{air}*} \frac{\partial T_{\text{air}*}}{\partial t} = \dot{Q} + \dot{Q}_v \tag{26}$$

where $V_{\text{air}*}$ and $c_{\text{air}*}$ is the volume and the specific heat of the air inside the sphere, respectively. $\dot{Q}_v$ is the heat generated within the system by e.g. an electric current. $\dot{Q}_v$ in the sphere is small and has been neglected in this simulation. $\dot{Q}$ is calculated as

$$\dot{Q} = qS = \kappa \left.\frac{\partial T_s}{\partial r}\right|_{r_i} 4\pi r_i^2 \tag{27}$$

where q is the heat flow per unit area and S is the surface area inside the sphere. The equation solved to obtain the temperature of the shell in time is

$$\rho_s c_s \frac{\partial T_s}{\partial t} = k_s \nabla^2 T_s \tag{28}$$

Considering a perfect sphere, Eq. (28) can be written using spherical coordinates as

$$\begin{aligned}\rho_s c_s \frac{\partial T_s}{\partial t} &= k_s \frac{1}{r^2}\frac{\partial}{\partial r}\left(r^2 \frac{\partial T_s}{\partial r}\right) = \\ &= k_s \left(\frac{\partial^2 T_s}{\partial r^2} + \frac{2}{r}\frac{\partial T_s}{\partial r}\right)\end{aligned} \tag{29}$$

4.2 Stagnation Temperature

A simulation of the stagnation temperature for a sphere released from rest at 90 km is shown in Fig. 11. A Mach and Reynolds number dependent C_D has been used.

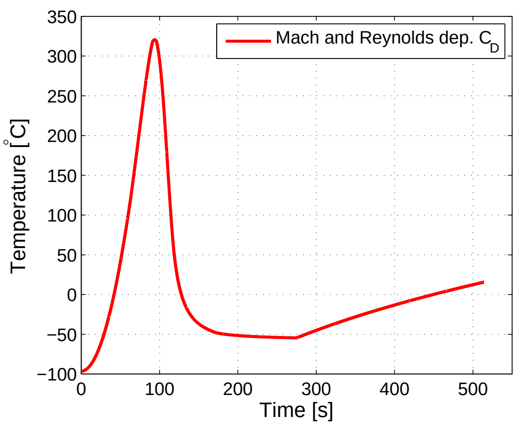

Figure 11: Stagnation temperature during the descent.

4.3 Sphere Temperature

The parameters used for the simulation of the temperature of the sphere are listed in Table 1.

Description	Value	SI Unit
Sphere inner radius (r_i)	0.061	m
Sphere outer radius (r_e)	0.062	m
Epoxy density (ρ_s) [11]	1140	kg/m^3
Epoxy thermal conductivity (κ_s) [11]	0.480	W/mK
Epoxy w. short glasfibers specific heat (c_s)[12]	800	J/kgK
Air specific heat (c_{air})	1006	J/kgK

Table 1: Sphere and air parameters.

The time steps in the numerical simulation of the heat transfer are done with the Runge-Kutta method which is of 4th order accuracy. The number of discrete points used in the shell to simulate the heat transfer is set to 20. The step in time is set to 0.002 s. A larger step size caused a divergence of the solution.

Two simulations are compared to see the effect of the initial temperature of the sphere shell and internal air. Simulation 1 and 2 were performed with an initial temperature of −10 °C and 10 °C respectively. The temperature of the outer surface of the sphere shell in simulation 1 and 2 as well as the stagnation temperature are shown in Fig. 12.

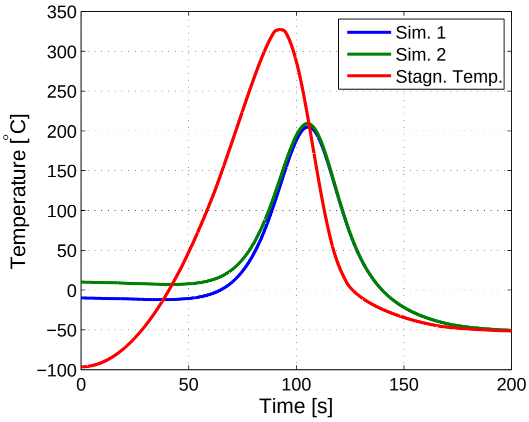

Figure 12: Temperature profiles.

The spheres are made of glass-fiber reinforced epoxy. The epoxy has an ISO 75 temperature resistance of 210–220 °C. Since the simulation consideres air at stagnation temperature surrounding the sphere on all sides, the results shown in Fig. 12 are expected to show an overestimation in temperature of the actual sphere.

To determine the effect of having atmospheric pressure at sea level inside the sphere during the descent, it is compared to a simulation where no air is present inside the sphere. Two simulations with an initial temperature of 10 °C are compared in Fig. 13.

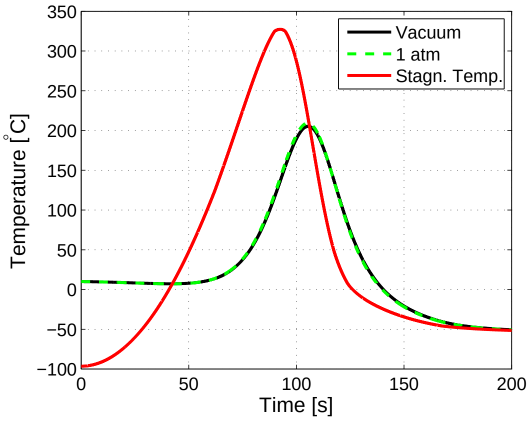

Figure 13: Skin temperature for different conditions inside the sphere.

It is shown that the difference between the two simulations is neglectible. The pressure inside the sphere will in reality be somewhere in between, as the pressure will equalize with the pressure outside the sphere through a small hole on the surface.

A simulation has been made to determine the difference in the temperature evaluation, had only a Mach dependent drag coefficient been considered.

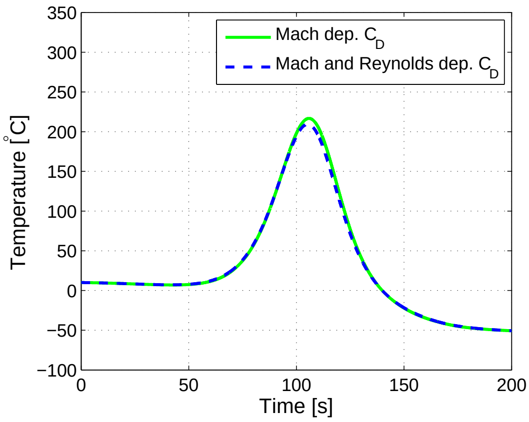

Figure 14: Skin temperature evaluated with different drag coefficients.

The difference of the maximum shell temperature between the two simulations is approximately 4 °C.

4.3.1 Shell thickness

The thickness of the shell is varied to determine its effect on the temperature of the shell. The outer radius of the sphere is fixed at 0.062 m. Three simulations are compared in Fig. 15. It is shown that if a safety margin is desired, adding one millimeter of thickness will greatly reduce the temperature of the shell.

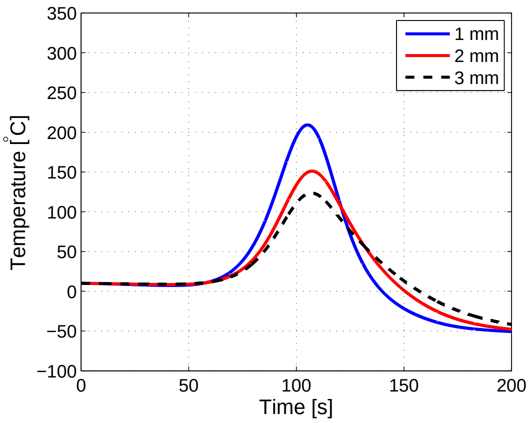

Figure 15: Skin temperatures for different shell thicknesses.

References

[1] Philip Hill and Carl Peterson. *Mechanics and Thermodynamics of Propulsion*. Addison-Wesley Publishing Company, Inc., 2nd edition, 2010.

[2] F. L. Bartman et. al. Upper-Air Density and Temperature by the Falling-Sphere Method. *Journal of Applied Physics*, 27(7), 1956.

[3] John D. Anderson Jr. *Fundamentals of Aerodynamics*. McGraw-Hill, 4th edition, 2007.

[4] M. Leroy Spearman and D. O. Braswell. Aerodynamics of a sphere and an oblate spheroid for Mach numbers from 0.6 to 10.5 including some effects of test conditions. Technical report, National Aeronautics and Space Administration, 1993.

[5] A.B. Bailey and J. Hiatt. Free-flight measurements of sphere drag at subsonic, transonic, supersonic and hypersonic speeds for continuum, transition and near-free-molecular flow conditions. Technical report, Von Karman Gas dynamics facility, 1971.

[6] W. R. Lawrence. Free-flight range measurements of sphere drag at low Reynolds numbers and low Mach numbers. Technical report, Von Karman Gas dynamics facility, 1967.

[7] K. L. Goin and W. R. Lawrence. Subsonic drag of spheres at reynolds numbers from 200 to 10,000. *Aiaa Journal*, 6(5):961–962, 1968.

[8] Heinrich et al. The drag coefficient of a sphere corresponding to a one meter robin sphere descending from 260,000 ft altitude (Reynolds NOS 789 to 23,448, Mach NOS 0,056 to 0,90). Technical report, G.T. Schjeldahl Company, 1963.

[9] Phillip P. Brown and Desmond F. Lawler. Sphere Drag and Settling Velocity Revisited. *Journal of Environmental Engineering*, March 2003.

[10] Williams D. Deveikis and Robert W. Walker. Local Aerodynamic Heat Transer and Boundary-layer Transition on Roughened Sphere-ellipsoid Bodies at Mach Number 3.0. Technical report, National Aeronautics and Space Administration, 1961.

[11] Overview of materials for epoxy, cast, unreinforced. `http://www.matweb.com/search/DataSheet.aspx?MatGUID=1c74545c91874b13a3e44f400cedfe39`, July 2012.

[12] Steve Lampman. *Characterization and Failure Analysis of Plastics*. ASM International, 1st edition, 2003.

MUSCAT Verification: RMU Rail Analysis

Marco Tito Bordogna

May 24, 2012

1 Introduction

The aim is to design the rails of the ejection system so that they do not deflect under loads from the launch.

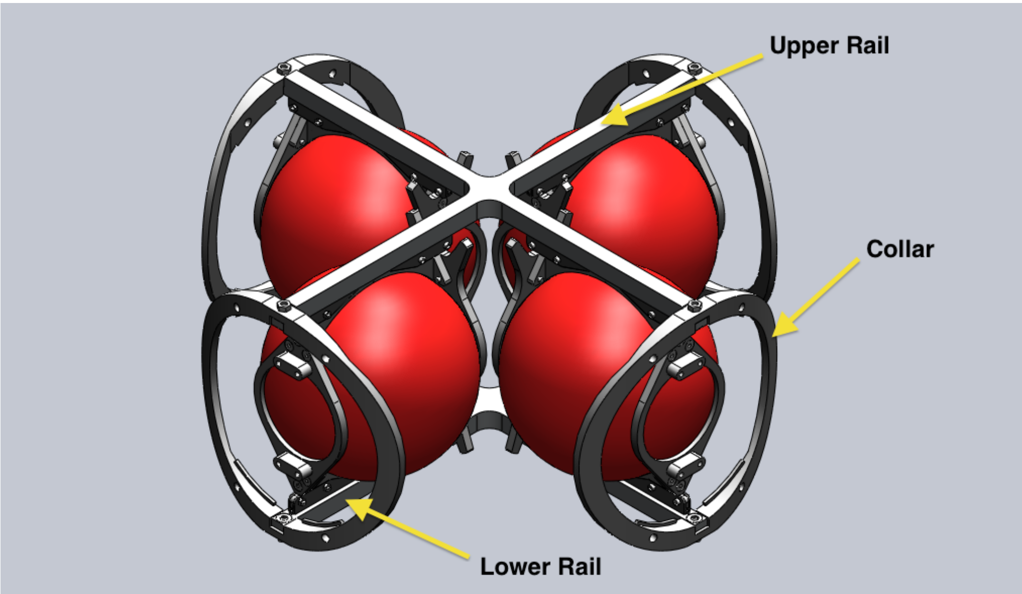

Figure 1.1: Isometric view of the ejection system

To fulfill their requirements the rails must be dimensioned so that the stresses in the rails are well below the yield stress of the material and that the maximum displacement of the rail is sufficient low so that the cage will not “jump out”.

2 Approach

During launch the rails will be subjected to both rocket acceleration and random vibrations. Using the Miles equation [1] it is possible to evaluate the equivalent static acceleration due to random vibrations. Once computed, this acceleration will be added to the acceleration of the rocket. This will allow to calculate both internal stresses and displacement of the rails.

2.1 Rail configuration

The analysis will be done on the *upper* and the *lower rail* for both longitudinal and lateral accelerations. Figures 2.1 and 2.2 explain the loading situation on the rails.

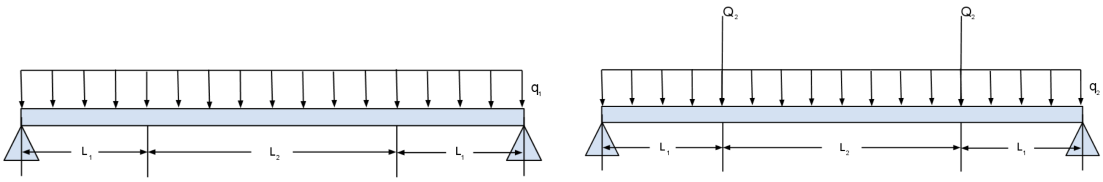

(a) *Longitudinal loads.* (b) *Lateral loads.*

Figure 2.1: Upper rail load configuration.

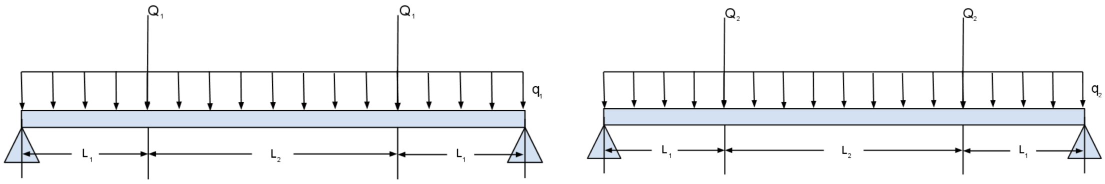

(a) *Longitudinal loads.* (b) *Lateral loads.*

Figure 2.2: Lower rail load configuration.

2.2 Natural Frequencies

Miles equation allow to find an equivalent static acceleration due to random vibrations. In order to get this acceleration the fundamental frequencies of the system, f_1, must be found.

Each rail can be divided into three base sections each described by the base case shown in Fig. 2.3. The first and third sections have a length, $L_1 = 68$ mm, and the second section has a length, $L_2 = 192$ mm. θ_1 and θ_2 are the deflection angles at the ends of the beam, while A and B are the reaction forces present at the end of the beams.

To solve the problem a FEM code has been used. The stiffness and mass matrix of the base section are:

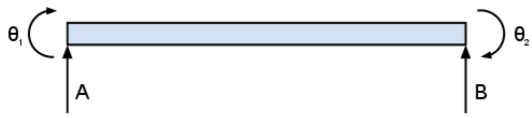

Figure 2.3: Base section

$$\mathbf{K_S} = \frac{EI}{L^3}\begin{bmatrix} 12 & 6L & -12 & 6L \\ 6L & 4L^2 & -6L & 2L^2 \\ -12 & -6L & 12 & -6L \\ 6L & 2L^2 & -6L & 4L^2 \end{bmatrix} \tag{2.1}$$

and:

$$\mathbf{M_S} = \frac{\rho AL}{420}\begin{bmatrix} 156 & 22L & 54 & -13L \\ 22L & 4L^2 & 13L & -3L^2 \\ 54 & 13L & 156 & -22L \\ -13L & -3L^2 & -22L & 4L^2 \end{bmatrix} \tag{2.2}$$

The matrices of the three sections will be assembled and in the mass matrix the masses of the FFU and the cage is added in the correspondent nodes, respectively at the point L_1 and $L_1 + L_2$. The boundary condition are applied by removing the column which represent the constraints.

$$\mathbf{K} = EI\begin{bmatrix} \frac{6}{L_1^2} & \frac{-12}{L_1^3} & \frac{6}{L_1^2} & 0 & 0 & 0 \\ \frac{4}{L_1} & \frac{-6}{L_1^2} & \frac{2}{L_1} & 0 & 0 & 0 \\ \frac{-6}{L_1^2} & \frac{12}{L_1^3} + \frac{12}{L_1^3} & \frac{-6}{L_1^2} + \frac{6}{L_2^2} & \frac{-12}{L_2^2} & \frac{6}{L_2} & 0 \\ \frac{2}{L_1^2} & \frac{-6}{L_1^3} + \frac{6}{L_2^3} & \frac{4}{L_1^2} + \frac{4}{L_2^2} & \frac{-6}{L_2^2} & \frac{2}{L_2^2} & 0 \\ 0 & \frac{-12}{L_2^3} & \frac{-6}{L_2^2} & \frac{12}{L_2^3} + \frac{12}{L_1^3} & \frac{-6}{L_2^2} + \frac{6}{L_1^2} & \frac{6}{L_1^2} \\ 0 & \frac{6}{L_2^2} & \frac{2}{L_2} & \frac{-6}{L_2^2} + \frac{6}{L_1^2} & \frac{4}{L_1} & \frac{2}{L_1} \\ 0 & 0 & 0 & \frac{-12}{L_1^3} & \frac{-6}{L_1^2} & \frac{-6}{L_1^2} \\ 0 & 0 & 0 & \frac{6}{L_1^2} & \frac{2}{L_1} & \frac{4}{L_1} \end{bmatrix} \tag{2.3}$$

and:

$$\mathbf{M} = \frac{\rho A}{420}\begin{bmatrix} 22L_1^2 & 54L_1 & -13L_1^2 & 0 & 0 & 0 \\ 4L_1^3 & 13L_1^2 & -3L_1^3 & 0 & 0 & 0 \\ 13L_1^2 & 156(L_1 + L_2) + \frac{420m}{\rho A} & -22(L_1^2 - L_2^2) & 54L_2 & -13L_2^2 & 0 \\ -3L_1^3 & -22(L_1^2 - L_2^2) & 4(L_1^3 + L_2^3) & 13L_2^3 & -3L_2^3 & 0 \\ 0 & 54L_2 & 13L_2^2 & 156(L_2 + L_1) + \frac{420m}{\rho A} & -22(L_2^2 - L_1^2) & -13L_1^2 \\ 0 & -13L_2^2 & -3L_2^3 & -22(L_2^2 - L_1^2) & 4(L_2^3 + L_1^3) & -3L_1^3 \\ 0 & 0 & 0 & 54L_1 & 13L_1^2 & -22L_1^2 \\ 0 & 0 & 0 & -13L_1^2 & -3L_1^3 & 4L_1^3 \end{bmatrix} \tag{2.4}$$

By solving the eigenvalue problem,

$$[\mathbf{M}^{-1}\mathbf{K} - \omega^2 \mathbf{I}] = 0 \tag{2.5}$$

we can find the natural frequencies of the system:

$$f = \frac{\omega}{2\pi} \tag{2.6}$$

The fundamental frequency, f_1, will be used in determining the equivalent static acceleration.

2.3 Equivalent Static Acceleration

To find the equivalent static acceleration for the upper and lower rails due to random vibration the Miles equation has been used. The random vibrations act in all direction, but for this case the most important directions are the lateral and the longitudinal.

For the longitudinal direction the Miles equation will lead to an equivalent static acceleration (using the 3σ concept) of:

$$\ddot{x}_2 = 3\sqrt{\frac{\pi}{2} f \gamma W(f)} \tag{2.7}$$

where the amplification factor γ=10 as indicated in [1], and the power spectral density, $W(f)$=0.018 g^2/Hz as indicated in [2]. For what concern the longitudinal acceleration the equation in the same but the linear acceleration of the rocket must be added:

$$\ddot{x}_1 = 3\sqrt{\frac{\pi}{2} f \gamma W(f)} + 20 \text{ g} \tag{2.8}$$

2.4 Static Analysis

Once the equivalent static acceleration is calculated it is possible to derive the value of the concentrated loads Q_1 or Q_2 and the distributed load q_1 or q_2 acting on the beam.

$$Q_1 = m\ddot{x}_1 \tag{2.9}$$

$$Q_2 = m\ddot{x}_2 \tag{2.10}$$

$$q_1 = \rho A \ddot{x}_1 \tag{2.11}$$

$$q_2 = \rho A \ddot{x}_2 \tag{2.12}$$

The internal moment of the upper rail under longitudinal load can be found using:

$$M_u^{LONG} = \frac{q_1 L_f^2}{8} \tag{2.13}$$

for lateral load:

$$M_u^{LAT} = \frac{q_2 L_f^2}{8} + Q_2 L_1 \tag{2.14}$$

The internal moment of the lower rail under longitudinal load can be found using:

$$M_l^{LONG} = \frac{q_1 L_f^2}{8} + Q_1 L_1 \tag{2.15}$$

for lateral load:

$$M_l^{LAT} = \frac{q_1 L_f^2}{8} + Q_1 L_1 \tag{2.16}$$

From the moment the internal stresses are given by:

$$\sigma = \frac{M^* h}{2I} \tag{2.17}$$

where M^* is the moment present in one point of the rail and h is the height of the rail.

2.5 Deflection Analysis

The deflection is calculated using superposition of the different loads. For the lower rail in both longitudinal and lateral direction the displacement can be found by superposition of a distributed load with two concentrated pint loads (where the FFUs are located). For the upper rail in lateral direction the displacement can be found by superposition of a distributed load with two concentrated pint loads (where the FFUs are located). For the upper rail in longitudinal direction the displacement depends only on the distributed load.

The deflection component of the rail under a distributed load under longitudinal loading is expressed as:

$$\delta_{q_1} = \frac{q_1 x}{24EI}(L_f^3 - 2L_f x^2 + x^3) \tag{2.18}$$

The deflection component of the rail under a distributed load under lateral loading is expressed as:

$$\delta_{q_2} = \frac{q_2 x}{24EI}(L_f^3 - 2L_f x^2 + x^3) \tag{2.19}$$

where x the coordinate along the rail and L_f is the total length of the rail.

The deflection component of the rail under one FFU point loads under longitudinal loading is expressed as:

$$\begin{cases} \delta_{Q_1} = \dfrac{Q_1 x b}{6L_f EI}(L_f^2 - x^2 - b^2) & \text{for x<a} \\ \delta_{Q_1} = \dfrac{Q_1 b}{6L_f EI}\left(\dfrac{L_f}{b}(x-a)^3 + (L_f^2 - b^2)x - x^3\right) & \text{for x>a} \end{cases} \tag{2.20}$$

Where a and b are explained in (2.4). The deflection component of the rail under one FFU point loads under lateral loading is expressed as:

$$\begin{cases} \delta_{Q_2} = \dfrac{Q_2 x b}{6L_f EI}(L_f^2 - x^2 - b^2) & \text{for x<a} \\ \delta_{Q_2} = \dfrac{Q_2 b}{6L_f EI}\left(\dfrac{L_f}{b}(x-a)^3 + (L_f^2 - b^2)x - x^3\right) & \text{for x>a} \end{cases} \tag{2.21}$$

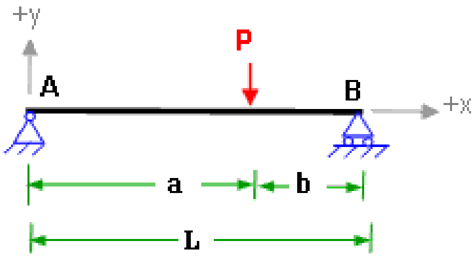

Figure 2.4: Definition of a and b used in Equations 2.20 and 2.21

3 Results and Analysis

To find the optimal rail dimensions the maximum stress, σ_{max}, in the rail and the maximum deflection, δ_{max}, at critical positions along the rail have been evaluated. The criteria for acceptable rails include:

$$\sigma_{max} = \frac{\sigma_{yield}}{S} \tag{3.1}$$

where S is the safety factor and it is equal to 2 and σ_{yield} is the yield stress for the material used in the rail. The material tested are A514 steel alloy (σ_{yield}=689 MPa) and 7075 T6 aluminium (σ_{yield}=550 MPa).

Material data used for the analysis are presented in Tab. 3.1

	Steel A514	**Aluminium 7075 T6**
E (GPa)	210	72
ρ (kg m^{-3})	7850	2800
σ_{yield} (MPa)	689	550

Table 3.1: Material Data [3]

For the displacement we must provide that the maximum longitudinal displacement, δ_{max}, at the place where the FFUs are located will never reach 0.1 mm. This deflection has been chosen based on the minimum allowable distance between the FFU cage and upper rail.

The analysis will be performed only for the lower rail since is the one that has higher loads. For the upper rail the dimensions chosen will be the same of the lower one. This is done in order to have a symmetry in the assembly that will allow the MUSCAT experiment to have less spare parts and a simpler design for the ejection system. The upper rail will be analyzed afterward in order to verify that the yield stress in not reached

Due to design constrain, the maximum dimension for the rail cannot exceed t$_{max}$=5 mm and b$_{max}$=10 mm. These constrains are due to the available space in the collar (Fig. 1.1). The first analysis will be done considering rails with a rectangular cross section; in case the requirements will not be fulfilled a T-section (see Fig. 3.1) will be analyzed.

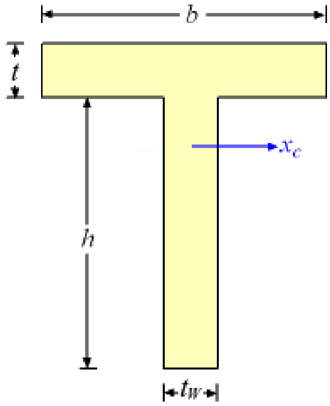

Figure 3.1: T cross section

The lightest lower rail that can withstand σ_{max}, does not deflect more than 0.1 mm, and is the lightest option will be chosen.

3.1 Equivalent Static Acceleration

The equivalent static acceleration for the lower rail has been computed for longitudinal and lateral load direction, for steel and aluminum alloy and for rectangular and T cross section.

Fig. 3.2 shows the equivalent static acceleration of the lower rail with rectangular cross section, made by aluminum alloy, under longitudinal and lateral load.

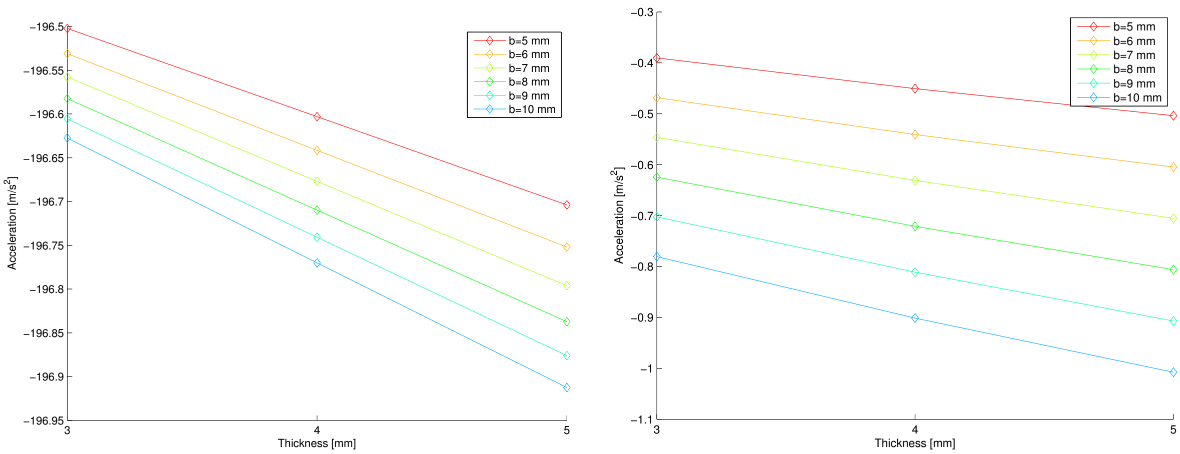

(a) *Longitudinal load.* (b) *Lateral load.*

Figure 3.2: Equivalent static acceleration for lower rail with rectangular cross section.

Fig. 3.3 shows the equivalent static acceleration of the lower rail with rectangular cross section, made by steel, under longitudinal and lateral load.

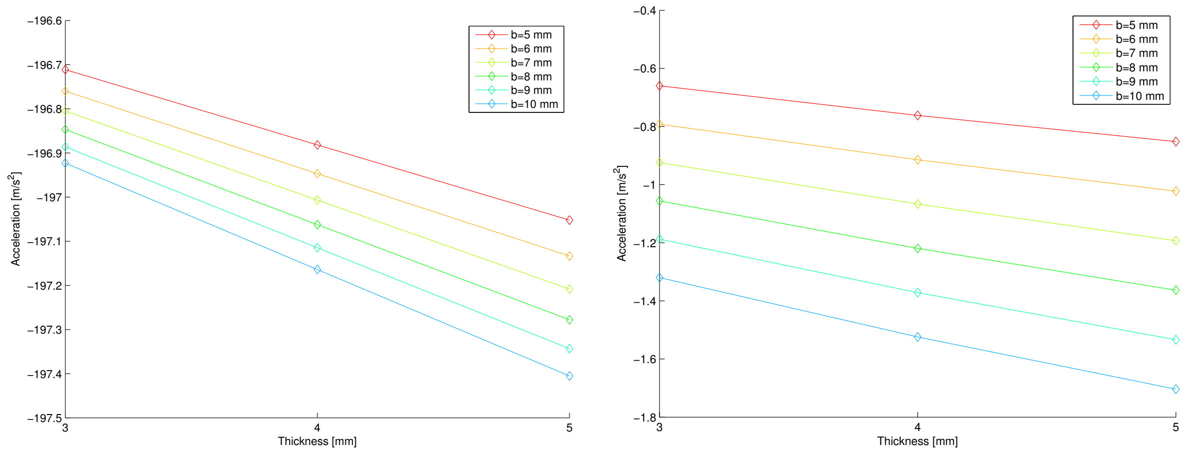

(a) *Longitudinal load.* (b) *Lateral load.*

Figure 3.3: Equivalent static acceleration for lower rail with rectangular cross section.

Fig. 3.4 shows the equivalent static acceleration of the lower rail with T cross section, made by aluminum alloy, under longitudinal and lateral load. The T cross section has fix value of b=b_{max} and t=t_{max} but variable h and t_w.

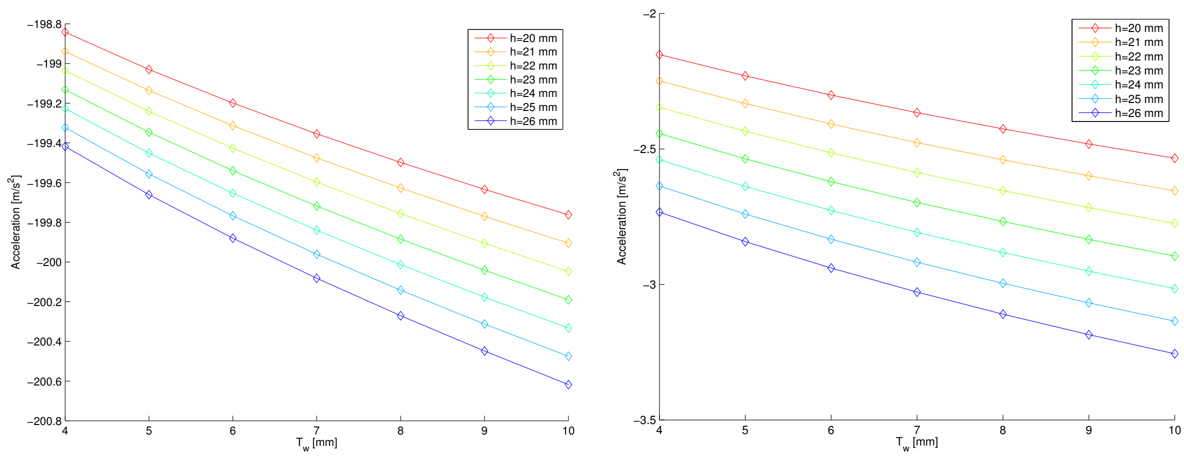

(a) *Longitudinal load.* (b) *Lateral load.*

Figure 3.4: Equivalent static acceleration for lower rail with T cross section.

Fig. 3.5 shows the equivalent static acceleration of the lower rail with T cross section, made by steel, under longitudinal and lateral load.

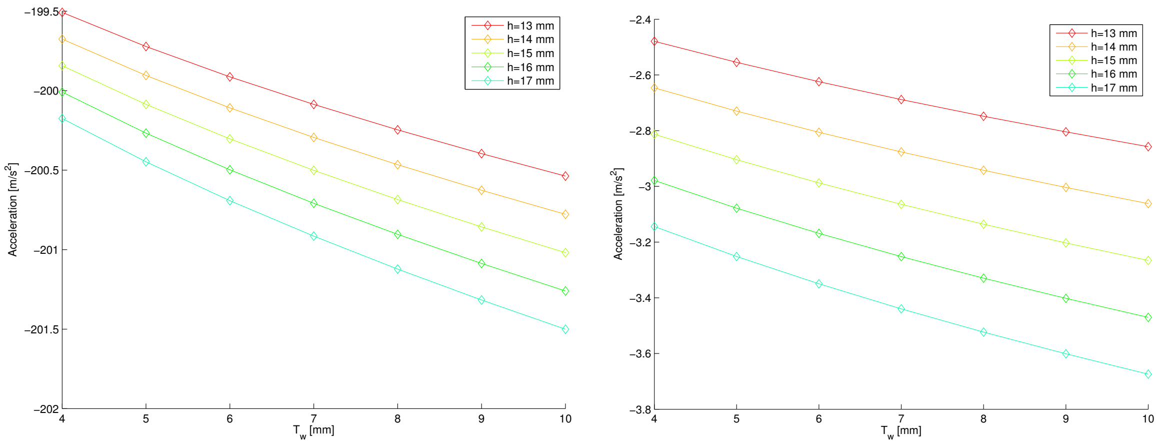

(a) *Longitudinal load.* (b) *Lateral load.*

Figure 3.5: Equivalent static acceleration for lower rail with T cross section.

3.2 Lower Rail

3.2.1 Rectangular Cross Section

In this section the results of the analysis of the lower rail are presented. First results will involve the rectangular cross section under longitudinal and lateral load for both materials. The results will be presented in graphs that show the relation between stress and displacement as function of t and b.

Fig. 3.6 shows the maximum stress present in a lower rail made from steel and aluminium as a function of width and height for the rectangular cross section rail under longitudinal load.

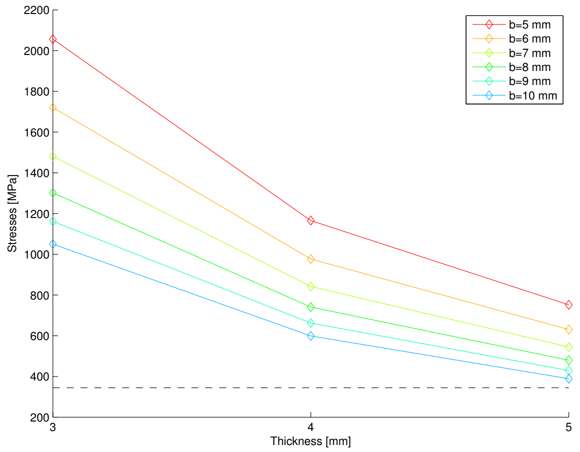

(a) *Steel.*

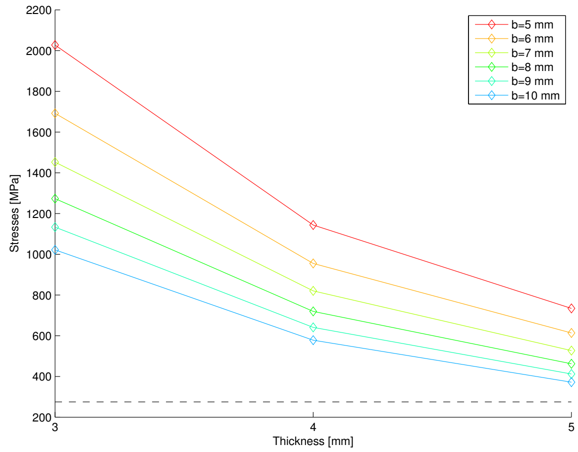

(b) *Aluminum.*

Figure 3.6: Stresses lower rail for longitudinal load with rectangular cross section.

Fig. 3.7 shows the maximum displacement, at FFU location, present in a lower rail made from steel and aluminium as a function of width and height for the rectangular cross section rail under longitudinal load.

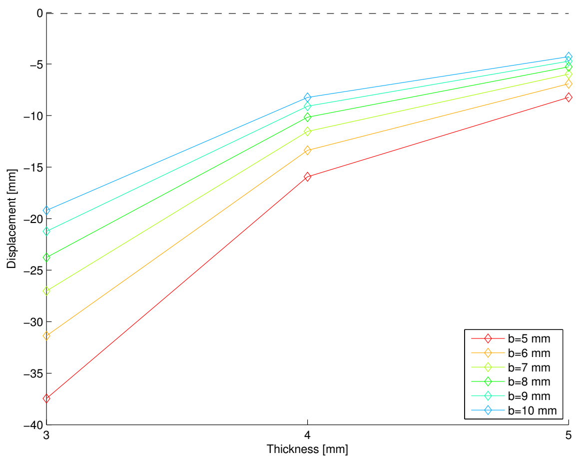

(a) *Steel.*

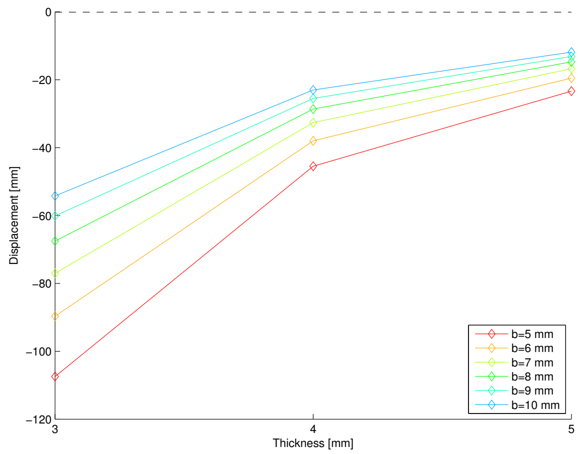

(b) *Aluminum.*

Figure 3.7: Displacement lower rail for longitudinal load with rectangular cross section.

Fig. 3.8 shows the maximum stress present in a lower rail made from steel and aluminium as a function of width and height for the rectangular cross section rail under lateral load.

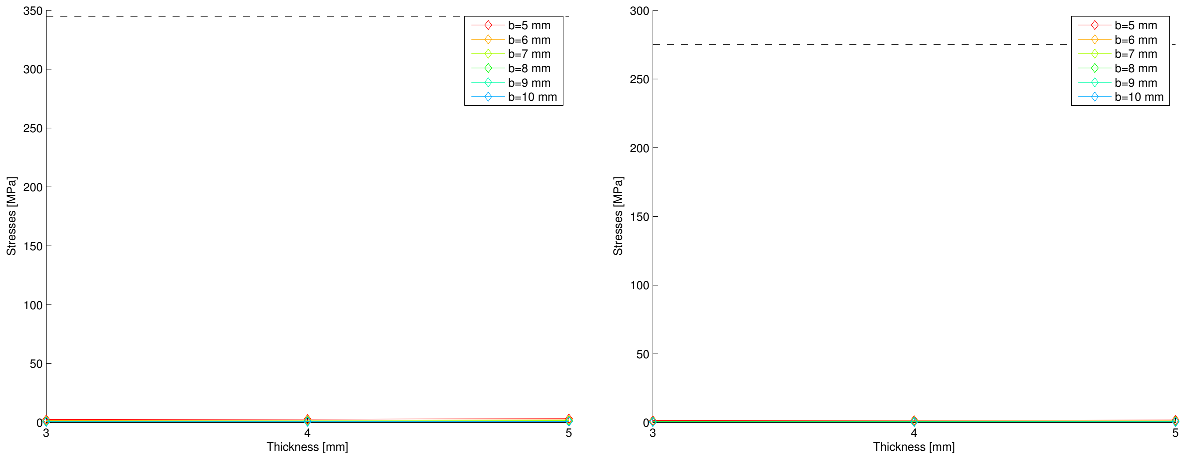

(a) *Steel.* (b) *Aluminum.*

Figure 3.8: Stresses lower rail for lateral load with rectangular cross section.

3.2.2 T Cross Section

Now the results for the T cross section will be presented. As mention in Sec. 3 the cross T cross section has fixed b=b$_{max}$ and t=t$_{max}$ but variable h and t_w.

Fig. 3.9 shows the maximum stress present in a lower rail made from steel and aluminium as a function of width and height for the T cross section rail under longitudinal load.

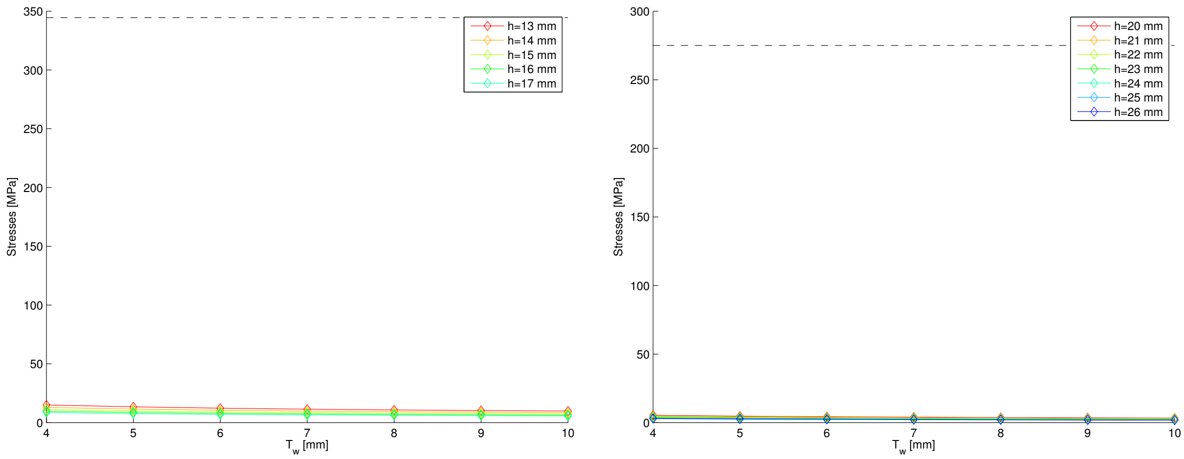

(a) *Steel.* (b) *Aluminum.*

Figure 3.9: Stresses lower rail for longitudinal load with T cross section.

Fig. 3.10 shows the maximum displacement, at FFU location, present in a lower rail made from steel and aluminium as a function of width and height for the T cross section rail under longitudinal load.

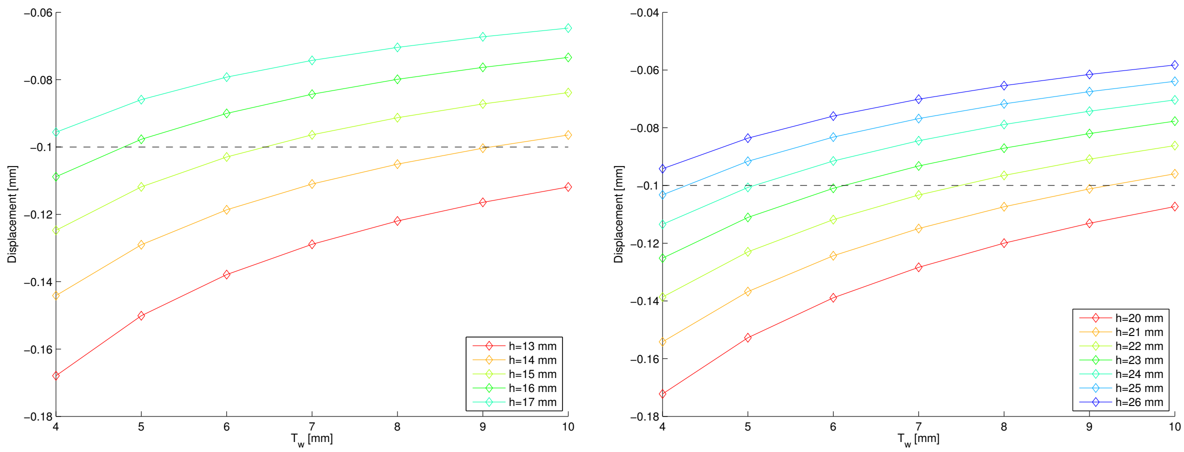

(a) *Steel.* (b) *Aluminum.*

Figure 3.10: Displacement lower rail for longitudinal load with T cross section.

Fig. 3.11 shows the maximum stress present in a lower rail made from steel and aluminium as a function of width and height for the T cross section rail under lateral load.

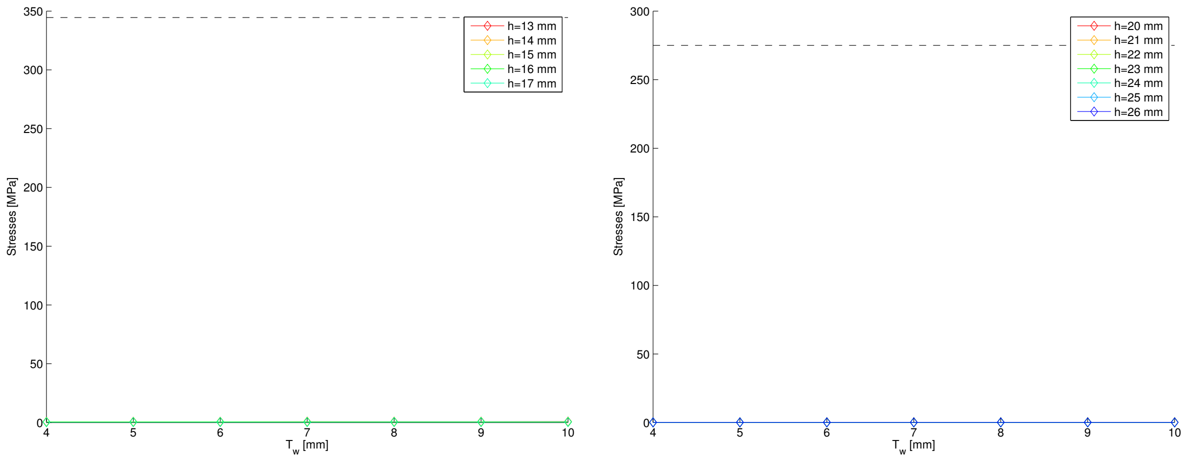

(a) *Steel.* (b) *Aluminum.*

Figure 3.11: Stresses lower rail for lateral load with T cross section.

3.3 Mass of the Rail

In this section we present the results for the mass analysis of the rail. Both material and cross section will be analyzed. Fig. 3.12 shows the mass of the rail made from steel and aluminium as a function of width and height of the rectangular cross section rail.

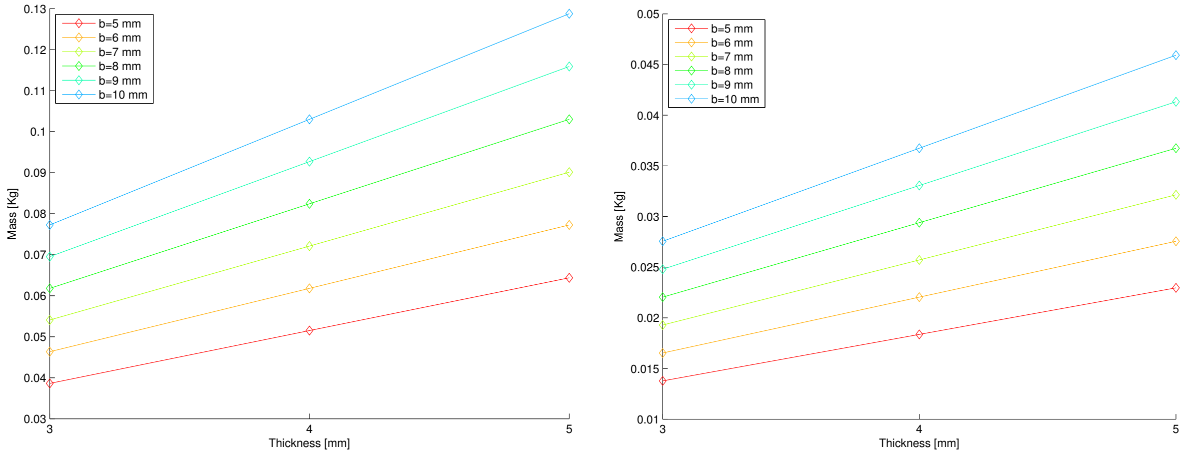

(a) *Steel.* (b) *Aluminum.*

Figure 3.12: Mass of the rail with T cross section.

Fig. 3.13 shows the mass of the rail made from steel and aluminium as a function of h and t_W of the T cross section rail.

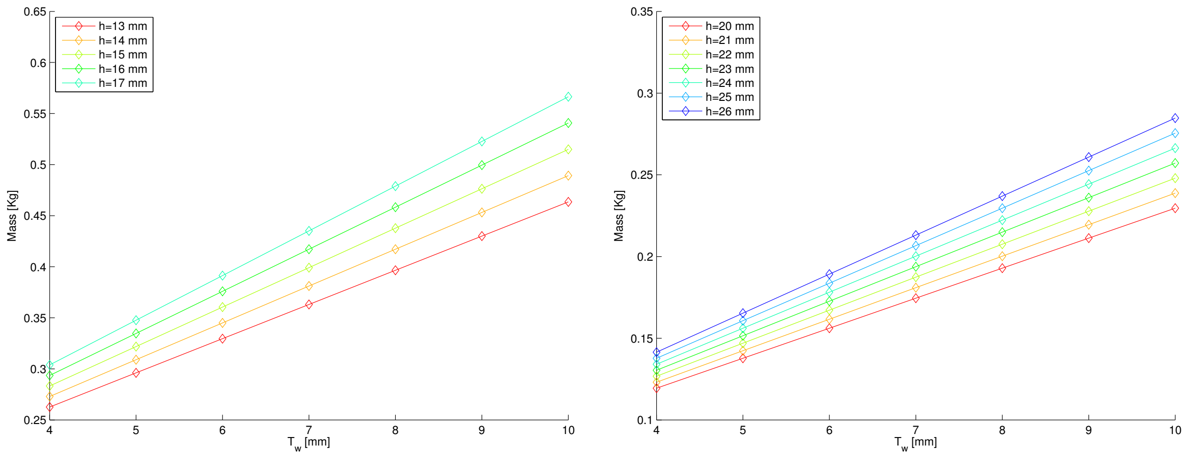

(a) *Steel.* (b) *Aluminum.*

Figure 3.13: Mass of the rail with T cross section.

4 Conclusion

As it is possible to see from Figures 3.7 and 3.6 that using the rectangular cross section will not fulfill both the requirement of maximum displacement and maximum stress. Therefore, the best option is to chose a T cross section. As it is possible to see from Figures 3.10 and 3.9 the T cross section will allow the rail to displace within the constraint of $\delta_{FFU} \leq \delta_{max}$ and the stresses are largely below σ_{max}.

Between the acceptable solutions the lighter will be chosen. By comparing Figures. 3.10 and 3.13 it has been sorted out that the optimal T cross section is (see Tab. 4.1):

	Steel A514	**Aluminium 7075 T6**
t	5 mm	5 mm
b	10 mm	10 mm
h	17 mm	26 mm
t_w	4 mm	4 mm
Weight	0.304 kg	0.141 kg

Table 4.1: Available solutions for lower rail

where the aluminium rail has the lowest mass.

Since it has been chosen to have a symmetry in the design of the ejection system it has been decided to have as upper rail a rectangular cross section aluminum beam with:

- t=5 mm;
- b=10 mm;
- mass=0.046 kg.

As shown if Fig. 1.1, the ejection system is composed by two upper rail and two lower rail. This will lead with a total mass for the system of M_{TOT}= 0.347 kg.

References

[1] J. Wijker, *Random Vibrations in Spacecraft Structures Design: Theory and Applications*. Springer, 2009.

[2] Euro Launch, *REXUS user manual*, 7.3 ed., 2011.

[3] `http://www.makeitfrom.com/material-data/?for=7075-T6-Aluminum`

Evaluation of suitable springs for the ejection system

Emilio J. Lozano

September 23, 2012

Nomenclature

E_k =Kinetic energy

E_p =Potential energy

$E_{p\text{-typen}}$=Potential energy associated to the spring type n

K =Stiffness constant of the spring

L_0 =Free length of the spring

L_1 =Maximum extended length of the spring

F_0= Force to start the elongation of the spring

F_s =Spring force

δ= Spring elongation

1. Introduction

The aim of this analysis is to select a set of springs suitable for the ejection system. The springs that have been considered suitable for the ejection system are extension springs. Extension springs are thus the only ones studied because of the architecture of the ejection system. Furthermore only springs from the manufacturer Lesjöfors [1] are considered because of the successful implementation of their products in previous experiments [2].

The approach for the analysis is to compute the elastic potential energy that can be stored in the springs and assume that this potential energy will become kinetic energy that the system will exchange with the FFUs in order to accelerate them.

2. Motivation of spring selection for the analysis

The springs selected for this analysis are extension springs from the manufacturer Lesjöfors[1] as mentioned above. Four different springs are selected: a stiff spring with small elongation, a weak spring with large elongation and two intermediate options. The characteristics of these four springs can be seen in Table number 1. The intention with the selection of these springs is to sweep all the combinations of mechanical properties of the springs that can be used. A stiff spring with large elongation has been ignored because of the large forces and all the inconvenient aspects that this fact could have in the loading process. The opposite option of a weak spring with small elongations does not make sense for the purpose of storing energy.

Spring number	Spring model	K (N/m)	L_0 (m)	L_1 (m)	F_0(N)
1	Extension-Spring-Serie-A-SS1774-05 9676	63600	0.0632	0.0733	114.3
2	Dragfjäder SF-DF-SS1774-04 3518	4360	0.07	0.114	40
3	Dragfjäder SF-DF-SS1774-04 3511	10070	0.07	0.094	45
4	Dragfjäder SF-DF-SS1774-04 3504	2570	0.06	0.105	23

Table1: Mechanical characteristics of the selected springs.

These springs have been chosen with the intention of matching the requirements of ejecting speed of 5 m/s. (this ejection speed was considered suitable for the RAIN experiment[2]) and minimization of the force required to compress the springs.

3. Computation of the stored potential energy and forces

The computation of the potential of energy of the spring can computed according with [3] by means of Equation (1)

$$E_p = \frac{1}{2} K \delta^2 \tag{1}$$

Applying Equation (1) to the springs mentioned in table 1, the potential energy stored in each spring can be computed and the result of this computation can be seen in Table 2

Spring number	Spring model	E_p(J)
1	Extension-Spring-Serie-A-SS1774-05 9676	4.39
2	Dragfjäder SF-DF-SS1774-04 3518	5.98
3	Dragfjäder SF-DF-SS1774-04 3511	3.17
4	Dragfjäder SF-DF-SS1774-04 3504	3.64

Table2: Potential energy stored in the spring at maximum elongation

Furthermore it is possible to compute the force resulting in from the loaded spring. This computation can be done by applying Hook's law [2] by means of Equation (2)

$$F_s = K(L_1 - L_0) \tag{2}$$

The results of the computation of the resultant force of the loaded springs can be seen in Table 3

Spring number	Spring model	F_s(N)
1	Extension-Spring-Serie-A-SS1774-05 9676	756
2	Dragfjäder SF-DF-SS1774-04 3518	232
3	Dragfjäder SF-DF-SS1774-04 3511	283
4	Dragfjäder SF-DF-SS1774-04 3504	138

Table 3: Force required to elongate the springs until their maximum elongation

As a conclusion for this section it should be mention that the springs number 2 and 4 shows more positive characteristics that the springs 1 and 3. This is due to the fact that a smaller force spring number 2 can store more potential energy that springs 1, 3 and 4. This is positive because it is possible to store more potential energy with less force although it should be mention that spring 4 is a interesting option because of its low spring stiffness it could be used in a parallel setting with a lower resulting force than the other 3 springs.

4. Computation of the kinetic energy and ejection speed

In the selection of the springs it is an important feature how fast the FFU is ejected. With the purpose of deriving this speed it is assumed that all the potential energy stored in the springs will become kinetic energy because the FFU is the only body that can interact with the springs. Therefore the potential energy of the springs should become kinetic energy of the FFU. Under this assumption and considering the definition of kinetic energy according to [3] that can be seen in Equation (3), the velocity of the FFU can be computed. The computed ejection velocity can be seen in Table 4 for an estimated mass of 0.8 kg for the assembly of the FFU plus the rest of parts that have to be ejected.

$$E_k = \frac{1}{2}\mathrm{m}v^2 \tag{3}$$

Spring number	Spring model	E_k(J)	V(m/s)
1	Extension-Spring-Serie-A-SS1774-05 9676	4.39	3.31
2	Dragfjäder SF-DF-SS1774-04 3518	5.98	3.86
3	Dragfjäder SF-DF-SS1774-04 3511	3.17	2.81
4	Dragfjäder SF-DF-SS1774-04 3504	3.64	3.01

Table 4: Ejection speeds created by each spring.

As it was expected due to the higher potential stored by the spring 2 the ejection speed is also higher for the spring number 2.There is a fact that deserves attention the fact that spring 4 although it is the weakest one in terms of stiffness it can create a similar ejection speed.

5. Conclusion

The spring Dragfjäder SF-DF-SS1774-04 3518, reference corresponding to the spring number 2 is the one that offers better performances among the springs analyzed of this study. With only one spring the ejection velocity would be 3.86 m/s as it can be seen in Table 4. However the design of the ejection system contains 4 springs. Four springs of type 2 would increase the ejection speed but also the forced caused by the springs. In opposition to the use of type 2, by using springs of type 4 the requirement of having an ejection speed over 5 m/s is fulfilled too. In the case of using springs type 4 the force to load the spring will lower than in the case of using 4 springs type 2. Then it can be concluded that the use of springs type 4 is the most suitable one because the requirement of ejection speed is fulfil and the force is smaller than if springs type 2 where uses. The ejection speed of the FFU using 4 springs type 4 can be calculated with Equation (4)

$$v = \sqrt{\frac{8E_{p-type4}}{\mathrm{m_{FFU}}}} = 6.03 \text{ m/s} \tag{4}$$

The forced created by 4 springs of type 4 can be calculated with the data present in Table 3. Using the data from Table 3 the force of 4 springs type 4 is 555N and the force of 4 springs type 2 is 928N.

Furthermore, it should be mention than the rocket will be rotating with an angular speed of 4 Hz. This rotation will make the ejection process easier because of the centrifugal force induced by the rotational movement. In any case the ejection speed will be above 5 m/s and this ejection speed was considered appropriate for the RAIN experiment [2]. Moreover, the loading force required by this spring is lower than for any of the other than can fulfil the requirement of ejection speed of 5 m/s. Finally, the lower load force of the selected spring will make the handling of it, easier and safer.

6. References

[1] Lesjöfors AB

http://www.solidcomponents.com/company/default.asp?SCCC=SCCIG82BO&Lang=44

&ClickLog=logo

[2] RAIN experiment SED

Document ID: RX1112-RAIN-v3.0-7September11.pdf

Mission: REXUS 11/12

[3] Dynamic of Solids- a primer

Mårten Olsson

Department of solid mechanics, KTH, march 2012

Estimation of the force on the collar from cable pre-stress

The force from the four extension springs of the ejection system must be balanced by the radial component of the cable force to keep the hatches closed. During launch, some extra loading conditions must be considered, which means that the cable must be pre-stressed to a larger force. The difference between the cable pre-stress and the spring force must be taken by the four stop blocks on the collar. The identified launch loading conditions which can be estimated are:

- Centrifugal force at 4 Hz
- Random vibrations
- Thermal expansion of the cable

Other loading conditions, such as creep and thermal effects on the extension springs cannot easily be estimated.

1. Properties of ejection system

Mass of one FFU: $m_{FFU} := 0.5 \cdot kg$

Mass of hatch: $m_{hatch} := 0.5 \cdot kg$

Mass of rib-ring and extension springs $m_{ribring} := 0.5 \cdot kg$

Diameter of rocket module: $D_{module} := 356 \cdot mm$

Opening diameter: $d_{opening} := 134 \cdot mm$

Spring stiffness of one extension spring: $k_{spring} := 1 \cdot \frac{N}{m}$

Elastic modulus of cable (lower than 210 GPa due to helical coling): $E_{cable} := 170 \cdot GPa$

Cross-section area of cable (2.5 mm diameter 7tr-1x7): $A_{cable} := 4.3 \cdot mm^2$

Spinning frequency: $f_{spin} := 4 \cdot Hz$

Height of hatch fork: $h_{fork} := 15 \cdot mm$

2. Force on collar from centrifugal force

Estimated radius for FFU: $r_{FFU} := \frac{D_{module}}{4}$ $\quad r_{FFU} = 89\,mm$

Estimated radius for hatch: $r_{hatch} := \frac{D_{module}}{2}$ $\quad r_{hatch} = 178\,mm$

Estimated radius for rib-ring: $r_{ribring} := \frac{D_{module}}{4}$ $\quad r_{ribring} = 89\,mm$

Force on collar from centrifugal force:

$$F_{collar.centri} := \left(m_{FFU} \cdot r_{FFU} + m_{hatch} \cdot r_{hatch} + m_{ribring} \cdot r_{ribring}\right) \cdot \left(2 \cdot \pi \cdot f_{spin}\right)^2$$

$$F_{collar.centri} = 112\,N$$

3. Force on collar from random vibrations

The force created by the random vibration is computed via the Miles equation assuming that the ejection spring and cable provide the stiffness for a single degree-of-freedom system in the radial direction:

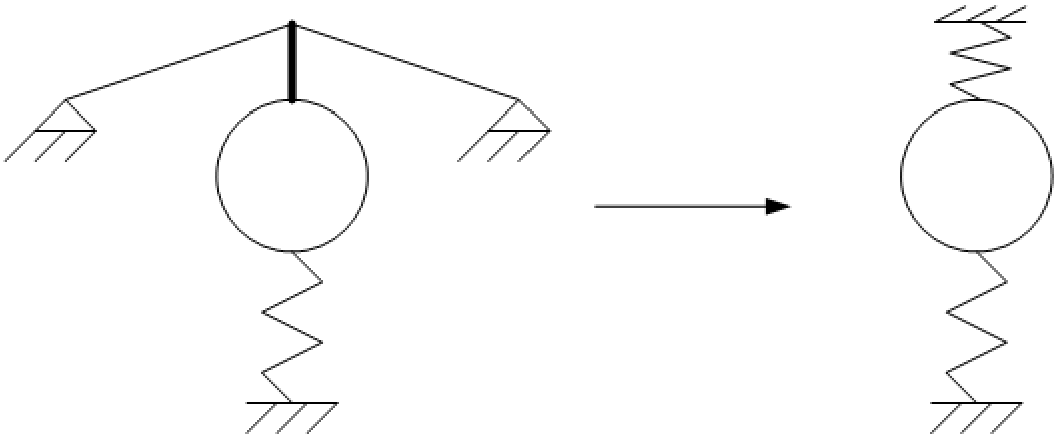

It is assumed that the friction between the cable and the rocket cylinder prevents any cable elongation for the cable part between the openings. Hence, only the cable part over the opening is used to calculate the equivalent spring stiffness in the radial direction:

Stiffness of four extension springs

$k_{springs} := 4 \cdot 2570 \cdot \frac{N}{m}$ $\qquad k_{springs} = 10.28 \, \frac{kN}{m}$

Total force from four springs: $\quad F_{springs} := 4 \cdot 23 \cdot N + k_{springs} \cdot (0.105 \cdot m - 0.060 \cdot m)$ $\qquad F_{springs} = 555 \, N$

Length of cable from opening to fork:

$$L_c := \sqrt{\left(\frac{d_{opening}}{2}\right)^2 + h_{fork}^2} \qquad L_c = 68.659 \, mm$$

Angle of cable over the hatch fork

$$\beta := \operatorname{atan}\left(\frac{2 \cdot h_{fork}}{d_{opening}}\right) \qquad \beta = 12.619 \, deg$$

Equivalent spring stiffness for cable (including only the material stiffness and thus neglecting the stress stiffness due to prestressing):

$$k_{cable} := 2 \cdot \frac{E_{cable} \cdot A_{cable}}{L_c} \cdot (\sin(\beta))^2 \qquad k_{cable} = 1.016 \, \frac{MN}{m}$$

Eigenfrequency of SDOF system: $f_{SDOF} := \frac{1}{2\cdot\pi}\cdot\sqrt{\frac{k_{springs} + k_{cable}}{m_{FFU} + m_{hatch} + m_{ribring}}}$ $f_{SDOF} = 132\,Hz$

Damping amplification factor in Mile's equation: $\gamma := 10$

Power spectral density for REXUS rocket: $W_f := 0.018\cdot g^2\cdot\frac{1}{Hz}$ $W_f = 1.731\,\frac{m^2}{s^3}$

3-sigma equivalent static acceleration according to Mile's equation: $g_{Miles} := 3\cdot\sqrt{\frac{\pi}{2}\cdot f_{SDOF}\cdot\gamma\cdot W_f}$ $g_{Miles} = 179.506\,\frac{m}{s^2}$

Force on collar from random vibrations:

$F_{collar.randvib} := \left(m_{FFU} + m_{hatch} + m_{ribring}\right)\cdot g_{Miles}$ $F_{collar.randvib} = 269\,N$

4. Force on collar from prestress to counteract thermal expansion

The assumption here is that the cable elongation due to heating should NOT lead to hatch opening at a given temperature difference. Here the maximum temperature is +120 C.

Maximum temperature (Celsius): $T_{max} := 120$ Minimum temperature (Celsius) i.e., assembly temperature: $T_{min} := 20$

Coefficient of thermal expansion for cable (m/m Celius): $CTE_{cable} := 16\cdot 10^{-6}$

Total thermal strain in cable: $\varepsilon_{thermal} := CTE_{cable}\cdot\left(T_{max} - T_{min}\right)$ $\varepsilon_{thermal} = 1.6\times 10^{-3}$

Required pre-stress to remove the effects of thermal strain = no opening of hatches:

$F_{cable.thermal} := E_{cable}\cdot A_{cable}\cdot\varepsilon_{thermal}$ $F_{cable.thermal} = 1.17\,kN$

Force on collar from thermal prestress:

$F_{collar.thermal} := 2\cdot F_{cable.thermal}\cdot\sin(\beta)$ $F_{collar.thermal} = 511\,N$

5. Total force on the collar and required prestress of the cable

The radial force on the cable due to centrifugal forces, random vibrations and thermal elongation of the cable has been estimated. To take into account creep and thermal effects of the extension springs, the total force is increased by 10% percent, giving the total estimated force on the collars as:

$$F_{collar.tot} := 1.10 \cdot \left(F_{collar.centri} + F_{collar.randvib} + F_{collar.thermal}\right) \qquad F_{collar.tot} = 0.98\,\mathrm{kN}$$

$$F_{collar.tot} = 100\,\mathrm{kgf}$$

The force in the cable which equilibrate the force from the springs is

$$F_{cable.springs} := \frac{F_{springs}}{2 \cdot \sin(\beta)} \qquad F_{cable.springs} = 1.269\,\mathrm{kN}$$

The additional pre-stress force in the cable to counteract the launch effects (equilibrated by the collar before launch):

$$F_{cable.launch} := \frac{F_{collar.tot}}{2 \cdot \sin(\beta)} \qquad F_{cable.launch} = 2.25\,\mathrm{kN}$$

$$F_{cable.launch} = 229\,\mathrm{kgf}$$

Total force in cable before launch

$$F_{cable.tot} := F_{cable.springs} + F_{cable.launch} \qquad F_{cable.tot} = 3.52\,\mathrm{kN}$$

$$F_{cable.tot} = 359\,\mathrm{kgf}$$

Minimum breaking load for cable: $F_{cable.breaking} := 6.77 \cdot \mathrm{kN}$

Factor of Safety Cable $\quad FOS_{cable} := \dfrac{F_{cable.breaking}}{F_{cable.tot}} \qquad FOS_{cable} = 1.93$

A cable factor of safety of around 2 seems acceptable considering that the cable has full strength up until +150 C.

The required Ultimate Factor of Safety (FOSU) and the Yield Factor of Safety (FOSY) for the Design Limit Load according to the "*European Cooperation for Space Standardization (ECSS), Space engineering: structural factors of safety for spaceflight hardware, ECSS-E-ST-32-10C, 6 March 2009.*" are

Ultimate Factor of Safety: $FOSU := 1.25$

Yield Factor of Safety: $FOSY := 1.10$

for satellites and launch vehicles according to Table 4.3 in ECSS-E-ST-32-10C.

One can compute a higher FOSU taking into account the uncertainties in the design using all the various design factors:

Local design factor: $K_{LD} := 1.2$ (according to 4.1.5.2b)

Margin policy factor: $K_{MP} := 1.1$ (10% marging assumed, see 4.1.5.3)

Model factor: $K_{M} := 1.2$ (according to 4.1.4.2b)

Project factor: $K_{P} := 1.0$ (not relevant according to 4.1.4.3)

Qualification test factor: $K_{Q} := 1.25$ (applied only for satellites according to 4.1.4.4)

$$FOSU := K_{LD} \cdot K_{MP} \cdot K_{M} \cdot K_{P} \cdot K_{Q} \qquad FOSU = 1.98$$

Thus, having a Factor of Safety around 2 indicates a safe design according to ECSS

5. Checking the capacity of the collars

The total force on one collar is: $F_{collar.tot} = 0.98\,kN$

The four stop blocks on the collar will be subjected to shear loads. The capacity of a rectangular section with width b and heigh h is:

$$F_{shear} = \frac{f_{02}}{\sqrt{3}} \cdot b \cdot h$$

Assuming aluminium 6061-T6, with a yield strength of 245 MPa,

$$f_{02.6061T6} := 245 \cdot MPa$$

the required cross-section area of one collar stop block is:

$$A_{req.collar.stop.block} := \frac{F_{collar.tot}}{4 \cdot \left(\frac{f_{02.6061T6}}{1.1 \cdot 1.2 \cdot \sqrt{3}} \right)} \qquad A_{req.collar.stop.block} = 2.29\,mm^2$$

Thus, a aluminium stop block of size 1 mm x 4 mm has sufficient capacity for the pre-stress force on the collars.

Cable analysis for the ejection system

Emilio J. Lozano

September 23, 2012

Nomenclature

T_c=Cable tension

$F_{4springs}$ =Force of extended set of springs.

β=Cable kink angle at the support

α=Half of the angular sector covered by the openings

D =Module diameter

d=Opening diameter

b= Distance from the hatch end to the idealized support point.

MBF = Minimum breaking force

SF = Safety factor

E = Young modulus

G =Shear modulus

ν = Poisson's ratio

CTE = Coefficient of thermal expansion

A_c =Area of the cable

L_c =Length of the cable

ΔL_c =Variation of the length of the cable

t_i = Temperature for the different calculations of the elongation

m_x =Mass of component x

r_x = Distance from the axis of rotation of component x

f_{SDOF} =Natural frequency of the single degree os freedom system

γ =Amplification factor of the Miles equation

W_f =Power spectra density

1. Introduction

The aim of this analysis is to calculate the required tension in the cable in the ejection system. In the case of the selection of the cable dimension the safety margin has been set to 2 at 150 °C. The cable properties have been provided by CERTEX [1]. This analysis was performed to obtain the maximum elongation of the cable under the worst load case.

The approach for the analysis is to assume that the length of the cable is such that the cable goes around the entire module plus a 10% of that length inside the module until the clamping mechanism. The tension can be derived analysing only one of the hatches by equilibrium of forces assuming that there is only one contact point. Furthermore, it is assumed that the bending stiffness of the cable is negligible and the cable will take only tension loads.

2. Tension and elongation estimation.

The springs selected for the ejection system of the FFUs, SF-DF-SS1774-04 3504, create a resultant force of 555 N when they are completely loaded. This resultant force will have to be equlibrated by the cable at the hatch support. In order to make a conservative estimation of the tension present in the cable a point support is assumed. The point support is a more critical configuration than the actual design solution of the hatches where a continuous support is used. In the case of continuous support at the hatches the load will be transfer to the cable in a bigger area avoiding stress concentrations.

The mechanical layout of the MUSCAT experiment includes 4 openings as it can be seen in Figure 1

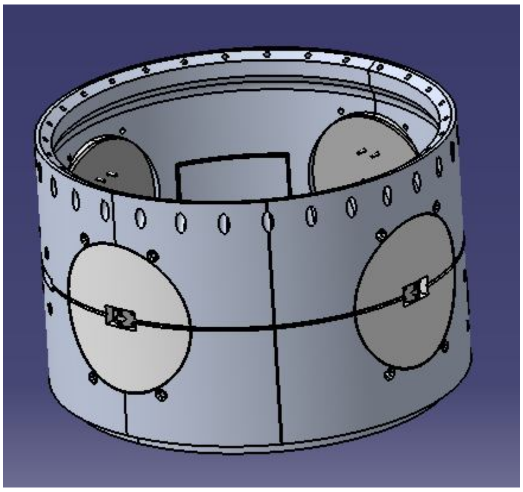

Figure 1, Muscat rocket cylinder.

The objective of this analysis goes through the groove that can be seen in Figure 1 and the through the groove at the hatches. The ends of the cable are attached to an internal hook in one end and it is clamped with a set of ruffled plates in the other after going around the external perimeter. The attachment to the hook includes a temperature resistant ferrule and a splice in stainless steel [1] Figure 2. This kind of configuration for the end attached is considered to have 90% of the cable load capacity [2].

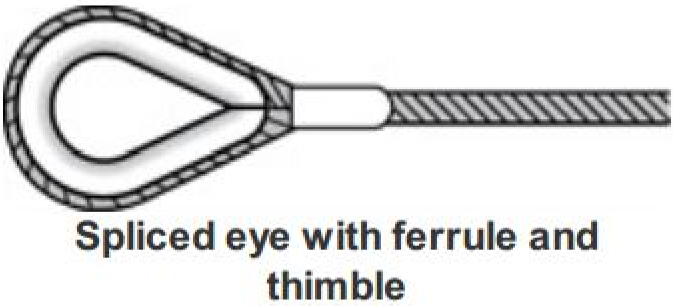

Figure 2, Configuration of the end attached to the hook.

However, the configuration of four identical hatches with four identical sets of spring and only one continuous cable, allows that analysis of only one hatch is required in order to derive the tension present in the cable. The mentioned configuration can be seen in Figure 3. Therefore, the equilibrium problem that has to be solved is the problem sketched in Figure 4.

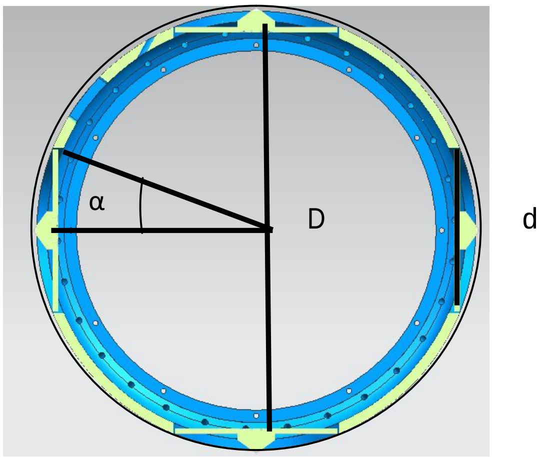

Figure 3, Section showing the configuration to analyze.

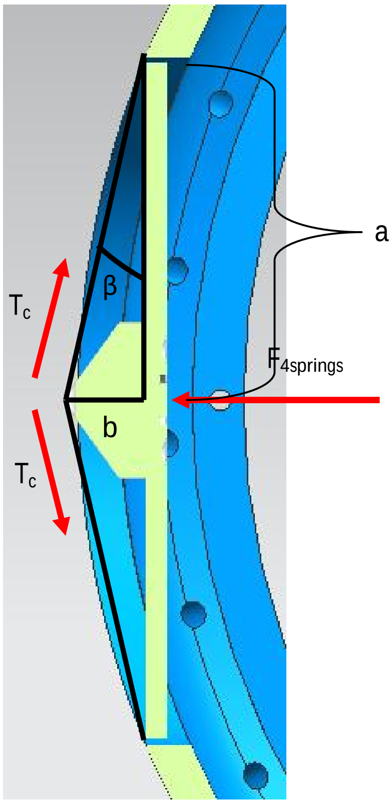

Figure 4, Sketch of the radial equilibrium.

The geometrical variables presented in Figure 3 and Figure 5 can be defined as follows:

D = 356 mm

d=134 mm

$a = \frac{d}{2} = 67$ mm

b = 15 mm (Obtained from the CAD model)

$\alpha = \sin^{-1}\frac{d}{D} = 22.11\ deg$

$\beta = \tan^{-1}\beta = \tan^{-1}\frac{b}{a} = 12.61\ deg$

After defining the geometrical variables the force equilibrium between the tension present in the cable (T_c) and the resultant force coming from the set of springs ($F_{4springs}$=555 N) can be stated as can be seen in Equation (1)

$$2T_c \sin\beta = F_{4springs} \tag{1}$$

Deriving from (1) the tension in the cable, the result of the tension present in the can be obtained as it can be seen in Equation (2)

$$T_c = \frac{F_{4springs}}{2\sin\beta} = 1271 \text{ N} \tag{2}$$

In order to determine the cable pre-tension so that the hatches do not open, there are other three loading conditions that should be added to the value derived in (2). These load conditions are:

- The centrifugal forced caused by the spinning of the rocket.

-The random vibrations induced by the launch.

-Pre-stressing tension that should absorb the effect of the possible thermal expansion.

-The centrifugal force (F_{centr}) can be computed according to Equation (3)

$$F_{centr} = (m_{FFU} \times r_{FFU} + m_{cage} \times r_{cage} + m_{hatch} \times r_{hatch}) \times (2\pi \times f_{spin})^2 \tag{3}$$

$$F_{centr} = (0.5 \times r_{FFU} + 0.5 \times r_{cage} + 0.5 \times r_{hatch}) \times (2\pi \times f_{spin})^2$$

$$F_{centr} = 112 \text{ N}$$

This force from the centrifugal force transmits to the cable 256N by analogy with (2).

-The equivalent static acceleration from the random vibrations is computed by means of Miles equation [6]. In order to apply the Miles equation to this case, it is assumed that the assembly of the FFU, hatch and cage is a system with one degree of freedom. The Miles equation is used then to compute the acceleration induced by the random vibrations as follows.

$$g_{Miles} = \sqrt{\frac{\pi}{2} f_{SDOF} \gamma W_f} \quad (4)$$

Where f_{SDOF} is the natural frequency of the system and it can be computed as show in (5)

$$f_{SDOF} = \frac{1}{2\pi}\sqrt{\frac{k_{springs}+k_{cable}}{m_{FFU}+m_{hatch}+m_{cage}}} = \frac{1}{2\pi}\sqrt{\frac{10280+1016000}{0.5+0.5+0.5}} = 132\text{ Hz} \quad (5)$$

$W_f = 1.731\frac{m^2}{s^3}$ and$\gamma = 10$, with all these inputs the acceleration computed by the Miles equation is $g_{Miles} = 179.8\frac{m}{s^2}$. This acceleration is used together with the mass of the system to compute the resultant forced that it will be transmitted to the cable according to (6).

$$F_{centr} = (m_{FFU} + m_{cage} + m_{hatch}) \times g_{Miles} = 269\text{N}$$

This force from the random vibration transmits to the cable 616N by analogy with (2).

-The tension required to absorb the effect of the thermal expansion can be computed as follows. The thermal strain of the cable can be computed by Equation (6)

$$\epsilon_{thermal} = CTE_{cable}(T_{max} - T_{\min}) \quad (6)$$

where $CTE_{cable} = 16 \times 16^{-6}\frac{1}{K}$, $T_{max} = 100°C$ and $T_{\min} = 20°C$ (temperature when thecable tensioned). With all these parameters $\epsilon_{thermal} = 1.6 \times 10^{-3}m$. With the known strain the tension needed in the cable can be computed according to Equation (7)

$$F_{Thermal\,T} = \epsilon_{thermal}\ A_{cable}\, E_{cable} \quad (7)$$

The result obtained from is 1.17kN as required tension to absorb the expansion caused by the variation of temperature.

Summing up all the forces, the resultant tension that should be pre-stressed in the cable is 3.3kN.

According to [3] the stainless steel cable SS1x7 with a 2.5 mm diameter has minimum breaking force of 6.77 kN. The safety factor when this cable is used under the loading conditions above is

$$\text{SF} = \frac{\text{MBF}}{T_c} = \frac{6.7}{3.3} = 2 \quad (8)$$

The cable SS1x7 with steel core is shown in Figure 5

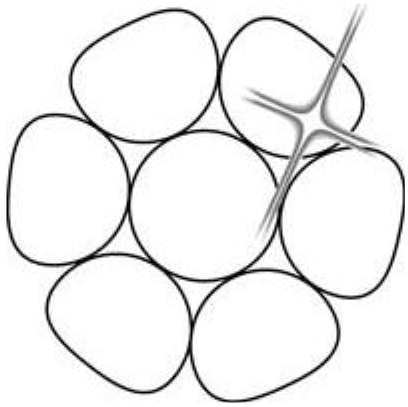

Figure 5, Layout of the fibres of the cable SS1x7 compacted Ø=2.5 mm

According to [1] the evolution of the strength of the cable with temperature follows the values indicated in Table 1

Temperature range (°C)	Decreasing factor	MBF(kN)	SF
- 40 to 100	1	6.77	2
101 to 150	1	6.77	2
151 to 200	0.9	6.09	1.8
201 to 300	0.75	5.08	1.5
301 to 400	0.65	4.4	1.3

Table 1, evolution of the SF and MBF with the temperature of the cable SS1x7 compacted Ø=2.5 mm

Furthermore, the materials used in the manufacturing of the cable according to [3] is stainless steel 316S31. This material according to reference [4], has the mechanical properties that can be seen in Table 2

Stainless Steel 316S31	
E	200 GPa
G	77 Gpa
ν	0.25
CTE(100°C)	16.0 µm/m°C
CTE(315°C)	16.2 µm/m°C
CTE(540°C)	17.5 µm/m°C

Table 2, mechanical properties of stainless steel 316S31

The evolution of the Young's modulus in [5] with the similar stainless alloy 316L can be used to predict the behaviour at different temperatures of the stainless steel alloy 316S31 because the composition of the alloy is almost the same and the safety margins are large enough to absorb small deviations. The evolution of the young modulus of the stainless steel 316L can be seen in Table 3

T(°C)	20	100	200	300	400	500
E(GPa)	200	194	185	177	169	160

Table 3, evolution of the young modulus of stainless steel 316L

3. Conclusion

The conclusions that can be drawn from this analysis are mainly related to two aspects. The first aspect is the strength of the cable, with the conclusions that the selected cable has sufficient strength to stand the launch loads. The safety margin is inside the limits marker by ECSS[7] until temperatures of 500 °C.

The second is the elongation of the cable. With a pre-tension of 3.3 N the elongation is negligible.

References

[1] CERTEX

http://www.certex.se/uk/teknisk-beskrivning/anvandning-i-ogynnsam-miljo__10836

[2] CERTEX

http://www.certex.se/uk/teknisk-beskrivning/andbeslag__14820

[3] CERTEX

http://www.certex.se/uk/rostfria-linor/stallina-rfr-1x1919-tr__2916

[4] Matweb

http://matweb.com/search/DataSheet.aspx?MatGUID=5edc39d3b0fd44efa9fdd90d049c3737&ckck=1

http://matweb.com/search/datasheet.aspx?MatGUID=3a413dabd215462da3408e6e8b761349

[5] Parr Instrument Company- Technical notes

http://www.parrinst.com/

http://www.parrinst.com/wp-content/uploads/downloads/2011/07/Parr_High-Performance-Stainless-Steels-Corrosion-Info.pdf

[6] Random vibrations in Spacecraft Structures design: Theory and Applications.

Wijker, Jaap

2009

SBN: 978-90-481-2727-6

E-ISBN: 978-90-481-2728-3

[7] European cooperation for space standardization.

ECSS-E-30

Part 2A

25 April 2000

Appendix C

Mechanical Components

This appendix contains a complete parts list of the MUSCAT experiment and technical drawings of all custom-made parts.

MUSCAT Universal Parts List

ID	Description	Status	Quantity in one RMU assembly	Quantity to be ordered/produced	Supplier/Manufacturer	Material	Expected delivery date	Delivery confirmation status	Material density kg/m^3	Volume of the CAD model, m^3	Part mass estimated using CAD, g	Collective part mass estimated using CAD, g	Notes
1.00.00.00	**FFU**		4	6	MUSCAT								
1.01.00.00	**Lower Hemisphere**		4	8									
1.01.00.01	Lower Hemisphere Shell	Arrived	4	8	SPP Workshop	Glass Fiber/Epoxy composite	10.1.12						
1.01.01.01	Internal Metal Ring	Arrived	4	10	Mixtrum	Aluminium 6082	03.29.12	Confirmed	2700		24		
1.01.01.02	External Metal Ring	Arrived	4	15	Mixtrum	Aluminium 6082	03.29.12	Confirmed	2700		18		
1.01.01.03	FFU Top PCB	Being soldered	4	10	MultiCAD AB		04.05.12	Confirmed					
1.01.01.04	FFU Bottom PCB	Being soldered	4	10	MultiCAD AB		03.30.12	Confirmed					
1.01.01.05	Battery cage	In production	4	8	SPP Workshop	Aluminium 6082	09.28.12		2700				
1.01.02.00	**Recovery System**		4										
1.01.02.01	Cross Parachute	Arrived	4	4	Top Flight Recovery LLC		02.15.12	Confirmed					Thin Mill Xform Chute Size 30" (XTPAR- 30TM)
1.01.02.02	Parachute String	Arrived	4		LIROS Ropes		04.15.12	Confirmed					LIROS DSL 350, 2mm
1.01.02.03	Eyebolt	Arrived	16	40	Oscarssons	Stainless Steel 7346	03.23.12	Confirmed	7850				
1.01.02.04	Fishing Line	Arrived	4										
1.01.03.00	**Thermal Cutter**		4										
1.01.03.01	Thermal Cutter Base	Designed	4	10	SPP Workshop	Aluminium 1050	03.28.12	TBC		59*10^-9	0.16		
1.01.03.02	Thermal Cutter Isolation	Arrived	4	8	SPP Workshop		03.28.12	TBC					
1.01.03.03	Thermal Cutter Wire Mount	Arrived	8	11	SPP Workshop	Copper	03.28.12	TBC					
1.01.04.00	**Winch**		4										
1.01.04.01	Winch Rotor	Arrived	4	12	SPP Workshop	Aluminium 6082			2700	638*10^-9	1.7		
1.01.04.02	Winch Base	Arrived	4	8	EKAB	Aluminium 6082	10.19.12		2700	288*10^-9	0.8		
1.02.00.00	**Upper Hemisphere**		4	6									
1.02.00.01	Upper Hemisphere Shell	Arrived	4	10	SPP Workshop	Glass Fiber/Epoxy composite	10.1.12						
1.02.00.02	Rib Ring	Arrived	4	8									
2.00.00.00	**RMU**		1	1									
2.01.00.01	Rocket Cylinder	In production	1	1	DLR	Aluminium 7075 T6			2700	478649*10^-9	5445		
2.01.00.02	RMU PCB	Designed	1	2									
2.02.00.00	**Ejector Module**		1	1									
2.02.01.00	**Rail System**		1	1									
2.02.01.11	Upper Cross 1	Arrived	1	1	SPP Workshop	Aluminium 6082	09.28.12						
2.02.01.12	Upper Cross 2	Arrived	1	1	SPP Workshop	Aluminium 6082	09.28.12						
2.02.01.13	Lower Cross	Arrived	1	1	Mixtrum	Aluminium 6082	09.19.12						
2.02.01.02	Collar	Arrived	4	6	Mixtrum	Aluminium 6082	08.10.12	Confirmed		36164*10^-9	97,643		
2.02.02.00	**FFU Cage**		4	6									
2.02.02.01	Inner Ring	Arrived	4	6	EKAB	Aluminium 6082	07.20.12	Confirmed		2117*10^-9	57,016		
2.02.02.02	Outer Ring	Arrived	4	6	EKAB	Aluminium 6082	07.20.12	Confirmed		11813*10^-9	31,896		
2.02.02.03	Rib	Arrived	16	20	EKAB	Aluminium 6082	07.20.12	Confirmed		1894*10^-9	7,815		
2.02.02.04	Slider	Arrived	8	20	EKAB	Teflon	07.20.12	Confirmed		1320*10^-9	6,063		
2.02.02.05	Spring	Arrived	16	20	Lesjöfors	Steel				4414*10^-9	34.65		SF-DF-3504 Lesjofors
2.02.02.06	Hook Bracket	Arrived	4	5	SPP Workshop	Aluminium 6082							
2.03.00.00	**Pyrocutter Assembly**		1	1									
2.03.00.01	Pyrocutter	Decided	2	2									TRW
2.03.00.02	Pyrocutter Bracket	Arrived	1	1	Hagal Machinery	SS304				56832*10^-9	153,447		
2.03.00.03	Ruffled Steel Plate 1	Arrived	1	1	SPP Workshop	Steel				10980*10^-9	29.65		
2.03.00.04	Ruffled Steel Plate 2	Arrived	1	1	SPP Workshop	Steel				6274*10^-9	16.941		
2.03.00.05	Cable Guide	Arrived	1	1	EKAB	SS304	10.19.12			3737*10^-9	29.41		
2.03.00.06	Cable Guide Cover	Arrived	1	1	EKAB	SS304	10.19.12						
2.03.00.07	Sleeve	Arrived	1	1	SPP Workshop	Steel							
2.04.00.00	**Camera Module**		1	1									
2.04.00.01	Camera	Arrived	1	1									
2.04.00.02	Camera Box	Designed	1	1	SPP Workshop	Aluminium 6082							
2.04.00.03	Camera Lid	In production	1	1	SPP Workshop	Aluminium 6082							
2.04.00.04	Camera Ring	Designed	1	1	SPP Workshop	Aluminium 6082							
2.04.00.05	Camera Collar	Designed	1	1	SPP Workshop	Aluminium 6082							
2.05.00.00	**Hatch Assembly**		4										
2.05.00.01	Hatch	Arrived	4	4	SPP Workshop	Aluminium 6082				54262*10^-9	152.48		
2.05.00.02	Triangular Fork	Arrived	4	4	SPP Workshop	Aluminium 6082				4441*10^-9	11.99		
2.05.00.03	Cork	In production	4	4	SPP Workshop	Cork							
2.06.00.00	**Safety Assembly**		1	1									
2.06.00.01	Safety Clip	Arrived	4	4	SPP Workshop	Aluminium 6082							
2.06.00.02	Upper Lock Plate	Arrived	1	1	SPP Workshop	Aluminium 6082							
2.06.00.03	Lower Lock Plate	Arrived	1	1	SPP Workshop	Aluminium 6082							
2.06.00.04	Threaded Rod	Arrived	4	4	SPP Workshop	Aluminium 6082							
2.07.00.00	**Umbilical Assembly**												
2.07.00.01	Center Piece 1	Arrived	1	1	SPP Workshop	Aluminium 6082	09.19.12						
2.07.00.02	Center Piece 2	Arrived	1	1	SPP Workshop	Aluminium 6082	09.19.12						
2.07.00.03	Umbilical Bracket	Arrived	1	1	SPP Workshop	Aluminium 6082							
2.08.00.00	**Gas Protection**												
2.08.00.01	Upper Cover	In production	1	1	SPP Workshop	Aluminium 6082	09.28.12						
2.08.00.02	Lower Cover	In production	1	1	SPP Workshop	Aluminium 6082	09.28.12						
2.08.00.03	Tunnel Backside	In production	1	1	SPP Workshop	Aluminium 6082	09.28.12						
2.08.00.04	Tunnel Side 1	In production	1	1	SPP Workshop	Aluminium 6082	09.28.12						
2.08.00.05	Tunnel Side 2	In production	1	1	SPP Workshop	Aluminium 6082	09.28.12						
2.08.00.06	Gas Cover Spacer	Arrived	8	8	SPP Workshop	Aluminium 6082							
Not in experiment assembly													
	Mold	Arrived	x	2	Mixtrum		03.28.12	Confirmed					

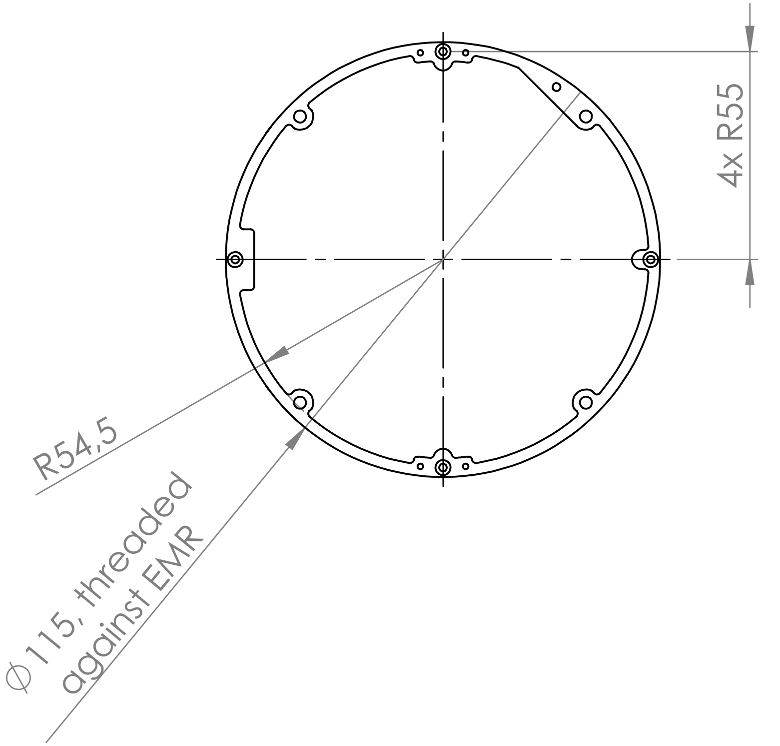

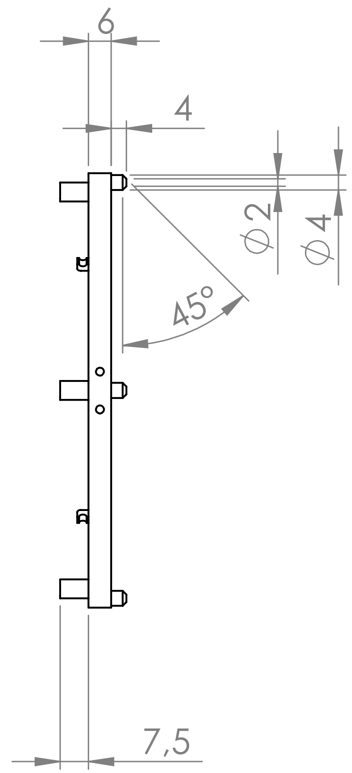

Top surface view

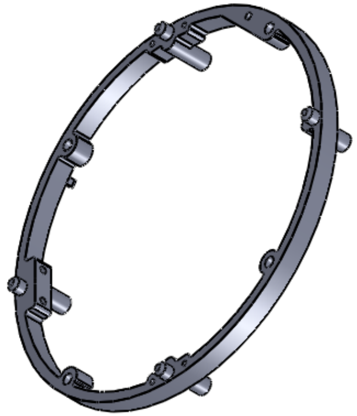

Bottom surface view

UNLESS OTHERWISE SPECIFIED: DIMENSIONS ARE IN MILLIMETERS TOLERANCES: 0.1 mm	FINISH:		DEBUR AND BREAK SHARP EDGES	DO NOT SCALE DRAWING	VERSION	1.0
	NAME	SIGNATURE	DATE	TITLE:		
Design	Marco Tito Bordogna		03.06.12	Internal Metal Ring		
DRAWN	Darri Kristmundsson		03.07.12			
CHK'D						
APPV'D						
			MATERIAL: Aluminium 6082	DWG NO. 1.01.01.01		A4
			WEIGHT:	SCALE:1:2	SHEET 1 OF 4	

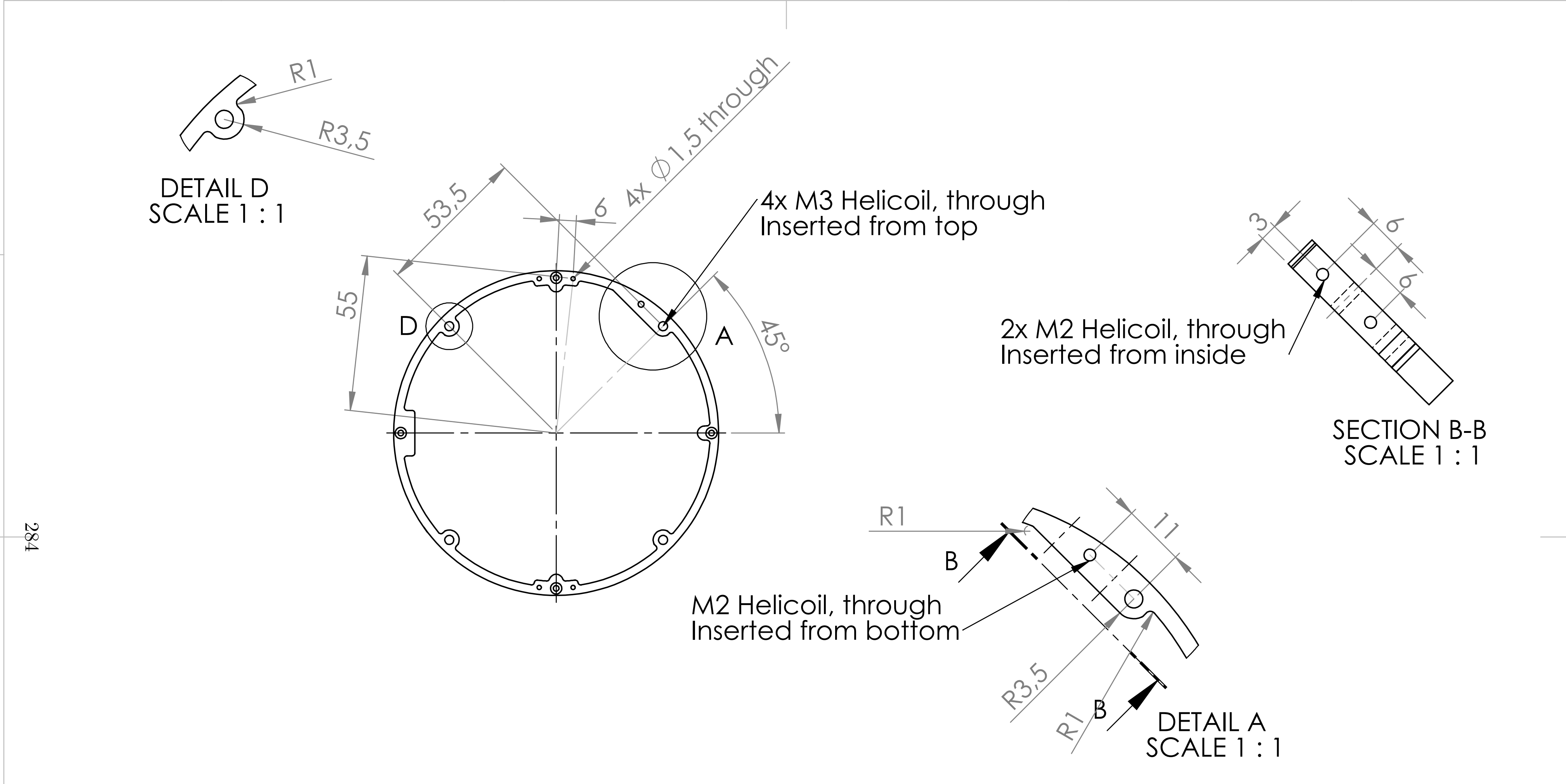

UNLESS OTHERWISE SPECIFIED: DIMENSIONS ARE IN MILLIMETERS TOLERANCES: 0.1 mm	FINISH:	DEBUR AND BREAK SHARP EDGES	DO NOT SCALE DRAWING	VERSION 1.0
			Eyebolt hole details	

	NAME	SIGNATURE	DATE
Design	Marco Tito Bordogna		03.06.12
DRAWN	Darri Kristmundsson		03.06.12
CHK'D			
APPV'D			

TITLE:

Internal Metal Ring

MATERIAL: Aluminium 6082

WEIGHT:

DWG NO. 1.01.01.01

A4

SCALE:1:2

SHEET 2 OF 4

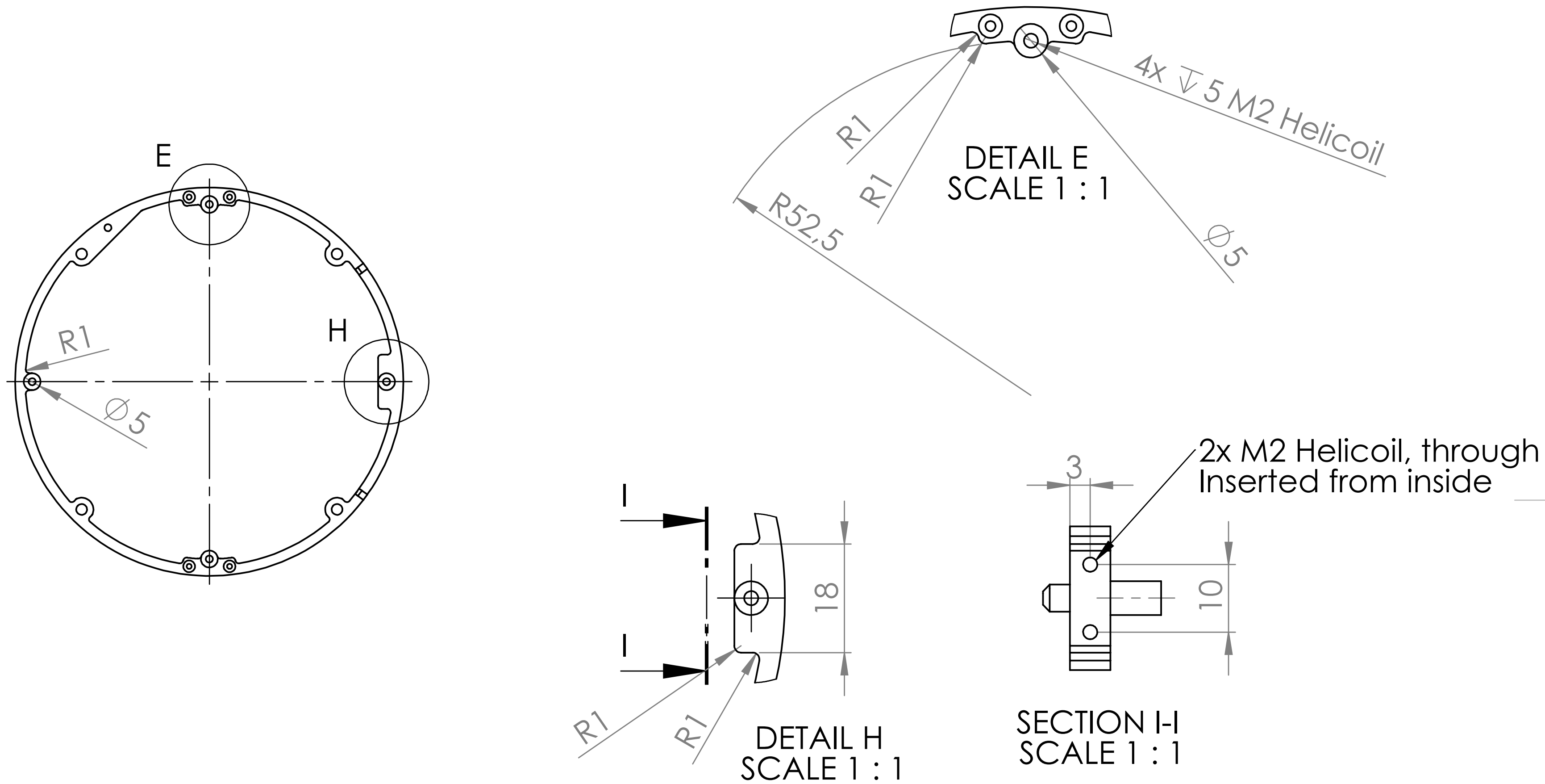

UNLESS OTHERWISE SPECIFIED: DIMENSIONS ARE IN MILLIMETERS TOLERANCES: 0.1 mm	FINISH:	DEBUR AND BREAK SHARP EDGES	DO NOT SCALE DRAWING	VERSION 1.0
			Bottom surface details	

	NAME	SIGNATURE	DATE
Design	Marco Tito Bordogna		03.06.12
DRAWN	Darri Kristmundsson		03.07.12
CHK'D			
APPV'D			

TITLE:

Internal Metal Ring

MATERIAL: Aluminium 6082

DWG NO. 1.01.01.01 | A4

WEIGHT: | SCALE:1:2 | SHEET 3 OF 4

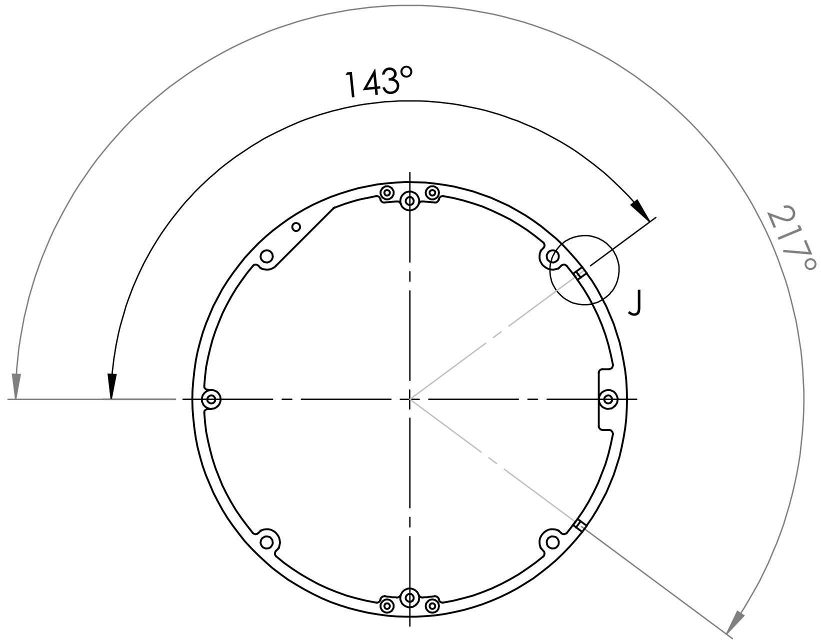

286

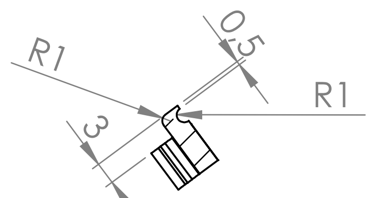

SECTION M-M
SCALE 1 : 1

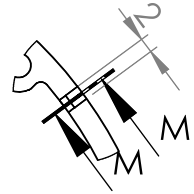

DETAIL J
SCALE 1 : 1

UNLESS OTHERWISE SPECIFIED:
DIMENSIONS ARE IN MILLIMETERS
TOLERANCES:
0.1 mm

FINISH:

DEBUR AND BREAK SHARP EDGES

DO NOT SCALE DRAWING

VERSION 1.0

Hook details

	NAME	SIGNATURE	DATE
Design	Marco Tito Bordogna		03.06.12
DRAWN	Darri Kristmundsson		03.07.12
CHK'D			
APPV'D			

TITLE:

Internal Metal Ring

MATERIAL: Aluminium 6082

WEIGHT:

DWG NO. 1.01.01.01

A4

SCALE:1:2

SHEET 4 OF 4

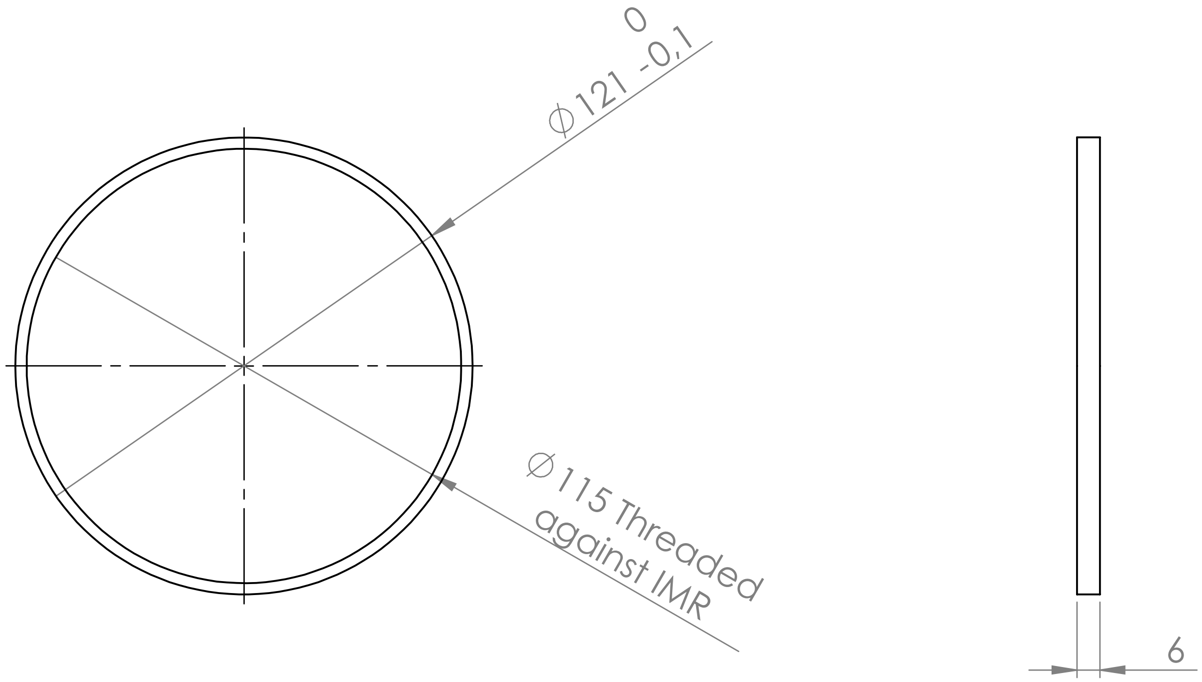

UNLESS OTHERWISE SPECIFIED: DIMENSIONS ARE IN MILLIMETERS TOLERANCES: 0.1 mm	FINISH:	DEBUR AND BREAK SHARP EDGES	DO NOT SCALE DRAWING	VERSION	1.0

	NAME	SIGNATURE	DATE
Design	Marco Tito Bordogna		
DRAWN	Darri Kristmundsson		07.3.12
CHK'D			
APPV'D			

TITLE:

External Metal Ring

MATERIAL: Aluminium 6082

DWG NO. 1.01.01.02 A4

WEIGHT:

SCALE:1:2

SHEET 1 OF 1

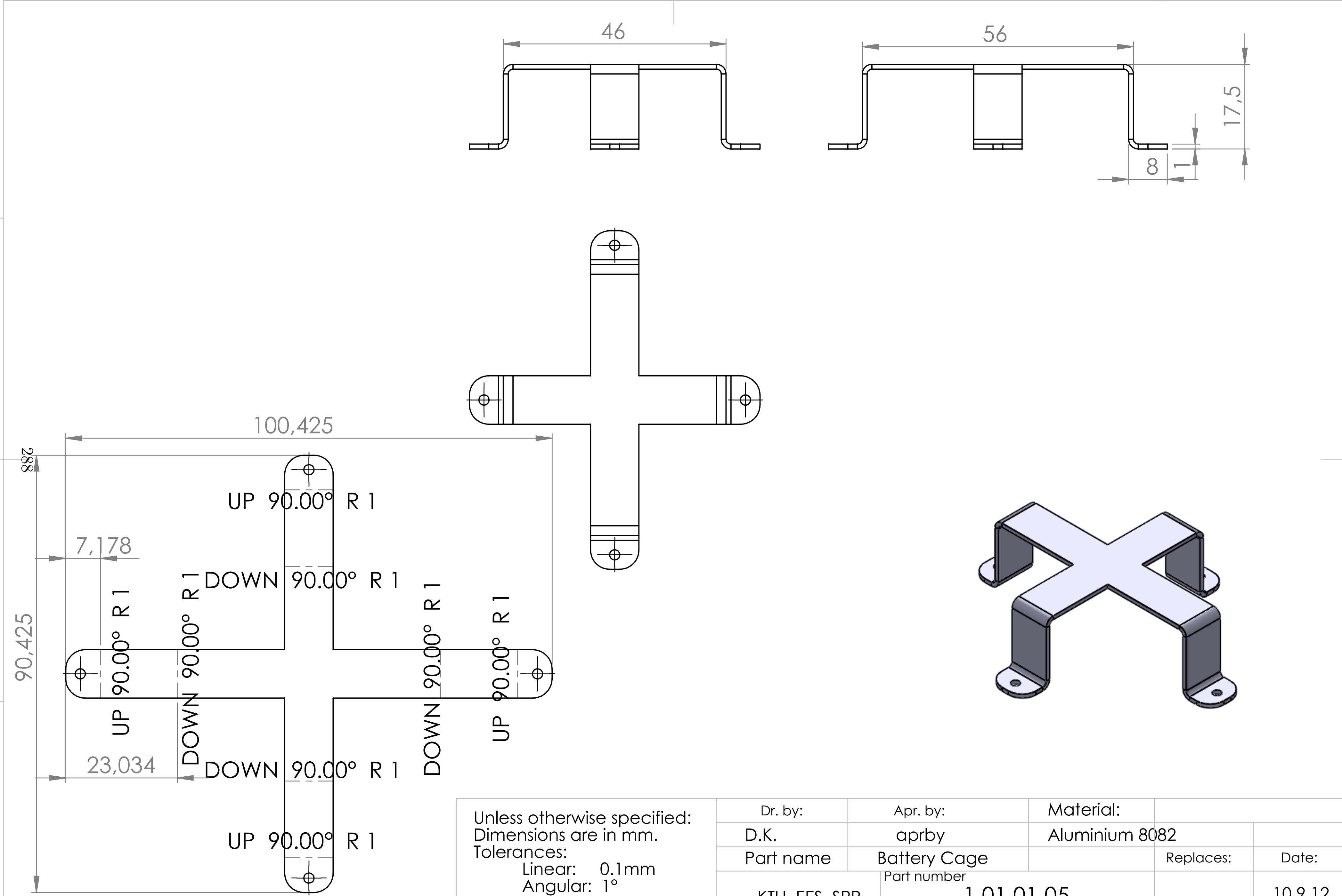

Unless otherwise specified:
Dimensions are in mm.
Tolerances:
Linear: 0.1mm
Angular: 1°

Dr. by:	Apr. by:	Material:		
D.K.	aprby	Aluminium 8082		
Part name	Battery Cage		Replaces:	Date:
KTH, EES, SPP	Part number 1.01.01.05			10.9.12
WEIGHT:	SCALE:1:1		SHEET 1 OF 1	

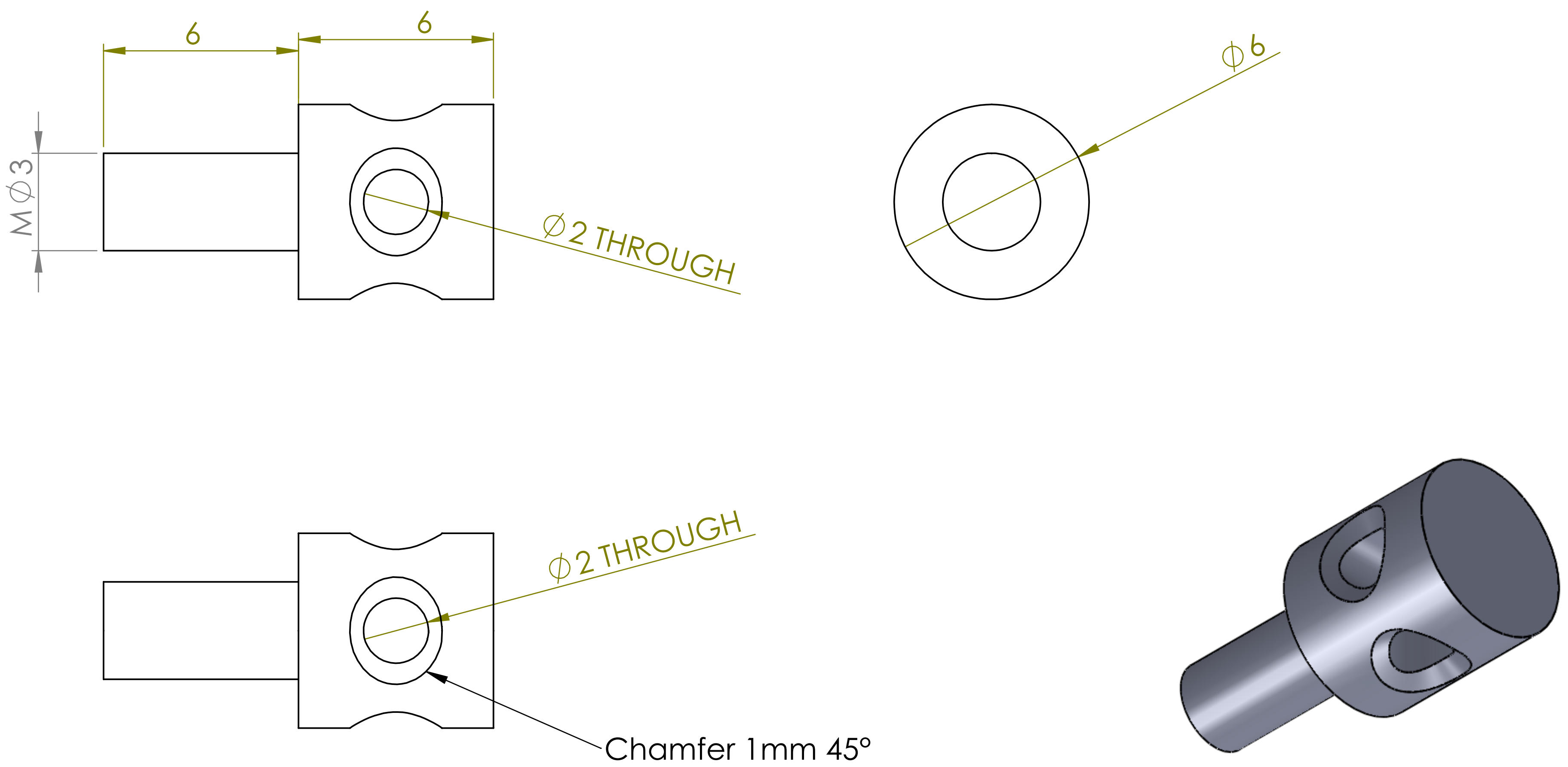

UNLESS OTHERWISE SPECIFIED: DIMENSIONS ARE IN MILLIMETERS TOLERANCES: 0.1 mm	FINISH:		DEBUR AND BREAK SHARP EDGES	DO NOT SCALE DRAWING	VERSION	1.0
	NAME	SIGNATURE	DATE	TITLE:	Eyebolt	
Design	Marco Tito Bordogna		03.06.12			
DRAWN	Darri Kristmundsson		03.07.12			
CHK'D						
APPV'D						
			MATERIAL: Stainless Steel 7346	DWG NO.	1.01.02.03	A4
			WEIGHT:	SCALE:5:1	SHEET 1 OF 1	

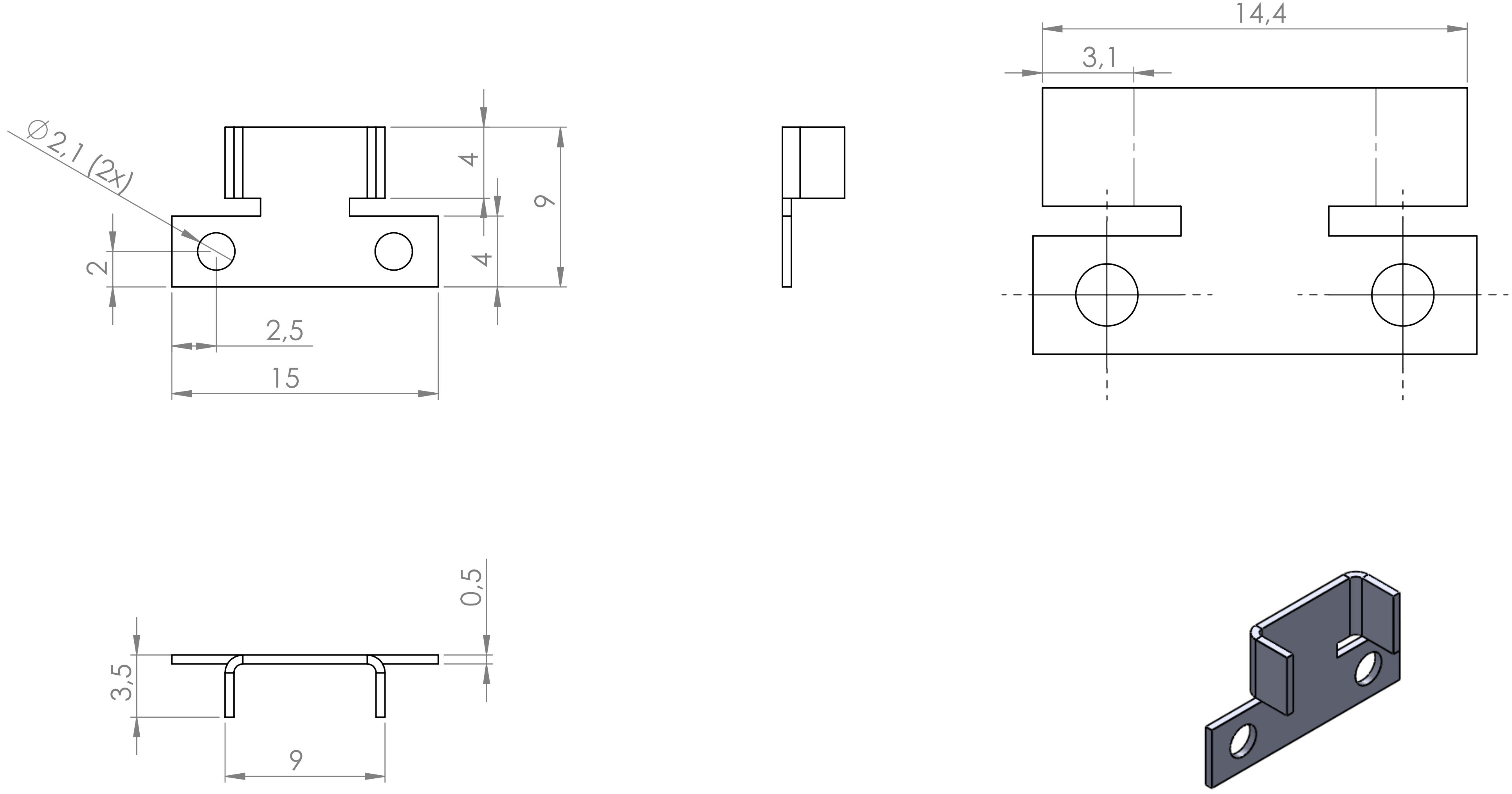

290

Unless otherwise specified:
Dimensions are in mm.
Tolerances:
Linear: 0.1mm
Angular: 1°

Dr. by:	Apr. by:	Material:	
D.K.	aprby	Aluminium 6082	
Part name	Thermal Cutter Base	Replaces:	Date:
KTH, EES, SPP	Part number 1.01.03.01		6.12.12

WEIGHT: SCALE:5:1 SHEET 1 OF 1

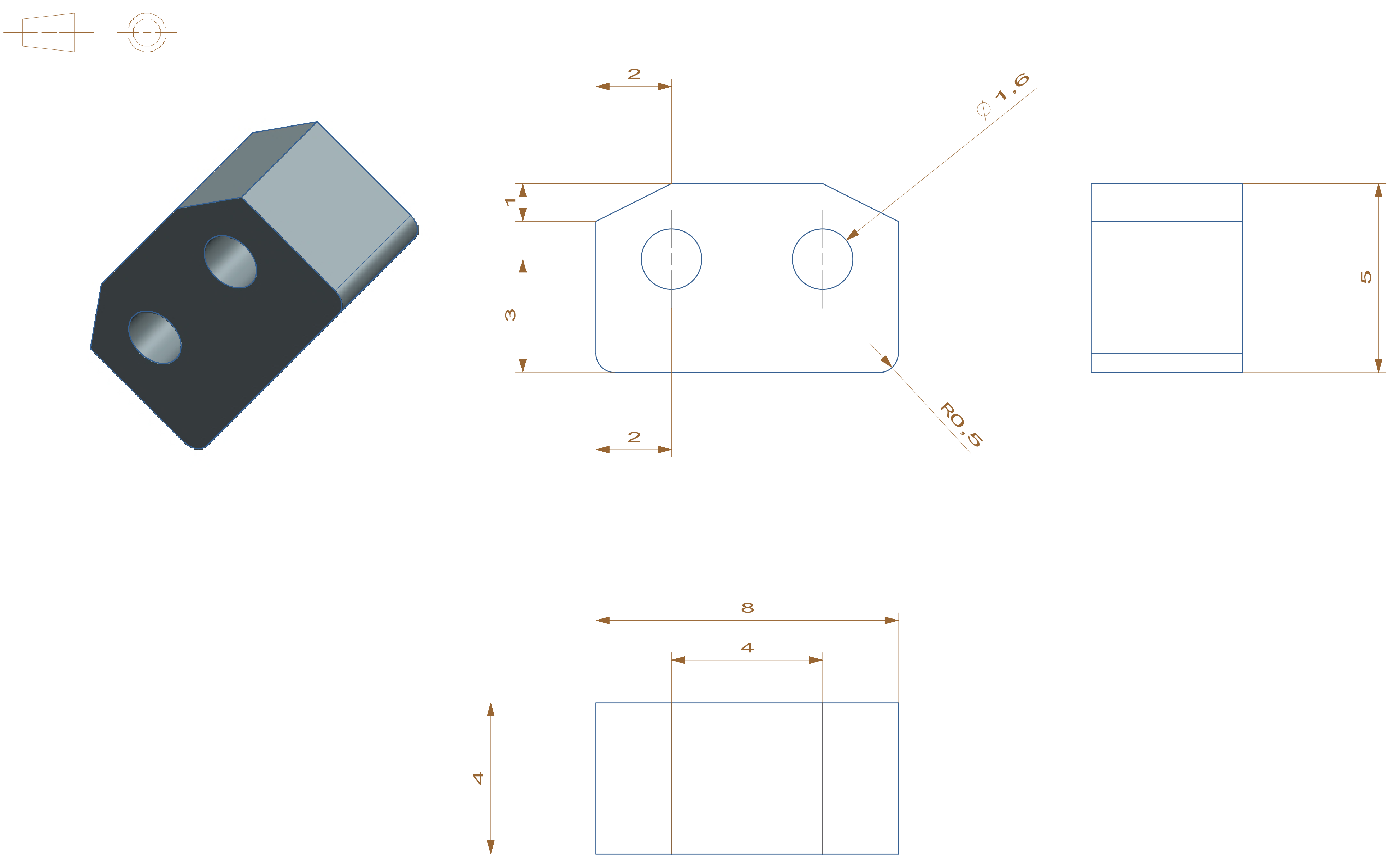

		1.01.03.02 Thermal Cutter Isolation		PVC			
Det.no.	No. of	Part name		Material		Remarks	
Designer: Bordogna	Dr. by: Bordogna		Ck. by: D.K.		Apr. by: D.K.	Replaces:	Replaced by:
KTH, EES, SPP							Date: 20120509
						Dwg no: 1.01.03.02	

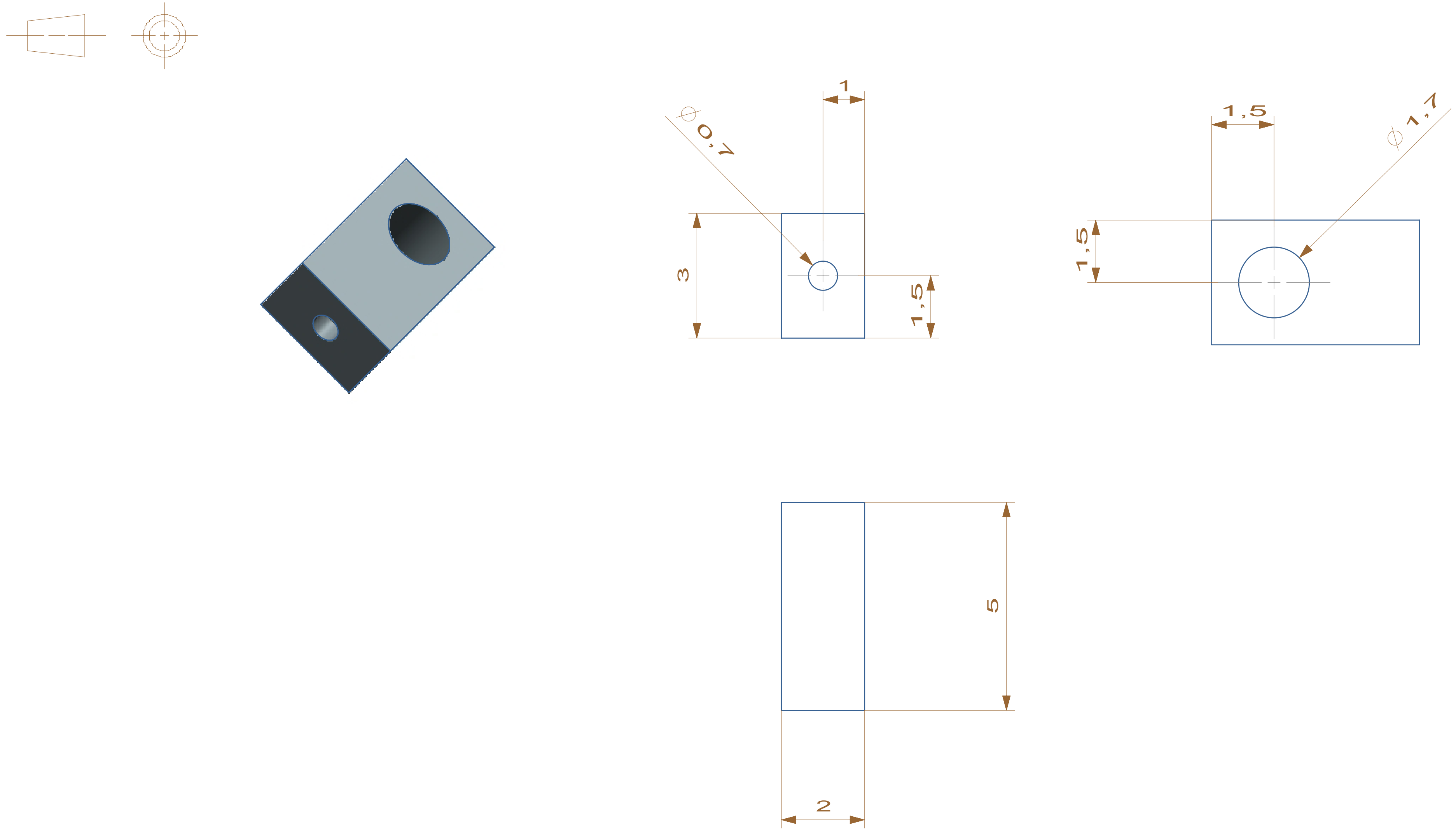

		1.01.03.03 Thermal Cutter Wire Mount	Copper			
Det.no.	No. of	Part name	Material		Remarks	
Designer: Bordogna	Dr. by: Bordogna	Ck. by: D.K.	Apr. by: D.K.		Replaces:	Replaced by:
KTH, EES, SPP						Date: 20120509
					Dwg no: 1.01.03.03	

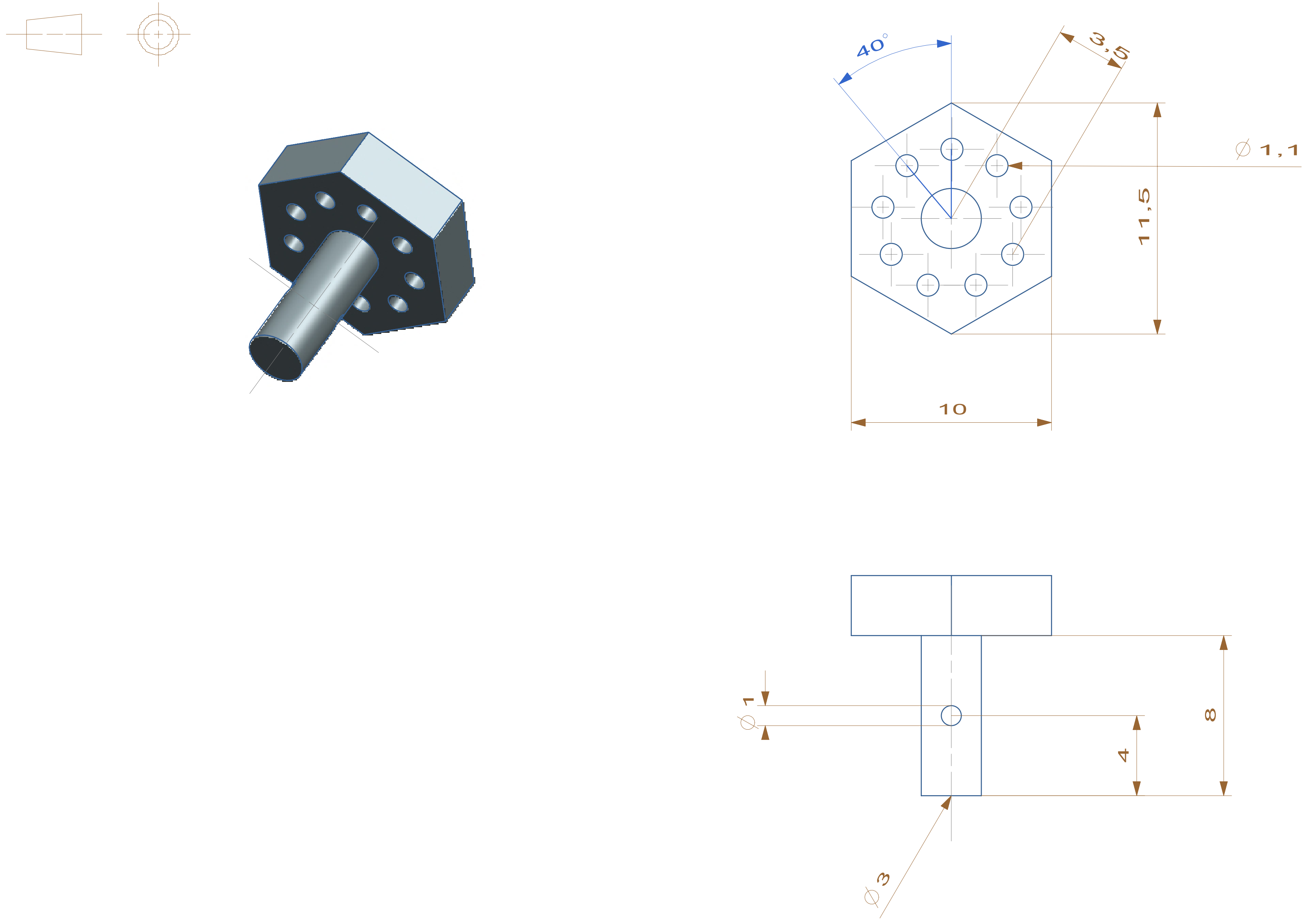

		1.01.04.01 Winch Rotor		Aluminium 6082		
Det.no.	No. of	Part name		Material	Remarks	
Designer: Bordogna	Dr. by: Bordogna		Ck. by: D.K.	Apr. by: D.K.	Replaces:	Replaced by:
KTH, EES, SPP						Date: 20120509
					Dwg no: 1.01.04.01 V.1	

294

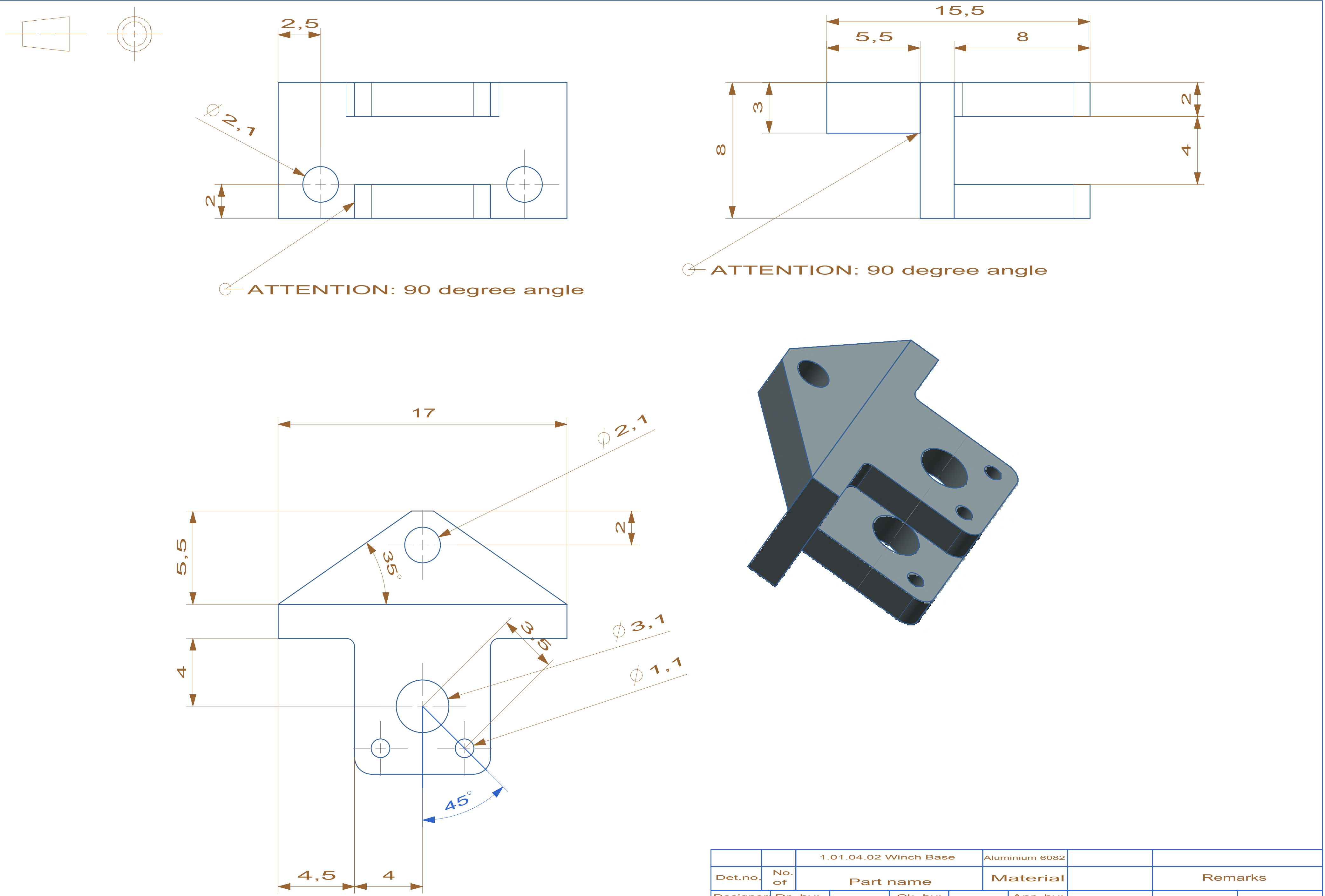

		1.01.04.02 Winch Base		Aluminium 6082		
Det.no.	No. of	Part name		Material		Remarks
Designer: Bordogna	Dr. by: Bordogna		Ck. by: D.K.	Apr. by: D.K.	Replaces:	Replaced by:
KTH, EES, SPP		Unless specified all corners can be rounded			Date: 20120706	
					Dwg no: 1.01.04.02 V.2	

295

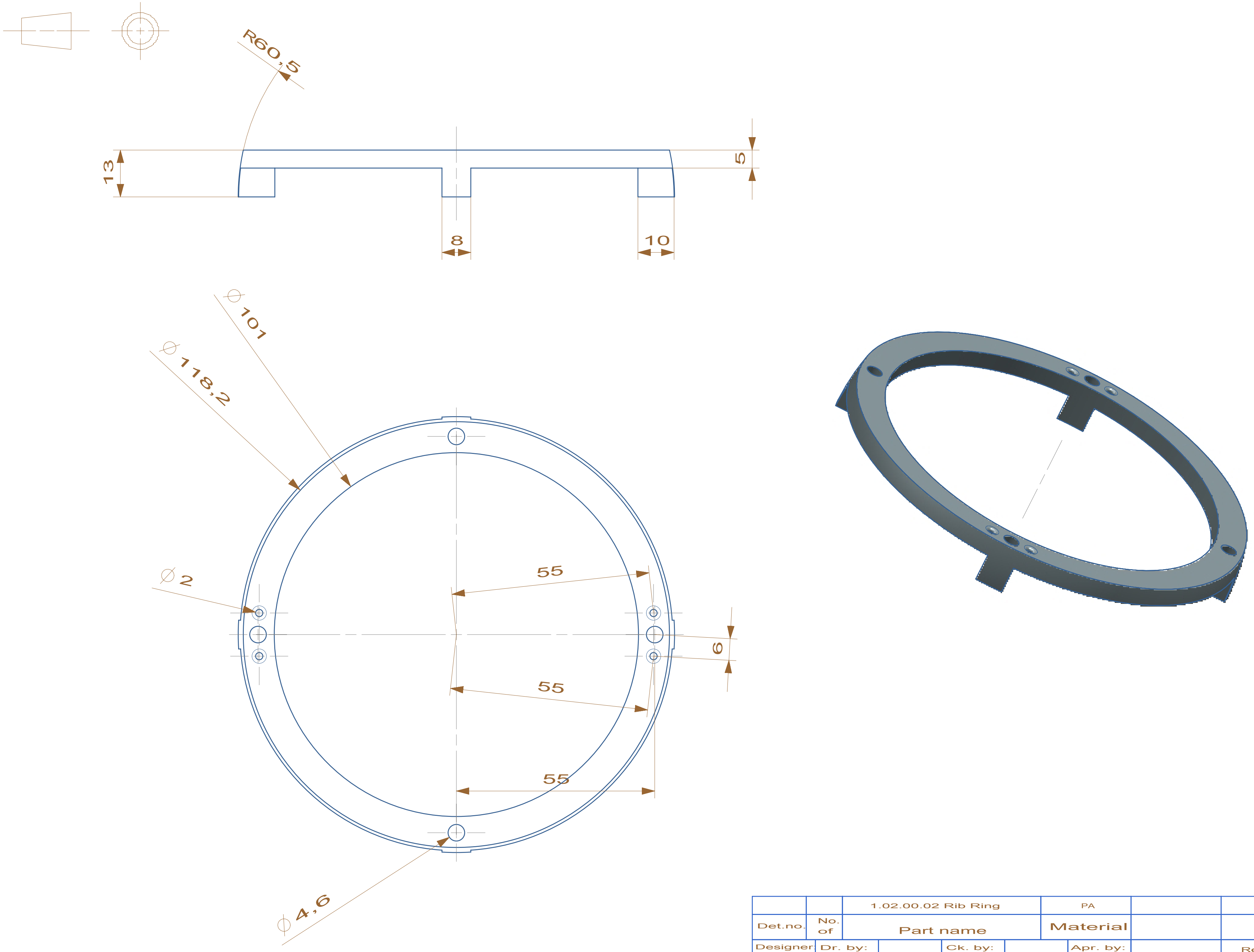

		1.02.00.02 Rib Ring		PA		
Det.no.	No. of	Part name		Material		Remarks
Designer Bordogna	Dr. by: Bordogna	Ck. by: Ivchenko		Apr. by: Ivchenko		Replaces: / Replaced by:
KTH, EES, SPP						Date: 20120605
						Dwg no: 1.02.00.02

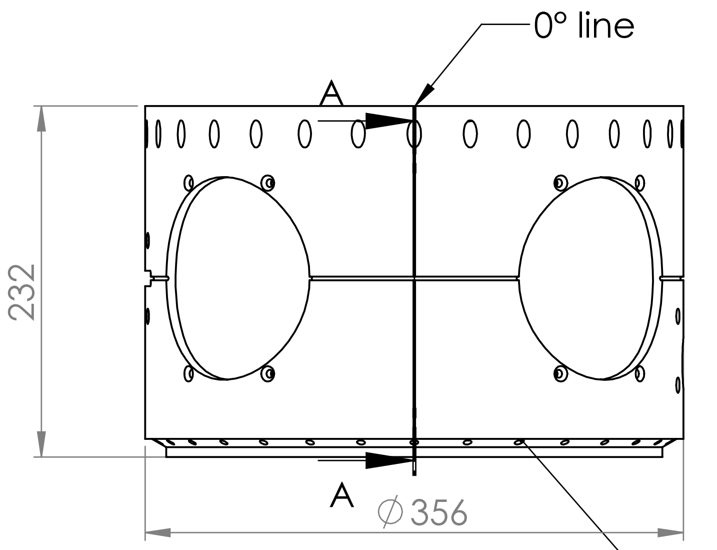

296

Rocket module screw joints top and bottom as per standard

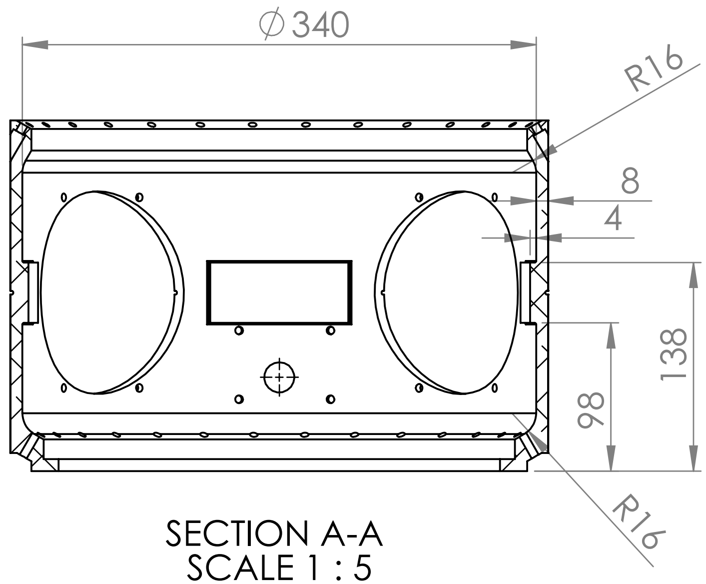

SECTION A-A
SCALE 1 : 5

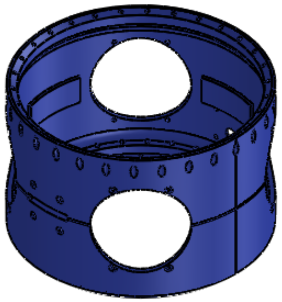

Hole details:
"Hole A" - for M5 screws, see detail E, sheet 3

Estimated mass of the modified rocket cylinder is 5,61 kg

Unless otherwise specified: Dimensions are in mm. Tolerances: ISO 2768-m	Dr. by:	Apr. by:	Material:		
	D.K.	aprby	Aluminium 7075 T6		
	Part name	Rocket Cylinder		Version	Date:
	KTH, EES, SPP	Part number 2.01.00.01		2.2	29.11.12
	WEIGHT:	SCALE:1:10		SHEET 1 OF 10	

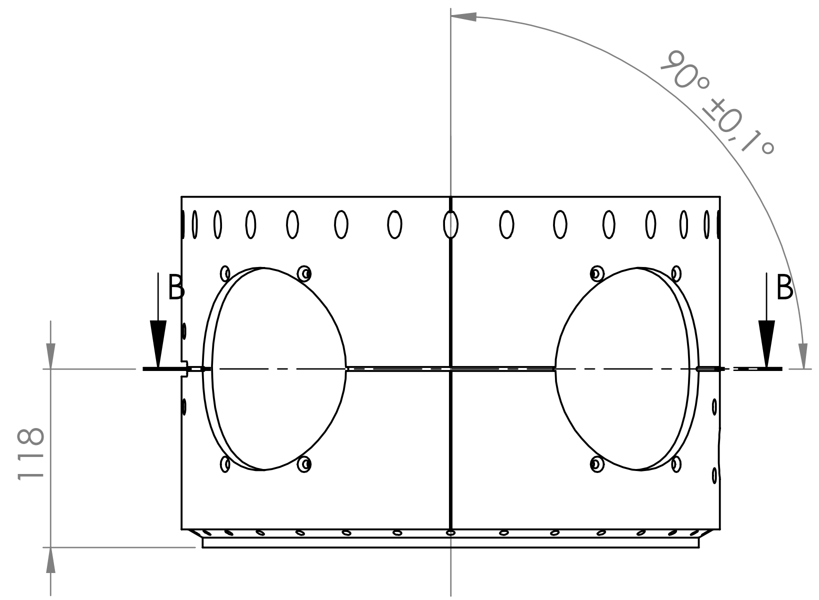

Details of special tolerance between the two ejection hole axes and the tolerance between the ejection hole plane and the rocket longitudinal axis

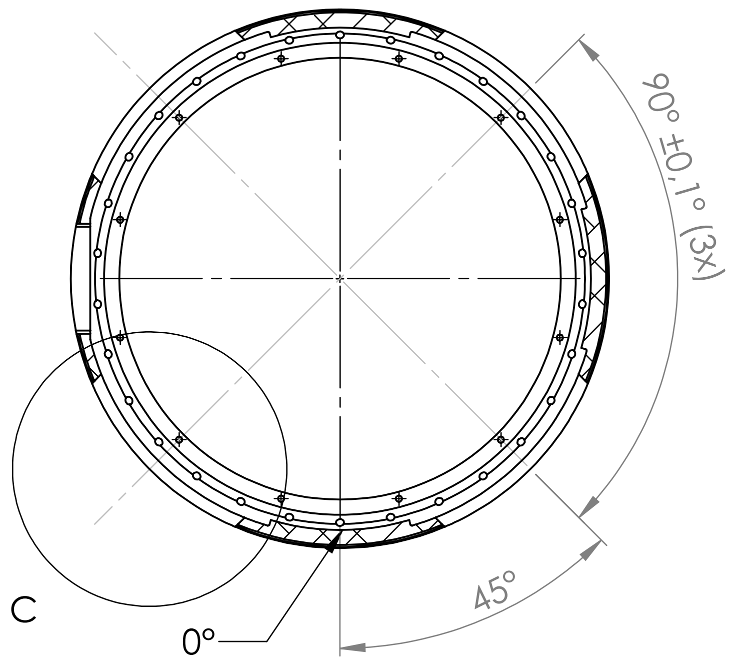

SECTION B-B
SCALE 1 : 5

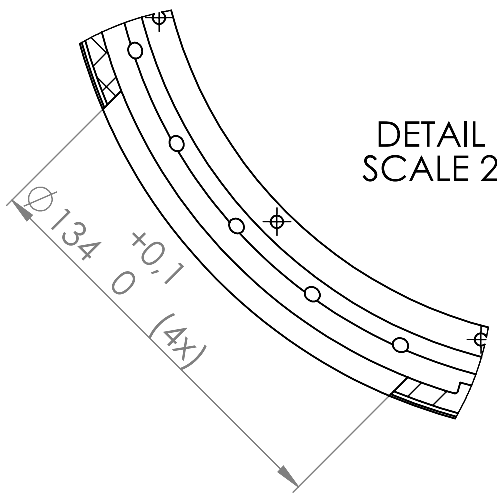

DETAIL C
SCALE 2 : 5

Unless otherwise specified: Dimensions are in mm. Tolerances: ISO 2768-m	Dr. by:	Apr. by:	Material:		
	D.K.	aprby	Aluminium 7075 T6		
	Part name	Rocket Cylinder		Version	Date:
	KTH, EES, SPP	Part number 2.01.00.01		2.2	29.11.12
	WEIGHT:	SCALE:1:10		SHEET 2 OF 10	

297

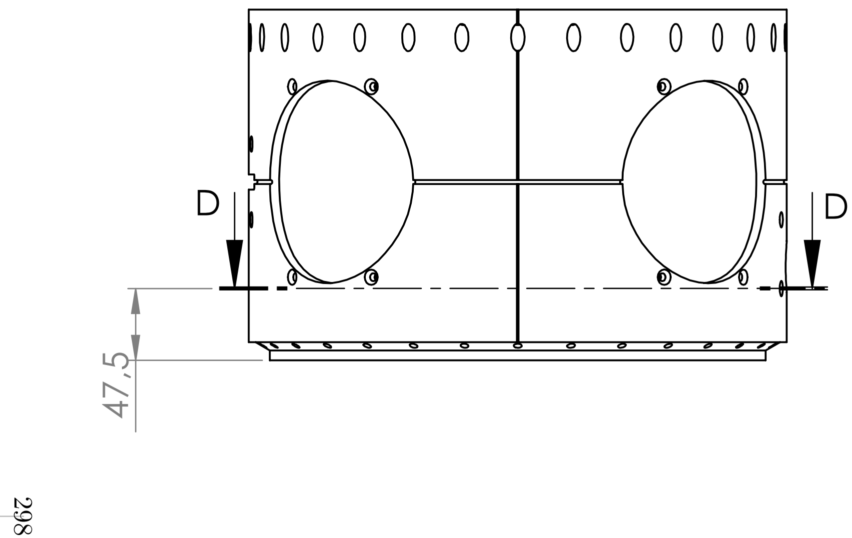

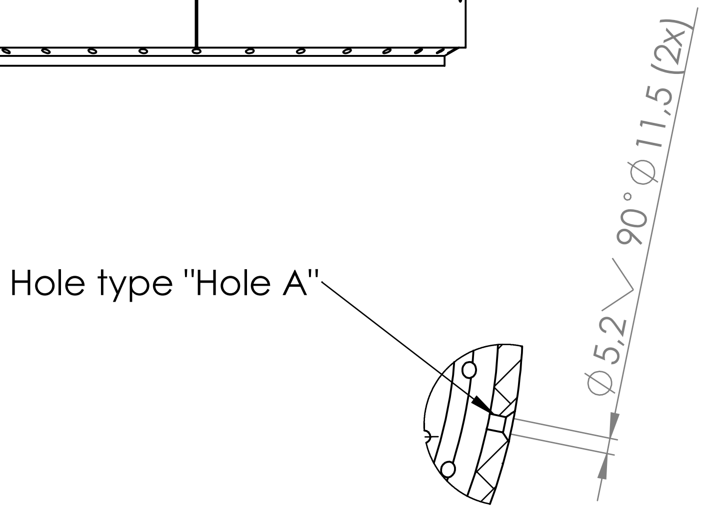

DETAIL E
SCALE 2 : 5

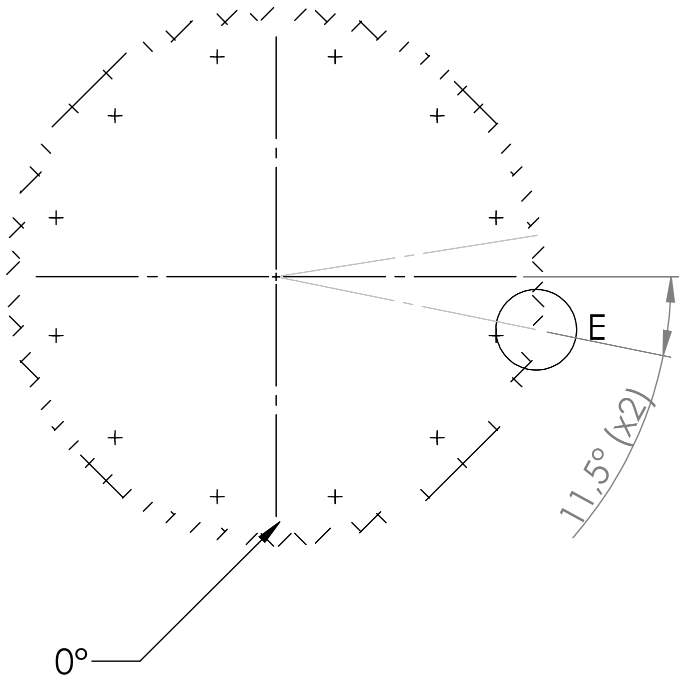

SECTION D-D
SCALE 1 : 5

Both holes in section D-D are of type "Hole A"

Unless otherwise specified: Dimensions are in mm. Tolerances: ISO 2768-m	Dr. by:	Apr. by:	Material:		
	D.K.	aprby	Aluminium 7075 T6		
	Part name	Rocket Cylinder		Version:	Date:
	KTH, EES, SPP	Part number 2.01.00.01		2.2	29.11.12

WEIGHT: SCALE:1:10 SHEET 3 OF 10

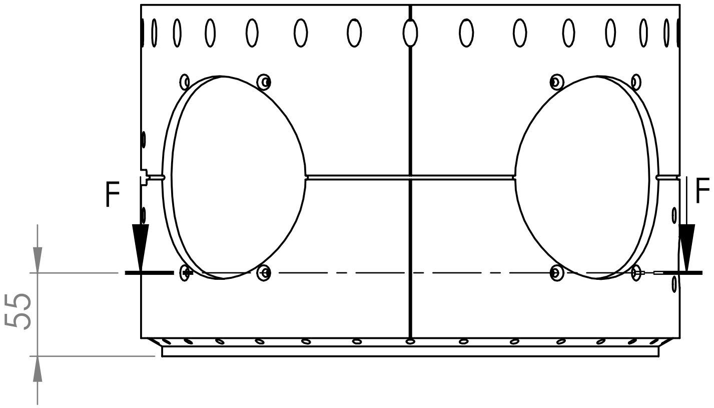

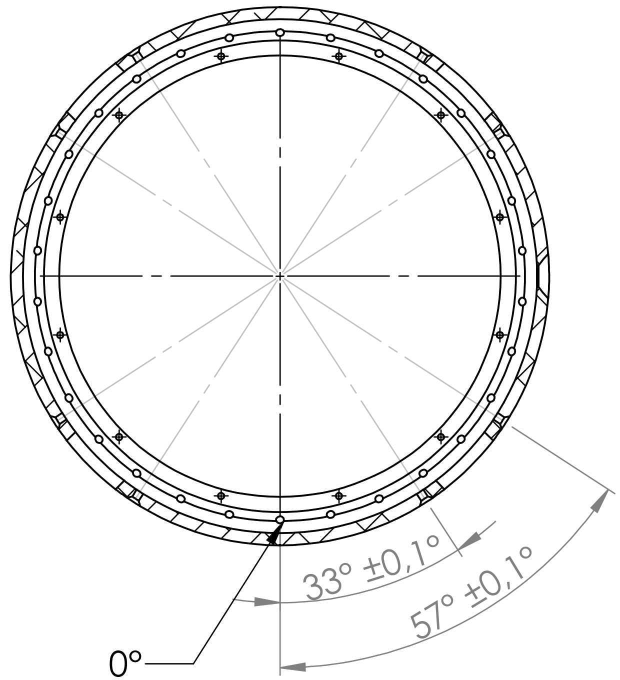

SECTION F-F
SCALE 1 : 5

299

All 8 holes in section F are of type "Hole A"

Unless otherwise specified: Dimensions are in mm. Tolerances: ISO 2768-m	Dr. by:	Apr. by:	Material:		
	D.K.	aprby	Aluminium 7075 T6		
	Part name	Rocket Cylinder		Version	Date:
	KTH, EES, SPP	Part number 2.01.00.01		2.2	29.11.12
	WEIGHT:	SCALE:1:10		SHEET 4 OF 10	

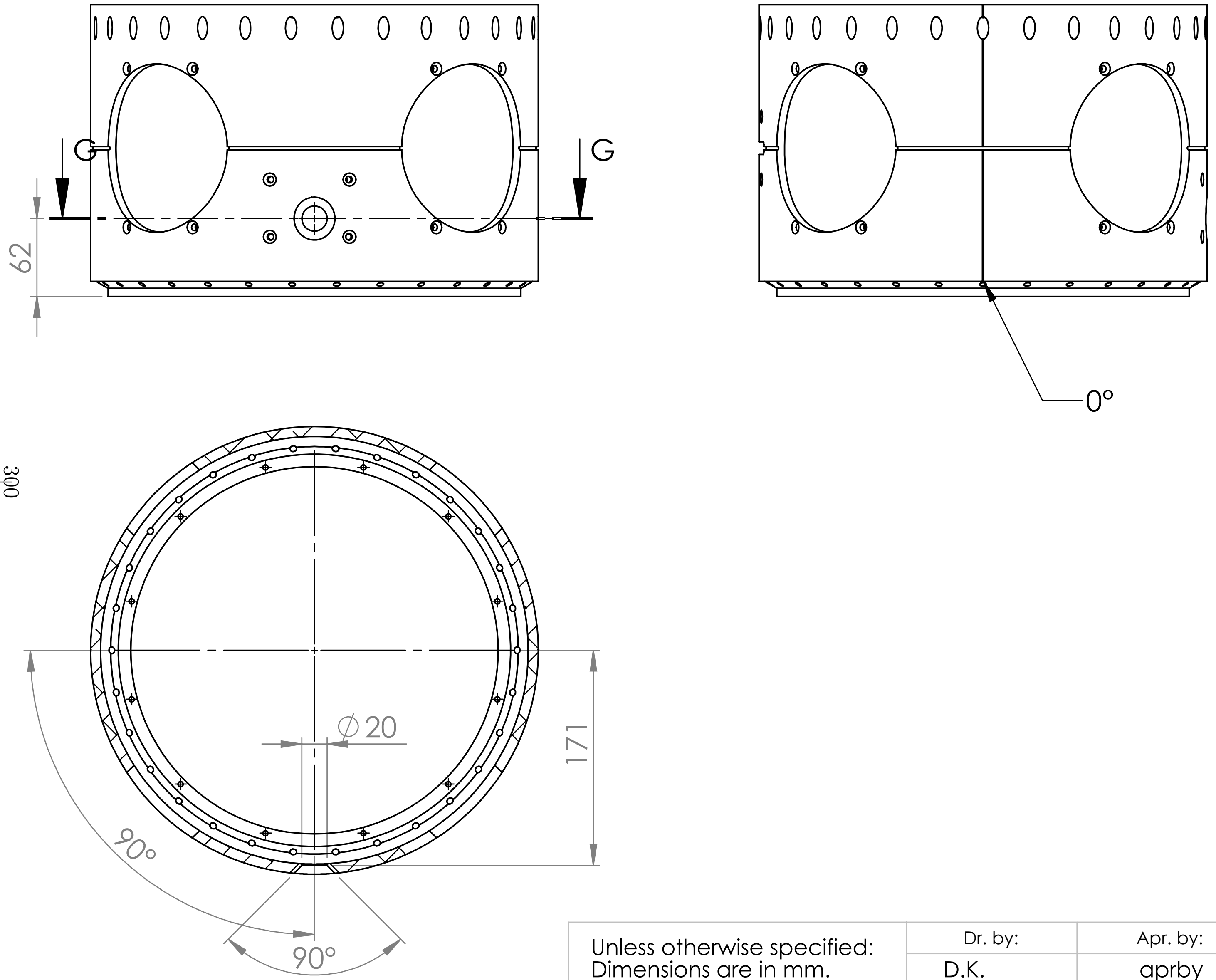

SECTION G-G
SCALE 1 : 5

Unless otherwise specified: Dimensions are in mm. Tolerances: ISO 2768-m	Dr. by:	Apr. by:	Material:		
	D.K.	aprby	Aluminium 7075 T6		
	Part name	Rocket Cylinder		Version:	Date:
	KTH, EES, SPP	Part number 2.01.00.01		2.2	29.11.12

WEIGHT: SCALE:1:10 SHEET 5 OF 10

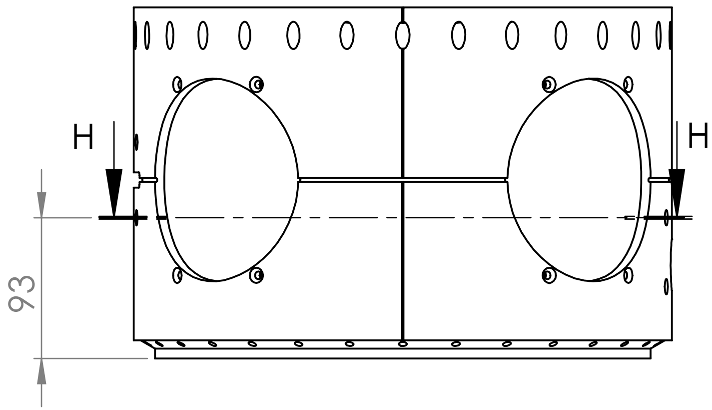

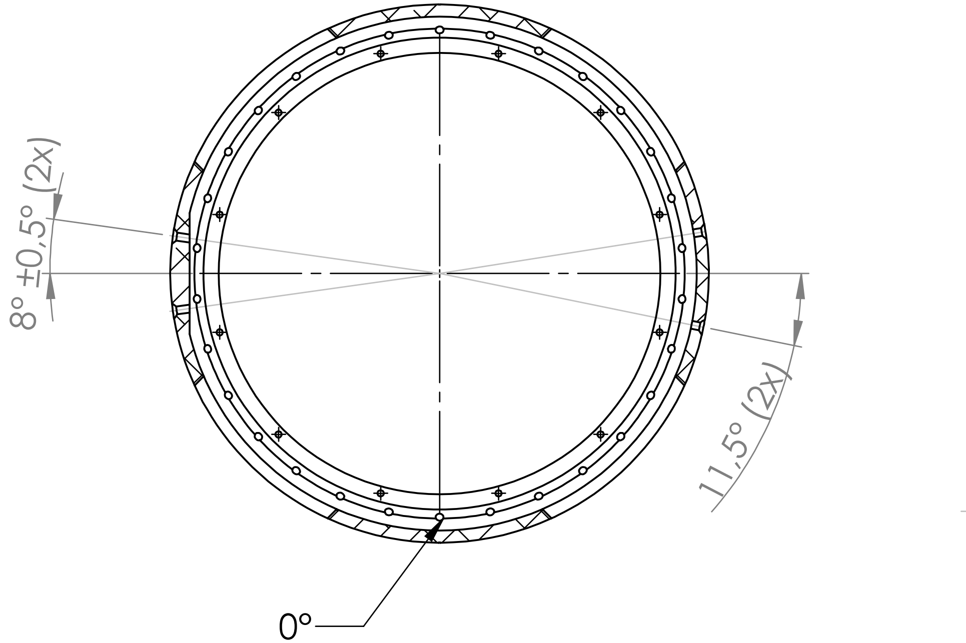

SECTION H-H
SCALE 1 : 5

All 4 holes in section H-H are of type "Hole A"

301

Unless otherwise specified: Dimensions are in mm. Tolerances: ISO 2768-m	Dr. by: D.K.	Apr. by: aprby	Material: Aluminium 7075 T6	
	Part name	Rocket Cylinder	Version: 2.2	Date: 29.11.12
	KTH, EES, SPP	Part number 2.01.00.01		
	WEIGHT:	SCALE:1:10	SHEET 6 OF 10	

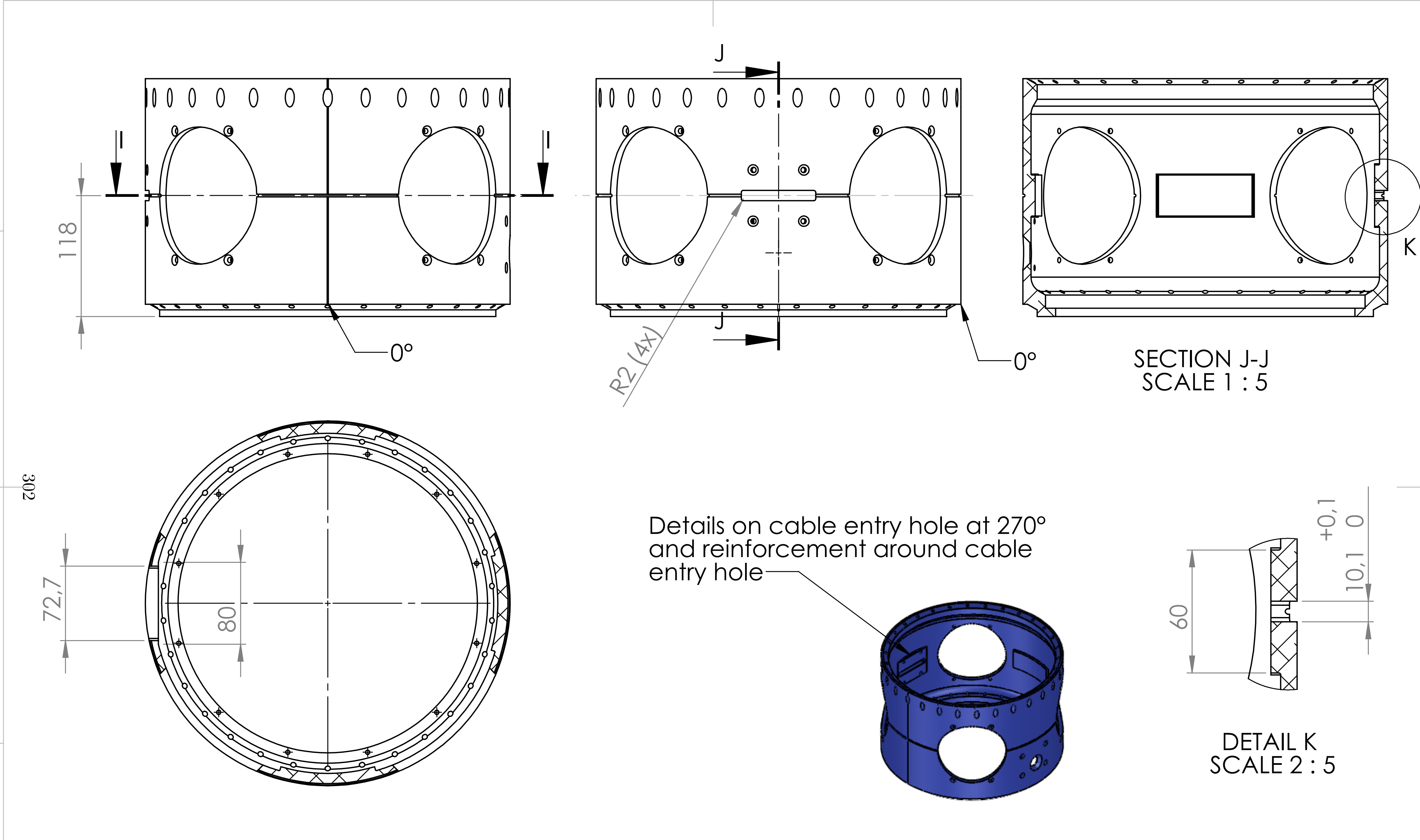

Unless otherwise specified: Dimensions are in mm. Tolerances: ISO 2768-m	Dr. by:	Apr. by:	Material:		
	D.K.	aprby	Aluminium 7075 T6		
	Part name	Rocket Cylinder		Version:	Date:
	KTH, EES, SPP	Part number 2.01.00.01		2.2	29.11.12
	WEIGHT:	SCALE:1:10		SHEET 7 OF 10	

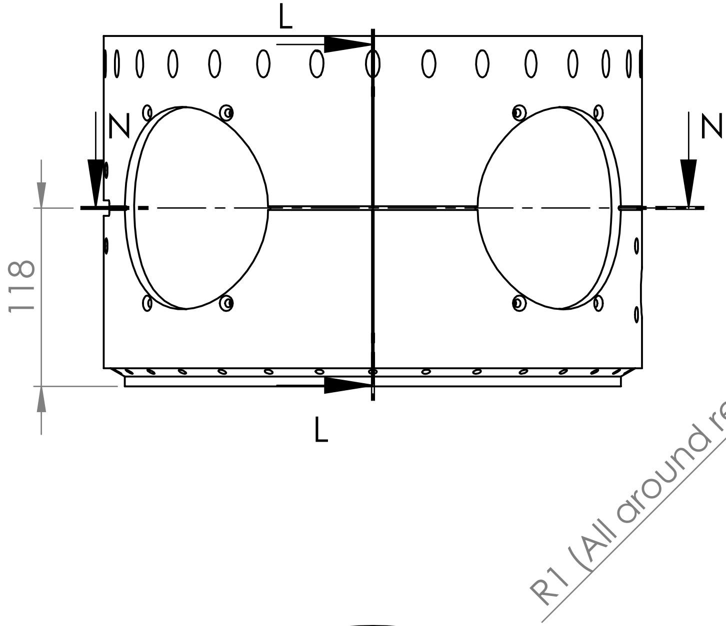

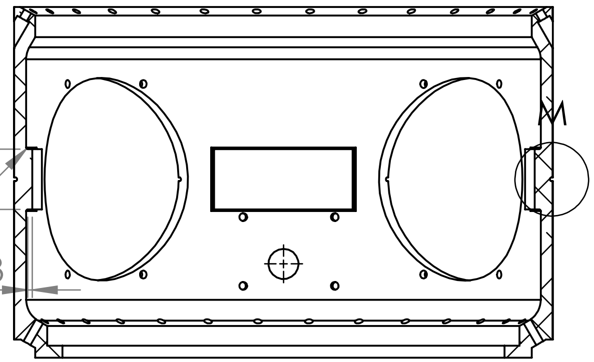

SECTION L-L
SCALE 1 : 5

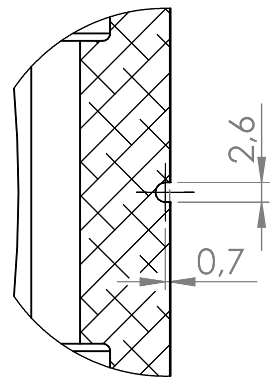

DETAIL M
SCALE 1 : 1

303

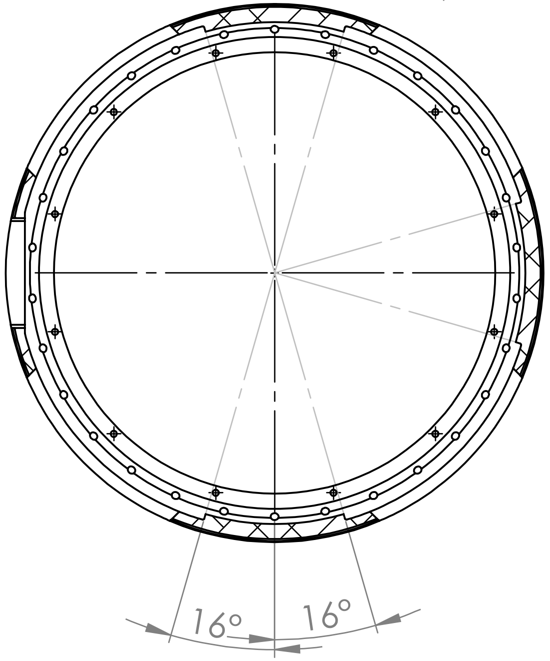

SECTION N-N
SCALE 1 : 5

Details on cable groove and
reinforcements around 0°, 90° and 180°

Unless otherwise specified: Dimensions are in mm. Tolerances: ISO 2768-m	Dr. by:	Apr. by:	Material:		
	D.K.	aprby	Aluminium 7075 T6		
	Part name	Rocket Cylinder		Version	Date:
	KTH, EES, SPP	Part number 2.01.00.01		2.2	29.11.12
	WEIGHT:	SCALE:1:10		SHEET 8 OF 10	

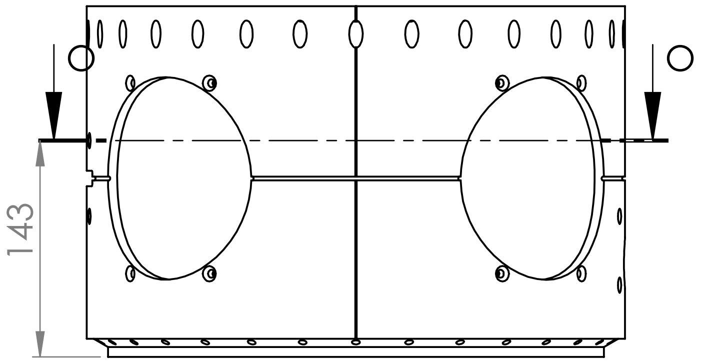

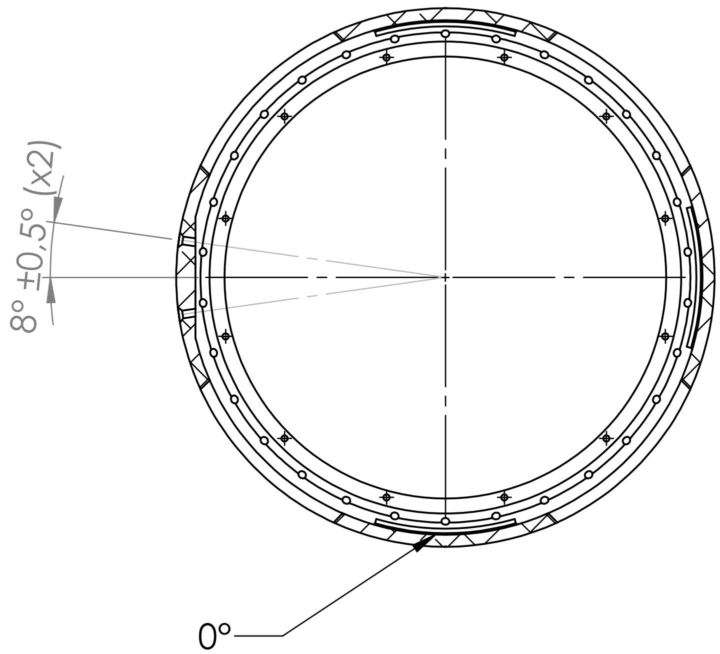

SECTION O-O
SCALE 1 : 5

Both 2 holes in section O-O of type "Hole A"

304

Unless otherwise specified: Dimensions are in mm. Tolerances: ISO 2768-m	Dr. by: D.K.	Apr. by: aprby	Material: Aluminium 7075 T6	
	Part name	Rocket Cylinder	Version	Date:
	KTH, EES, SPP	Part number 2.01.00.01	2.2	29.11.12
	WEIGHT:	SCALE:1:10	SHEET 9 OF 10	

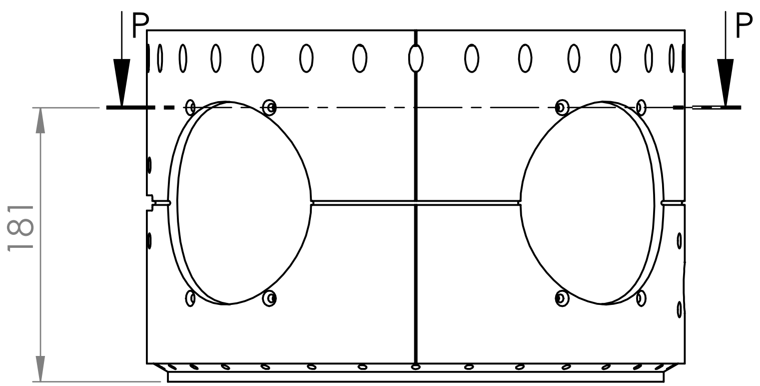

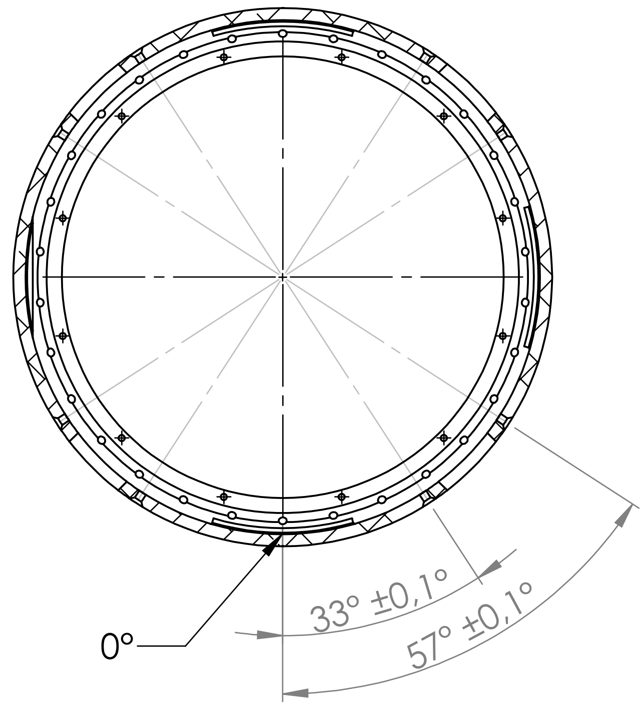

SECTION P-P
SCALE 1 : 5

305

All 8 holes in section P-P of type "Hole A"

Unless otherwise specified: Dimensions are in mm. Tolerances:	Dr. by:	Apr. by:	Material:		
	D.K.	aprby	Aluminium 7075 T6		
	Part name	Rocket Cylinder		Version:	Date:
ISO 2768-m	KTH, EES, SPP	Part number 2.01.00.01		2.2	29.11.12
	WEIGHT:	SCALE:1:10		SHEET 10 OF 10	

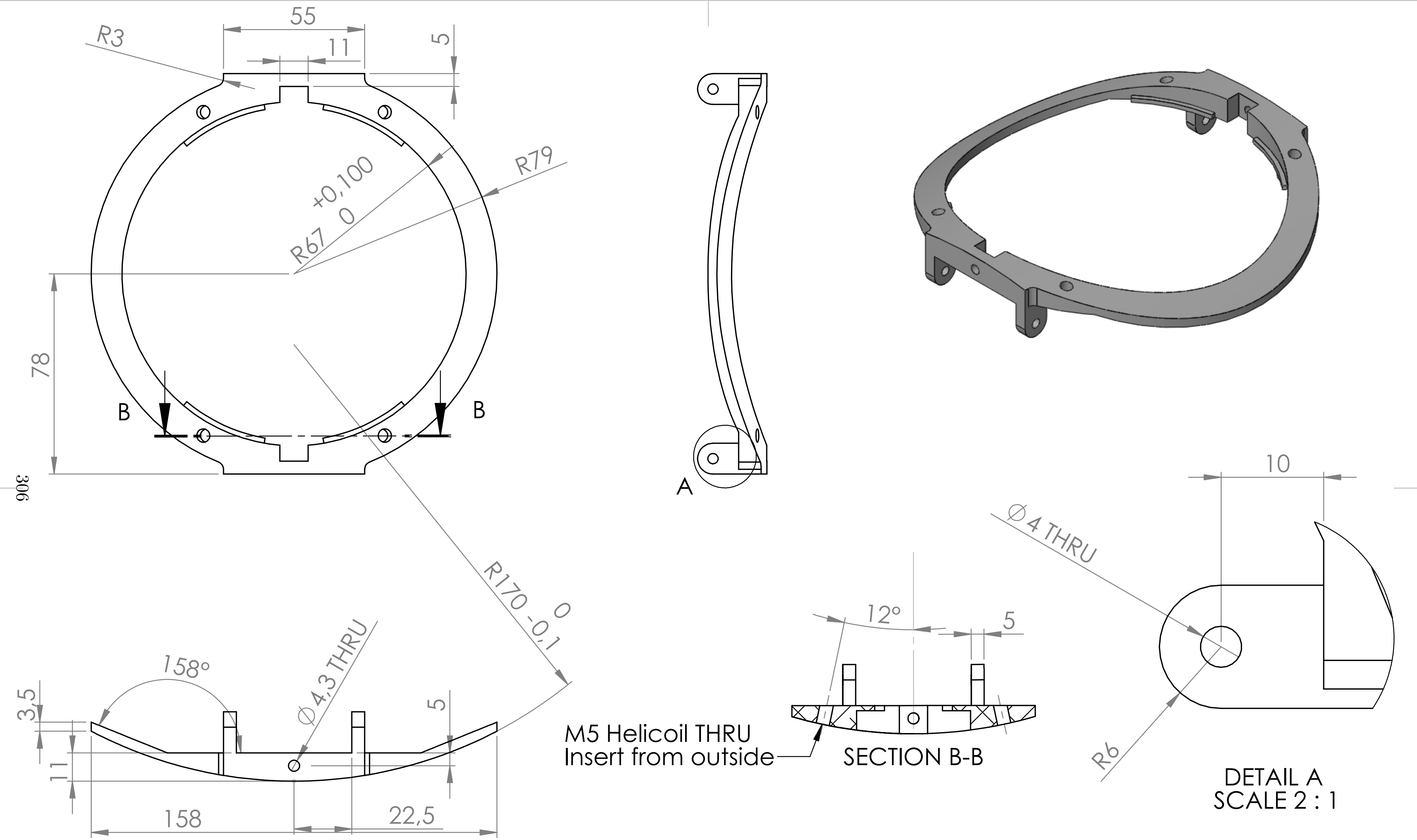

Unless otherwise specified:
Dimensions are in mm.
Tolerances:
Linear: 0.1mm
Angular: 1°

Dr. by:	Apr. by:	Material:		
D.K.	aprby	Aluminium 7075		
Part name	Collar		Replaces:	Date:
KTH, EES, SPP	Part number 2.02.01.02			16.5.12

WEIGHT: SCALE:1:2 SHEET 1 OF 2

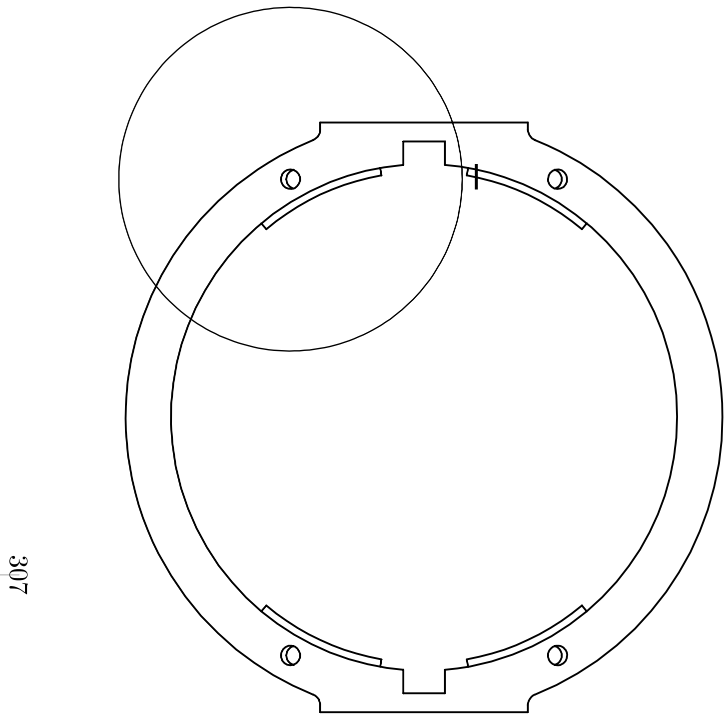

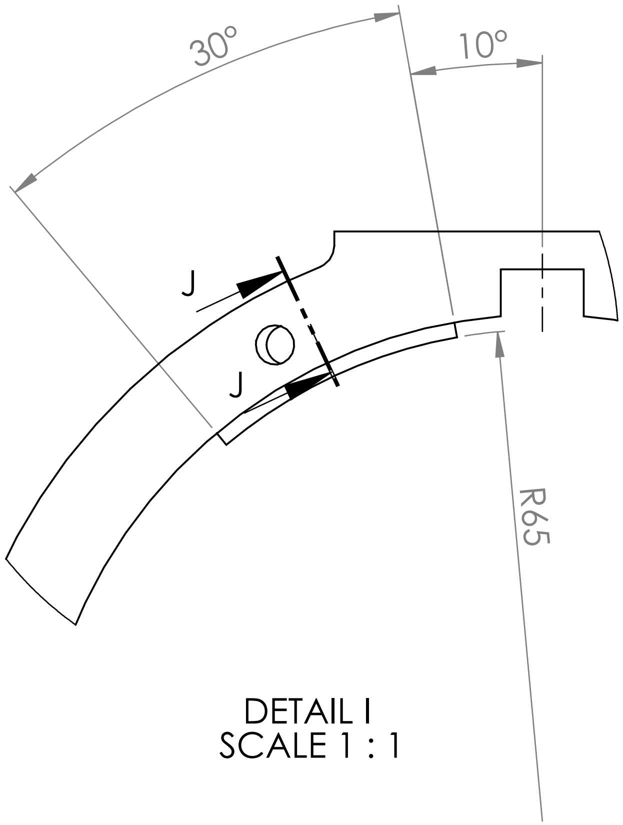

DETAIL I
SCALE 1 : 1

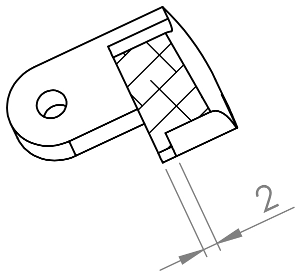

SECTION J-J
SCALE 1 : 1

Unless otherwise specified: Dimensions are in mm. Tolerances: Linear: 0.1mm Angular: 1°	Dr. by:	Apr. by:	Material:		
	D.K.	aprby	Aluminium 7075		
	Part name	Collar		Replaces:	Date:
	KTH, EES, SPP	Part number 2.02.01.02			23.5.12

WEIGHT: SCALE:1:2 SHEET 2 OF 2

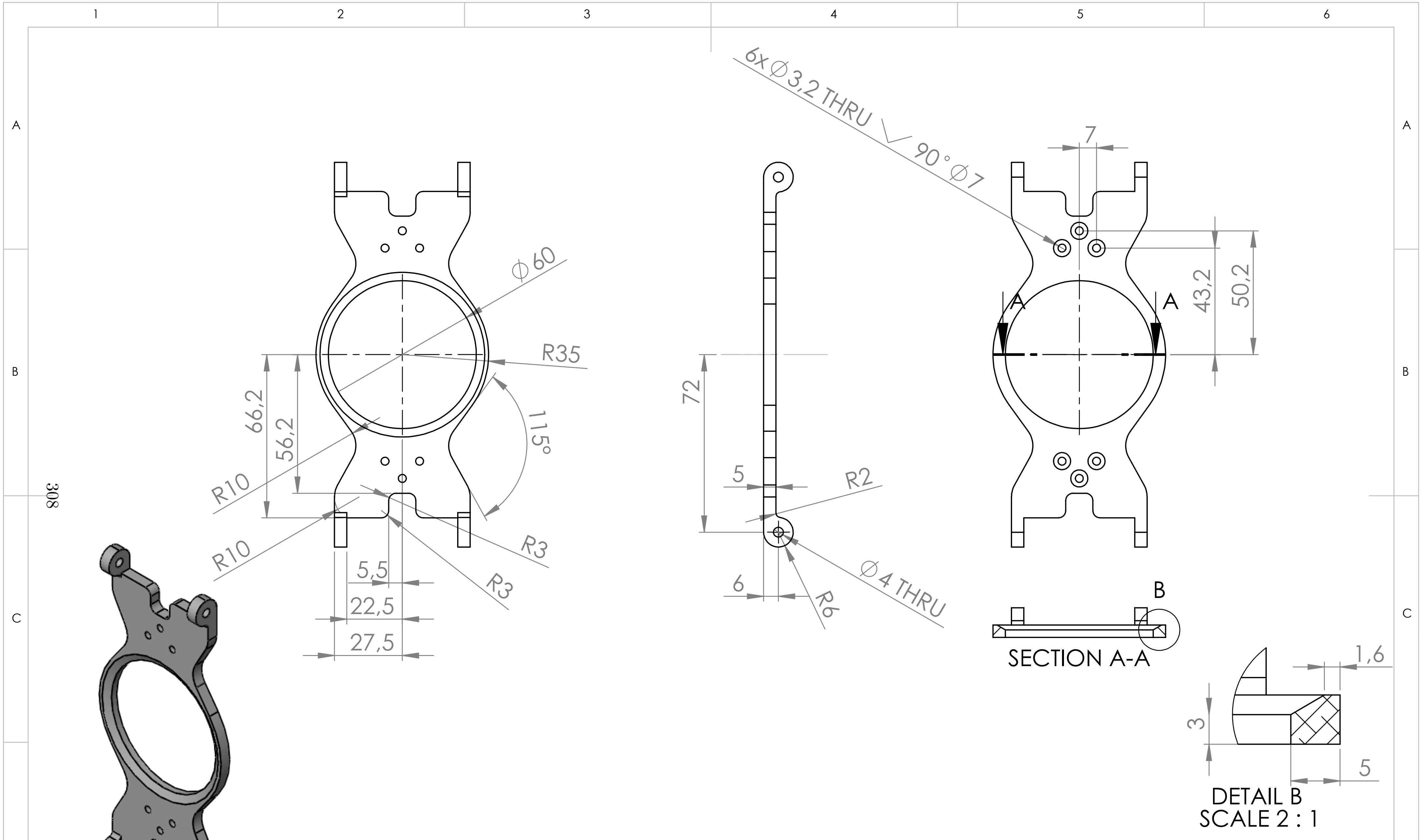

Unless otherwise specified:
Dimensions are in mm.
Tolerances:
Linear: 0.1mm
Angular: 1°

Dr. by:	Apr. by:	Material:	
D.K.	aprby	Aluminium 7075	
Part name	Inner Ring	Replaces:	Date:
KTH, EES, SPP	Part number 2.02.02.01		18.5.12

WEIGHT: SCALE:1:2 SHEET 1 OF 1

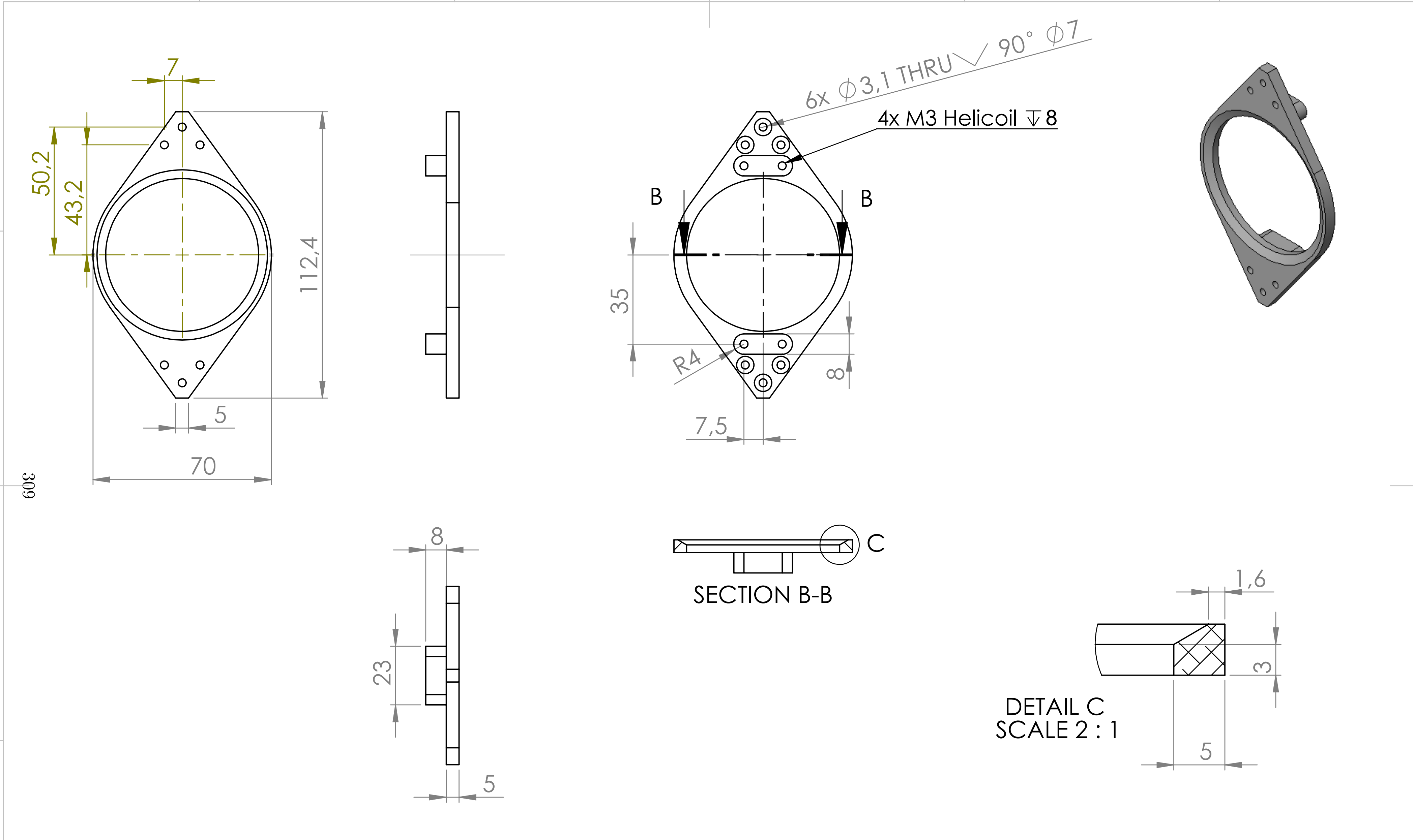

Unless otherwise specified:
Dimensions are in mm.
Tolerances:
Linear: 0.1mm
Angular: 1°

Dr. by:	Apr. by:	Material:		
D.K.	aprby	Aluminium 7075		
Part name	Outer Ring		Replaces:	Date:
KTH, EES, SPP	Part number 2.02.02.02			16.5.12

WEIGHT: SCALE:1:2 SHEET 1 OF 1

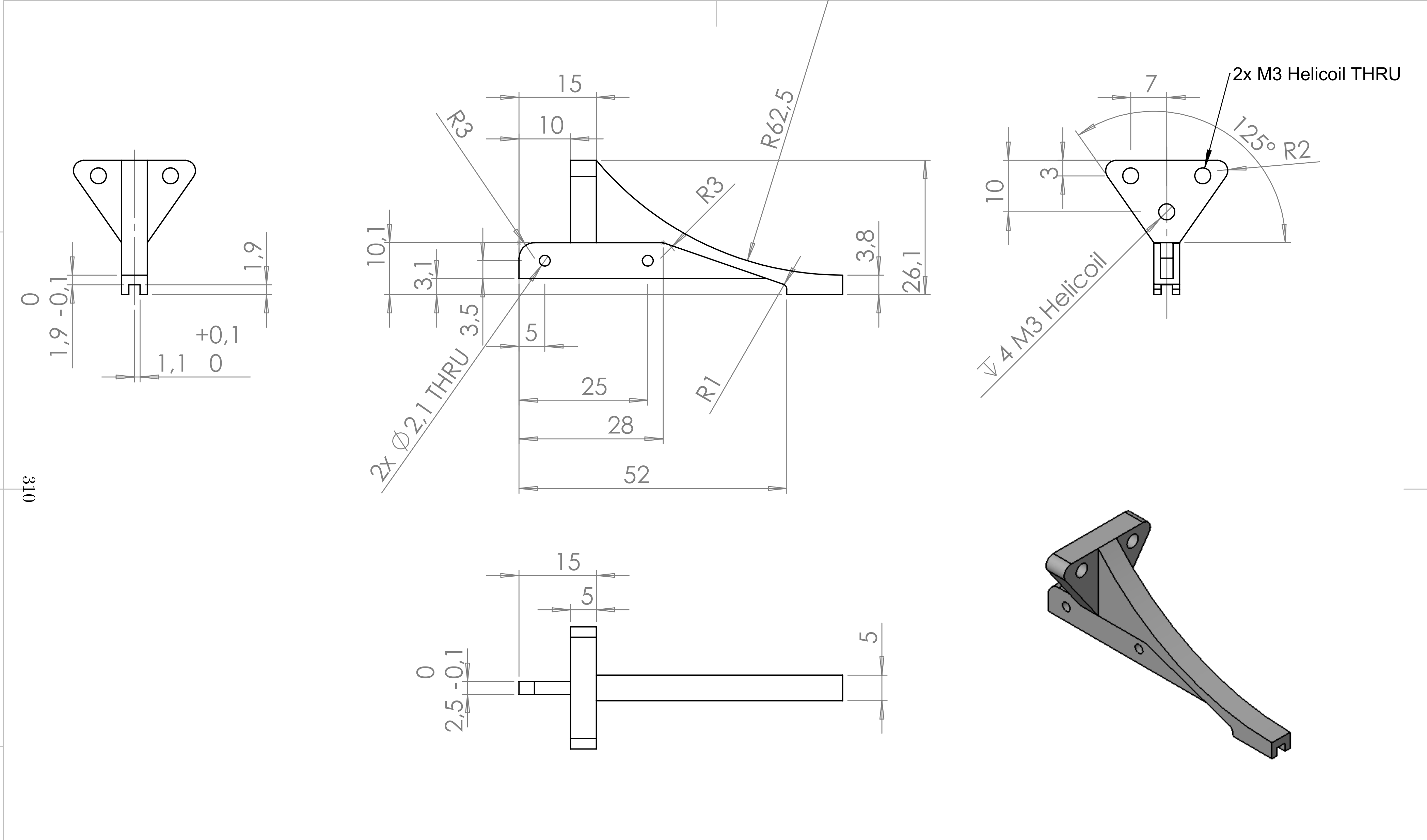

Unless otherwise specified: Dimensions are in mm. Tolerances: Linear: 0.1mm Angular: 1°	Dr. by:	Apr. by:	Material:		
	D.K.	aprby	Aluminium 7075		
	Part name	Rib		Replaces:	Date:
	KTH, EES, SPP	Part number 2.02.02.03			16.5.12
	WEIGHT:	SCALE:1:1		SHEET 1 OF 1	

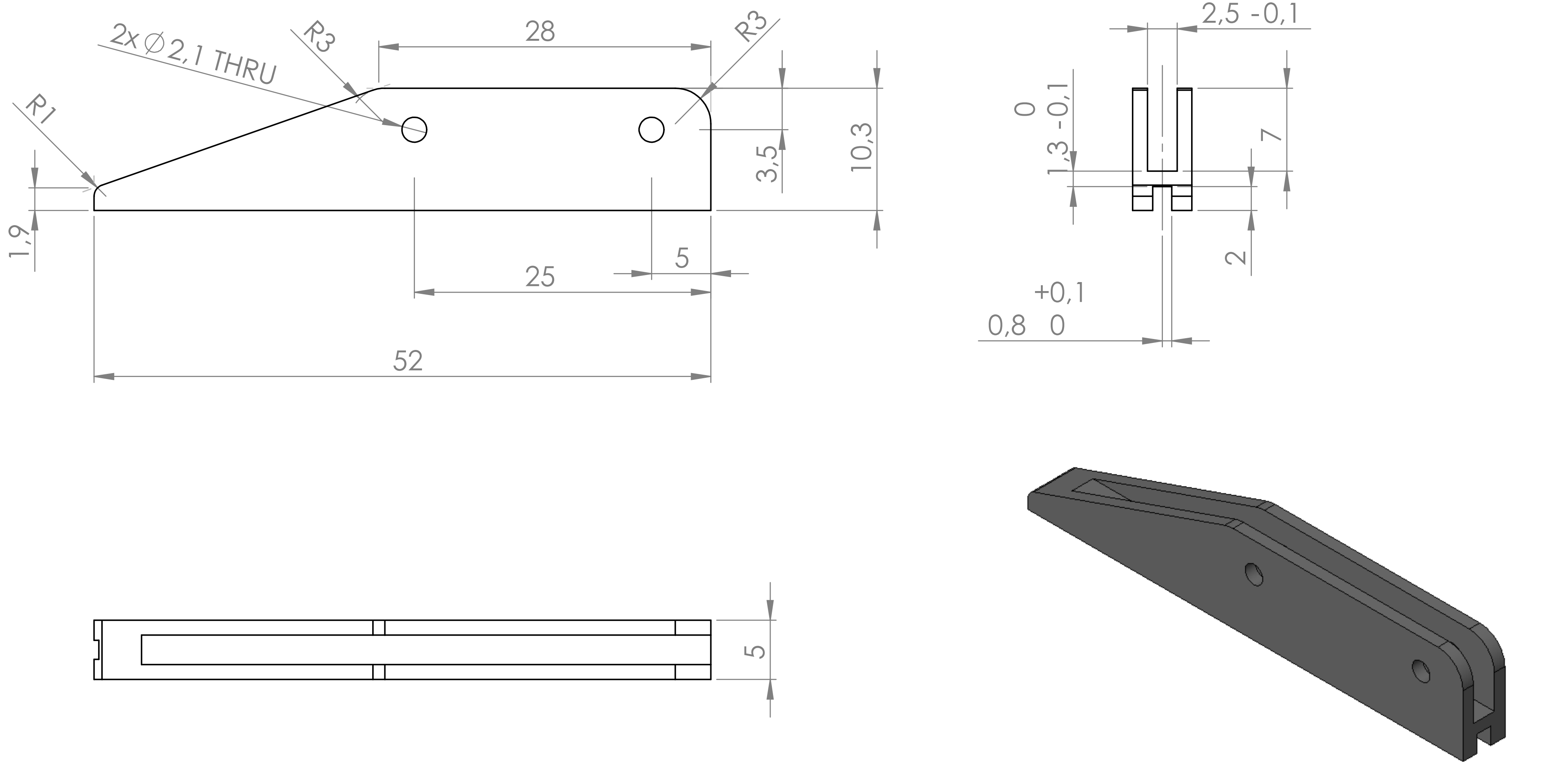

Unless otherwise specified:
Dimensions are in mm.
Tolerances:
Linear: 0.1mm
Angular: 1°

Dr. by:	Apr. by:	Material:		
D.K.	aprby	PTFE (Teflon)		
Part name	Slider		Replaces:	Date:
KTH, EES, SPP	Part number 2.02.02.04			16.5.12

WEIGHT: SCALE:2:1 SHEET 1 OF 1

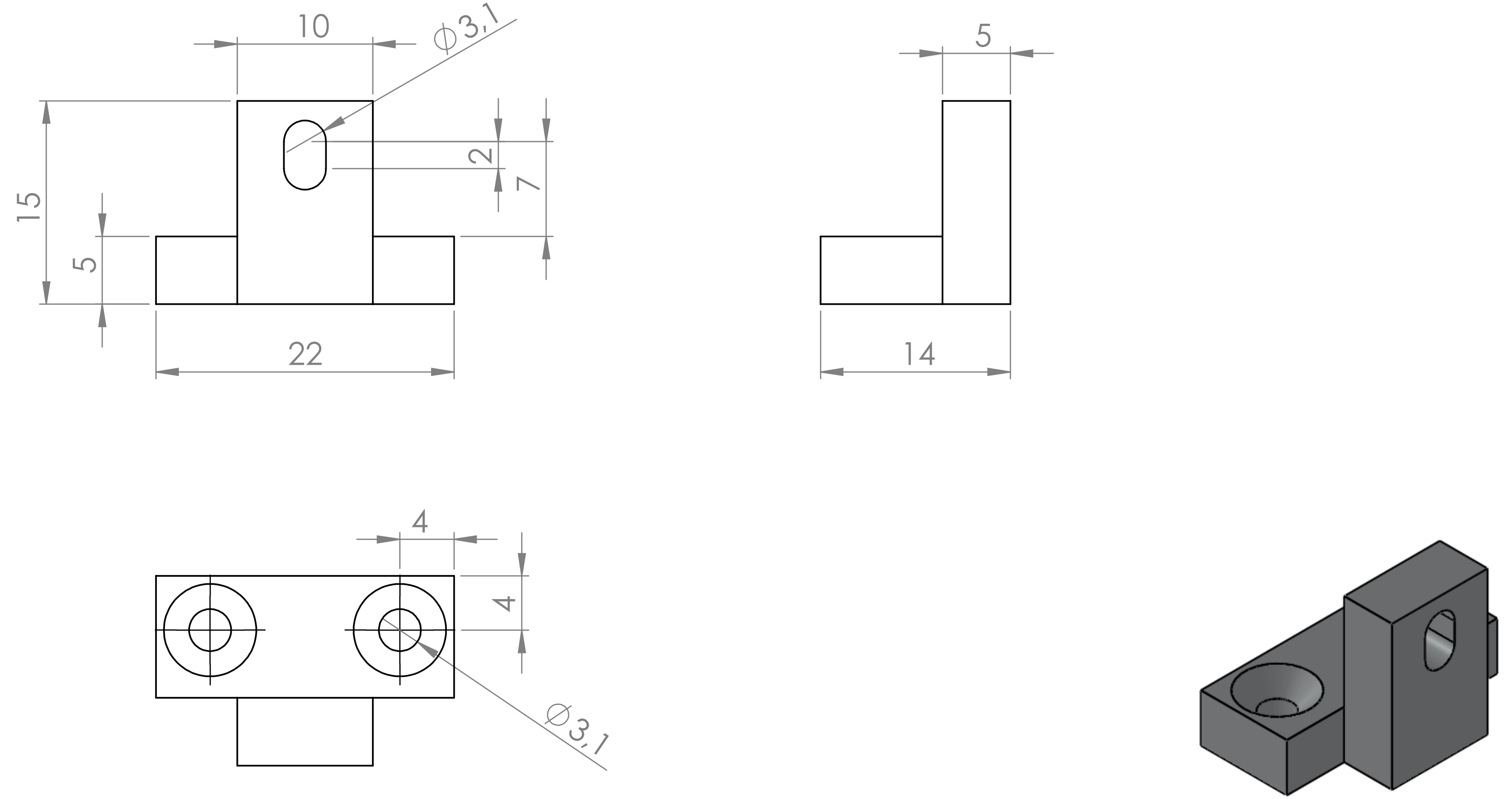

Unless otherwise specified: Dimensions are in mm. Tolerances: Linear: 0.1mm Angular: 1°	Dr. by:	Apr. by:	Material:	
	D.K.	aprby	Aluminium 6082	
	Part name	Hook bracket	Replaces:	Date:
	KTH, EES, SPP	Part number 2.02.02.06		20.11.12
	WEIGHT:	SCALE:2:1	SHEET 1 OF 1	

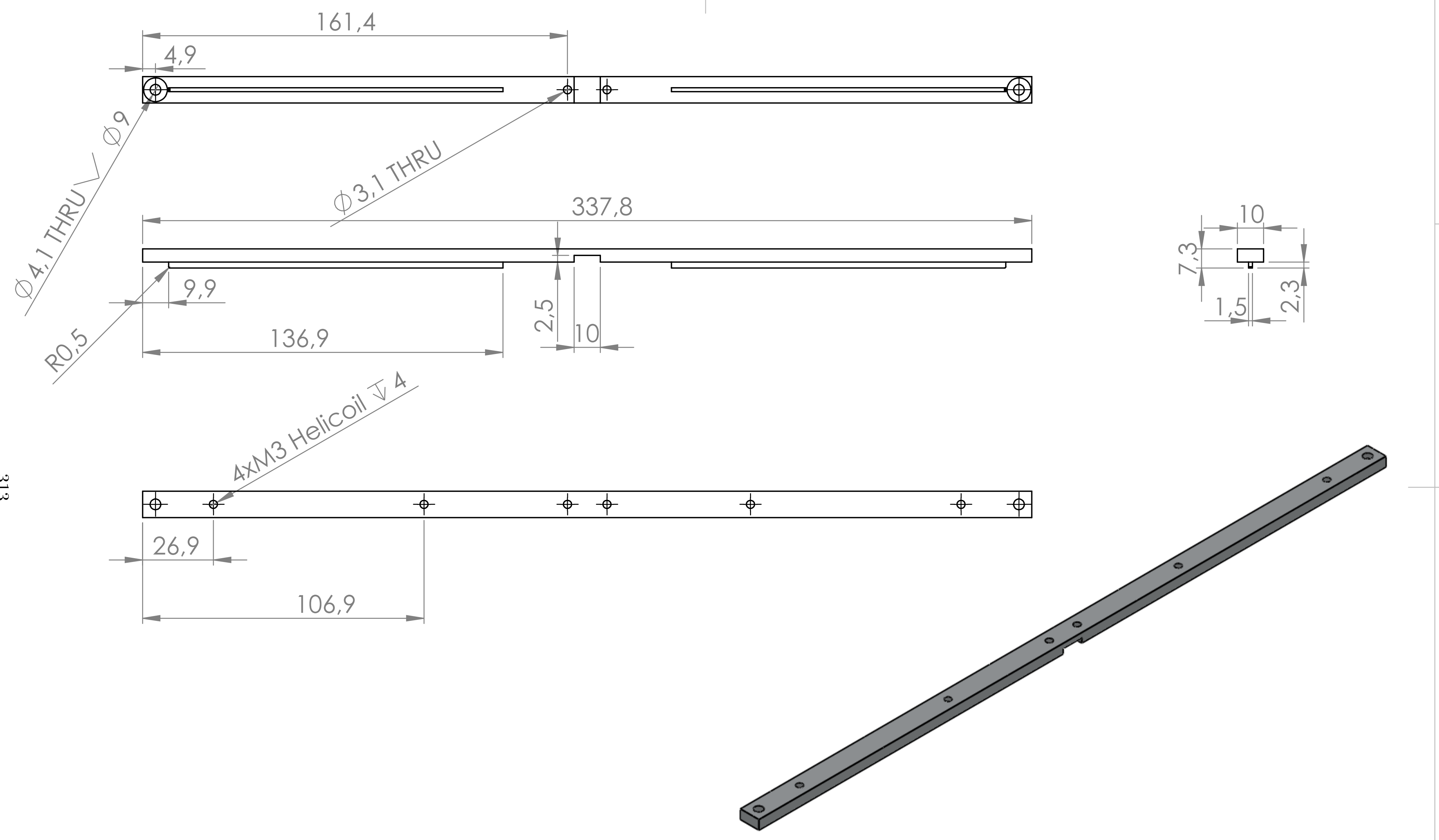

313

Unless otherwise specified:
Dimensions are in mm.
Tolerances:
Linear: 0.1mm
Angular: 1°

Dr. by:	Apr. by:	Material:		
D.K.	aprby	Aluminium 6082		
Part name	Upper Cross 1		Replaces:	Date:
KTH, EES, SPP	Part number 2.02.01.11		2.02.01.11	11.9.12
WEIGHT:	SCALE:1:5		SHEET 1 OF 1	

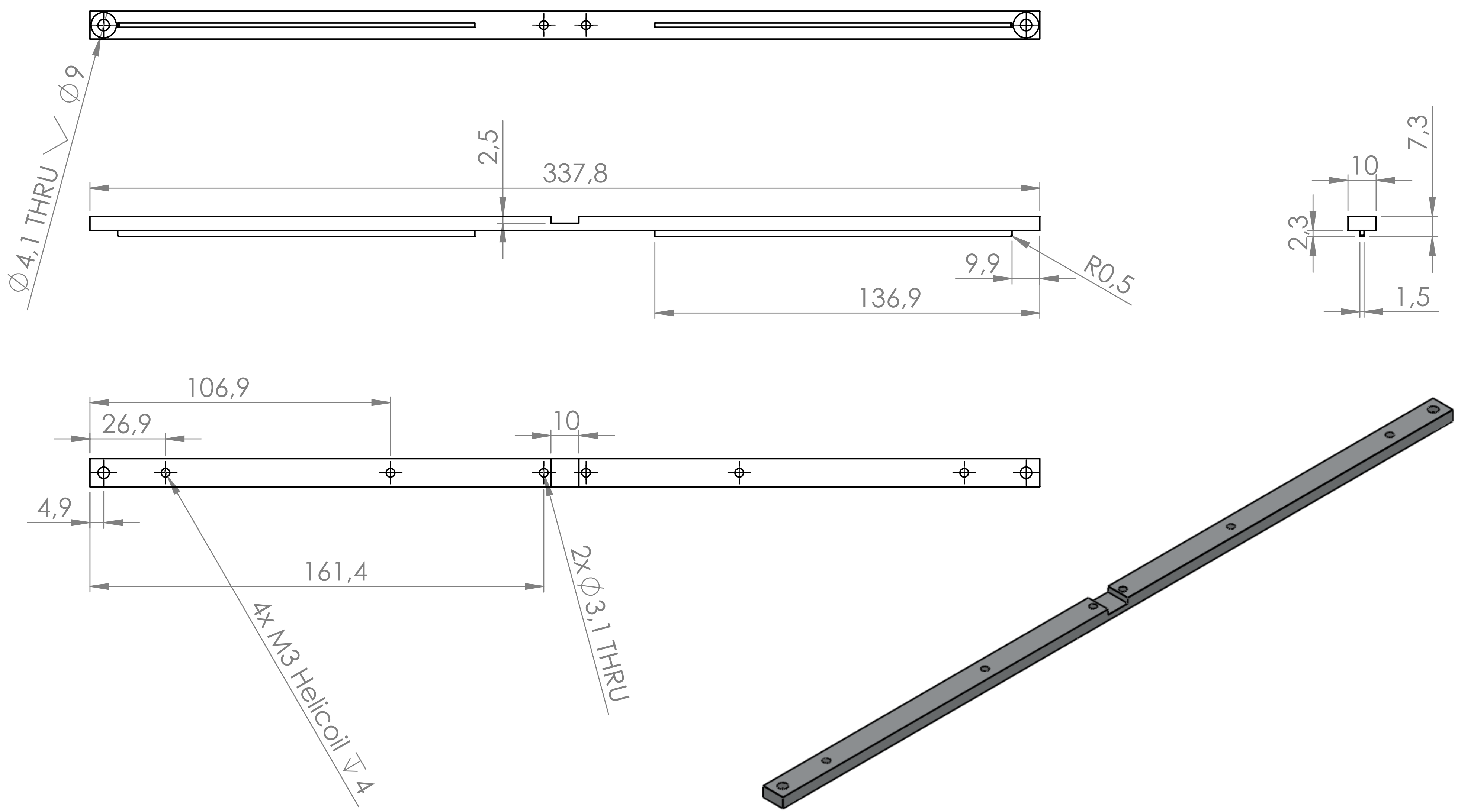

Unless otherwise specified:
Dimensions are in mm.
Tolerances:
Linear: 0.1mm
Angular: 1°

Dr. by:	Apr. by:	Material:		
D.K.	aprby	Aluminium 6082		
Part name	Upper Cross 2		Replaces:	Date:
KTH, EES, SPP	Part number 2.02.01.12			11.9.12

WEIGHT: SCALE:1:5 SHEET 1 OF 1

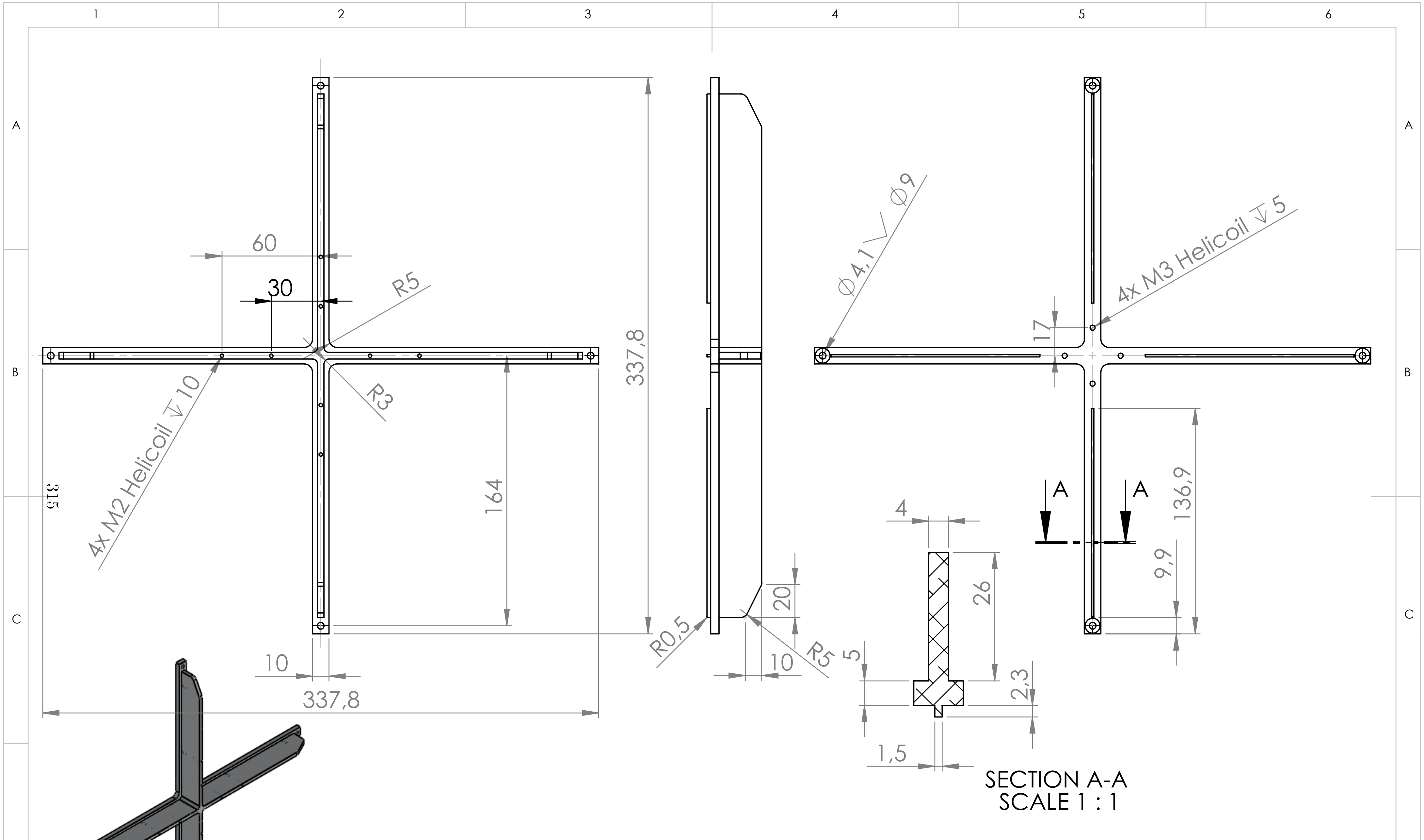

Unless otherwise specified:
Dimensions are in mm.
Tolerances:
Linear: 0.1mm
Angular: 1°

Dr. by:	Apr. by:	Material:		
D.K.	aprby	Aluminium 6082		
Part name	Lower Cross		Replaces:	Date:
KTH, EES, SPP	Part number 2.02.01.13			21.9.12

WEIGHT: SCALE:1:5 SHEET 2 OF 2

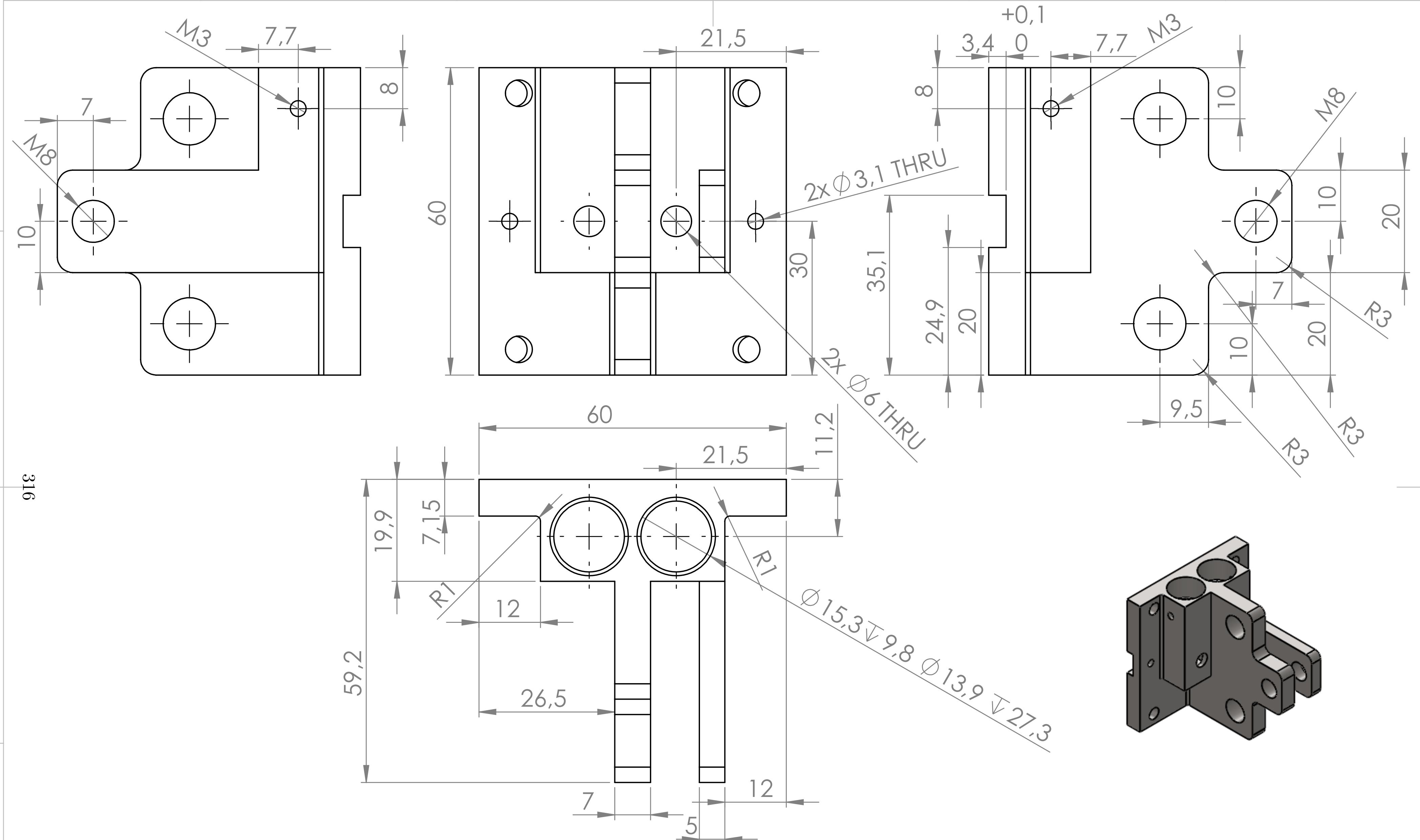

Unless otherwise specified: Dimensions are in mm. Tolerances: Linear: 0.1mm Angular: 1°	Dr. by:	Apr. by:	Material:		
	D.K.	aprby	SS 304		
	Part name	Pyrocutter Bracket		Version:	Date:
	KTH, EES, SPP	Part number 2.03.00.02		2.3	02.10.12
	WEIGHT:	SCALE:1:2		SHEET 1 OF 2	

317

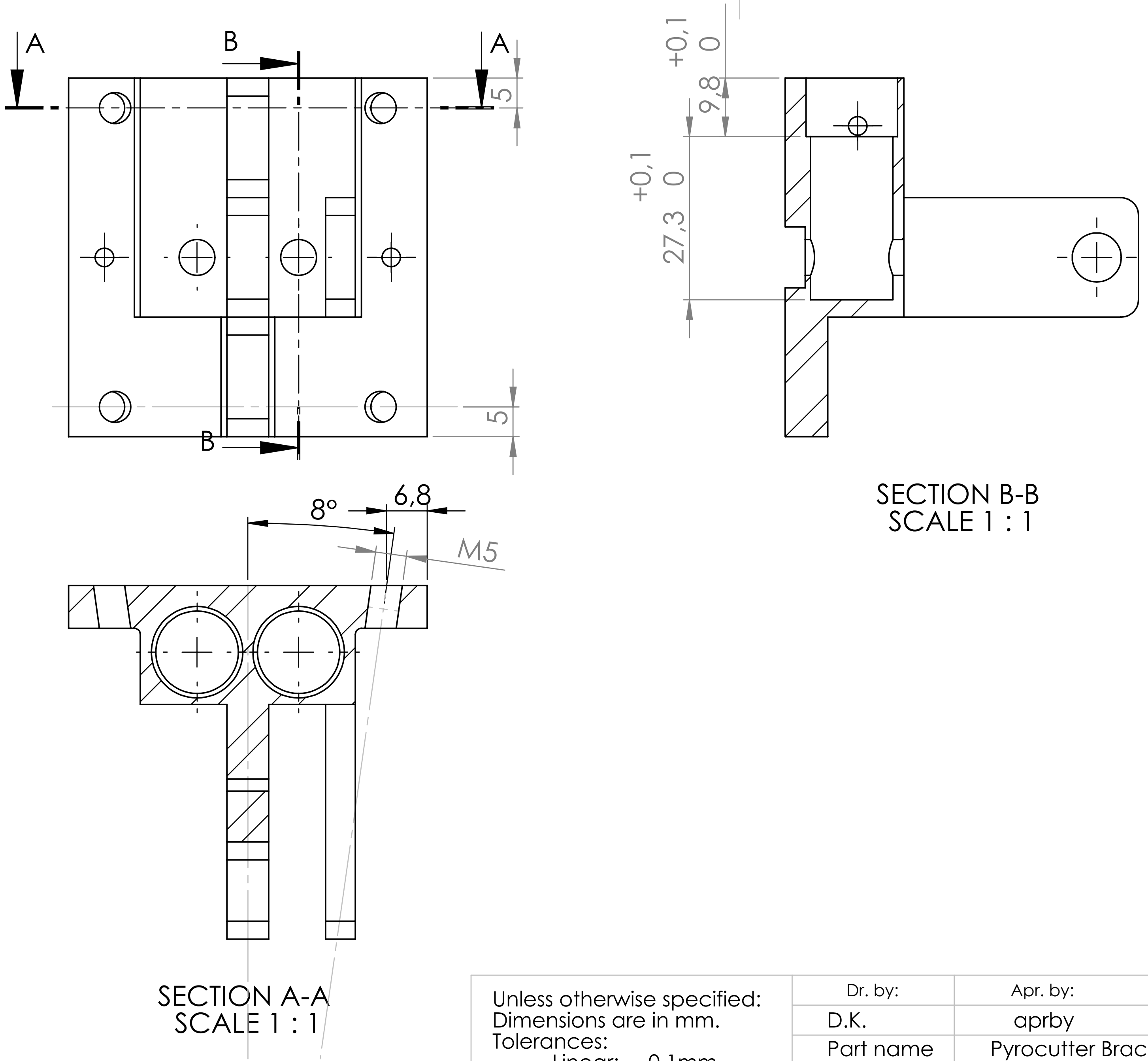

Unless otherwise specified:
Dimensions are in mm.
Tolerances:
Linear: 0.1mm
Angular: 1°

Dr. by:	Apr. by:	Material:		
D.K.	aprby	SS 304		
Part name	Pyrocutter Bracket		Version:	Date:
KTH, EES, SPP	Part number 2.03.00.02		2.3	02.10.12
WEIGHT:	SCALE:1:2		SHEET 2 OF 2	

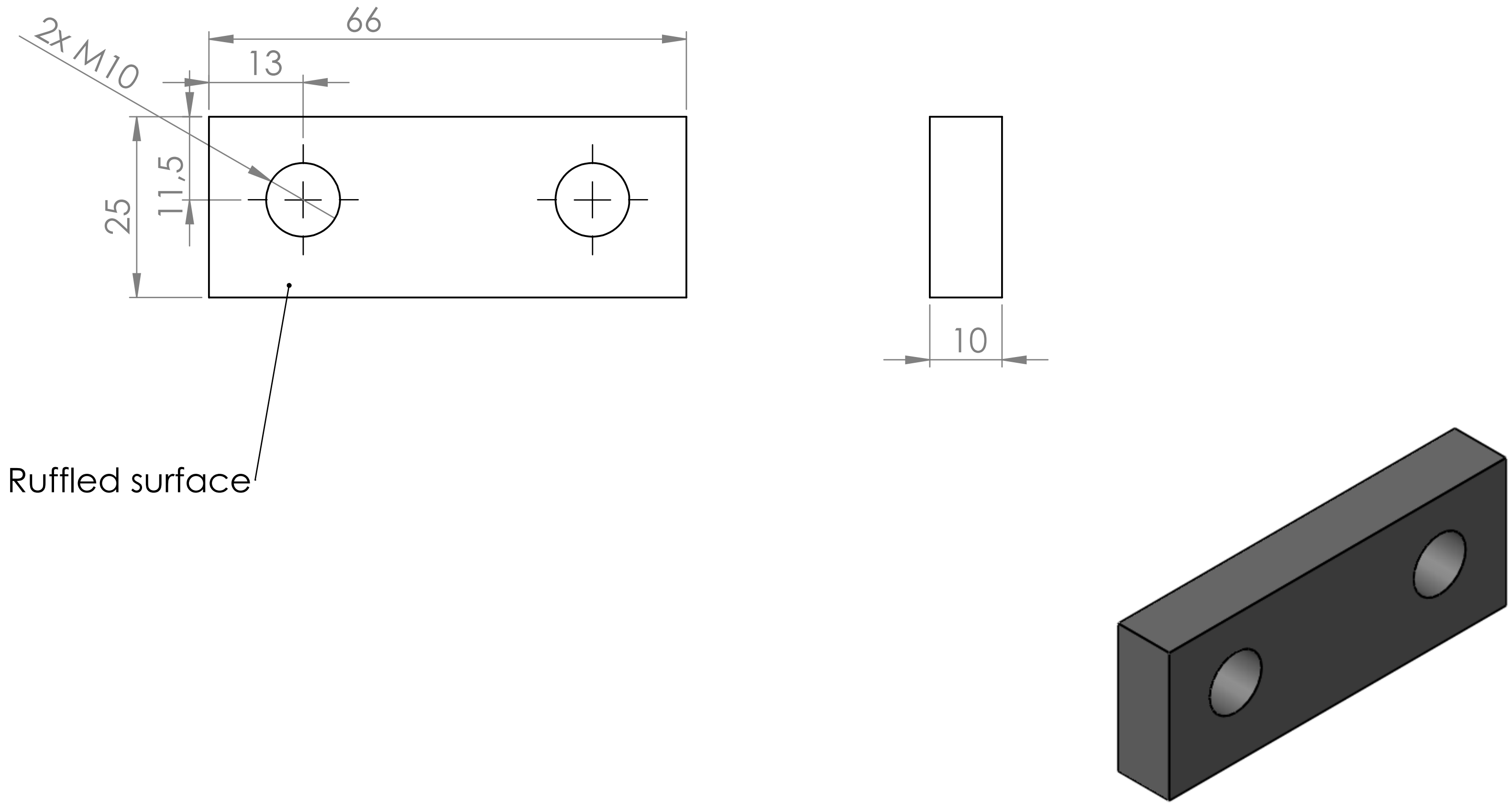

Unless otherwise specified:
Dimensions are in mm.
Tolerances:
Linear: 0.1mm
Angular: 1°

Dr. by:	Apr. by:	Material:		
D.K.	aprby	Steel		
Part name	Ruffled Steel Plate 1		Replaces:	Date:
KTH, EES, SPP	Part number 2.03.00.03			01.10.12

WEIGHT: SCALE:1:1 SHEET 1 OF 1

319

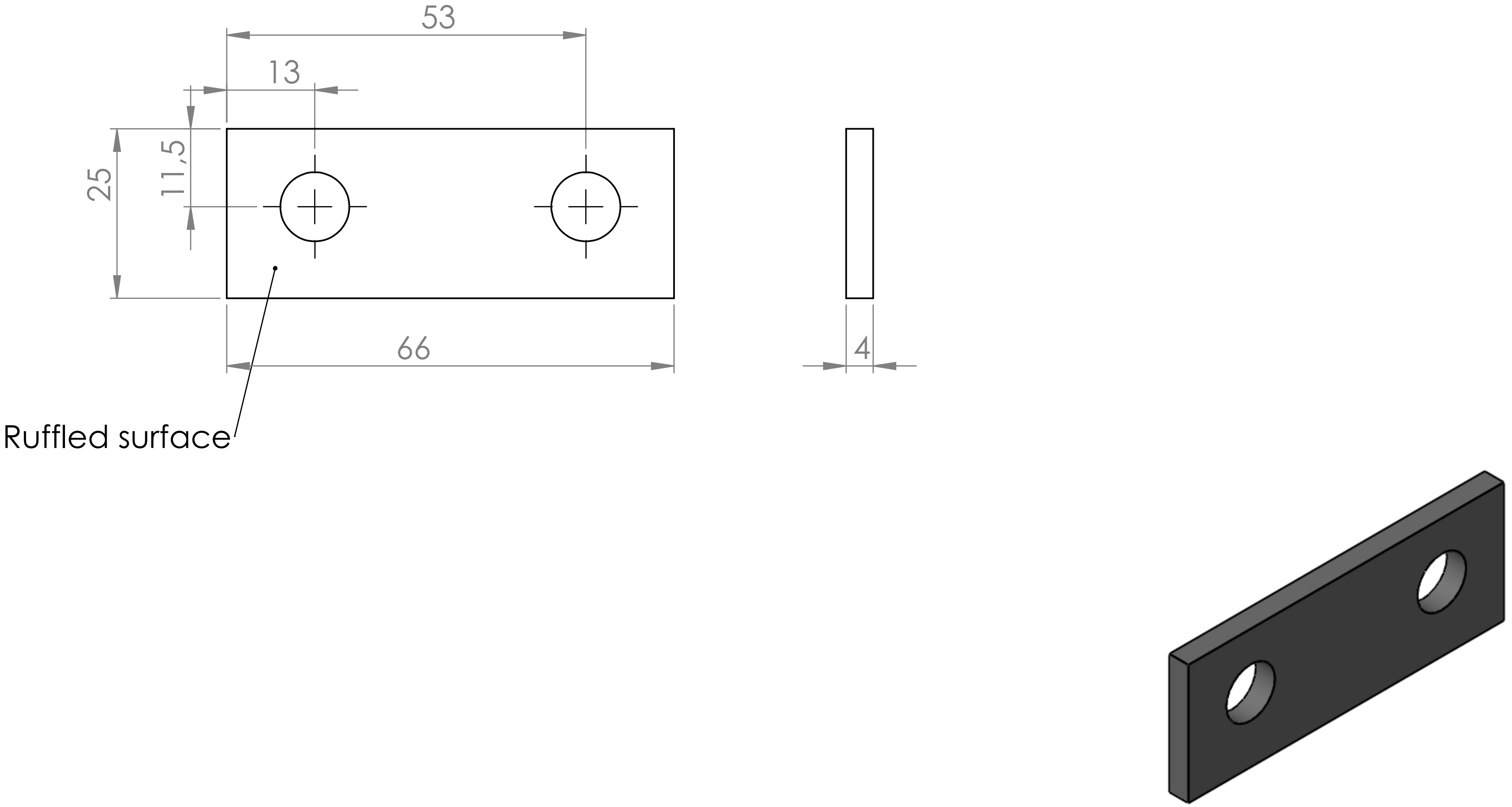

Unless otherwise specified: Dimensions are in mm. Tolerances: Linear: 0.1mm Angular: 1°	Dr. by:	Apr. by:	Material:	
	D.K.	aprby	Steel	
	Part name	Ruffled Steel Plate 2	Replaces:	Date:
	KTH, EES, SPP	Part number 2.03.00.04		01.10.12
	WEIGHT:	SCALE:1:1	SHEET 1 OF 1	

Assemble with 2.03.00.06 to check fit

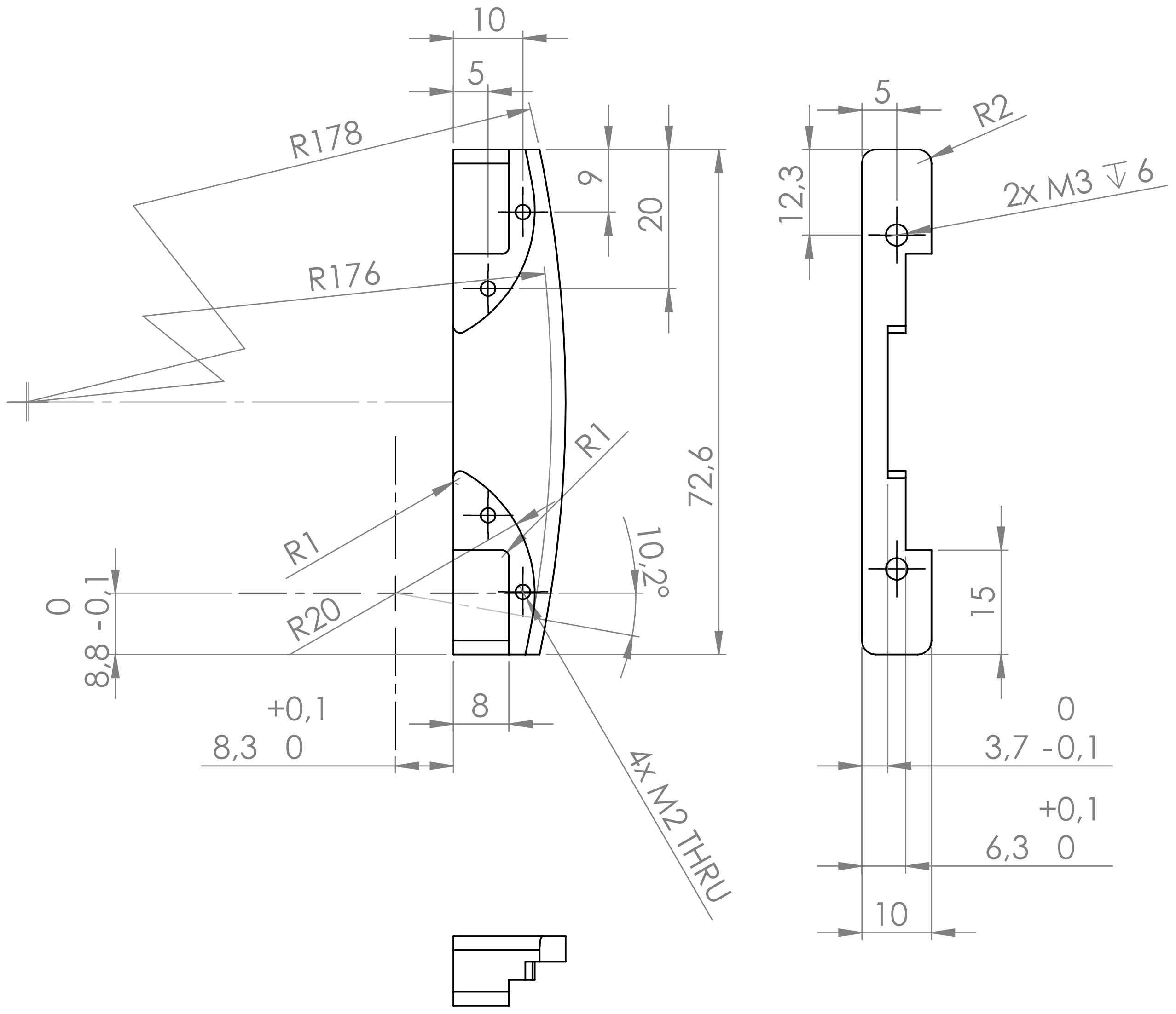

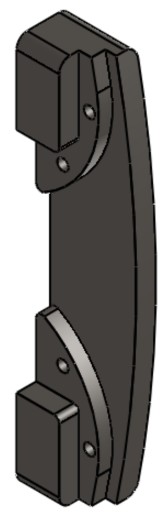

Unless otherwise specified: Dimensions are in mm. Tolerances: Linear: 0.1mm Angular: 1°	Dr. by:	Apr. by:	Material:		
	D.K.	aprby	SS 304		
	Part name	Cable Guide		Version	Date:
	KTH, EES, SPP	Part number 2.03.00.05		2.0	18.9.12
	WEIGHT:	SCALE:1:1		SHEET 1 OF 1	

321

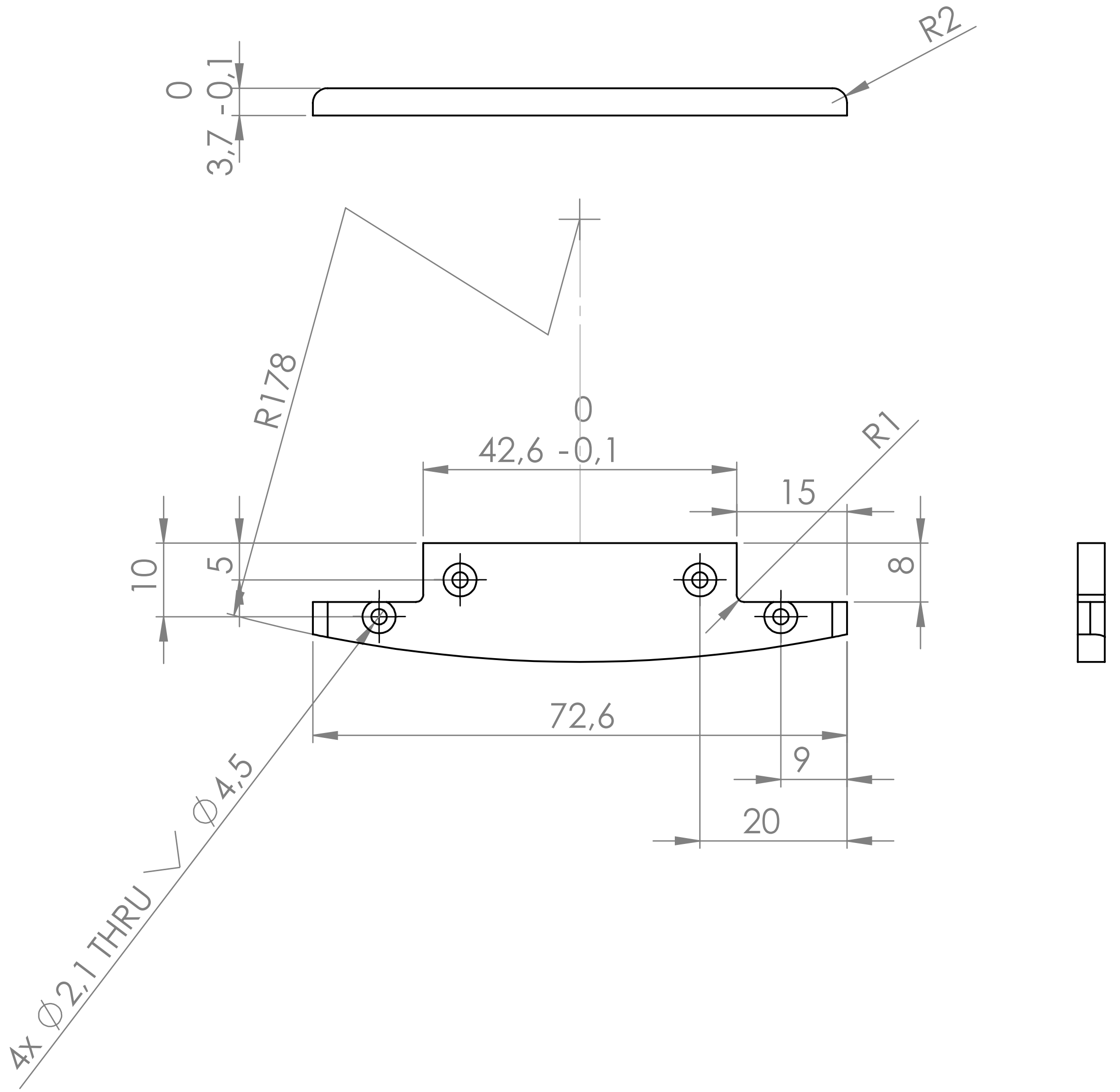

Unless otherwise specified:
Dimensions are in mm.
Tolerances:
Linear: 0.1mm
Angular: 1°

Dr. by:	Apr. by:	Material:		
D.K.	aprby	SS 304		
Part name	Cable Guide Cover		Version	Date:
KTH, EES, SPP	Part number 2.03.00.06		2.0	18.9.12

WEIGHT: SCALE:1:1 SHEET 1 OF 1

322

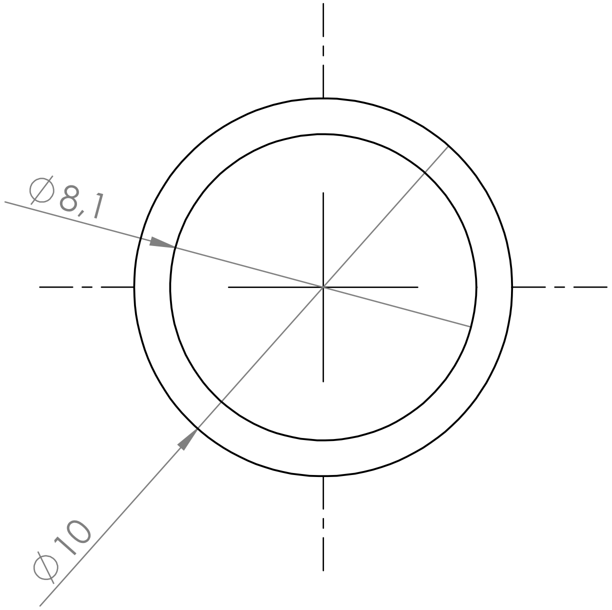

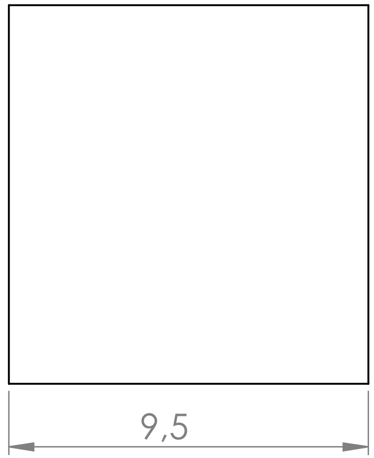

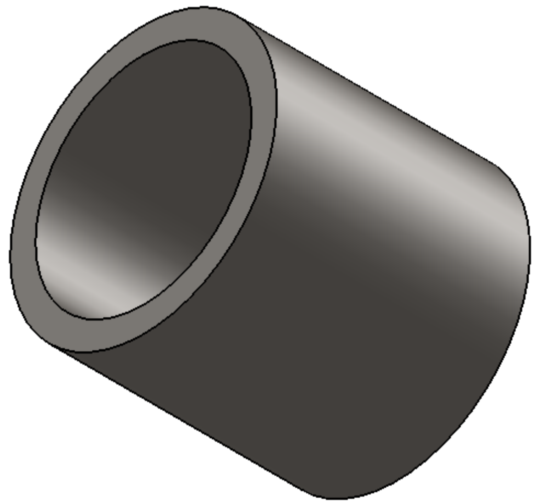

Unless otherwise specified:
Dimensions are in mm.
Tolerances:
Linear: 0.1mm
Angular: 1°

Dr. by:	Apr. by:	Material:		
D.K.	aprby	Steel		
Part name	Sleeve		Replaces:	Date:
KTH, EES, SPP	Part number 2.03.00.07			07.9.12
WEIGHT:	SCALE:5:1		SHEET 1 OF 1	

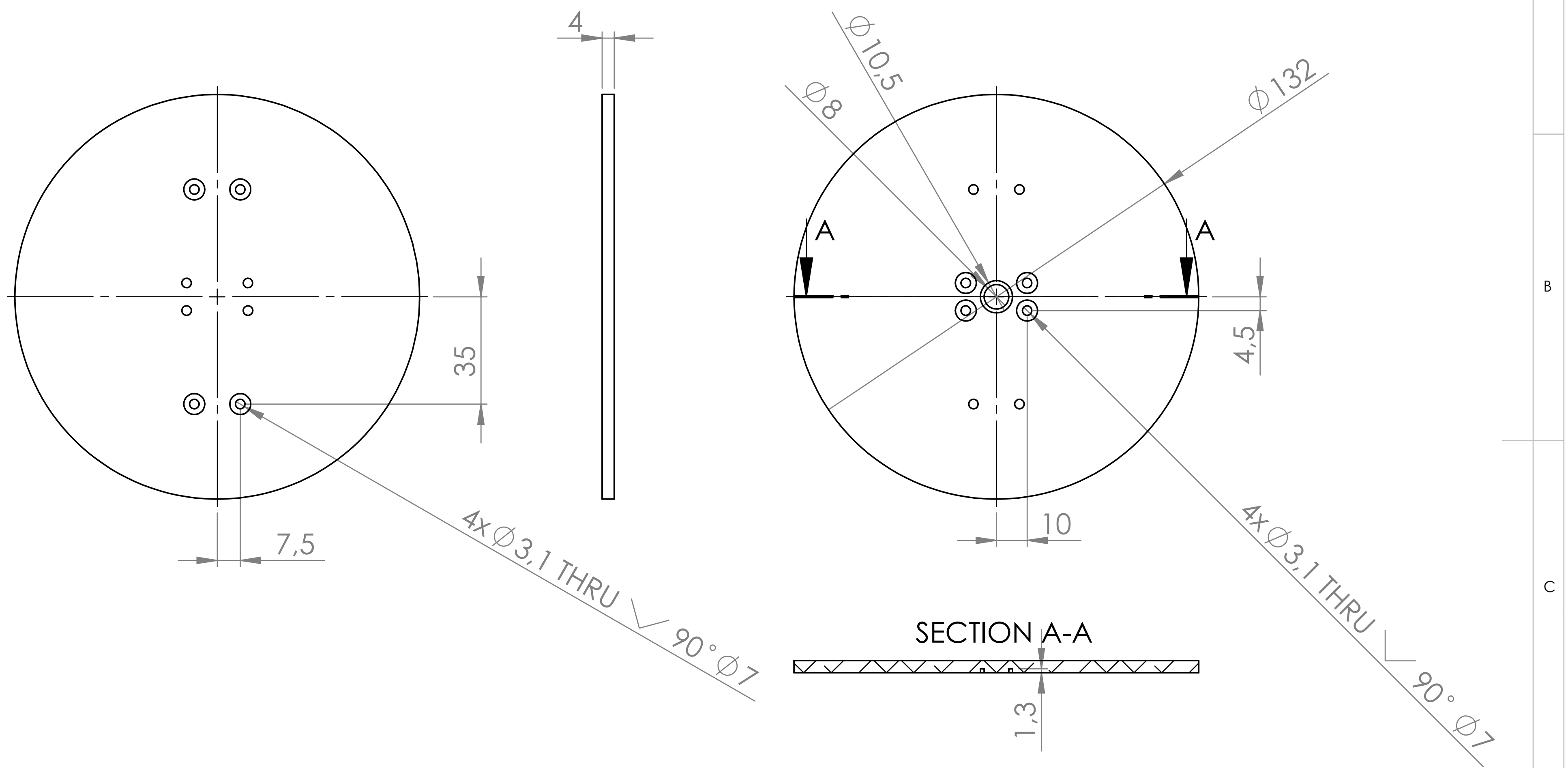

Unless otherwise specified:
Dimensions are in mm.
Tolerances:
Linear: 0.1mm
Angular: 1°

Dr. by:	Apr. by:	Material:		
D.K.	aprby	Aluminium 7075		
Part name	Hatch		Replaces:	Date:
KTH, EES, SPP	Part number 2.05.00.01			16.5.12
WEIGHT:	SCALE:1:2		SHEET 1 OF 1	

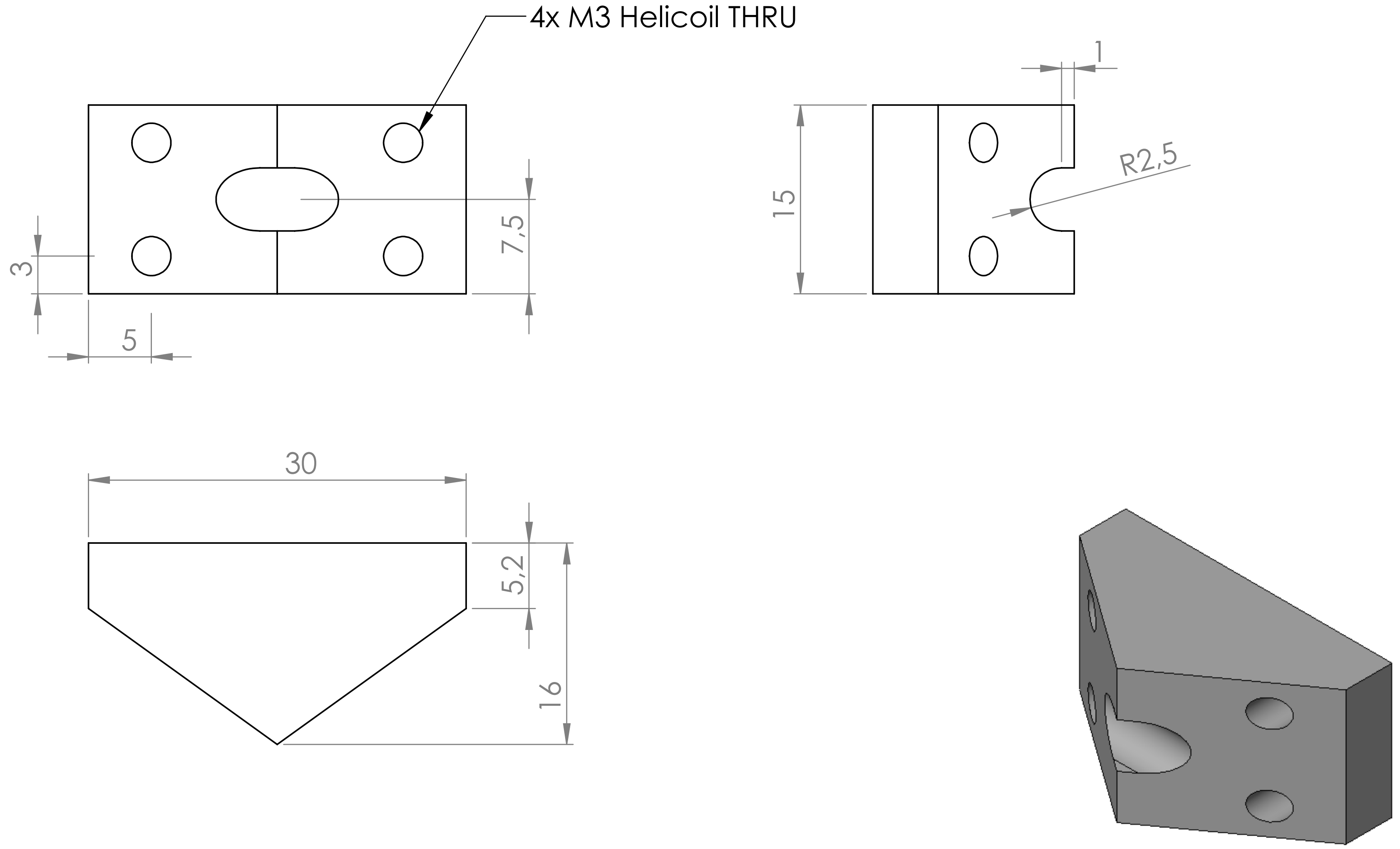

Unless otherwise specified: Dimensions are in mm. Tolerances: Linear: 0.1mm Angular: 1°	Dr. by:	Apr. by:	Material:		
	D.K.	aprby	Aluminium 7075		
	Part name	Triangular Fork		Replaces:	Date:
	KTH, EES, SPP	Part number 2.05.00.02			17.5.12
	WEIGHT:	SCALE:2:1		SHEET 1 OF 1	

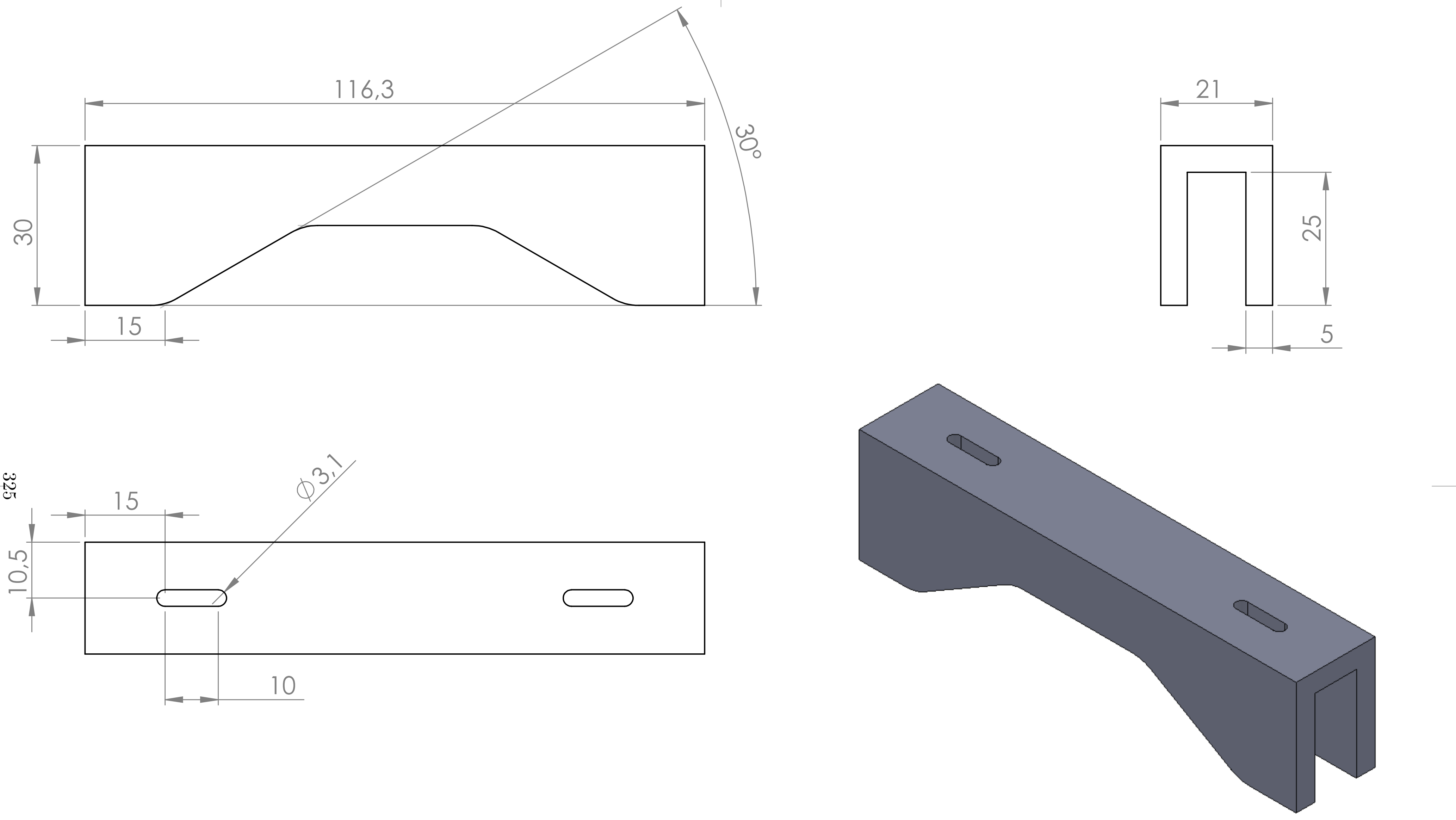

Unless otherwise specified:
Dimensions are in mm.
Tolerances:
Linear: 0.1mm
Angular: 1°

Dr. by:	Apr. by:	Material:		
D.K.	aprby	Aluminium 7075		
Part name	Safety Clip		Replaces:	Date:
KTH, EES, SPP	Part number 2.06.00.01			18.5.12

WEIGHT: SCALE:1:1 SHEET 1 OF 1

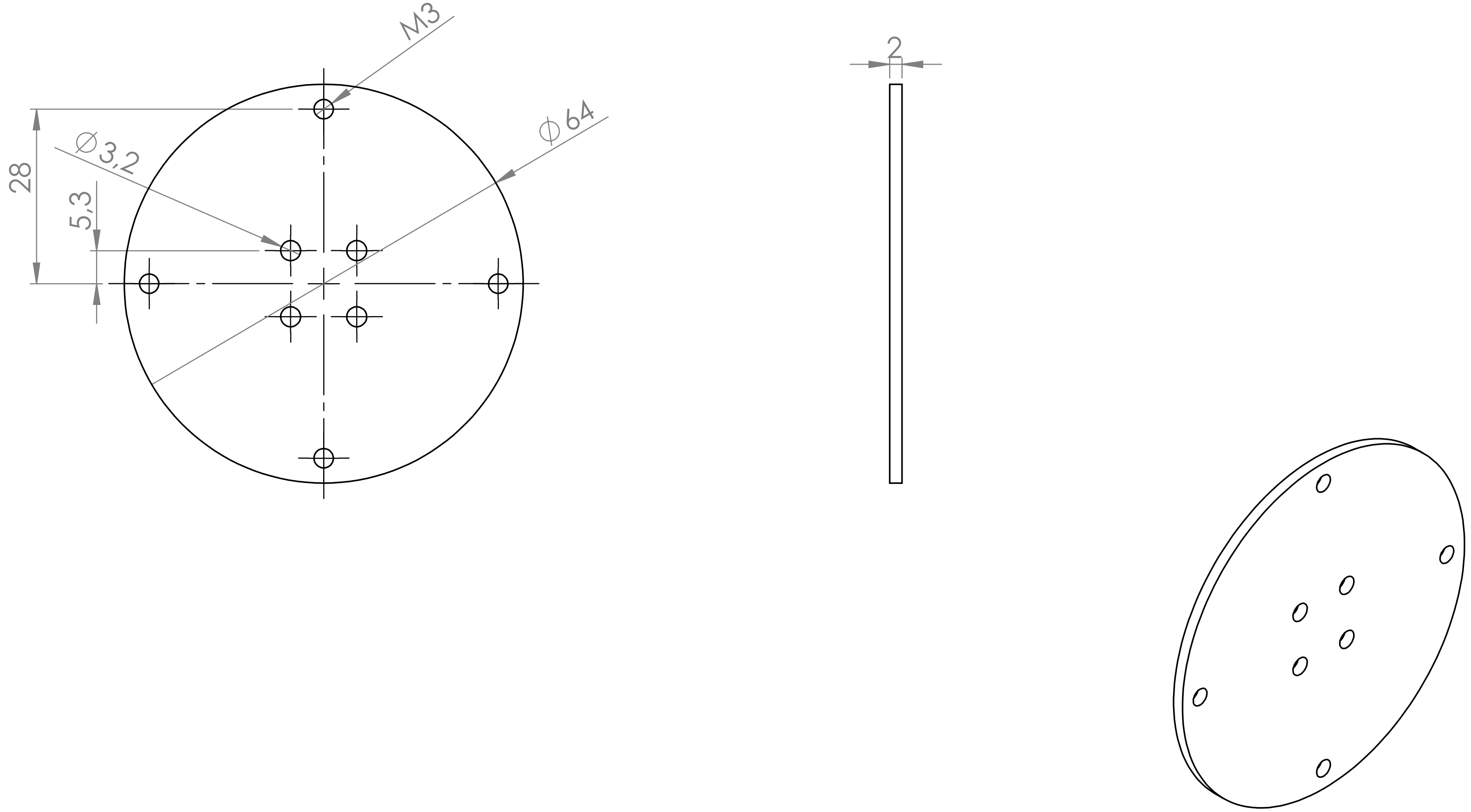

Unless otherwise specified:
Dimensions are in mm.
Tolerances:
Linear: 0.1mm
Angular: 1°

Dr. by:	Apr. by:	Material:		
D.K.	aprby	Aluminium 6082		
Part name	Upper Lock Plate		Replaces:	Date:
KTH, EES, SPP	Part number 2.06.00.02			20.11.12
WEIGHT:	SCALE:1:1		SHEET 1 OF 1	

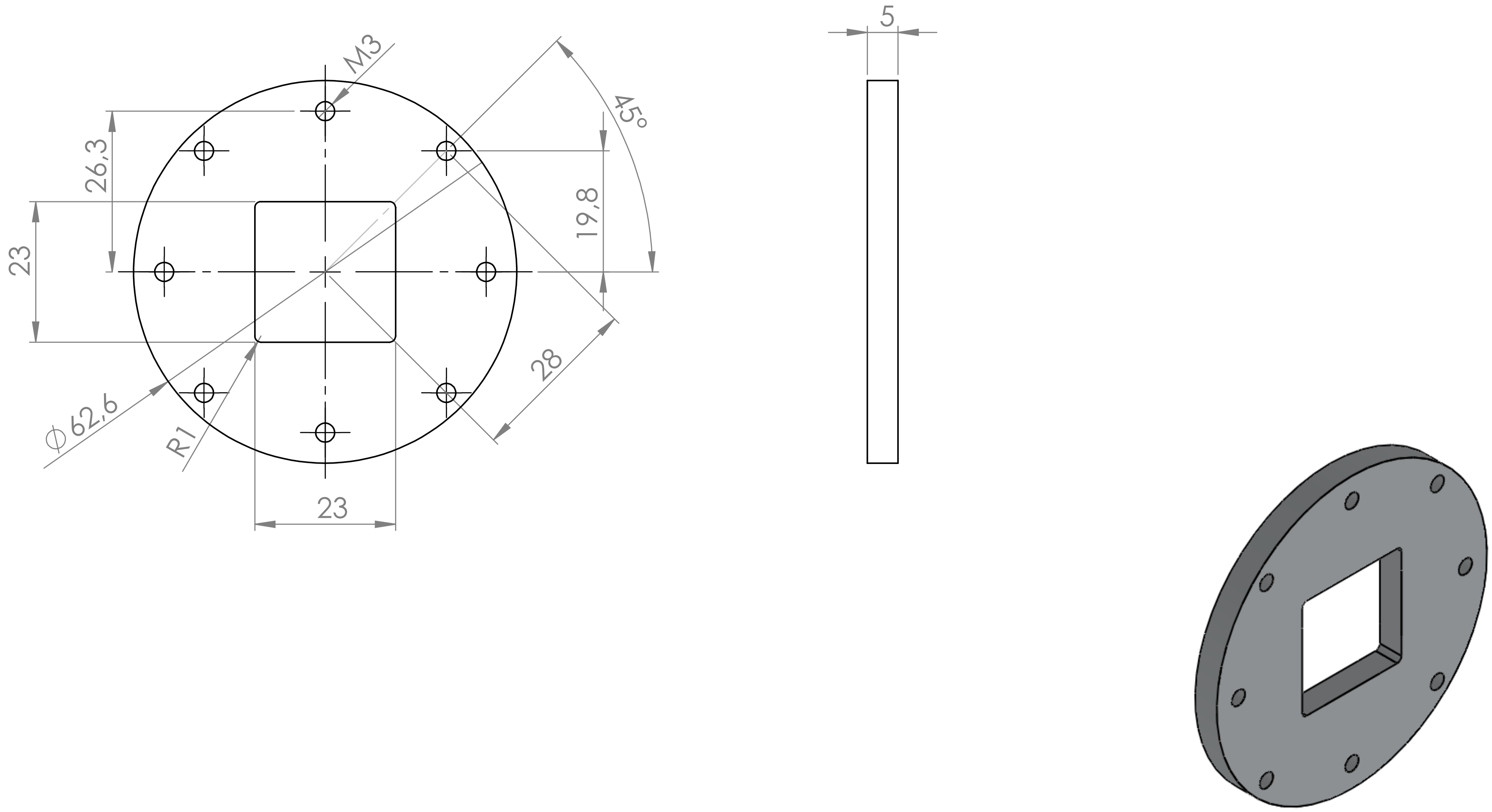

327

Unless otherwise specified:
Dimensions are in mm.
Tolerances:
Linear: 0.1mm
Angular: 1°

Dr. by:	Apr. by:	Material:		
D.K.	aprby	Aluminium 6082		
Part name	Lower Lock Plate		Replaces:	Date:
KTH, EES, SPP	Part number 2.06.00.03			20.11.12
WEIGHT:	SCALE:1:1		SHEET 1 OF 1	

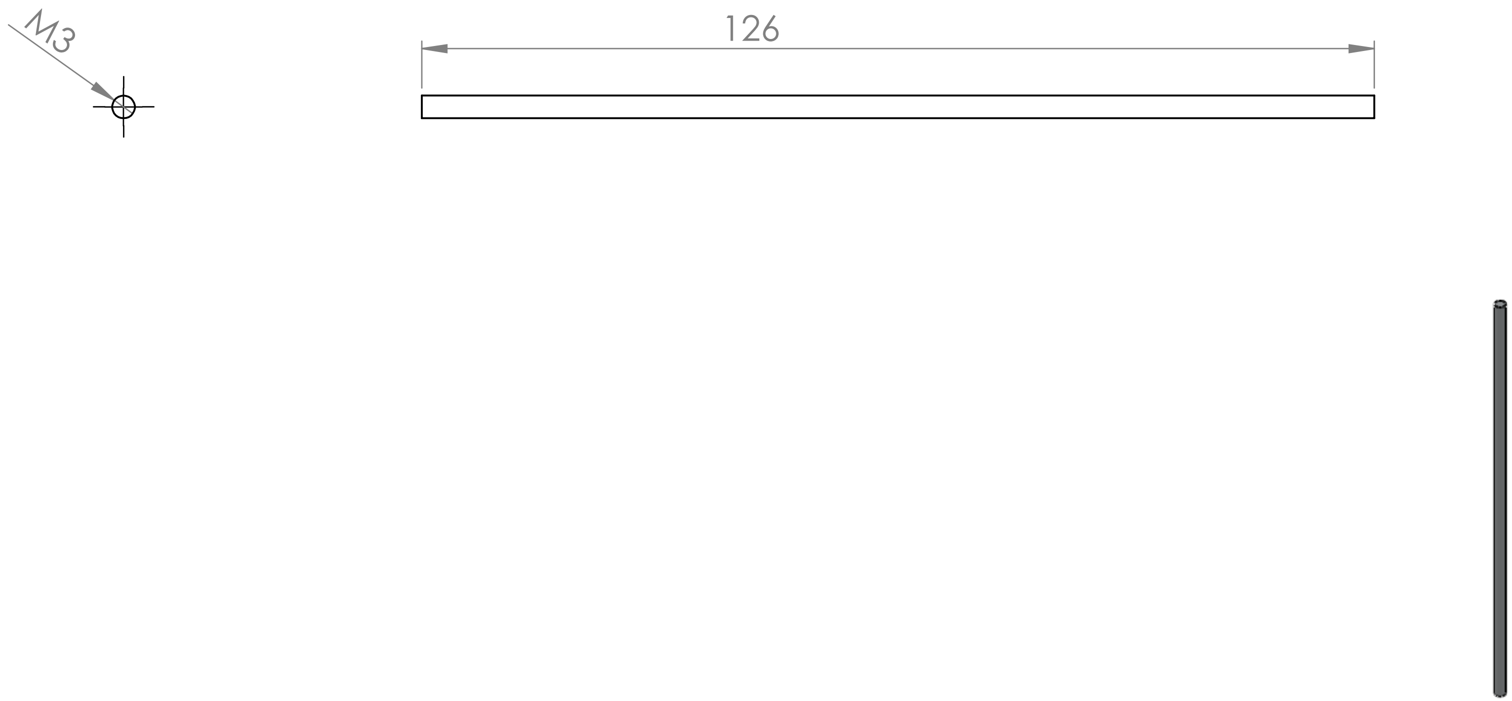

328

Unless otherwise specified: Dimensions are in mm. Tolerances: Linear: 0.1mm Angular: 1°	Dr. by:	Apr. by:	Material:		
	D.K.	aprby	Aluminium 6082		
	Part name	Threaded Rod		Replaces:	Date:
	KTH, EES, SPP	Part number 2.06.00.04			20.11.12
	WEIGHT:	SCALE:1:2		SHEET 1 OF 1	

329

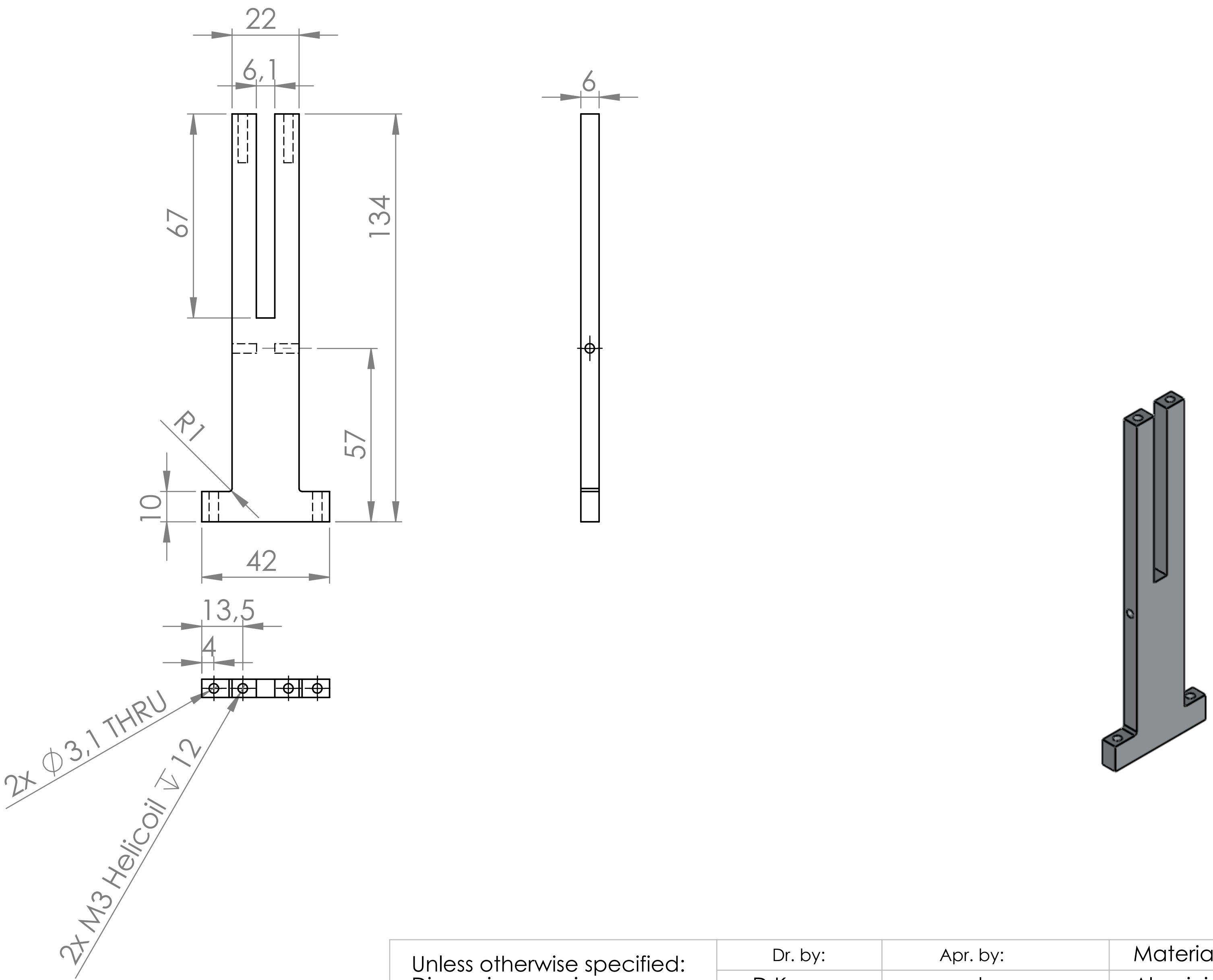

Unless otherwise specified:
Dimensions are in mm.
Tolerances:
Linear: 0.1mm
Angular: 1°

Dr. by:	Apr. by:	Material:		
D.K.	aprby	Aluminium 6062		
Part name	Center Piece 1		Replaces:	Date:
KTH, EES, SPP	Part number 2.07.00.01			01.10.12
WEIGHT:	SCALE:1:2		SHEET 1 OF 2	

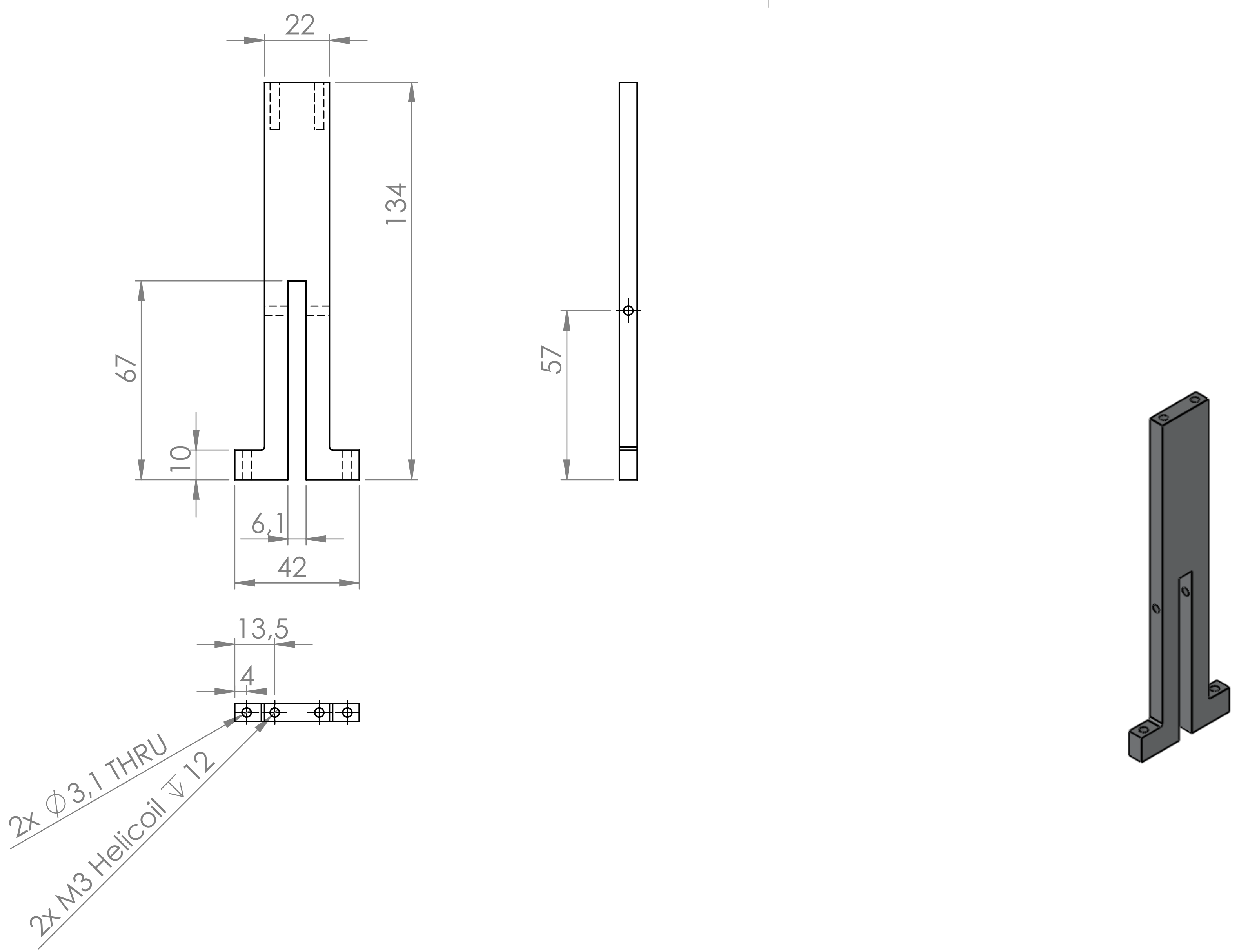

Unless otherwise specified:
Dimensions are in mm.
Tolerances:
Linear: 0.1mm
Angular: 1°

Dr. by:	Apr. by:	Material:		
D.K.	aprby	Aluminium 6062		
Part name	Center Piece 2		Replaces:	Date:
KTH, EES, SPP	Part number 2.07.00.02			01.10.12
WEIGHT:	SCALE:1:2		SHEET 2 OF 2	

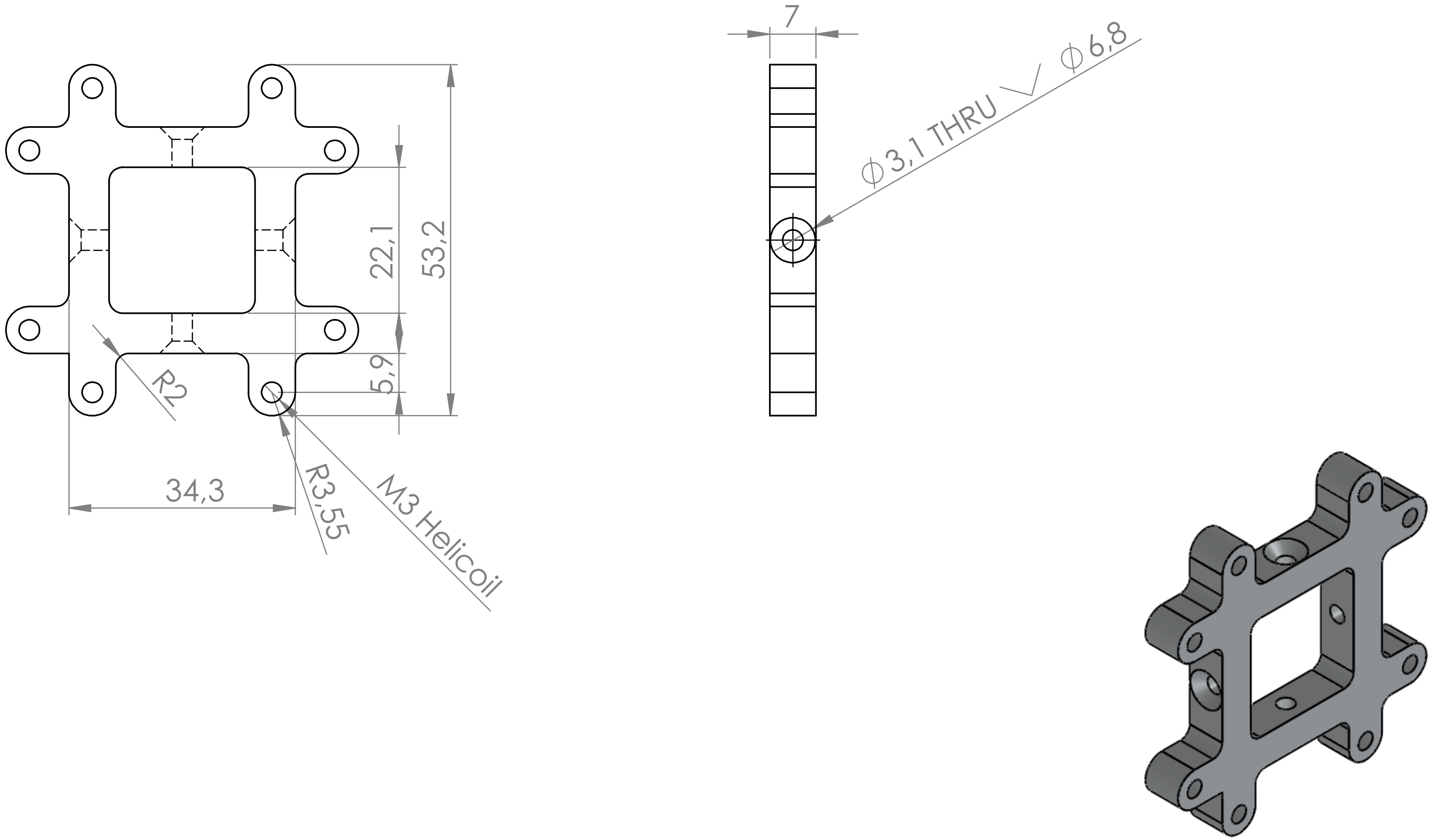

Unless otherwise specified: Dimensions are in mm. Tolerances: Linear: 0.1mm Angular: 1°	Dr. by:	Apr. by:	Material:	
	D.K.	aprby	Aluminium 6082	
	Part name	Umbilical bracket	Version:	Date:
	KTH, EES, SPP	Part number 2.07.00.03	2.0	02.10.12
	WEIGHT:	SCALE:1:1	SHEET 1 OF 1	

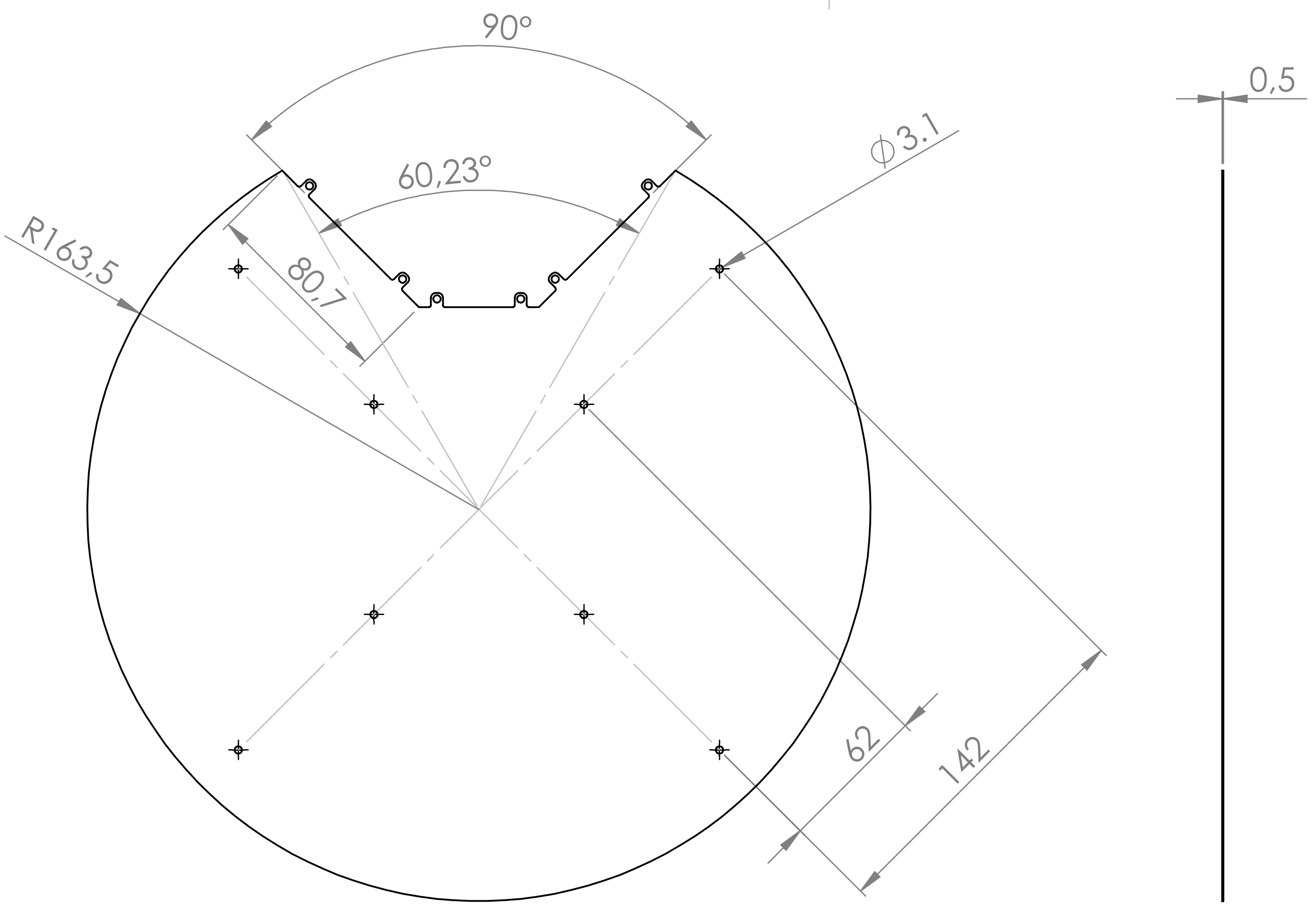

332

Unless otherwise specified: Dimensions are in mm. Tolerances: Linear: 0.1mm Angular: 1°	Dr. by:	Apr. by:	Material:		
	D.K.	aprby	Aluminium 7075		
	Part name	Upper Cover		Replaces:	Date:
	KTH, EES, SPP	Part number 2.08.00.01			18.7.12
	WEIGHT:	SCALE:1:5		SHEET 1 OF 1	

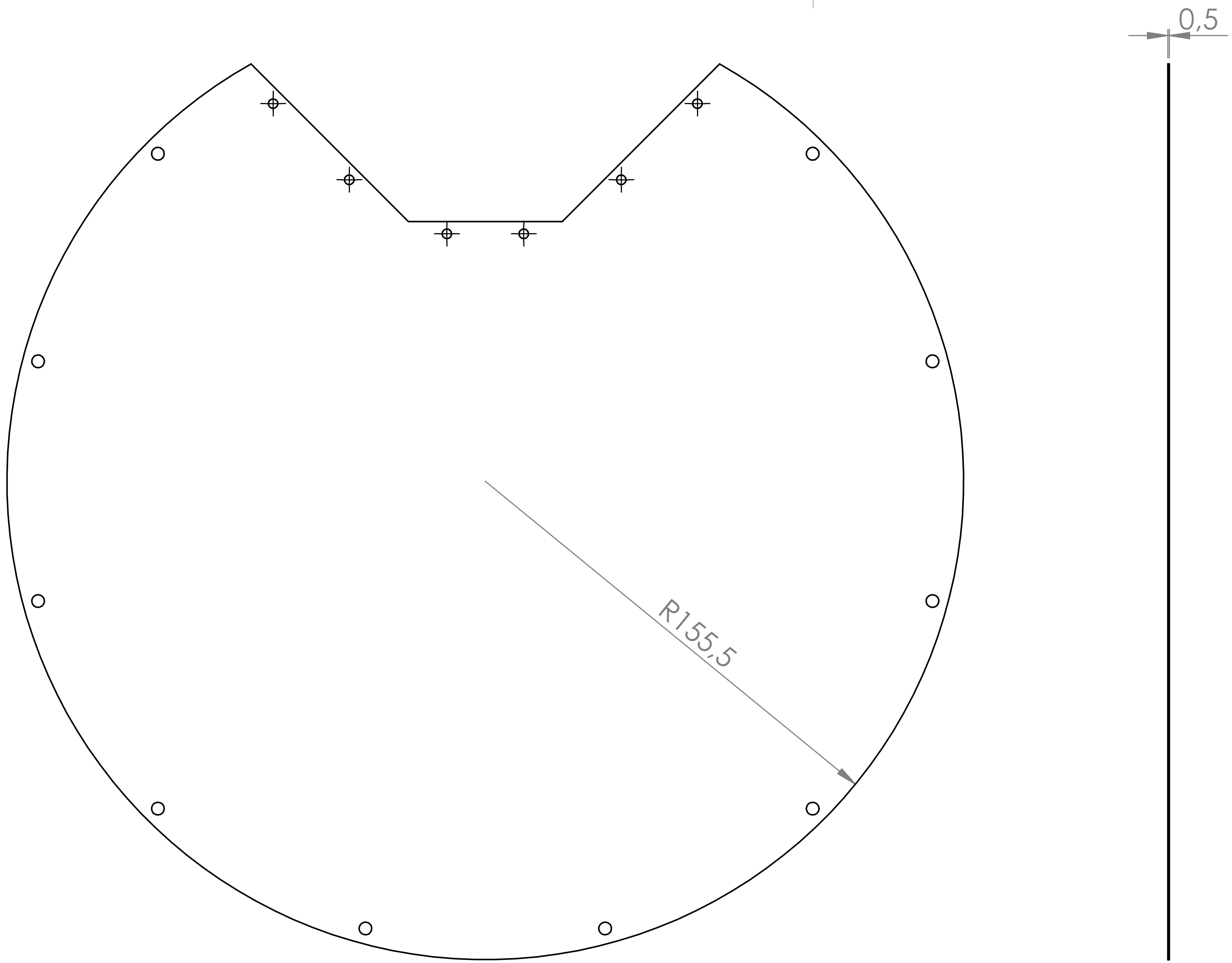

Unless otherwise specified:
Dimensions are in mm.
Tolerances:
Linear: 0.1mm
Angular: 1°

Dr. by:	Apr. by:	Material:		
D.K.	aprby	Aluminium 7075		
Part name	Lower Cover		Replaces:	Date:
KTH, EES, SPP	Part number 2.08.00.02			04.9.12
WEIGHT:	SCALE:1:5		SHEET 1 OF 1	

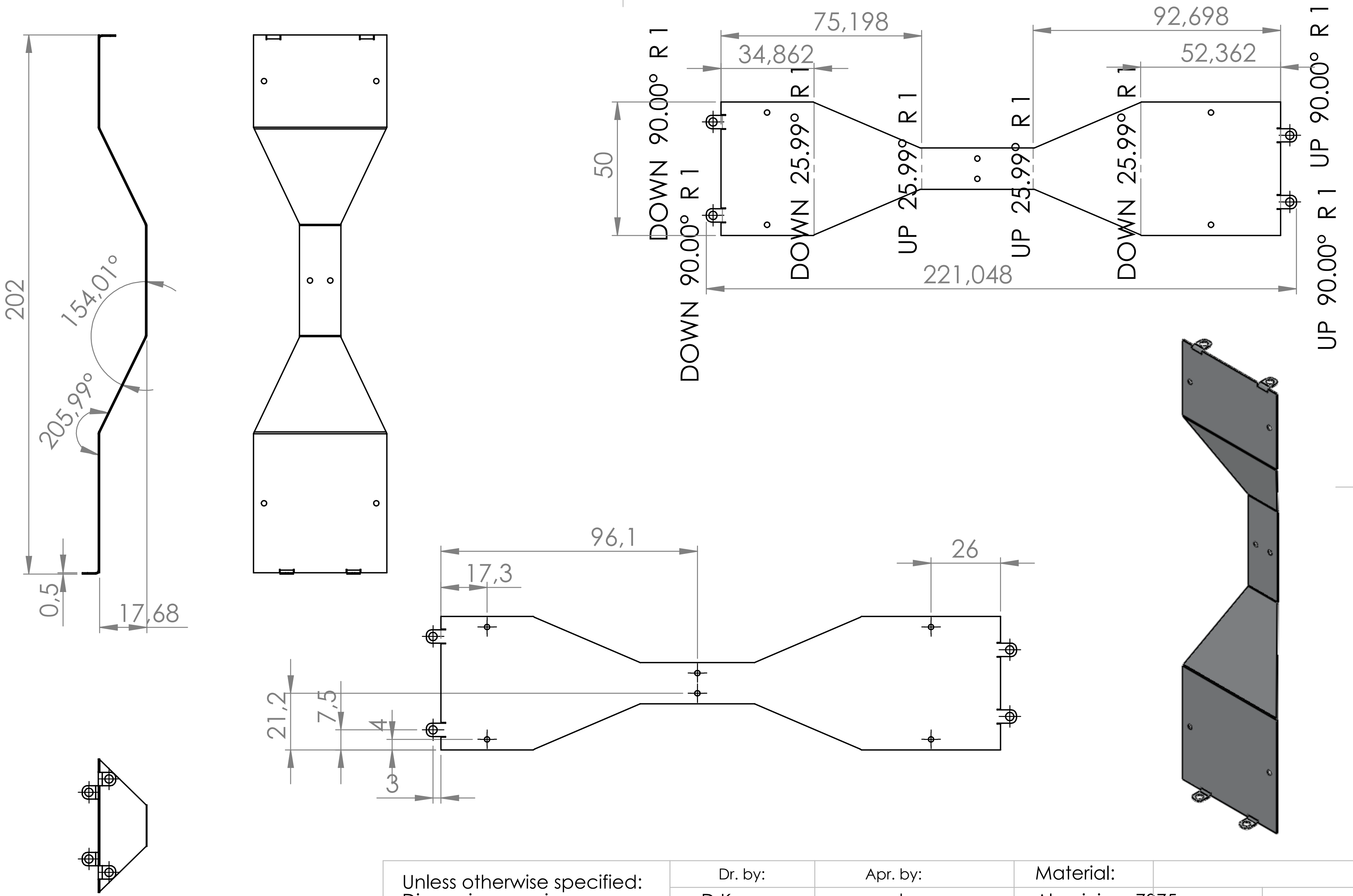

Unless otherwise specified: Dimensions are in mm. Tolerances: Linear: 0.1mm Angular: 1°	Dr. by:	Apr. by:	Material:	
	D.K.	aprby	Aluminium 7075	
	Part name	Tunnel Backside	Version:	Date:
	KTH, EES, SPP	Part number 2.08.00.03	v2.0	5.2.13
	WEIGHT:	SCALE:1:5	SHEET 1 OF 1	

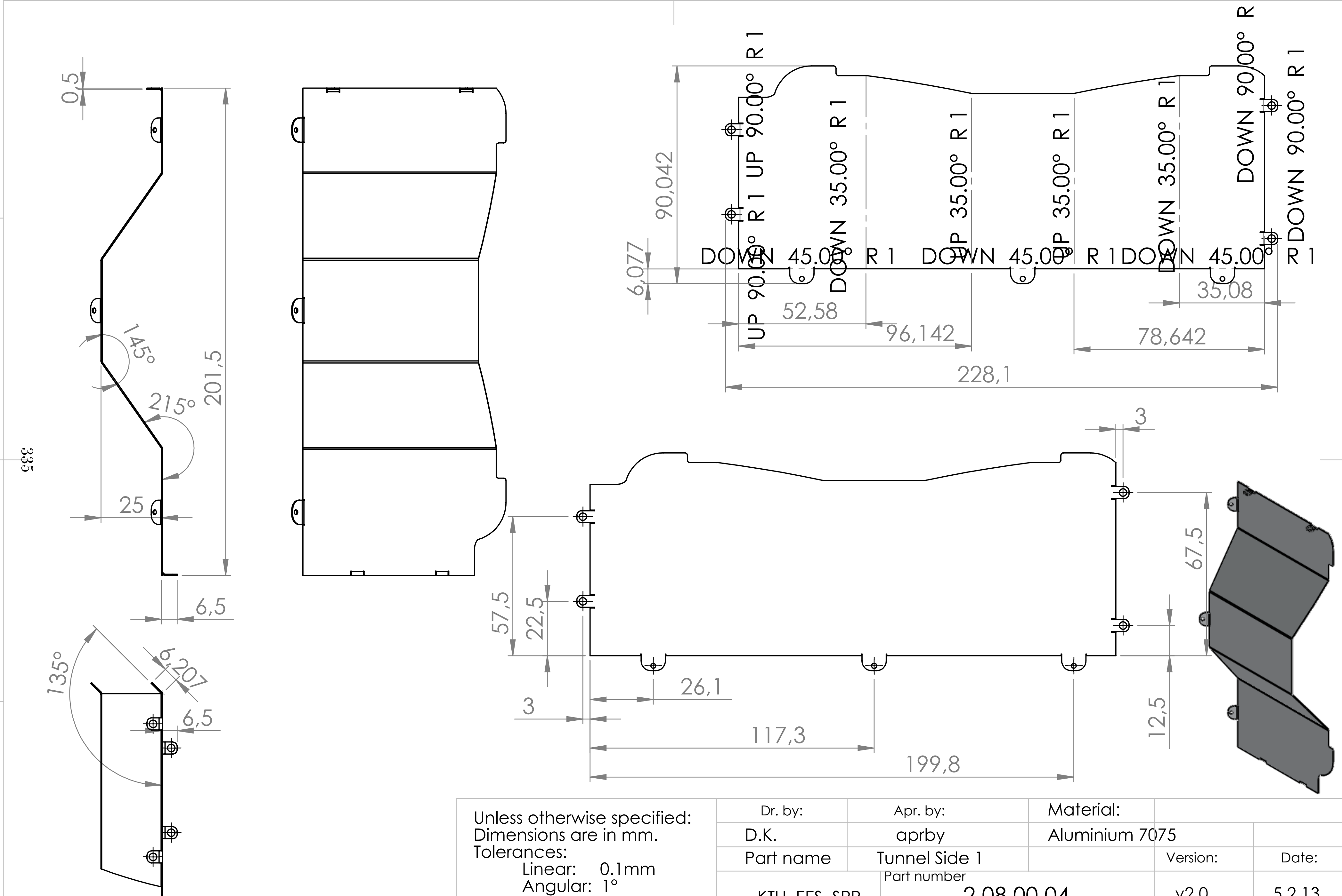

Unless otherwise specified:
Dimensions are in mm.
Tolerances:
Linear: 0.1mm
Angular: 1°

Dr. by:	Apr. by:	Material:	
D.K.	aprby	Aluminium 7075	
Part name	Tunnel Side 1	Version:	Date:
KTH, EES, SPP	Part number 2.08.00.04	v2.0	5.2.13

WEIGHT: SCALE:1:5 SHEET 1 OF 2

Mirror of 2.08.00.04

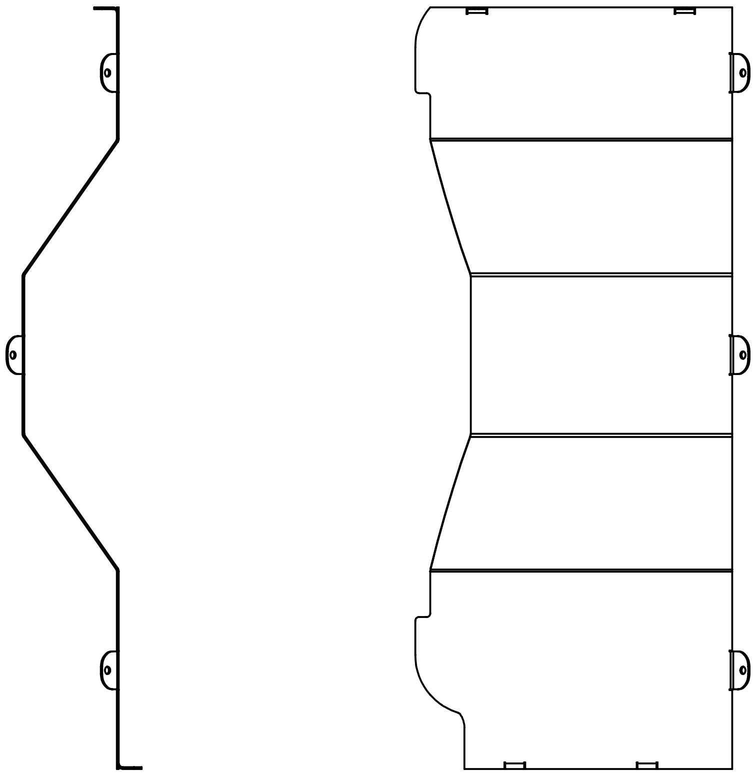

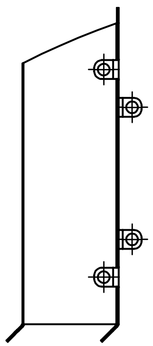

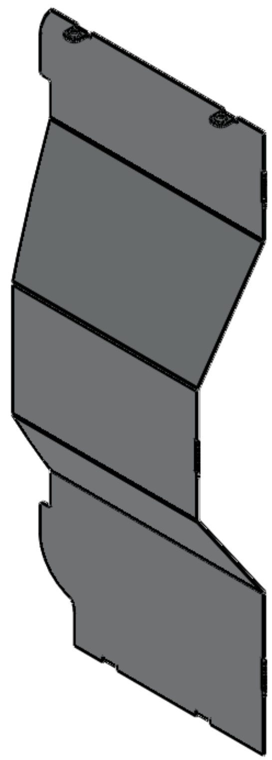

Unless otherwise specified:
Dimensions are in mm.
Tolerances:
Linear: 0.1mm
Angular: 1°

Dr. by:	Apr. by:	Material:		
D.K.	aprby	Aluminium 7075		
Part name	Tunnel Side 2		Replaces:	Date:
KTH, EES, SPP	Part number 2.08.00.05			04.9.12

WEIGHT: SCALE:1:5 SHEET 2 OF 2

Unless otherwise specified:
Dimensions are in mm.
Tolerances:
Linear: 0.1mm
Angular: 1°

Dr. by:	Apr. by:	Material:		
D.K.	aprby	POM		
Part name	Gas Cover Spacer		Replaces:	Date:
KTH, EES, SPP	Part number 2.08.00.06			04.9.12
WEIGHT:	SCALE:2:1		SHEET 1 OF 1	

Appendix D

Schematics and Layouts

The following chapter shows the schematics and layout for the MUSCAT electronics sub-systems.

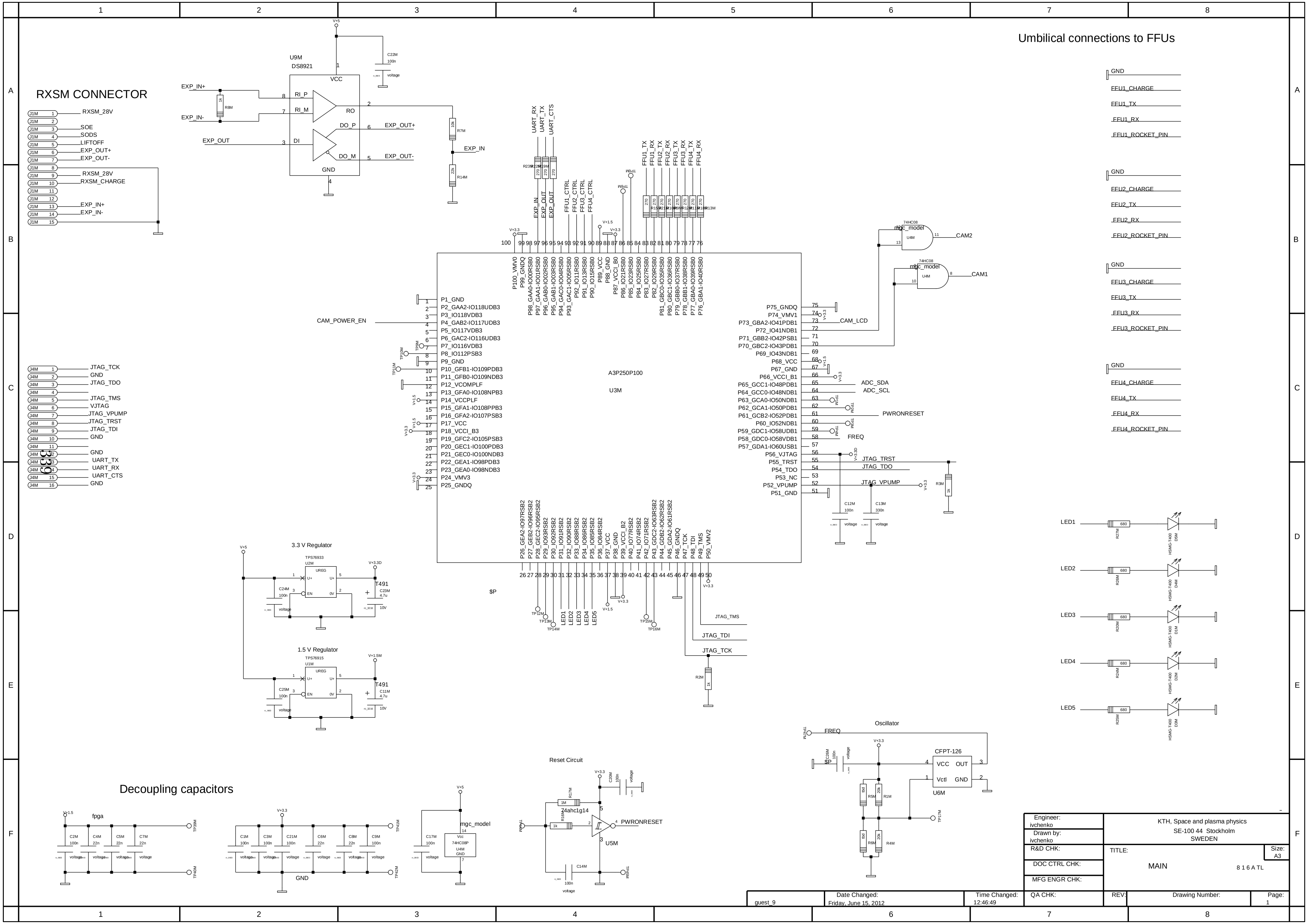
Umbilical connections to FFUs
RXSM CONNECTOR
RXSM_28V
SOE
SODS
LIFTOFF
EXP_OUT+
EXP_OUT-
RXSM_28V
RXSM_CHARGE
EXP_IN+
EXP_IN-
U9M
DS8921
EXP_IN
EXP_OUT
CAM_POWER_EN
JTAG_TCK
GND
JTAG_TDO
JTAG_TMS
VJTAG
JTAG_VPUMP
JTAG_TRST
JTAG_TDI
UART_TX
UART_RX
UART_CTS
A3P250P100
U3M
CAM1
CAM2
CAM_LCD
ADC_SDA
ADC_SCL
PWRONRESET
FREQ
FFU1_CHARGE
FFU1_TX
FFU1_RX
FFU1_ROCKET_PIN
FFU2_CHARGE
FFU2_TX
FFU2_RX
FFU2_ROCKET_PIN
FFU3_CHARGE
FFU3_TX
FFU3_RX
FFU3_ROCKET_PIN
FFU4_CHARGE
FFU4_TX
FFU4_RX
FFU4_ROCKET_PIN
LED1
LED2
LED3
LED4
LED5
HSMG-T400
3.3 V Regulator
TPS76933
1.5 V Regulator
TPS76915
Reset Circuit
74ahc1g14
U5M
Oscillator
CFPT-126
U6M
Decoupling capacitors
fpga
mgc_model
74HC08P
Engineer:
ivchenko
Drawn by:
ivchenko
R&D CHK:
DOC CTRL CHK:
MFG ENGR CHK:
QA CHK:
KTH, Space and plasma physics
SE-100 44 Stockholm
SWEDEN
TITLE:
MAIN
Size:
A3
8 1 6 A TL
REV:
Drawing Number:
Page:
1
guest_9
Date Changed:
Friday, June 15, 2012
Time Changed:
12:46:49

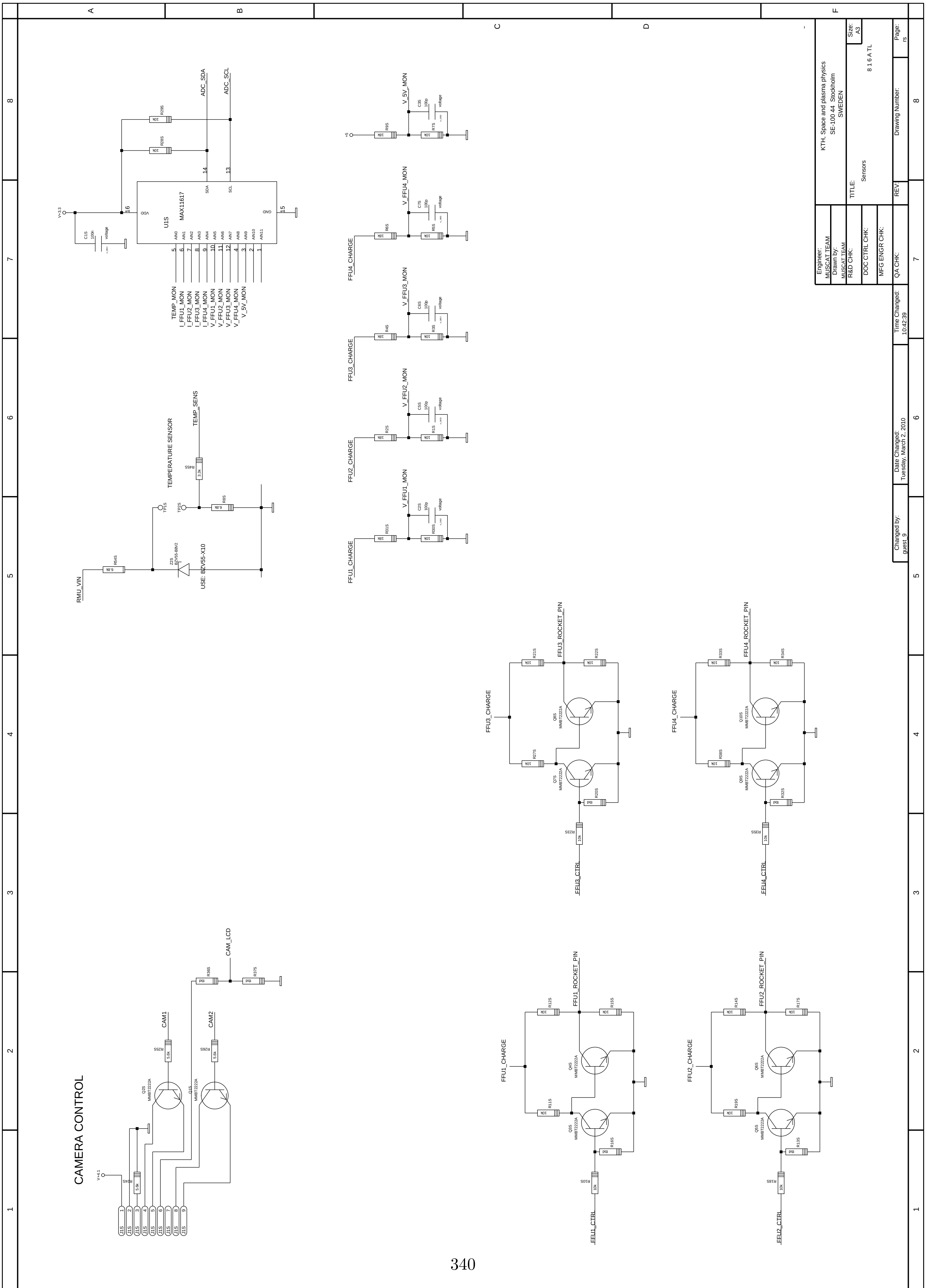
CAMERA CONTROL
CAM1
CAM2
CAM_LCD
TEMPERATURE SENSOR
TEMP_SENS
RMU_VIN
USE: BZV55-X10
MAX11617
ADC_SDA
ADC_SCL
TEMP_MON
I_FFU1_MON
I_FFU2_MON
I_FFU3_MON
I_FFU4_MON
V_FFU1_MON
V_FFU2_MON
V_FFU3_MON
V_FFU4_MON
V_5V_MON
FFU1_CHARGE
FFU2_CHARGE
FFU3_CHARGE
FFU4_CHARGE
FFU1_ROCKET_PIN
FFU2_ROCKET_PIN
FFU3_ROCKET_PIN
FFU4_ROCKET_PIN
FFU1_CTRL
FFU2_CTRL
FFU3_CTRL
FFU4_CTRL
KTH, Space and plasma physics
SE-100 44 Stockholm
SWEDEN
TITLE:
Sensors
Engineer:
MUSCAT TEAM
Drawn by:
MUSCAT TEAM
R&D CHK:
DOC CTRL CHK:
MFG ENGR CHK:
QA CHK:
Size:
A3
Drawing Number:
8 1 6 A TL
Page:
rs
REV:
Time Changed:
10:42:39
Date Changed:
Tuesday, March 2, 2010
Changed by:
guest_9

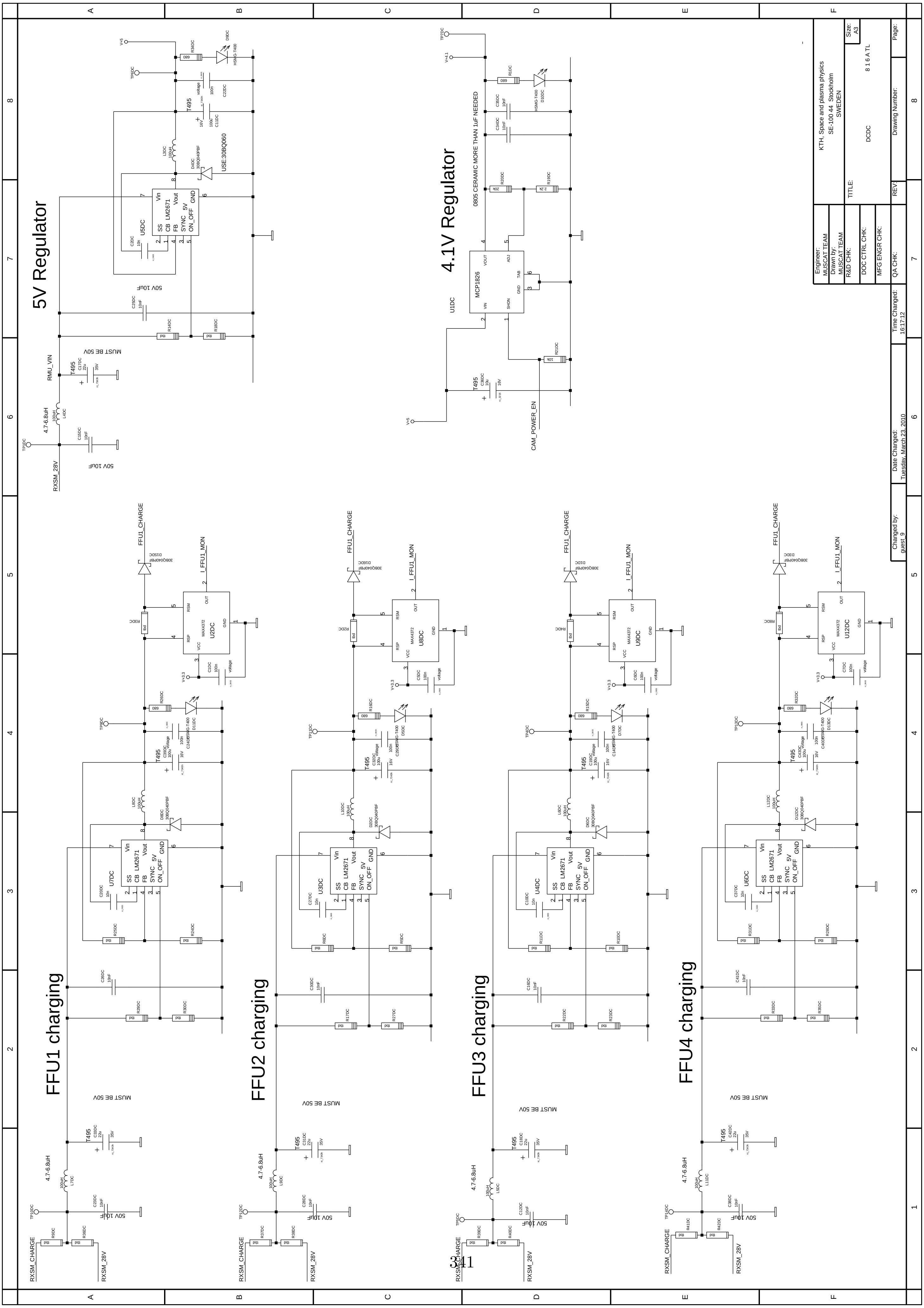
5V Regulator
4.1V Regulator
0805 CERAMIC MORE THAN 1uF NEEDED
FFU1 charging
FFU2 charging
FFU3 charging
FFU4 charging
MUST BE 50V
50V 10uF
RXSM_28V
RXSM_CHARGE
RMU_VIN
CAM_POWER_EN
FFU1_CHARGE
I_FFU1_MON
LM2671
MCP1826
MAX4372
KTH, Space and plasma physics
SE-100 44 Stockholm
SWEDEN
DCDC
Engineer: MUSCAT TEAM
Drawn by: MUSCAT TEAM
R&D CHK:
DOC CTRL CHK:
MFG ENGR CHK:
QA CHK:
TITLE:
Size: A3
Drawing Number:
Page:
REV:
Time Changed: 16:17:12
Date Changed: Tuesday, March 23, 2010
Changed by: guest_9

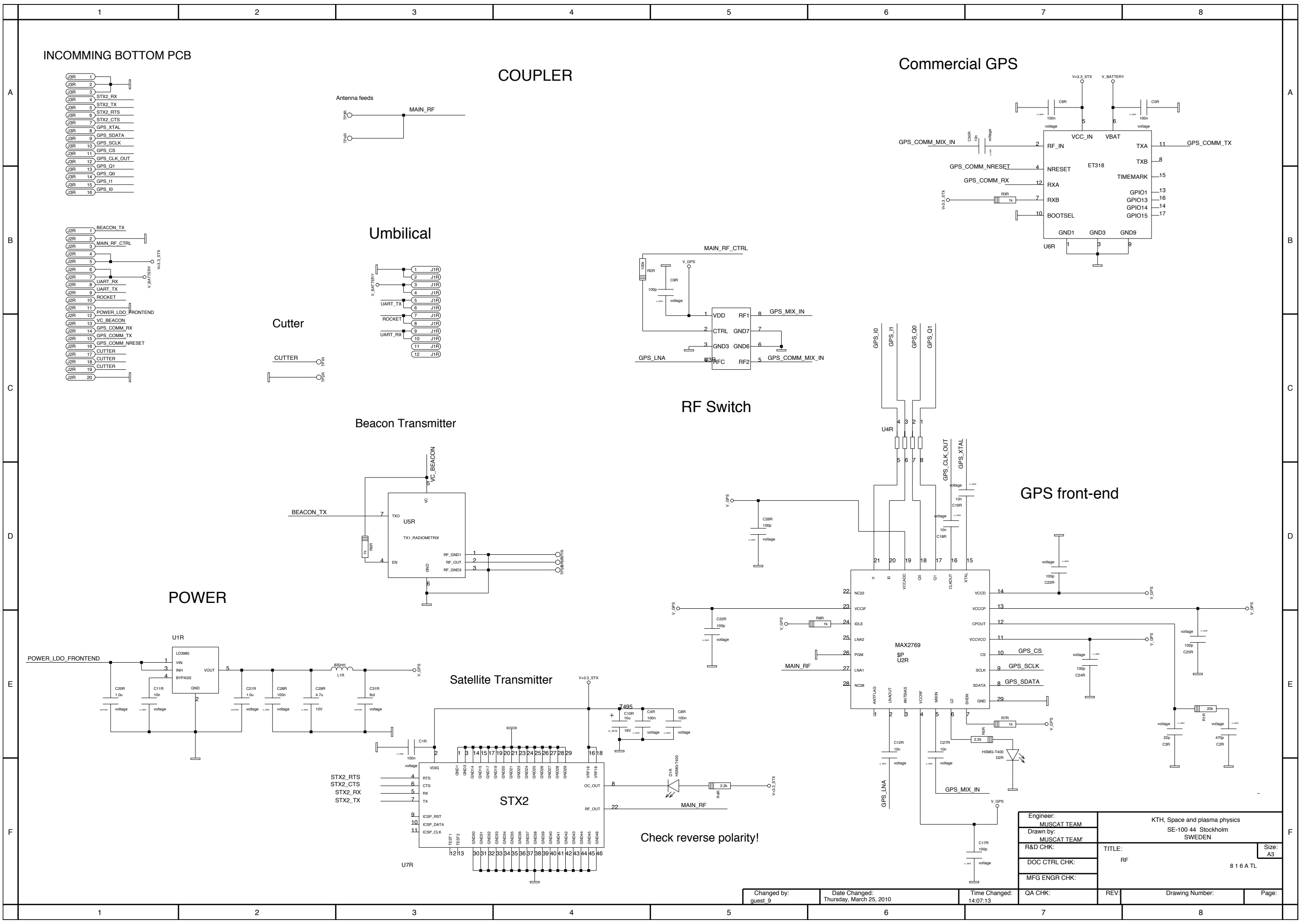
INCOMMING BOTTOM PCB
COUPLER
Commercial GPS
Umbilical
Cutter
RF Switch
Beacon Transmitter
GPS front-end
POWER
Satellite Transmitter
STX2
Check reverse polarity!
MAX2769
ET318
Engineer: MUSCAT TEAM
Drawn by: MUSCAT TEAM
KTH, Space and plasma physics
SE-100 44 Stockholm
SWEDEN
TITLE: RF
Changed by: guest_9
Date Changed: Thursday, March 25, 2010
Time Changed: 14:07:13

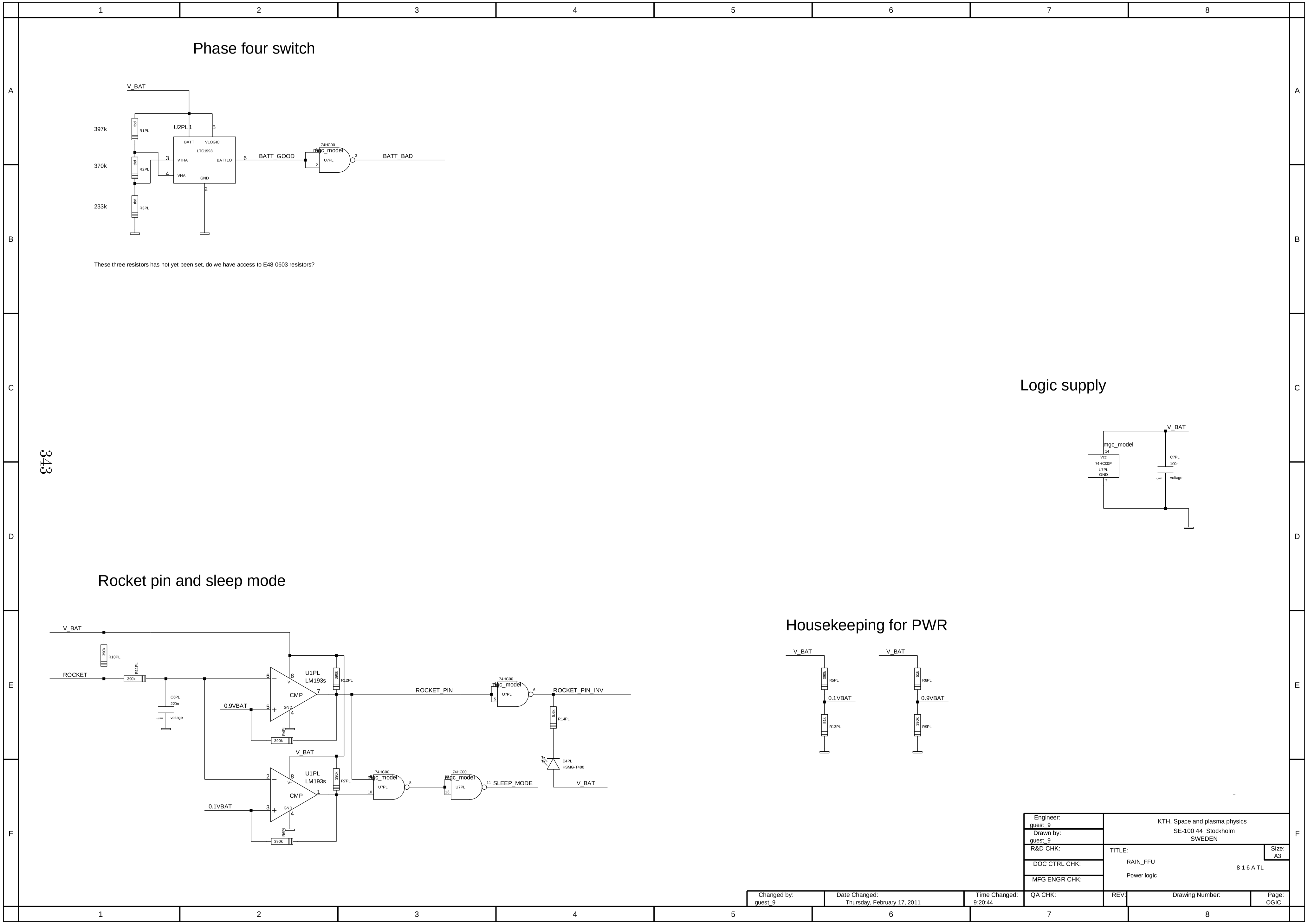
Phase four switch
V_BAT
U2PL
LTC1998
BATT_GOOD
BATT_BAD
74HC00
mgc_model
U7PL
397k
370k
233k
R1PL
R2PL
R3PL
These three resistors has not yet been set, do we have access to E48 0603 resistors?
Logic supply
C7PL
100n
74HC00P
Rocket pin and sleep mode
ROCKET
R10PL
R11PL
C6PL
220n
0.9VBAT
0.1VBAT
U1PL
LM193s
CMP
R12PL
R7PL
ROCKET_PIN
ROCKET_PIN_INV
SLEEP_MODE
R14PL
5.6k
D4PL
HSMG-T400
Housekeeping for PWR
R5PL
R13PL
R8PL
R9PL
390k
51k
Engineer:
guest_9
Drawn by:
guest_9
R&D CHK:
DOC CTRL CHK:
MFG ENGR CHK:
QA CHK:
KTH, Space and plasma physics
SE-100 44 Stockholm
SWEDEN
TITLE:
RAIN_FFU
Power logic
Size:
A3
8 1 6 A TL
Changed by:
guest_9
Date Changed:
Thursday, February 17, 2011
Time Changed:
9:20:44
REV:
Drawing Number:
Page:
OGIC

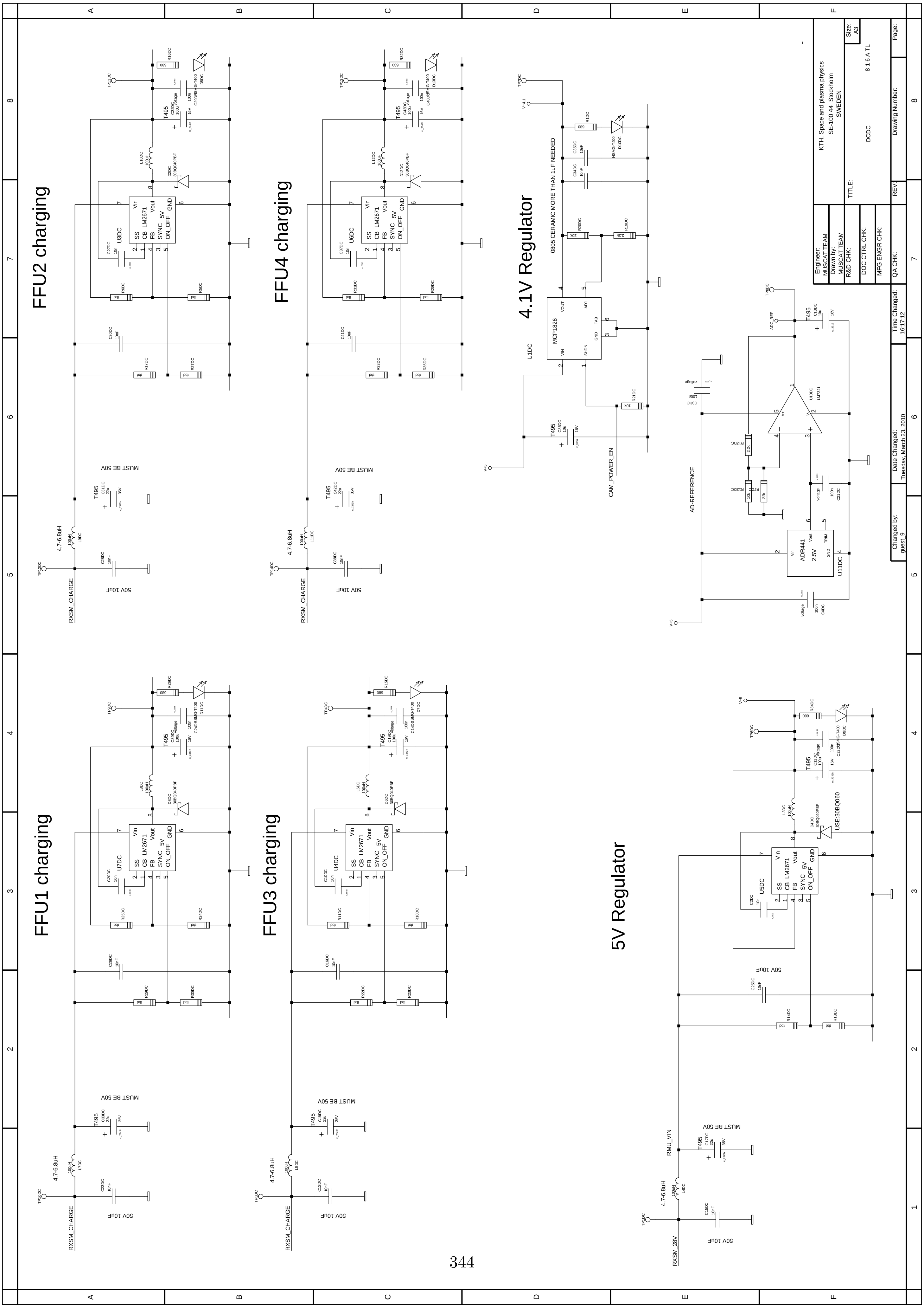
FFU2 charging
FFU4 charging
4.1V Regulator
0805 CERAMIC MORE THAN 1uF NEEDED
MCP1826
U1DC
CAM_POWER_EN
AD-REFERENCE
ADR441
LM7321
FFU1 charging
FFU3 charging
5V Regulator
USE:30BQ060
LM2671
RXSM_CHARGE
RXSM_28V
RMU_VIN
MUST BE 50V
50V 10uF
4.7-6.8uH
KTH, Space and plasma physics
SE-100 44 Stockholm
SWEDEN
Engineer: MUSCAT TEAM
Drawn by: MUSCAT TEAM
R&D CHK:
DOC CTRL CHK:
MFG ENGR CHK:
QA CHK:
TITLE: DCDC
Size: A3
Drawing Number:
Page:
REV:
Date Changed: Tuesday, March 23, 2010
Time Changed: 16:17:12
Changed by: guest_9

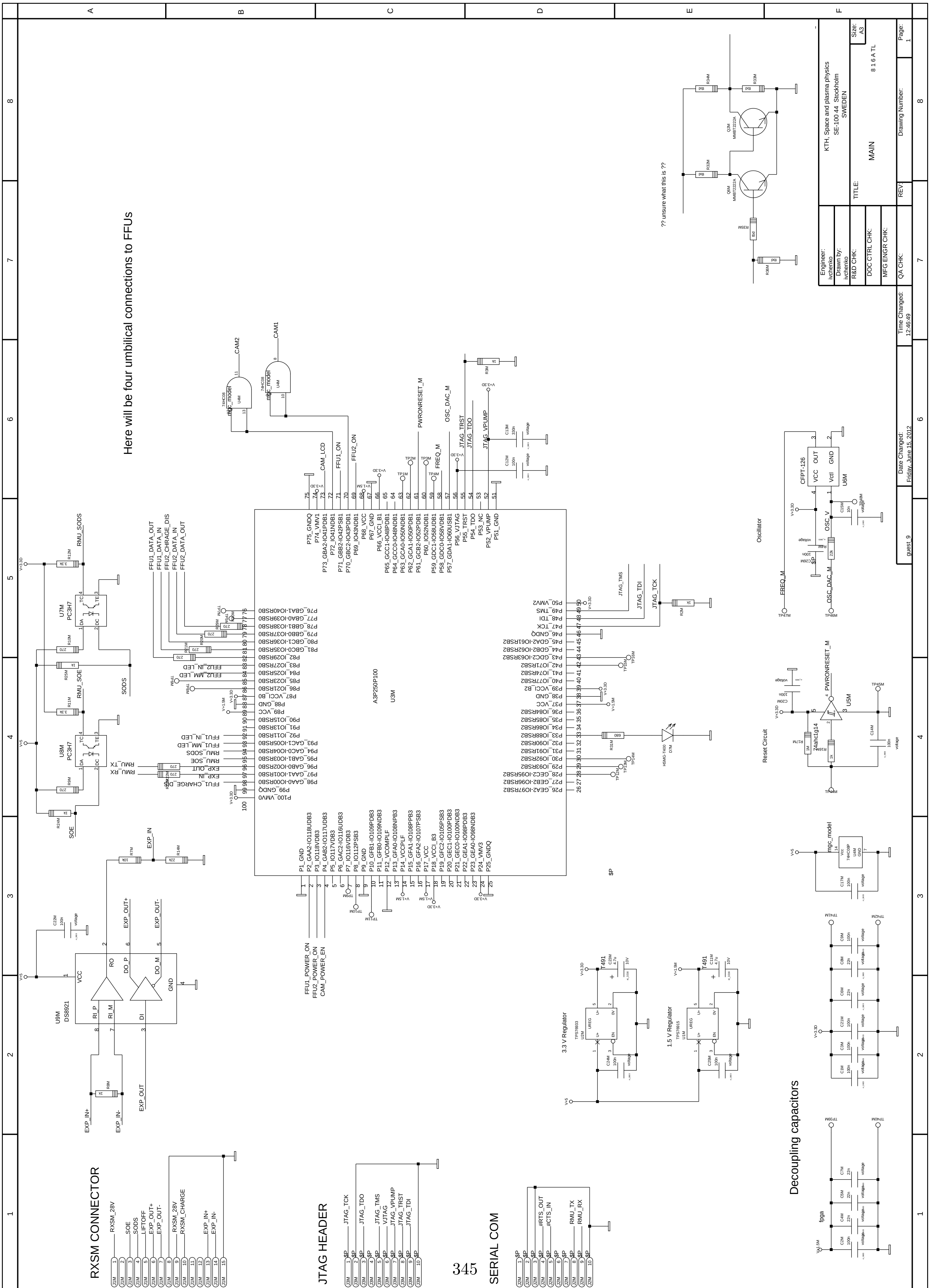
Here will be four umbilical connections to FFUs
RXSM CONNECTOR
JTAG HEADER
SERIAL COM
Decoupling capacitors
Oscillator
Reset Circuit
3.3 V Regulator
1.5 V Regulator
A3P250P100
U3M
?? unsure what this is ??
KTH, Space and plasma physics
SE-100 44 Stockholm
SWEDEN
MAIN
8 1 6 A TL
Engineer: ivchenko
Drawn by: ivchenko
Date Changed: Friday, June 15, 2012
Time Changed: 12:46:49
guest_9

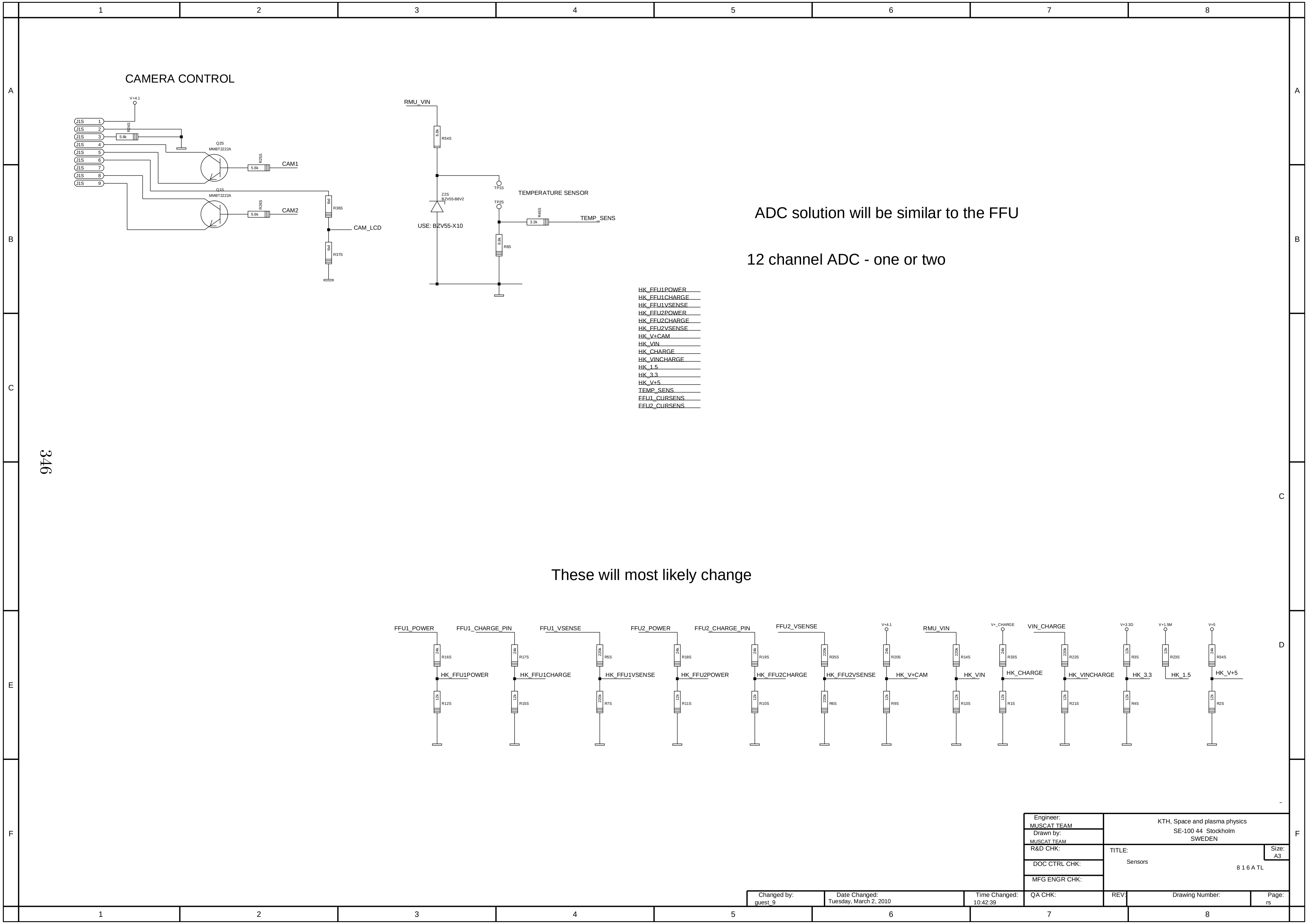
CAMERA CONTROL
V+4.1
J1S
Q2S
MMBT2222A
Q1S
MMBT2222A
CAM1
CAM2
CAM_LCD
RMU_VIN
TEMPERATURE SENSOR
TEMP_SENS
USE: BZV55-X10
ADC solution will be similar to the FFU
12 channel ADC - one or two
HK_FFU1POWER
HK_FFU1CHARGE
HK_FFU1VSENSE
HK_FFU2POWER
HK_FFU2CHARGE
HK_FFU2VSENSE
HK_V+CAM
HK_VIN
HK_CHARGE
HK_VINCHARGE
HK_1.5
HK_3.3
HK_V+5
TEMP_SENS
FFU1_CURSENS
FFU2_CURSENS
These will most likely change
FFU1_POWER
FFU1_CHARGE_PIN
FFU1_VSENSE
FFU2_POWER
FFU2_CHARGE_PIN
FFU2_VSENSE
RMU_VIN
VIN_CHARGE
Engineer:
MUSCAT TEAM
Drawn by:
MUSCAT TEAM
R&D CHK:
DOC CTRL CHK:
MFG ENGR CHK:
QA CHK:
KTH, Space and plasma physics
SE-100 44 Stockholm
SWEDEN
TITLE:
Sensors
Size:
A3
8 1 6 A TL
Changed by:
guest_9
Date Changed:
Tuesday, March 2, 2010
Time Changed:
10:42:39
REV:
Drawing Number:
Page:
rs

Appendix E

Software schematics

This appendix includes schematics of our VHDL code.

MUSCAT SYSTEM CLOCK AND COUNTERS

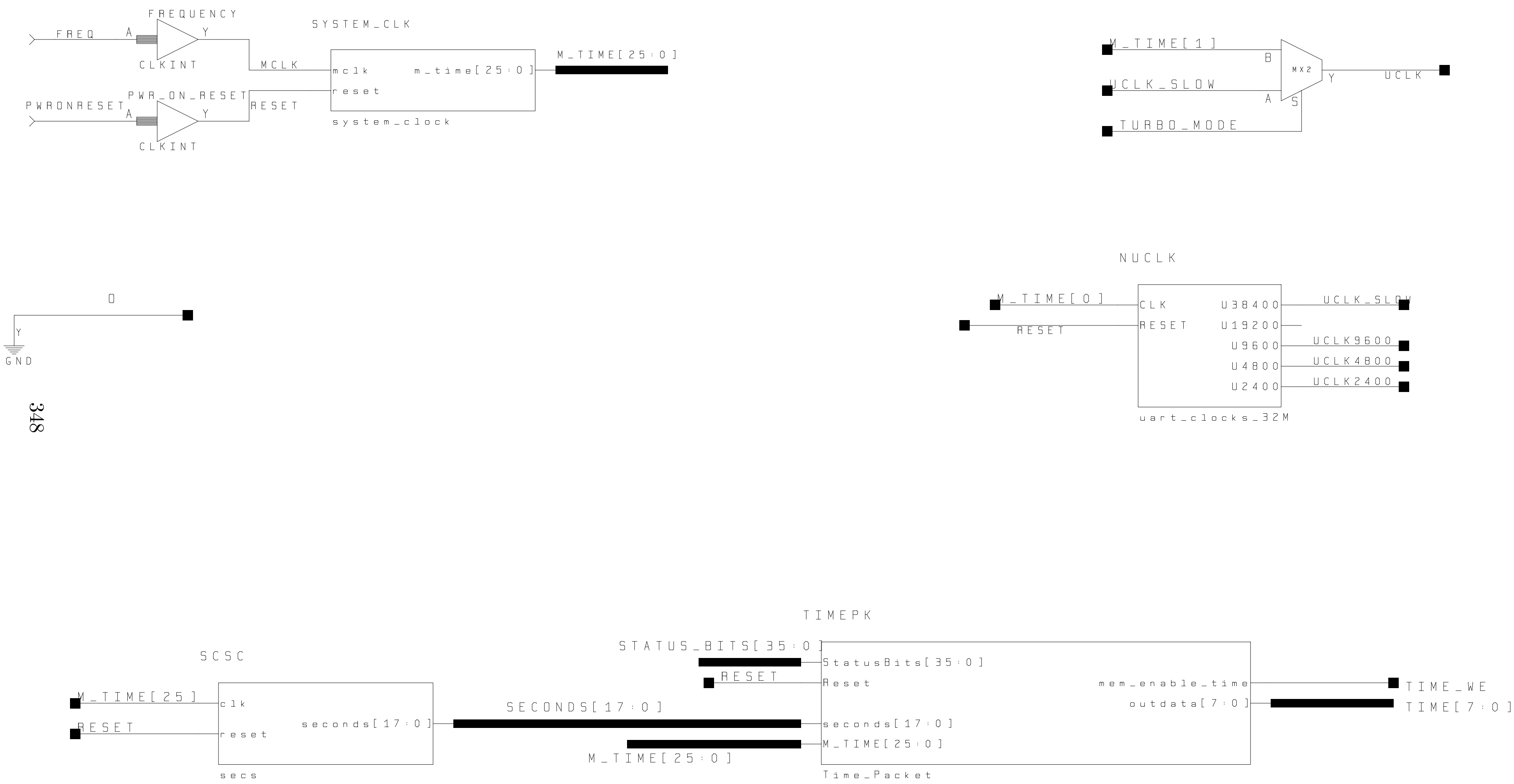

348

MUSCAT MODE, MEMORY, UART RX/TX, SWITCH

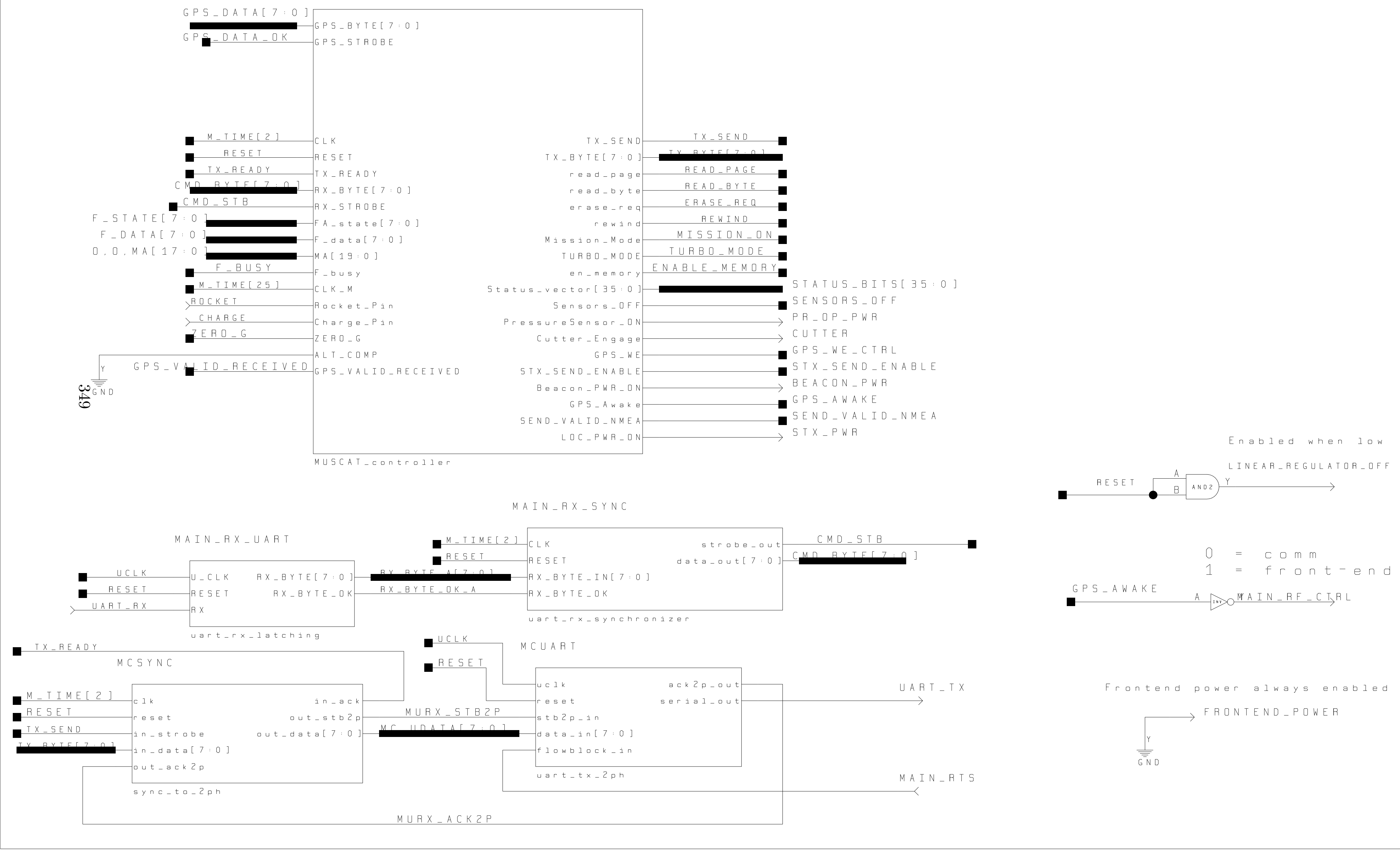

349

S E N S O R   I N T E R F A C E

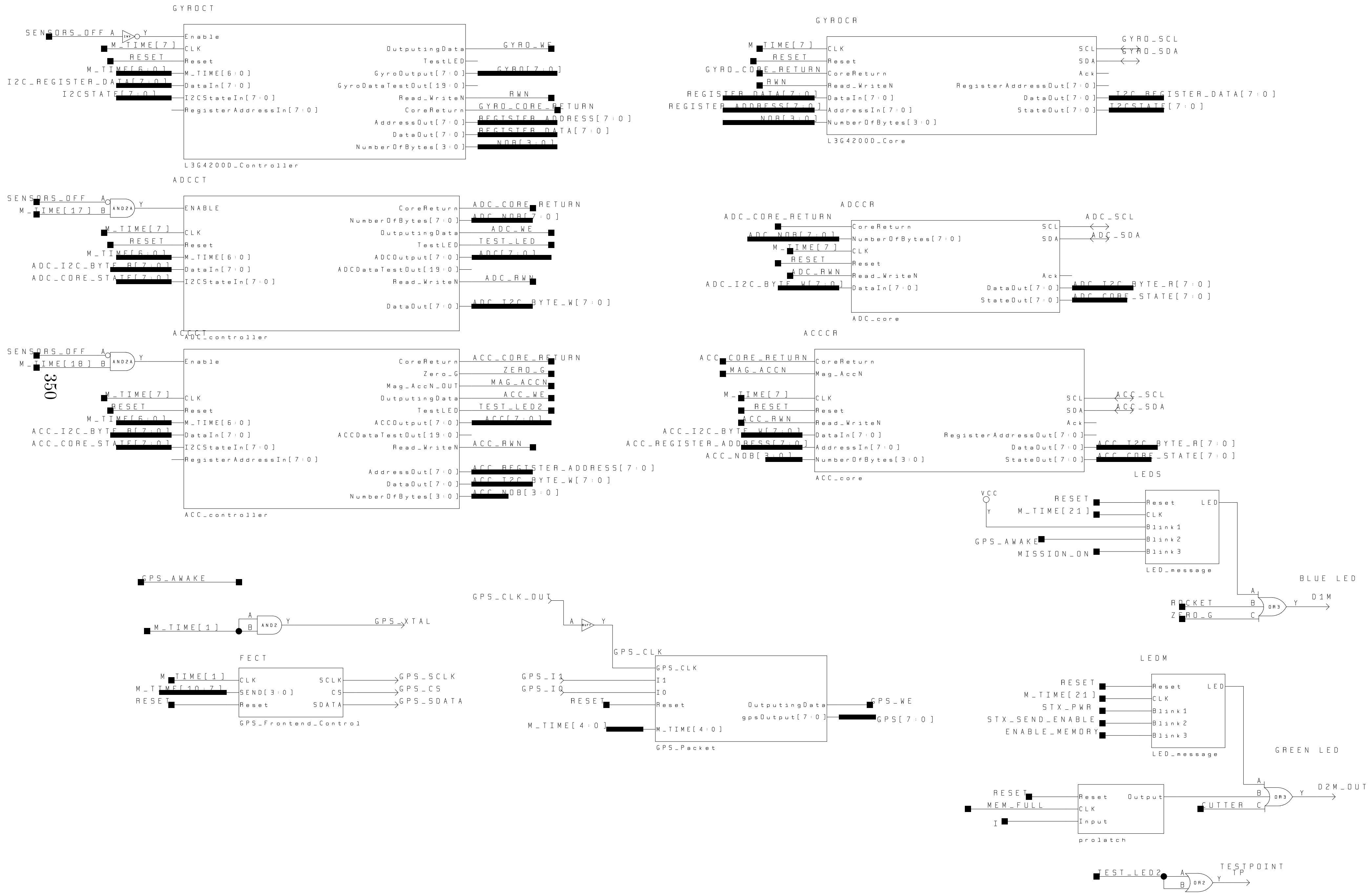

MEMORY HANDLING

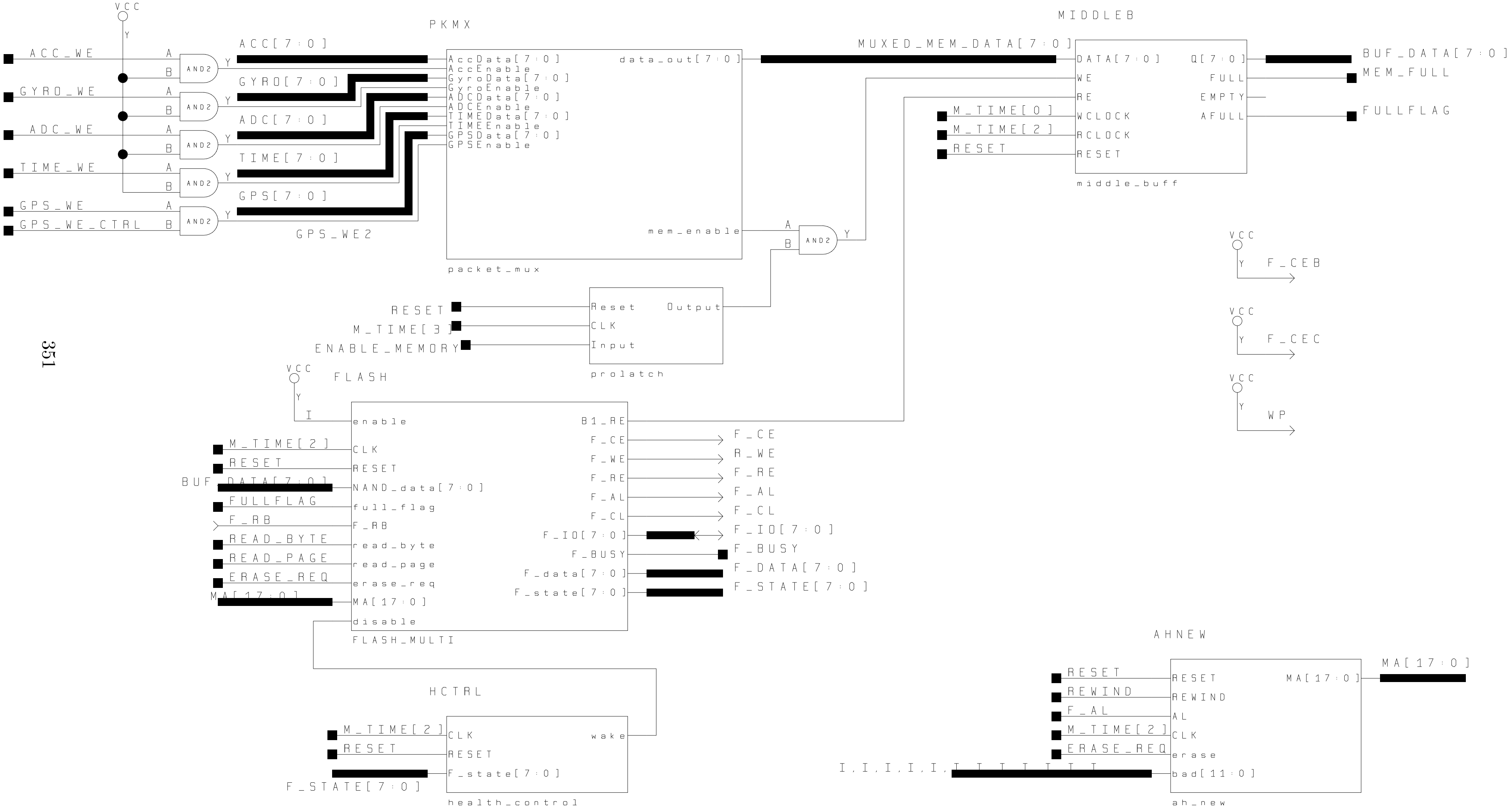

LOCALISATION SYSTEM

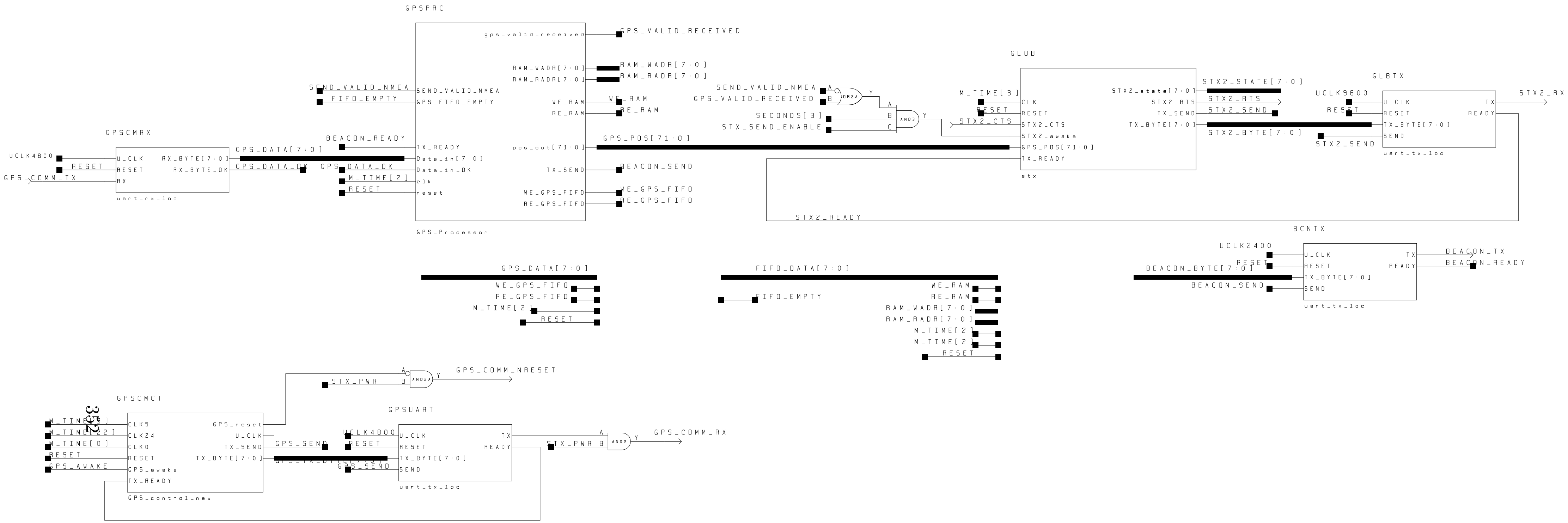

Appendix F

Procedures and Checklists

This appendix includes procedures and checklists regarding FFU and RMU operations.

Royal Institute of Technology, MUSCAT Experiment

MUSCAT Manual: FFU Assembly Procedure

Marco Tito Bordogna
Emilio Lozano
Andreas Myleus

February 4, 2013

1 Introduction

The present manual describe step by step the entire assembly procedure of the FFU: assembly of the PCBs to the structure, folding procedure of the FFU's parachute and how to arm the deployment system of the parachute.

The manual is used for assembly of the FFUs for launch and also of the test FFU that are used for the drop test.

Since the assembly of the FFU for the drop test is done multiple times, during the re-assembly of the FFU the steps to follow are the **bold** one.

2 Procedure

Step 1

Take the *Thermal Cutter (1.01.03.00)* and fix it with 2 x M2x6 and washers to the *Internal Metal Ring (1.01.01.01)*. Take the *Winch (1.01.04.00)* and fix it with 1 x M2x4 and 2 x M2x8 on the internal metal ring (see Fig. 2.1 and Fig. 2.2).

Every screw must be secured using locktight, as soon as one screw is locktight it must be marked immediately with a color. <u>(This must be done ONLY for the flying FFU)</u>

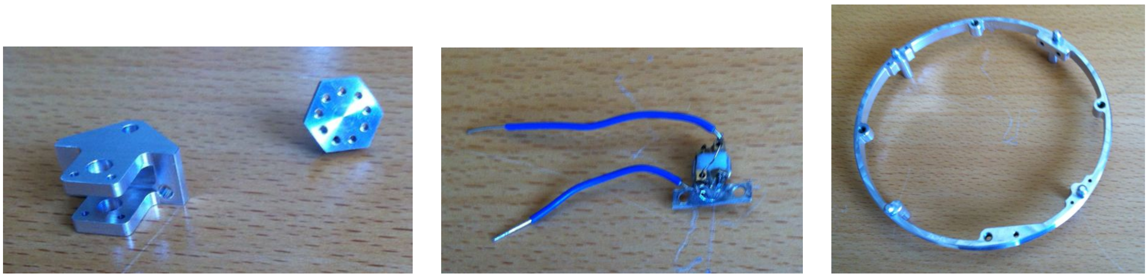

(a) *Winch* (b) *Thermal Cutter* (c) *Internal Metal Ring*

Figure 2.1

(a) *Winch*

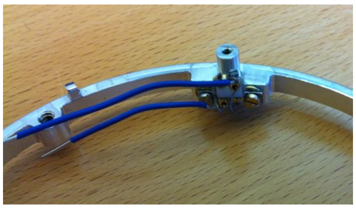

(b) *Thermal Cutter*

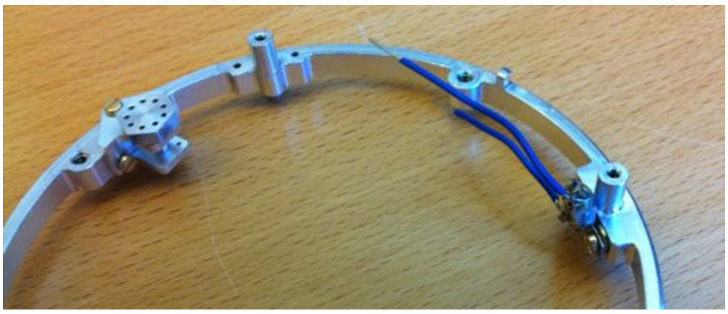

(c) *Winch and Thermal Cutter*

Figure 2.2

Step 2

Take 4 x *Parachute Strings(1.01.02.02)* (15 cm) and 4 x M3 *Eyebolts (1.01.02.03).* Insert the ropes through the eyebolts and knot them around (see Fig. 2.3), also sew the knot to secure [see 3.1]. Make same knot in the other end [see 3.1].

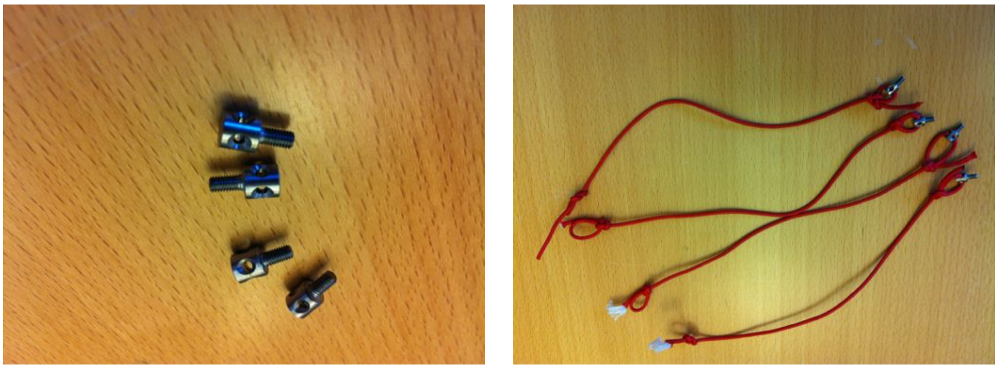

(a) *Eyebolt* (b) *Eyebolt with Parachute Ropes*

Figure 2.3

Step 3

Insert the eyebolts as they are after Step 2 in the holes of the internal metal ring in order to clamp the *Top PCB (1.01.01.03)* between the eyebolts and the ring (see Fig. 2.4).

Secure the eyebolt using locktight. As soon as one eyebolt is locktight it must be marked immediately with a color. (This must be done ONLY for the flying FFU).

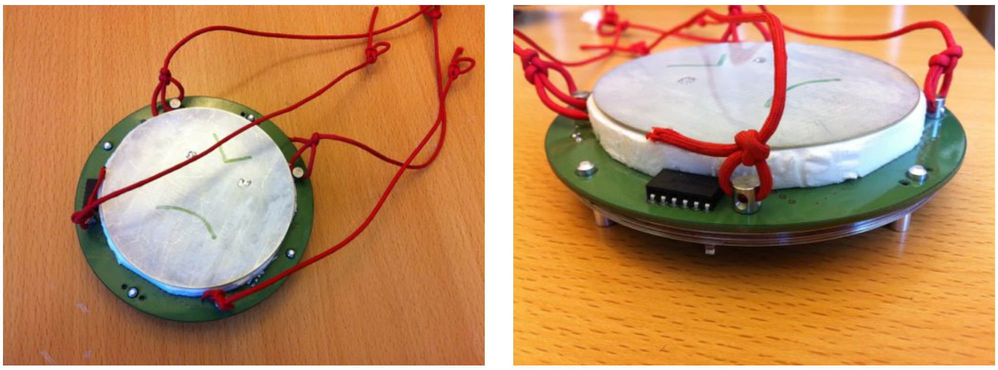

(a) (b)

Figure 2.4: Top PCB clamped to the Internal Metal Ring using Eyebolts

Step 4

Solder the thermal cutter wires to the top PCB (see Fig. 2.5).

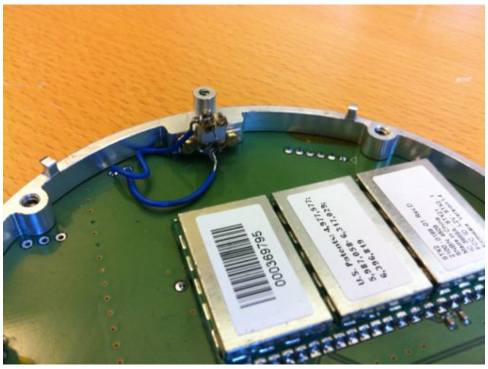

Figure 2.5: Thermal Cutter's connectors soldered to the PCB

Step 5

Take the *Parachute (1.01.02.01)* and the *Parachute Rope (...)* (1.5 m). Insert one end of the parachute cable through the parachute chords and knot them around [see 3.1](see Fig. 2.6).

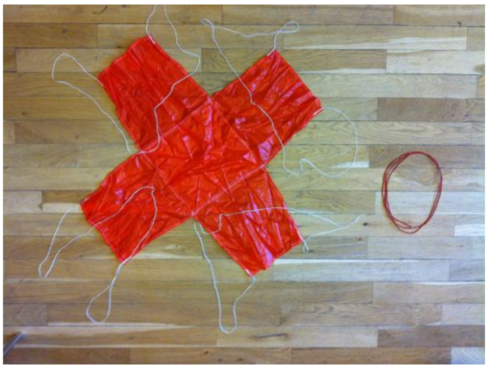

(a) *Parachute and Cable*

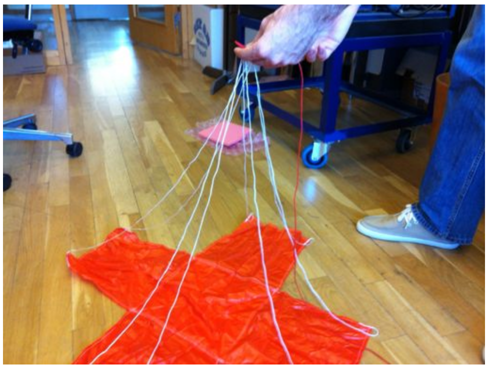

(b) *Parachute Chords*

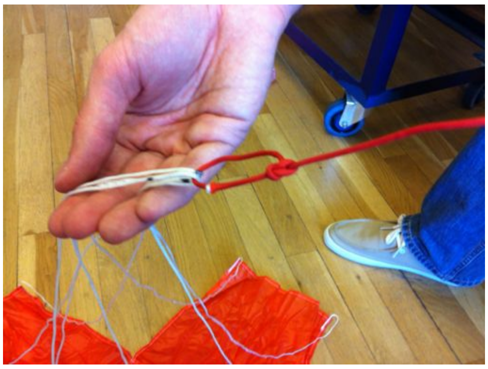

(c) *Knot*

Figure 2.6

Step 6

Take the parachute and untangle the chords. See Fig. 2.6 to see how to check if the lines are tingled or not.

Step 7

Take the parachute and fold it along one of the middle square's diagonals (see Fig. 2.7).

Figure 2.7: Parachute folding procedure

Step 8

Fold the parachute once again along the symmetry line of the middle triangle (see Fig. 2.8).

Figure 2.8: Parachute folding procedure

STEP 9

Fold the parachute along the symmetry line. Always pay attention to not tangle the chords (see Fig. 2.9).

Figure 2.9: Parachute folding procedure

STEP 10

Fold the parachute upwards towards the supporting cords (see Fig. 2.10).

Figure 2.10: Parachute folding procedure

Step 11

Take the parachute and a *Upper Hemisphere (1.02.00.00)*. Follow the next images (see Fig. 2.11) to fold the parachute in the hat. First, introduce the top corner of the parachute in the hemisphere, and then fold the parachute around it.

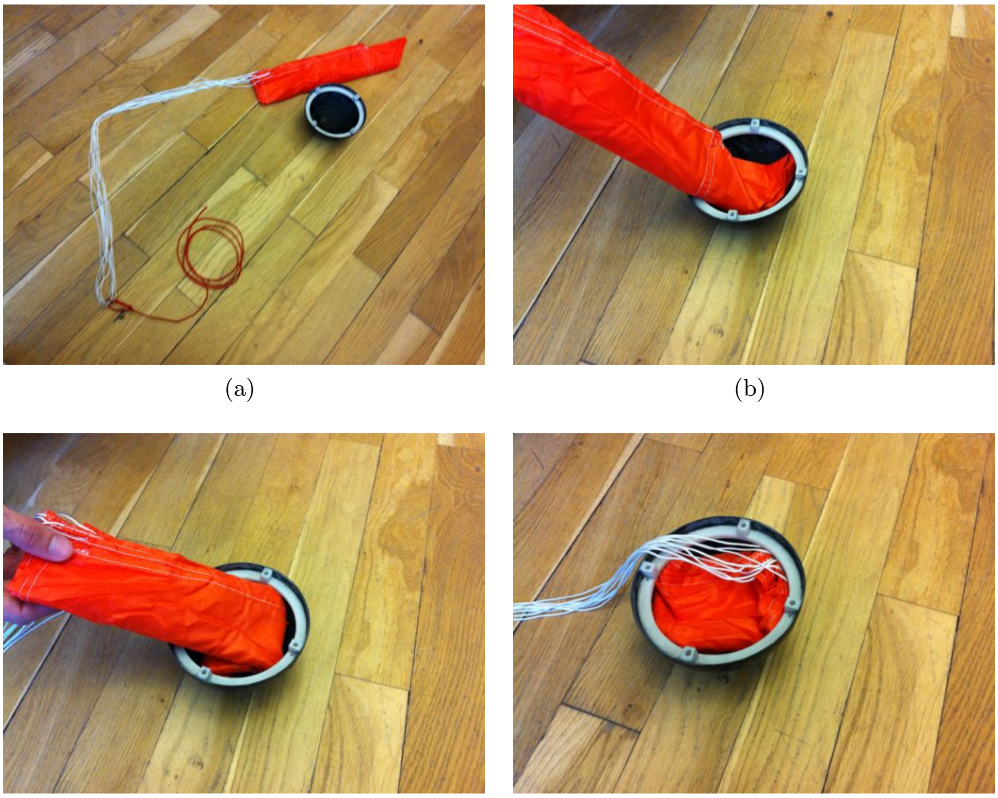

(a) (b) (c) (d)

Figure 2.11: Parachute folding procedure

Step 12

Take the parachute chords and fold them along the inner wall of the hat, in the place where is the least parachute material (see Fig. 2.12).

TIP: To do this rotate the upper hemisphere with respect of the vertical axis and in the meanwhile place the parachute chord inside the hemisphere.

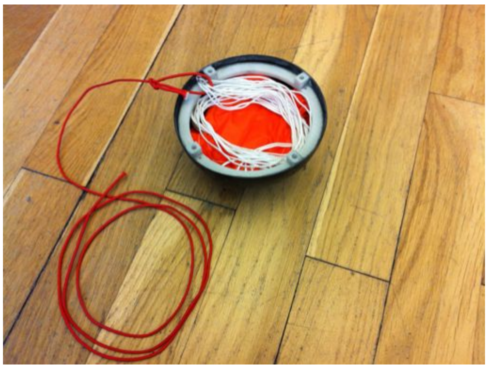

Figure 2.12

Step 13

Take the parachute cable to which the parachute is attached and fold it in the place with the least parachute and rope material (see Fig. 2.13).

TIP: To do this rotate the upper hemisphere with respect of the vertical axis and in the meanwhile place the parachute cable inside the hemisphere.

Figure 2.13

Step 14

Before assembly the upper hemisphere (with the parachute) to the rest of the FFU, take the other end of the parachute cable (not the one used in Step 3) and the parachute rope (attached to the internal metal ring) and knot them around [see 3.1] (see Fig. 2.14).

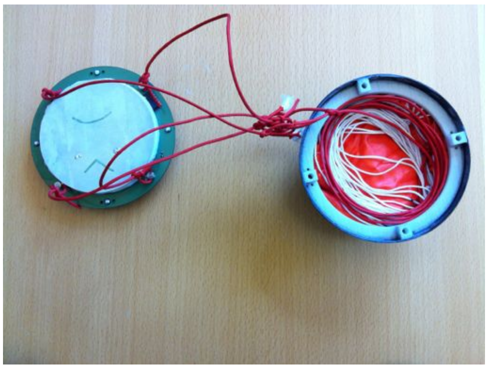

Figure 2.14: Parachute attached to the Internal Metal Ring

Step 15

Now the parachute is correctly folded in the upper hemisphere and it is possible to proceed with the assembly of the upper hemisphere to the top PCB and the internal metal ring.

Step 16

Take the *Finishing Line (...)*, fix one end [see 3.2] to the internal metal ring and go through all the holes as shown in Fig. 2.15 and Fig. 2.16.

IMPORTANT: Check that the fishing line is not stuck into the brackets.

IMPORTANT: Place spring between points: 1-2, 3-4, 7-8 and 9-10.

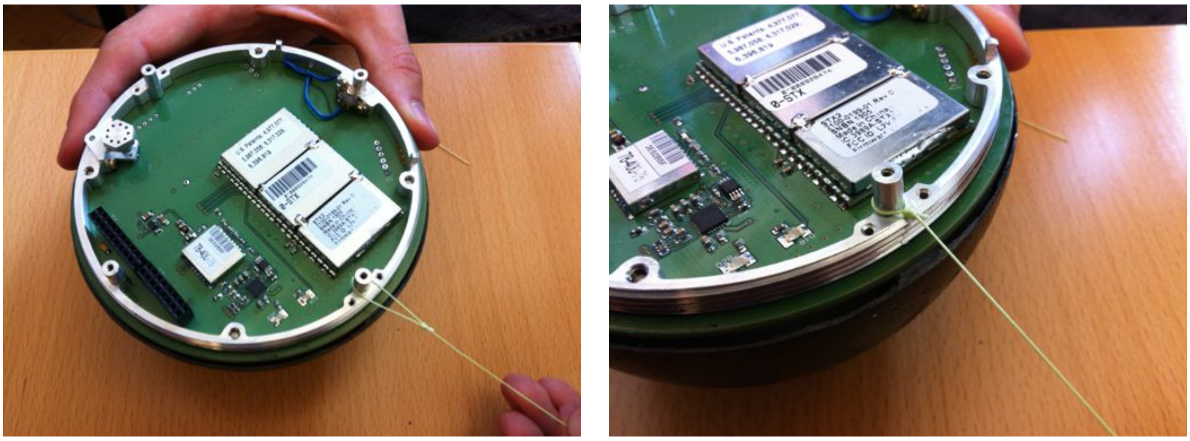

(a) (b)

Figure 2.15: One end of the fishing line fixed to the Internal metal ring

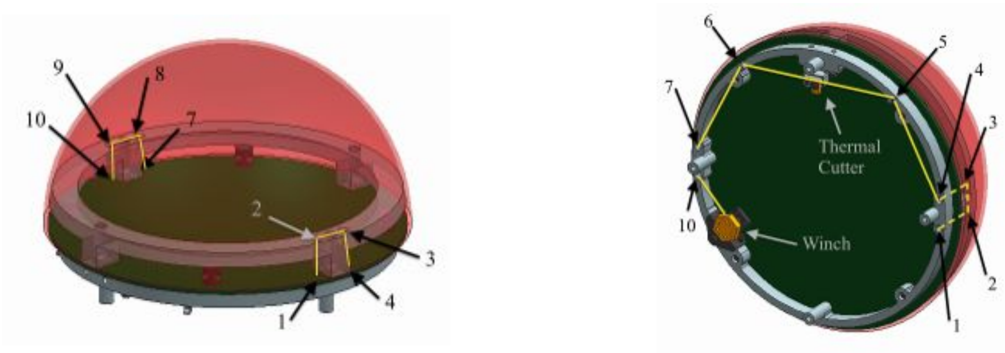

(a) (b)

Figure 2.16: Route of the fishing line

Step 17

Make sure you go through the thermal cutter (see Fig. 2.17). The fishing line must be on the kantal wire cable of the thermal cutter.

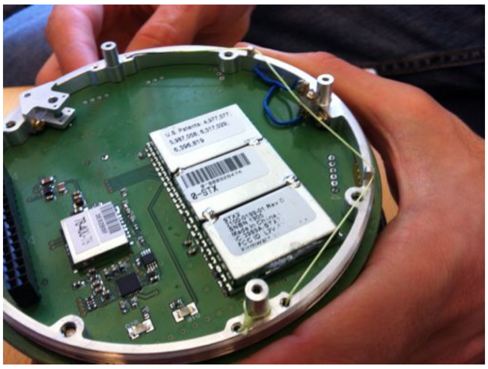

Figure 2.17: Fishing line passing through the thermal cutter

Step 18

Fix the fishing line to the *Winch Rotor (1.01.04.01)* by means of a knot [see 3.1] and tight the cable (see Fig. 2.18). Put M1 screw trough hole and secure with M1 nut.

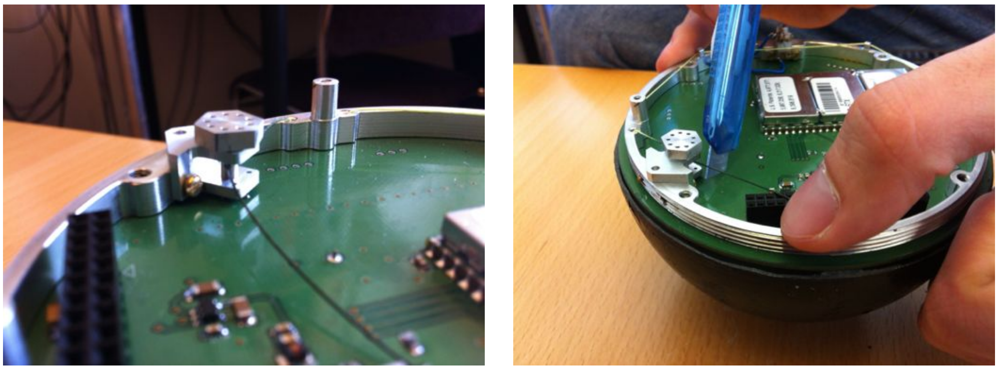

(a) (b)

Figure 2.18

Step 19

Take the *Battery Cage (1.01.01.05)* and insulate the feet of the cage using kapton film. Fix battery cage with *Battery (...)* to the bottom side of *bottom PCB (1.01.01.04)* using 4 x M2x6 screws and 4 x M2 nuts. The screws will be on the bottom side of the bottom PCB and the nuts on the top side. Use padding to prevent movement of the battery if necessary.

Solder the cables of the battery to the bottom PCB (see Fig. 2.19).

<u>WARNING:</u> Bottom PCB and all the components attached on it MUST NOT BE TOUCHED by metal tools. Moreover screws MUST NOT BE DROPPED on it.

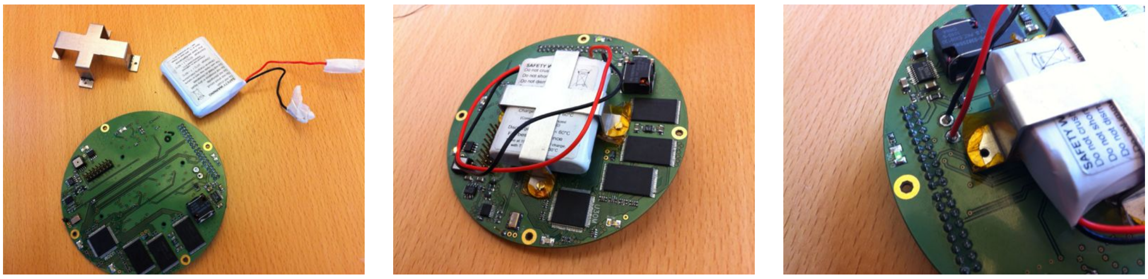

(a) (b) (c)

Figure 2.19: Battery Cage assembled on the Bottom PCB

Step 20

Fix the bottom PCB to the internal metal ring (see Fig. 2.20) using 4 x M2x8 screws and 4 x washers.

Every screw must be secured using locktight, as soon as one screw is locktight it must be marked immediately with a color.<u>(This must be done ONLY for the flying FFU)</u>.

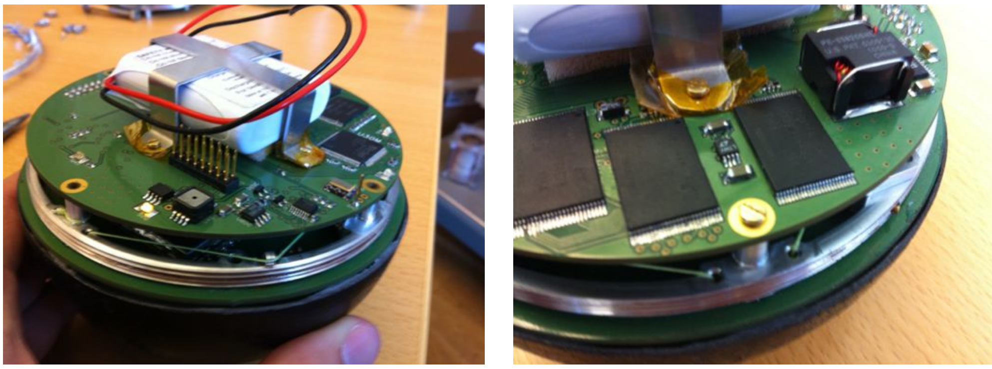

(a) (b)

Figure 2.20

Step 21

Update software, flight mode and others....

Step 22

Check if there is lubricant along the threads of both metal rings. Then screw together the upper and lower part of the FFU (see Fig. 2.21).

Secure the two part using locktight. <u>(This must be done ONLY for the flying FFU)</u>.

(a) (b)

Figure 2.21

3 Note

3.1 Gassa d'amante

All the knots done to with the parachute ropes (Step.2,5,14) are *Gassa d'amante* (see Fig. 3.2).

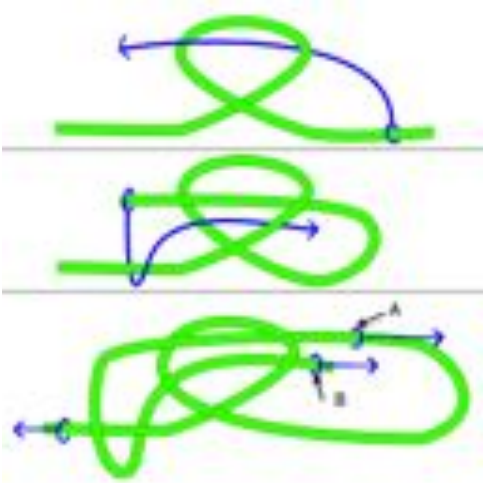

Figure 3.1: Knot: Gassa d'amante

To increase the reliability of the knot sewing will be made between the point A and B in Fig. 3.2.

3.2 Hangman's knot

The not done to fix one end of the fishing line to the internal metal ring (Step.16) is the *Hangman's knot*.

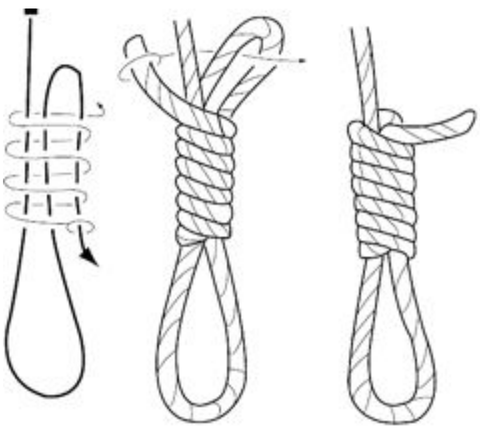

Figure 3.2: Knot: Hangman's knot

Royal Institute of Technology, MUSCAT Experiment

MUSCAT Manual: RMU Loading Procedure

Marco Tito Bordogna
Darri Kristmundsson
Miguel Galrinho

February 8, 2013

1 Materials Checklist

ID	Item	Quantity	Check
2.00.00.00	RMU Assembly	1	
	Loading Mechanism	1	
	Compression Handles	2	
	Compression Plate	4	
	Tensioning Mechanism	1	
	Steel Cable	1	
	Auxiliary Spring	4	
2.05.00.00	Hatch	4	
2.06.00.01	Safety Clamp	4	
	Safety Straps	2	
	Pyrocutter	2	

2 Loading Procedure

Step 1

Place the two Pyrocutters in the Pyrocutter Assembly *(2.03.00.00)* and secure them by using the small screws in Figure 2.1. ☐

IMPORTANT: Orient the pyrocutters so that the signal cap will fit in. ☐

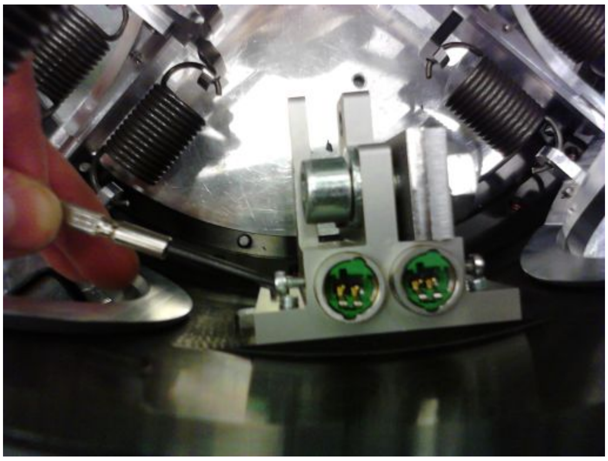

Figure 2.1

Step 2

Fix the looped end of the steel wire to the Pyrocutter Assembly *(2.03.00.00)* using the Slave Ring *(2.03.00.07)* (Figure 2.2) and the SPECIAL SCREW (Figure 2.3). Let the cable go outside the RMU by passing through the Cable Guide *(2.03.00.05)*. ☐

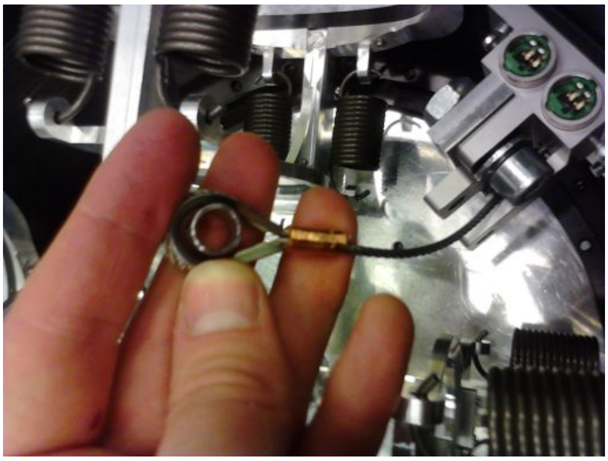

Figure 2.2

Figure 2.3

Step 3

Tighten the bottom screw of of the Pyrocutter Assembly so that the lower parts of the Ruffled Steel Plates *(2.03.00.03 & 2.03.00.04)* are almost in touch (Figure 2.4). This simplify the securing of the steel wire in Step 15. ☐

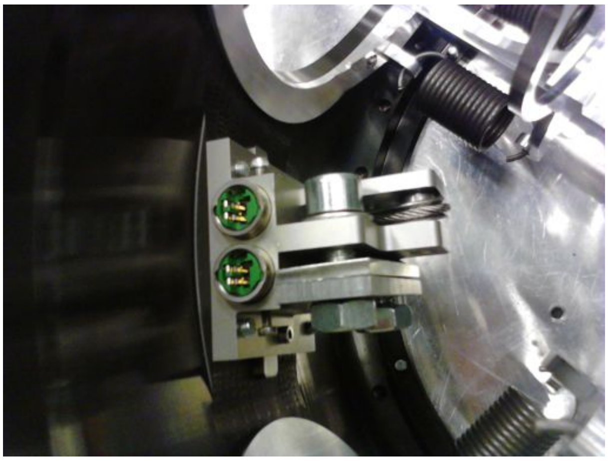

Figure 2.4

Step 4

Take the four Compression Plates and place them inside the inner part of the FFU cages Figure 2.5). ☐

Step 5

Take the Loading Frame (Figure 2.6) and place it around the RMU. Pay attention that the frame is perfectly horizontal. ☐

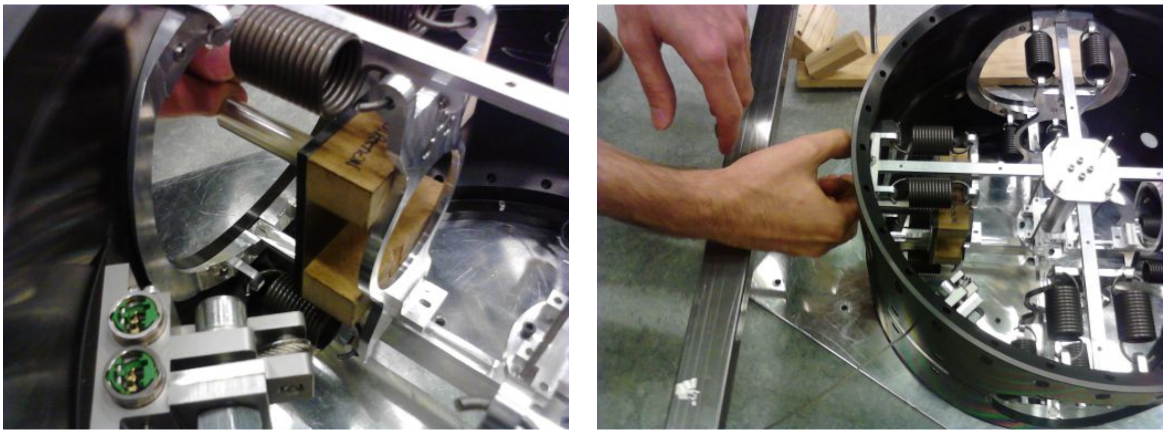

(a) (b)

Figure 2.5

Figure 2.6

Step 6

Center the frame with respect to the RMU by screwing the threaded roods so that they are inside the compression plates (Figure 2.7) and the plates are slightly pressed against the inner part of the FFU cage. This step is very important since the loading frame and the RMU are not fixed on a common support. □

Step 7

Each two inner cages in front of each other are loaded at a time (Figure 2.8). To load the cages use the compression handle and twist the threaded roods. Maintain this loading configuration while the process is repeated for the other two inner cages. □

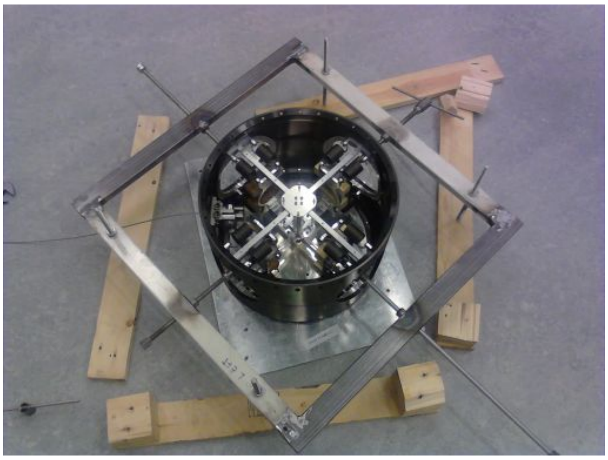

Figure 2.7

Figure 2.8

Step 8

Lock down the safety block by unscrewing the nuts on top (Figure 2.9) then place the security clamps (Figure 2.10). The final configuration is shown in Figure 2.11. □

Step 9

Now that the inner part of the FFU cages are secured it is possible to remove the loading frame (Figure 2.12). □

Step 10

It is now possible to insert the FFUs inside the RMU. The FFUs have to be put in contact with the inner part of the FFU cage and the umbilical must be aligned and connected. Immediately after the insertion of the each FFU the hatch *(2.05.00.00)* have to be placed (Figure 2.13). This will avoid any rotation of the FFU and will prevent any bending of the umbilical connector. □

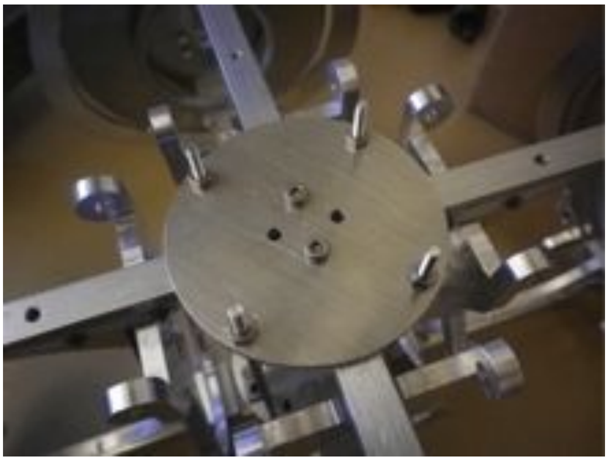

Figure 2.9

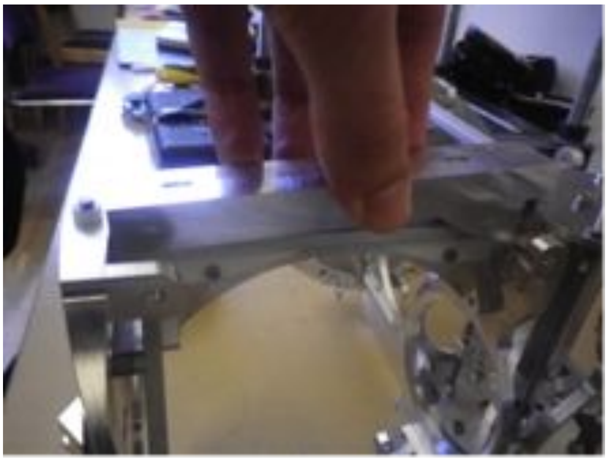

Figure 2.10

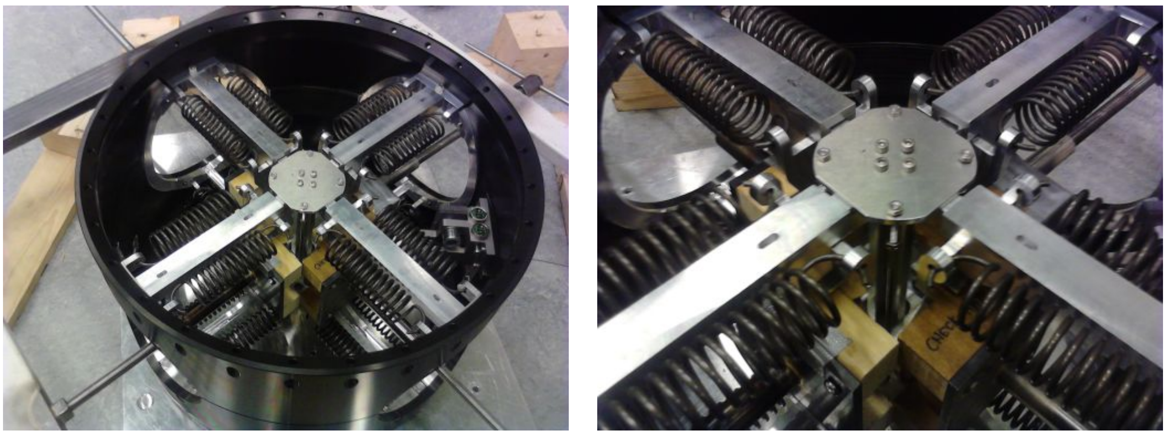

(a) (b)

Figure 2.11

Figure 2.12

It is important to check that every hatch has the internal auxiliary spring (Figure 2.14). □

Figure 2.13

Figure 2.14

Step 11

Let the steel wire go all around the RMU following the groove and going inside the groove in the pyramids of the hatches (Figure 2.15). When the steel wire goes inside the RMU check the it goes between the two ruffled plates. ☐

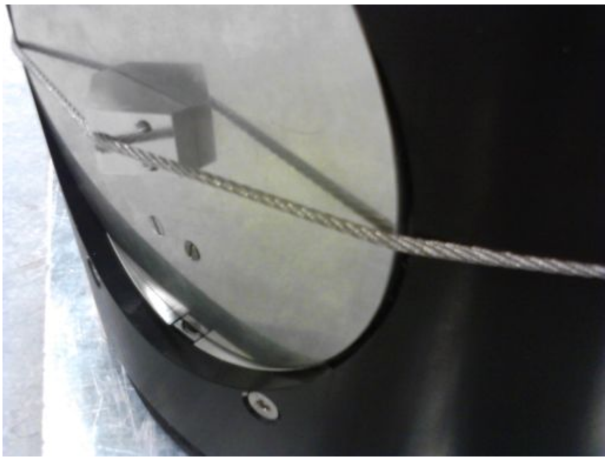

Figure 2.15

Step 12

Once the steel wire is inside the RMU put the tensioning mechanism on top or the RMU (Figure 2.16). Check that the cable guide of the tensioning mechanism is in touch with the ruffled plate of the pyrocutter assembly (Figure 2.17). ☐

Secure the end of the steel cable at the end of the turnbuckle using the block in Figure 2.18. ☐

Step 13

Place again the loading frame around the RMU. This time use the wooden circular plate to compress the hatches. Paying attention that the circular plate is covering all the cork! Load the hatches until they touch the stopper of the collar (Figure 2.19). ☐

Step 14

Now that the hatches are perfectly in touch with the RMU use the turnbuckle of the tensioning mechanism to tight the steel wire. ☐

Step 15

Now it is possible to tight the ruffled plate. Since the lower screw has already been tightened (Step 3), the upper screw has to be tightened first. Than if it is necessary tight the lower screw. ☐

Figure 2.16

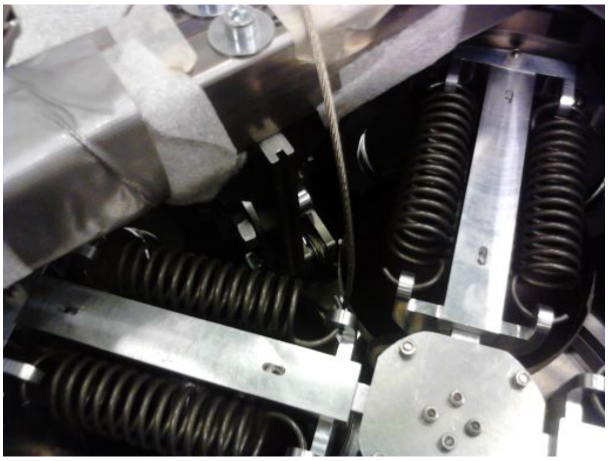

Figure 2.17

Step 16

Now remove the tensioning mechanism, the loading frame and cut the extra wire. At the end of the wire put same block used for the tensioning mechanism. Once this is done take the safety strap and place it around the RMU. Pay attention that the strap goes over the groove and the pyramids (Figure 2.20). ☐

The RMU is now ready to be moved or be placed on the REXUS 13.

Figure 2.18

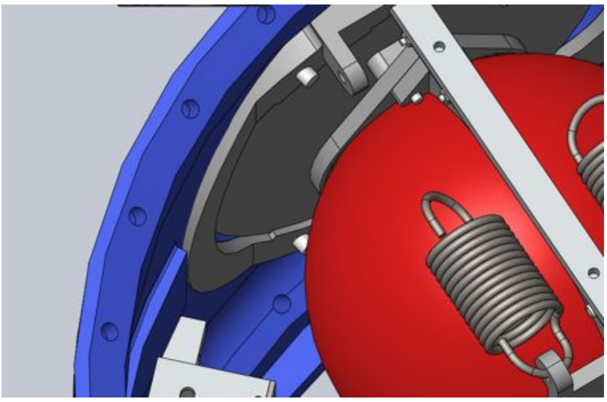

Figure 2.19

3 Rocket Assembly

Step 1

Once the RMU is place on the rocket it is possible to remove both safety clamps and safety block. □

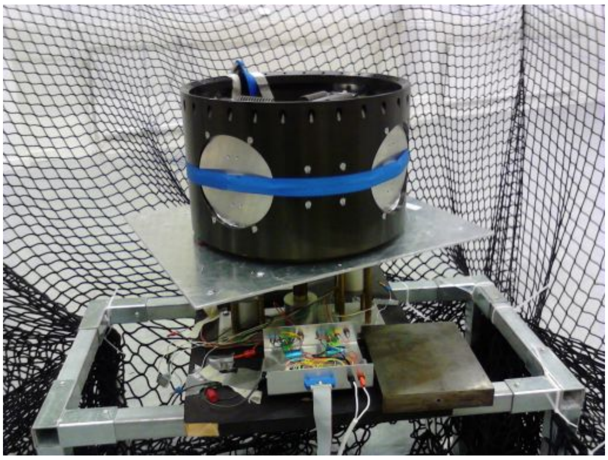

Figure 2.20

Step 2

Once this is done the upper plate of the gas protection can be placed. ☐

Step 3

It is important to remember that before lift of the safety strap must be removed. ☐

Appendix G

Reports from projects made in courses at KTH

KTH Royal Institute of Technology

SD2414 Fiber Composites - Materials and Manufacturing

Project Report: Spherical shell for MUSCAT Experiment

Author:
Marco Tito Bordogna (bordogna@kth.se)
Emilio Lozano (emiliolozano13@gmail.com)

Supervisor:
Magnus Burman

August 1, 2012

Contents

1 Abstract

The report will focus on the product design and production aspects of a composite external shell for spherical probes used in the MUSCAT experiment. The product design and analysis is done buy mean of the "Rule of Mixture" theory and by FE based software considering different configurations. Furthermore different material evaluation and process manufacturing are evaluate in order find the optimal solution for the shell.

2 Nomenclature and abbreviations

C_D	Drag Coefficient
v_i	Volume fraction of material i
E	Young Modulus
β_i	Efficiency factor for direction i
ν_i	Poisson ration for material i
ρ_i	Density for material i
G	Shear Modulus
ϵ_1^{T*}	Longitudinal tensile strain
ϵ_1^{C*}	Longitudinal compressive strain
ϵ_2^{T*}	Transverse tensile strain
ϵ_2^{C*}	Transverse compressive strain
γ_{12}^*	In-plane shear strain
DLR	Germany's national research center for aeronautics and space
ESA	European Space Agency
ESRANGE	European Sounding Rocket Launching Range
FFU	Free Falling Unit
GPS	Global Positioning System
MUSCAT	Multiple Spheres for Characterization of Atmospheric Temperature
RAIN	Rocket deployed Atmospheric probes conducting Independent measurements in Northern Sweden
REXUS	Rocket Experiments for University Students

3 Introduction

This report will cover the entire design process of the external shell for the spherical probes used in the **MUSCAT** experiment [1]. The main topics involve from the product specification to the material evaluation until the manufacturing process.

MUSCAT stands for **MU**ltiple **S**pheres for **C**haracterization of **A**tmospheric **T**emperature. The experiment is built by a team of **11** students from the Royal Institute of Technology (KTH) cooperating with Stockholm University and it will be placed on the **REXUS 13/14** sounding rocket [2]. The scientific objectives of the experiment include retrieval of multiple temperature and wind profiles, in the lower atmosphere, using active spherical probes based on GPS technology.

To derive temperature and density the MUSCAT experiment wants to measure, throughout GPS, the deceleration and velocity of the probe during free falling. Once those data are collected the team, using a post-processing approach, will be able to derive profiles of temperature and pressure in the lower atmosphere.

Another objective of the experiment is also to demonstrate multiple small deployable subpayloads that are reliable, robust and easy to manufacture.

As an external shell, the component, will acts as protective layer for all the internal components and sensors of the probe. Therefore the product will have to stands severe requirements and specifications in order to guarantee the reliability of the experiment.

The main advantage in creating the shell in composite materials is that they can provide good damage tolerance, stiffness and robustness without increasing the weight. Moreover, given that the shell will be an assembly of different parts, the choice of composites will enable the team to assembly all component by means of adhesives without loosing structural integrity.

4 Product specification

4.1 Requirements

The atmospheric probes, or FFUs (Free Falling Units), are going to be housed inside a rocket that will reach 90 kilometers of altitude, then the probes will be ejected. This mission presents several handicaps for the probes in order to perform properly during the entire process of launch, flight and landing. Furthermore the FFUs have to pass the certification process of the European Space Agency in order to be allowed to be in the rocket.

The first requirement for the atmospheric probes is that they must be complete transparent to electromagnetic radiations, because there are antennas collecting GPS data located in different positions that have to able to emit and receive data without interferences during the whole mission.

The second requirement for the atmospheric probes is that they have to be as light as possible. The minimum weight criteria is required because during the launch the acceleration can reach peaks of 21 g's and any extra weight in the probes means an heavier structure to withstand the additional inertia forces created by any additional extra weight. The experiment has a weight limitation that can not be exceed and this weight is directly related with the weight of the structure that houses the atmospheric probes.

The third requirement for the atmospheric probes is that they have to have a good resilience. The resistance to impact has to be high for three reasons. First, the probes are supposed to land in the forest, where the worst case scenario for the probes will be to hit a rock at the terminal speed of the probe (8 m/s). Second the ejection system will hit the probes during the ejection process. Third during the mounting of the probes, they should stand accidents like falling from the workbench.

The fourth requirement for the atmospheric probes is that they should have smooth outer surface. The experiment is based on the record of the influence of the air on the probe, so having a smooth surface will guarantee a constant drag independently from the orientation of the probe during free fall. Furthermore a controlled smooth surface guarantees that the measured values of aerodynamic coefficients in the wind tunnel of one probe are applicable to the other manufactures probes.

The fifth requirement for the atmospheric probes made in composite material is that they should not be affected by outgassing, or at least the effect of outgassing should be minimized. Since the low pressure reached can accelerate the outgassing rate this must be taken into account in the design stage. The requirement of no outgassing is due to that both the integrity of the probes and the shape of the outer surface can not be compromised in any stage of the mission and since the value of C_D has a vital role in the experiment.

The sixth requirement for the atmospheric probes is the ESA certification process that must be fulfilled in order to be able to place the probes in the rocket. The requirements set by ESA related to the mechanical design of the probes are that they should be able to stand all the loads caused during the flight and stand temperatures from -40 °Cuntil 80 °C. Unfortunately since the FFUs will be in free fall outside the rocket skin the evaluated temperature that that have to stand is approximatively 320 °C.

Is it possible to resume the requirements in Table 1.

Requirement	**Priority**
Complete transparency to electromagnetic waves	High
Lightweight structure	High
Resilience to impact	Medium
Smooth outer surface	Medium
Outgassing	Low
Stand all load and temperature	High

Table 1: Requirements for MUSCAT FFUs.

4.2 Mechanical Design

The shell is composed of two parts: Upper hemisphere (UH) and Lower hemisphere (LH). These two components will be joint together using two metal rings (Fig. 2) that will manufacture by an external company.

The external shape of the two hemisphere is the same, but since the two parts have different role and function the internal structure of the UH is different from the LH. The characteristics of the shell are described in Table 2.

Diameter (mm)	*Thickness* (mm)	*Mass* (kg)
124	~ 1	< 0.1

Table 2: Shell Characteristics

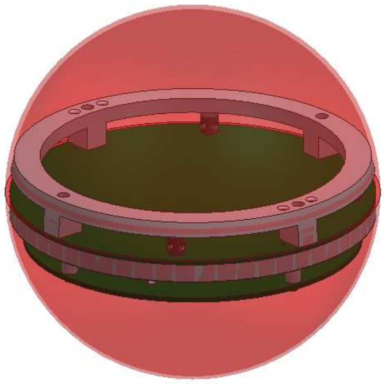

Figure 1: FFU: Entire structure.

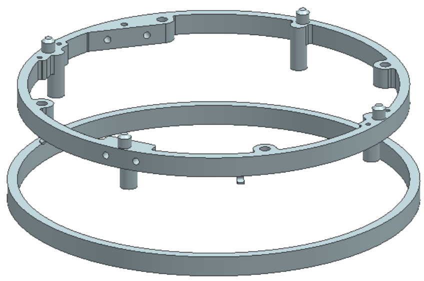

Figure 2: Metal Rings.

4.2.1 Lower hemisphere

The LH is the simplest part of the shell. Inside the LH there be attached, by means of an adhesive, one of the two metal rings as shown in Fig 3

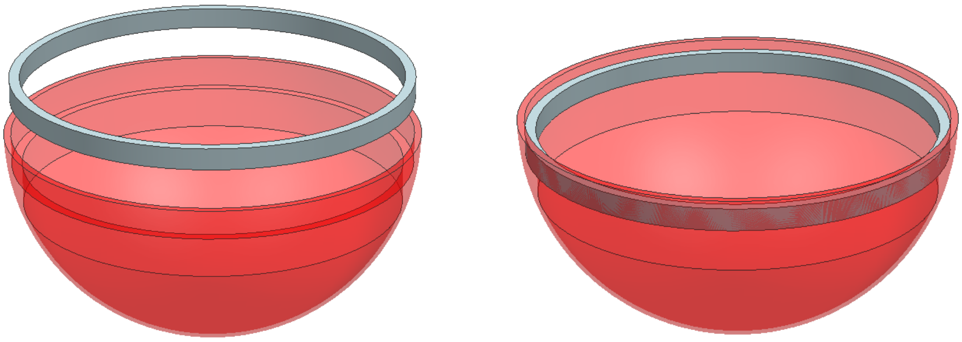

(a) *FFU: LH and metal ring* (b) *FFU: LH and metal ring assembly*

Figure 3: FFU: Lower Hemisphere.

4.2.2 Upper hemisphere

The UH is more complex than the LH due to the fact that it requires a mounting, called Rib Ring, to fulfill some constrain requirement. This Rib Ring, with some cone shaped support, will force the UH to remain in a fixed position with respect to the second metal ring, Fig 4.

The Rib Ring will be manufactured using PA reinforced with fiberglass and attached to the UH using the adequate adhesive, this will guarantee continuity and integrity to the structure.

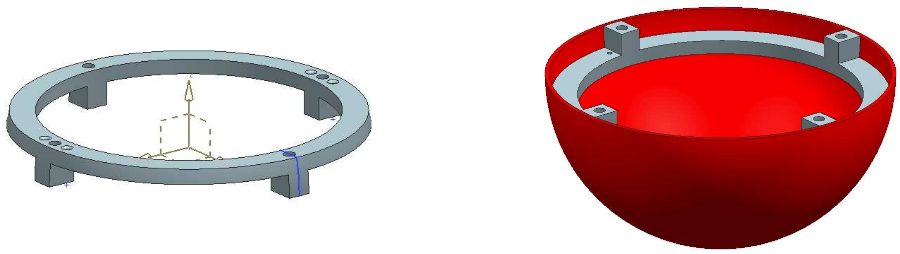

(a) *FFU: Rib Ring* (b) *FFU:Upper Hemisphere and Rib Ring*

Figure 4: FFU: Upper Hemisphere and Rib Ring.

5 Material evaluation

In order to justify the selection of the fibre reinforcement and matrix a research process is performed with the purpose of finding the materials that fulfill the stated requirements. Furthermore in this section a general estimation of thickness and weight is done by means of the lamina theory. The thickness and hence the weight are estimated taking into account the loads that should be beard by the FFU during the mission.

5.1 Material Selection

The key property of the fibre reinforcement and the matrix that will be chosen for the manufacturing of the FFU is the electromagnetic transparency (This means that the material should have low dielectric constant). It must be taken into account that the satisfactory performance of the FFU depends on its capability to transmit the acquired data during the flight to the receiver with the minimum distortion. Therefore electromagnetic transparency is an indispensable characteristic that the selected material should possess.

In the second step in terms of priority properties of the selected materials for the fibre reinforcement and the matrix is the low density. Low density is desirable because as every aerospace application the weight is a parameter that should be kept as low as possible. Therefore low density material are desirable but with priority of the electromagnetic transparency.

In the mechanical properties section there is no high demand because the FFU will only have to bear its own weight during the mission. The two most important load cases are: the launch, where the FFU will be subjected to accelerations up to 21 g's, and the landing, because the FFU should be able to stand a landing at 8 m/s over a tough surface. Those situations are not critical because the total weight of the FFU will be approximately 0.6 Kg.

5.1.1 Fiber choice motivation

According to the important requirement of electromagnetic transparency there is a big group of fibre reinforcements that is automatically removed from the options. The fibre reinforcement that cannot be used according to the electromagnetic transparency criteria is the carbon fibre reinforcement because according to Chung [6] carbon fibre reinforced polymers has a high electromagnetic interference (EMI) shielding effectiveness. Therefore it should not be used to emit through it.

There are other smaller fibre reinforcements group that cannot be used according to the electromagnetic transparency criteria. These groups are boron fibers because of high dielectric constants in comparison with glass fibers according the online database matweb.com [7] .Moreover boron fibers and silicon carbide (SiC) fibers should not be used in the design of the

FFU because they are very brittle materials according to the online database matweb.com [7].

In terms of fibre reinforcement that can be used there are the following options left: glass fibers, Silica or quartz (SiO_2) fibers and aramid fibers.

According to the online database matweb.com [7] and Astrom [3] silica and quartz fibers are used in applications like high temperature insulation and stealth aircraft due to its astonishing good thermal properties and its good dielectric behavior. Nevertheless these applications are far away from the mission that the FFU should carry out. Furthermore, it is also mentioned in the online database matweb.com [7] that silica quartz reinforced materials are used in applications where the thermal and mechanical properties of glass fibre are not enough. Nevertheless in the case of the FFU thermal and mechanical properties are not over the properties that the glass fibre can provide. Thus it would be not logic to choose the silica fibre as reinforcement.

In the case of the of the aramid fibers their use is recommended when the mechanical properties and resilience are important properties to have, according to Astrom [3]. Furthermore in the design with aramid fibers it must be taken into account their low matrix compatibility, the high price and the difficulties that imply to shape aramid fibers because of their toughness, according to Astrom [3] .Thus aramid fibers are not a logical choice for the FFU reinforcement. At this point all the options have been found not optimal but glass fibers.

In the case of glass fibers there characteristics that are desired to include in the FFU because the glass fibers have good dielectric behavior, good enough mechanical properties and are easy to work with, according to Astrom [3] . Therefore it will be easy to accommodate the fabrics of glass fibre to the shape of the FFU. Thus glass fibers are the logical choice as reinforcement for the FFU. Among of the glass fibers there is a kind that has the best dielectric behavior, according to the online database matweb.com [7]. Furthermore this glass fibre has low relatively low density and mechanical properties that would allow it use un the design of the FFU. This is type of glass fibre id the D glass fibre and this will be the material used as fibre reinforcement of the FFU. The properties of the D glass fibre can be seen in the Table 3.

5.1.2 Matrix choice motivation

The selection of the matrix has different parameters and facts that will influence the final choice of it. Among these parameters and facts there are not only mechanical and electromagnetic properties but also process and manufacturing considerations. In this stage of selecting the matrix it is important to take into account what kind of chemicals components are involved, because in the application of the matrices there are aggressive chemicals products involved that makes them undesirable to work with.

Physical Properties	**Metric**
Density	2.11 g/cc
Mechanical Properties	**Metric**
Tensile Strenght, Ultimate	2415 MPa
Elongation at Break	4.60%
Modulus of Elasticity	51.7 GPa
Poisson Ratio	0.30
Electrical Properties	**Metric**
Dielectric Constant	3.80
Thermal Properties	**Metric**
CTE	2.50 μm/m-°C

Table 3: Properties of D-Fiber Glass [7].

The matrix as the fibre reinforcement should have a low dielectric constant in order to be as transparent to electromagnetic radiation as possible. The mechanical properties of the matrix should be as good as possible in order to get a thin light structure, hence a low density and high strength are also desired.

With these specifications that have been set, the most suitable matrices are thermosets matrices. Thermosets matrices are suitable because they have low dielectric constant, low density and as difference between thermosets and thermoplastic matrices, thermosets have better mechanical properties (With some exceptions like PEEK which has very good mechanical properties). These affirmations are stated according to the data study performed in the online data base matweb.com [7]. Furthermore first thermal analysis of the descending trajectory indicate that the temperature in the skin can be high therefore thermoplastic with low Tg should be avoided.

Therefore from now on the selection of matrix will be focused in thermoset matrices. Among thermoset matrices according to Astrom [3] there the following group of possible thermoset matrices, vinilesters, epoxies, phenolics and polyesters.

As mentioned above in this stage the kind of chemicals products that are involved should be taken into account, hence matrices that can produce dangerous environments as the unsaturated polyester should be avoided. According to Astrom [3] the monomers present in this matrix at the time of starting the process of manufacturing can create an unhealthy work environment. Another drawback of polyester is its Tg of 70° C and, since the FFU should stand 80° C according to the specifications by ESA, polyester is not valid because thermosets should not be used beyond their Tg.

About the phenolics there is a mayor drawback that forces their rejection as matrix, they are brittle and the mayor mechanical requirement for the FFU is to stand a landing over a tough surface at 8 m/s. Therefore phenolics matrices are rejected. Vinilesters have slightly better properties than polyesters in terms of temperature and mechanical performances and they do not have problem with dangerous gases generation but there is a better option.

The best option among the thermoset are the epoxies due to its outstanding mechanical properties, low dielectric constant, low density and Tg over the certification temperature of the FFU. All these conclusions have been achieved studying the data available in the online data base matweb [7] and in the book written by Astrom [3] Therefore it can be concluded that epoxy resin is the most suitable option in order to select a matrix materials that will provide the best result for the design of the FFU. The data for average properties of epoxy resin obtained from the online data base matweb.com [7] can be seen in the Table 6.

Physical Properties	**Metric**
Density	$0.049 - 1.80$ g/cc
Mechanical Properties	**Metric**
Tensile Strenght, Ultimate	$7.58 - 96.5$ MPa
Elongation at Break	$0.70 - 96.5$%
Modulus of Elasticity	$1.54 - 10.0$ GPa
Poisson Ratio	$0.35 - 0.42$
Electrical Properties	**Metric**
Dielectric Constant	$2.80 - 4.20$
Thermal Properties	**Metric**
CTE	$33.0 - 65.0$ μm/m-°C

Table 4: Properties of Epoxy [7].

5.2 Analysis

5.2.1 Load Analysis

The FFU has to withstand the entire mission, thus structural failure is not admitted, so an analysis of the loads must be performed. It has been sorted out that the most critical load case is during the launch, when the probe has to stand up to 21g's of acceleration.

The load in that situation is:

$$P = 21 \cdot g \cdot m \tag{1}$$

where:

g gravity acceleration;
m mass of the FFU ($= 0.6$ Kg *estimated*).

in order to be conservative the mass used for the calculation is 0.8 Kg. By doing this the load value is: $P = 164.98\ N \cong 165\ N$.

During the flight the FFU will be carried inside a cage (Figure 5) that will prevent any movement. Ideally the cage will be able to distribute the total load along two lines.

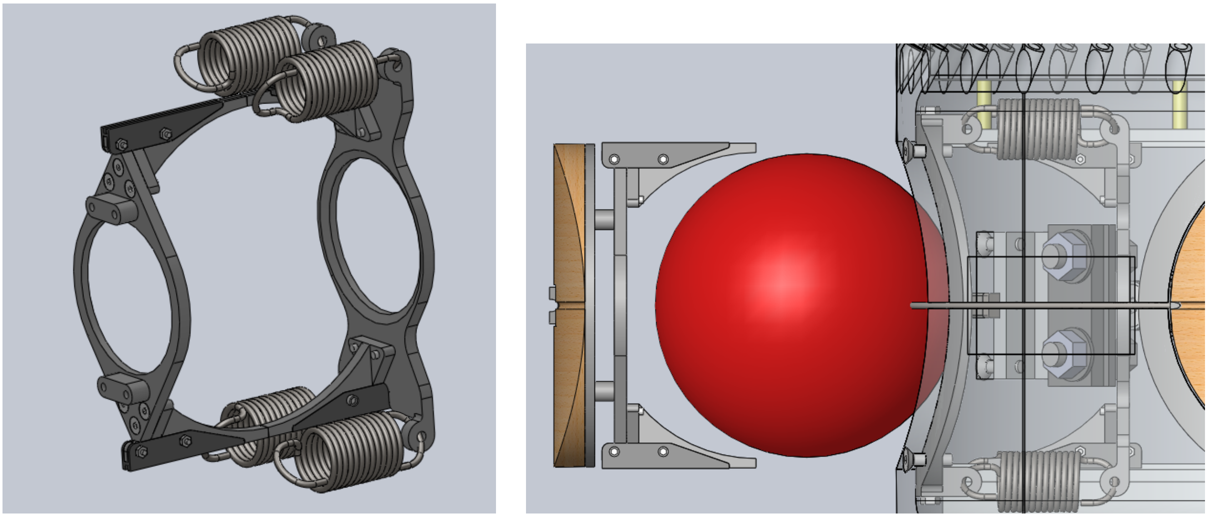

(a) *Cage.* (b) *Lateral view of FFU and Cage.*

Figure 5: Cage of the FFU.

since the design of the FFU must be conservative the analysis of the load will be done by assuming that the total load will be transmitted to the FFU in a single point. In this way, even if the FFU will not be perfectly in contact with the cage, the shell will stand the load.

5.2.2 FEM Analysis

Due to the difficulties if finding analytical solutions for a sphere under a concentrated external load in handbooks or other sources, it has been decided to use finite elements method to find out internal strains and stresses of the shell. The program used for the FEA is ABAQUS [9].

The idea is to use ABAQUS to model the effect of the concentrated external load on the sphere. In order to find strains and stresses some parameters of the material used are needed. This parameters will be derived using the simple lamina theory and the entered in the FEA software.

The simulations are performed using two different values for the thickness (1 or 2 mm) of the shell. In order to evaluate which thickness can stand the load, once stresses and strains are obtained, they are used in failure criteria.

Results from ABAQUS showing the behavior of the sphere under the load are available on request.

5.2.3 Lamina Theory

It has been decided to use a fabric of D-Fiber Glass with Epoxy.All the properties will be estimated, using a simple lamina theory, for different values of volume fraction of fibers.

The volume fracture analyzed are:

- $v_f = 0.4$;
- $v_f = 0.5$;
- $v_f = 0.6$.

Since there are different kind of epoxies, for the calculations average values of the important characteristics are taken.

Physical Properties	**Metric**
Density	1.40 g/cc
Mechanical Properties	**Metric**
Modulus of Elasticity	3.00 GPa
Poisson Ratio	0.35

Table 5: Properties of Epoxy used for calculations.

The fabric chosen is not unidirectional so, for the estimation of the Young's module, the efficiency factors are taken into account.

$$E_{0,90} = \sum_i \beta_i v_i E_i \tag{2}$$

where:

β_i is the efficiency factor for direction i ($= 0.5$ *for bidirectional*);
v_i is a volume fraction.

For all the other parameters needed the formulas used are:

$$\nu_{12} = \nu_f v_f + \nu_m v_m \tag{3}$$

$$\rho_l = \rho_f v_f + \rho_m v_m \tag{4}$$

$$G_l = \frac{G_m G_f}{G_m v_f + G_f v_m} \tag{5}$$

The result, for the different kind of volume fraction are:

Volume fracion	Young's module	Poisson ratio	Density	Shear module
0.4	12.14 GPa	0.330	1.684 g/cc	4.96 GPa
0.5	14.43 GPa	0.325	1.755 g/cc	4.07 GPa
0.6	16.71 GPa	0.320	1.826 g/cc	3.45 GPa

Table 6: Properties of Lamina.

5.2.4 Failure Criteria

For evaluating which thickness and volume fraction is the most suitable for the FFU's shell it has been decided to use the failure criteria of the maximum strain. This criteria is more appropriate since from the FEM software it is not possible to calculate the different stresses in matrix and fibers. Therefore, since the strain is equal for both components of the lamina, the maximum strain criteria is the most suitable failure criteria for the shell.

The criteria consist in:

$$\begin{cases} \epsilon_1 \geq \begin{cases} \epsilon_1^{T^*}, (\epsilon_1 > 0) \\ -\epsilon_1^{C^*}, (\epsilon_1 < 0) \end{cases} \\ \epsilon_2 \geq \begin{cases} \epsilon_2^{T^*}, (\epsilon_2 > 0) \\ -\epsilon_2^{C^*}, (\epsilon_2 < 0) \end{cases} \\ \gamma_{12} \geq \gamma_{12}^* \end{cases} \tag{6}$$

where:

$\epsilon_1^{T^*}$ longitudinal tensile strain
$\epsilon_1^{C^*}$ longitudinal compressive strain
$\epsilon_2^{T^*}$ transverse tensile strain
$\epsilon_2^{C^*}$ transverse compressive strain
γ_{12}^* in-plane shear strain

To calculate the value of the maximum strain, it has ben used the Hook's law on the maximum stresses that the GFP woven can stand [8].

$$\sigma_1^{T^*} = 367 \text{ MPa}$$
$$\sigma_1^{C^*} = -549 \text{ MPa}$$
$$\sigma_2^{T^*} = 367 \text{ MPa}$$
$$\sigma_2^{C^*} = -549 \text{ MPa}$$
$$\tau_{12}^* = 97 \text{ MPa}$$

the result obtained is:

$$
\begin{cases}
\dfrac{\sigma_1^{C^*} - \nu\sigma_2^{C^*}}{E} < \epsilon_1 < \dfrac{\sigma_1^{T^*} - \nu\sigma_2^{T^*}}{E} \\
\dfrac{\sigma_2^{C^*} - \nu\sigma_1^{C^*}}{E} < \epsilon_2 < \dfrac{\sigma_2^{T^*} - \nu\sigma_1^{T^*}}{E} \\
\gamma_{12} < \dfrac{\tau_{12}^*}{G}
\end{cases} \tag{7}
$$

$$
\begin{cases}
\epsilon_1^{C^*} < \epsilon_1 < \epsilon_1^{T^*} \\
\epsilon_2^{C^*} < \epsilon_2 < \epsilon_2^{T^*} \\
\gamma_{12} < \gamma_{12}^*
\end{cases} \tag{8}
$$

From the ABAQUS analysis of the strain it is possible to conclude that with both 1 and 2 mm thickness and with any of the volume fraction proposed the shell can withstand the load (numerical results are available on request).

5.2.5 Results

From the analysis performed and according to the assumption stated it is possible to conclude that the hemispheres shall be done using D-glass fiber and epoxy. Moreover due to the difficulties in laying up the fiber glass the best woven to use , due to its good drapability, is the *sateen*.

It has been sorted out that all the thicknesses and the volume fractions tested can be used, without any problem for what concern the load bearing capacity, so no conclusion can be found out looking at the loads. After that the next biggest limitation in the choice of the material is the weight. So it has been chosen to use 1 mm thickness lamina with a volume fraction of 0.4 for the fibers. From calculations it can be shown that the thickness may be reduced to $0.5 \sim 0.6$ mm, unfortunately this would created difficulties in the manufacturing process, so it has been chosen to keep 1 mm thickness. In this way it is possible to use the lowest density and obtain a very lightweight shell.

The two hemispheres to produce, 124 mm diameter and 1 mm thickness, will weight approximatively 83 g for both hemispheres.

6 Processing

In this section the attention is focused on the production aspect of the realization of the FFU's shell. The production method is a very important aspect since it doesn't affect only the mechanical properties of the produced object but also other aspects such:

- Costs (labour, raw material, equipment and tools);
- Cycle time;
- Quality;
- Series length;
- Health aspects.

The aspect treated in this report are mainly all costs and "know how" knowledge required. Nevertheless some minor considerations on health aspect, quality and series length are analyzed.

6.1 Processing method

The process that should be used in the manufacturing of the spheres should fulfill the following conditions. The process must allow a good controlled exterior surface and tolerate a double curvature geometry, it has to be possible to use very conformable reinforcing fabrics, it should not require expensive equipment or facilities, the "know how" needed to manufacture under the method should not be advanced and the health concerns should be minimized. Furthermore, for the election of the process it should be taken into account the production rate will not be high although the amount of parts manufactured can be around twenty five parts per year according to initial estimations. In case the experiment is successful and four spheres are placed in all coming sounding rockets that are launched from ESRANGE the amount of produced spheres can experience a rise in the demand.

When the above mentioned considerations are taken into account there are certain manufacturing processes that are rejected. The processes involving pre-impregnated fabrics are rejected because the conformability of a pre-impregnated fabric is lower in comparison with the conformability of the some dry fabric and since the shape is a vital parameter for this project the best drapability should be pursued. The processes involving expensive equipment like presses, autoclaves, dedicated tooling like the equipment needed for the filament winding or pressurized spry pistols are rejected because of the high cost of the equipment that would make the accomplishment of the project impossible because of budget limitations. Furthermore, there are processes that cannot be used due the semi spherical shape of the manufactures parts. This process is pultrusion, because this method requires a constant section and spray lay up because the difficulties to control the amount of matrix deposed. Finally all processes involving chop fibre or thermoplastic are not going to be considered because of the limitations set by the already chosen materials.

After the considerations exposed above there is a limited range of processes available. These processes are injection moulding, resin transfer moulding (RTM), vacuum injection moulding, reinforced reaction injection moulding (RRIM) and structural reaction injection moulding (SRIM) which are the processes under the liquid moulding classification. Among the liquid moulding there is a method that does not require pressurizing the resin for its injection and only require the creation of vacuum in the mould which can be an advantage in terms of simplicity. This manufacturing method is the *vacuum injection moulding*, therefore this will be the chosen method.

Vacuum injection moulding fulfill all the requirements, it allows a controlled outer surface, the drapability of the fabrics is not affected by the manufacturing process (therefore the double curvature shape only depends on the fabric), the "know how" required to implement this manufacturing method is low, the equipment required do not required any high investment and the health concerns are low according to Astrom [3].

6.1.1 Mould

For what concern the mould two aspects are important: the material and the fabrication process. If not considered and designed carefully those to aspect can lead to undesired results during the curing precess.

The influence of the material is directed connected to the difference of the coefficient of thermal expansion (CTE) between the mould and the composite material. Due to the fact that during cure processes there are chances in temperature, if the CFE of mold and composite are difference, this lead to inaccuracy of dimensions and residual stresses. For these reason the CTE must be taken into account.

Since the dimension of the shell are not standard (124 mm diameter) it has been decided to fabricate the mould through direct machining from a solid block. Due to the fact that the mould could be used for several times it has been decided to fabric them using aluminum. This allow the MUSCAT team to re-use them several time without the risk of damaging them.

Aluminum has a good compatibility with glass-reinforced epoxy material as can be see in Table.7:

Material	$\alpha[10^{-6}\ °C^{-1}]$
Aluminum	22.5
Glass-reinforced epoxy prepreg	20
Glass-reinforced epoxy, wet layup	$22-25$

Table 7: Coefficient of thermal expansion [3].

6.2 Post-processing steps

The post processing steps required by the parts after the manufacturing process is completed is the finishing of the edges. The post processing of the edges is required in order to guarantee the right relative positioning between the two hemispheres the compound each sphere.

After the de-moulding of the part there will be extra material in the edges that should be removed in order to reach the design shape . To remove this extra material the most suitable option is to trim these edges with a carbide based cutting tool such as a disc saw. Finally the mountings, or Ribs, will be fixed to the Upper Hemisphere using adhesives.

6.3 Processing time and governing process parameters

As a consequence of the fact that the process chosen is *vacuum injection moulding*, the governing process parameters for the manufacturing technique are room temperature and atmospheric pressure. Therefore the processing time can be evaluated by looking at the technical instruction provided by the producer of the epoxy for curing at room temperature and atmospheric pressure.

The curing time for the resin used varies from 48 h to 24 h depending on the hardened used with the resin.

7 Conclusion and Further improvements

It is possible to conclude that a spherical shell made in D-fiber glass and epoxy can fulfill all the strict requirements for the FFU. The election of composite materials to manufacture the spherical probes of the MUSCAT experiment is an appropriate choice because of its light weight, electromagnetic transparency and mechanical properties

The improvements that can be implemented in the current product are add a final coating to the outer surface of the spheres, improve the finishing of the inner surface of the sphere and develop the co-curing of components in the inner surface.

The coating it is a desirable feature for future development because the spheres can be made more visible by adding color coating to the outer surface during the manufacturing process.

The finishing of the inner surface it is a feature that can be improved by means of modifying the manufacturing method. This improvement has no impact in the performance of the spheres but it would improve the appreciated quality of the product. In order to implement this improvement other manufacturing method that can control the finishing of the inner and outer surface should used. A method that would allow the control of the inner and outer surface would be forming by pressing, but his process has a big con, its high price.

The co-curing of components to the inner surface it is an option that the customer could desire in order to implement more sensors o different equipment. The implementation of co-cured part s in the inner surface would make the spheres a more versatile and interesting product. The co-curing it is also desirable from the point of view of the manufacturing because structural components can be directly attached decreasing the amount of pieces involved in the assembly of the spheres.

References

[1] MUSCAT Official Website, `http://muscatexperiment.se/`

[2] REXUS/BEXUS Website, `http://www.rexusbexus.net/`

[3] B.Y.Astrom (1997). *Manufacturing of Polymer Composites*, Nelson Thornes.

[4] Easy Composites, `http://www.easycomposites.co.uk/Default.aspx`

[5] The Wagner Companies, `http://www.shopwagnerb2c.com/`

[6] Chung, Deborah D.L. (1994). *Carbon Fiber Composites. (pp: 102)*, Elsevier. Online version available at: `http://www.knovel.com.focus.lib.kth.se/web/portal/browse/display?_EXT_KNOVEL_DISPLAY_bookid=517&VerticalID=0`.

[7] Matweb, `www.matweb.com`.

[8] Lecture Note *Composite Strength and Failure Criteria (slide 16)* of the course of *SD2414 Fiber Composites - Materials and Manufacturing.*

[9] Dassault Systemes Simulia Corp. Rising Sun Mills, 166 Valley Street, Providence, RI 02909-2499, USA.

Antenna project,
Patch antenna for MUSCAT

Applied antenna theory

Authors: Ben Oakes, Patrick Magnusson and Ólafía Lára Lárusdóttir
Supervisors: Anders Ellgardt, Peter Fuks and Nickolay Ivchenko
Date: June 15, 2012

Abstract

A lightweight, transmitting and receiving antenna is required for the rocket experiment MUSCAT (MUltiple Spheres for Characterisation of Atmospheric Temperature). This antenna must be capable of receiving raw GPS signals at 1.575 GHz and transmitting the position of the experiment back to Globalstar satellites at 1.615 GHz. The fractional -10 dB return loss bandwidth of the antennas should be 3%. In this document a 90 degree hybrid coupler is designed using AWR, then further simulated in CST (Computer Simulation Technology) and tested using a Network analyzer. Furthermore a square and a circular patch antenna are designed analytically, simulated and optimized in CST (Computer Simulation Technology) and their properties compared. Finally circular patch antennas are built, measured and tested extensively. The result of this project is a well matched, broadband, very circularly polarized and well functioning antenna system for high efficiency for the frequencies required for the MUSCAT experiment.

Contents

Preface

The aim of this paper is to present our project design in the course EI2400 "Applied Antenna Theory". We gratefully thank our supervisors Anders Ellgardt, Peter Fuks and Nickolay Ivchenko. We also thank sponsors of MUSCAT, EVONIK especially, for their part in making our antenna work.

1 Introduction

This project treats the procedure of building a GPS antenna for the MUSCAT (MUltiple Spheres for Characterization of Atmospheric Temperature) rocket experiment. At least four identical antennas will be made and four of them will be placed in the four FFUs (free falling units) of MUSCAT which collect raw GPS and sensor data between the altitudes 15 - 80 km to estimate a temperature profile in this region. When the FFUs have fallen to approximately 5 km altitude they will transmit their position via the Globalstar satellites using the satellite modem, STX2. Former experiments used two antennas in one FFU to serve these purposes. The purpose of our antenna project is to make an antenna that can receive GPS signals and transmit STX messages containing the FFUs position so the FFU can be tracked.

In this paper the requirements of the antenna are discussed first, followed by the design procedure, simulations and testing of a coupler and then the antenna. Simulations and tests of the complete design of the antenna, the coupler, and coaxial connections are illustrated. Also, results from the integration of the whole system in a FFU are discussed.

2 Requirements

The antenna has to receive the GPS signal and transmit STX messages along with fitting in a FFU. In the next sections requirements will be presented.

2.1 Functional requirements

Functional requirements state what functions our antenna should have. These are the basic requirements for ensuring a functional antenna as the end result.

2.1.1 Frequency

The antenna shall be able to transmit STX2 messages with the STX and be able to receive GPS signals. The carrier wave of the GPS signals from satellites $L1$, commercial GPS band, has a frequency of 1575.42 MHz. The null to null bandwidth of a L1 C/A is 2.046 MHz [1]. At the end of the project the transmitted signal containing the FFU position is sent on 1615 MHz with a resolution of 2.5 MHz, but the STX2 can be set to a frequency between 1611 MHz to 1618 MHz.

This gives us a center frequency of 1595 $\pm$2 MHz, which is where the resonance should be at. The fractional bandwidth is mainly decided by the two carrier frequencies as those are the biggest limitation, if a single resonant antenna is used, and is $\approx$3 %.

2.1.2 Polarization

As the GPS signal is right hand circularly polarized, RHCP, and the STX2 signal is left hand circularly polarized, LHCP, the antenna needs to be able to receive RHCP signals and transmit LHCP signals.

2.1.2.1 Reduction of multi paths The antenna should be able to discriminate between direct and reflected signals. If reflected waves reach the antenna, the path of the signal will not be a straight line and the calculated GPS position will be inaccurate. When the FFU is still falling this is not a big problem but when it is on the ground it will have greater effect.

GPS satellites send RHCP waves. When a RHCP wave is reflected, for example on the ground or on some other surface, it will become LHCP and if LHCP wave is reflected it will become RHCP. Furthermore when a LHCP wave enters a RHCP antenna the polarization losses will be greater than the received RHCP waves so, the LHCP waves will just act as a noise.

2.2 Design requirements

The design requirements are constraints that have been put on the antenna, for example size constraints or constraints regarding interfaces.

2.2.1 Mechanical constraints

As the antenna is placed within the MUSCAT FFU it needs to fit and work under those conditions. A exploded view is presented in Figure 1 and it can be seen that the antenna is going to be placed on the top PCB, on the top side. On the top side there are small metal objects that limit how big the antenna can be, a parachute is placed there as well and finally a top hemisphere made of glass fiber and epoxy, will be placed on for more than half of the mission.

To fit on the top PCB the antenna should be less then 104 mm in diameter and less then 30 mm high.

2.2.2 Electrical constraints

The antenna needs to be able to work with the satellite modems, STX 2, and the two GPS receivers, a GPS-front end and a commercial GPS. The STX 2 modem output connection is 50 Ω and outputs 18dBm ±2 RMS power on a 50 Ω load [2]. The amplifier input-impedance of the GPS front end is 50 Ω and the maximum RF Input Power is 15dBm [3]. The commercial GPS is located after the GPS front end amplifier and has a 50 Ω input impedance and the output VSWR should be 1.5 max, see [4] for further details.

2.3 Performance requirements

The performance requirements is how well the functions should be fulfilled.

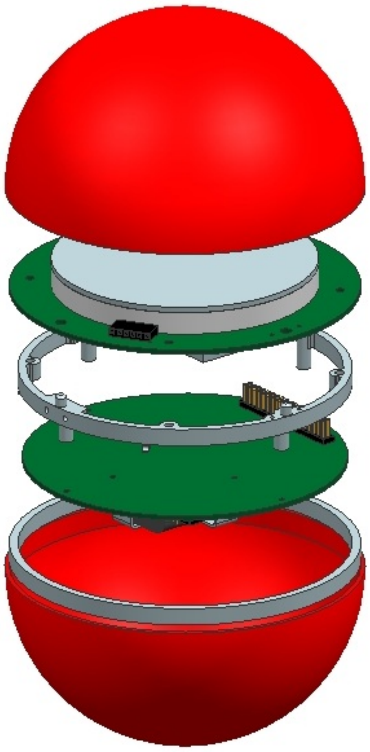

Figure 1: Drawing of the MUSCAT FFU with antenna on top

2.3.1 Radiation pattern

The antenna should be able to receive signal from as many GPS satellites as possible to be able to get a good approximation of speed and position of the FFU. This gives us the requirement that the antenna should have quite low directivity and a quite wide main lobe. The best solution would be to have an omnidirectional pattern on the upper hemisphere, i.e. have a directivity of 3 dB.

2.3.2 Bandwidth and losses

The dielectric and conductive losses can't be affected so much, but losses due to impedance mismatching are easier to affect. A normal level for the return loss criteria is that the return loss should be bigger than 10 dB. Our definition of bandwidth from here on will therefore be that the amplitude of S_{11} and S_{22} is less then -10 dB.

2.3.3 Polarization

To not lose too much power the polarization needs to be matched. The requirement is that the axial ratio of the main beam at 0 degrees, should be lower than 3 dB.

2.3.4 Vibrations and temperature

The antenna needs to withstand the conditions the FFU is subjected to like a temperature range of $-40°$ C to $60°$ C, be vacuum proof and survive vibrations of the rocket.

2.4 Link budget when our antenna is the receiving antenna

The link budget is based on [5] and [6]. In table 1 is the link budget for the downlink. The values for satellite EIRP, the propagation is taken from [5]. We assume that the antenna noise temperature and the antenna temperature is 3 K. From the data sheet of our GPS receiver, [3] we get a noise figure of 1.4 dB. Using the design mentioned in later chapters we get that the gain of our receiving antenna is G=8.69 dB. This results in C/N=6.64 dB, with a link margin of 2.24 dB.

Satellite transmitter	
Transmitter power (25 Watts)	14 dBW
RF Losses in transmitter path	-1.25 dB
Antenna gain (with respect to an isotrope)	13.5 dBi
Satellite EIRP	**26.25 dBW**
Propagation	
Atmospheric and polarization losses	-0.5 dB
Distance, d	$\approx$ 25236 km
Speed of light, c	$3 \cdot 10^8$ m/s
Frequency, f	$1.575 \cdot 10^9$ Hz
Wavelength, $\lambda = \frac{c}{f}$	3/16 m
Free space loss $= 10\log_{10}((\frac{\lambda}{4\pi d})^2)$	-184.43 dB
Received power on Earth (EIRP+Losses)	**-158.68 dBW**
Noise figure	
Estimated antenna noise temperature T	3 K
Boltzmann's constant k_B	-228.6 dBJ/K
Noise bandwidth of the receiver B	2500000
Noise figure of our GPS receiver	-1.4 dB
Total noise power	-161.4 dB
Gain of receiving antenna	
Effective radius	0.0562 m
G_{rad}	0.004
Directivity $D_0 = \frac{(k_0 a_e)^2}{120 G_{rad}}$	7.38
Gain of receiving antenna	8.69 dB
$G/T = G_{dB} - 10\log(T_A)$	3.92 dB
Carrier power per noise $C/N = (EIRP + G/T + Losses - TNP)_{dB}$	**6.64 dB**
BER	10^{-3}
$(C/N)_{required}$ according to [6]	4.4 dB

Link margin $(C/N)_{available} - (C/N)_{required}$	2.24 dB

Table 1: Downlink link budget

2.5 Summary of design specifications

A summary of our requirements are listed in table 2

Center frequency	1.597 GHz
Fractional bandwidth	3% defined as when S_{11} and S_{22} is below -10 dB
C/N	4.4 dB
Polarization	Circular, left hand sending, right hand receiving
Radiation	As omnidirectional as possible above the antenna
Size	Radius smaller than 104 mm
Impedance	Matched to 50 Ω

Table 2: Specifications for our patch design

3 Choice of design

For a hemispherical coverage and circular polarization at the GPS frequency, several antenna design options come to mind. These are the patch antenna, helix antenna and conical spiral antenna. The latter two require no extra microwave component for circular polarization. They do however only have one type of polarization, either right or left hand circular polarization. Furthermore they "stick out", taking up a lot of space which we don't have in this application. Moreover, they are difficult to make with precision even if they are very broadband. The patch antenna has the benefit of being flat, low profile, capable of fitting well inside the FFU without too much height, low cost, easy manufacturing and light weight. The disadvantage of a patch antenna is that both pattern and impedance bandwidth are narrow. Although patches are relatively narrowband, we chose to go with the patch option.

3.1 Patch antenna

In this section we describe how we overcame the various shortcomings of a patch antenna.

3.1.1 Ways of making a patch antenna more broadband

The patch antenna is generally quite narrowband. There are a few ways to increase the bandwidth of patch antennas that have already been investigated, such as electrically thick elements, stacked multipatch, multilayer elements, multiple-resonator elements and a reactive matching technique. For the first four of those their increased bandwith makes the radiation characteristics poorer [7]. Increasing the substrate thickness increases excitation of substrate waves [7] as well as causing matching problems [8]. Using substrate material with lower dielectric constant, e.g. $\varepsilon_r = 1$ decreases the excitation of the substrate waves [7]. Also if two feeds are placed symmetrically located with respect to the antenna center the losses can be further decreased [9].

3.1.1.1 Available substrate material The PCB on which electrical components of the FFU are placed on is FR4, which has dielectric constant $\varepsilon_r \approx 4.4$. If this material is used as a substrate it will cause a lot of substrate waves, which will increase the losses of the antenna. A material that was found with a dielectric constant close to 1 is from Evonik industries and is called ROHACELL 31 and it has dielectric constant, $\varepsilon_r \approx 1.08$ at 2 GHz and dissipation factor of $\tan\delta = 0.0001$ at 2 GHz.

3.1.2 Ways of feeding a patch antenna to obtain circular polarization

There are a few ways to achieve circular polarization with a patch antenna. One way is to build an antenna in such a way that the currents move in circles, for example a square antenna with a slot in the center of the antenna. Another way is to position a feed in the right place of the patch antenna. The third way is to use two feeds and make 90 degree phase shift between the two feeds. The phase shift can be achieved by for example using stubs or a hybrid 90 degree branch-line coupler.

3.1.3 Position and shape of the patch

The patch will be placed on the top of the top PCB in the FFU in order to reduce losses and interference from other components. The ground plane of the PCB will act as the ground plane of the microstrip antenna and ROHACELL will be placed in between the patch and ground plane. In order to get a symmetrical feed we need a antenna that is symmetrical around two axis through the center of the patch. The most obvious and easiest designs are a square and a circular shape. Both of those will be considered in this text. As the geometry of these kind of antennas will not produce circular polarization, a branch-line coupler will need to be added and designed to provide two linearly polarized waves with 90° phase shift between each other, this design will be discussed in next section.

4 Branch-line coupler for circular polarization

Circular polarization is achieved with a branch-line coupler. This section describes how it works and the design of it.

4.1 How it works

Figures 2 and 3 view the coupler from the back of the ground plane. The direction of propagation of the wave is indicated by the $\hat{k}$ Poynting vector directed in through this paper. For right hand circular polarization (RHCP), the phase shift moves around the branch-line in a clockwise direction looking from the back of the ground plane. Placing your right thumb in the direction of the wave, the fingers of your right hand will curl in the direction of the phase shift, the wave is thus RHCP, see figure 2. Changing the terminated end to port 1 instead of 4 and transmitting though port 4 will phase shift the wave in the other direction around the branch-line. Sticking your left thumb in the direction of the wave, your left fingers will curl in the direction of the phase shift. The wave is thus in this case LHCP, see figure 3.

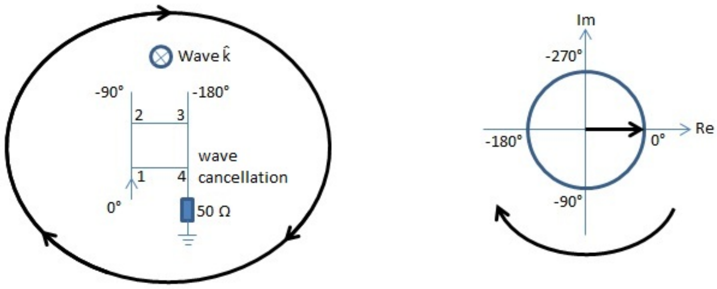

Figure 2: Coupler terminated to obtain RHCP

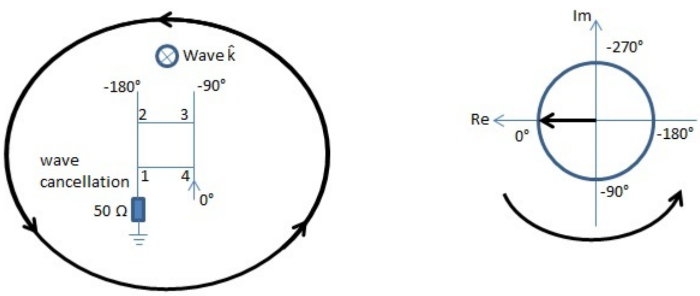

Figure 3: Coupler terminated to obtain LHCP

When measuring the s-parameter with the hybrid connected one has to think of what happens to the reflections. One can think that the s-parameters only goes down 3 dB lower, because of simple power division if there was no hybrid there but we also need to think about what happens to the phase. In Figure 4 we can see what happens to the signals when it is sent in from port 1.

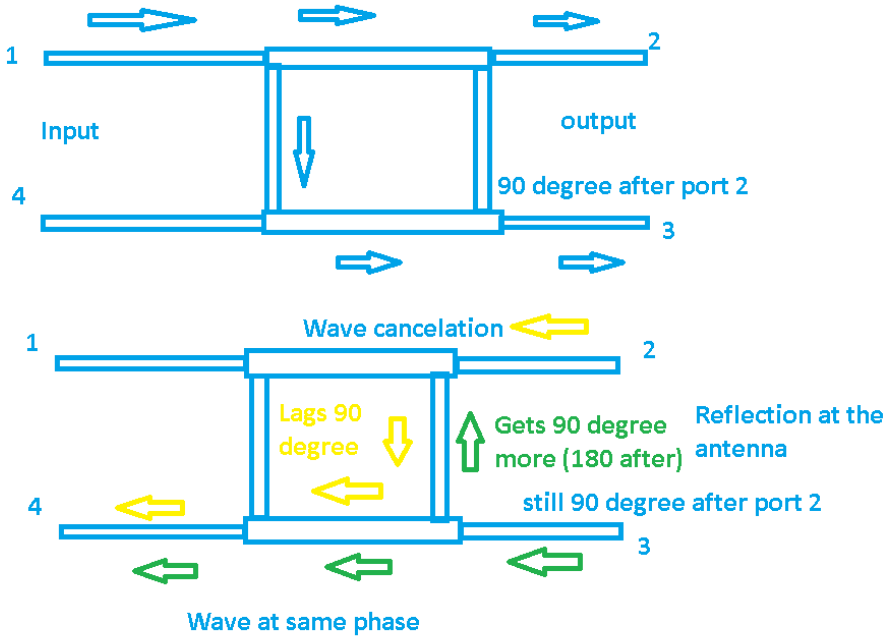

Figure 4: Explanation of what happens to the reflection of the antenna when the signal is sent through the hybrid. In the top picture the wave enters from port 1. In the picture below the wave is reflected at port 2 and 3, the yellow arrows are reflections from port 2 and the green are reflections from port 3. We can see that the signal to port 4 is added constructively and signal to port 1 is canceled.

As we know the signal is split into two signals with equal amplitude, the one going to port 2 has 90 degree phase shift seen from the wave put in at port 1 and port 3 has a 180 degree phase shift. When the signal is reflected again at the end of the hybrid both signals are split into two parts again. The split signal from port 2 going toward port 3 will get a 90 degree more phase shift and adds constructively to the signal going from port 3 and toward port 4. On the other hand the signal from port 3 going toward port 2 also gets a 90 degree phase shift more and will cancel the signal from port 2 against port 4. So what was see on S_{11} and S_{22} is only the coupling of the two outputs as that is affected opposite of a reflection. In S_{21} and S_{12} the coupling is canceled but not the reflection from the antenna so S_{12} and S_{12} should be showing the mean value, 3 dB down, of the reflection of port 1 and port 2.

4.2 Design procedure

For low profile and in order to minimize disturbances from surrounding objects, the coupler will be inside the PCB on which the ground plane of the antenna sits on, sandwiched between two FR-4 layers of the PCB. These FR-4 layers will hence be wedged in between two equally thick PEC layers which in turn are sandwiched between two ground planes. The coupler dimensions are heavily influenced by the fact that it is between two conducting layers equidistantly placed from it.

4.2.1 Specifications for coupler

The sought parameters are the widths of the stripline and other dimensions of the coupler. In order to calculate these we will need the parameters that are already specified, which can be seen in table 3.

Parameter	Value	Description
f_c	1597 MHz	center frequency
ε_r	4.4	relative permittivity of substrate (FR-4)
h	735 μm	distance between ground planes
t	35 μm	thickness of stripline
Z_c	50 Ω	system impedance

Table 3: Design specifications for coupler

The material of the stripline will be the same as that for the patch and ground plane, copper.

4.3 AWR environment simulations

As mentioned before the coupler is positioned between two ground planes and thus it is a stripline. Although the length of each "side" of the coupler is merely $\lambda/4$, the width of stripline is more difficult to calculate analytically. The time this would take and the non-reliability of the results are good reasons to use numerical tools. For designing this, we use AWR environment and verify the obtained results in CST.
The specified parameters of the coupler mentioned in table 3 were plugged into a module in the AWR environment which has a built in calculator for dimensioning striplines. To obtain a system impedance of 50 Ω, all striplines in the coupler except two should have an impedance of 50 Ω and thus they have the same width. The ones that do not have the same impedance as the rest are the upper and lower parts of the branch-line, see figure 7. They will have an impedance of the wanted system impedance divided by the square root of 2 so $50/\sqrt{2}\ \Omega$ and will thus have a different width. The widths of the different striplines were first calculated separately and lengths were thereafter optimized with the AWR program.

The input windows from simulation for 50 Ω and 35.35 Ω striplines can be seen in figures 5 and 6.

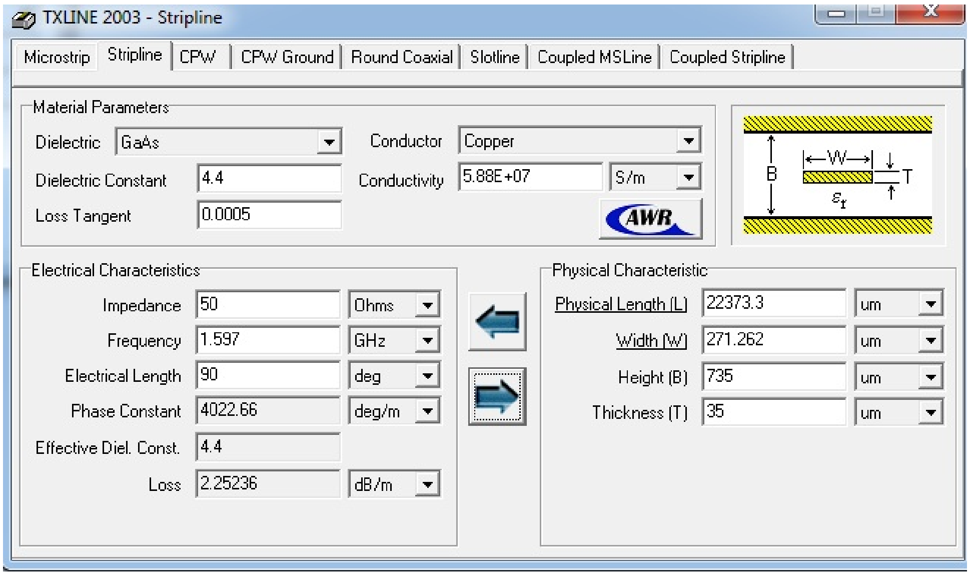

Figure 5: Dimensions for 50 Ω stripline

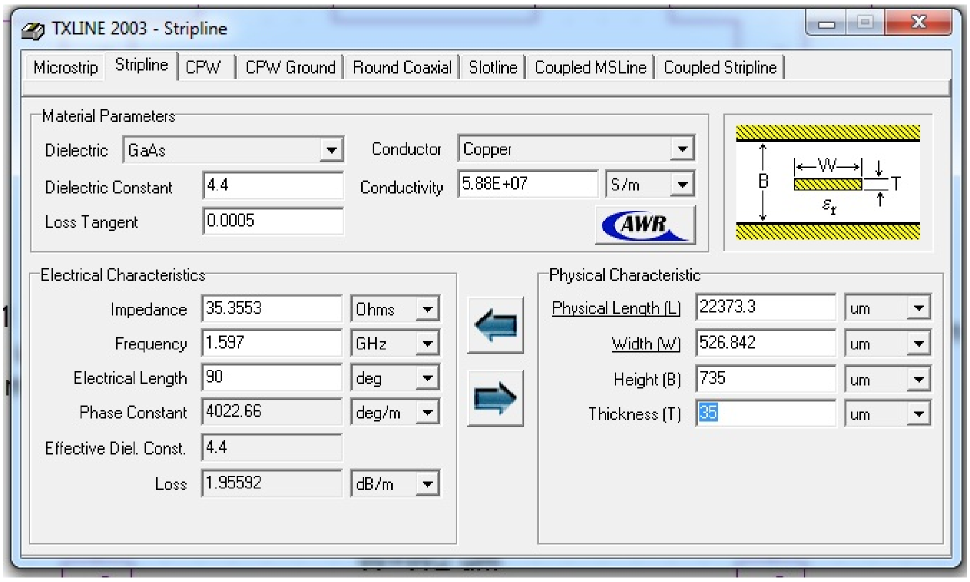

Figure 6: Dimensions for 35.35 Ω stripline

4.3.1 Results from simulation in AWR design environment

The resulting dimensions of the coupler can be viewed in figure 7. The impedance in each stripline with width $W1$ is 50 Ω and the impedance for the two strips of width $W2$ is $50/\sqrt{2} \approx 35.35$ Ω.

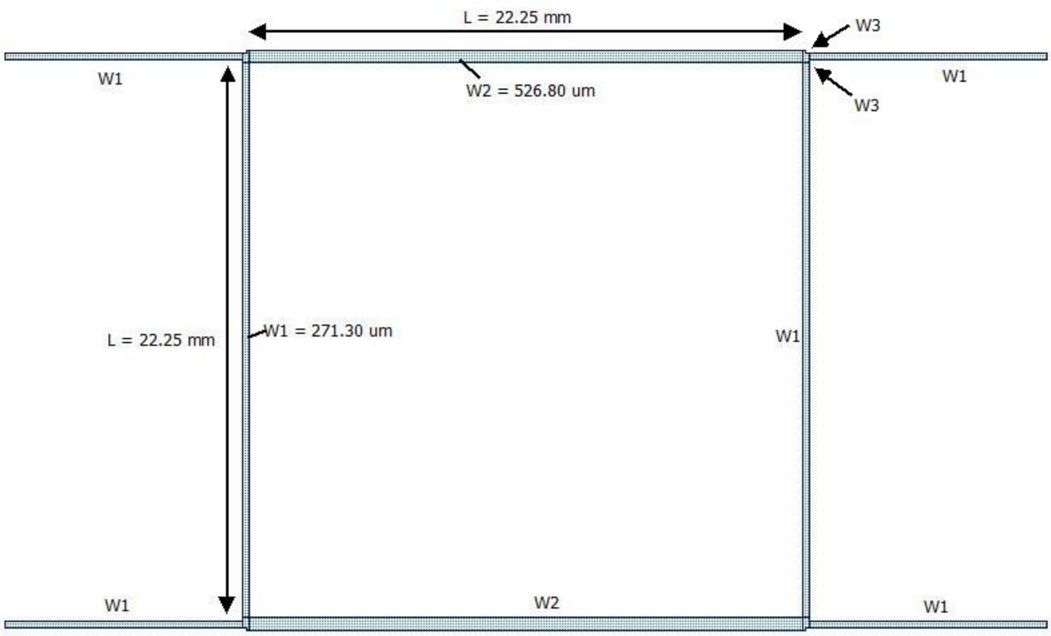

Figure 7: Layout, dimensions

Where $W3 = \frac{W1-W2}{2}$ is the width the arrows indicate in figure 7 and is the same in all corners so the ports are centered on the striplines. The corners of the coupler (at the ports) are not seen so clearly in the figure above. Figure 8 shows the top left corner and its exact dimensions. The rest of the corners are identical.

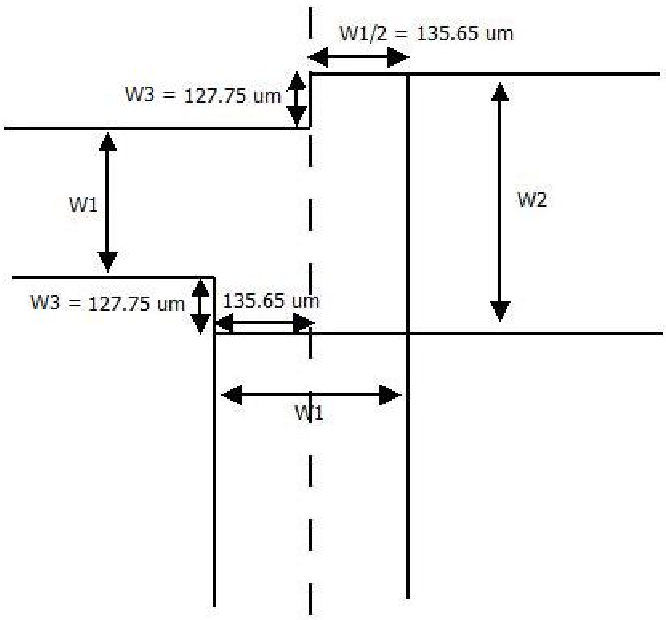

Figure 8: Corner dimensions of the coupler

A more detailed schematic from AWR of the resulting coupler and its dimensions can be viewed in figure 9. Substrate permittivity and stripline thickness can for example be viewed there.

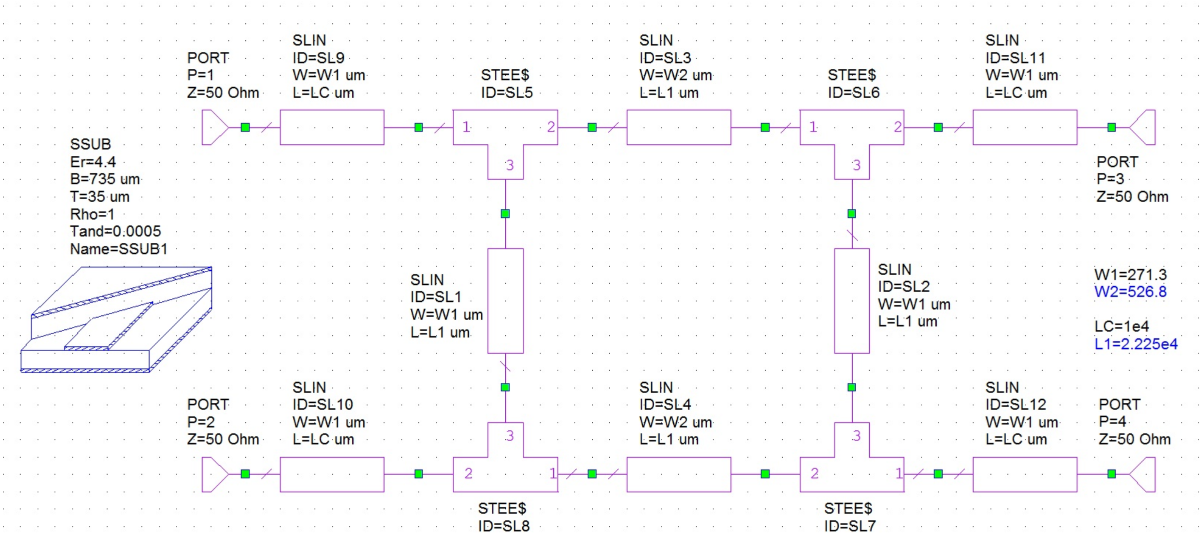

Figure 9: Dimensions from AWR environment

4.3.2 S-parameters

The S-parameters of the coupler from AWR environment were also checked. AWR's first coupler design had a resonance slightly off the desired center frequency so a parameter sweep was made for optimizing the coupler. The results obtained after the optimization can be seen in figure 10.

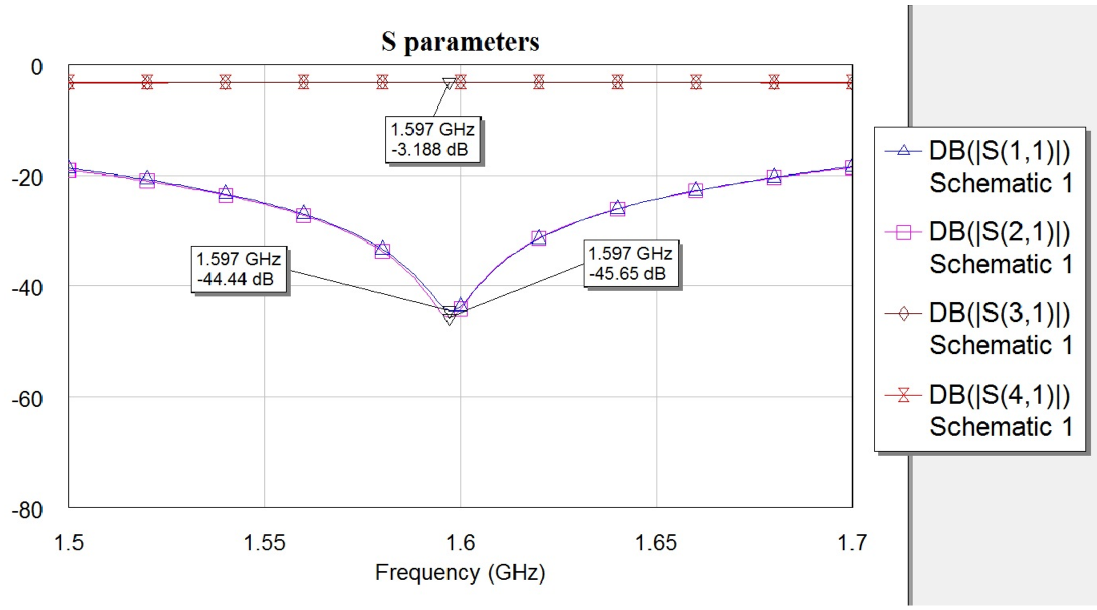

Figure 10: S parameters of the coupler in AWR

As can be seen from figure 10, the coupler is broadband enough for our design.

4.3.3 Simulations in CST

The coupler with dimensions resulting from simulations in AWR environment was then simulated in CST to verify results and see if the dimensions needed to be further optimized. Figure 11 shows the coupler in CST embedded in the substrate.

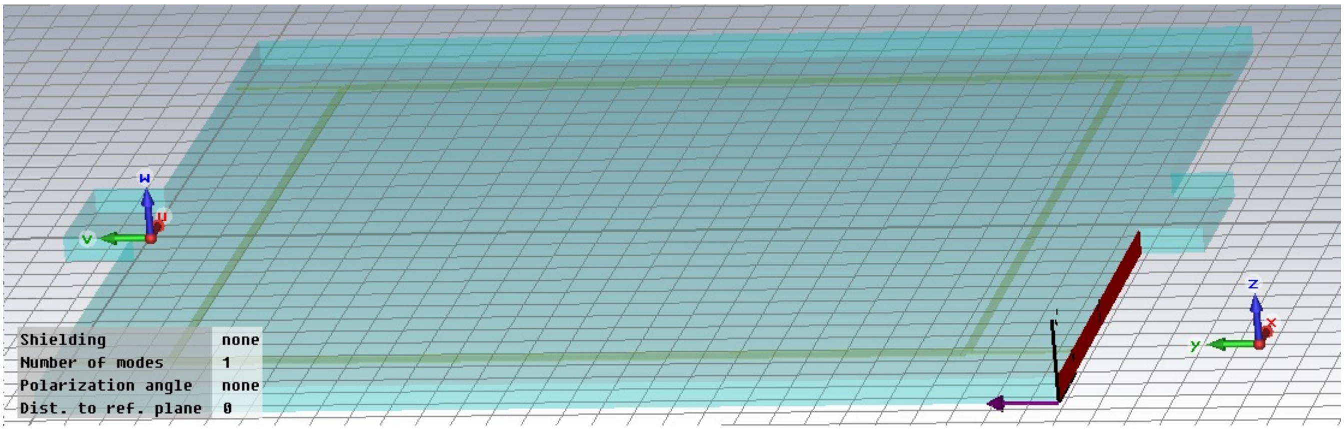

Figure 11: The coupler in CST embedded in FR-4 substrate with 4 waveguide ports

Simulation results of time domain solver were made. The interesting results concerning the coupler are mainly the S-parameters, which where made with adaptive meshing in CST for higher precision. These can be viewed in figure 12.

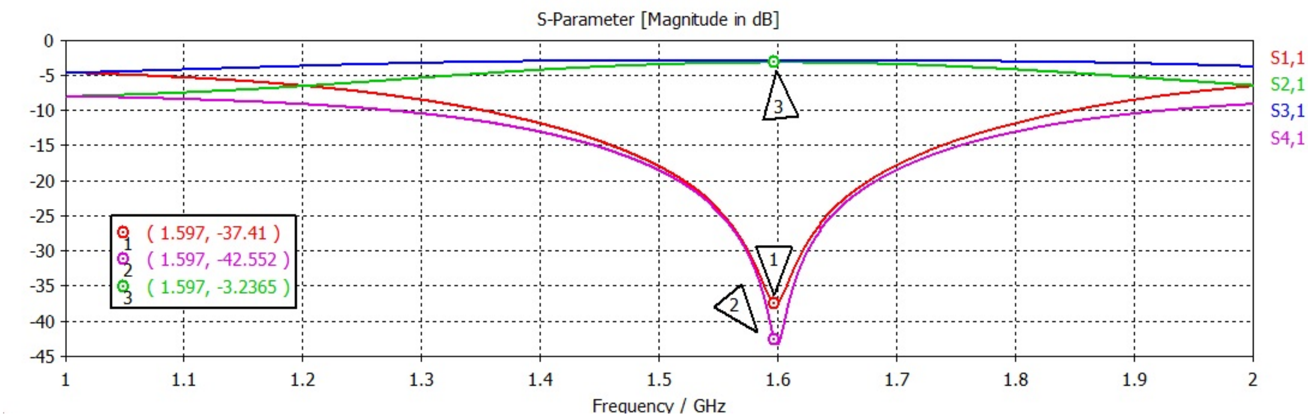

Figure 12: S-parameters of coupler

These show what fraction of the power sent into ports 1, 2, 3 and 4 comes out of port 1. Port 2 and 3 are the output ports and ports 1 and 4 are the input ports. Ideally very little of the signal is reflected and very little goes between the STX modem and GPS front-end, hence the S-parameters results are good. Results from figure 12 and 11 are very similar so there is a degree of trust that this design will work.

4.4 Testing the coupler with the Vector Network Analyzer

When the coupler came from the manufacturer, S-parameter tests were made with the Vector Network Analyzer, VNA. The most important feature of the coupler is that the phase difference between the two outputs port 3 and 4 when sending from from port 1 (see port numbering in figure 9) should be 90° at the resonance frequency. This measurement was performed on several frequencies of interest; 1.5 GHz (interesting to see how s-parameters vary further away from the resonance frequency), 1.575 GHz (the GPS frequency L_1), 1.597 GHz (center frequency of antenna) and 1.618 GHz the transmitting frequency. The results of the measurements are in table 4. Minimal reflection will be achieved if the phase shift between port 3 and 4 is 90° at these frequencies. The phase difference between port 3 and 4 is compared for the frequency sampled closest to 1.597 GHz see figures 13 and 14.

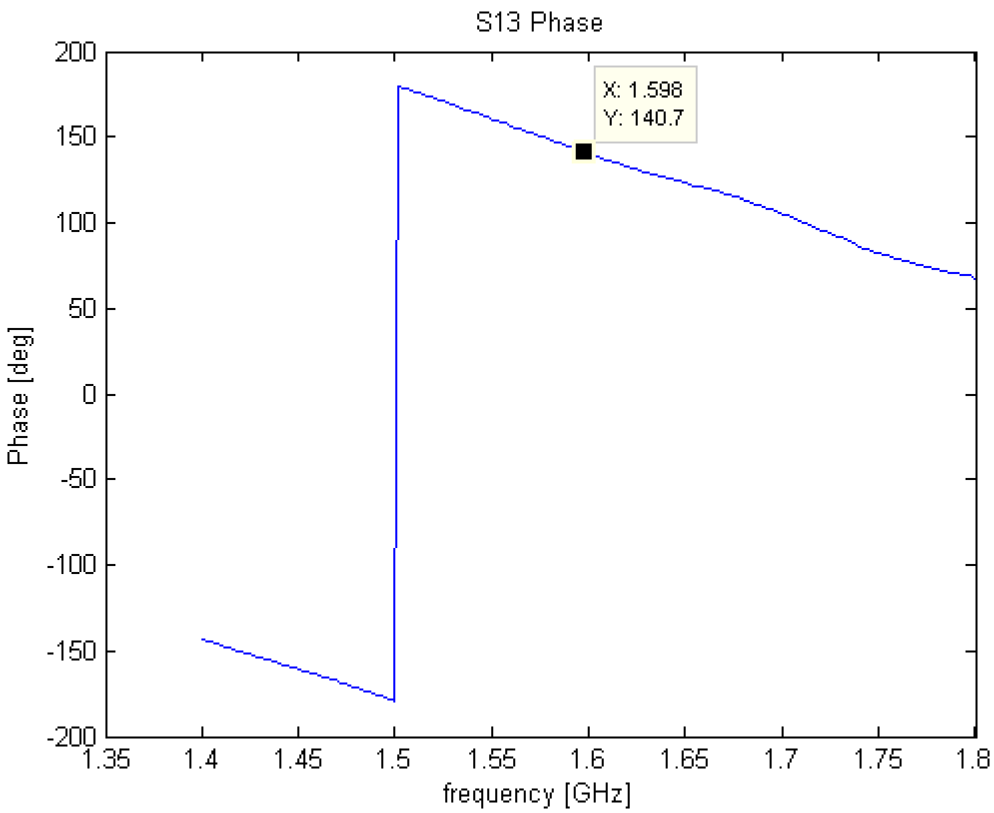

Figure 13: Phase diagram showing phase of S13 at 1598 MHz

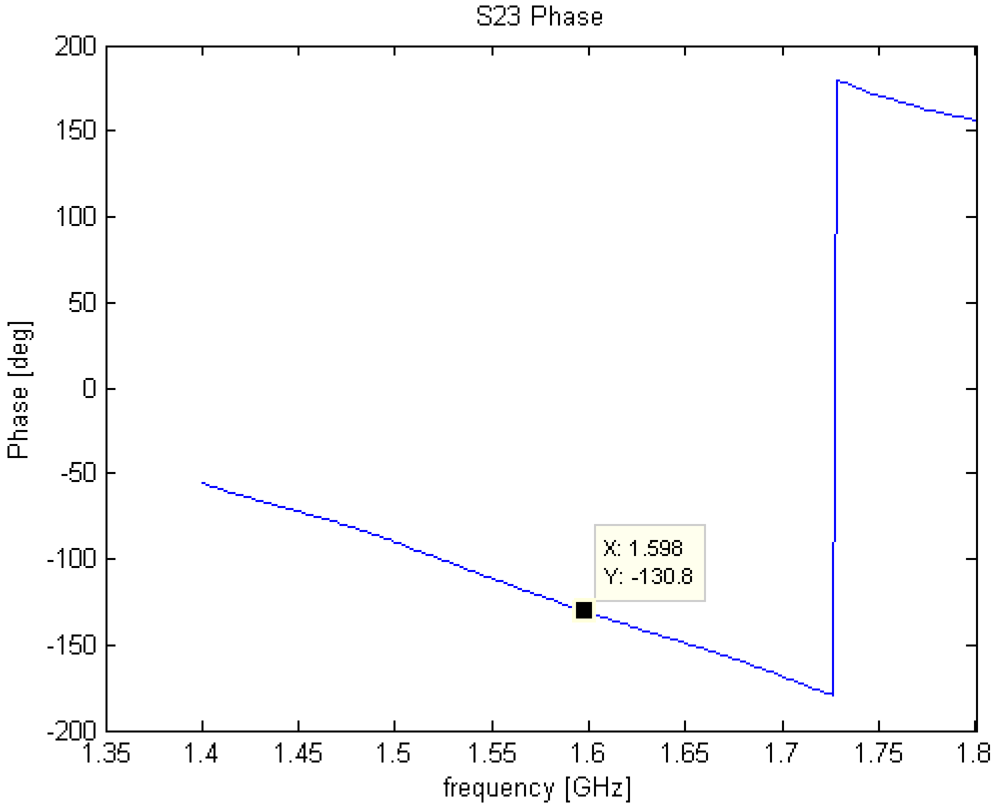

Figure 14: Phase diagram showing phase of S23 at 1598 MHz

	1.500 GHz	1.576 GHz	1.598 GHz	1.618 GHz
Phase angle of S_{13}	-179.73°	149.42°	140.74°	133.08°
Phase angle of S_{23}	-90.34°	-122.40°	-130.78°	-137.91°
Phase difference	89.39°	88.18°	88.48°	89.01°

Table 4: Phase at frequencies of interest of various S-parameters

As we have seen before in the design, the coupler is very broadband and works well for all these frequencies.

5 Patch design

Two types of patch where designed and compared to see which is most suitable, a square patch and a circular patch.

5.1 Design procedure

The radius and feed points of the patch were dimensioned analytically to begin with. For this, several parameters are known, namely the center frequency of the antenna f_c, the relative permittivity of the substrate ε_r and the height of the substrate h.
The substrate between patch and ground plane is of the available material in store at KTH; ROHACELL. The dielectric constant, ε_r, is as previously stated close to that of air, unity, for ROHACELL [10]. The thickness of this material is 9 mm.

The following parameters will be used to design two kinds of patch antennas:

- $f_c = 1597\ MHz$
- $\varepsilon_r = 1$
- $h = 9\ mm$

5.2 Square patch antenna

5.2.1 Width and length of the antenna

The width of a square patch antenna can be found using cavity model. It states that

$$W = L = \frac{\lambda_0}{2\sqrt{\varepsilon_r}} \tag{1}$$

where W and L are the width and length of the patch respectively, λ is the center wavelength and ε_r is the dielectric constant of the substrate. This gives

$$W = L = \frac{0.1875}{2 \cdot 1} = 0.09375 \text{ m} \tag{2}$$

5.2.2 Feed position of the antenna

To achieve circular polarization the antenna must have two feeds equally spaced away from the center and the angle between them seen from the center of the patch needs to be 90°, see figure 15. The distance they should be spaced away from the center is found by looking at the conductance and see when it fits to 50 Ω. This can be found using equation (14-12) from Balanis [11] namely

$$G_1 = \frac{I_1}{120\pi^2} \tag{3}$$

where

$$I_1 = -2 + \cos(X) + XS_i(X) + \frac{\sin(X)}{X} \tag{4}$$

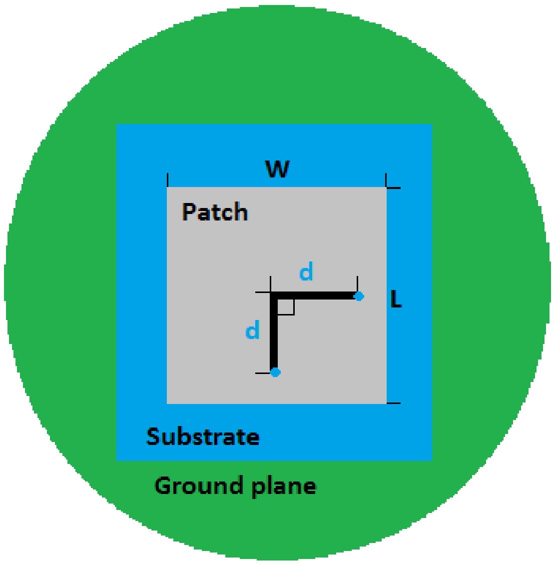

Figure 15: Square patch antenna and it's dimensions

where X=k_0W and k_0 is the wave number for the center frequency. In order to find the impedance the mutual conductance is also needed. The mutual conductance is given with the formula

$$G_{12} = \frac{1}{120\pi^2} \int_0^\pi \left[\frac{\sin(\frac{k_0W}{2}\cos(\theta))}{\cos\theta} \right]^2 J_0(k_0L\sin(\theta))\sin^3\theta d\theta \tag{5}$$

Putting this into the following MATLAB script and using equation (14-17) in Balanis [11] with the (+) sign because of the odd field distribution between the radiating slots for the dominant TM_{010} mode.

```
% Pre-req. for lab 3 in applied antenna theory
clear all
close all
f0=1.6*10^9;
lambda0=3*10^8/f0;
k0=2*pi/lambda0;
W=0.09375;
L=0.09375;
X=k0*W;
G1=(-2+cos(X)+X*sinint(X)+sin(X)/X)/(120*pi^2)
syms theta
Gfun12=@(theta) (sin(k0.*W.*cos(theta))./cos(theta)).^2.*besselj(0,k0.*L.*sin(...
    theta)).*(sin(theta)).^3/(120*pi^2);
G12=quad(Gfun12,0,pi)

Rin=1/(2*(G1+G12))
```

This results in $R_{in} = 700.51\Omega$. In order to get a match with 50Ω we have formula (14-20a) in Balanis [11]

$$R_{in}(y = y_0) = R_{in}(y = 0)\cos^2\left(\frac{\pi y_0}{L}\right) \tag{6}$$

This gives $\frac{\pi y_0}{L} = \arccos(\sqrt{50/700.51})$, i.e.

$$y_0 = \frac{0.09375}{\pi}\arccos(\sqrt{50/700.51}) = 0.0388 \text{ m} \tag{7}$$

this means that the distance from the center of the patch should be

$$d = W/2 - y_0 = 0.0081 \text{ m}. \tag{8}$$

5.2.3 Square patch simulations

After the preliminary analytical calculations a model of the antenna was built and simulated in CST (Computer Simulation Technology). The first simulation was run with the parameters from the analytical calculations. The second simulation was a parameter sweep for many different values of the feed position and the width and length of the square patch.

5.2.3.1 Initial simulation As said before the antenna consists of a ground plane, substrate and a patch. The purpose of the initial simulation was to approve or reject what was found with analytical calculations. In table 5 are the parameters that were used during the simulation. In order to simplify things we used only one feed for this calculations as well as disturbing objects in the FFU were neglected.

Radius of ground plane	62 mm
Height of ground plane	6 mm
Material of ground plane	PEC
Length and width of square substrate	93.5 mm
Height of square substrate	9 mm
Material of substrate	New material with default settings, i.e. $\varepsilon_r = 1$
Length and width of square patch	93.5 mm
Height of square patch	1 mm
Material of patch	PEC
Number of feeds	1
Diameter of feed	0.75 mm
Height of feed	15 mm
Material of feed	PEC
Diameter of vacuum around feed	1.5 mm
Height of vacuum feed	6 mm
Position of feeds center	8.1 mm from center
Frequency	1-2 GHz

Table 5: Parameters used in the simulation

The solver used was Frequency Domain Solver with default settings and a far field monitor. In figure 16 it can be seen that the center frequency of this antenna is below 1.4 GHz. This is not an acceptable antenna in any way, it is far to big for the FFU as well as being far from our center frequency. In next section we go through several parameter sweeps that where made in order to improve the square patch solution.

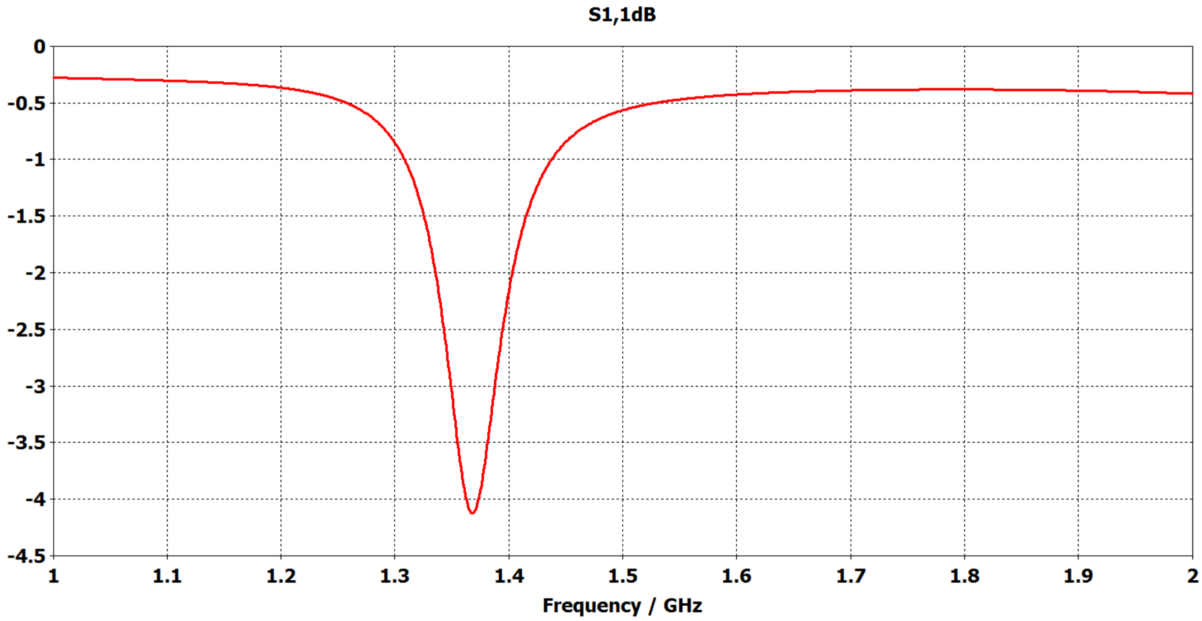

Figure 16: S_{11} parameter we got from simulations

5.2.3.2 Parameter sweep The first parameter sweep done after realising that the analytical design didn't work out was to keep all the parameters in 5 constant except the width of the patch and the position of the feeds center. In table 6 the changes of parameter for each run can be seen. The parameter sweep was run with frequency domain solver with default settings.

Run nr.	Width and length of the patch [mm]	position of the feeds center [mm]
Run 1	93.75	7
Run 2	93.75	8
Run 3	93.75	9
Run 4	93.75	10
Run 5	75	8.1
Run 6	80	8.1
Run 7	85	8.1
Run 8	90	8.1
Run 9	95	8.1

Table 6: Parameter sweep nr. 1 of the width and the feedposition

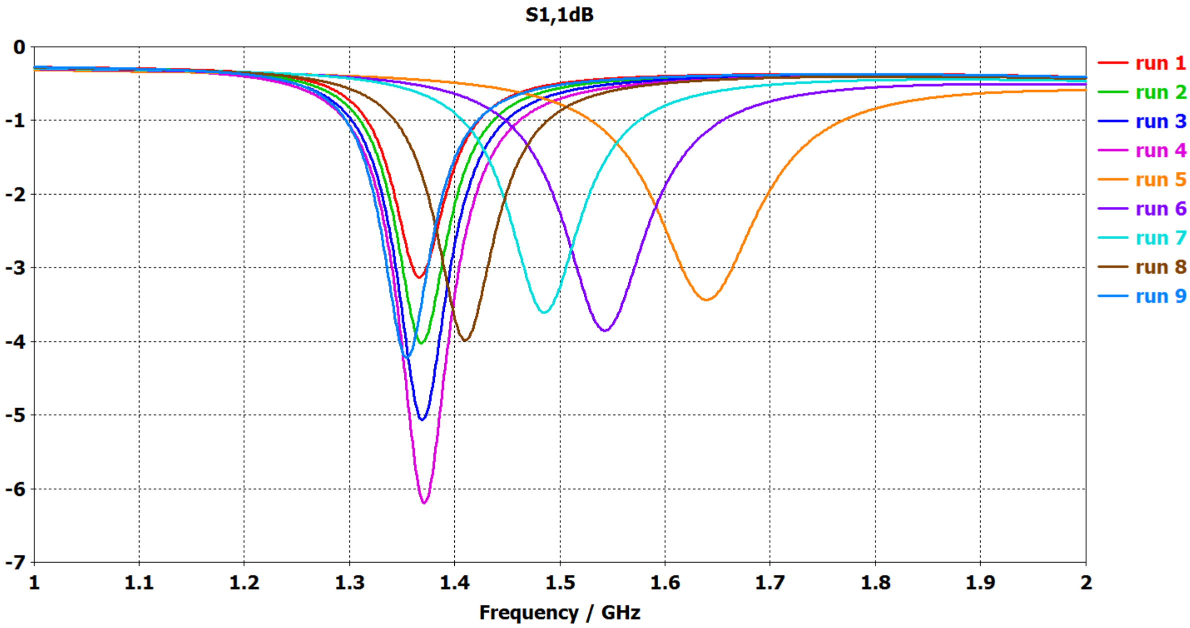

Figure 17: S_{11} parameter we got from parameter sweep nr. 1

From figure 17 it can seen that moving the feed position further out increases the signal that is sent out and moves the center frequency a little bit to the desired center frequency. Furthermore it can be seen that the smaller the patch is the bigger the center frequency is, which is quite obvious considering that the center frequency depends inversely on the size of the patch. Next we simulated various feeds for a patch with the width 80 mm and then with various widths and constant feed position of 20 mm from center. Details of this can be seen in table 7. The same procedure was used as before.

Run nr.	Width and length of the patch [mm]	position of the feeds center [mm]
Run 1	80	20
Run 2	80	21.6667
Run 3	80	23.3333
Run 4	80	25
Run 5	70	20
Run 6	71.25	20
Run 7	72.5	20
Run 8	73.75	20
Run 9	75	20

Table 7: Parameter sweep nr. 2 of the width and the feedposition

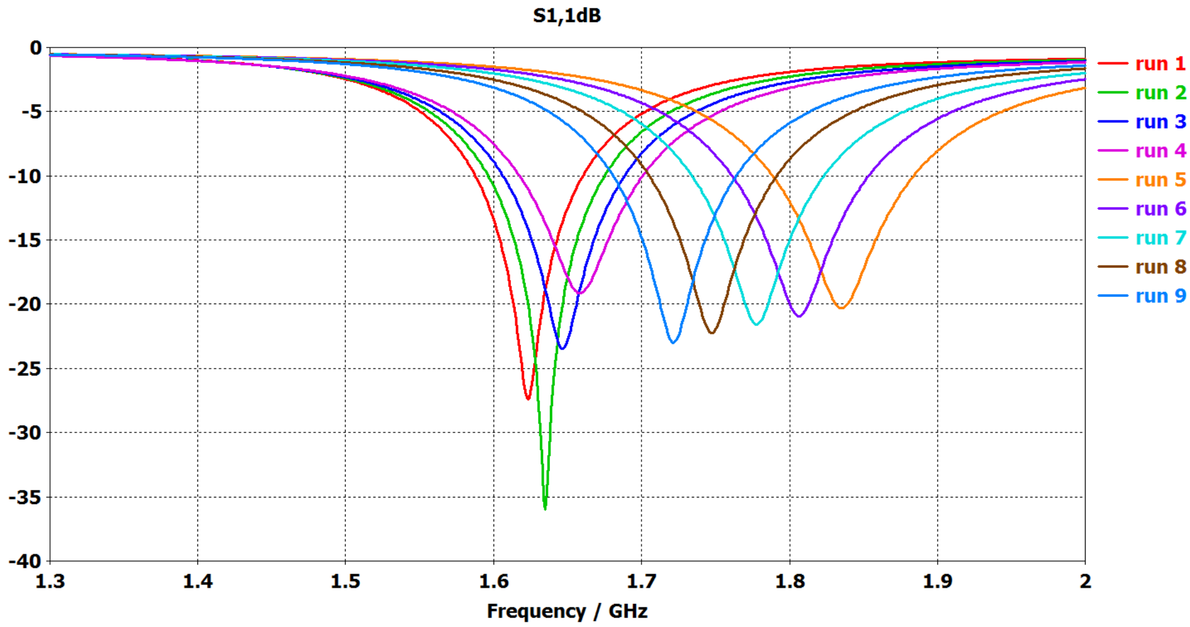

Figure 18: S_{11} parameter we got from parameter sweep number 2

From figure 18 it can be seen that all the results were above the desired frequency so we decided, especially the ones with widht of 70-75 mm. The best return loss is in run 2, where we had a feed of 21.6677 mm from the center. So in the next sweep the feed position was held constant at 21.5 mm from the center while the width was changed as can be seen in table 8.

Run nr.	Width and length of the patch [mm]
Run 1	80
Run 2	82.5
Run 3	85
Run 4	87.5
Run 5	90

Table 8: Parameter sweep nr.3 of the width and the feed position

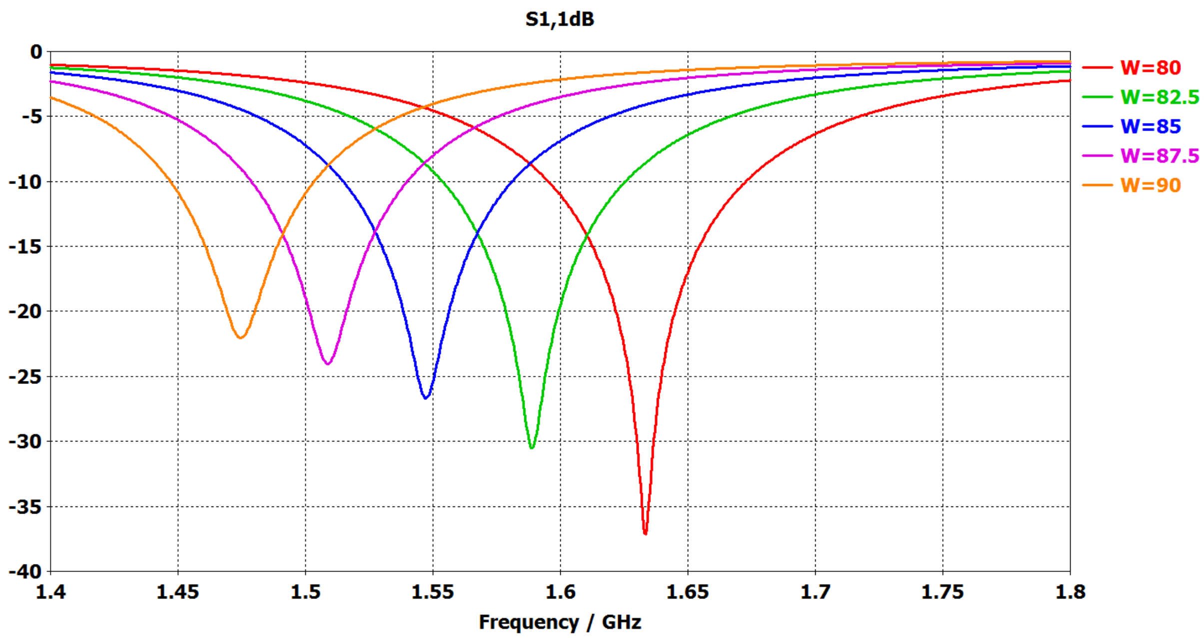

Figure 19: S_{11} parameter we got from parameter sweep number 3

From figure 19 we can see that the best width is between 80 mm to 82.5 mm. So another sweep for width and length of the patch between 80 and 82.5 mm was done. The width of each run can be seen on figure 20

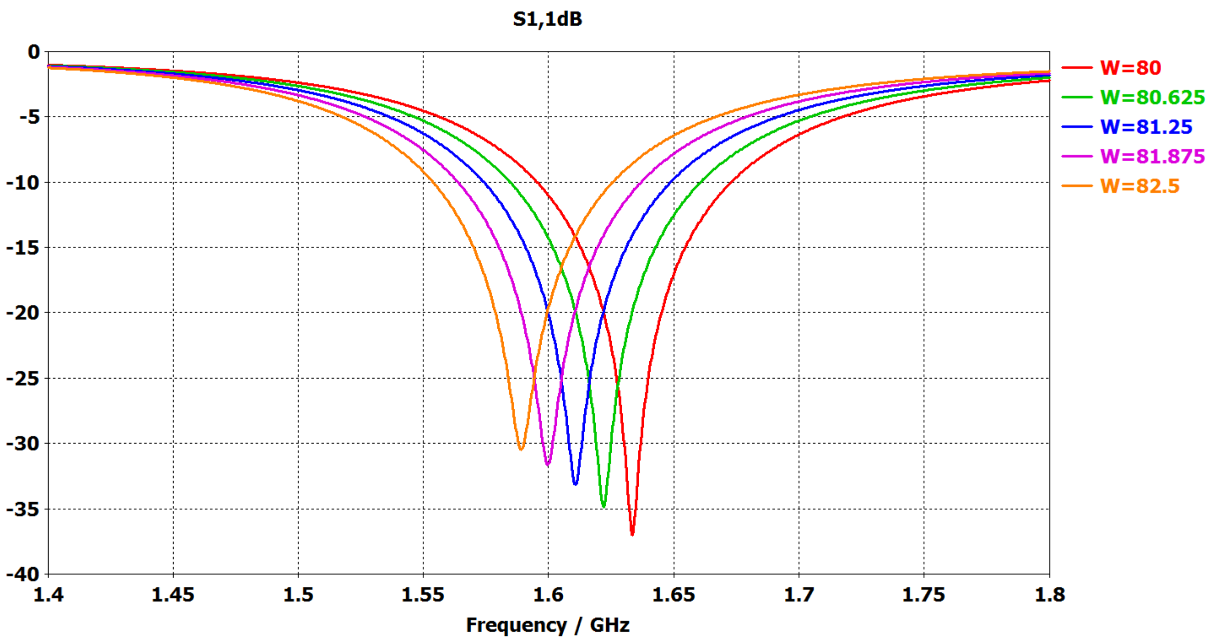

Figure 20: S_{11} parameter we got from parameter sweep number 4

This showed that 82 mm width would be the best one, so a final parameter sweep was done where the width and length was kept constant at 82 mm and the feed position was varied. The results and values of the feed position can be seen in figure 21. From this the best square patch would be 82 mm wide and long with feed position at 21.33 mm from the center.

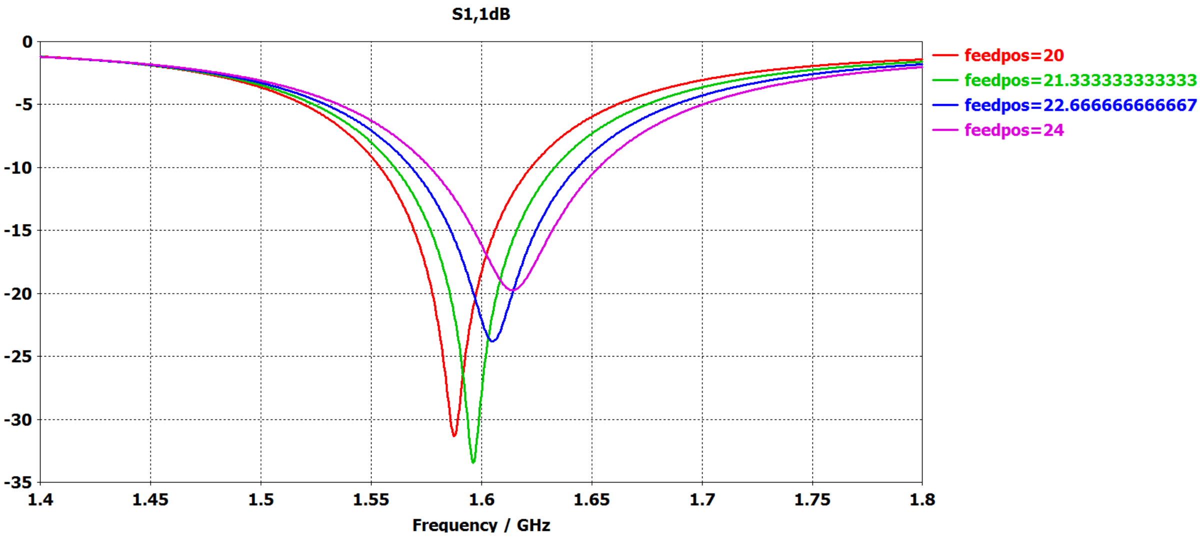

Figure 21: S_{11} parameter we got from parameter sweep number 5

5.3 Circular patch

Here, the design, simulations and testing of the circular patch antenna are illustrated.

5.3.1 Calculating the radius of the patch

To get a approximation of the size of the circular patch antenna we can treat the space between the circular patch and the ground plane as a circular cavity. The modes that the cavity is able to support are primarly TM^Z, where Z is perpendicular to the patch, when the substrate height is small ($h \ll \lambda$). In [11], equation 14-69, the radius a of the patch is given by

$$a = \frac{F}{\{1 + \frac{2h}{\pi \varepsilon_r F}[ln(\frac{\pi F}{2h}) + 1.7726]\}^{1/2}} \tag{9}$$

Where h is the height of the substrate in cm, ε_r is the relative permittivity of the substrate and F is

$$F = \frac{8.791 \cdot 10^9}{f_r \sqrt{\varepsilon_r}} \tag{10}$$

where f_r is the wanted center frequency in Hz. Plugging in our values for f_c, ε_r and h gives:

$$a = \frac{\frac{8.791 \cdot 10^9}{1597 \cdot 10^6 \sqrt{1}}}{\{1 + \frac{2 \cdot 0.9 \cdot 10^{-3}}{\pi \cdot 1 \frac{8.791 \cdot 10^9}{1597 \cdot 10^6 \sqrt{1}}}[ln(\frac{\pi \frac{8.791 \cdot 10^9}{1597 \cdot 10^6 \sqrt{\varepsilon_r}}}{2 \cdot 0.9 \cdot 10^{-3}}) + 1.7726]\}^{1/2}} = 4.62 \text{ cm} \tag{11}$$

this is the actual radius of the patch but because of the fringe fields, the antennas will have an effective radius given by 14-67 in [11],

$$a_e = a\{1 + \frac{2h}{\pi a \varepsilon_r}[\ln(\frac{\pi a}{2h}) + 1.7726]\}^{1/2} \tag{12}$$

which gives $a_e = 5.62$[cm] for this case. This is required for calculating the feed position in the next section.

5.3.2 Calculating the position of feed points

The input resistance, R_{in}, of the circular patch is purely real at resonance and according to [11], equation 14-81 can be expressed as

$$R_{in}(\rho' = \rho_0) = \frac{1}{G_t}\frac{J_1^2(k\rho_0)}{J_1^2(ka_e)} \tag{13}$$

where ρ_0 is the position of the feed, J_1 is the first zero of the Bessel function, k is the wave number and G_t is the total conductance given by

$$G_t = G_{rad} + G_c + G_d \tag{14}$$

$$G_{rad} = \frac{(k_0 a_e)^2}{480}\int_0^{\pi/2}[\acute{J}_{02}^2 + \cos^2(\theta)J_{02}^2]\sin(\theta)d\theta \tag{15}$$

$$G_c = \frac{\varepsilon_{m0}\pi(\pi\mu_0 f_r)^{-3/2}}{4h^2\sqrt{\sigma}}[(ka_e)^2 - m^2] \tag{16}$$

$$G_d = \frac{\varepsilon_{m0}\tan(\delta)}{4h\mu_0 f_r}[(ka_e)^2 - m^2] \tag{17}$$

where k_0 is the wave number, $\varepsilon_{m0} = 1$ because of assumed dominant TM110 mode, σ is the conductivity in copper, $\tan(\delta)$ is the loss tagent in the substrate, $m = 1$ because of TM110 mode and

$$\acute{J}_{02} = J_0(k_0 a_e \sin(\theta)) - J_2(k_0 a_e \sin(\theta)) \tag{18}$$

$$J_{02} = J_0(k_0 a_e \sin(\theta)) + J_2(k_0 a_e \sin(\theta)) \tag{19}$$

after putting in the parameters we and calculate G_c and G_d, G_{rad} was read from figure 14.25 in [11], we get an input resistance of 49.1Ω when the feed is placed 16 mm from the center.

To get an approximation of the bandwidth we can look in [11] figure 14.27 and see that for $\varepsilon_r = 2.2$ with $\frac{h}{\lambda} = 0.5$ we have a bandwitdth of roughly 7% and as we use $\varepsilon_r = 1$ we should get better results than that which would fullfill our criteria.

5.3.3 Circular patch simulations

After the preliminary analytical calculations had been performed a model of the antenna was built in CST. The first iteration of the model uses the calculated values. The model was then modified to include the surrounding conducting objects, the model of the patch was made more realistic and the feed was changed from the symbolic Coax feed to the real feed using strip lines. Finally a parameter sweep was done in order to optimize the design.

5.3.4 Initial simulation

The preliminary analytical calculations yielded that the radius of the patch should be 46.2 mm and the feed position should be 16 mm from the center. Furthermore the substrate thickness should be 9 mm and with a dielectric constant equal to one, $\varepsilon_r = 1$. A basic model was put together according to those specifications, except the patch radius was 46.1 mm. The patch was made of PEC, Perfect Electric Conductor, with a thickness of 0.07 mm and the ground was also made of PEC and made 5.3 mm thick, mainly to be able to get three mesh cells feed for the solver. Only one feed was used and it was a coax feed with dimensions so that the feed had impedance of 50 Ω, which gave the inner conductor a radius of 1.2 mm.

The boundaries were kept open with added space for the solver to be able to calculate the full near field and the transient solver was used. Adaptive meshing was not turned on so the result may be a bit from the "true" value but as this model is fairly simple we trust that the results are close to what they should be. From the amplitude of the S_{11} parameter, presented in Figure 22 we can see that the center frequency is 1.627 GHz and the fractional bandwidth, defined by -10dB> in reflection to incident wave ratio, is 4.8%.

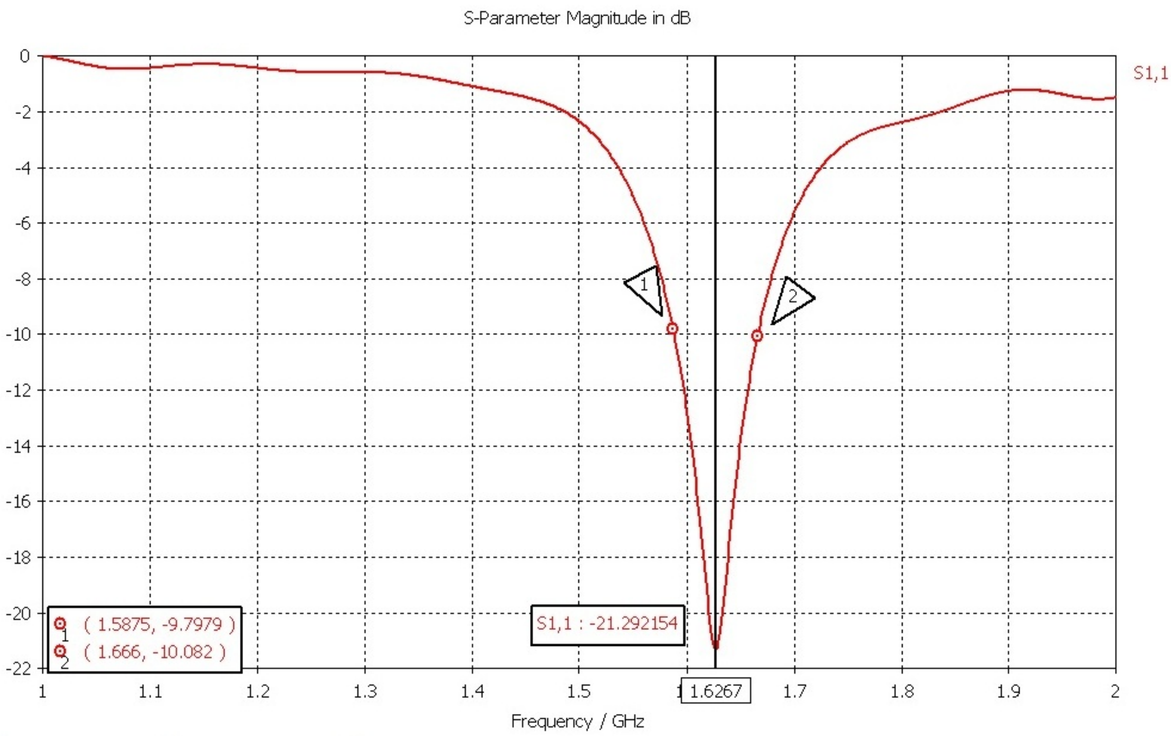

Figure 22: The simulated S-parameter of the circular patch antenna gotten from the analytical calculations

5.3.5 The model made more realistic

After the initial simulations the model was refined step by step. As the mechanical team of MUSCAT planned to place a few screws and other conducting objects close to the antenna the first things that were added were screws placed near the antenna. This of course affected the resonance because of the changed impedance, see next paragraph. At the time we started the simulations we had not done a literature study so the next thing that was done was checking if a smaller antenna with a substrate with a higher dielectric constant, ε_r but this was quickly rejected after doing the literature study. The next thing that was added to to the model was a hemisphere. Then we changed the feed from coaxial feed to strip line feed. Later a second port was added and finally a few parameter sweeps were run in order to get the best value for our antenna.

5.3.5.1 Strip line feed The actual antenna does not have a coax feed as has been used so far during the simulations. It will be fed by a pin going from the patch through the ground plane as in a coax feed but instead of the pin being the coax inner conductor it goes to a strip line inside the PCB. The pin decided upon is 0.4 mm in radius. The PCB has several layers of copper with thickness of 0.035 mm per layer and with a spacing of 0.35 mm with FR-4 between the layers. There is a ground plane on top of the PCB and it is modeled as a full copper piece with the exception close to the strip line feeds. The strip line feeds are located on the second layer and are bricks, 0.035 mm thick, 0.27 mm wide and are in the final version 16 mm long. The strip line feeds are made so they have plenty of space to fulfill the 3 mesh cells requirement by the solver. Around the the strip line feeds, FR-4 is placed with a thickness of 0.735, as it is in the PCB. The final waveguide port in the simulation model is 10 mm in width and 0.735 mm in height.

At first the model was not done exactly as described above but with FR-4 covering the whole space between layer one and three in the PCB and the waveguide port was not so wide. This was changed because problems arose, the port mode changed to Quasi-TEM and the S-parameter did not look good at all anymore, results presented in Figure 23 and 24. After that the ports were remade to be bigger and the FR-4 was limited to the surrounding of the port. In figure 39 one can see how the port should look like for a stripline.

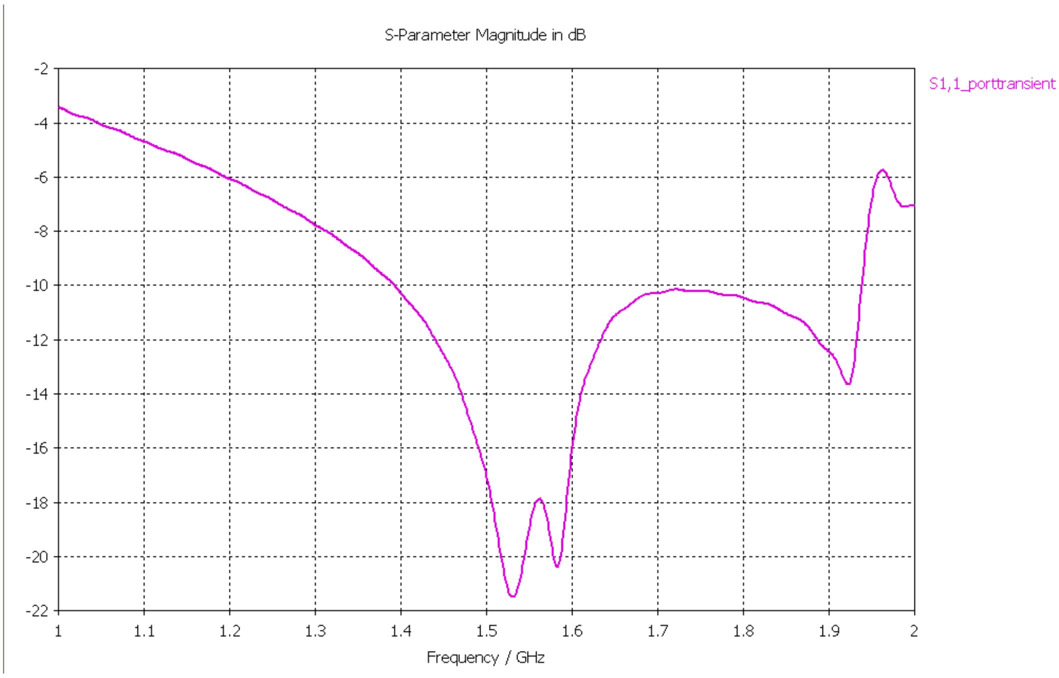

Figure 23: This is the s-parameter plot from when the model started to behave incorrectly when the feed was changed from coax to stripline

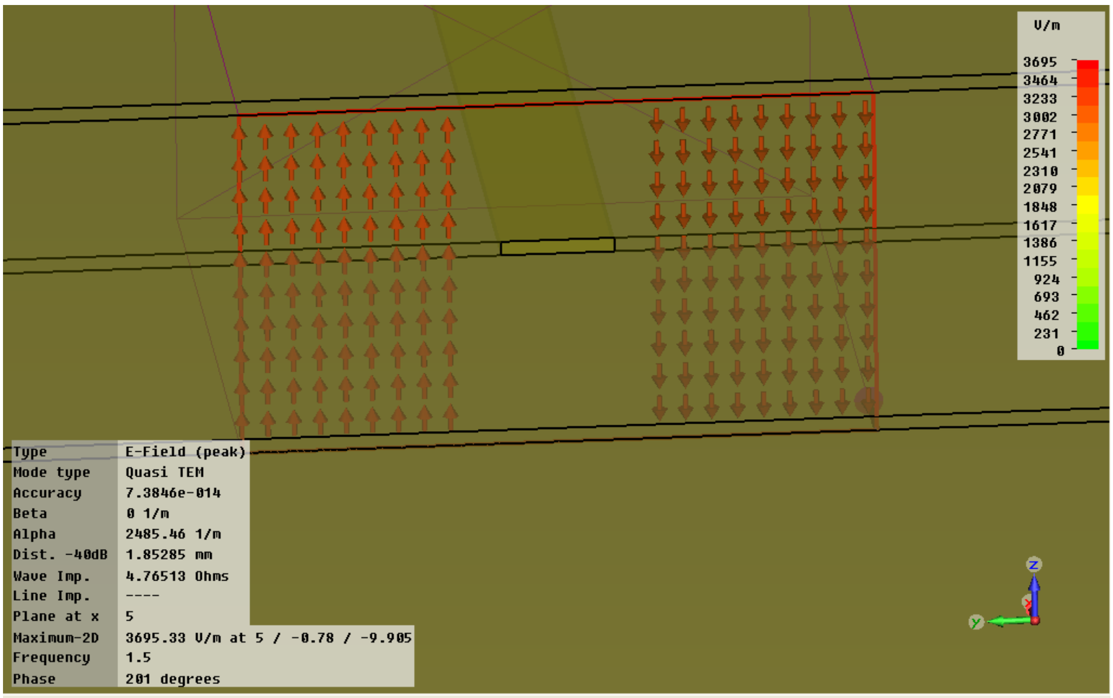

Figure 24: This is the port plot from when the model started to behave incorrectly when the feed was changed from coax to stripline

5.3.5.2 Second port added When the first port was working again the second feed was added, exactly as the first feed but with a 90 degrees angle between them seen from the center. Around the feed pins solder pads were added on all the modeled layers (first, second and bottom layer) which have 2 mm more in radius than the holes them self. We also had some problems with the initial meshing here so local mesh criteria had to be put in so the initial mesh looked like the model. The results of adding a second feed can be seen in figure 25, where the green line is the s_{11} parameter when we have two feeds but the red line is the s_{11} parameter when we have one feed. It can be seen that the return is less when we have two feeds. This is because the voltage changes over the patch when we add the second feed, so that the voltage becomes higher on the patch and at the same time the impedance becomes higher, which gives better match, since the s parameter is lower.

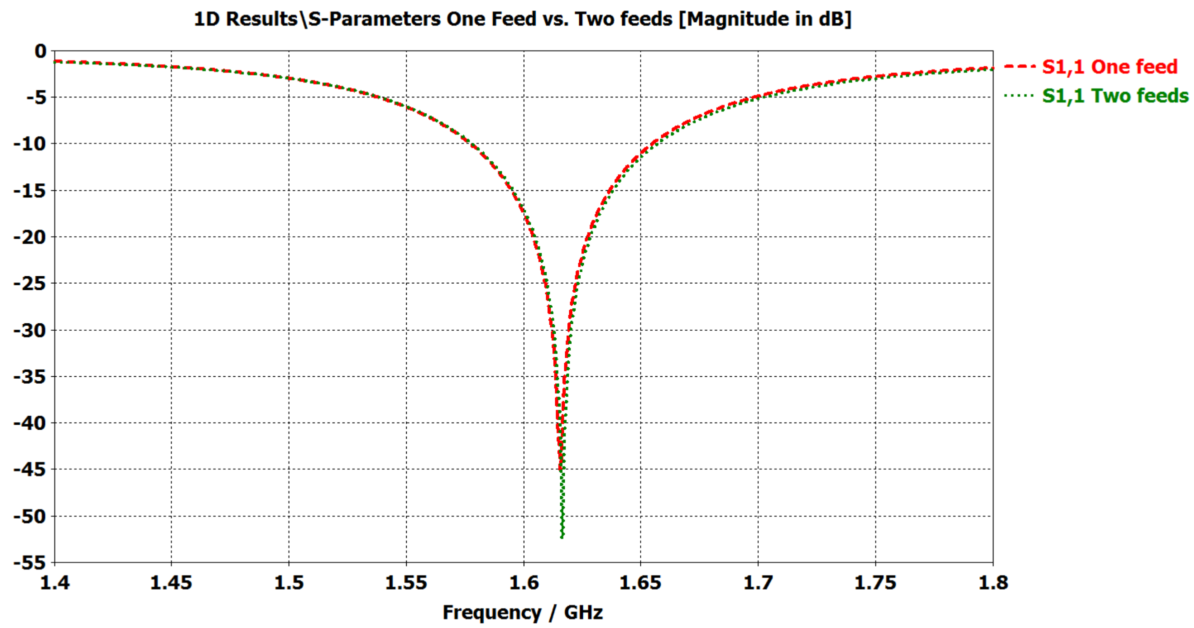

Figure 25: S_{11} port parameters of the feeds with one, and two feeds

5.3.5.3 Simulation with eye bolts and cones After getting the specifications for the screws and the other objects that will be close to the antenna they where placed in the model without the hemisphere on top. There are a total of 9 objects that could interfere with our model, four eye bolts, four cones that serve as a constraint on the upper hemisphere and a umbilical connector block. The four eye bolts were modeled as four cylinders, the four cones were modeled as cylinders as well and the umbilical connector was modeled as a rectangular block. Furthermore the real patch used was put into the model along with changing the ground to copper. The real patch is made out of a very thin substrate of FR-4 with metal layer on top. The metal layer is 0.035 mm thick and was modeled as a copper and the FR-4 layer is 0.35 mm thick. In figure 26 it can be seen that when we place these objects around the patch antenna, the center frequency of all the s-parameters move to a slightly lower value, this might be explained by the fact that we are making our antenna larger, because we add more conducting objects around it. This results in bigger resonance wavelength which again makes the center frequency smaller. In figure 27 we can see that the total efficiency without the disturbing objects for port 1 and 2 are the same and that with the disturbing objects they are not the same, this can easily be explained because with the umbilical connector there, the antenna is no longer symmetrical around all the axis, so the feeds are not symmetrically placed with respect to the umbilical connector. In figures 28 and 29 we can see that the radiation pattern has become less broad as well as we get kind of a disturbance where the umbilical connector is positioned. This can be explained because patch induces current in the disturbing objects, which results in smaller "sight angle".

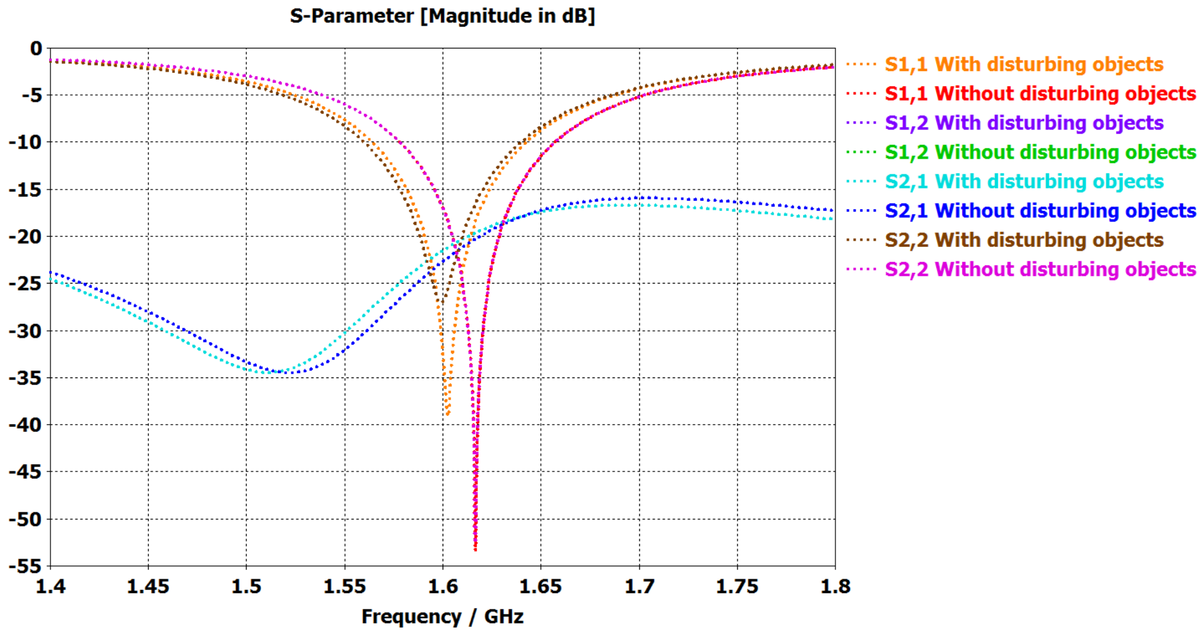

Figure 26: The simulated S-parameters of the circular patch antenna with and without the disturbing objects

Figure 27: The simulated efficiency of the circular patch antenna with and without the disturbing objects

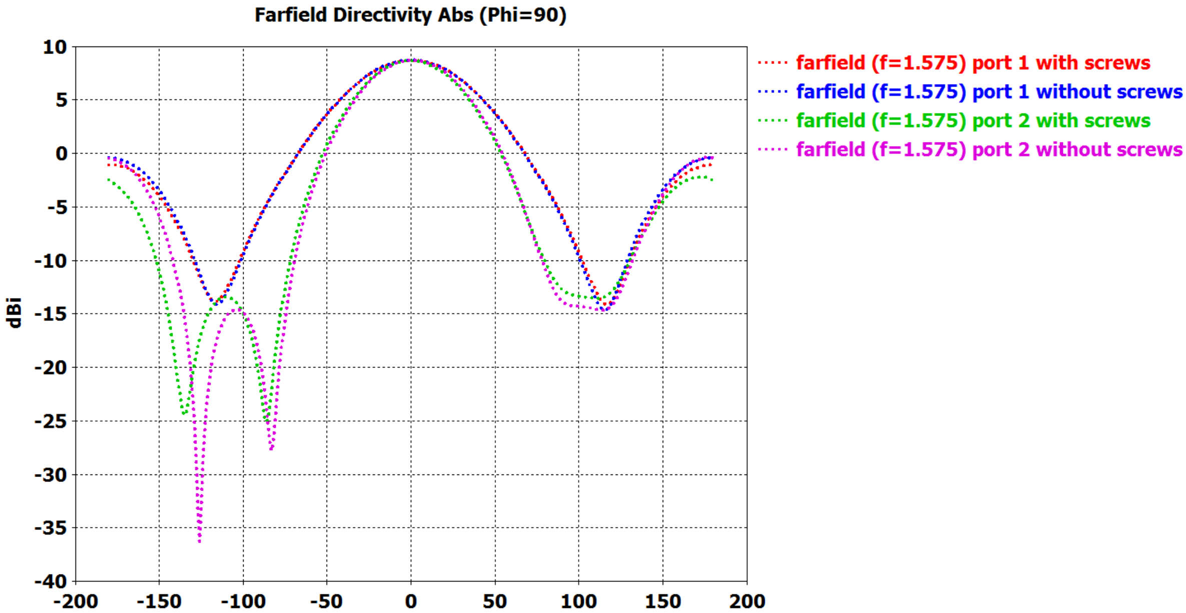

Figure 28: The far field of the antenna with and without the disturbing objects at 1.575 GHz

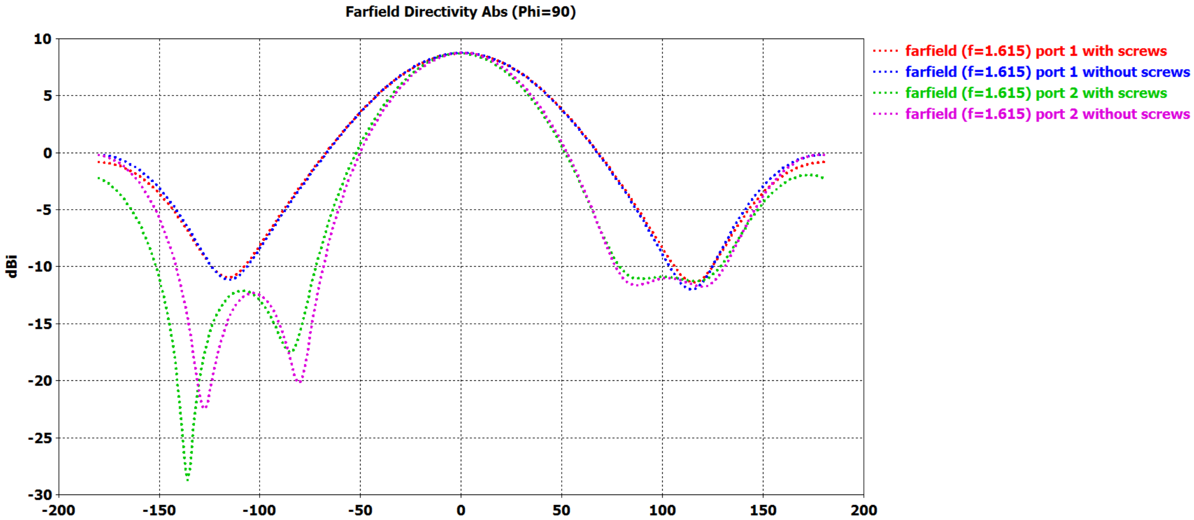

Figure 29: The far field of the antenna with and without the disturbing objects at 1.615 GHz

5.3.5.4 Simulation with a top hemisphere As the antenna will be under a hemisphere, as can be seen from figure 1, for most of the time the MUSCAT experiment is conducted, the antenna was simulated with that on top. The MUSCATs mechanical team tried to find a material for the hemispheres that had low dielectric constant and ended their search with epoxy with a worst case dielectric constant of $\varepsilon_r = 5.6$ and E and S-2 glass fiber with dielectric constants $\varepsilon_r = 5.34$ and $\varepsilon_r = 6.6$ respectively. Preliminary simulations were done to see what happened to the resonance. In the top hemisphere above the antenna there are also a parachute along with parachute cords and a beacon antenna. The beacon antenna was was deemed to difficult to model, since it had not been designed yet and the parachute along with the cords was considered to have less effect on the simulations than the half sphere.

Before the results of which material to use for the hemispheres were known we modeled the top hemisphere as 1 mm thick with an outer radius of 60 mm with $\varepsilon_r = 4.5$ and $\tan(\delta) = 0.001$. The substrate parameters were $\varepsilon_r = 1.05$ and $\tan\delta = 0.0002$. This was one of the earlier models with coax feed and without disturbing objects. For the simulation a transient solver with adaptive meshing was used. The results from modeling the antenna with top hemisphere was quite good, see Figure 30, where the resonance frequency did not change much but the return loss changed more.

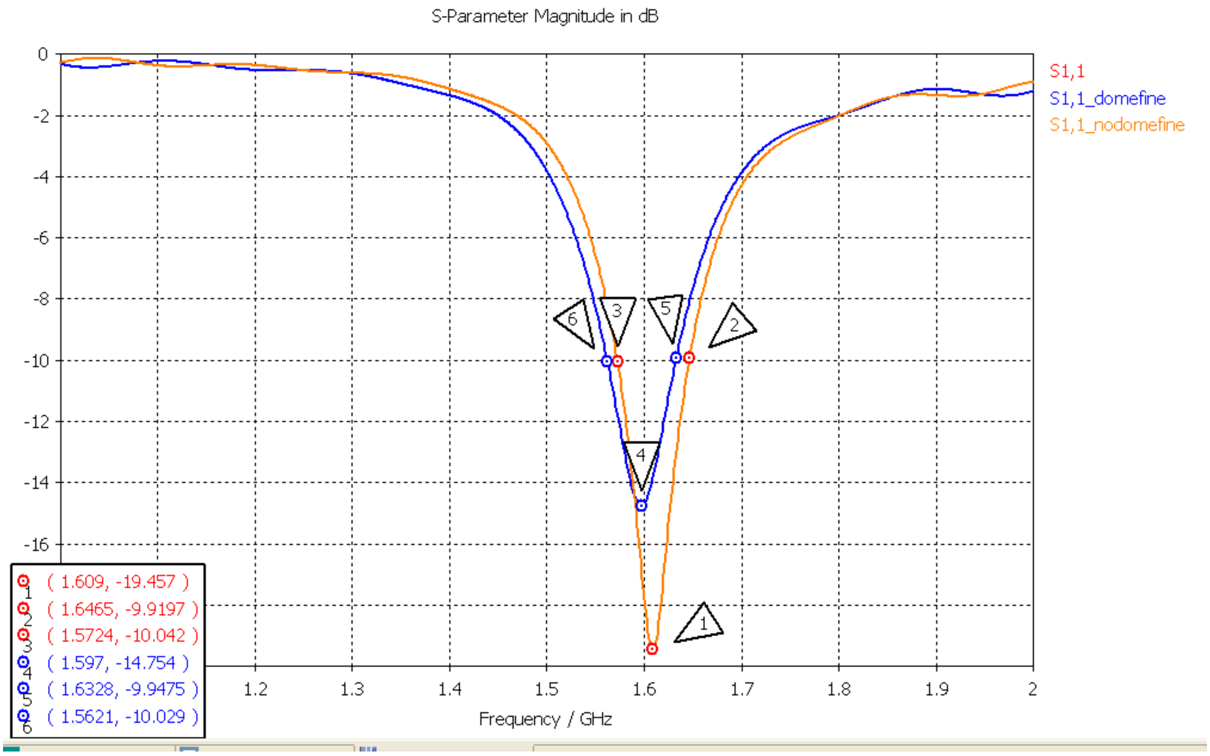

Figure 30: The simulated s-parameter of the initial sphere model without disturbing objects.

When the model was finished and the materials found for the sphere another simulation could be done. The used glass-fiber was of type E with $\varepsilon_r = 6.3 - 6.6$ at 1 MHz and with a dissipation factor, $\tan(\delta)$, of 0.0025 at 1 MHz [12]. The glass-fiber is mixed with epoxy to create the sphere, and the epoxy used here is made to withstand high temperatures, with an $\varepsilon_r = 3.3 - 5.4$ and dissipation factor of 0.01 [13]. The half-sphere was modeled as 1 mm thick, $\varepsilon_r = 6.3$, $\tan\delta = 0.007$. In the model everything else was as for the final model. The frequency solver was used and the results for the s-parameter is shown in Figure 31 and for the directivity in Figure 32. As seen on the picture the resonance and impedance changes and because of the sphere with the high permittivity it seems larger. This is good as when the sphere is on only the GPS is used and as can be seen the reflection coefficient gets better for the GPS with the sphere on. The directivity is not changed very much.

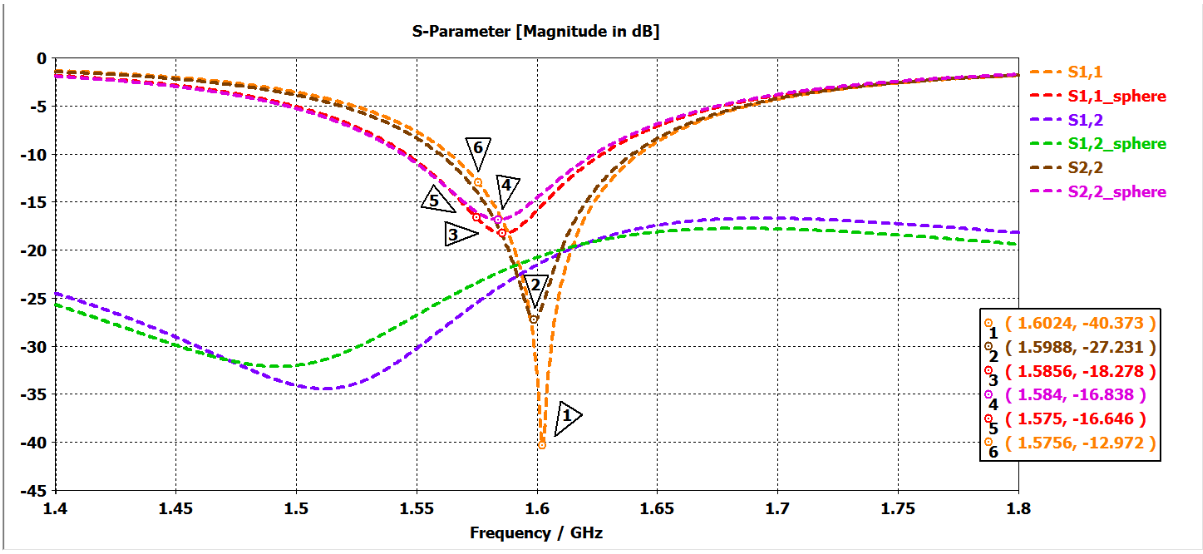

Figure 31: The simulated s-parameter of the final model with the sphere and without the sphere.

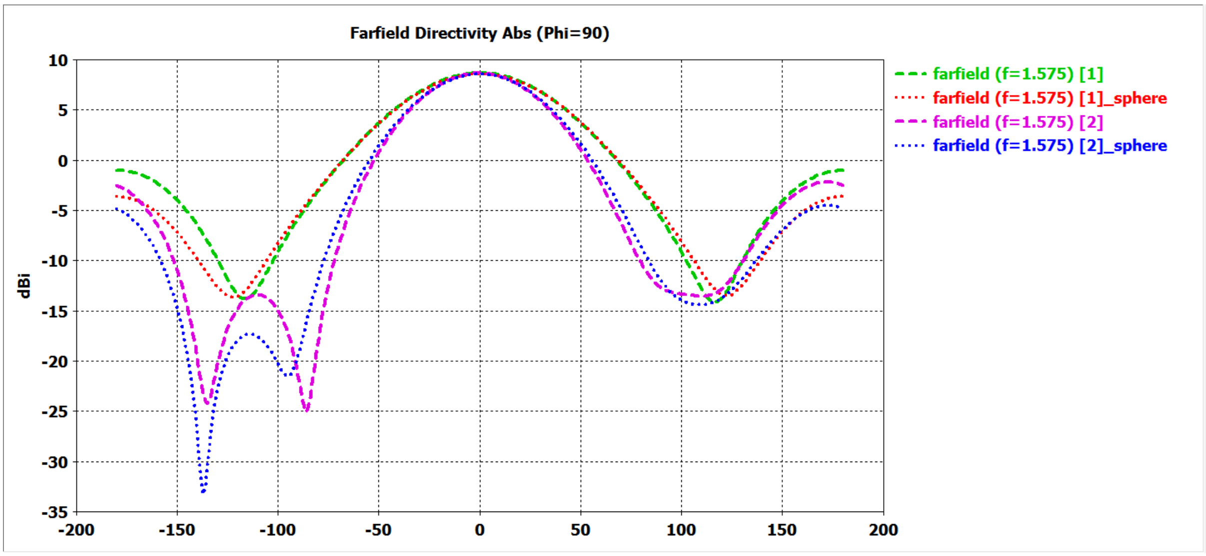

Figure 32: The simulated Directivity of the final model with the sphere and without the sphere.

5.3.5.5 Parameter sweeps After the second feed was put in we did some parameter sweeps to find the optimal feed position, antenna radius along with how big the distance from the feeds solder pads to the ground plane should be. The best results at the time for ordering test antennas was to have the feeds placed 22 mm from the center, the antenna radius should be 47 mm and the distance from the center of the feed to the ground plane should be 0.93 mm. In table 9 you can see the values we put in for the broad parameter sweep. We used frequency domain solver for the parameter sweep and changed all the metal materials to PEC and the FR-4 to lossless FR-4. In figures 33 and 34 we can see that the best results the position of the frequency is run 11, but the best results for the s parameters is run 1. As we had learned from the square patch the s parameter goes further to the left on the graph when we make the patch bigger and it goes further to the right and down when we make the feed be further away from the center.

Run nr.	Radius of antenna [mm]	position of the center of the feeds [mm]
Run 1	47	22
Run 2	45	22
Run 3	45.5	22
Run 4	46	22
Run 5	46.5	22
Run 6	47.5	22
Run 7	48	22
Run 8	47	18
Run 9	47	19
Run 10	47	20
Run 11	47	21
Run 12	47	23
Run 13	47	24
Run 14	47	25

Table 9: Parameter sweep nr. 1 of the radius and the feed position for the circular patch

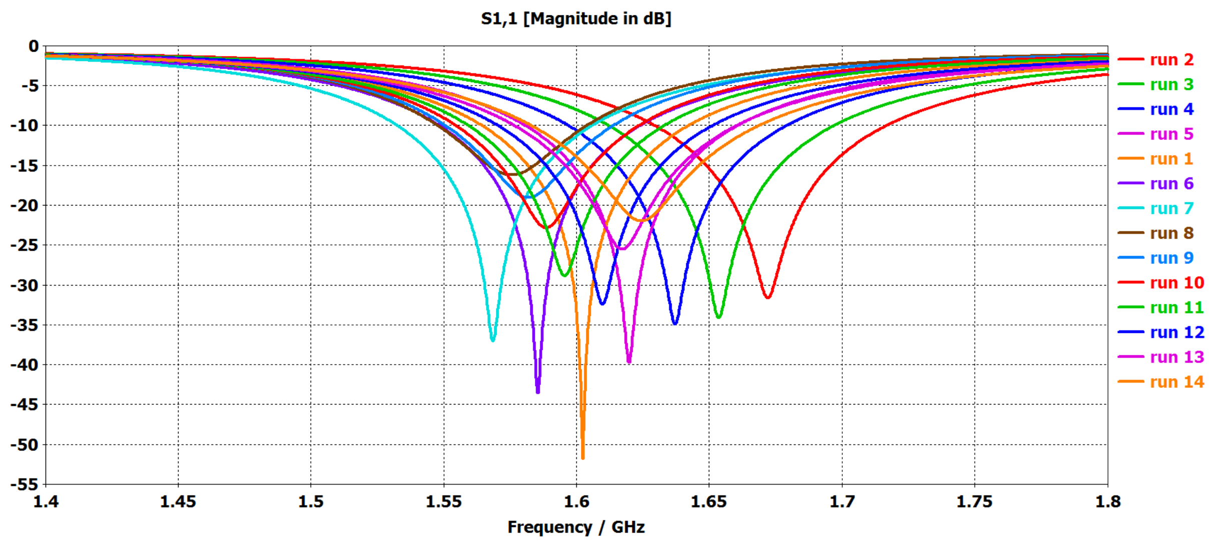

Figure 33: The results of the first parameter sweep for S_{11}.

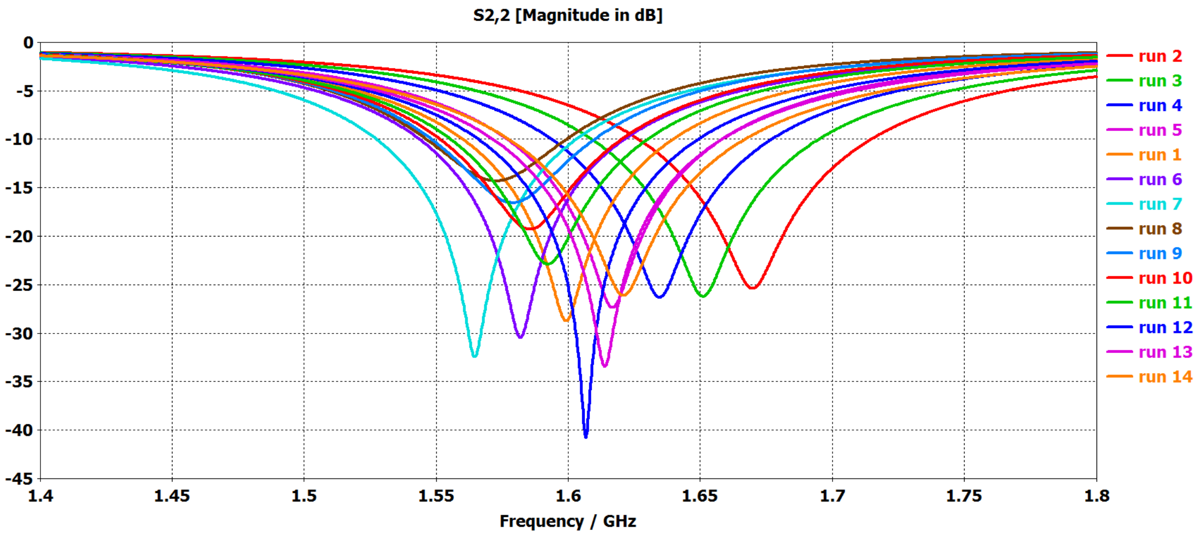

Figure 34: The results of the first parameter sweep for S_{22}.

So we did another simulation that was close to the good values found in the first parameter sweep, see table 10 for variables. The results can be seen in figures 35 and 36. From the figures we can see that the best results we get when the radius of the circular patch antenna is 47 mm and the feed of the antenna is 22 mm from the center.

Run nr.	Radius of antenna [mm]	position of the center of the feeds [mm]
Run 1	46	22
Run 2	46.1091	22
Run 3	46.2182	22
Run 4	46.3273	22
Run 5	46.4364	22
Run 6	46.5455	22
Run 7	46.6545	22
Run 8	46.7636	22
Run 9	46.8727	22
Run 10	46.9818	22
Run 11	47.0909	22
Run 12	47.2	22
Run 13	47	19
Run 14	47	20
Run 15	47	21
Run 16	47	22
Run 17	47	23
Run 18	47	24
Run 19	47	25

Table 10: Parameter sweep nr. 2 of the radius and the feed position for the circular patch

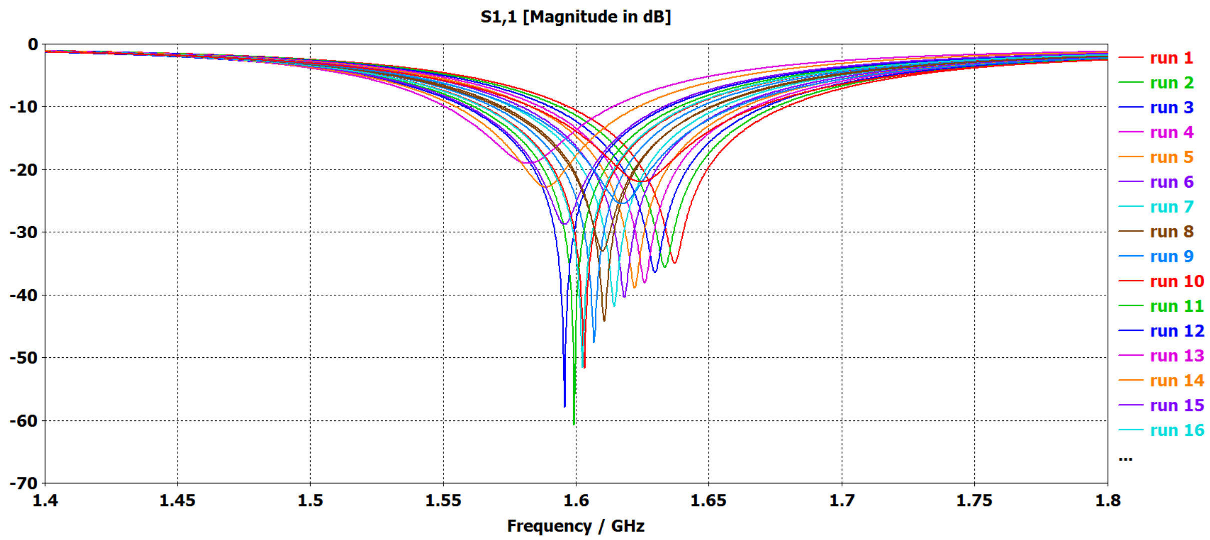

Figure 35: The results of the second parameter sweep for S_{11}.

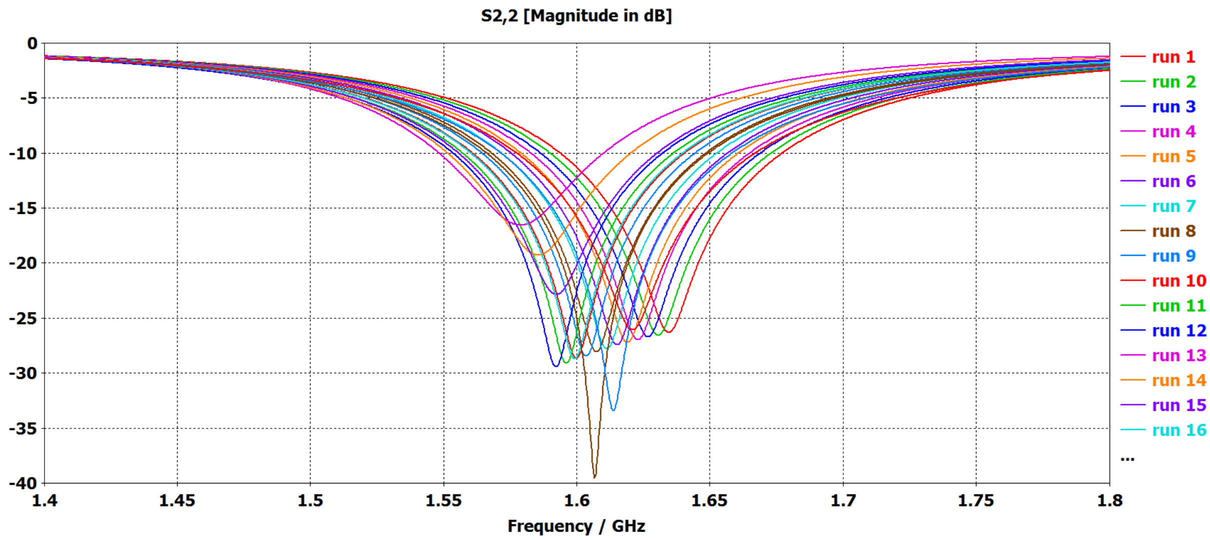

Figure 36: The results of the second parameter sweep for S_{22}.

5.3.6 The final model

After all the parameter sweeps, the best model we could simulate is given in tables 11 and 12. We can see a picture of the final model in Figure 37

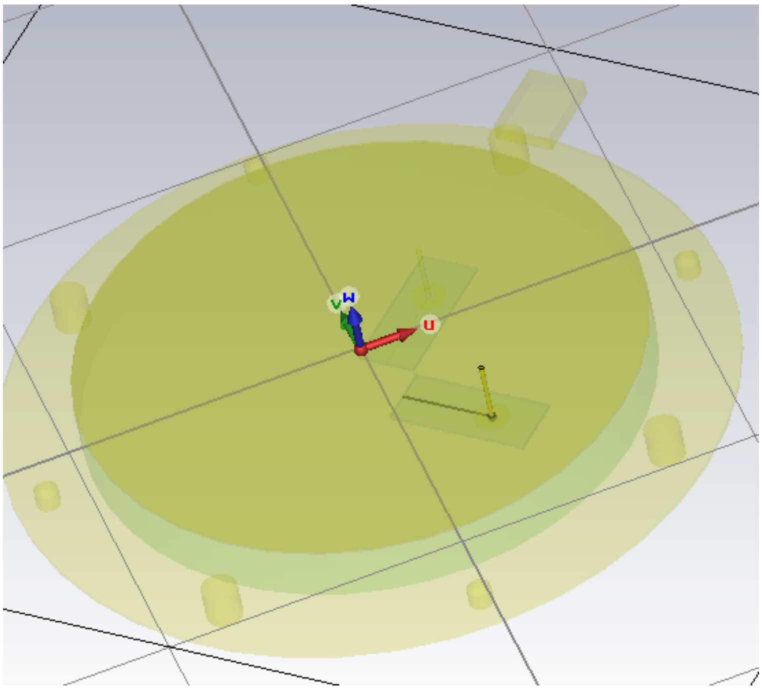

Figure 37: This is how the final model looked like.

Item	**Size**	**Material**	**Else**
Umbilical	Width 10 mm, length 40.5 mm, height 2 mm	Copper	Position Y:from 58to 17.5, X:from 5 to(-)5, Z=from (-)9 to(-)7
Four "eye bolts"	Cylinders, radius 3mm, height 6 mm	Aluminum	Position 0, 90, 180, 270 degrees at a radius 53.5 from the center
Four cylinders with cones placed on top	Radius of cylinder and bottom of cone is 2 mm, top radius of cone is 1 mm, height of cylinder is 3 mm and height of cone is 1 mm high	Aluminum	Position 45, 135, 225,315 degrees at a radius 55 from center
Substrate	Radius 47 mm, height 9 mm	Rohacell 31	
Patch	Radius 47 mm, height of FR4 0.35 mm, height of copper 0.035 mm	FR4 (Lossy)and copper	

Feed connectors	Height 14.45 mm, radius 0.4 mm	Copper	Position Center is 22 mm from center of antenna at 0 degrees and 90 degrees.From the center of the feed it is 0.93 mm to the ground plane and the solder pads have a radius of 0.4-0.6 mm
Ground plane	Thickness 0.77 mm, radius 60.5 mm	Copper	
Strip line boxes	Thickness 0.735 mm, width 10 mm, length 24 mm	FR4	Position placed 0.035 mm down in the ground layer
Strip line	Thickness 0.035 mm, length 16 mm, width 0.28 mm	Copper	

Table 11: Information about all the items in the simulation

Material	**Dielectric constant** ε_r	**Dissipation factor** $\tan(\delta)$	**Relative permeability** μ_r	**Conductivity** σ	**Frequency**	**Reference**
ROHACELL HF 31	1.05	0.0002			2.5 GHz	[10]
FR-4	4.4	0	1			[?]
FR-4 lossy	4.4	0.025	1			[?]
Copper				5.8e+007		[?]
Aluminum				3.56e+007		[?]

Table 12: Material used in CST and their properties

The results of simulating the final model with frequency solver are presented in table 13 and in figures, 38, 39 and 40. In figure 38 you can see the S-parameters of our design, in figure 39 you can see the gain for port 1 at 1.575 GHz, th GPS frequency and in figure 40 you can see the E-field for port 1.

	Port 1	**Port 2**
Total efficiency	at 1.575 GHz 93.9 % and at 1.618 GHz 97.1 %	at 1.575 GHz 95.2% and at 1.618 GHz 96.7%
Line impedance on port	48.95 Ω	48.95 Ω
Directivity	8.7dB	8.7 dB
Half power beam width	80°	65°

Back lobe level	-1 dB	- 2.5 dB
Fractional bandwidth	5 %	5 %
Center frequency	1.602 GHz	1.599 GHz
	Amount	
Amount of mesh cells to achieve the 10^{-5} criteria for the solver	160 000	

Table 13: Results from simulation of final model

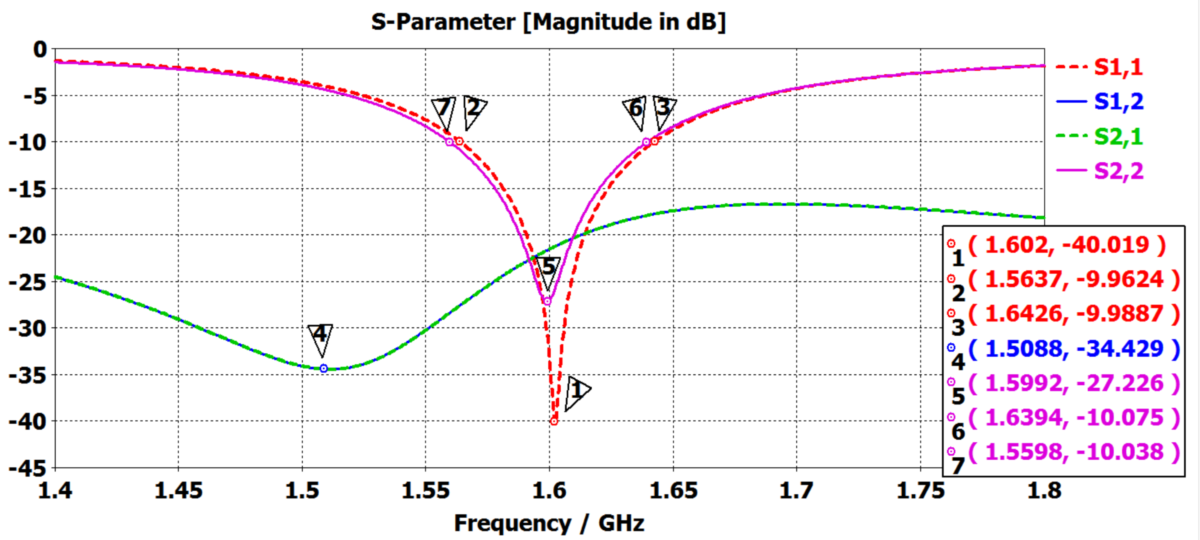

Figure 38: This is the final model with s-parameter plot, the port mode is TEM

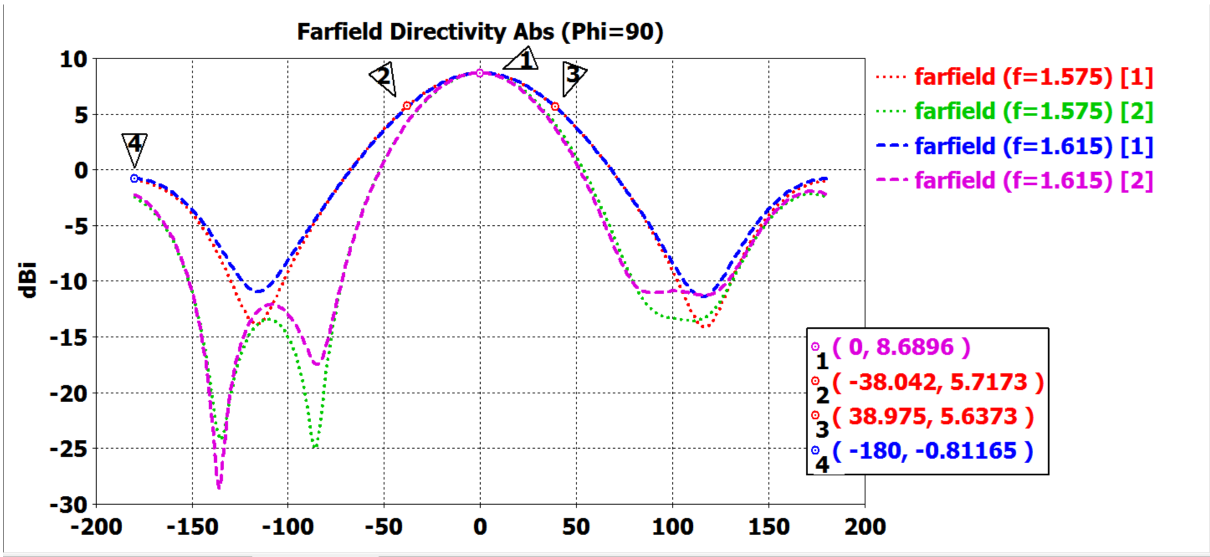

Figure 39: This is the final model with the directivity plotted for 1.575 GHz and 1.618 GHz for port 1 and 2

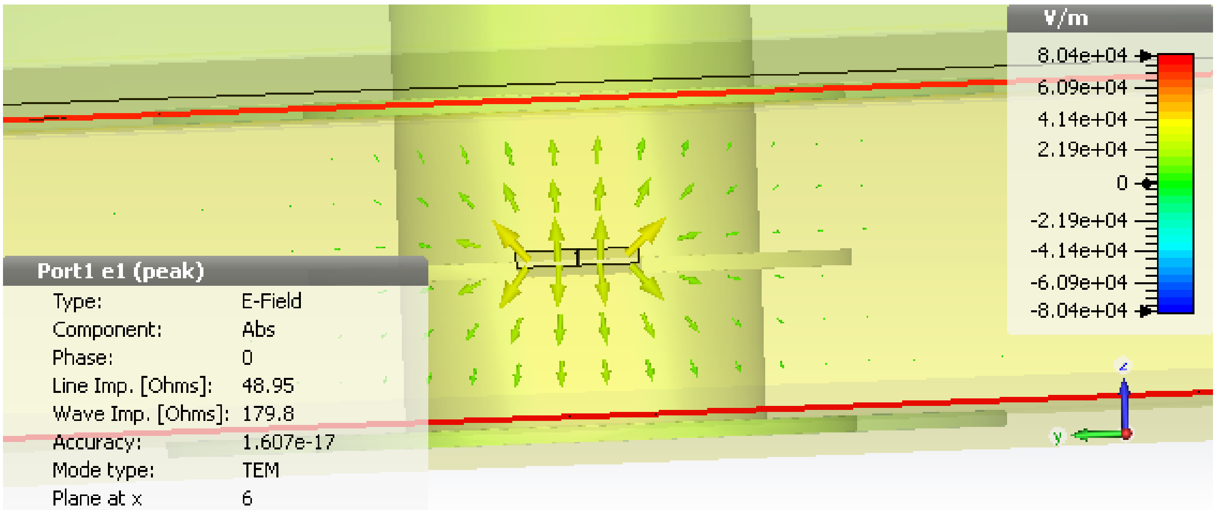

Figure 40: This is the final model with the e-field port plot for port 1

5.3.7 Polarization

As we want to have circular polarization we want to simulate this. To do this, four far field monitors where placed on both ports and on the GPS and the STX frequency in CST. After running the simulation in the frequency solver the results from the two ports for the far field monitors was combined so the amplitude was the same but one was 90 degrees phase shifted. After that plots where made of the axial ratio. Left hand polarization is when port 2 is phase shifted + 90 degrees and right hand polarization port

1 should be phase shifted +90 degrees. In Figure 41 it can be seen that the axial ratio is low for left hand polarization on both 1.575 and 1.618 GHz and that it is the same situation for right hand polarization in Figure 42. In the plots the 3 dB point have been marked.

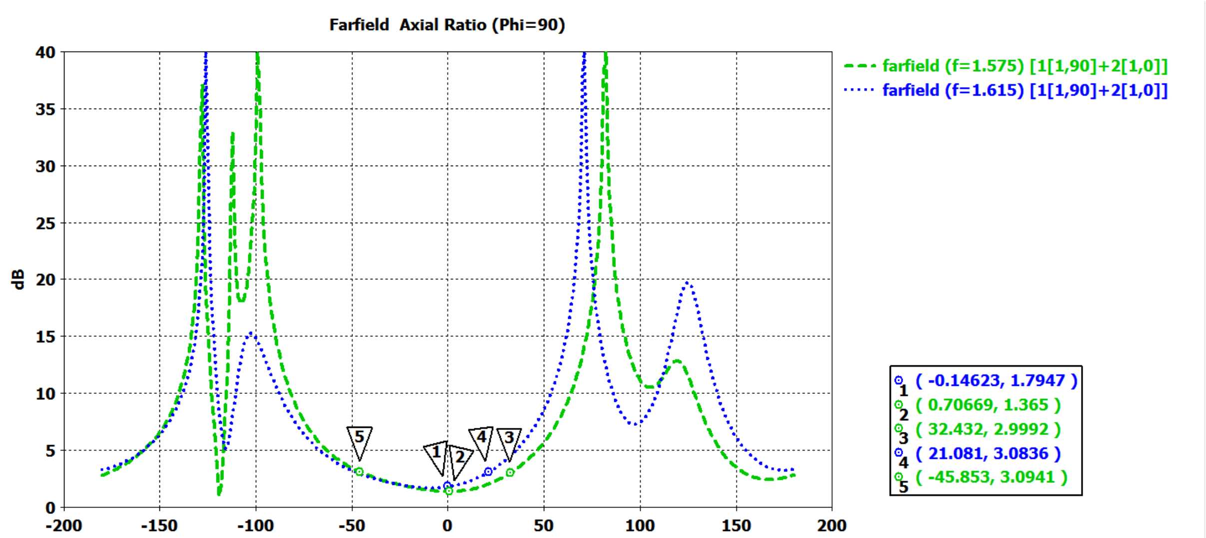

Figure 41: This is the final model where the axial ratio is plotted for left hand polarization.

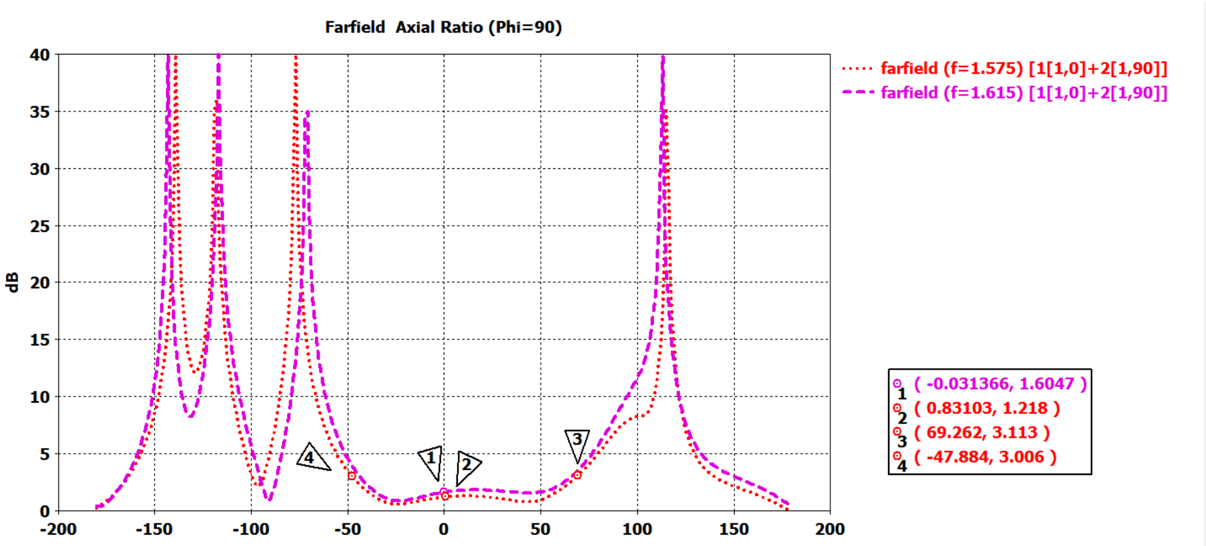

Figure 42: This is the final model where the axial ratio is plotted for right hand polarization.

After the sphere simulation axial ratio plots of the GPS was also made to compare between the no sphere case and the sphere case. In Figure 43 the axial ratio for right hand polarization is presented. The results for all the presented polarization simulations are summarized in Table 14

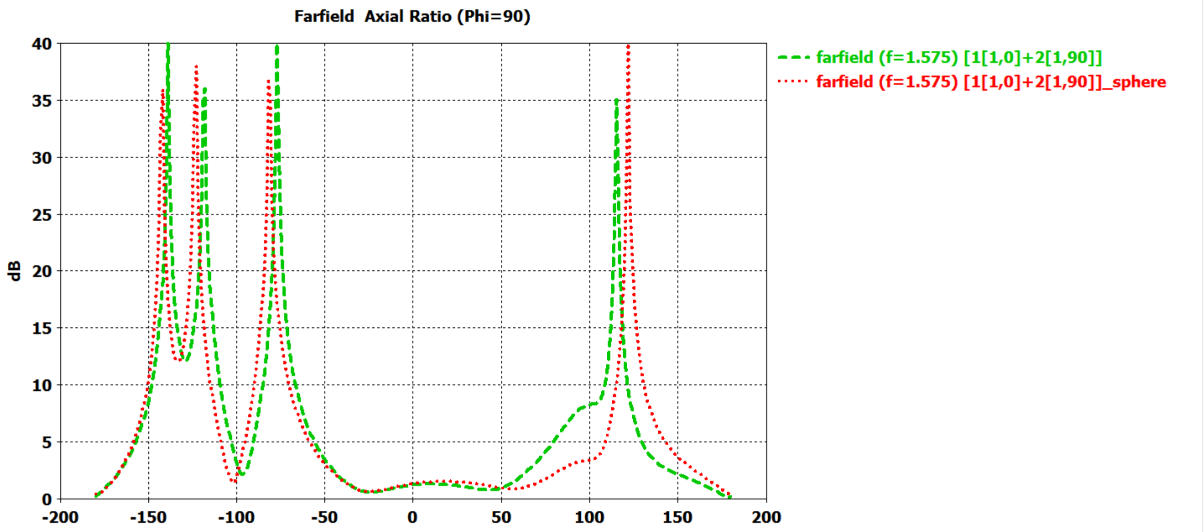

Figure 43: This is the final model where the axial ratio is plotted for right hand polarization. A comparison between with sphere and without is shown

	RHP	**LHP**
Axial ratio at Theta=0	1.2 dB at 1.575 GHz ,1.6 dB at 1.615 GHz	1.3 dB at 1.575 GHz ,1.8 dB at 1.615 GHz
Range of Theta where axial ratio$< 3dB$	115° at 1.575 GHz,115° at 1.615 GHz	75° at 1.575 GHz,65° at 1.615 GHz
Axial ratio at Theta=0 with sphere	135 ° at 1.575 GHz,	

Table 14: Results from simulation of the polarization

5.4 Hybrid and Antenna simulation

The hybrid and the antenna have been simulated before by them self but as they are going to be mounted together it is good to simulate them together. This was done by connecting them together in CST, in the schematic view, and then running the full model. The S-parameter of this simulation is shown in Figure 44. As previously explained in the hybrid chapter the S_{11} and S_{22} shows the coupling between the antenna elements and the S_{12} and S_{21} shows the reflection from the antenna.

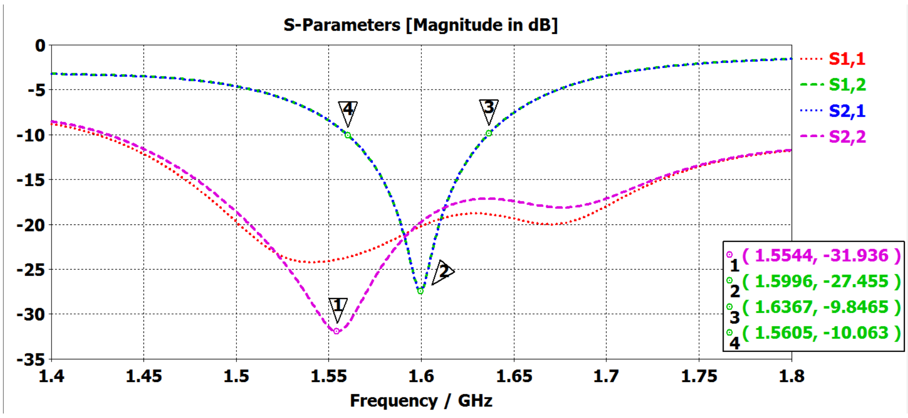

Figure 44: The S-parameters when the hybrid and antenna are connected together.

5.5 Comparing the results for the square patch antenna and the circular patch antenna.

From the simulations we got that the square patch should have width=length=82 mm and that the circular patch should have a radius=47 mm. If we use Pythagoras rule to calculate the distance between two horns of the square we get that this diagonal length is $82\sqrt{2}$ =116 mm. According to our requirements this is to big for MUSCAT's FFU, see requirements section. Furthermore, since the FFU has some disturbing objects the circular patch fits better into the FFU, as well as the distance from the patch to the end of the ground plane along the circumference is the same, which gives better radiation and impedance characteristics.

5.6 Building MUSCATs antenna

After simulating the antenna extensively in CST we built three prototypes. We ordered the patch, the PCB with the ground planes and the ROHACELL 31 substrate. The first prototype had wrong height of FR-4 patch, due to manufacturing error, where the height was 1.6 mm instead of 0.35 mm. Since we were in a hurry we decided to build the antenna anyway and measure the axial ratio. We cut three ROHACELL 31 substrates into circles, straightened a wire Anders found in the Hertz lab, stripped the wire and cut it into pieces for the feed. Then we punched holes into the ROHACELL substrate. Next we cleaned the PCB and the patch and soldered the wires to the PCB and to the patch. We also made fake cones and fake eye bolts cutting aluminum rods, we found in SPP, into right shape. Then we used a copper tape that has conducting glue on both sides and glued the fake eye bolts and cones to the PCB. Then we went to the lab and connected one port of the antenna to the network analyzer but left the other port open. The axial ratio was excellent for frequency of approximately 1.5 GHz but for 1.6 GHz the results where quite bad. We debugged the antenna, started with the hybrid coupler and found out that it works very well as can be seen from section 4.4. Then we thought about that the open port of the antenna should have been terminated with a 50 Ω. We were interested in seeing what effect the wrong patch height would have on the antenna so we simulated the antenna with this added height of FR-4 and we got the results in figure 45. Together with the open port this explains how we got so bad results for 1.6 GHz but good results for 1.5 GHz. Finally the manufacturer sent us the correct patch and we built two,

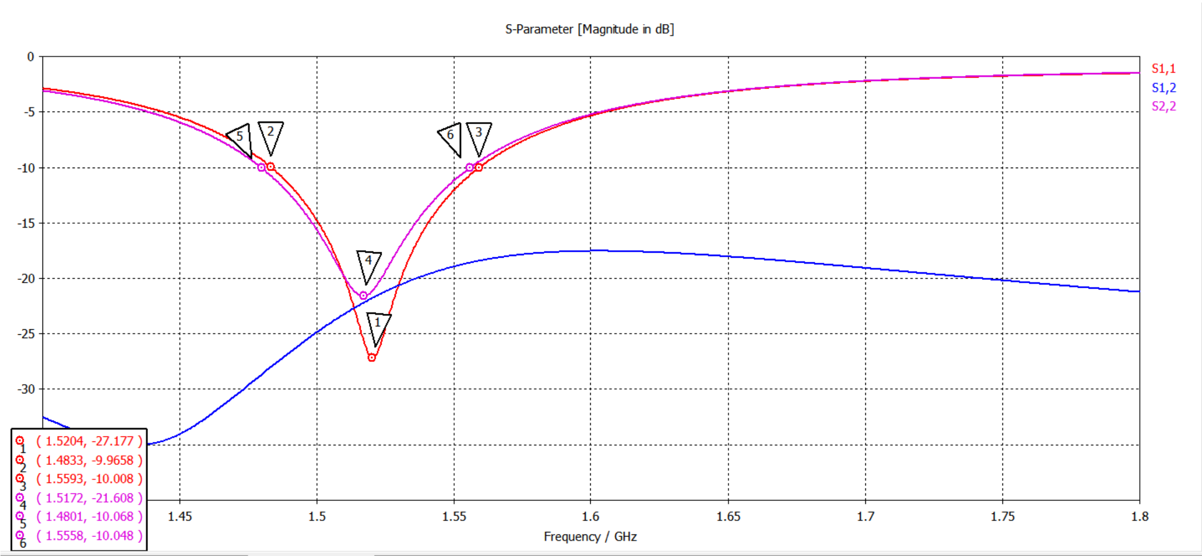

Figure 45: Simulation in CST with wrong patch height

antennas according to the simulations, with two different feed positions. One with 46.2 mm feed position and one with 47 mm feed position. They were built in a similar manner as the incorrect antenna but in this case the feeds were legs that were cut of a resistor component we found in the REXUS room. This we did because when we disassembled the incorrect antenna the feeds we had made from the wire were wrinkled. This was then tested in lab see section 6 and you can see a picture of the antenna in Figure 46. When the antenna had been tested extensively in the lab, substrate and patch was connected to the MUSCATs PCB in similar fashion as it had been built before. The antenna was tested in that system, see section 7.

6 Antenna testing in the lab

When the antenna with correct patch height had been assembled several measurements where made in the lab. These include S-parameter, axial ratio and radiation pattern measurements.

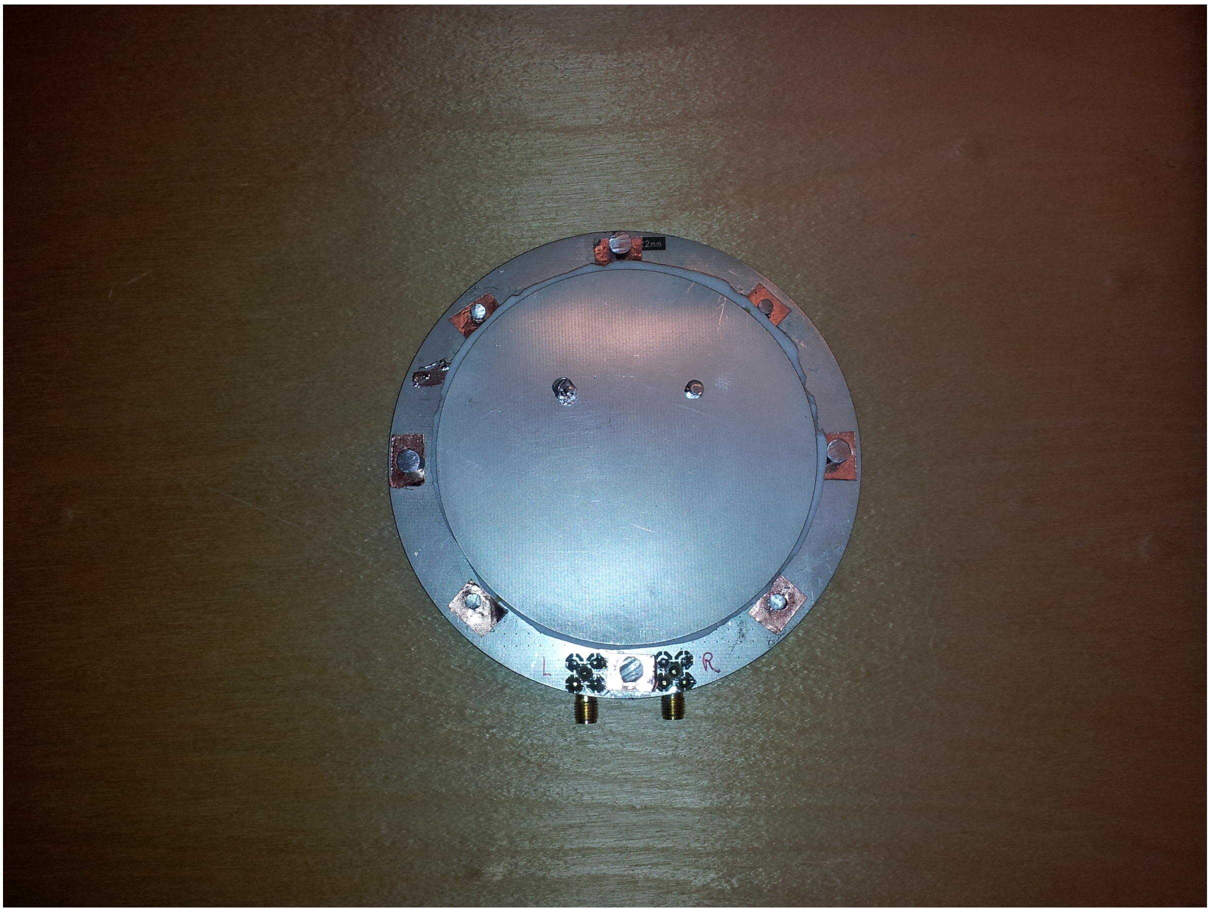

Figure 46: The built and tested antenna

6.1 S-parameter test

Testing both antenna and coupler as a single unit, we have two S-parameters of interest one is S_{11} for measuring the coupling between the two output ports of the antenna and the other is S_{21}, where we can see the reflections from the antenna. This was measured with the VNA by loading port 2 (port numbering can be seen from 9) with 50 Ω for S_{11} measurements. For the S_{21} measurements, both ports were connected. The measured S_{21} and S_{11} can be seen in 47 and 48.

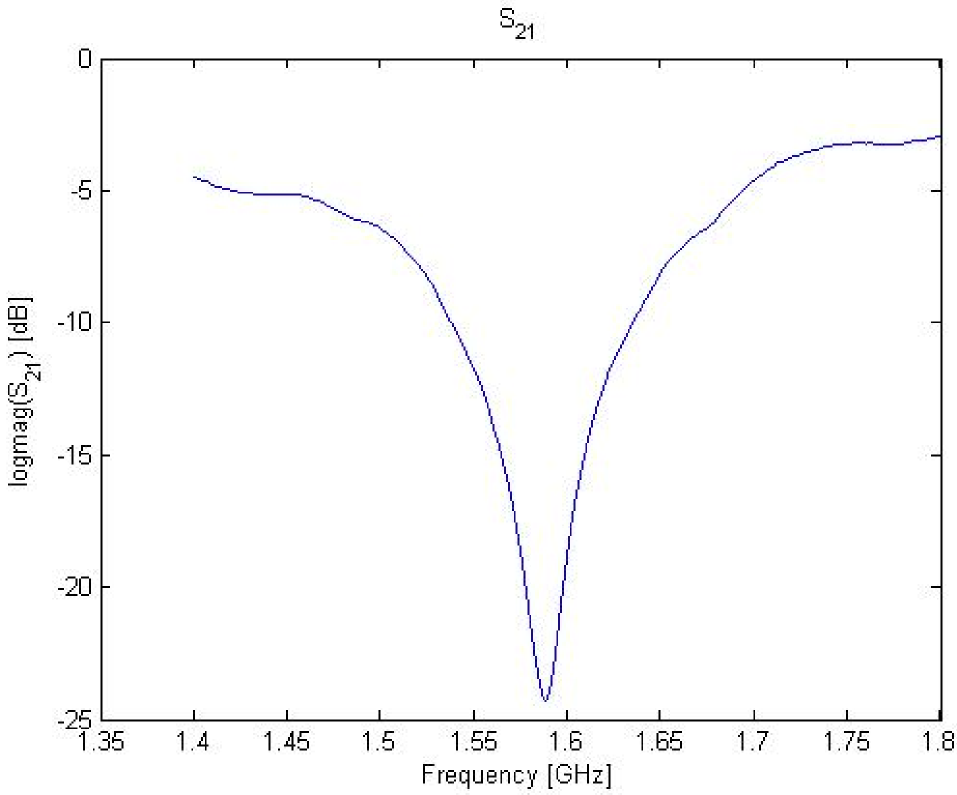

Figure 47: S_{21}

From the above figure, we see that the -10dB bandwidth of the antenna is around 100 MHz giving a fractional bandwidth of $100 \cdot 10^6 / 1.6 \cdot 10^9 = 6.3\%$, which is rather common for patches as they are quite narrow band, so this is expected. The frequency range well covers the upper and lower frequencies we wish to accommodate for.

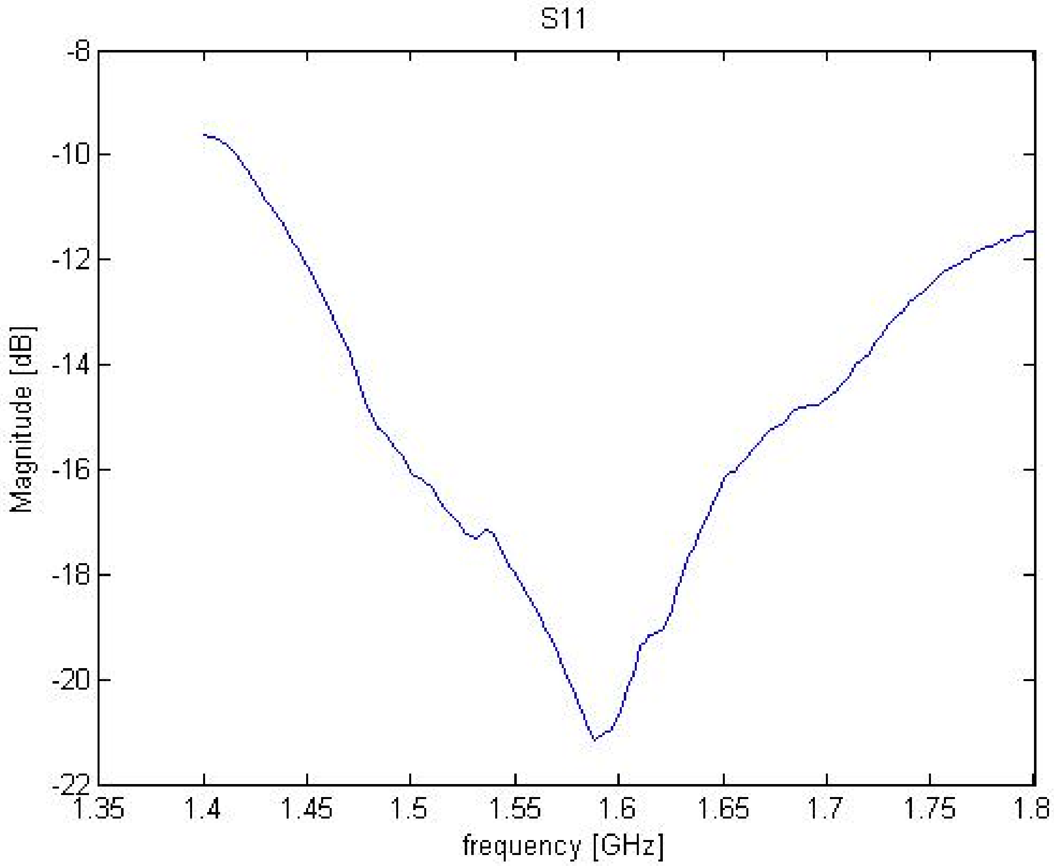

Figure 48: S_{11} with a 50 Ω load on port 2

As we can see, the coupling between the ports is very small over a wide range of frequencies around the resonance frequency which is good as the losses due to this will be small. Note that since the coupler and the antenna we tested are symmetrical, it is reciprocal to measure S_{22} and not necessary. S_{11} is enough. Similarly, the same applies for S_{12} and S_{21}.

6.2 Axial ratio test

An axial ratio test was also made. This is basically a measure of how circularly polarized the antenna is. The test involves one transmitting antenna which is linearly polarized and our antenna as the receiving one because our antenna is the unknown antenna. The patch antenna was rotated as shown in the figure 49, starting at a 90° angle to the right and turned 180° stepwise (2° steps) and the LHCP was measured. The patch receives several frequencies throughout the whole measurement and the signal is sampled for each step the patch is turned. The received power is plotted as a function of the rotation angle. If the patch is circularly polarized, the difference between the maximum and minimum received power should not exceed 3dB as mentioned earlier, else the difference between extrema will be greater. This measurement was also done exactly the same for the RHCP.

Which feed was chosen for which polarization is shown in figures 2 and 3. When one port was connected the other one was terminated with 50 Ω. The results can be seen in figures 50, 51,52 and 53. The rotation was done using the robot in the Tesla lab at KTH, Molly.

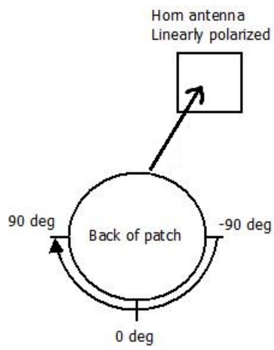

Figure 49: Patch antenna rotated 180° to the left

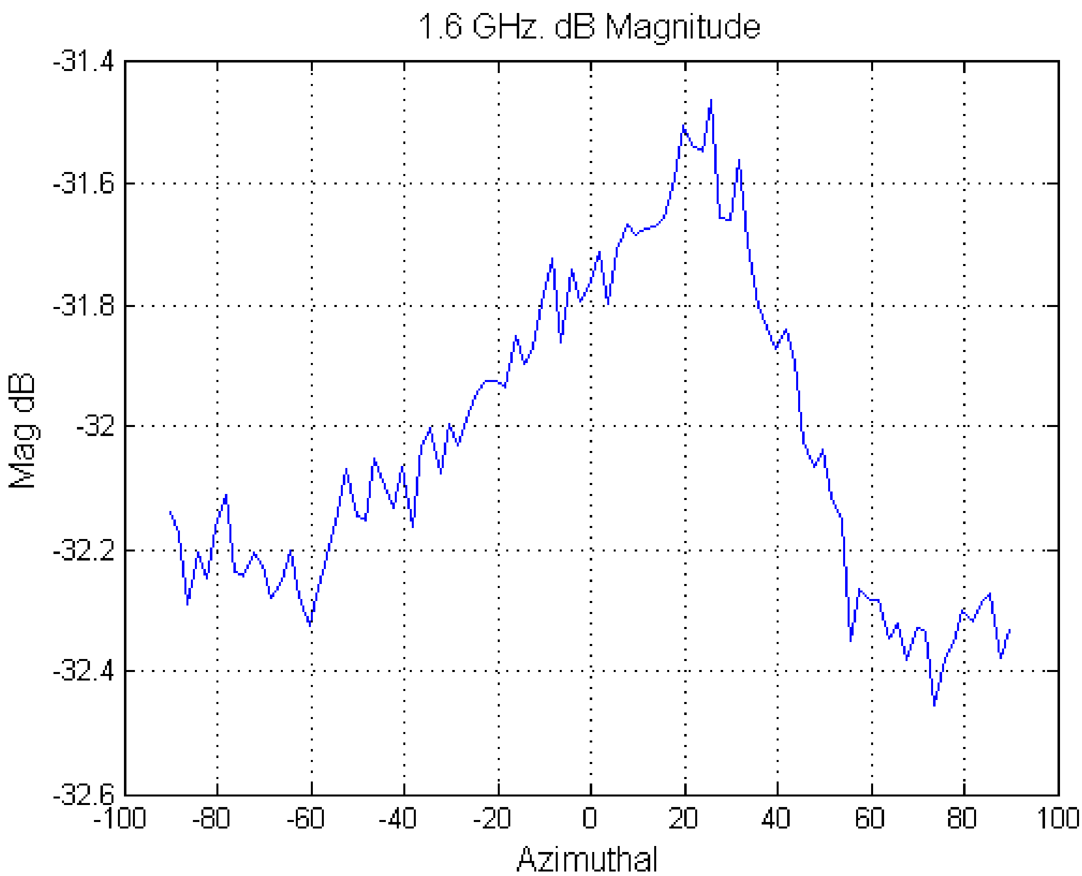

Figure 50: Received power as a function of rotation angle for the LHCP port

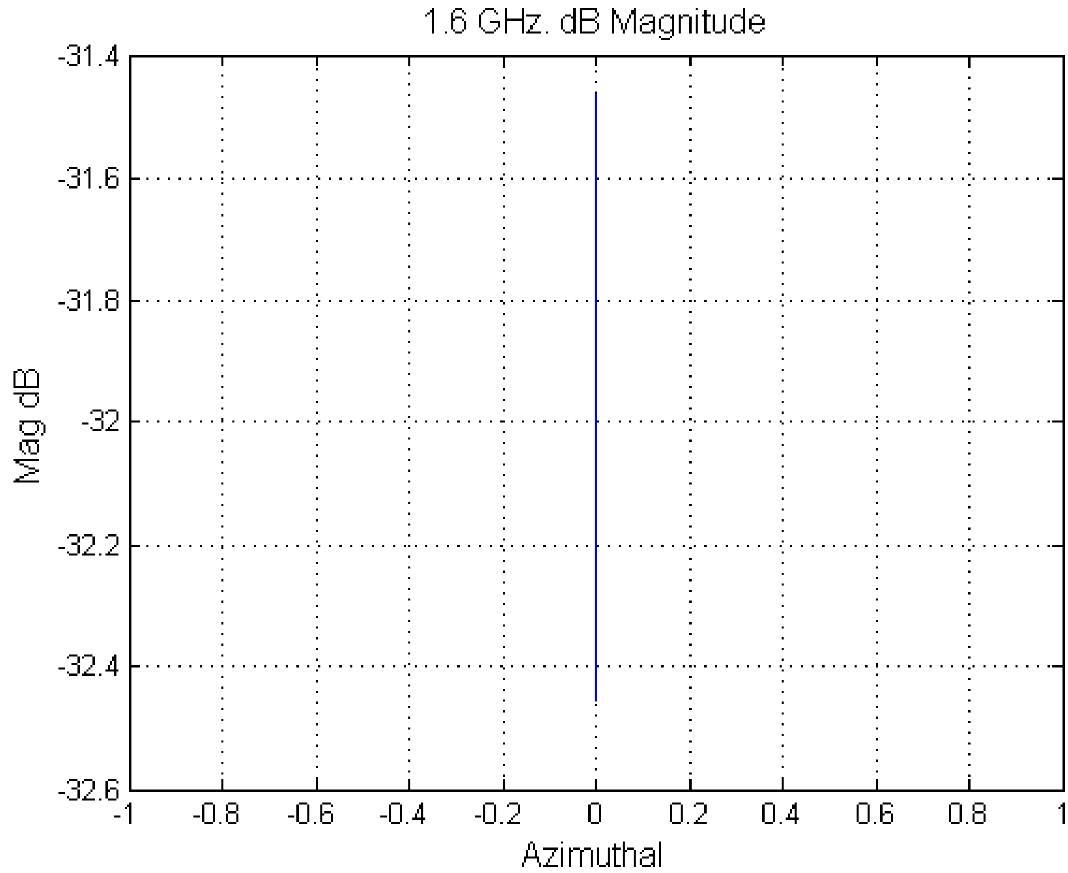

Figure 51: Showing the maximum and minimum of the above plot for LHCP

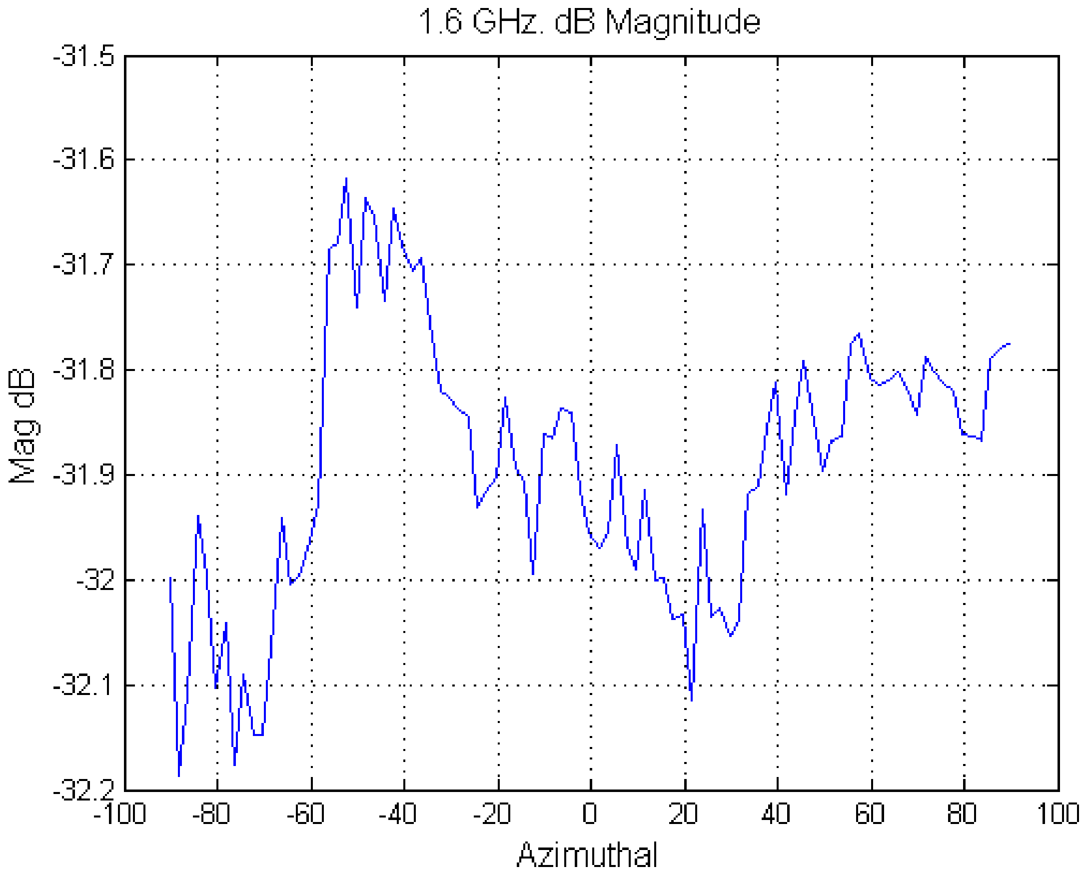

Figure 52: Received power as a function of rotation anglefor the RHCP port

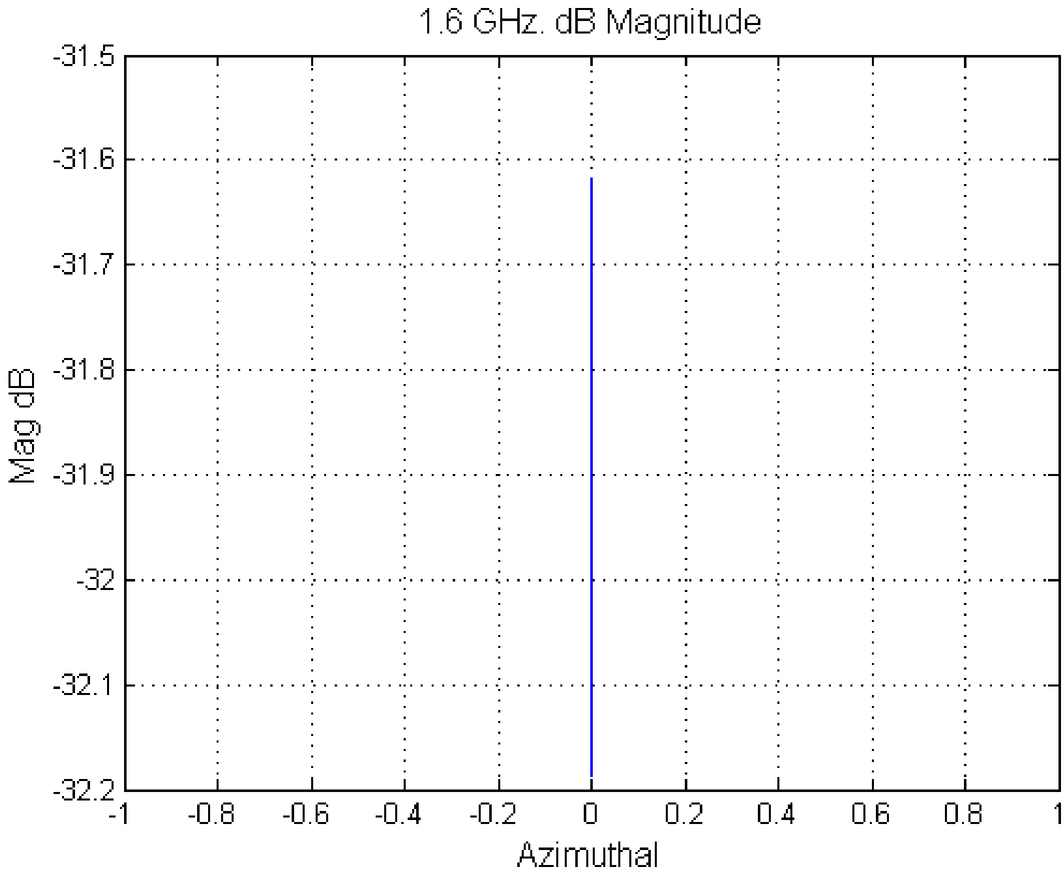

Figure 53: Showing the maximum and minimum of the above plot for RHCP

As we can see from the above, the axial ratio for RHCP is about 0.6 dB and for LHCP it is about 1dB which is remarkably good. The antenna is very circularly polarized.

6.3 Radiation pattern

A radiation pattern measurement was also made in the Tesla lab with Molly. It was made with the left port connected to the network analyzer and the other port terminated with 50 Ω see figure 55. The patch was mounted on Molly and turned as in figure 54 and also the patch antenna was the receiving antenna and the horn was the transmitting one on the measurement.

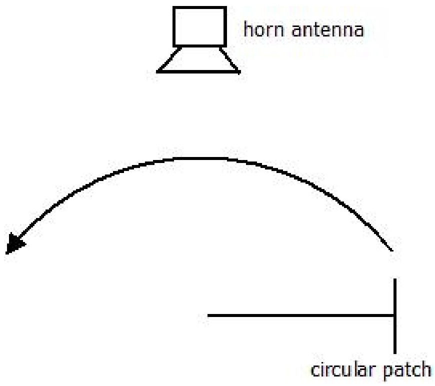

Figure 54: Rotation of patch antenna for radiation pattern measurement

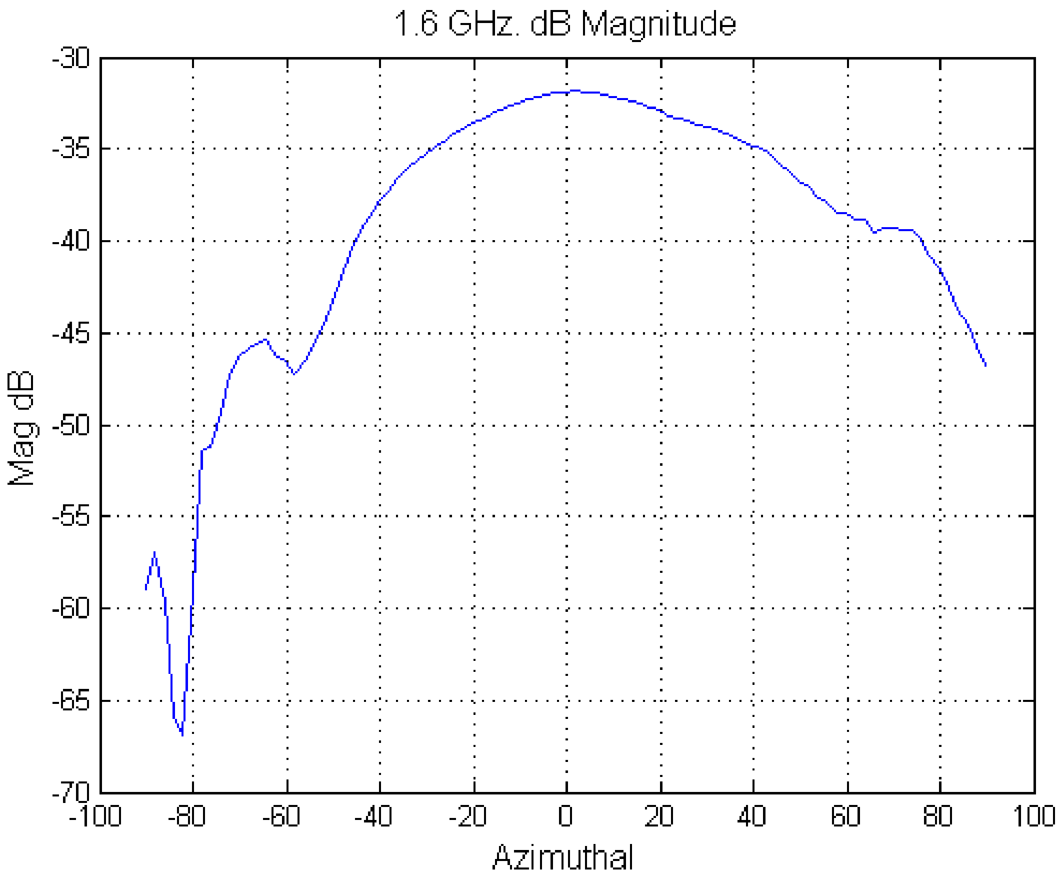

Figure 55: Power received by patch through port 1 transmitted from horn

We can see from this that the pattern is quite uniform over the whole room even though we had some disturbance on the left side in figure 55. The asymmetry may have to do with some object causing reflections.
The pattern however look promising, as it shows a wide HPBW around 60°, indicating a low directivity as desired.
More accurate results could have been obtained if we had used the semi echo free chamber

in the Hertz lab, but this was enough for our purpose. In the Tesla lab where the measurements were performed, there were conducting devices which were prone to cause reflections and give rise to imperfect measurements.

7 Integration

As has been said before the antennas are supposed to be inside MUSCATs FFU. This has been kept in mind during the full process of designing the antenna and the disturbing objects like eye-bolts and cones have been taken into account as well as the finite ground plane. The spherical cover has also been simulated to see how it affects the antenna. But the things left to simulate are all the connecting lines, this will be discussed in coming sections.

7.1 Strip lines and micro strip lines

In this sub-section we take into account how to feed the antenna and hybrid. The feeds for the antenna, as stated before, are two strip lines going to two pins which feed the patch antenna. As the hybrid is not the same size as the distance between the feeds the strip lines have to be turned somehow which of course can cause problems. The transmission lines were bent with a quite small angle without calculations or simulations and this solution has been proved to work. In Figure 56 it is shown how it was done in the test antenna, in the real system the PCB and that layer, layer two, is used for other things as well but the hybrid and feeds are encapsulated with vias between two ground layers.

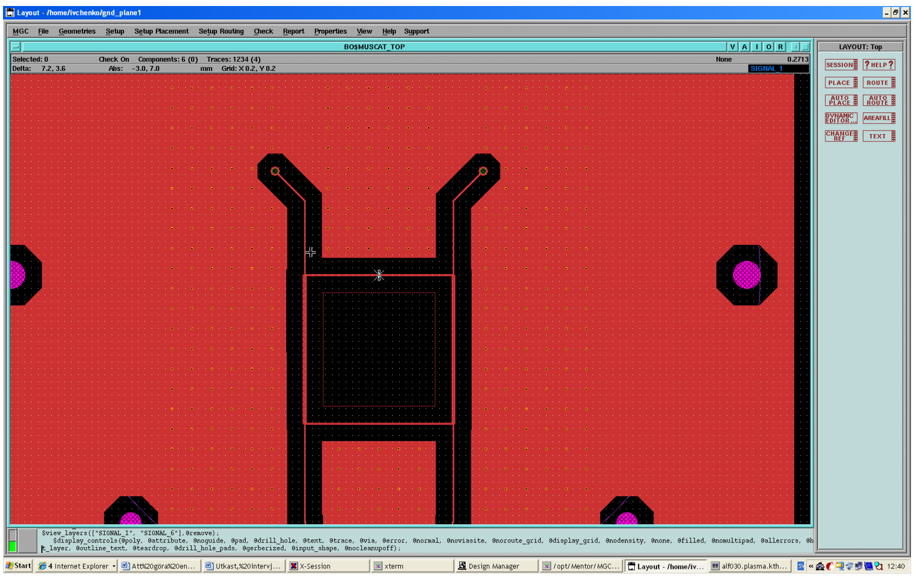

Figure 56: The hybrid and feeds for the antenna in the test antenna

In order to get 50 Ω the striplines have a thickness of 0.271 mm. The thickness of the micro stripline was also calculated. First it was calculated according to the following formulas found in [14]. First using formula 3.5.1.1 from [14] we can find w'

$$Z_0 = \frac{\eta_0}{2\sqrt{2}\pi\sqrt{\varepsilon_r + 1.0}} ln \left\{ 1 + \frac{4h}{w'} \left[\frac{14 + 8/\varepsilon_r}{11} \frac{4h}{w'} + \sqrt{\left(\frac{14 + 8/\varepsilon_r}{11}\right)^2 \left(\frac{4h}{w'}\right)^2 + \frac{1 + 1/\varepsilon_r}{2}\pi^2} \right] \right\}$$

where $\eta_0 = 120\pi$, $Z_0 = 50\Omega$, $\varepsilon_r = 4.4$, h=0.35, solving for w', gives w'=0.6681 mm. Then we use equation 3.5.1.5

$$w = w' - \Delta w'$$

and equation 3.5.1.4

$$\Delta w' = \frac{t}{\pi} \ln \left[\frac{4exp(1)}{\sqrt{(t/h)^2 + (\frac{1/\pi}{w/t+1.1})^2}} \right]$$

from [14]. From 3.5.1.4 we get $\Delta w' = 0.0521$ which gives the width of the micro strip to be

$$w = 0.616 \text{ mm}.$$

This we further confirmed using the macro impedance calculator in CST, see figure 57. We started with the calculated value but the final value we got was W=0.6226 mm.

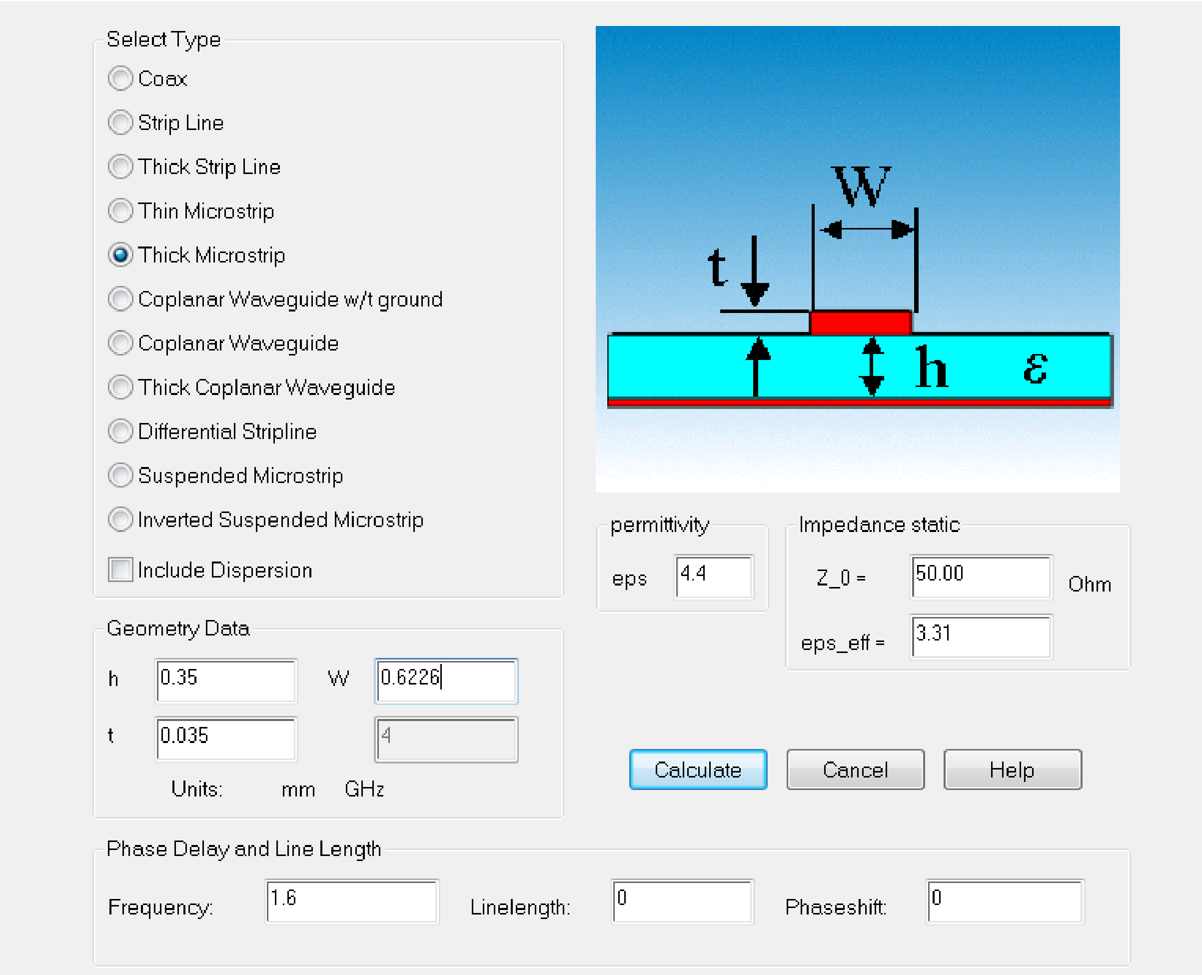

Figure 57: The impedance calculator from CST and calculated values of the thick microstrip

The micro strip line is on the bottom side of the card going to the STX, GPS-front end and commercial GPS. The simulation for transition from strip line to micro strip line can be found in the via model section.

The feed for the LHCP-input to the hybrid is taken directly to the STX modem but the feed for the RHCP-input is first routed to the GPS-front end. In the front end the signal is amplified from a amplifier with 19dB in Gain and with a noise lever of 0.8 dB[3], if there is a AC-capacitor which is not there which could increase the noise. After the amplification the signal goes out again and into a RF-switch which can be turned so the it goes into the GPS-front end again for raw data sampling or into the commercial GPS for getting a location fix. Unfortunately the maker of the layout for the PCB did not put in the correct width for the micro stripline coming out from the GPS-front end but it is working anyhow.

7.2 Via model

A crude model of the coaxial connection between the stripline (coupler) and the micro stripline (PCB with STX and GPS-front end) was made in CST. There are four layers of FR-4 between the stripline and the micro stripline and between these three conducting grounded layers. These layers are however not taken into account in the CST design as there will be very little coupling between them and the via. These are therefore replaced with FR-4 in the model so the entire substrate the conductors are embedded in is FR-4. A plane of PEC was however placed above the stripline for a more accurate result. Refined meshing was required as the stripline between the two conducting plates is a rather complex geometry.
The model can be viewed in figure 58. All boundaries are set to "open" except for underneath the thick ground plane on the bottom where the boundary condition is electric ground. The conducting PEC plate was not placed all the way out to the edge normal to the x-axis (coming through the left hand wall of the substrate in the figure) as it would be excited by the waveguide port on that edge for exciting the stripline. Note the thick micro stripline on the top and the end of the stripline coming out through the right hand wall of the substrate.

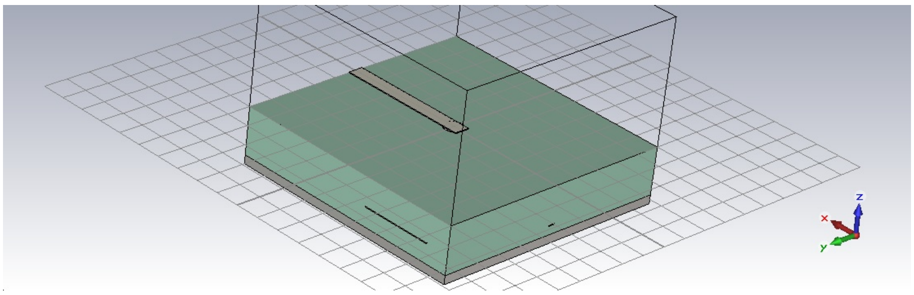

Figure 58: The via model from stripline to micro stripline

The reflections caused due to the via were estimated in CST and the S-parameter S_{11} can be viewed in figure 59.

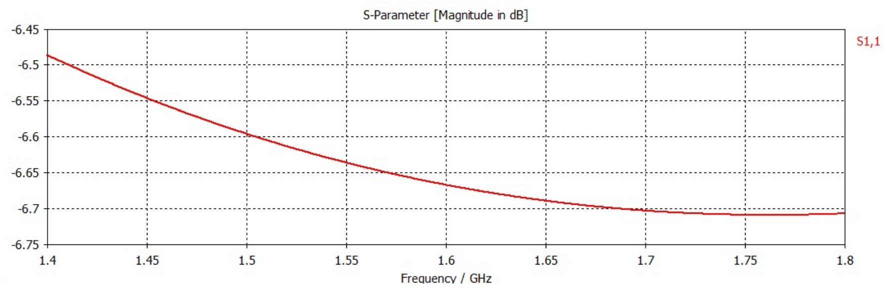

Figure 59: The via model from stripline to microstrip line

The reflections are not bad but they are not so good either. The via connection will cause reflections no doubt. The boundary conditions and the geometry could however be improved. For instance, a ground boundary condition should be placed on the PEC plate above the stripline. An attempt was made to make the two walls in contact with the ends of this plane (the walls normal to the y-axis) have the BC electric ground so that this plate would be grounded. This however caused errors in CST so the open sided option was chosen.

7.3 STX functionality

To verify the functionality with the full system for STX transmissions the STX was asked to send periodically by the FPGA. This has been performed both with clear sight to sky, inside a room, and sticking out through the window. All the tested locations have worked and we can see a lot of received messages on a Internet portal that displays the messages.

The STX functionality of our antenna has also been tested with another probe from last years REXUS program, RAIN [15], where the test antenna was connected to the RAIN probe with a 2 m coax cable. The probe was told to send periodically and the antenna was stuck out through the window. This also worked.

7.4 Commercial GPS

The commercial GPS worked the first time it was tested but soon problems started to appear. It turned out that a clock signal to the GPS-front end disturbed the commercial GPS. The antenna was proven to work well and now the system with the commercial GPS is working as well, as long as the clock is turned off.

The commercial GPS have also been tested with the RAIN system during the same conditions as for the STX tests for the RAIN system and been proved to work.

7.5 GPS front end

There have been more problems getting the GPS front end to work. The first problem was to get the software to work and there could also be problems with disturbances. The GPS front end worked once where we used a software GPS-receiver that could track satellites with good result. This GPS measurement was performed on Arboga airfield. The result is presented in Figure 60 where we can see that the software GPS-receiver tracks 10 satellite, which is really nice, along with having high CN_0 values, carrier to noise density. The carrier to noise density is defined as the carrier power divided with the noise power spectral density [16]. The position could also be derived from the data and is shown in Figure 61.

The GPS-front end has also been tested using the RAIN probe with our antenna showing good results.

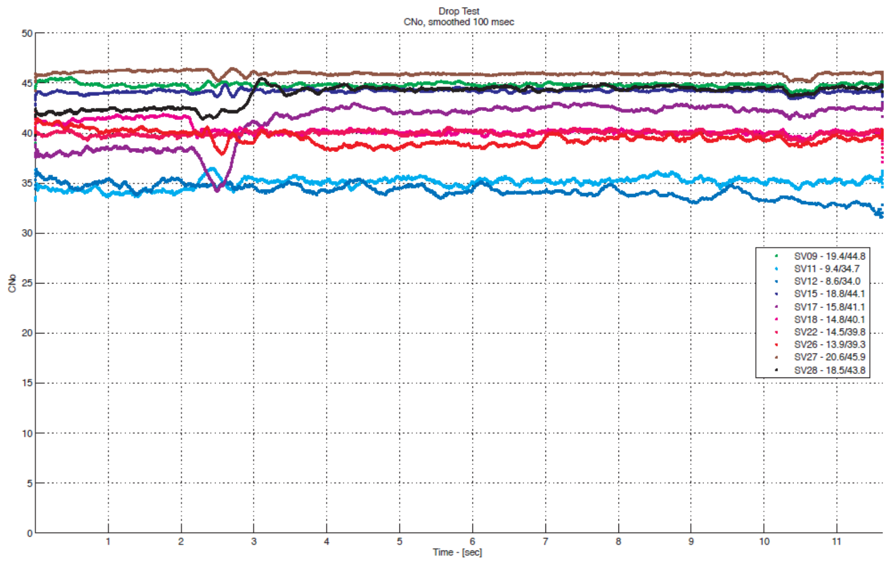

Figure 60: Tracking of GPS satellites using data from Arboga

7.6 Sphere

At Arboga airfield a drop test was conducted to test the FFU falling from a balloon. This was done to test it during "real" circumstances and the STX and commercial GPS was tested along with the system with a half sphere and parachute on. The results was that the STX could send out messages that was received by the Global Star satellites and the commercial GPS was able to get a position fix.

8 Discussion

8.1 Comparison between theoretical, simulation and measurement results

As stated in the the theoretical parts of the report, the formulas used are only approximations. It can be seen that some of the formulas are empirical which means that even if you have close to perfect conditions such as an infinite ground plane etc, the result will still not be 100 % correct. As we can see from the circular patch section, we get similar results from the simulation but still the center frequency is almost 30 MHz off. This is of course not all too bad but since our antenna is quite narrowband a difference of 30 MHz could move the curve so much that the antenna no longer fulfills our requirements. Then the question is what to trust the most, the theory or simulations. In this case we trust the simulations because even if some of the results presented were from runs without adaptive meshing turned on ther are no strange things happening in the simulation. We would thus say that the simulation is better than the empirical formula. Regarding the

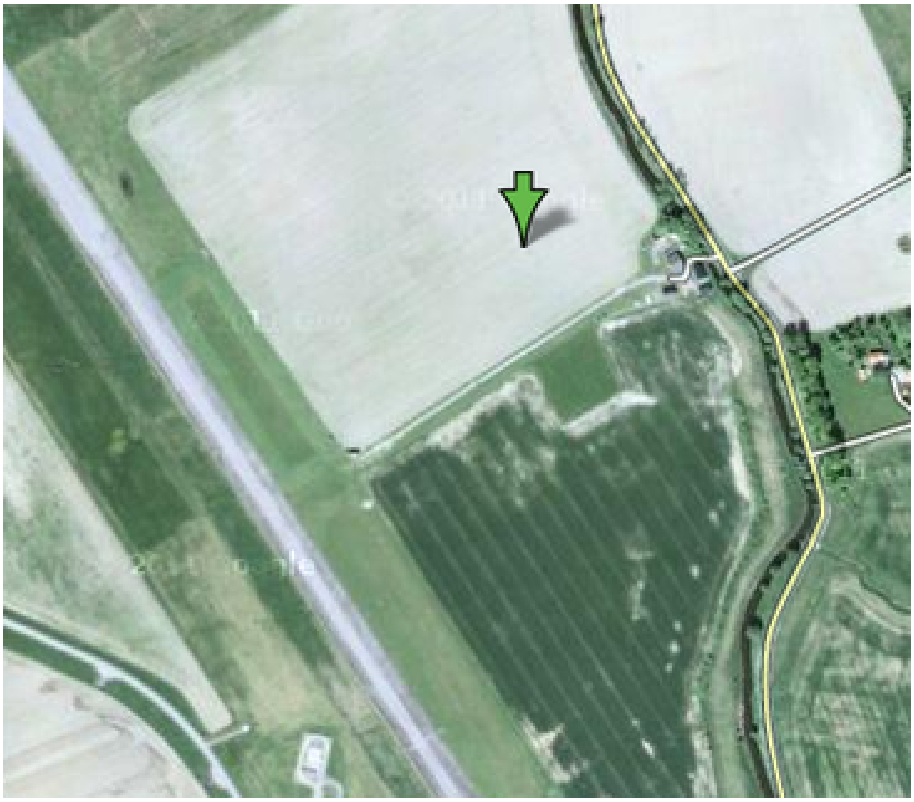

Figure 61: Position derived using data from Arboga

feed position calculated from theory we see quite a low return loss at the resonance which would indicate that the feed is not totally missplaced.

Regarding the measurement compared to the simulations with the complete model, we can see that the resonance is roughly at the predicted spot in the simulations. We also see that it is well matched and the radiation pattern is very similar from what we got from the simulation but it would be quite hard to get something with high directivity from a single patch antenna so it is not so impressive. The axial ratio measurement compares the maximum value with the value at 0 degrees on the simulation. We see that there is no big difference between the simulated and measured values.

8.2 Simulations of circular patch

The circular patch model in CST was the most complex model we did during the project. During the building of the model we ran into some problems. The first problem arose when implementing the stripline port and did not get the right port mode. What we did was to make the port wider so the right mode could be calculated in the port. Another small problem we found out during simulation is that if you create several objects of the same material which are connected there can still be some separation of the field between them even if there should not be. This phenomena could perhaps arise from how the different objects are treated numerically, perhaps a surface mesh is created on every single object. The solution was of course to add the objects together so CST treated them as one single object.

Another problem which was created when adding the stripline feed was that the initial mesh/viewable mesh looked really bad. As we have understood it the initial mesh is created and then during mesh refinement and so on the mesh cells "lock" onto the initial mesh, so if the initial mesh looks bad it will keep looking bad during mesh refinement. This can of course cause problems when a round feed looks more like a rectangle and to fix this local mesh requirement was set.

The last encountered problem was that the port mode changed to QTEM mode when the FR-4 material was specified as lossy. We do not know why as the material is the same all around the port the wave should not get different propagation speed as it is for QTEM mode. We did a small comparison between the cases and they where roughly the same, some of the differences could simply be explained by the losses in the FR-4.

Now when we do not find any more problems do we trust the simulation? Well we got TEM port mode which we would expect, the other results like S-parameters, directivity and axial ratio seem to be as expected as well. So before comparing with the measurements we have some faith in the model and when we compare with the test results we can see that it is probably alright.

How efficient is the model then? It takes up 160 000 mesh cells to get the frequency solver to be happy so it is quite big, but would it need to be as big? Probably not, for the first the change from PEC to copper on the ground plane and patch perhaps is a bit unnecessary but from the few tries we have done it does not seem to reduce the amount of mesh cells a lot. It could be because the things we changed had not high concentration of mesh cells, but probably it effects the speed of the calculation, depending on how the program is built. Having copper on the feed is perhaps a bit easier to defend but the question is if it really matters? One other thing that might have been over the top is adding the extremely small losses in the substrate, compared to the FR-4. Overall having a very small structure, the stripline feed, in a much bigger structure, the antenna, is something that made the automatic meshing become quite bad and then putting manual mesh refinements to fix that might generally have gone a bit to far.

8.3 STX frequency

We have had a small misunderstanding within the team what our center frequency is. This is because the STX can be set to send at 1618 MHz but if the settings are not changed it sends on 1615 MHz. It is not a big deal as the frequency is so close to each other but would have been better to be consistent through the whole report.

8.4 Comparison between requirements and the antenna

At the beginning of the report we set out a few requirements for our antenna. The fractional bandwidth defined as -10 dB in reflection coefficient was stated to be 3 %, the measured value for S_{11} shows a fractional bandwidth of 6 % which is quite good.

The polarization is also fulfilled of having both LHCP and RHCP. The axial ratio is good since it is less then 1 dB difference and therefor fulfills our requirement. Even if we think we have the data for the axial ratio versus frequency, we only plotted for one frequency due to time constraints but from the simulations we see that it should be fulfilled for both the GPS and STX.

The size constraints have of course been met along with creating a antenna with a quite broad main beam where the half power beam width is around 60 degrees. It also works well with a sphere, actually it seems like the GPS works better with the sphere on which is very good as it is the only thing which is used with the sphere on. The efficiency is also high at around 95 %.

9 Conclusion

This project resulted in an antenna which fulfills the requirements we prescribed before building it. The antenna not only agrees with the requirements, it performs better than is required in several ways. The frequency range it accommodates for is more than good enough for covering our required frequencies. This is thought to be due to the broad banded coupler and the low substrate permittivity of ROHACELL. Also, the polarization is more perfectly circular than expected, clearly deceding 3dB. An efficiency estimate was made only taking the patch into account, without coupler, coaxial connections and losses in transmission line etc. A high efficiency is mainly due to our near vacuum, non-lossy substrate.

Since we had not measured the radiation intensity in all directions and determined the maximal radiation intensity on the surface of a sphere surrounding the antenna, we could not obtain a measured directivity. We can however see that the simulated radiation patterns are close to the measured and hence, the directivity obtained in simulations is fairly accurate.

The characteristics of the final antenna can be viewed in table 15.

Axial ratio	1dB (LHCP), 0.6dB (RHCP)
Bandwidth	6.3 %
Efficiency	94%-97% (simulated)
Directivity	8.7dB (simulated)
Half power beamwidth	$\approx 70°$

Table 15: Example of table

Starting with requirements, we chose the design, made preliminary dimensions from theory, ran numerical simulations to verify and optimize results and finally built the antenna in reality. After running the tests, we see that the results were successful.

References

[1] L. Chen, "Dual frequency patch antenna design for global navigation satellite system," master thesis, The Russ College of Engineering and Technology of Ohio University, June 2007.

[2] Axonn, *Gen 2 Satellite Transmitter Product Data Sheet*, 1.4 ed., 2005.

[3] Maxim, *MAX2769 Universal GPS Receiver*, 2 ed., 2010. `http://www.maxim-ic.com/datasheet/index.mvp/id/5241` acessed 2012-05-17.

[4] USGlobalSat, *User guide ET-318*, 1.3.1 ed. `http://www.usglobalsat.com/store/download/52/et318_ug.pdf` accessed 2012-05-31.

[5] NavtechGPS, *GPS L1 Link Budget*. `http://www.navtechgps.com/pdf/GPS\%20L1\%20Link\%20Budget\%20EIRP.pdf` accessed 2012-05-17.

[6] C. Langton, *Link Buget*, 1998. `http://www.complextoreal.com/chapters/linkbud.pdf` accessed 2012-05-17.

[7] H. F. Pues and A. R. V. D. Capelle, "An impedance-matching technique for increasing the bandwidth of microstrip antennas," *IEEE transaction on antennas and propagation*, vol. 37, November 1989.

[8] D. Pozar and B. Kaufman, "Increasing the bandwidth of a microstrip antenna by proximity coupling," *Electronics letters*, vol. 23, April 1987.

[9] P. Hall, "Probe compensation in thick microstrip patches," *Electronics letters*, vol. 23, May 1987.

[10] Evonik Industries, *Product Information; ROHACELL HF*, 2011. `http://www.rohacell.com/sites/dc/Downloadcenter/Evonik/Product/ROHACELL/product-information/ROHACELL\%20HF\%20Product\%20Information.pdf` acessed 2012-05-31.

[11] C. A. Balanis, *Antenna Theory Analysis and Design*. John Wiley & Sons, 3 ed., 2005.

[12] "E-glass fiber, generic." Internet. From `www.Matweb.com` accesed: 2012-05-29.

[13] "Overview of materials for epoxy, high temperature." Internet. From `www.Matweb.com` accesed: 2012-05-24.

[14] B. C. Wadell, *Transmission line design handbook*. Artech House, Inc., 1991.

[15] REXUS/BEXUS Programme, *Student Experiment Documentation; RAIN*, v4.0 ed., 2012.

[16] "Gps carrier-to-noise density," tech. rep., Northwood Labs LLC, February 2003. `http://202.114.120.10/gnss/docs/AN101.pdf` accessed 2012-05-24.

A Adjusted model

Quite late the mechanical team wanted to add springs to the top side where the antenna sits to "shoot of" the top hemisphere during parachute deployment. The springs are ejected with the top hemisphere so they are only on for part of the mission. The springs are 2 mm high and have 1.5 mm in radius and are placed on two sides of two of the cones on a radius of 55 mm 5 mm from the cones. The cones was also found to be to high as the PCB thickness was not taken into account when putting them into the model. Last the umbilical was moved to its correct location.

Two more models where made one with hemisphere, Figure 62, and one without ,Figure 63. The results are shown below.

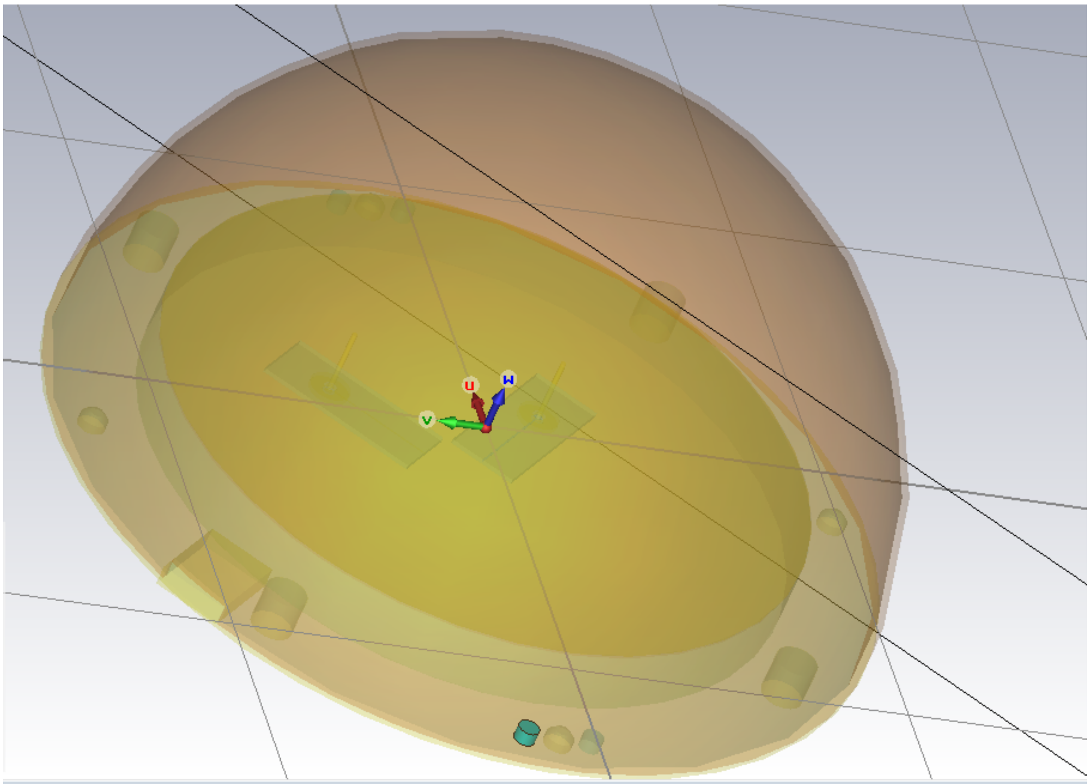

Figure 62: Sphere model geometry

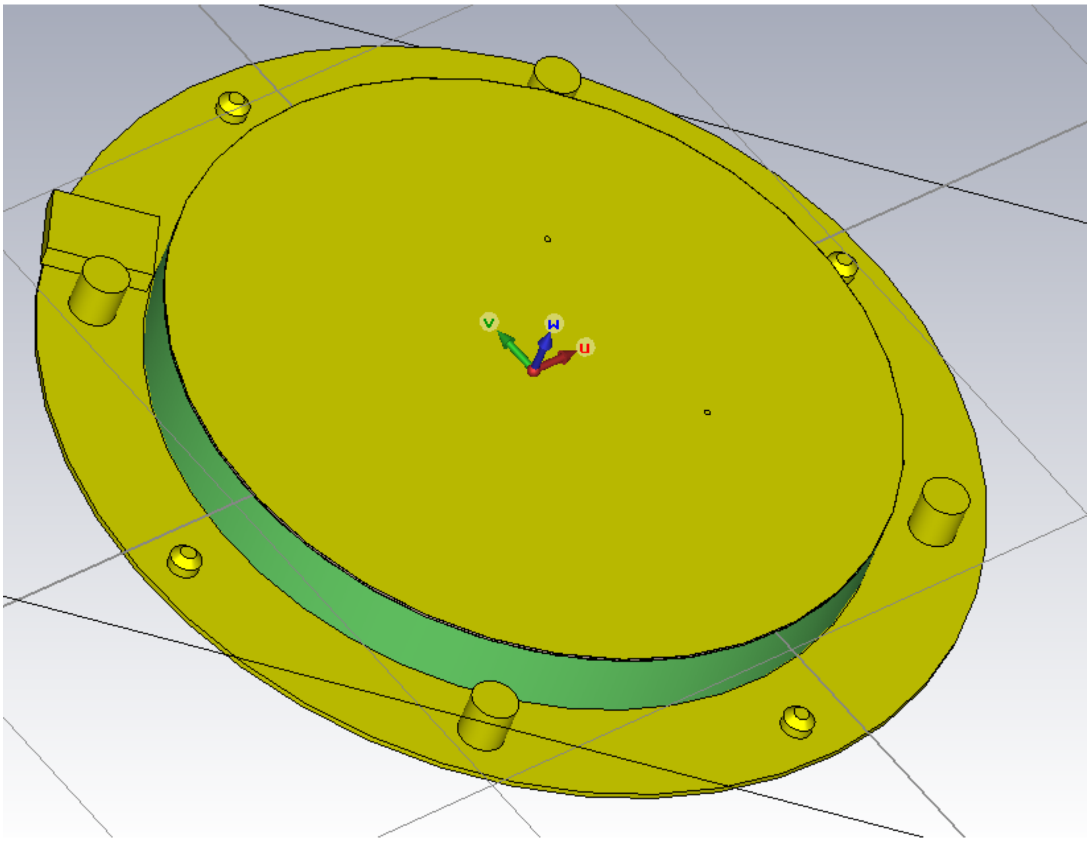

Figure 63: No Sphere model geometry

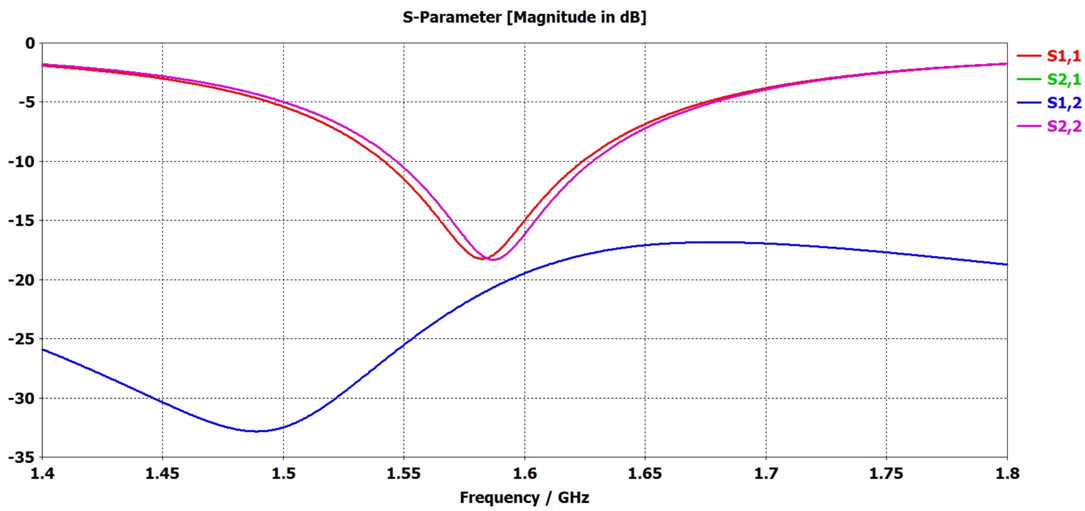

Figure 64: Sphere: S-parameters

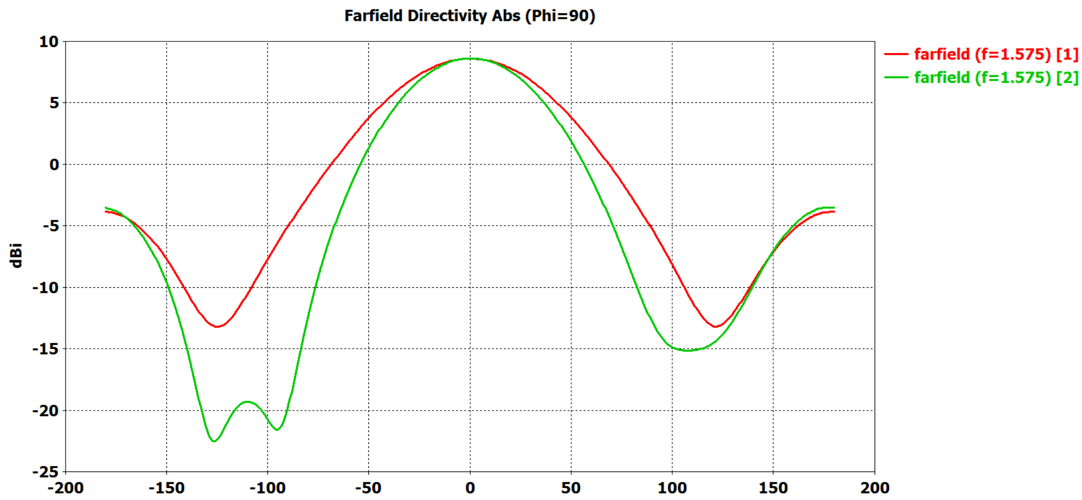

Figure 65: Sphere: Directivity

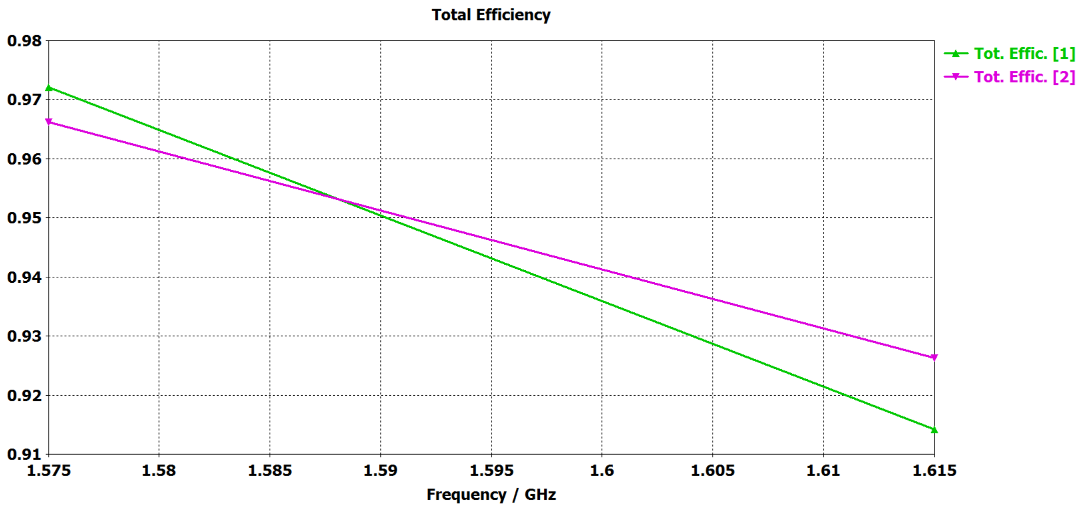

Figure 66: Sphere: Efficiency

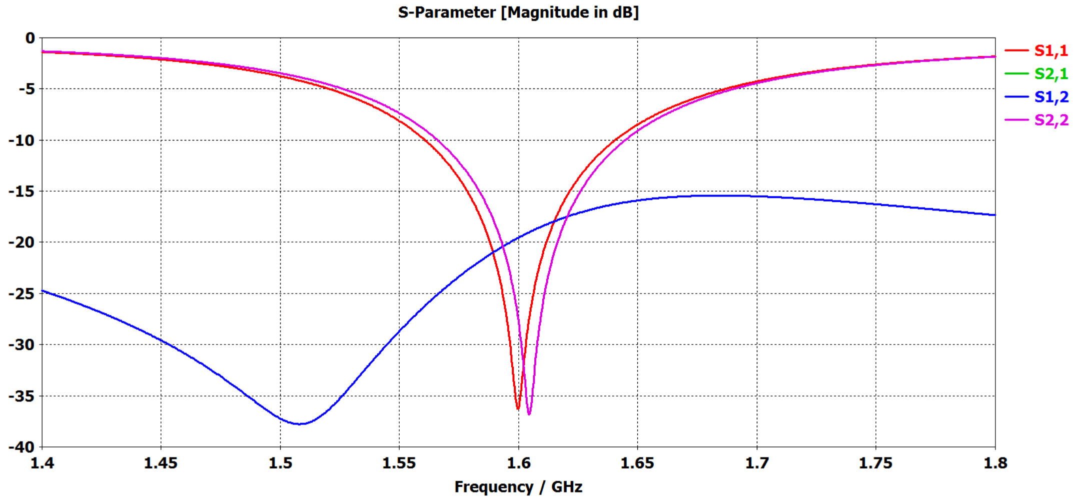

Figure 67: No Sphere: S-parameters

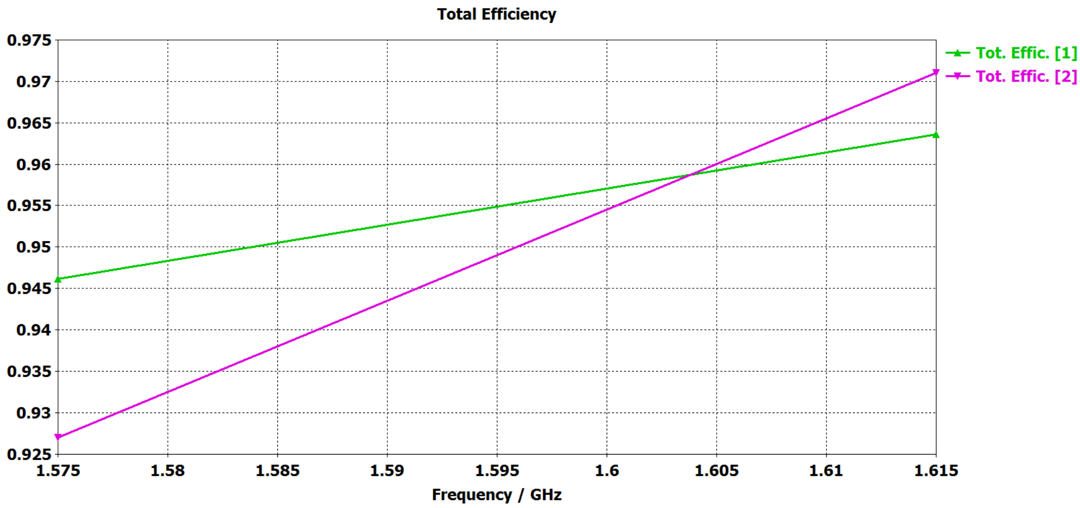

Figure 68: No Sphere: Efficiency

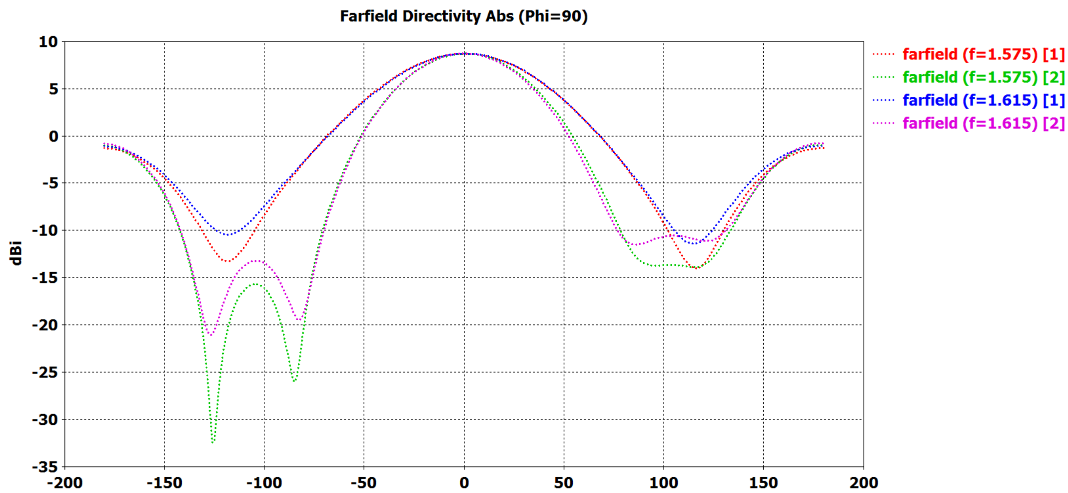

Figure 69: No Sphere: Directivity